The Dissertation Committee for Ying Lai Certifies that this is the approved version of the following dissertation

Laboratory Model Tests on Drag and Dynamically Embedded Plate Anchors in Layered Clay Profiles

Committee:

Robert B. Gilbert, Supervisor

Ellen M. Rathje

Charles P. Aubeny

Brady R. Cox

John L. Tassoulas

Laboratory Model Tests on Drag and Dynamically Embedded Plate Anchors in Layered Clay Profiles

by

Ying Lai

Dissertation

Presented to the Faculty of the Graduate School of

The University of Texas at Austin

in Partial Fulfillment

of the Requirements

for the Degree of

DOCTOR OF PHILOSOPHY

The University of Texas at Austin

August 2017

Dedication

To my parents,

Yuanming Lai and Man Hua

and my husband

Yubing Wang

and my son

Zezheng Wang

Acknowledgements

I would like to express my appreciation and gratitude to my supervisor, Dr. Robert B. Gilbert, for his encouragement and guidance. I appreciate the opportunity to work with him and being inspired from his knowledge and wisdom. I am grateful to Dr. Charles P. Aubeny for his guidance and help throughout this research. I would like to express my thanks to my committee members, Dr. Ellen M. Rathje, Dr. Brady R. Cox, and Dr. John L. Tassoulas for their valuable support and comments for my dissertation.

I would like to express my thanks to Dr. Paul M. Bommer for his help and support. I appreciate to being his teaching assistant and inspired by his enthusiasm about teaching.

I would also thank every faculty member in Geotechnical Division at The University of Texas at Austin, Drs. Cox, El Mohtar, Gilbert, Rathje, Stokoe, Zornberg, have been making the program excellence all over the world.

My life has been enriched by knowing amazing friends and fellow classmates in past six years. I would like to express my special thanks to Dr. Hande Gerkus, Dr. Asitha Senanayeke, Mr. Yunhan Huang, Mr. Jonas Bauer, Mr. Sebastian Farkas, Mr. Ian McMillan, and Mr. James Munson for being great colleagues. I would like to appreciate Dr. Hande Gerkus and Ms. Yanjun Chu for their friendship and support.

Last, I would like to express my heartful gratitude to my parents for encouraging me to pursue my Ph.D. I am grateful to my husband, Dr. Yubing Wang, for his support. I would also thank my son, Zezheng Wang, for the joy he brings to me.

Laboratory Model Tests on Drag and Dynamically Embedded Plate Anchors in Layered Clay Profiles

Ying Lai, Ph.D.

The University of Texas at Austin, 2017

Supervisor: Robert B. Gilbert

Layered soil profiles can complicate the ability to install a foundation and affect the performance of a foundation and therefore increase the cost of an offshore foundation. The goal of this research is to explore concepts to improve anchor performance in layered soil profiles of clay by further understanding (1) the drag trajectory and capacity for a drag embedded plate anchor in layered soil profiles; (2) the drag trajectory and capacity of tandem drag embedded plate anchor systems; and (3) the free-fall penetration trajectory and resistance of a dynamically embedded plate anchor in layered soil profiles. The methodology is to perform drag embedment and free-fall penetration tests with model anchors in a variety of test beds containing marine clays with different profiles of undrained shear strength versus depth.

For a drag embedment anchor, model tests with a single anchor in different sizes show that the ratio of normal to tangential displacement is affected by model scale, with smaller ratios applying to larger anchors. By appropriately adjusting this factor in a prediction model, the model is able to represent well the model test results and can be used rationally to predict behavior for a field-scale anchor. The drag embedment tests and analytical results in layered soil profile show that anchor can penetrate into stiff layer with shear strength 1.5 times higher than the surrounding soil and cannot penetrate into stiff layer with shear strength 5 times higher than the surrounding soil. In

the layered soil profile with stiff layer of shear strength 2 to 4 times higher than the surrounding soil, the anchor may be able to penetrate the stiff layer if the pitch of the fluke as it approaches the layer is at about 30°.

For a tandem system with two drag embedded anchors, the capacity of the system can be more than twice the capacity of a single anchor provided that the spacing between two anchors is at least two fluke lengths. The second anchor in the tandem system can penetrate deeper than a single anchor and the front anchor.

For a dynamically embedded plate anchor, the strain rate effect from undrained shearing is higher than that from bearing as measured from pure normal and pure in-plane shearing tests. A calibrated predication model accounting for the strain-rate effects strain rate parameters produces results similar to the model test results, generally matching or slightly under-predicting the actual penetration in non-layered and layered soil profiles. A dynamically embedded plate anchor can penetrate through stiff layers that would cause difficulty for a conventional drag embedded anchor.

Table of Contents

Lists of Tables

Lists of Figures

Chapter 1. Introduction

1.1 Introduction and Motivation

The cost of the foundation can be a significant percentage of the total cost for an offshore structure producing energy (e.g., Musial and Butterfield, 2006). Furthermore, layered soil profiles (e.g., layers of sand in clay or layers of stiff clay in soft clay) are common due to the glacial and sedimentation and can significantly increase the cost of an offshore foundation. Layers complicate the ability to install a foundation (e.g., inability to drive a pile through a dense sand) and can also detrimentally affect the performance of a foundation (e.g., loss of suction due to drainage around a suction caisson).

Plate anchors provide an economical solution for offshore foundations because they are very efficient as measured by the holding capacity achieved relative to the weight of the foundation. Plate anchors include drag embedment anchors (Figure 1.1), vertically loaded anchors (Figure 1.2), suction embedded plate anchor (Figure 1.3), dynamically embedded plate anchor (Figure 1.4) and a new concept currently under development, the Flying Wing Anchor® (Figure 1.5). The drag embedment anchor evolves from conventional ship anchors, and has a fixed fluke-shank angle between 30° to 50°. Vertical loaded anchors (VLAs) are based on the traditional drag embedment anchor with a fixed fluke-shank angle. VLAs has a thinner shank or a bridle, and can dive deeper than the traditional drag embedment anchor with 7 – 10 fluke lengths (Randolph and Gourvenec, 2011). SEPLA and DEPLA were developed to combine the benefits of high efficiency of plate anchor and certainty of suction caisson or torpedo pile, therefore anchors can start dive deeper because of a provided deeper initial embedment depth by suction or torpedo. The Flying Wing Anchor® is designed to installed by gravity and the capacity can be maximized with fluke nearly

perpendicular to the shank, which overcomes the problem of loss embedment for SEPLA and DEPLA. These types of anchors may provide an effective solution for layered soils. For example, two drag embedment anchors can be attached in tandem to provide greater holding capacity with less penetration (Figure 1.6). Also, the Flying Wing Anchor® may be able to penetrate into and through stronger layers during free-fall installation.

Existing research on the performance of plate anchors in layered soil profiles is limited. Baglioni et al. (1982) studied the stability of jack-up rig foundation in the soil profile with a relatively thin layer of sand underlain by a weak clay layer. Centrifuge modelling of spudcan foundations (Hossain and Randolph, 2011) was performed in the multi-layered soils with interbedded stronger layers. House (1998) applied a limit equilibrium solution of static anchor capacity to estimate the capacity of drag embedment anchors in stratified soil. However, a plate anchor installed by drag or by free-fall penetration in layered soil profiles has not been studied.

The motivation of this research is to investigate the performance of the plate anchors installed by drag or by free-fall penetration in layered soil profiles.

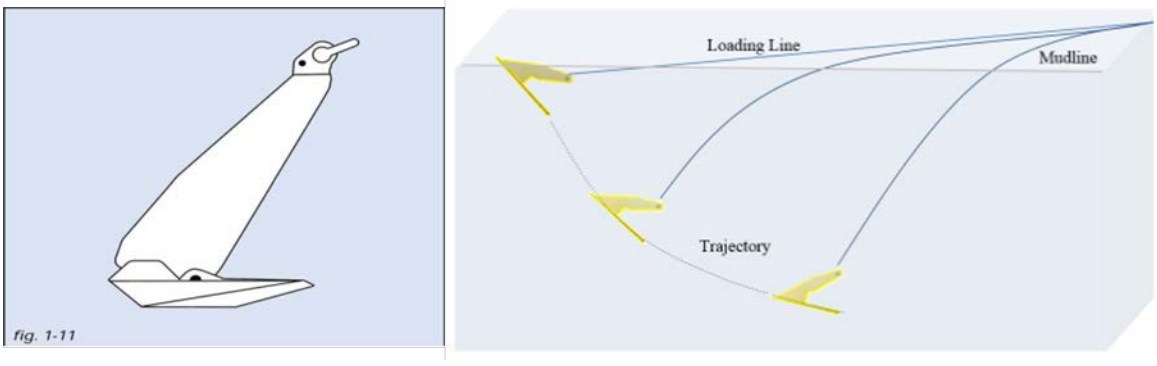

Figure 1.1. Example of Drag Embedment Anchor (Vryhof, Vryhof Anchors, Krimpen ad Yssel, 1999) and Trajectory (Gerkus, 2016)

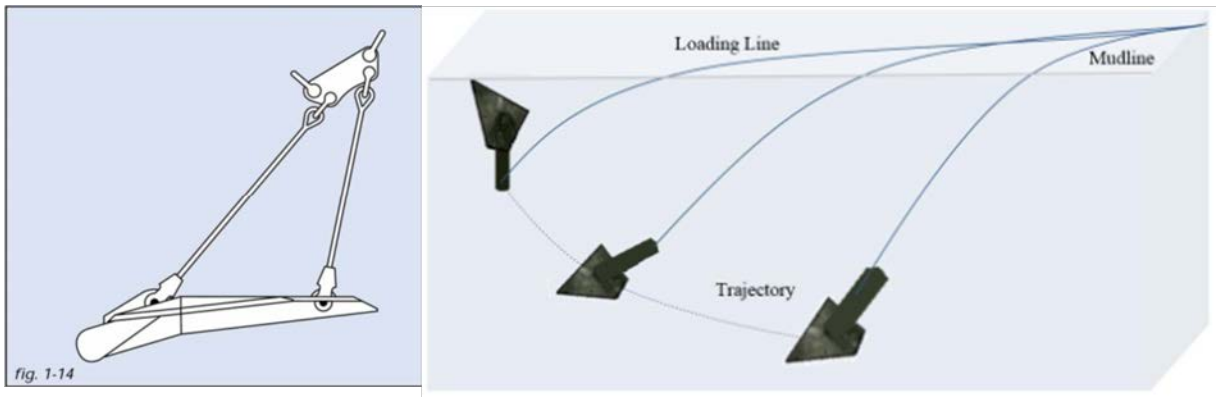

Figure 1.2. Example of Drag-in Plate Anchor – Stevmanta Vertical Loaded Anchor (Vryhof, Vryhof Anchors, Krimpen ad Yssel, 1999) and Trajectory (Gerkus, 2016)

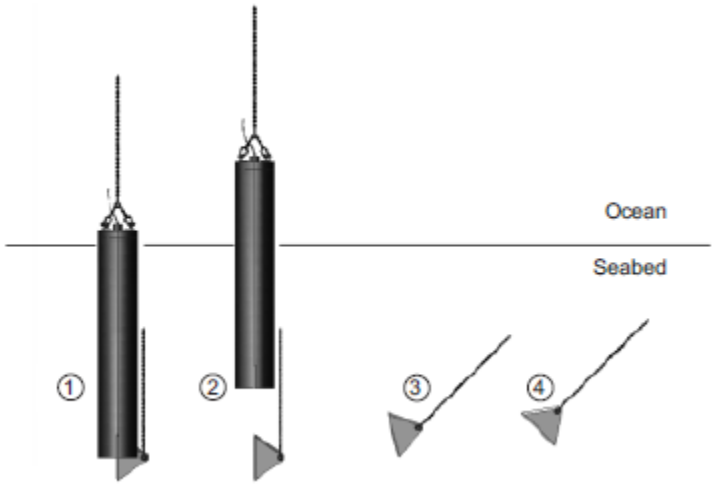

Figure 1.3. Example of Suction Embedded Plate Anchor (Gaudin et al., 2006)

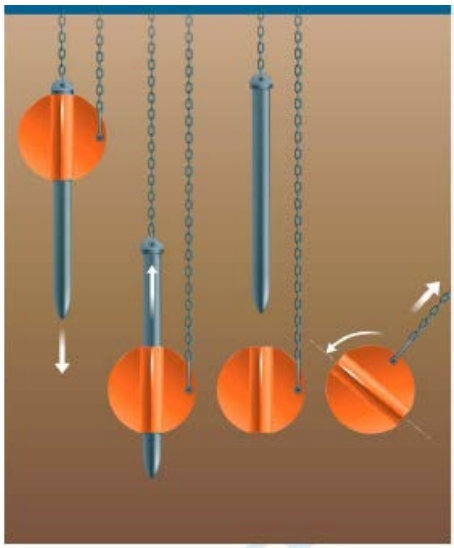

Figure 1.4. Example of Dynamically Embedded Plate Anchor (Blake et al., 2015)

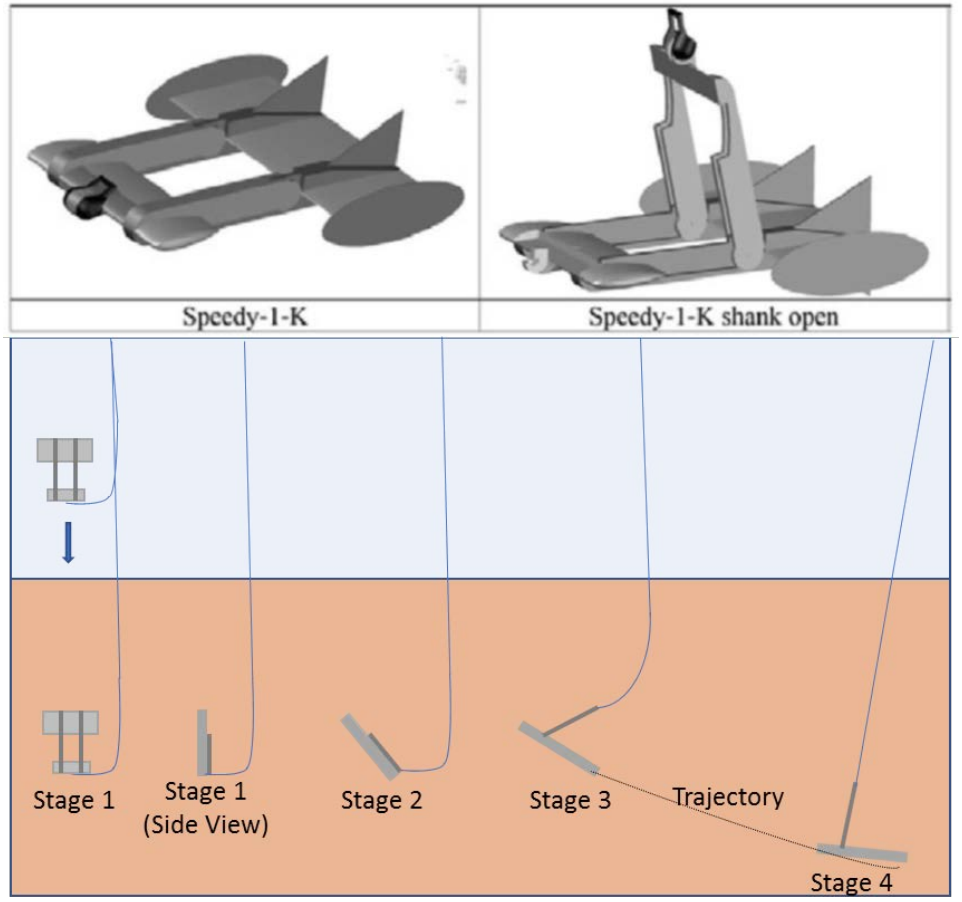

Figure 1.5 Speedy Flying Wing Anchor® Configurations (Gilbert et al., 2015) and Trajectory

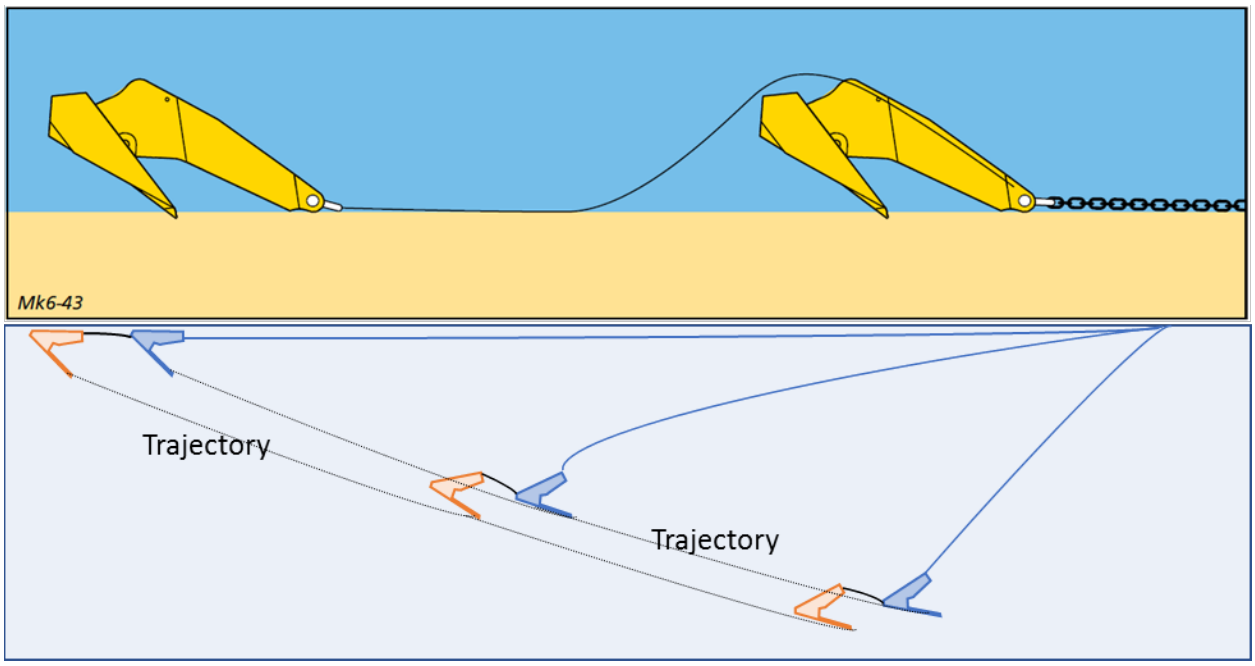

Figure 1.6. Example of Tandem Anchor (Vryhof, 2015) and Trajectory

1.2 Research Objectives

The objectives of this research are:

1. To further understanding of the drag trajectory and capacity for a plate anchor in layered soil profiles.
2. To further understanding of the drag trajectory and capacity of tandem anchor systems.
3. To further understanding of the free-fall penetration trajectory and resistance of a plate anchor in layered soil profiles.
4. To develop and explore concepts to improve anchor performance in layered soil profiles.

1.3 Methodology

The objectives will be achieved through the following tasks:

1. Perform pure loading tests in clay to measure the non-dimensional yield capacity factor, pure normal loading capacity factor, pure in-plane shearing capacity factory and pure rotational in pitch capacity factor for drag embedment anchor with scale of 1:30.
2. In the constructed layered soil profiles with remolded or consolidated Gulf of Mexico clay, conduct drag embedment tests to investigate anchor trajectory, the line load at the mudline and pitch angle. Experimentally perform sensitivity analyses on how the behavior of drag anchor affected by the shear strength, thickness and depth of stiff layer in the constructing layered soil profiles. The load cell can measure the line load at the mudline. The magnetometer with a sensor attached on the anchor can track anchor location (x,y,z) and orientation (yaw, pitch, roll).
3. Conduct drag embedment tests with tandem system anchor in a normally consolidated soil profile. Tandem system anchors with different test configurations are studied by varying tailing line thickness, spacing between two anchors, and attachment point of the second anchor.
4. Perform T-bar tests and pure loading tests of a circular plate with a diameter of 4 inch, and a thickness of 0.1 inch at different loading rate to establish the dependence of undrained shear strength on applied rate of strain.
5. Conduct free-fall penetration tests with Flying Wing Anchor® in different shear strength profiles constructed in the Gulf of Mexico clay, including normally consolidated, over consolidated and layered shear strength profile. Investigate impact velocity and drop height of anchors with different ratios of weight to surface area.

6. Compare and analyze the plasticity-based limit prediction model and experimental results. Extrapolate the experimental results to estimate the behavior of a prototype anchor in the field.

1.4 Structure of the Dissertation

- Chapter 1: A description of the introduction, motivation, and methodology in this dissertation
- Chapter 2: A summary of literature review on offshore structure, mooring system, offshore anchors, and design methods.
- Chapter 3: A description of test facilities in this study.
- Chapter 4: A description of pure loading tests and presents the experimental and analytical results of normal bearing and in-plane shearing capacity factor for drag embedment anchor.
- Chapter 5: A description of drag embedment anchor tests in single layer soil profile (normally consolidated and linearly increasing shear strength profile) and layered soil profiles, and presents the experimental and analytical results in terms of capacity, trajectory and pitch.
- Chapter 6: A description of tandem system anchor with two drag embedment anchors and shows the measured trajectory and capacity of tandem system anchor compared with that of single anchor. Additionally, the experimental results of configuration that second anchor attached to the back of fluke of front anchor are compared with analytical results.

- Chapter 7: A description of tests to study strain rate effect by conducting pure loading tests with a thin steel plate at different loading rate. Presents free-fall penetration tests with Flying Wing Anchor® in constant shear strength profile and layered soil profiles. The experimental results are compared with analytical solution.
- Chapter 8: A description of scale effect by conducting drag embedment tests with drag embedment anchor in different size and Flying Wing Anchor® with different weight to area ratio.
- Chapter 9: A Summary of main findings in this study.

Chapter 2. Literature Review

2.1 Introduction

This chapter reviews offshore structures, mooring systems, and types of offshore anchors typically used in deepwater offshore. The chapter also reviews the plasticity-based limit methods widely applied for prediction of anchor capacity and trajectory.

2.2 Background

2.2.1 Offshore Structures

The selection of appropriate foundation for offshore structure is based on site conditions (water depth, soil condition in construction site and reserve size), economic consideration, and operating interests (French, et al., 2006). The definition of shallow and deepwater depth has been evolved with technology, but nowadays the shallow water depth is less than 500m, deep water is 500 m - 1500 m, and ultra-deep water is over 1500 m (Colliat, 2002; and Randolph and Gourvenec, 2011).

Figure 2.1 shows main types of offshore foundations. Fixed Platfrom (FP) with a gravity base or steel jackets is selected when water depth shallower than 600 m due to economic consideration. If water depth from 300 m to 600 m, a compliant tower (CT) is selected due to its flexibility in bending so it can sustain higher lateral load without significant lateral deflection. Tension Leg Platform (TLP) with vertical tendons is selected if water depth is 300 m to 2000m. The vertical tendons are capable to maintain in tension in extreme loading condition like storm. Spar Platform (SP) can be developed if water depth is less than 3000m. SP includes a large cylindrical hull which supports platform and buoyancy chamber within the hull to provide buoyancy of platform. Floating Production Storage and Offloading Facility (FPSO) is also capable to develop in water

depth less than 3000m. FPSO consists of a vessel and storage facilities, which enables the development of FPSO is suitable for the remote filed without pipeline installed. Subsea systems are feasible for any water depth and in service for either a single or multiple platform.

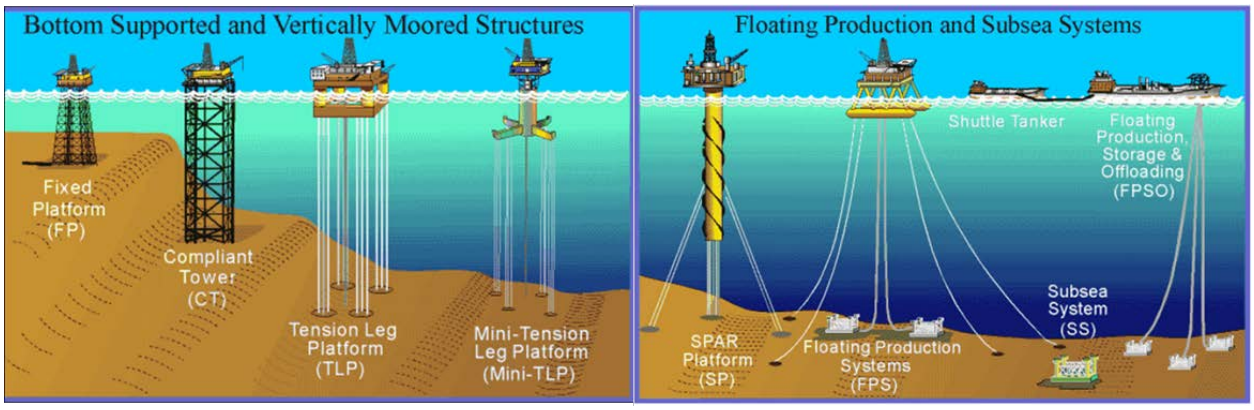

Figure 2.1. Offshore Development Systems (http://www.gomr.mms.gov)

2.2.2 Mooring Systems

Floating offshore structures can be anchored by catenary or taut mooring line (Figure 2.2). Catenary mooring line has zero-line angle at the seabed, as opposed to taut mooring line sustains 40° to 50° line angle. The catenary mooring line can transmit horizontal loads to seabed from offshore structure, in contrast, the taut mooring line is capable to transmit both horizontal and vertical load. Therefore, lateral load governs the design of catenary mooring line while vertical capacity controls designs of taut-leg mooring line (Eltaher et al., 2003). The self weight of catenary mooring line provides the restoring force, but for the taut mooring line, the mooring line elasticity is the main component for restoring force which indicates that water depth should be sufficient to make mooring length retain the required elasticity. Vryhof (1999) concluded from field experience that the selection of mooring system is limited by the design of the platform, weight and length of mooring line. In general, as water depth increase, the taut mooring line is

chosen other than the catenary mooring line. Taut mooring line can significantly reduce the possibility of interaction with existing facilities like pipelines or adjacent structures (Aubeny et al., 2001); additionally, cost on the mooring line can be saved by choosing taut mooring line with a shorter length compared with catenary mooring line.

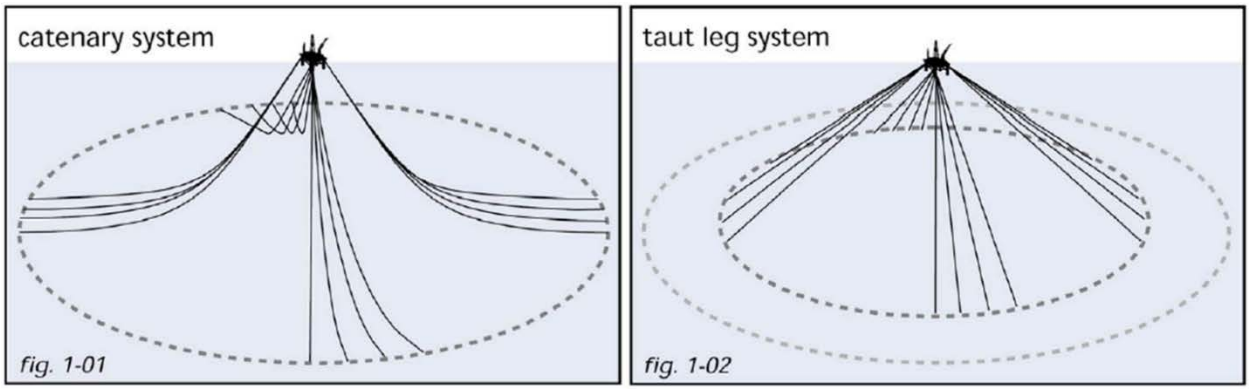

Figure 2.2. Catenary and Taut Leg Mooring System (Vryhof, 2015)

2.2.3 Offshore Anchors

Floating offshore structures are anchored to seabed by different type of anchors. The selection of anchors is based on the size and service life of structure, the geotechnical characteristics of construction site, and limitation of economy and installation convenience. This section briefly reviewed a couple of anchors commonly employed in practice.

2.2.3.1 Drag Embedment Anchors

A drag embedment anchor (DEA) embeds into seabed by dragged horizontally with an anchor-handling vessel (AHV). DEA designs were advanced by field experience (Figure 2.3). In general, DEA consists of a wide fluke which provides bearing capacity, a thick shank which provides shearing resistance, and an attachment point (padeye or shackle) for connecting mooring line.

Since the major capacity of DEA is from the bearing by fluke, thus DEA is not designed for sustain a large vertical load and are usually used as temporary anchor with catenary mooring system in deep water.

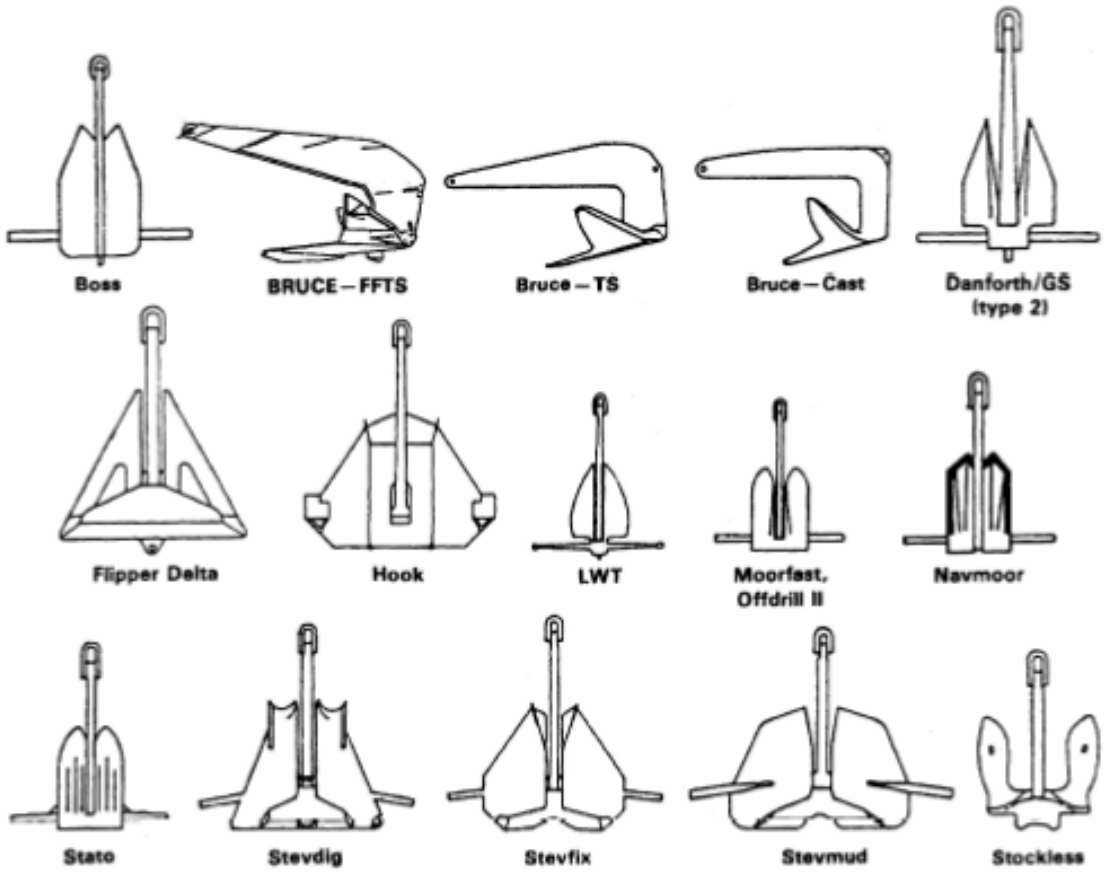

Figure 2.3. Drag Embedment Anchors (NCEL, 1987)

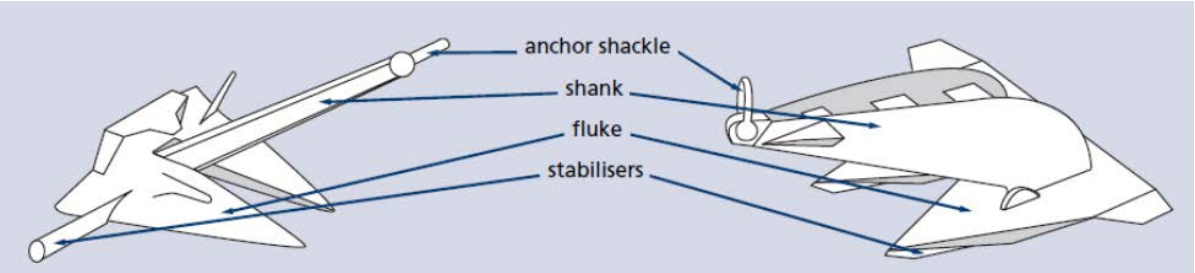

Figure 2.4. Components of Drag Embedment Anchor

A higher holding capacity can be achieved by embedding DEA deeper since the increase of soil shear strength which results in an increase of overburden pressure on fluke and higher resistance on shank and embedded anchor line. To facilitate DEA dives deeper, three features of DEA are designed. First, the front fluke is with two symmetric sharp triangular shape in the dragging direction (Figure 2.4). Second, for better performance, a stabilizer may be attached to on DEA (Figure 2.4). Third, different fluke-shank angle is designed for different site condition: angle with 30° for sand, and 50° for mud. The fluke-shank angle is fixed during installation, and it is preset by connecting shank to different notches on fluke (Figure 2.5). A typical DEA can have efficiency of 5 to 55 (efficiency is defined as anchor holding capacity over anchor self-weight).

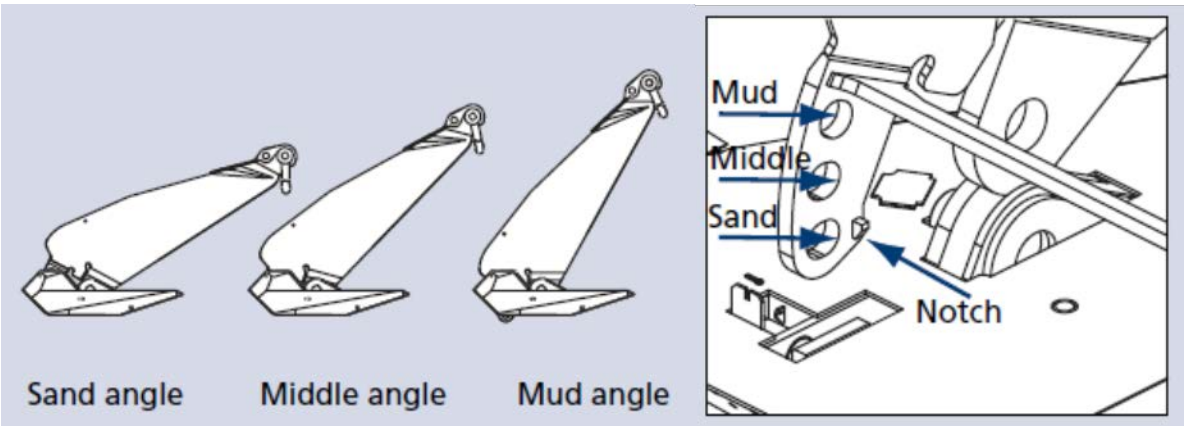

Figure 2.5. Schematic of Vryhof Drag Embedment Anchor (Vryhof, 2005)

2.2.3.2 Vertically Loaded Anchors

Vertically loaded anchors (VLA) is designed to sustain vertical load from offshore structure in the taut mooring system. The capacity of VLA is mainly provided by fluke which can be considered as an embedded bearing plate. The shank of VLA is a thin rigid bar or bridle and is allowed to rotate around the conjunction point of fluke and shank (Figure 2.6). VLA shares a

similar installation process with DEA, however, the fluke-shank angle of VLA increases along the horizontal drag, and shank is almost perpendicular with fluke at the end of installation while fluke is almost parallel to the seabed surface. This final configuration mobilizes the maximum bearing capacity on fluke (Murff et al., 2005).

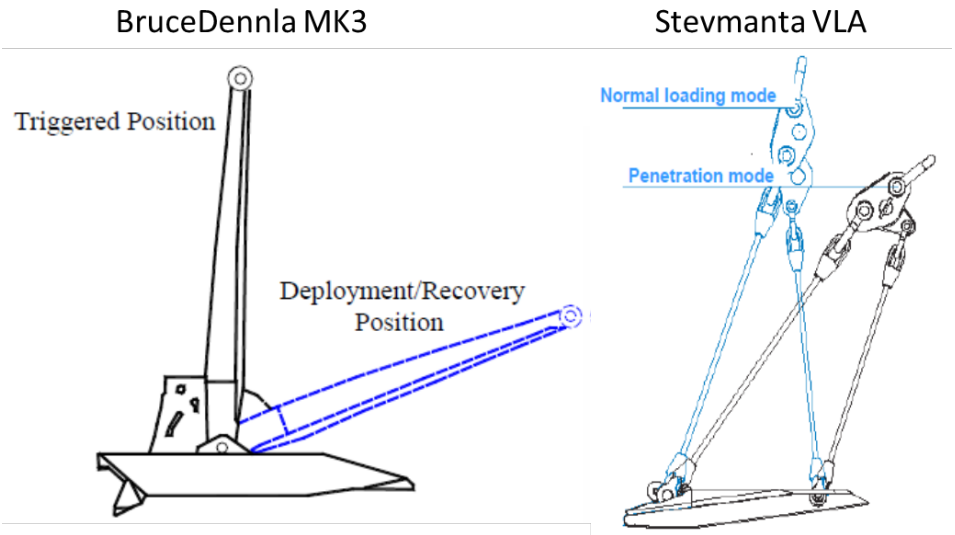

Figure 2.6. VLA Anchor

Two VLA commonly in use are shown in Figure 2.6. In order to achieve a relative normal fluke-shank angle, a shear pin is designed so it will break at a centain installation and anchor shifts from installation mode to normal loading mode (Figure 2.7). In the normal loading mode, VLA is acting as a embedded plate and sustain a high resistance against pulling out load (Murff and Anderson, 2001).

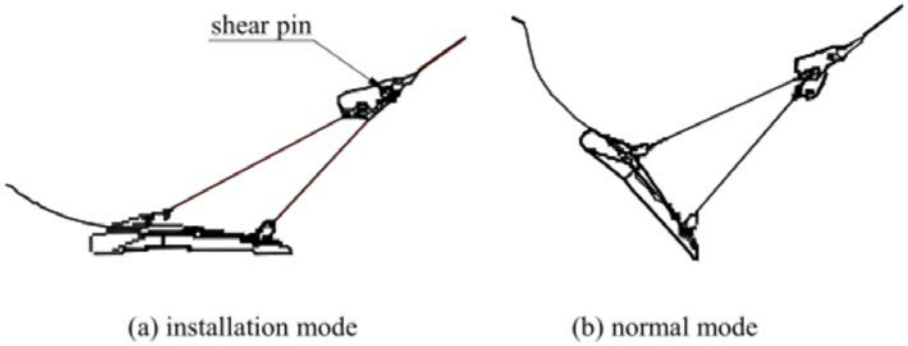

Figure 2.7. Different Mode of VLA

2.2.3.3 Piggy-back Anchor

Multiple drag anchors either DEA or VLA (Tandem system anchor shown in Figure 2.8) are connected to achieve a higher capacity compared with using a single anchor. The tandem system anchor is preferred in the following two situations: (1) the installation of large size anchor is limited by the reserve size or transport and handling facility; (2) the capacity of pre-selected anchor is inadequate for design load requirement. The total capacity of tandem system anchor highly depends on the way of second anchor being attached to the front anchor and the stability of the front anchor. Inappropriate attachment will result in a breakout or pulling-out of the front anchor and rotation of the second anchor (Oregon Wave Energy Trust, 2009). If the front anchor is unstable, it is impossible to mobilize full capacity for both anchor since the front anchor rolls and slides on seabed surface and prevents the second anchor diving into seabed. However, appropriate attaching the second anchor can lead to the total capacity of tandem systems equal to or higher than two anchors to be embedded separately.

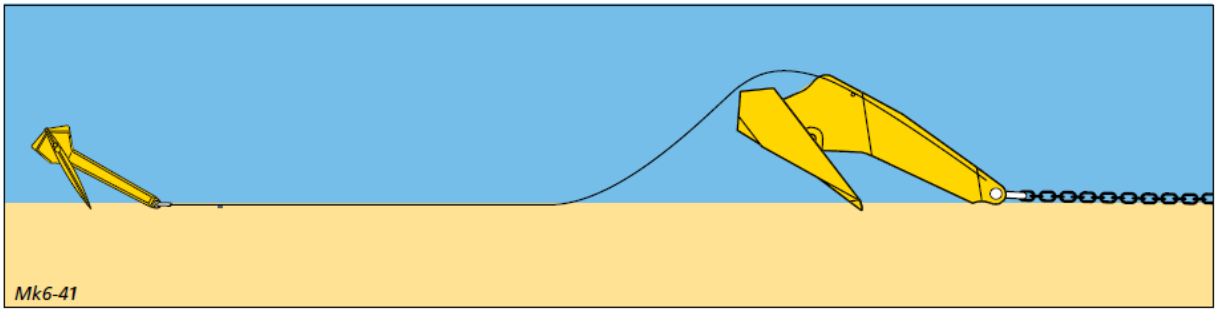

Figure 2.8. Example of Tandem Anchor (Vryhof, 2005)

2.2.3.4 Torpedo Pile

The torpedo pile is a cost-effective anchor since it is installed by its self-weight, and it was first developed in 1996 by the Brazilian energy company Petrobras for a riser flow-line restraint (Medeiros, 1997). The shape of torpedo pile is a tubular pile with a cone tip, fins attached at the rear and padeye on the top. As shown in Figure 2.9, the inside of tubular pile is filled with ballast or concrete (Medeiros, 2001 and Medeiros , 2002) to increase the self weight and lower down the center of gravity of pile. Typically, four to eight piles were transported by an anchor-handling vessel (AHV). Two lines are connected to pile, the installation line and mooring line. The installation line is used to lower the anchor to the designated drop height and is disconnected to allow anchor free falling through water column and impacting the seabed (Figure 2.10).

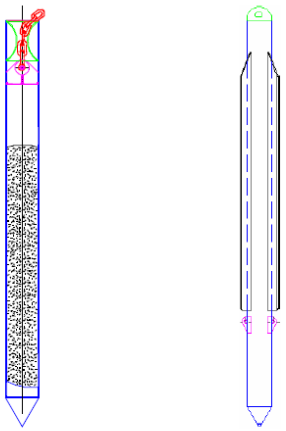

Figure 2.9. Torpedo Anchor (Medeiros, 2001)

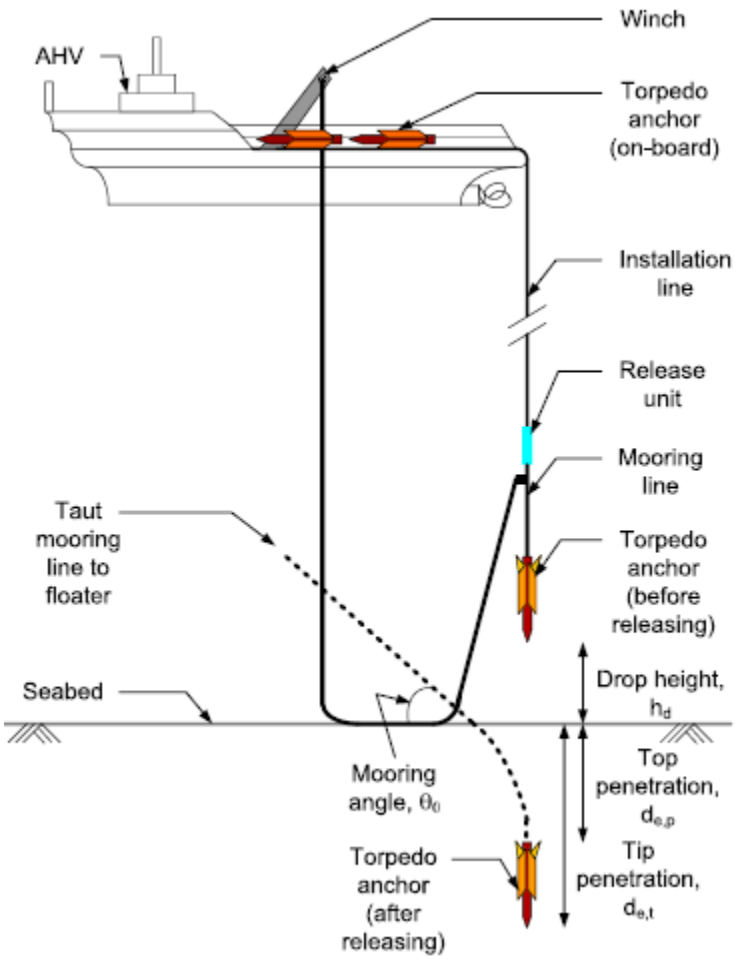

Figure 2.10. Torpedo Pile Installation (Hossain, 2014)

2.2.3.5 Deep Penetration Anchor

Deep Penetration Anchor (DPA) is a conceptually similar to torpedo pile but with shorter and wider fins attached on the cylindrical pile (Figure 2.11). The length of cylindrical pile of DPA is arranging from 10 to 15 m (32 to 49 ft), the diameter is between 1 to 1.2 m (3.3 to 3.93 ft), and weighs 50 to 100 tons (110 to 220 kips). The installation procedure of DPA is the same as torpedo pile. The installation line and mooring line is connected to the padeye located on the top of the pile, and the installation line is disconnected when DPA reaches the target deploying height and DPA is installed by gravity.

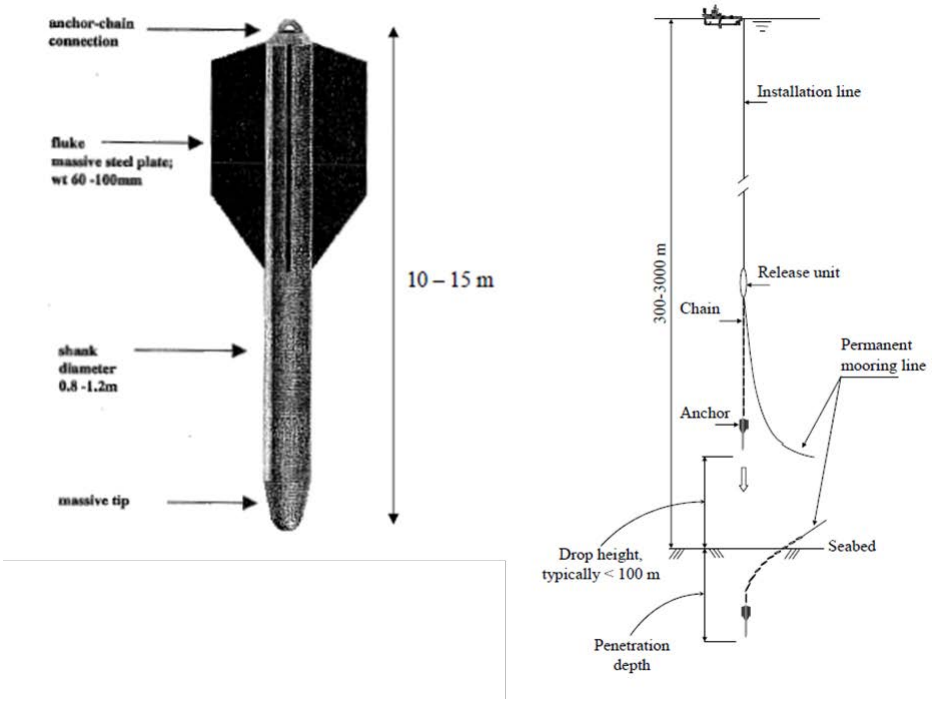

Figure 2.11. Torpedo Pile and Its Installation Procedure (Lieng et al., 1999)

2.2.3.6 Omni-Max Anchor

Zimmerman et al. (2005) firstly brought a new concept of dynamically installed anchor, which was named as self-penetrating embedment attachment rotating anchor (SPEAR), and later in 2007 was named as OMNI-Max anchor (Figure 2.12). OMNI-Max is a rocket shaped anchor with two sets of three fins. The set of fins with larger size is located on the upper part of anchor, and the smaller ones are at the bottom. This design makes the resistance along anchor equilibrium since the shear strength of seabed is linearly increasing with depth. OMNI-Max shares the similar installation procedure as torpedo pile and DPA but can rotate after penetration because of a new design of adjustable flukes and 360° rotation mooring attachment located on the one third of anchor. As shown in Figure 2.13, the mooring attachment point allows anchor to rotate to the position perpendicular to the applied load, which makes the anchor fluke maximize its bearing force. The adjustable fluke was designed for increase or reduce of anchor surface area make the shear resistance larger or smaller. In the normal loading condition, OMNI-Max anchor remains vertical. As the applied load increases up to 20% of design load, OMNI-Max starts to rotate until the frictional and bearing on the upper part flukes are equal to the lower part of flukes. With the further increase of load, the anchor starts diving like drag embedment anchor to the deeper soil where the shear strength is higher and can provide higher resistance.

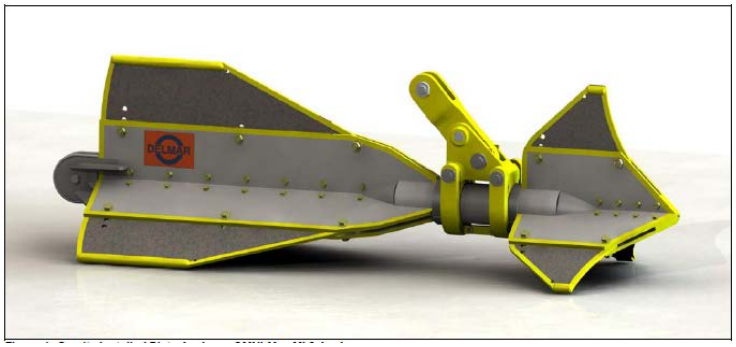

Figure 2.12. OMNI-Max Anchor (Shelton et al., 2011)

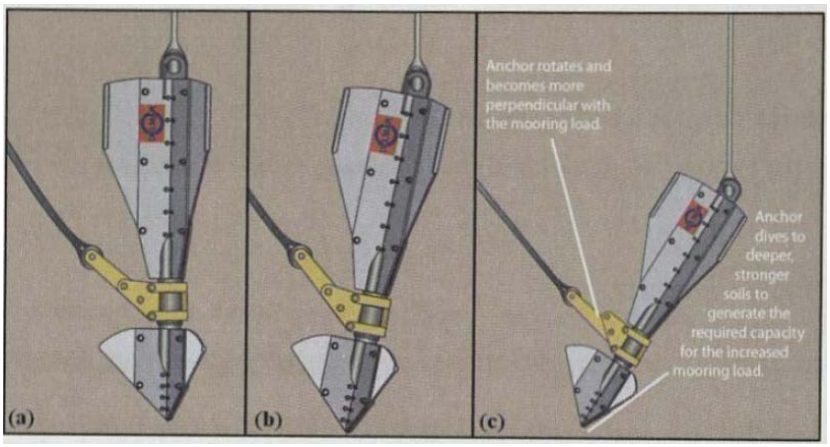

Figure 2.13. Installation of OMNI-Max Anchor (Delmar Systems Inc., 2011)

2.2.3.7 Suction Embedded Plate Anchor (SEPLA)

Suction Embedded Plate Anchor (SEPLA) is a hybrid anchor which is a plate anchor installed by suction caisson (Figure 2.14). It combines the advantages of dynamically installed anchor and the embedded plate. It can be accurately released from any desired height and location by self weight, and it can withstand the horizontal and vertical load which makes SEPLA applicable for catenary and taut mooring system. The installation process of SEPLA is shown in Figure 2.15, during installation, the water inside in caisson is pumped out to make the caisson penetrate deeper. After the caisson and embedded plate penetrates, the suction caisson is retrieved while the water is pumped back, and the embedded plate rotates to the position perpendicular to the load.

Figure 2.14. Suction Embedded Plate Anchor (http://www.energetics.com)

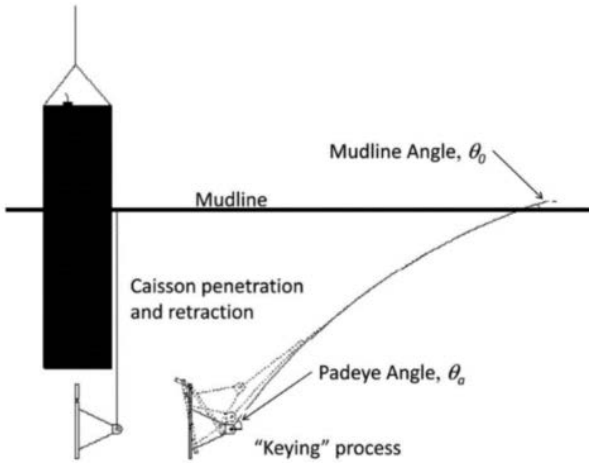

Figure 2.15. Installation Process of SEPLA (Yang et al., 2011)

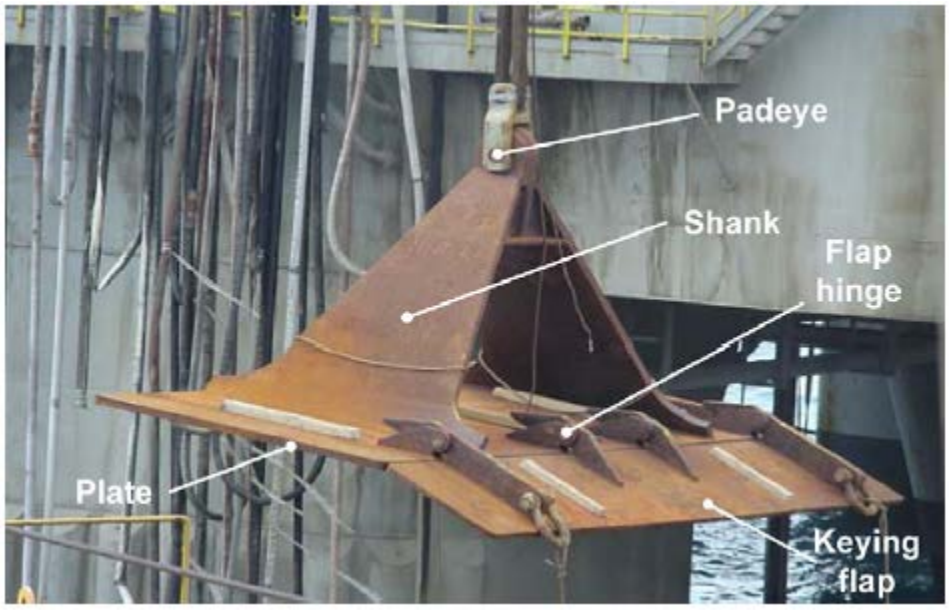

Figure 2.16. Typical SEPLA with Keying Flap (Courtesy of ExxonMobil)

The shortcomings of SEPLA are: (1) the potential to loss embedment during keying process; (2) the potential to break during penetration process specially if encounters stiffer soil; and (3) lower final capacity due to the weakened soil zone formed during retrieval of follower. Ehlers et al. (2004) reported that the keying process of SEPLA result in inaccurate estimation on final

embedment depth. Gaudin et al. (2006) illustrated that a weakened soil zone can be formed either during installation or retrieval of follower. This weakend soil zone can be extended from the seabed to the embedded anchor, which leads to a lower final capacity. The loss of embedment during keying has been studied experimentally (O'Loughlin et al. 2006; Song et al., 2009) and numerically (Song et al., 2008)), and a keying flap (Figure 2.31) was porposed by Gaudin et al. (2010b) to reduces the embedment loss.

2.2.3.8 Dynamically Embedded Plate Anchor (DEPLA)

Dynamically embedded plate anchor is another hybrid anchor combines the advantage of dynamic installed anchor and plate anchor. DEPLA has a tubular cylinder with a cone tip and four symmetric cylindrical fins (Figure 2.17). The installation line is attached to the top of follower, and the mooring line is attached to the padeye located on the flukes which are later also used for keying process. The installation process of DEPLA shares the similar procedures as SEPLA. After dynamic penetration of follower and fluke, the follower is retrieved back for future installation, and the fluke rotates to the position perpendicular to service load (Figure 2.18).

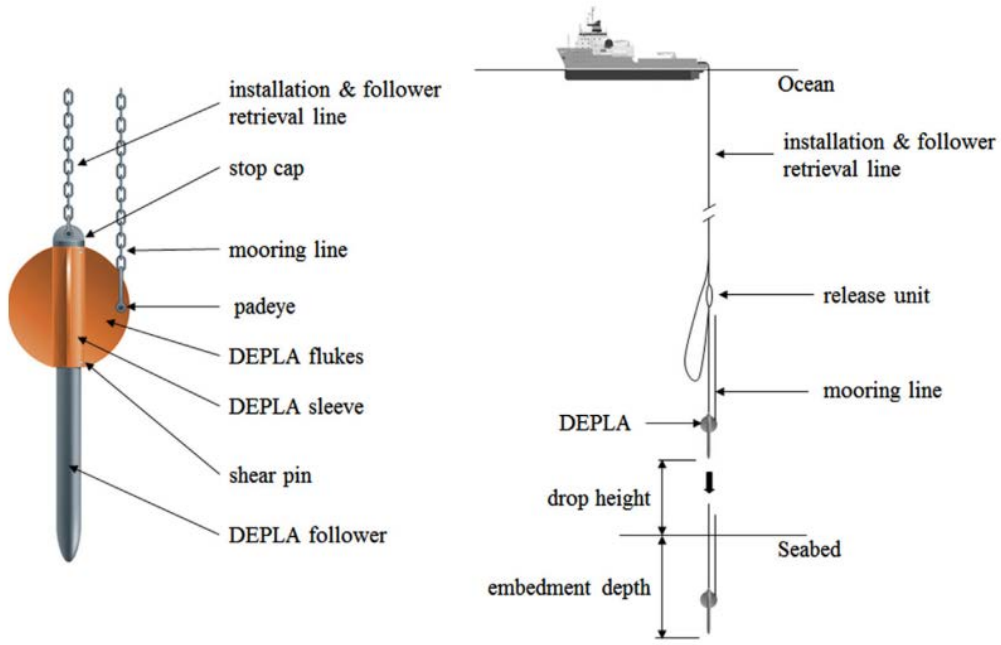

Figure 2.17. DEPLA Anchor (O'Loughlin et al., 2014)

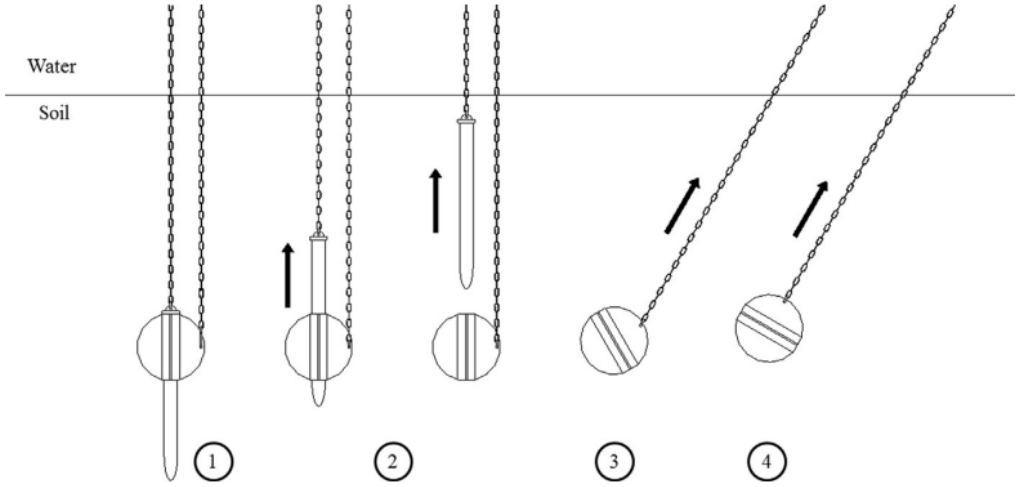

Figure 2.18. Installation of DEPLA (O'Loughlin et al., 2014)

2.2.3.9 Flying Wing Anchor ®

The Flying Wing Anchor®, was developed at The University of Texas at Austin, is a sustainable anchor for offshore wind turbines in deep water. This anchor combines torpedo piles and vertically loaded plate anchors, and it maximizes the advantages of both anchors. The installation steps of the Flying-Wing Anchor are presented in Figure 2.19. The Flying Wing Anchor® is installed by gravity (Figure 2.19) like torpedo pile, and its wing-shaped plates (shown in Figure 2.20 and Figure 2.21) provide hydrodynamic stability. The center of lift of Flying Wing Anchor® is designed above the center of mass when the trajectory of anchor in water is perpendicular to seabed. The shank of Flying Wing Anchor® is closed at the end of installation and keeps closing if anchor capacity meets the load requirements. When the environmental loads increases, as the result that the tension force in the mooring line which connects anchor and wind turbine increases, and Flying Wing anchor® starts pitching upward (Figure 2.20) from its current vertical position. During the first stage of pitching, the shank is closed and attached with the fluke-shank coupling mechanism. The second stage of pitching is triggered when the anchor rotates to the design pitch angle, then the fluke-shank coupling mechanism releases the shank and the shank gets aligned with the mooring line (Gilbert et. al, 2015). The tension in the mooring line further increases, which drives the anchor diving deeper and a greater anchor capacity can be attained. The maximum bearing capacity will be reached at an extreme load condition, when the fluke surface is in bearing and the shank is nearly perpendicular to the fluke.

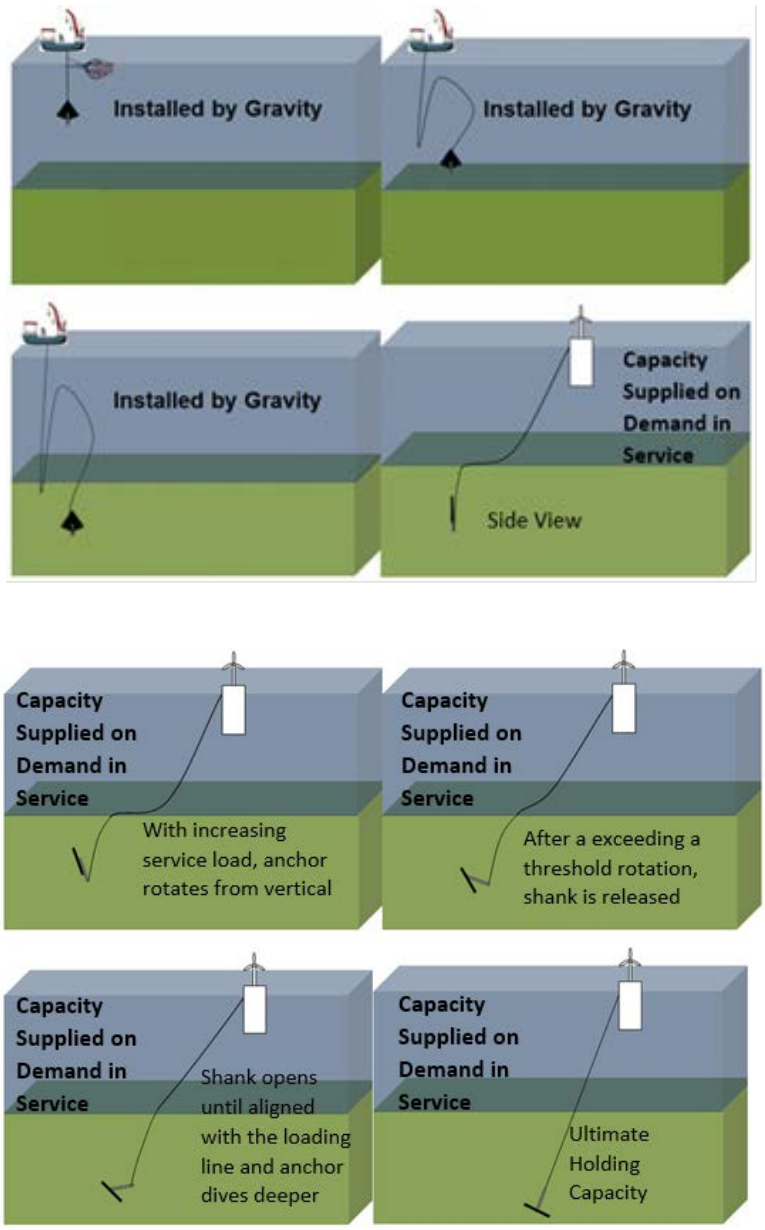

Figure 2.19 Schematic Illustration of Installation and Service for Flying Wing Anchor® (Gerkus et al., 2016)

The simplified Flying Wing Anchor® shown in Figure 2.20 are two possible design configurations, one is diamond-shape configuration, and the other is bi-wing shape configuration. In Figure 1.5, the Speedy Flying Wing Anchor® is designed by reducing the size of front fluke of bi-wing shape and modifying the front of fluke into a teardrop shape. Moreover, the fluke-shank

coupling mechanism is hidden when the shank is close. These modifications make the Speedy Flying Wing Anchor® more hydrodynamic stable when travelling through water.

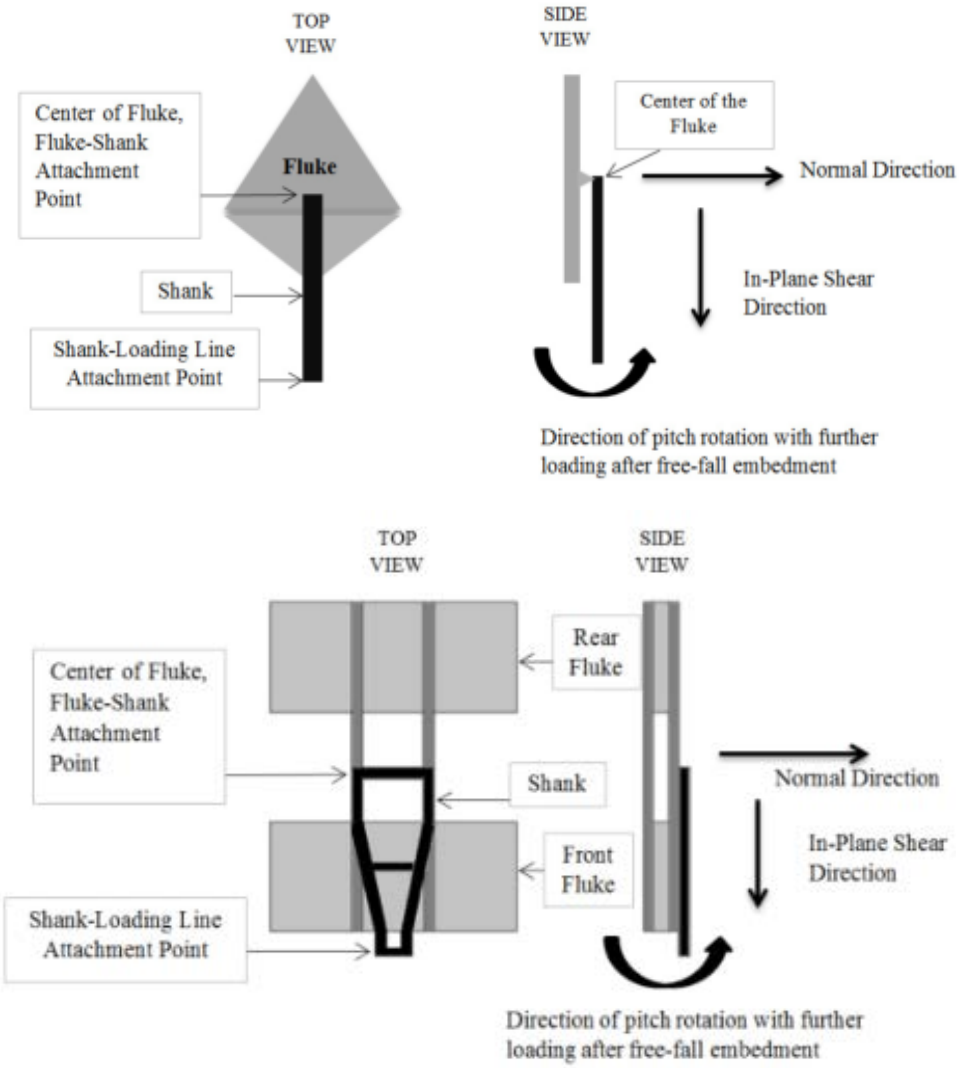

Figure 2.20 Simplified Diamond-Wing and Bi-Wing Shaped Anchor Designs (Gerkus et al., 2016)

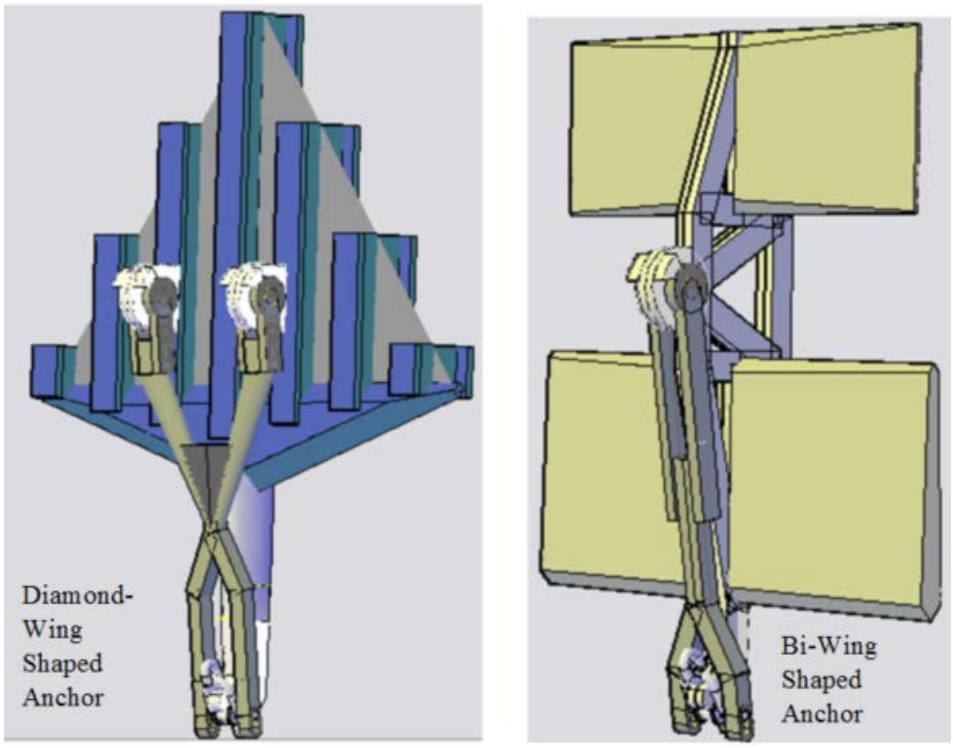

Figure 2.21 Diamond-Wing and Bi-Wing Shaped Flying Wing Anchor® Configurations (Gilbert et al., 2015)

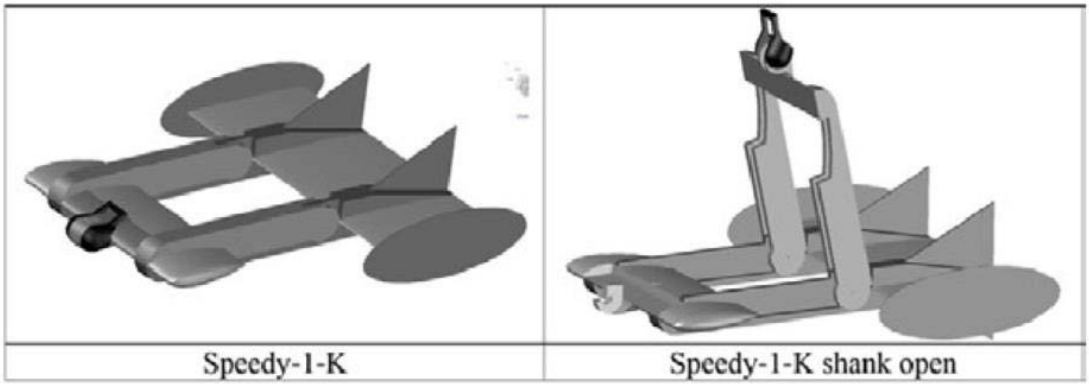

Figure 2.22 Speedy Flying Wing Anchor® Configurations (Gilbert et al., 2015)

2.3 Physical Tests of Different Types of Anchor

2.3.1 Drag Embedment Anchors

2.3.1.1 Field Tests

Taylor (1987) performed the field tests at Indian Island with different types of DEA (Table 2.1). The tested anchor weights ranges from 25 lbs to 800 lbs. The tested site consists normally consolidated organic silty clay. The shear strength at mudline is 0 psf, and the shear strength gradient is 10 psf/ft. The anchor capacity and efficiency is summarized in Table 2.1. For all the drag tests, the tested anchors remained stable. The maximum load among tested anchor is 105,300 lbs by 5000-kg (11023-lb) STEVFFIX anchor at drag distance of 45 ft. The STEVFIX was possible to dive deeper however the fluke is blocked to open and anchor rolled at 33.5 degrees. The maximum anchor efficiency is achieved by 500-kg (1102.3-lb) Bruce Twin-Shank with efficiency of 11.5 at drag distance of 42 ft.

Table 2.1. Data Summary for DEAs at Indian Island Tests

Test No.	Anchor	Anchor Weight (lb)	Anchor Load (lb)	Anchor Efficiency	Peak Mooring Load (lb)	Anchor Drag Distance (ft)	Chain Weight on Seafloor (lb)	Remarks
1-81	8K Two-Fluke Balanced	8000	23200	2.9	--	60	6392	Anchor was stable with drag
2-81	8K Two-Fluke Balanced	8000	20900	2.6	24800	47	6940	Anchor was stable with drag
3-81	6K MOORFAST	5400	28700	5.3	34100	40	3721	Anchor was stable with drag
4-81	6K MOORFAST	5400	29500	5.5	33900	45	3541	Anchor was stable with drag
5-81	8K Two-Fluke Balanced	9800	20100	2.5	24000	43	6541	Anchor was stable with drag
8-81	8K Two-Fluke Balanced	9800	21800	2.7	24800	42	6167	Anchor was stable with drag
7-81	500-kg Bruce Twin-Shank	1100	11300	10.3	17100	47	9089	Anchor was stable with drag
8-81	500-kg Bruce Twin-Shank	1100	12600	11.5	17500	42	9026	Anchor was stable with drag
9-81	645-kg PRISMA	1895	--	--	18600	42	9259	Anchor was stable with drag
10-81	645-kg PRISMA	1895	--	--	20100	51	8686	Anchor was stable with drag
11-81	5000-kg STEVFIX	11000	9200	<1	17500	20	15818	Flukes did no trip
12-81	5000-kg STEVFIX	11000	105300+	9.6+	118700+	94	0	Flukes blocked open

2.3.1.2 Scaled Model Tests

Lynk (2009) performed drag embedment tests with two types of DEA (Figure 2.23) in the normally consolidated kaolinite, the grey on with double shank, and the yellow one with a single shank. The capacity was measured for each type of anchor, however, due to the limitation of testing facilities, there is no trajectory measured in this study. The capacity of the grey anchor double shank was 1.5 times higher than the yellow anchor with a single shank.

Figure 2.23. Tested DEAs (Lynk, 2009)

Beemer (2011) performed drag embedment tests with in Laponite gel which represents clay. Laponite was selected because it can provide visibility of embedded anchor. An example of testing anchor in the Laponite testing bed with tested anchor is shown in Figure 2.24. The anchor was attached with different sizes of anchor line, 1/32 inch, 1/16 inch and 1/8 in. The fluke length of tested DEA is 4.5 inch, and the shank length is 4.5 inch. The fluke-shank angle is 50 degrees. The trajectory of anchor in the tested bed was captured by camera and extracted by Matlab program

LoctAnch (Figure 2.25). Beemer (2011) concluded that the increase of anchor line diameter leads to an increase of measured capacity. However, the relationship between the anchor line size and the anchor trajectory was not obvious. This can be explained that the Laponite gel has the different properties (shear strength and yield surface) than soil, and the anchor behavior in the Laponite cannot be interpreted into the behavior in soil.

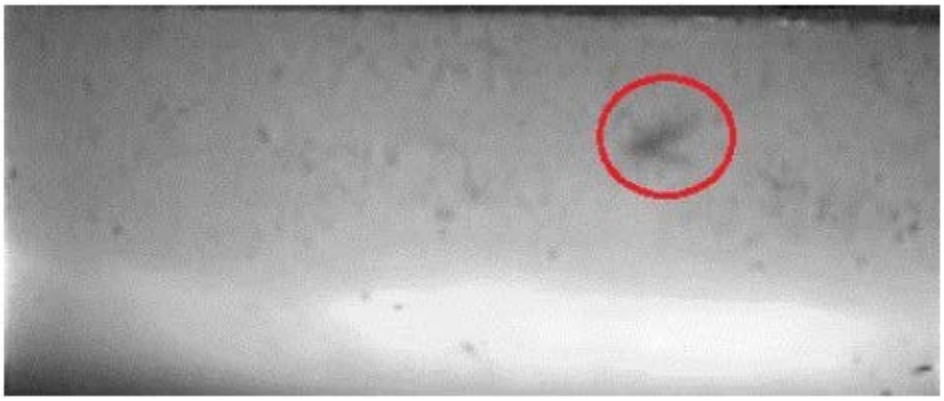

Figure 2.24. Example of Tested DEA in Laponite Gel (Beemer, 2011)

Figure 2.25. Example of Trajectory of DEA Extracted from Camera Images (Beemer, 2011)

2.3.2 Vertically Loaded Anchors

2.3.2.1 Field Tests

VLA with Stevmanta design was tested in the field initially in 1996 and 1998 at Gulf of Mexico and Offshore Brazil. Runien and Degenkamp (1999) reported that the VLA with Stavmanta was tested in very soft clay and achieved anchor efficiency with 2 to 3. Agenevall (1998) reported that the first VLA (118 ft^2 Stevmanta) applied to offshore structure is at P-27 field in Compos Bassin Offshore Brazil.

2.3.2.2 Scaled Model Tests

Elkhatib et al. (2002) performed drag embedment tests with model Vryhof Stevmanta (scale of 1:100). The scaled model anchor (Figure 2.26) is shown in The thickness of fluke is 0.75 mm (0.03 inch) and length of fluke is 35 mm (1.38 inch). The anchor line thickness is 1.8 mm (0.07 inch). The fluke-shank angle is 49°. The weight of model anchor 15 grams (0.03 lbs).

Figure 2.26. Scaled Vryhof Stevmanta (Elkhatib et al., 2002)

Due to the limitation of length strong box, the drag distance is limited up to 7 fluke lengths. Elkhatib et al. (2002) achieved a longer drag distance over than 7-fluke length by separating drag tests into two stages: (1) dragged the anchor starting at the mudline and measured the penetration depth at the end of tests; (2) place the anchor to the depth corresponding with the depth from the first stage and continued dragging the anchor (Figure 2.27). The final embedment depth is averaged at 4.5 fluke length.

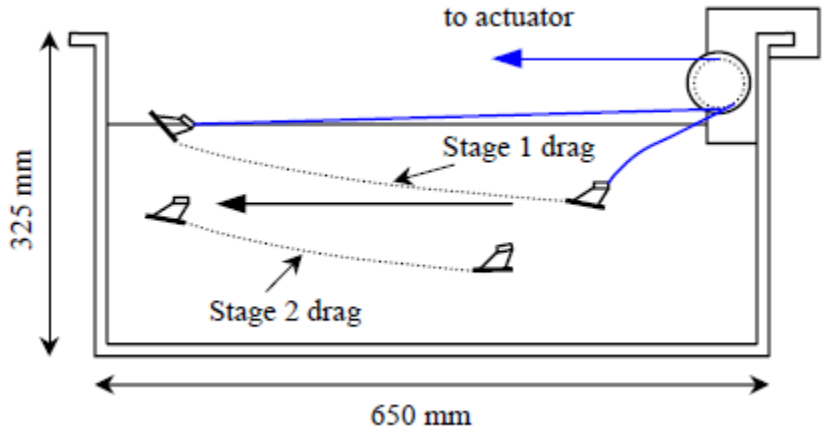

Figure 2.27. Drag Embedment Tests (Elkhatib et al., 2002)

2.3.3 Piggy-back Anchor

2.3.3.1 Field Tests

Taylor (1987) performed tandem system anchor field testing in Port Hueneme and San Francisco. For all of the tests reported by Taylor (1987), the second anchor was connected to the back of fluke of front anchor. He tested tandem system anchor with connecting two STATO anchors or two NAVMOOR anchors or one STATO to NAVMOOR. He found that either STATO or NAVMOOR anchor demonstrated good stability when set as the front anchor. From their site

investigations, the test site at Port Hueneme consisted of well-graded fine sand. The soil at San Fracisco Bay Hunters Point was classified normally consolidated silty clay with 0 psf undrained shear strength at seabed and 10 psf/ft increaseing rate. Three different tandem system anchors were tested with anchor in different size connected: the first two sets is two 1000-pound anchors connected and the third test with two 6000-pound NAVMOOR anchors connected. The first test with two 1000-pound anchors show that the total capacity was at least twice higher than two single anchor installed seperatly. The second test with two 1000-pound anchors and the third test with two 6000-pound anchor stopped in the middle of drag since the anchor capacity reached the maximum reading of load cell. The same conclusion were draw from the tamdem system tests in normally consolidated clay: the total capacity can be at least twice higher than a single anchor. The advantage of using tandem system is to maintain high anchor efficiency since the anchor efficiency decreased with the increase of size of anchor if a single anchor installed.

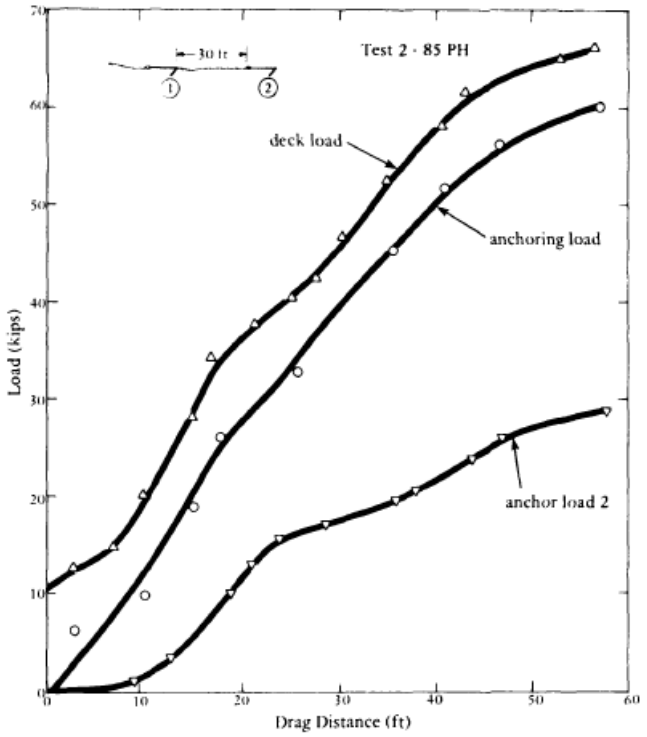

Figure 43. 1,000-pound tandem NAVMOOR Anchor performance in dense gravelly sand at Port Hueneme.

Figure 2.28. Tandem System Test Results in Dense Sand at Port Hueneme (Taylor, 1987)

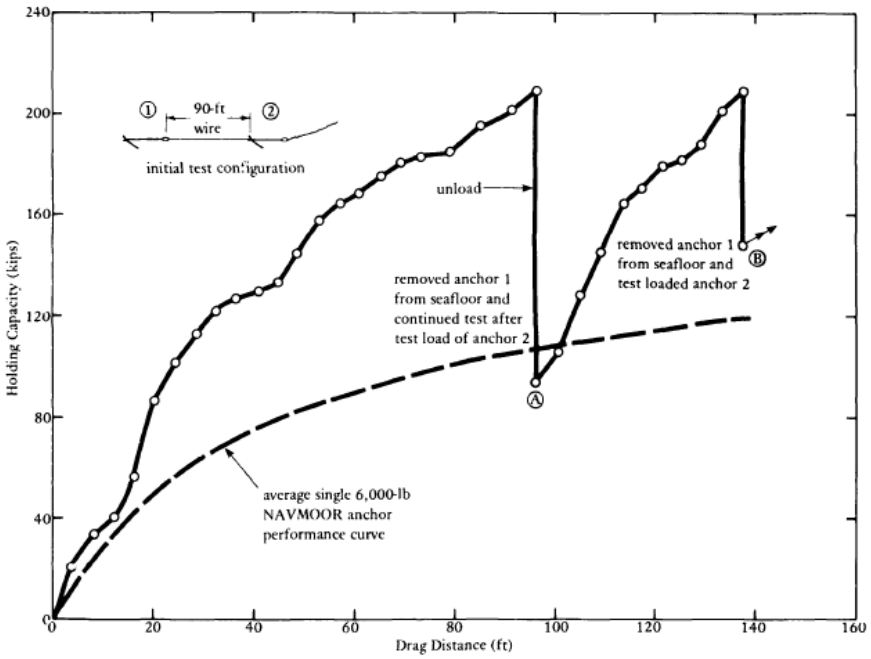

Figure 49. 6,000-pound tandem NAVMOOR Anchor performance in San Francisco Bay mud, showing results of sequential testing.

Figure 2.29. Tandem System Tests in San Fracisco Bay Hunters Point (Taylor, 1987)

2.3.3.2 Scaled Model Tests

Walker and Taylor (1983) performed eighty-two tests of tandem system anchor tests with two STATO anchors in sand by varying the attachment point and spacing between two anchors. From their model tests, they arrived at the same conclusion with Taylor (1987) that tandem system anchor had at least twice capacity compared with a single anchor with appropriate selection of attachment point. In their tests, they connected the shackle of the second anchor to the center of crown of the front anchor; connected the shackle of the second anchor to the upper tripping palm of the front anchor; the shackle of the second anchor to different locations on the shank of the front anchor; connect two anchors with an additional shackle in the front of both anchor and make them parallel (Figure 2.30). As shown in Figure 2.31, in their first attachment configuration, shackle to

center of crown, they found both anchors behaved as single anchor. The second and the third attachment configuration, palm-shackle rigging method and shackle to shank method made anchor unstable and the front anchor rolled during penetration while the second anchor was affected by this rotation. Moreover, this rotation was worse if the spacing between two anchors were smaller. The total capacity by the ground-shackling method highly depended on the spacing between two anchors. If the spacing was zero, then both anchors were unstable and rolled. With the increase of anchor spacing, the total capacity of tandem system anchors increased.

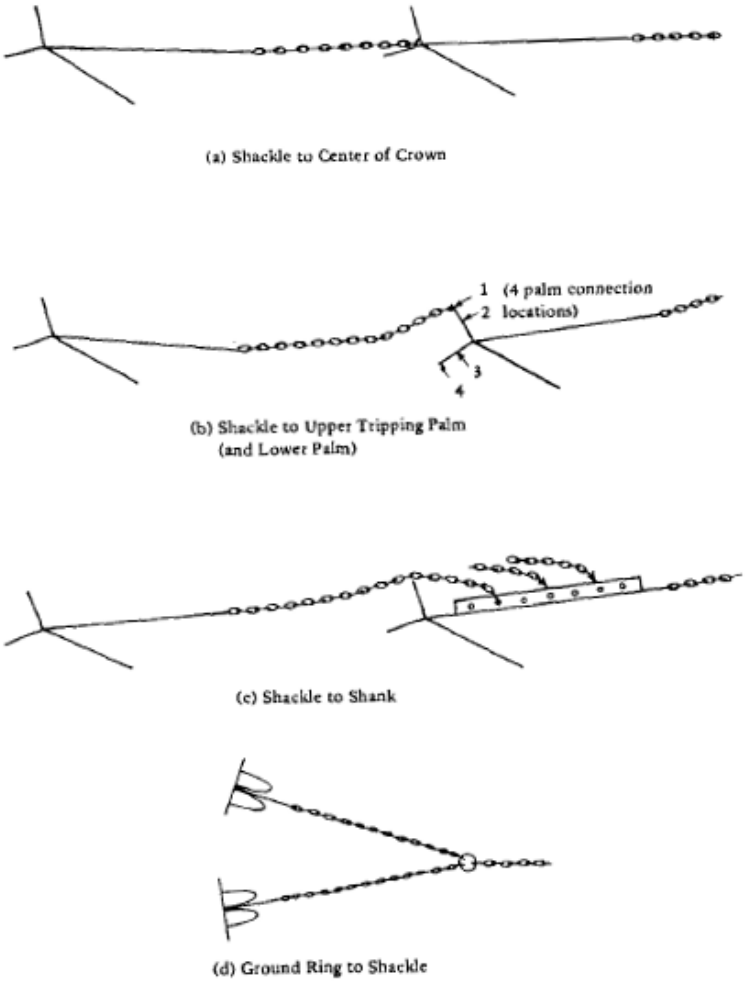

Figure 2.30. Multiple Anchor Test Methods (Walker and Taylor, 1987)

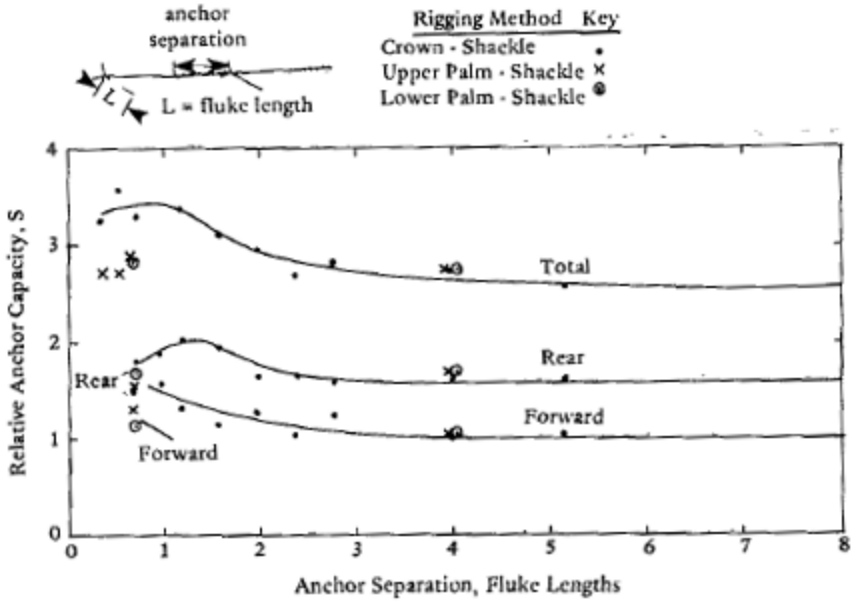

Figure 2.31. Total Capacity of Tandem System Anchors (Walker and Taylor, 1987)

2.3.4 Torpedo Pile

2.3.4.1 Field Tests

Petrobras developed a variety of types of torpedo piles for different offshore structures and successfully installed over 1000 torpedo piles in offshore Brazil (Acteon, 2009; Wilde, 2009). The types of torpedo piles were named by the anchor weight including T-24s, T-43s, and T-98s. T-24s is a 24-tons torpedo pile with small size fins which is designed to prevent pile rolling on the deck of handling vessels while provide small amount of frictional resistance to holding capacity. T-43s is a 43-ton torpedo pile with larger fins compared with T-24s and designed for MODU. T-98s is a 98-ton torpedo pile with fins for FPSO. From December 2001 to January 2000, the Petrobras installed over 90 torpedo piles either for MODUs or FPSO. Since 1996 torpedo piles installed by

Petrobras composed a database including installation information such as accelerometer and inclinometer data. Unfortunately, this database is unavailable for publics.

Medeiros (2002) reported a set of torpedo piles field tests performed in the Campos Basin. The 12-m (39.37 ft) long, 762-mm (2.5 ft) diameter and zero-fin torpedo pile with dry weight of 400 kN (89.9 kips) was dropped from 30 m (98.4 ft) above sea level and the water depth was around 1000 m (3280 ft). The tip penetration in different sites in Campos Basin is summarized in Table 2.2. Brandão et al (2006) published three full-scale filed tests with a 74-tons torpedo pile. In the published data, the tip angle, drop height, impact velocity, embedment depth at padeye and final pile inclination were listed (Table 2.3), however, no detailed description on anchor dimension was released. Denney (2007) decribed the installaion of torpedo pile for P-50 FPSO vessel. This torpedo pile was 17 m (55 ft) long, with a diameter of 1.07 m (3.5 ft) and four fins with 10 meters in length and 0.9 meters in width. The impact velocity was 26.8 m/s (87.9 ft/s), the tip embedment was 37.4 m (122.7 ft) and pile inclined 10°.

Table 2.2. Field Tests Tip Penetrations (Medeiros, 2002)

Site	Penetration Depth
Normally Consolidated Clay	29 m (95 ft)
Overconsolidated Clay	13.5 m (44.3 ft)
Calcareous Sand	15 m (49.2 ft)
Find Sand Overlying Normally Consolidated Clay	22 m (13m (42 ft) in sand and 9 m (29.5 ft) in normally consolidated clay)

Table 2.3. Full-Scale Filed Tests (Brandão et al., 2006)

	Test 1	Test 2	Test 3
Tip Angle	60°	30°	30°
Water Depth	1195 m (3920 ft)	1180 m (3871 ft)	940 m (3080 ft)
Drop Height	40 m (131 ft)	135 m (443 ft)	97 m (318 ft)
Impact Velocity	16.3 m/s (53.5 ft/s)	23.0 m/s (75.5 ft/s)	24.0 m/s (78.7 ft/s)
Padeye Embedment Depth	9.0 m (29.5 ft)	16.0 m (52.5 ft)	17.5 m (57.4 ft)
Pile Inclination After Set-up	3.0°	9.0°	5.0°

2.3.4.2 Scaled Model Tests

Gilbert et al. (2008) conducted a series of 1g tests with 1:30 scale aluminum model torpedo pile in normally consolidated kaolinite. The model pile consisted of a tubular shaft and a conical tip, and was deployed from 0 inch to 36 inches above the mud line. The dry weight of torpedo pile depends on the ballasted material inside of pile; it weighed 1.3 pounds in air if it was ballasted with tungsten and lead, and 0.7 pounds without ballast. The surface water above mud line arranged from -1 inches to 2.3 inches. They found the embedment depth increases as the drop height and anchor weight increases.

Table 2.4. 1g Torpedo Pile Tests Summary (Gilbert et al., 2008)

Test Identification	X Coord (in.)	Y Coord (in.)	Air Dry Weight (lb)	Bouyant Weight in Soil (lb)	Drop Height Above Mud Line (in.)	Water Level Above Mud Line (in.)	Embedment Mud Line to Tip (in.)	Predicted Penetration (in)	Prediction Performance Over = Pos. Under = Neg
3-001	89	7	0.69	0.22	12	1.0	12.0	12.2	1.8
3-002	89	13	1.30	0.82	24	1.8	22.6	23.8	5.3
3-003	89	19	1.30	0.82	24	1.8	21.4	23.8	11.2
3-004	89	25	1.30	0.82	24	1.8	20.8	23.8	14.4
3-005	89	31	1.30	0.82	24	1.8	23.0	23.8	3.4
3-006	83	31	1.30	0.81	24	2.3	24.8	23.8	-3.9
3-008	83	19	1.30	0.82	24	2.0	21.0	23.8	13.3
3-009	83	7	1.30	0.82	24	2.0	22.2	23.8	7.2
3-011	72	12	1.30	0.82	24	1.5	21.8	23.8	9.4
3-013	66	12	1.30	0.82	24	2.0	21.4	23.8	11.3
4-001	37	40	1.30	0.80	24	0.5	29.0	30.2	4.1
4-002	37	32	1.30	0.81	0	0.5	22.0	15.9	-27.9
4-003	37	24	1.30	0.81	12	0.5	25.2	24.4	-3.1
4-004	37	16	1.30	0.81	6	0.2	24.0	20.7	-13.7
4-005	29	32	1.30	0.80	30	0.3	30.8	32.4	5.5
4-006	29	40	1.30	0.80	36	0.1	32.5	34.8	7.1
4-007	29	16	0.69	0.22	12	0.0	13.1	14.3	9.2
4-008	17	40	0.69	0.21	24	0.0	15.3	18.7	22.9
4-009	17	14	2.76	2.23	6	-1.0	49.8	43.8	-11.9
4-010	17	30	1.01	0.52	36	1.3	24.3	29.0	19.5
4-011	17	6	2.76	2.23	0	1.3	50.6	38.5	-23.8
5-010	40	40	1.01	0.53	18	1.5	33.4	33.7	1.0
5-011	32	40	1.01	0.54	0	1.5	25.4	24.4	-4.2
5-012	24	40	0.70	0.24	0	2.1	16.1	18.4	14.4
5-013	16	40	0.70	0.23	6	2.1	21.4	21.9	2.3
5-014	8	40	0.70	0.23	12	2.3	24.9	24.6	-1.0
5-015	8	48	0.70	0.23	9	2.3	23.3	23.3	0.1
5-016	16	48	0.70	0.24	3	2.3	19.6	20.3	3.4
5-017	32	48	0.70	0.23	15	1.9	22.9	25.8	12.5
5-018	24	48	0.70	0.23	18	2.3	25.1	26.9	7.1
5-019	32	56	1.01	0.54	12	1.6	27.0	31.2	15.4
5-020	24	56	0.70	0.23	12	1.9	24.8	24.6	-0.5
5-026	16	64	1.01	0.54	12	1.6	26.8	31.2	16.4
5-029	40	72	1.01	0.53	9	1.1	30.3	29.7	-1.8
5-030	16	72	0.70	0.23	12	1.3	21.8	24.6	13.2
5-031	24	72	0.70	0.23	12	1.3	21.0	24.6	17.3
5-032	32	72	0.70	0.23	12	1.3	21.6	24.6	13.9
5-033	8	72	0.70	0.23	12	1.3	22.8	24.6	8.3
5-035	20	84	0.70	0.24	12	1.1	20.0	24.6	23.2
5-037	28	84	2.76	2.27	0	1.0	44.2	55.7	26.0
5-038	32	64	0.70	0.23	12	0.9	20.8	24.6	18.4

2.3.5 Deep Penetration Anchor

2.3.5.1 Field Tests

The field test data with full-scaled DPA is limited, but the data with 1:3 scale DPA is available. The first field test with 1:3 scale DPA was conducted in 2003, however, data were not available since the failure during the extraction of the instrumented anchor. In 2008, the second reduced scale data were performed at Troll Field in Norway. Sturn et al. (2011) released this set of field test data. The DPA is 2.9 t (6.4 kips), 4.4 m long and with diameter of 0.4 m (1.31 ft). The fluke width is 0.5 m (1.64 ft) and length is 2 m (6.56 ft). The water depth at test side was 300 m. The DPA was dropped from 15 m (49.2 ft) to 75 m (246 ft) from seabed. The impact velocity was around 13 m/s to 15 m/s and embedment depth was 7.04 m (23 ft) to 8.8 m (28.8 ft) (1.6 to 2 fluke length). The final inclination of DPA is around 2.8°. In 2009, another two full-size DPA with weight of 80 tons (176.4 kips) were tested at Gjøa Field in Norway. The DPA with length of 13 m (42.65 ft) and with fluke of 1.2 m (3.93 ft) in diameter was deloyed from 50 m (164 ft) and 75 m (246 ft) above sea level, and the embedment depth was 24 m (78.7 ft) (1.6 fluke length) and 31 m (101.7 ft) (2.4 fluke length). The undrained shear strength of soil in test site was not reported but only generally characterized as stiffer soil. The inclination at final orientation of DPA was less than 2°.

2.3.5.2 Scaled Model Tests

The database for DPA tested in centrifuge is larger than the field test. A DPA with 1:200 scale was conducted in normally consolidated kaolinite with shear strength ingradient of 0.83 to 1.5 kPa/m (17 to 31.33 psf/ft) (Richardson, 2008; O'Loughlin et al., 2004a; O'Loughlin et al., 2004b). The length of model DPA was 75 mm (2.95 inches) and diameter was 6 mm (0.24 inches). Three

types of DPA were tested, zero-fins, three-fins, and four fins (Figure 2.32). The tests results indicated that the anchor can penetrate 2 to 3 fluke length, and the final embedment depnds on drop height and anchor mass. O'Loughlin (2013b) concluded the impact velocity depends on aspecte ratio and surface area from a series of centrifuge tests (Figure 2.33).

Figure 2.32. 1:200 Scale DPA (O'Loughlin et al., 2004b)

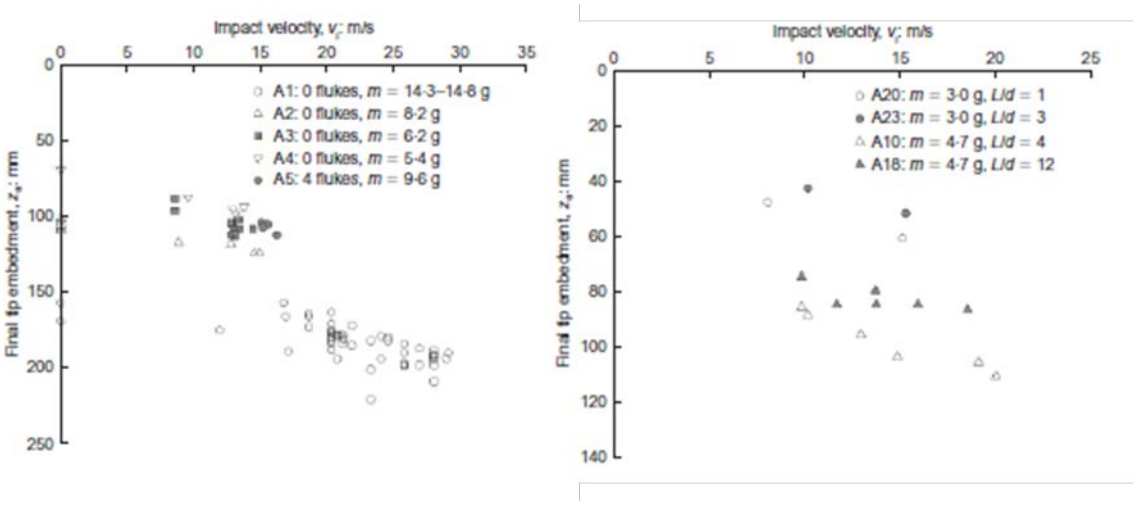

Figure 2.33. Centrifuge Test results with DPA (O'Loughlin et al., 2013b)

2.3.6 Omni-Max Anchor

2.3.6.1 Field Tests

Full-scale OMNI-Max anchor test was performed at Green Canyon in Gulf of Mexico. The tested anchor is 9.7m long and weight is 38 t. Shelton (2007) summarized that the water depth at the test site is around 1650 m. However, there is no detailed soil characterization information.

The anchor was dropped from 76 m above sea level, and penetrated 12m (39.4 ft) (1.2 fluke length) measured at the tip. Zimmerman et al. (2009) published OMNI-Max installation for MODU. The length of anchor is 9.15 m (30 ft) , the fluke is 2.9 m (9.5 ft), and the weight is 39 tons (85 kips). The tip embedment of anchor is around 1.17 to 2 fluke length at the initial installation. After a hurrican, post analysis showed that anchor rotated about 45°, with the tip embedment 2 flukes deeper.

2.3.6.2 Scaled Model Tests

Gaudin et al. (2013) performed a series of centrifuge tests in overconsolidated kaolinite with a shear strength gradient of 1.1 kPa/m (23 psf/ft) and calcareous silt. The fluke length is 34 mm (1.34 inches) and width of fluke is 16 mm (0.63 inches). The tests in silt showed that higher impact velocity leads to a deeper tip penetration, however, the restuls in kaolinite shows more scatter which might caused by the mooring line (Figure 2.34).

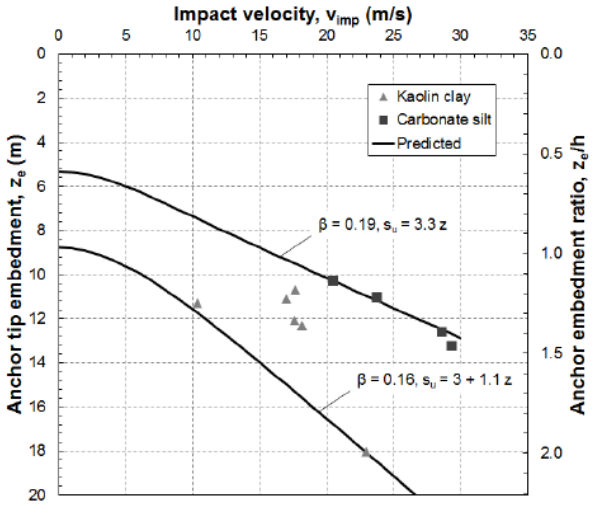

Figure 2.34. Centrifuge Tests Results with OMNI-Max Anchor (Gaudin et al., 2013)

2.3.7 Suction Embedded Plate Anchor (SEPLA)

2.3.7.1 Field Tests

Wilde et al. (2001) reported that CSO AMC designed and fabricated a SEPLA with a scale of 1:4 but with a full-sized follower in 1998. CSO AMC aimed to use this small scaled SEPLA with full-sized follower to confirum the follower installation, capacity and recoverility. After successful testing the follower at Gulf of Mexico Ship Shoal Area Block 332, the AHV Seacor Vanguard and the CAHT Dove successfully deployed a full size SEPLA at Mississippi Canyon Block 126 (MC-126). The test site had water depth of 1300 m (3280 ft). The final embedment depth of SEPLA was 25 m (82 ft). The SEPLA was first applied to taut leg mooring JIP on the MODU Ocean Victory. For this SEPLA, the embedment depth was 35 to 36 ft, and the tension at the runing-line tensionmeter (RLT) was 380 kips which was consistetn with prediction of 375 kips.

2.3.7.2 Scaled Model Tests

In 1998, CSO AMC performed small-scaled model test with SEPLA in Laponite for subsequent development of SEPLA (Wilde, 2001). Gaudin (2006) performed a series of centrifuge tests with $1/145^{th}$ scaled SEPLA in normally consolidated clay. The SEPLA plate in this study is a square plate with 35 mm (1.34 inch) high and 1 mm (0.04 inch) thick, which is equivalent to 5.075 m (16.6 ft) high and 0.145 m (0.45 ft) thick prototype SEPLA. The surface of the anchor was smooth. The 1 mm thick triangular-shaped plate represented the shank and the padeye on the shank was located with 23 mm eccentricity (66% relative to the anchor height). The purpose of making the padeye with eccentricity was to avoid the padeye leveling up with the caisson tip. From Gaudin (2006)'s tests, the embedment loss of plate was between 0.9 to 1.5 anchor height. Gaudin (2006) concluded that the embedment loss strongly was correlated with the padeye chain

inclination. Thus, keying the plate anchor at a lower inclination angle may reduce the embedment loss.

2.3.8 Dynamically Embedded Plate Anchor (DEPLA)

2.3.8.1 Field Tests

Blake et al. (2015) conducted a field test with DEPLA which has 9-m (29.5 ft) follower, 0.72-m (2.4 ft) flukes and 37 t (81.6 kips) in dry weight. The test site was located in Lower Lough Erne, a glacial lake in County Fermanaph, Northern Ireland. The soil is normally consolidated soft clay with shear strength gradient of 1.5 kPa/m (31.33 psf/ft), and moisture content of 270% to 520%, plastic limits of 130% to 180%, and liquid limits of 250% to 315%. The load-displacement measured in the field is consistent with the model centrifuge tests, and N_c from field tests (14.3 to 14.6) is close to N_c (15) from centrifuge tests. However, the embedment loss in field tests during keying was 1D to 1.8D, which is higher than the centrifuge data (0.7D).

2.3.8.2 Scaled Model Tests

O'Loughlin et al. (2014) performed a seried of centrifuge tests with DEPLA with cylindrical fins and square fins. The follower length is ranging from 51 mm (2 inches) to 76 mm (3 inches), and the diameter of fluke is around 16 mm (0.63 inches) to 30 mm (1.18 inches). The tests were conducted under 200g, which makes the model anchor equivalent to 10.3 m (33.8 ft), 15.2 m (50 ft), and 20.3 m (66.6 ft) respectively. The centrifuge tests results presented that DEPLA had similar behavior as DPA during installation process, and can reach a similar penetration depth which is 1.6 to 2.8 fluke length. After installation, the follower is retrieved, and the fluke rotates

into the perpendicular position to service load. The load measrued from retrieval process of follower was 3 times smaller than the anchor self weight. The load-displacement curve of keying and pull-out response contains three stages: stiff response at the beginning of keying, softening response afterwards when rotation angle increases, and stiff response again when the full capacity of fluke mobilizes. The loss of embedment is 0.5B to 0.66B during keying. The bearing capacity factor is between 14.2 to 15.8.

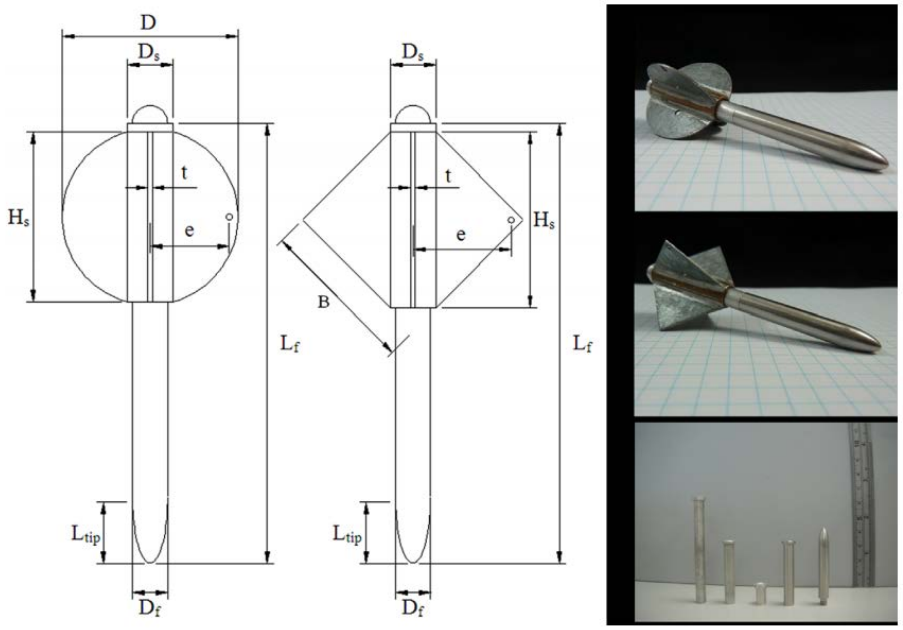

Figure 2.35. 1:200 DEPLA (O'Loughlin et al., 2014)

2.3.9 Flying Wing Anchor®

2.3.9.1 Field Tests

In December 2015, the scaled Flying Wing Anchor® in Paloma design was tested in Scottish Sea. The main purpose of testing Flying Wing Anchor® in Paloma is to evaluate the coupling mechanism underwater. Before deploying Paloma, the behavior of the coupling mechanism was

checked first in the air (Figure below). From the field tests, the Paloma was successfully embedded, but was not dragged to penetrate deeper afterwards. Moreover, due to the malfunction of measuring equipment, the tests data regarding on anchor capacity and embedment depth were unavailable.

Figure 2.36. Flying Wing Anchor® in Field Test (Jose Eugenio Iturriaga Flores, 2016)

2.3.9.2 Scaled Model Tests

Gerkus (2016) performed a series of scale model tests with three different designs of Flying Wing Anchor®, the Diamond, the Paloma, and Speedy (Figure 2.37). All three model anchors were printed by 3D printer. The Diamond model had a fluke area of 11.44 in^2, and weight of 0.114 lbs and fluke thickness between 0.1-0.75 inches. The Paloma model anchor had a fluke area of 12 in^2, and weight of 0.12 lbs. The Speedy had a fluke area of 9.7 – 19.29 in^2, and weight of 0.2 lbs. The anchor loading line thickness was a 0.025 in diameter nylon rope.

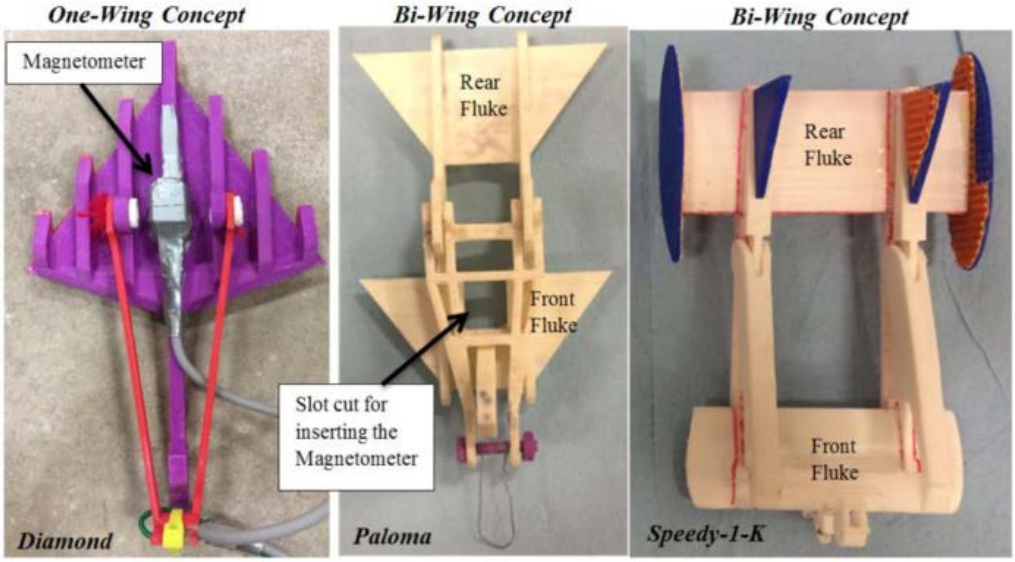

Figure 2.37. Scaled Model Flying Wing Anchor® (Gerkus, 2016)

For the Diamond Anchor, Gerkus (2016) concluded that the anchor dove deeper and the pitch angle increased. Gerkus (2016) placed the anchor with initial pitch of 45 degree and depth with 0.8 fluke width or 1.5 fluke width below mudline, and the final embedment depth was 1.4 fluke width or 2.1 fluke width. One example tests results for the Diamond are shown in Figure 2.38. For the Paloma Flying Wing Anchor® testing, the anchor line was loaded at 0.04 in/sec before the shank being released, and the loading rate was 0.8 in/sec. The tests results show that shank was released with the load at 4.2 lbs and pitch at 52 degrees. After the shank being released, the load dropped to 1.9 lbs. Correspondingly, the equilibrium capacity factor dropped from 4 to 1.8 at the point where shank was released. One example tests results for the Paloma are shown in Figure 2.39. The Speedy anchor was embedded 0.6 fluke width to 1.2 fluke width initially, and the equivalent bearing capacity factor for the Speedy was 10-12. One example tests results for the Speedy anchor is shown in Figure 2.40

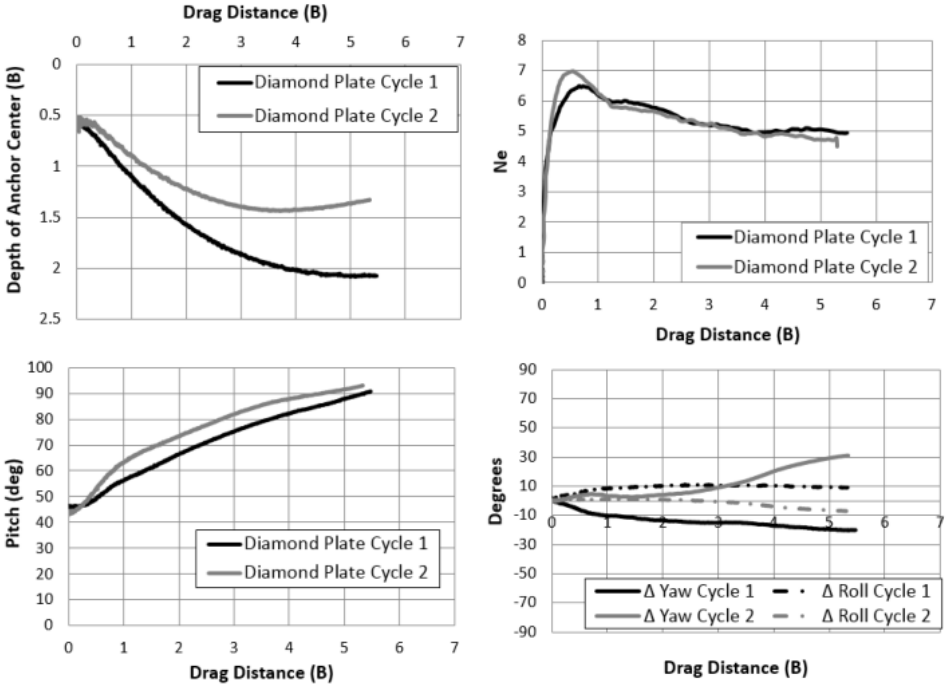

Figure 2.38. Example Tests Results with Diamond-Shaped Flying Wing Anchor® (Gerkus, 2016)

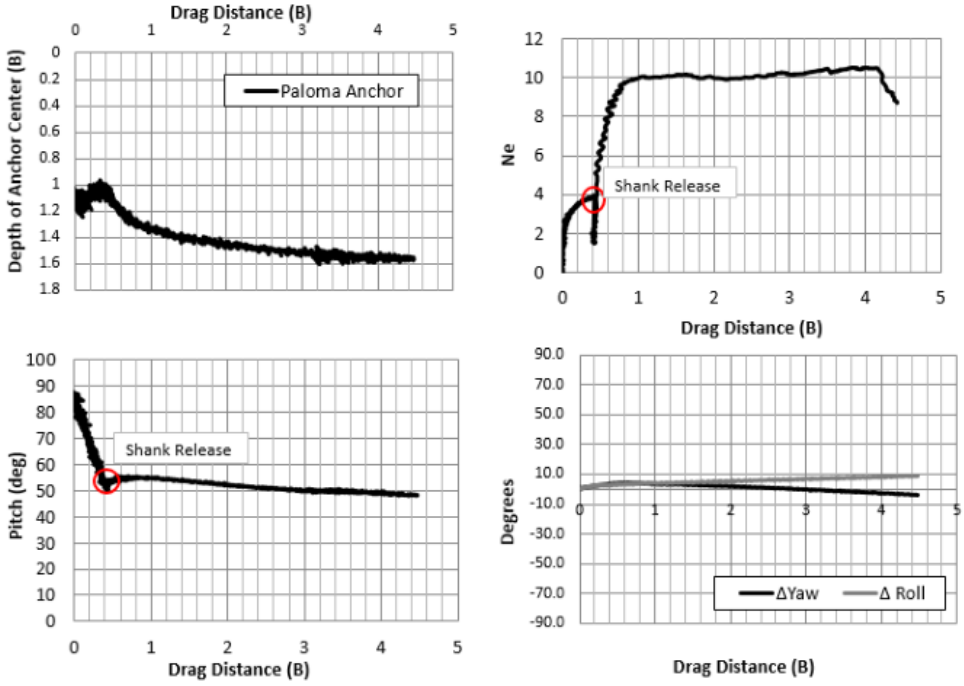

Figure 2.39. Example Tests Results with Paloma Flying Wing Anchor® (Gerkus, 2016)

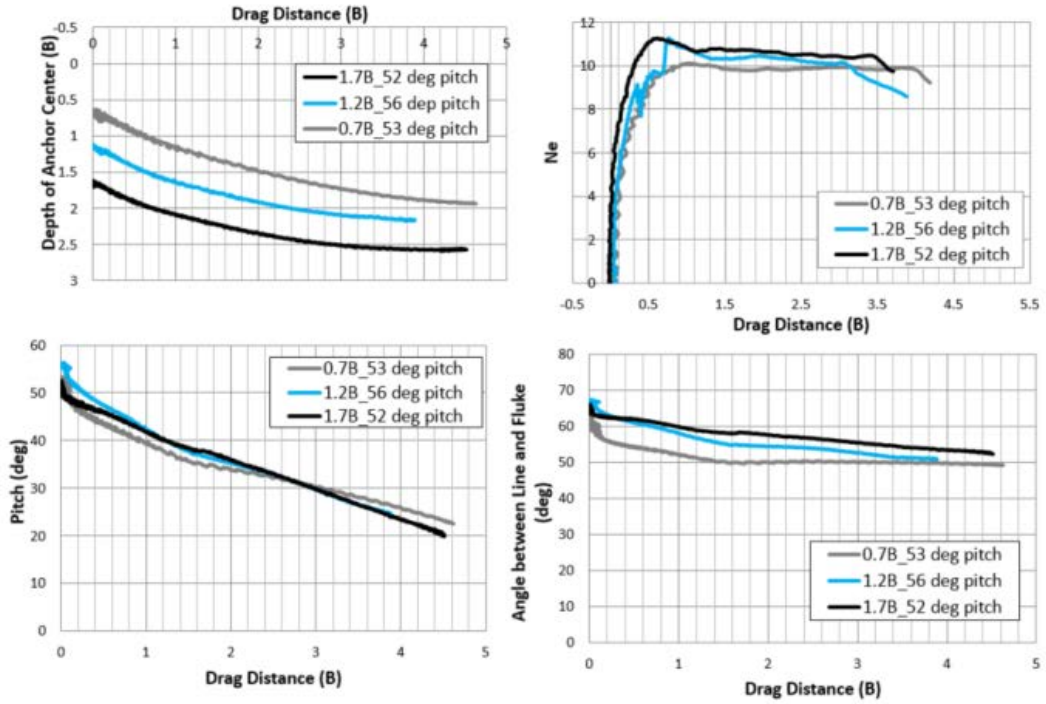

Figure 2.40. Example Tests Results of Speedy Flying Wing Anchor® (Gerkus, 2016)

2.4 Embedment Prediction Methods

In this section, the embedment prediction methods for drag embedment anchors and free-fall penetration anchors are briefly reviewed. For the drag embedment anchor prediction methods, empirical method, limit equilibrium method, plastic limit method, and upper bound collapse load method are reviewed. For the free-fall penetration prediction, Young's method, Ove Arup and Partners method, True's method, and modified True's method are reviewed.

2.4.1 Drag Embedment Prediction Methods

2.4.1.1 Empirical Method - Design Chart

The empirical method was designed to estimate holding capacity and embedment depth of a specific type of anchor. The chart was developed based on empirical equation and regression of tests data. This section briefly summarized the current design charts commonly used for different types of drag embedment anchors.

2.4.1.1.1 NCEL Method

Naval Civil Engineering Laboratory (NCEL) developed an empirical design chart for different types of anchors. From experiences, the holding capacity is related to the self weight of anchor. This relation was regressed as

$$F = a \times \left(\frac{W_a}{C}\right)^b \qquad \text{Eq.(2.1)}$$

where F is the anchor capacity in kips

a is a parameter for type of anchor in kips

W_a is the anchor weight in kips

b is a dimensionless parameter for type of anchor

C is a constant parameter equal to 10 kips

Figure 2.41 shows the capacity estimate design chart by NCEL. The capacity of anchor can be estimated by either calculating based on Equation 2.1 or finding the line corresponds with the designed anchor in log-log plot shown in Figure 2.41. For example, if we estimate capacity of

Bruce FFTS anchor, then a = 250 kips, and b = 0.92; if we estimate capacity of Vryhof Stevpris, then a = 189 kips, and b = 0.92. However, it is well known that the drag embedment capacity depends on the drag distance because a further drag makes anchor dives deeper which makes higher soil bearing on fluke and resistance on shank due to the higher undrained shear strength form normally consolidated profile. Therefore, NCEL (1997) proposed another chart for different types of anchor for estimate capacity at a certain drag distance. The drag distance in this chart is normalized by fluke length, and the estimated capacity is normalized total capacity from Figure 2.41.

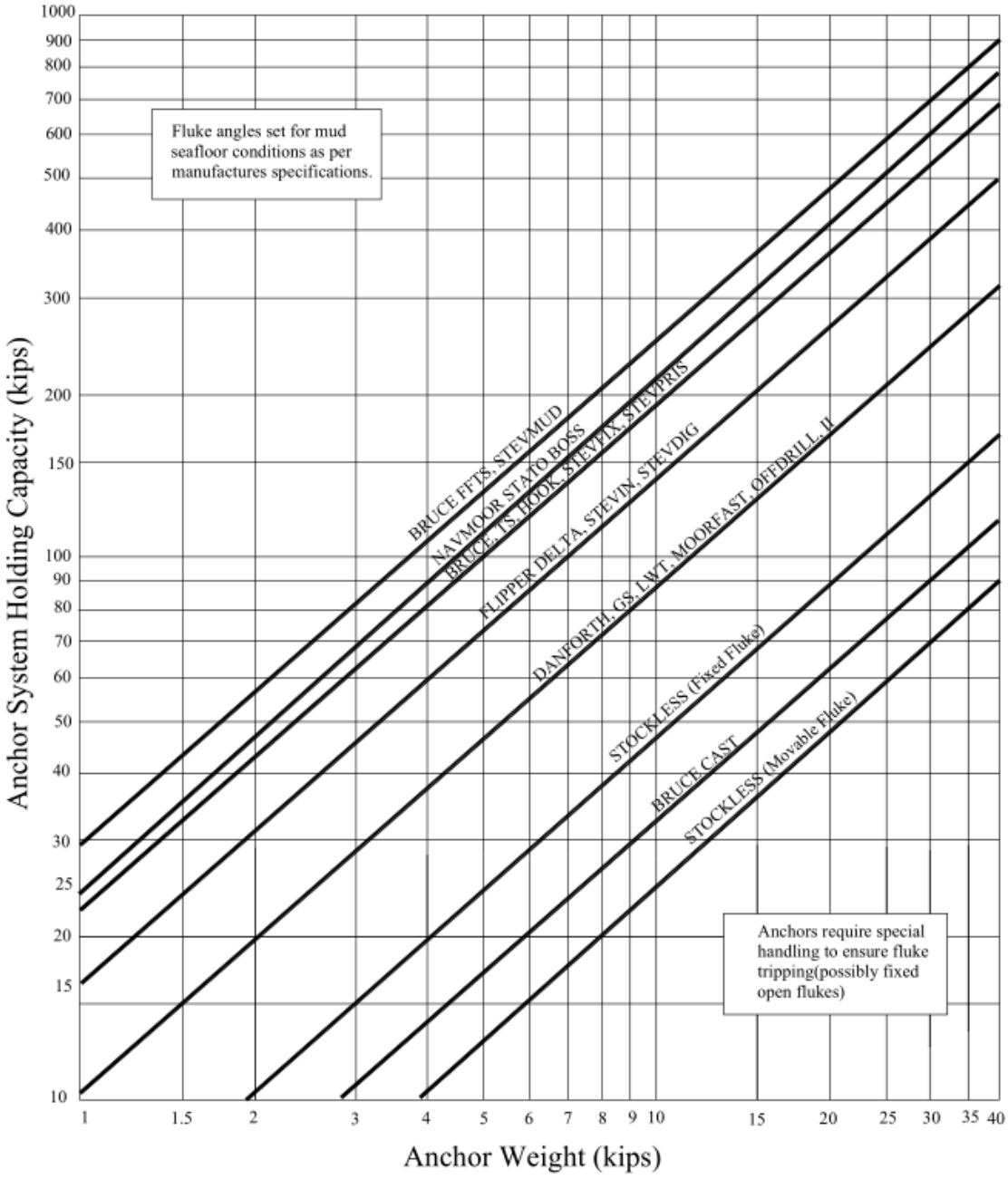

Figure 2.41. NCEL Design Chart (NCEL, 1987)

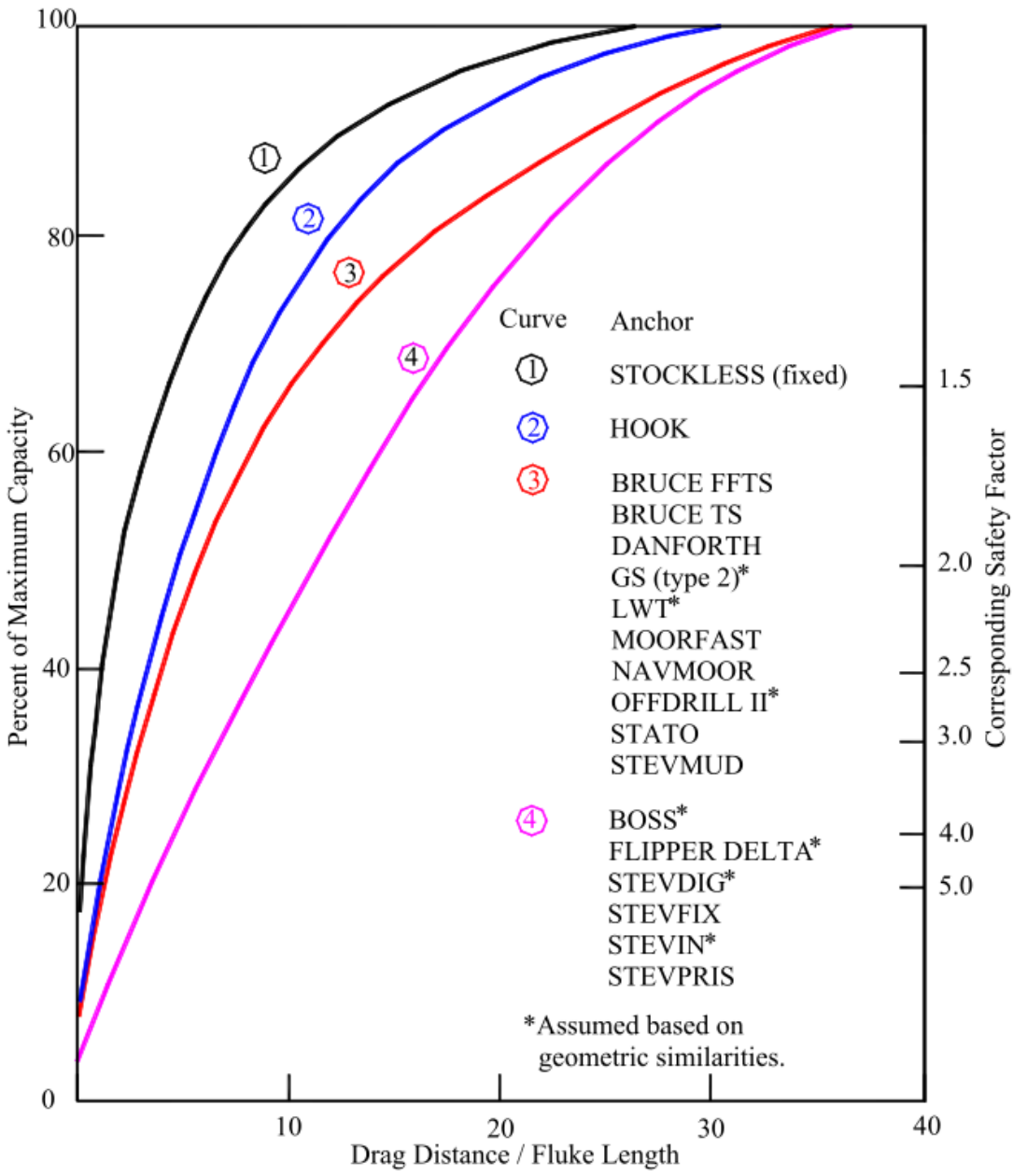

Figure 2.42. Anchor Capacity in Terms of Drag Distance (NCEL, 1987)

2.4.1.1.2 Vryhof Anchor Method

Vryhof Anchor (2010) developed empirical design chart and table to estimate holding capacity in terms of drag embedment depth. Similar to design chart by NCEL (1987), the design chart for

each anchor is different. However, the difference is that Vryhof takes the soil condition into the estimate of holding capacity. For example, the holding capacity curve for the same anchor is different in sand or hard clay, medium clay and very soft clay (Figure 2.43). The holding capacity read from the chart is the maximum holding capacity which corresponds with the deepest penetration depth. However, this extreme condition may not be reached during installation. Thus, a table to correct the maximum holding capacity was proposed (Table 2.5). The correction is based on the percentage of current drag distance over maximum drag distance.

Table 2.5. Correction Factor for Vryhof Anchor (Vryhof, 2010)

Anchor load as percentage of UHC	Drag as of percentage maximum drag distance	Penetration as percentage of maximum penetration depth
70	48	80
60	37	68
50	27	55
40	18	42
30	9	23

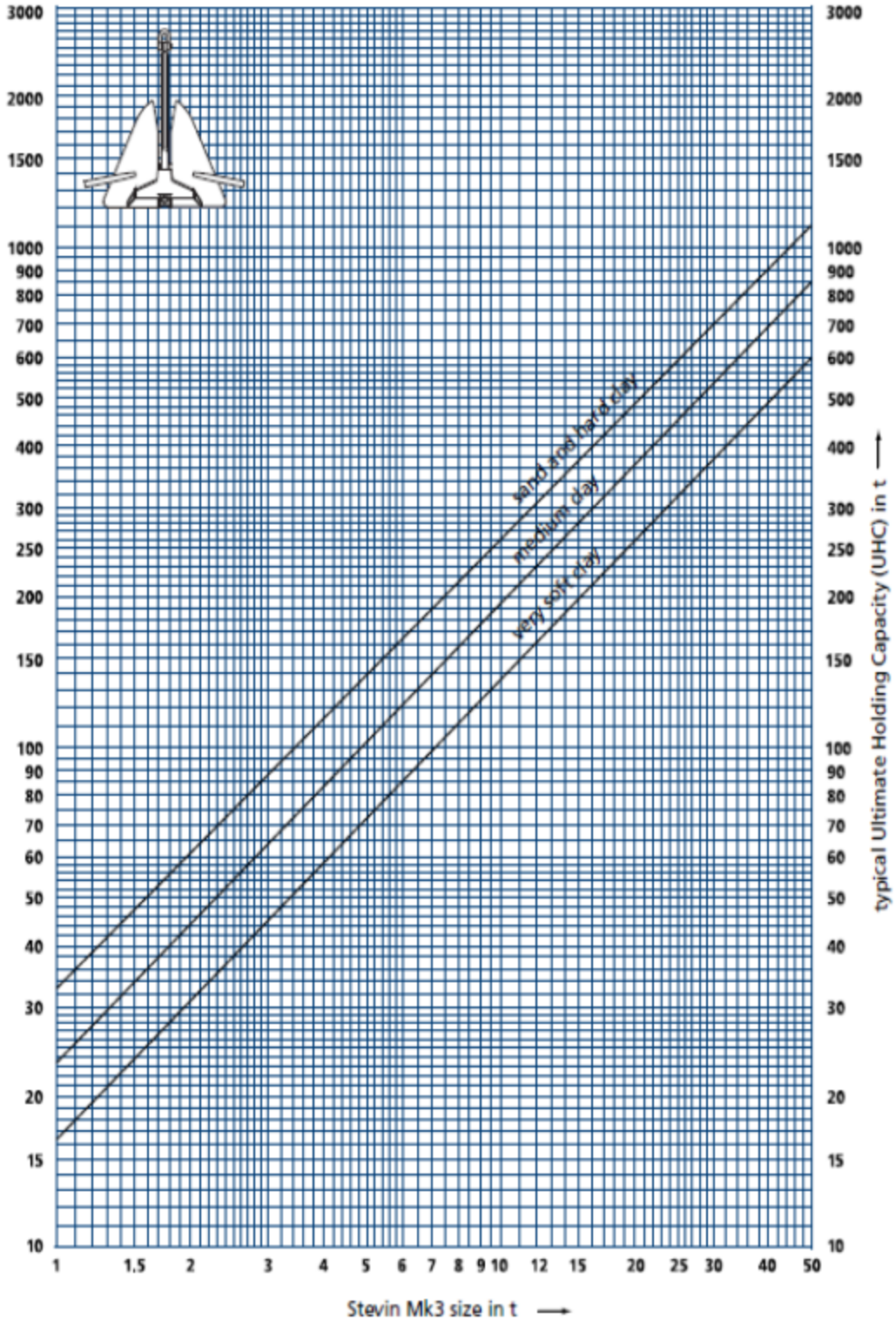

Figure 2.43. Vryhof Design Chart for Stevin MK3 Anchor (Vryhof, 2010)

2.4.1.1.3 Bruce Anchor Method

Similar to design chart by NCEL and Vryhof, the proposed design chart by Bruce also depends on anchor weight. The major difference of Bruce design chart is taking thickness of mooring line into capacity estimation. One example of design chart for Bruce PM Anchor is shown in Figure 2.44. The corresponding empirical equation is shown in Equation 2.2 to 2.4.

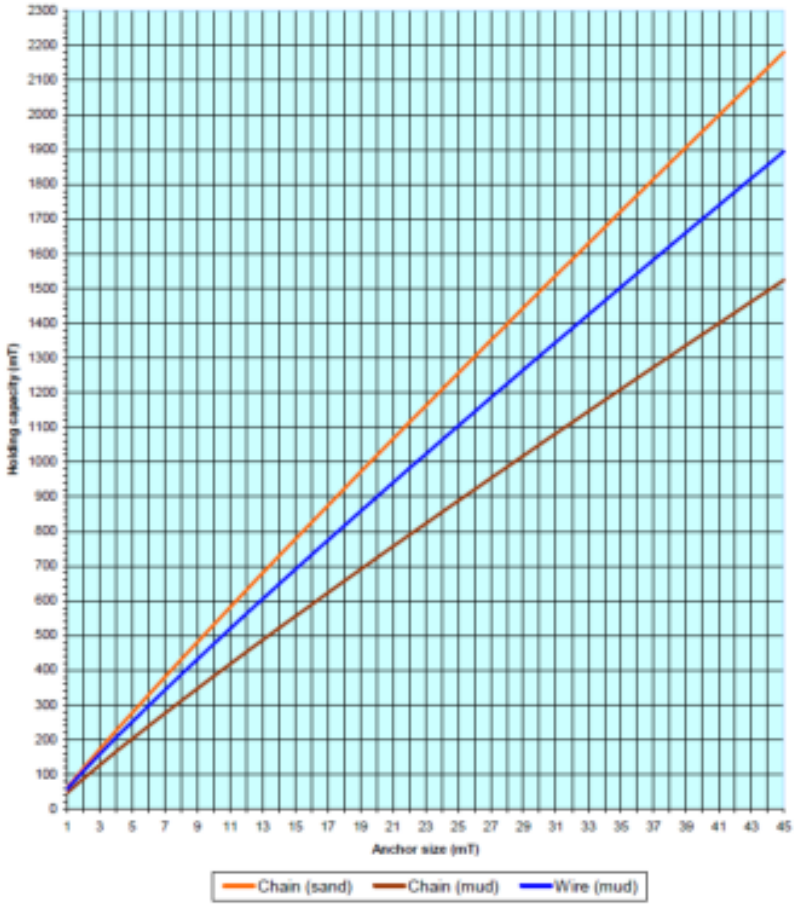

Figure 2.44. Brace PM Anchor Design Chart (Courtesy by Bruce Anchor)

$$HC_{(chain/sand)} = 60.92\ W^{0.94} \qquad \text{Eq.(2.2)}$$

$$HC_{(chain/mud)} = 45.94\ W^{0.92} \qquad \text{Eq.(2.3)}$$

$$HC_{(wire/mud)} = 57.11\ W^{0.92} \qquad \text{Eq.(2.4)}$$

2.4.1.2 Limit Equilibrium Method

Limit equilibrium method for predicting anchor trajectory, capacity and pitch along drag is assumed that the forces on anchor are in equilibrium at any point of horizontal drag. Different researchers have different assumptions of the magnitude of soil resistance as well as the direction and location applied. In this section, limit equilibrium method proposed by Neubecker and Randolph (1996b) and Throne (1998) is briefed reviewed.

2.4.1.2.1 Neubecker and Randolph

Neubecker and Randolph (1996) proposed a limit equilibrium approach based on static and kinematic behavior of drag anchor in cohesive soil (Stewart, 1992) and sand (Lelievre and Tabatabaee, 1981). In this approach, it was assumed that soil resistance on a weightless anchor is a function of undrained shear strength, static bearing capacity, and the frontal projected area in the direction of movement. Coupling with chain solution by Neubecker and Randolph (1995), the tension at padeye, anchor trajectory and orientation can be achieved.

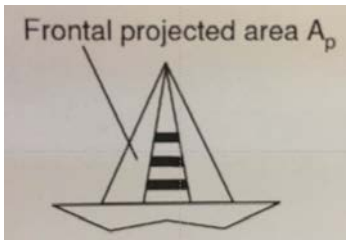

Figure 2.45. Frontal Projected Area A_p (Randolph and Gourvenec, 2011)

The forces acting an anchor is shown in Figure 2.46. T_p is the soil resistance parallel to fluke, and can be calculated by Equation 2.5. For a weightless anchor, a bearing force normal to fluke, T_n, combines with T_p, a resultant force T_w can be determined based on Equation 2.6. T_w at shackle makes anchor oriented to θ_w, which changes over horizontal drag. During embedment, there will be an angle between the fluke and the horizontal, which is defined as β. The angle between Tw and Ta is defined as ψ. Then, the angle at padeye, θ_a, can be calculated (Equation 2.7). It should be noted that T_w is independent with anchor weight; however, T_a, the tension at padeye depends on weight of anchor.

$$T_p = \text{f } A_p N_c s_u \qquad \text{Eq.(2.5)}$$

where f is the a from factor for anchor, which can be considered as the correction factor for bearing capacity factor N_c

A_p is projected anchor area in the direction of movement (Figure 2.45)

N_c is bearing capacity factor (commonly use 9)

S_u is the local undrained shear strength

$$T_w = \frac{T_p}{cos\ (\theta_w)} \qquad \text{Eq.(2.6)}$$

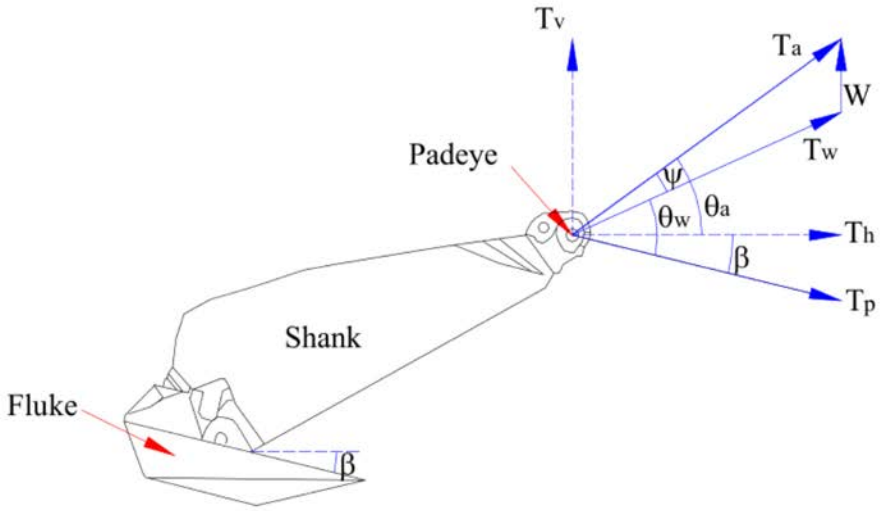

Figure 2.46. Force Acting on an Anchor (Neubecker and Randolph, 1996)

$$\theta_a = \theta_w + \psi - \beta \qquad \text{Eq.(2.7)}$$

The trajectory, capacity, and orientation of anchor is calculated by the following steps:

1. At the initial embedment, we know the fluke angle β.
2. Advance a horizontal increment, Δx, then the embedment depth, Δz, at this horizontal increment can be calculated.
3. Calculate the resistance parallel to fluke by Equation 2.5, and the angle at padeye by Equation 2.7, and tension at padeye by using force polygon formed by T_w and anchor weight (Figure 2.46).
4. Advance anchor movement to another increment Δx then repeat from step 2.

2.4.1.2.2 Throne (1998)

Throne (1998) proposed an equilibrium limit method to describe anchor movement in terms of its orientation and location. This method assumed that anchor will move until the it overcame the soil resistance parallel to fluke. The general drag force on an anchor is shown in Figure 2.47 and can be expressed as

$$\text{drag} = DA_i\, DF_i\, S_u \qquad \text{Eq.(2.8)}$$

where DA_i and DF_i is the area and drag factor for the ith component.

These small components drag force will be added to calculate the total drag forces as shown in Figure 2.48 by Equations 2.9 to 2.11.

$$\text{TDFN} = \sum_{i=1}^{i=n} -DA_i DF_i s_u \sin\alpha_i \qquad \text{Eq.(2.9)}$$

$$\text{TDFP} = DA_f \cdot DF_f \cdot S_u + \sum_{i=1}^{i=n} DA_i DF_i s_u \cos\alpha_i \qquad \text{Eq.(2.10)}$$

$$\text{TDFM} = \sum_{i=1}^{i=n} DA_i DF_i s_u \cos\alpha_i \cdot (Distx_i \cdot \sin\alpha_i + Disty_i \cdot \cos\alpha_i) \qquad \text{Eq.(2.11)}$$

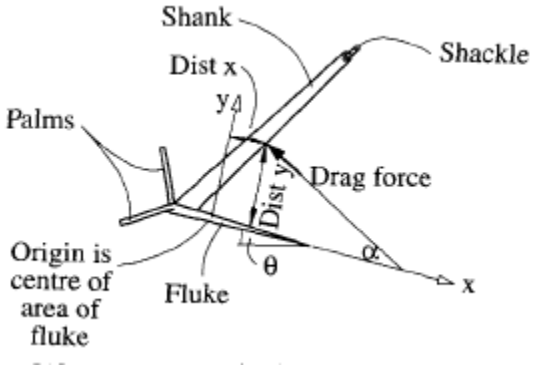

Figure 2.47. Elements for Conventional Anchor (Throne, 1998)

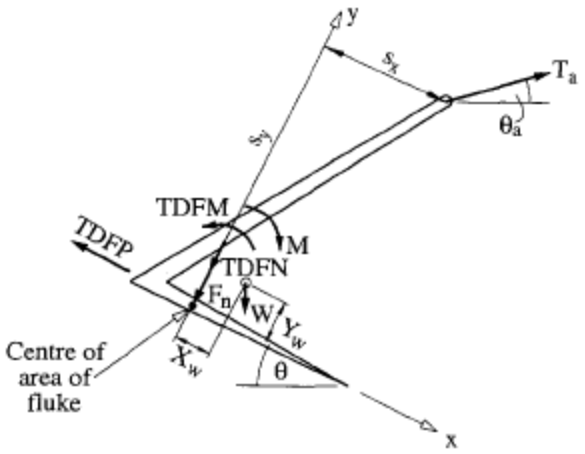

Figure 2.48. Equilibrium of Anchor During Penetration

If an anchor with fluke angle, θ, and the chain angle at the shackle θ_a, Throne (1998) set a rule that anchor stays static condition unless anchor overcomes all components of the soil resistance which is normal, parallel, and moment. At the moment where anchor is about to move, he assumed all the forces are in equilibrium state. The expressions about normal, parallel forces and moment are shown in Equation 2.12 to 2.14.

$$T_a \cos(\theta + \theta_a) = \text{TDFP} - W \sin\theta \qquad \text{Eq.(2.12)}$$

$$F_n = T_a \sin(\theta + \theta_a) - W \cos\theta - \text{TDFN} \qquad \text{Eq.(2.13)}$$

$$\text{M} = \text{T}_\text{a}\,(\text{S}_\text{x} \sin(\theta + \theta_a) - \text{S}_\text{y} \cos(\theta + \theta_a)) + \text{TDFM} - W\,(\text{Y}_\text{w} \sin\theta + \text{X}_\text{w} \cos\theta) \qquad \text{Eq.(2.14)}$$

2.4.1.3 Plastic Limit Method

O'Neill et al. (2003) proposed a prediction method for anchor trajectory based on the yield loci and plastic potential framework. This method was investigated by finite element analysis on the

interaction between anchor fluke and soil. For a given foundation and soil property around the foundaiton, the yield locus is

$$f(V, H, M) = 0 \qquad \text{Eq.(2.15)}$$

This mathematical expression of yield locus can be plotted as shown Figure 2.49 if only vertical and horizontal load applied (M=0). Chen (1975) assumed that soil interacted with foundation obeys normality rule, and Bransby and Randolph (1998) confirmed this assumption through finite element analysis on combined loading subjected to a skirt foundation. This approcach was applied to offhsore foundation by Martin and Houlsby (2001). Thus, it was verified that there is no volumne change in plastic flow for soil in undrained condition.

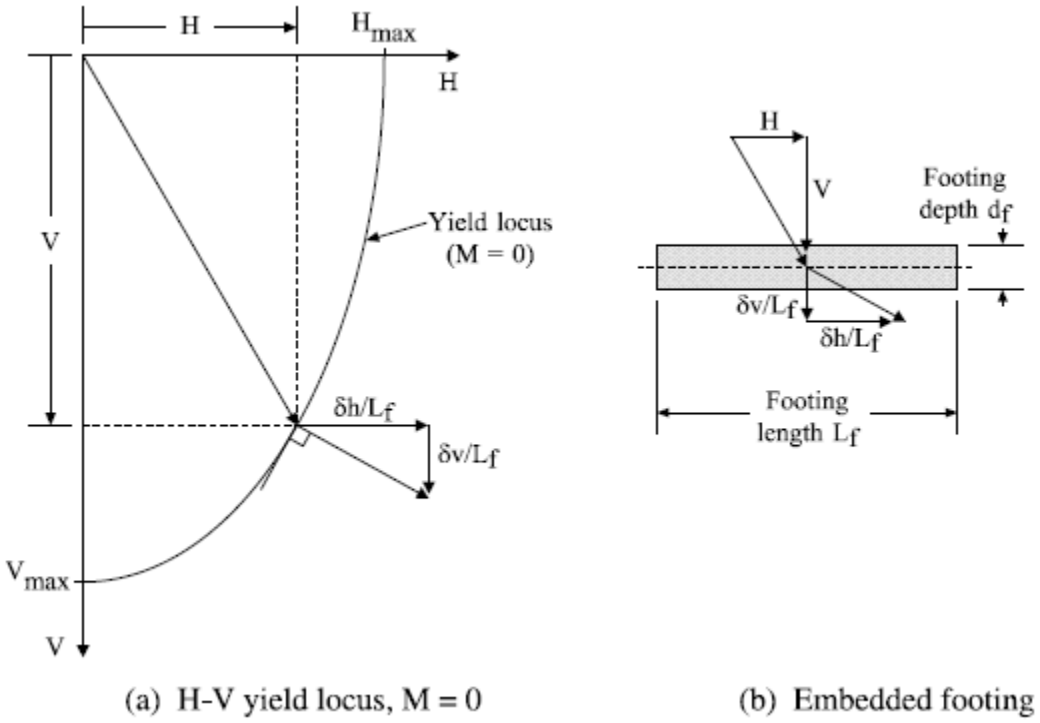

Figure 2.49. The Yield Locus and Plastic Potential Function (O'Neill et al., 2003)

O'Neill et al. (2003) extended this plastic framwork to a deeply embedded drag anchor. To simplify the analysis, he assumed that the anchor is weightless plate without shank as well as assumming chain load at padeye is subjected to a reference point on fluke. This weightless anchor without shank are under a loading conidion with force parallel (H) , force perpendicular (V), and moment (M) as shown in Figure 2.50. Anchor experineces with the subjection of H, V and M, the anchor experiences failure and moves parallely to fluke (δh), perpendicular to fluke (δv), and rotatiaonally to fluke ($\delta \beta$) about the same point on the fluke (Figure 2.49).

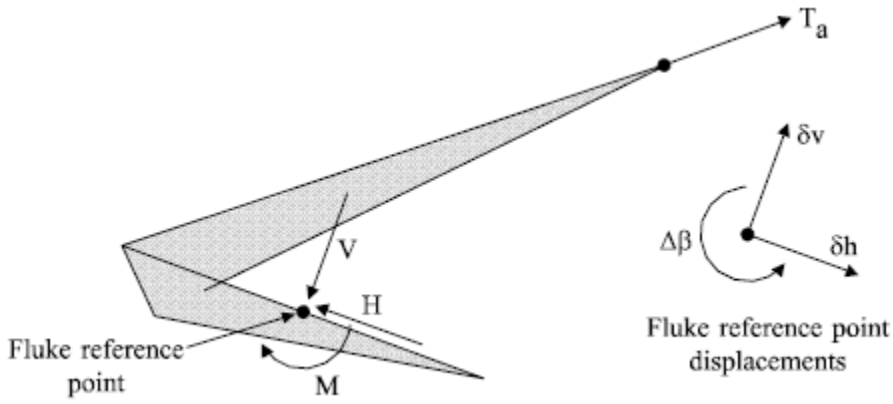

Figure 2.50. Loads and Displacements at Failure for a Simplified Drag Anchor (O'Neill et al., 2003)

Murff (1994) proposed an offset form of yield loci which gives the best fit to the anaylsis results (Equation 2.16)

$$f = \left(\frac{V-V_1}{V_{max}-V_1}\right)^q + \left[\left(\frac{M-M_1}{M_{max}-M_1}\right)^m + \left(\frac{H-H_1}{H_{max}-H_1}\right)^n\right]^{\frac{1}{p}} - 1 = 0 \quad \text{Eq.(2.16)}$$

The maximum vertical load (V_{max}), horizontal load (H_{max}), and moment (M_{max}) are shown in Equation 2.17 to 2.19 , respectively. The offset vertical load (V_1), horizontal load (H_1), moment (M_1) were from finite element analysis. The interaction coefficients, m, n, p, and q are obtained by least square regression (Table 2.6).

$$\frac{V_{max}}{L_f s_u} = 4\left(\pi - \alpha + \frac{\tan\alpha}{2}\right) + 4\frac{d_f}{L_f}\left(\frac{1}{2} + \cos\alpha\right) \quad \text{Eq.(2.17)}$$

$$\frac{H_{max}}{L_f s_u} = 4\frac{t}{L_f}\left(\pi - \alpha + \frac{\tan\alpha}{2}\right) + 4\left(\frac{1}{2} + \cos\alpha\right) \quad \text{Eq.(2.18)}$$

$$\frac{M_{max}}{L_f^2 S_u} = \frac{\pi}{2}\left[1 + \left(\frac{t}{L_f}\right)^2\right] \quad \text{Eq.(2.19)}$$

where L_f is the length of fluke

t is the thickness of fluke

α is the angle of rigid wedge (shown in Figure 2.51 and Figure 2.52)

Table 2.6. Interaction Coefficients

	Bransby and O'Neil (1999)	Elkhatib and Randolph (2005)	Murff et al. (2005)	Gilbert et al. (2009)	Yang et al. (2010)
m	1.26	2.58	1.56	1.56	1.35
n	3.72	3.74	4.19	4.19	3.11
p	1.09	1.09	1.57	1.57	1.38
q	3.16	1.74	4.43	4.43	4.3

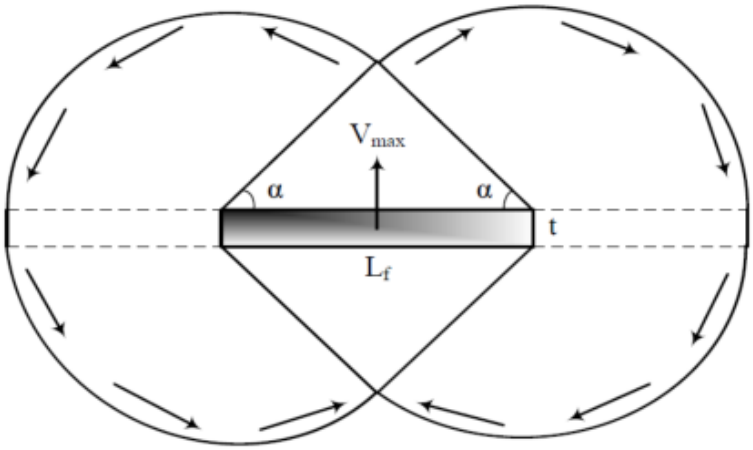

Figure 2.51. Upper Bound Mechanisms of Simplified Anchor Subjected by Pure Normal Load (O'Neill et al., 2003)

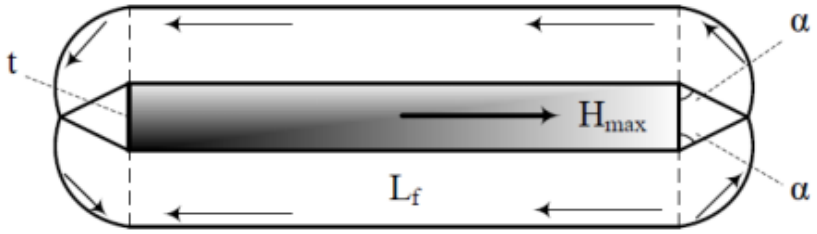

Figure 2.52. Upper Bound Mechanisms of Simplified Anchor Subjected by Pure Shear Load (O'Neill et al., 2003)

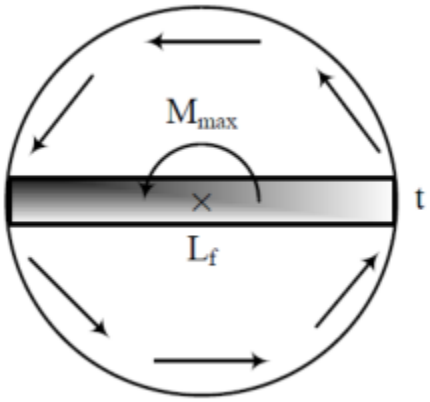

Figure 2.53. Upper Bound Mechanisms of Simplified Anchor Subjected by Pure Rotational Moment (O'Neill et al., 2003)

Figure 2.51 to Figure 2.53 presents the upper bound mechanisms for an anchor without shank. The movement of anchor is controlled by the direction which is normal to the yield locus. With the assumption of the associated flow rule, the vertical displacement increment relative to the horizontal displacement increment and the rotational movement to horizontal displacement increment is shown as following:

$$\frac{\delta v}{\delta h} = \frac{\delta f}{\delta V} \Big/ \frac{\delta f}{\delta H} \qquad \text{Eq.(2.20)}$$

$$\frac{\delta \beta}{\delta h / L_f} = \frac{\delta f}{\delta(\frac{M}{L_f})} \Big/ \frac{\delta f}{\delta H} \qquad \text{Eq.(2.21)}$$

The horizontal displacement increment is determined in advance, then the vertical and rotational movement of anchor fluke can be updated by the following equations:

$$\Delta v = (\frac{\delta f}{\delta V} \Big/ \frac{\delta f}{\delta H})\, \Delta h \qquad \text{Eq.(2.22)}$$

$$\Delta \beta = (\frac{\delta f}{\delta(\frac{M}{L_f})} \Big/ \frac{\delta f}{\delta H})\, (\Delta h \,/\, L_f) \qquad \text{Eq.(2.23)}$$

2.4.1.4 Upper Bound Collapse Load Analysis

Aubeny et al. (2008) developed an anchor trajectory and load prediction method based on the anchor line solution by Neubecker and Randolph (1995) and the capacity solution by upper bound collapse load analysis. The anchor chain solution is shown below

$$\frac{T_a\,(\theta_a^2 - \theta_0^2)}{2} = \mathrm{z}E_n N_c \mathrm{b}\; (N_c b\; (S_{u0} + \mathrm{kz}/2) \qquad \text{Eq.(2.24)}$$

where T_a is the anchor line tension at shackle

θ_a is the anchor line angle from horizontal at shackle point

θ_0 is the anchor line angle from horizontal at mudline

E_n is the multiplier to be applied to chain diameter

N_c is the bearing factor for anchor line

b is diameter of anchor line

S_{u0} is the undrained shear strength at mudline

k is the shear strength gradient

z is the depth

The line angle θ_a at the shackle can be calculated as

$$\frac{d\theta_a}{d\hat{z}} = \frac{\frac{E_n N_c}{\hat{T}_a} - \frac{\theta_a^2 - \theta_0^2}{2\left(\frac{1}{\eta} + \hat{z}\right)}}{\left(\theta_a - \theta_0 \frac{d\theta_0}{d\theta_a}\right) + \frac{1}{\hat{T}_a} \frac{d\hat{T}_a}{d\theta_{as}} \frac{\theta_a^2 - \theta_0^2}{2} \left(1 - \frac{d\theta_s}{d\theta_a}\right)} \qquad \text{Eq.(2.25)}$$

where $\hat{z}$ is the normalized depth of shackle = z/b

$\hat{T}_a$ is the normalized tension at shackle = $T_a / s_{ua} b^2 = N_e A_f / b^2$; and s_{ua} is the soil shear strength at shackle, and N_e is the equilibrium bearing capacity factor which is the capacity factor when anchor is in the equilibrium condition.

$\frac{d\hat{T}_a}{d\theta_{as}}$ is the slope of anchor capacity curve

$\frac{d\theta_s}{d\theta_a}$ is the rate of change in mudline angle with respect to θ_a

η is the strength gradient parameter = bk/s_{u0}

The anchor trajectory can be calculated as following steps:

1. Set a movement Δt which is parallel to the fluke, and a fluke angle θ_f .

2. Calculate the horizontal and vertical displacement by combining the current rotational angle θ_f. $\Delta z = \Delta t \sin \theta_f$, $\Delta x = \Delta t \cos \theta_f$ (Figure 2.54). Moreover, the displacement normal to fluke can be calculated ($\Delta n = \Delta x \cdot \sin \theta_f - \Delta z \cdot \cos \theta_f$), and then the ratio of displacement normal to displacement parallel to fluke ($R_{nt} = \Delta n / \Delta t$) can be defined.
3. Calculated line angle by Equation 2.25.
4. Update fluke angle θ_f and anchor line angle at the next step θ_a

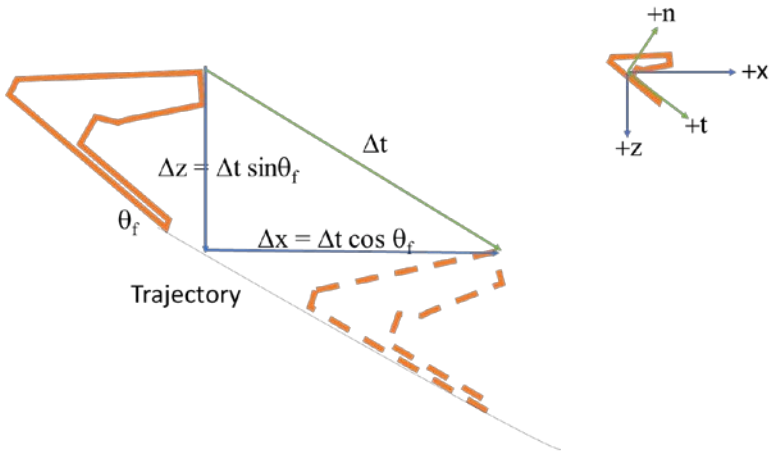

Figure 2.54. Sketch of Anchor Displacement

2.4.2 Free Fall Embedment Prediction Methods

For the free fall embedment prediction, four different methods are reviewed in this section. The Young's (1969) method was developed empirically based on database with full scale tests, Ove Arup and Partners Methods (1982) develop prediction for the disposal of radiactive waste in seabed sediment by free-fall penetrometer. True (1976) extended prediction for penetrometer based on Schmid (1969) and Migliore and Lee (1971). The widely applied prediction for penetrometer is the modified True's method.

2.4.2.1 Young's Method

Young (1969) proposed a prediction model for free-fall penetrometer based on an extensive database of full scale field tests. Revised prediction by Young (1981) and Young (1997) were porposed. Young (1969, 1981, and 1997)'s method:

1. is suitable for impact velocity less than 4000 ft/s
2. cannot accurately predict displacement and velocity within three fluke lengths
3. is not applicable for layered soil profile
4. is not applicable for weight less than 5 lb.

In a uniform soil, the displacement can be predicted by the following equation only if the velocity is less than 200 ft/s

$$z = 0.3\ SNK_s\ (\frac{m}{A_p})^{0.7} \ln\ (1+ 2\times10^{-5} v_i^2) \qquad \text{Eq.(2.26)}$$

If velocity is more than 200 ft/s

$$z = 0.00178\ SNK_s\ (\frac{m}{A_p})^{0.7} (v_i - 100) \qquad \text{Eq.(2.27)}$$

where z is the displacement

N is coefficient depends on the tip shape

For ogive shape tip

$$N = 0.18\ \frac{L_{tip}}{D} + 0.56 \qquad \text{Eq.(2.28)}$$

For a conical shape tip

$$N = 0.25 \frac{L_{tip}}{D} + 0.56 \quad \text{Eq.(2.29)}$$

v_i is the impact velocity in ft/s

m is the weight in lbs

A_p is the projected from area in ft^2

K_s is a correction factor for the penetrometer less than 60 lbs

$$K_s = 0.2m^{0.4} \quad \text{Eq.(2.30)}$$

S is the fitting parameter depends on the soil property shown in Table 2.7.

Table 2.7. Soil Penetrability of Typical Soil Types (Young, 1997)

Material	S
Dense, dry, cemented sand	2-4
Sand without cementation, very stiff and dry clay	4-6
Moderately dense to loose sand, no cementation	6-9
Soil fill material, various levels of compaction	8-10
Silt and clay, low to medium moisture content	5-10
Silt and clay, moist to wet	10-20
Very soft, saturated clay – very low shear strength	20-30
Clay marine sediments – Gulf of Mexico	30-60

The strain effect and fluke length is not included in Young's method, which leads to inaccurate prediction on shear strength of soil when penetrometer travelling through soil and inaccurate prediction of bearing and shearing force on penetrometer. In addition, the prediction highly depends on the determination of material factor, S, which makes difficult to extend Young's method to stiff materials such as stiff clay and rock.

2.4.2.2 Ove Arup and Partners Method

Ove Arup and Partners (1982) proposed a method to estimate the penetrometer embedment depth for a disposal of radiactive waste in seabed sediment by free-fall penetrometer. In the estimation method developed by Ove Arup and Partners (1982), there was no inertial drag effect included. The estimation contained separte prediction for full and partial penetration. The part for full penetration is brieftly reviewed here.

The projectile of penetrometer during free-fall process can be described by

$$-\mathrm{m}\frac{d^2z}{dt^2} = A_2\mathrm{z} + B_2 \qquad \text{Eq.(2.31)}$$

where A_2 and B_2 can be expressed as

$$A_2 = \frac{\pi D^2}{4} N_{ed}\ \mathrm{k} + \pi \mathrm{DLk}\alpha_d \qquad \text{Eq.(2.32)}$$

$$B_2 = \frac{\pi D^2}{4}\left(N_{ed}\ (S_{u,sea} + \mathrm{kL})\right) + \pi \mathrm{DL}\alpha_d\left(S_{u,sea} + \mathrm{k}\left(\frac{L}{2}\right)\right) - W_s \qquad \text{Eq.(2.33)}$$

and

$$N_{ed} = N_{cd} + \frac{N_{chd}}{S_t} \qquad \text{Eq.(2.34)}$$

where N_{cd} is the bearing capacity factor for penetrometer, and N_{cd} is resistance factor for dynamic trail, and S_t is the soil sensitivity.

By differentiate Equation 2.31, and modified by Poorooshasb and James (1989), the penetration depth can be expressed

$$Z = \frac{B_2}{A_2}(\cos(Kt) - 1) + \frac{V_i}{K}\sin(Kt) \qquad \text{Eq.(2.35)}$$

where $K = A_2/m$

The velocity then can be obtained by differentiating Equation ,

$$V = -(\frac{B_2}{A_2})K\sin(Kt) + V_i\cos(Kt) \qquad \text{Eq.(2.36)}$$

This method successfully predicted the velocity, bearing and resistance force during free-fall, however, it lacks the consideration of strain rate effect of soil shear strength caused by penetrometer travelling through soil with wide range of velocity.

2.4.2.3 True's Method

True (1976) developed a method based on Schmid (1969) and Migliore & Lee (1971) to predict free-fall object travelling through soil with velocity up to 400 ft/s. This method includes the strain rate, remodling effect on shear strength of soil adhere to side of penetrating object and inertial drag effects. This method is recommended to apply with the velocity over 3 ft/s. If the object is lower than 3ft/s, a static penetration analysis is recommended.

The prediction equation proposed by True (1976) is shown as following:

$$F = W_s - F_b - F_s - F_d \qquad \text{Eq.(2.37)}$$

where F is from Newton's Law

$$F = mv\left(\frac{dv}{dz}\right) \quad \text{Eq.(2.38)}$$

W_s is the submerged weight of penetrating object

F_b is the tip resistance can be expressed

$$F_b = s_{u,tip} S_e \, N_t A_p \quad \text{Eq.(2.39)}$$

where $s_{u,tip}$ is the undrained soil shear strength at a D/2 below penetrating object, and A_p is the cross-sectional area of penetrating object

S_e is the strain rate factor can be expressed by

$$S_e = \frac{S_e^*}{1+\frac{1}{[\frac{C_e V}{s_u D_{eq}}+C_0]^{0.5}}} \quad \text{Eq.(2.40)}$$

where S_e^* is the maximum strain rate factor, C_e and C_0 is strain rate coefficient, V is penetrating object velocity, D_{eq} is the equivalent diameter of penetrating object. For a long cylindrical object, S_e^* = 4, C_e = 4 and C_0 = 0.11.

N_t is tip resistance factor can be expressed by

$$N_t = 5\,[1 + 0.2(\frac{D}{L})]\,[1 + 0.2(\frac{z}{D})] \leq 10 \quad \text{Eq.(2.41)}$$

F_s is the side friction with the assumption that no gap is between soil and penetrating object

$$F_s = (\frac{S_{u,ave}}{S_t}) S_e A_s \quad \text{Eq.(2.42)}$$

where $S_{u,ave}$ is the undrained shear strength over the penetrating object

S_t is soil sensitivity

A_s is the side surface area.

The prediction flow chart is shown in Figure 2.55. In general, calculating v_i for each depth increment, then update current depth z, and v_{i+1} for the next iteration.

$$v_i = v_0 + (\frac{1}{v_0}) [(\frac{\Delta z}{m}) (W_{si} - F_{bi} - F_{si} - F_{di})] \quad \text{Eq.(2.43)}$$

$$v_{i+1} = v_{i-1} + 2\Delta v_i \quad \text{Eq.(2.44)}$$

$$z = z_i \Delta z (\frac{v_i}{v_i - v_{i+1}}) \quad \text{Eq.(2.45)}$$

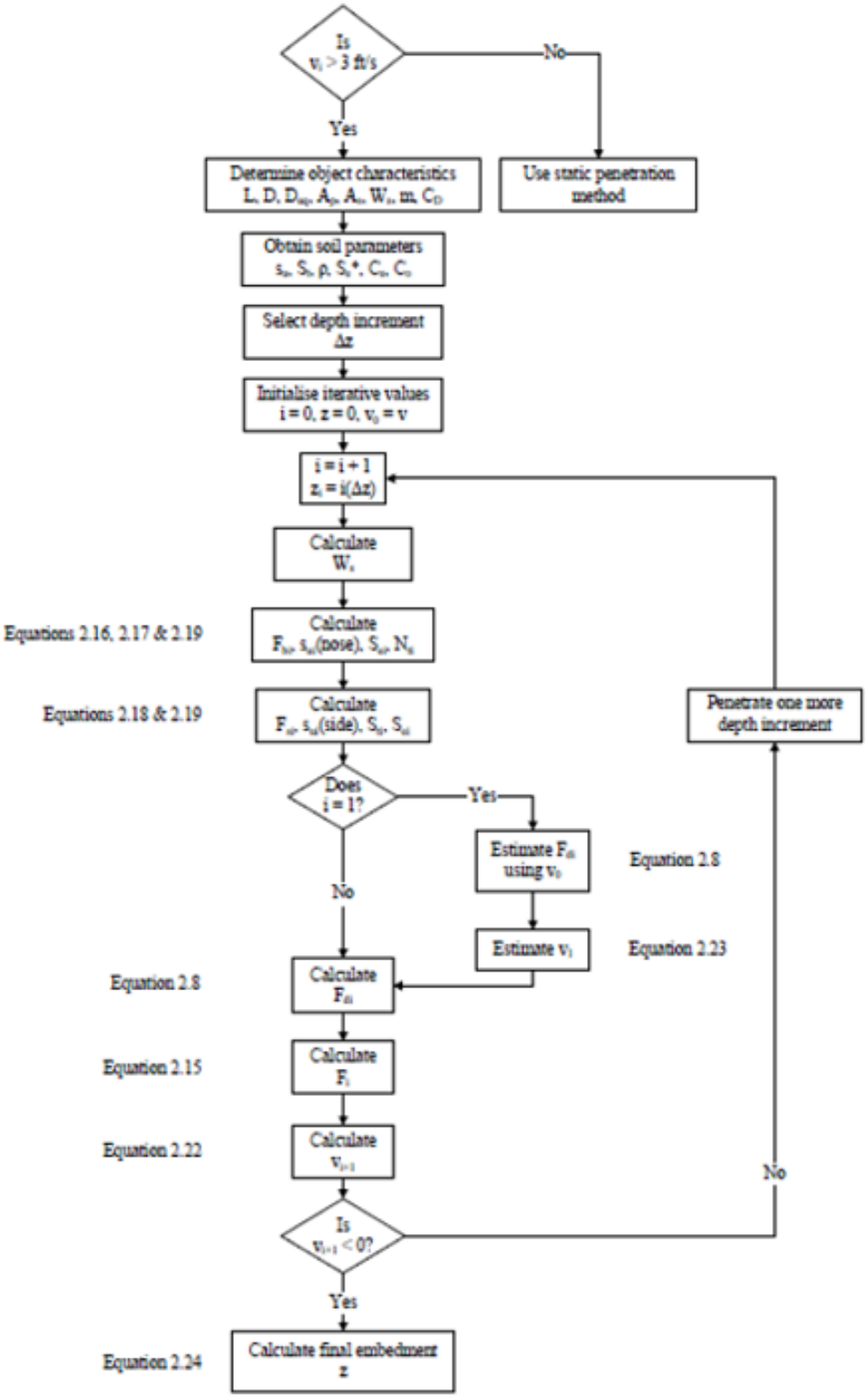

Figure 2.55. Prediction Flow Chart (True, 1976)

2.4.2.4 Modified Ture's Method

The embedment prediction model currently widely employed is the modified True's method with the semi-logarithmic or power-lower rate function included (Lisle, 2001; Wemmie, 2003; Aubeny and Dunlap, 2003; Shi, 2005; Aubeny and Shi, 2006). The model can be expressed as

$$m' \frac{d^2z}{dt^2} = W' - R_f (F_b + F_s) - F_d \qquad \text{Eq.(2.46)}$$

where m' is the submerged mass of anchor

W' is the submerged weight of anchor

R_f is the strain rate effect function depends on the velocity of penetrating object and detailed explained in Section 2.4.2.4.3.

F_b and F_s are detailed discussed in Section 2.4.2.4.1

F_d is detailed discussed in Section 2.4.2.4.2

2.4.2.4.1 Bearing, Frictional and Buoyancy Forces

The bearing force and resistance force in the modified True's method can be written as

$$F_{bear} = s_u N_c A_p \qquad \text{Eq.(2.47)}$$

$$F_{frict} = \alpha s_u A_s \qquad \text{Eq.(2.48)}$$

where s_u is the undrained shear strength, N_c is bearing capacity factor, A_p is the frontal projected area, α is an interface friction ratio ($1/S_t$), and A_s is the side area.

Normally, N_c for the bearing tip is taken as 12 (O' Loughlin et al., 2004a; O' Loughlin et al., 2009; O'Loughlin et al., 2013b), 15 (Freeman et al., 1990), 10 (Mulhearn et al., 1998), 17 (Gilbert

et al., 2008) and 14 (Steiner et al., 2014). N_c = 7.5 is typically adopted for the upper and lower end of dynamically installed anchor flukes (Skempton, 1951) based on a solution for deeply embedded strip footings. The adhesion factor, α, is estimated as the inverse of soil sensitivity (Andersen et al., 2005). For Gulf of Mexico clay, the sensitivity is 1.6 to 1.8 (Gerkus, 2016).

2.4.2.4.2 Inertial Drag

The drag force is acting on the penetrating object, and is in the opposite direction with the movement of penetrating object. The soil inertial force accelerates soil mass from rest to velocity capable to move along penetrating object. The soil inertial force is analogous to the drag force in water when penetrating object travels through water. The drag force consists two parts, the pressure drag and the frictional drag. The pressure drag is formed by the pressure difference between the tip and the back of penetrating object, and mathematically obtained by integrating pressure on the projected frontal area; while the frictional drag is formed by the shear stress on surface area of penetrating object. Raie and Tassoulas (2009) showed that the frictional drag contributes 12% to the total resisting force on a torpedo pile. Achenbach (1968, 1971) showed that the friction drag is only 2% to 3% for total resistance for a sphere. Therefore, the frictional force is omitted. The inertial drag force can be expressed as

$$F_d = ½\ C_d\ \rho A_p v^2 \qquad \text{Eq.(2.49)}$$

where C_d is drag coefficient, ρ is the soil or water density A_p is frontal projected area, and v is the penetrating velocity. C_d is a function of shape and surface roughness of penetrating object as well as the Reynolds number (R_e),

$$R_e = \frac{\upsilon D}{v} \qquad \text{Eq.(2.50)}$$

where D is the effective diameter of penetrating object, and υ is the viscosity of fluid, and v is the penetrating object velocity.

As a penetrating object moves through water or soil, the drag coefficient changes with Reynold Number or different flow conditions as shown in Figure 2.56 and Figure 2.57. In the case of Low Reynold numbers represent laminar flow, the drag force is linearly proportional to the velocity. The drag coefficient remains relatively constant.

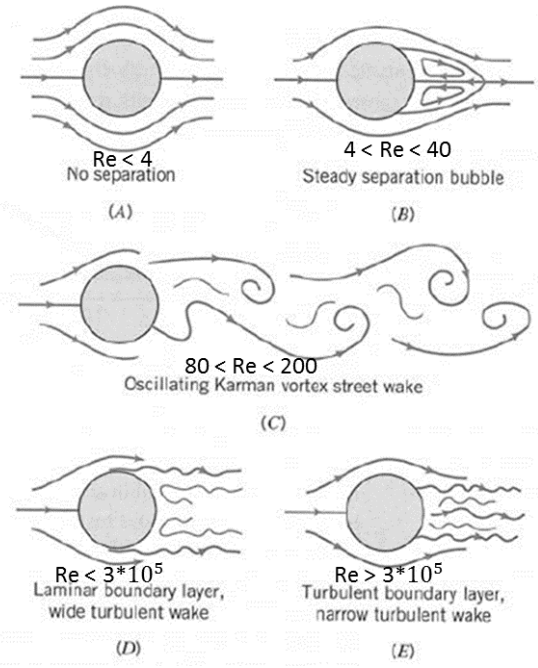

Figure 2.56. Flow Patterns Past Cylinder (Brown and Lawler,2003)

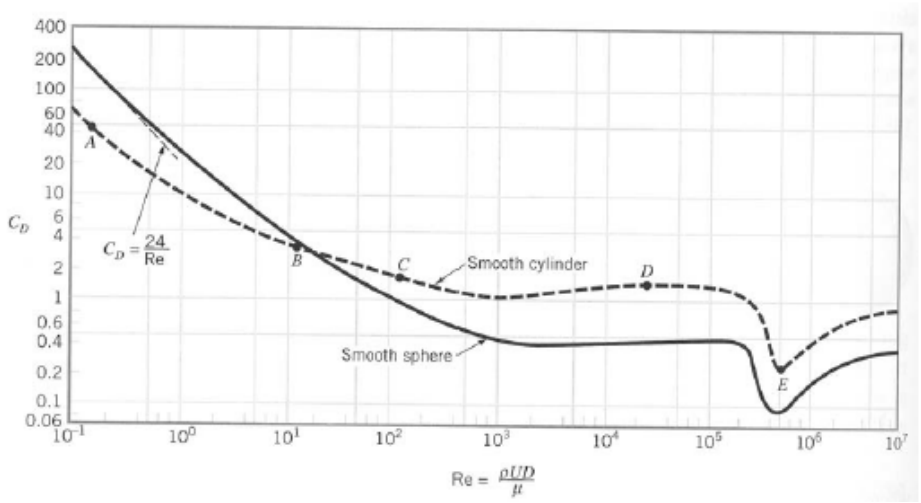

Figure 2.57. Subcrictal Sphere Drag Data Corrected for Wall Effect (Brown and Lawler, 2003)

The most of studies on dynamically installed anchor assumes the drag coefficient remains constant and has no variation with Reynolds number. In addition, when penetrating object travels from water to soil, we should separate the drag coefficient for two media due to the difference of viscosity of two medium. However, usually one drag coefficient set for water and soil is because the change in Reynolds number during free-fall is small and the inertial drag force contributes small portion of total resistance. For the range of velocities, True (1976) adopted 0.7 for calculating drag force in soil and water. Freeman et al. (1984) recommended 0.15 to 0.18 for the ESP, and 0.64 for four-fluke steel DPA. Shelton (2007) suggested 0.65 for OMNI-Max anchor. Richardson (2008) recommended 0.63 for DPA with an ellipsoidal tip. Cenac II (2011) showed a scaled OMNI-Max with scale ratio of 1:15 has 0.46 to 0.83 drag coefficient.

Blake and O'Loughlin (2015) proposed experimental measurement for anchor drag coefficient, $C_{d,a}$. They measured the acceleration by accelerometer attached to anchors with different scales,

quantified the motion of anchors during free-fall in water (Equation 2.51), and back calculated $C_{d,a}$ for each anchor by substituting $F_{d,a}$ and $F_{d,l}$ with Equations 2.52 and 2.53 into Equation 2.51, then rearranged into the from shwon in 2.54

$$(m + m')\frac{d^2s}{dt^2} = W_s - F_{d,a} - F_{d,l} \qquad \text{Eq.(2.51)}$$

where m is the anchor mass

m' is the added mass (the mass of the fluid accelerated with anchor) which is negligible for slender bodies such as the DEPLA

s is the distance travelled by the anchor

t is the time

W_s is the component of the submerged weight of the anchor acting in the direction of motion

$F_{d,a}$ is the fluid drag resistance actin on the anchor

$F_{d,l}$ is the fluid drag resistance actin on the mooring and follower recovery lines

$$F_{d,a} = ½\ C_{d,a}\ \rho_w A_f v^2 \qquad \text{Eq.(2.52)}$$

where $C_{d,a}$ is the drag coefficient for the anchor, ρ_w is the water density, and A_f is the frontal area (of the follower, sleeve, and lfukes).

$$F_{d,l} = ½\ C_{d,l}\ \rho_w A_s v^2 \qquad \text{Eq.(2.53)}$$

where $C_{d,l}$ is the drag coefficient of the mooring and follower recovery lines, A_s is the surface area of the mooring and follower recovery lines in contact with water.

$$C_{d,a} = \frac{W_s - \text{ma} - 1/2\, C_{d,l}\, \rho_w A_p v^2}{½\, \rho_w A_p v^2} \qquad \text{Eq.(2.54)}$$

$$\text{Re} = \frac{\rho_w v D_{eff}}{\mu} \qquad \text{Eq.(2.55)}$$

From Equations 2.54 and 2.55, Blake and O'Loughlin showed that the drag coefficient of acnhor depends on the size of the anchor, and they back calculated $C_{d,a}$ for each scale of tested anchor. The Reynolds number (0.33×10^6) is oabtained by the anchor with scale of 1:4.5 approximately remains at a constant, which implies that the drag coeffeicient for the 1:4.5 size anchor is a constant at 0.7. For the anchor with scale of 1:12 and 1:7.2, the Renolds number is smaller and not a constant, which implies that the drag coefficient for those two sizes anchor may not be a constant. However, the anchor with different scale is geometrically identical, the drag coefficient obtained from 1:4.5 scale of anchor can be applited to other two anchors.

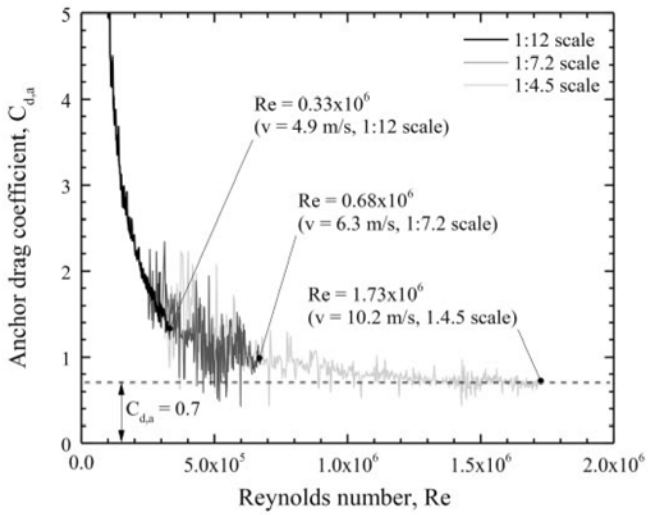

Figure 2.58. Dependence of DEPLA Drag Coefficient on Reynolds Number (Blake and O'Loughlin, 2015)

2.4.2.4.3 Strain Effects

It is generally recognized that the undrained shear strength highly depends on the strain rate (Casagrande et al., 1951) and varies in a wide range for in situ tests and laboratory tests, which is supported by vane shear tests (Biscontin et al., 2001) and triaxial compression tests (Sheahan et al., 1996). Einav and Randolph (2006) indicated that triaxial compression tests are usually with the strain rate of 1%/hr which corresponds with 3×10^{-6} s^{-1}, and strain rate of vane shear tests is 2×10^{-3} s^{-1}. For a dynamically installated anchor, the strain rate is normally in the order of 10^{-1} s^{-1}, which is seven orders of magnitude greater than strain rates from triaxial compression tests and four orders of magnitude greater than those from vane shear tests. Therefore, it is difficult to extroplate the strain rate effect for dynamically installed anchor from laboratory tests.

True (1974) took the strain effects into the prediction of penetration anchor by empirically assessed the strain effects with model penetrometer tests (Section 2.4.2.3). The relationship between the shear strain rate and the undrained shear strength can be expressed by semi-logarithmic or power-law form:

$$s_u = s_{u,ref} \left[1 + \lambda \log \left(\frac{\dot{\gamma}}{\dot{\gamma}_{ref}}\right)\right] \qquad \text{Eq.(2.56)}$$

$$s_u = s_{u,ref} \left(\frac{\dot{\gamma}}{\dot{\gamma}_{ref}}\right)^{\beta} \qquad \text{Eq.(2.57)}$$

where $\dot{\gamma}$ is the strain rate, β and λ are strain rate parameters, and $\dot{\gamma}_{ref}$ is a reference strain associated with the measurement of undrained strength. The strain rate, $\dot{\gamma}$ can be quantified as v/D, such that:

$$s_u = s_{u,ref}\,[1 + \lambda \log(\frac{v/D}{(v/D)_{ref}})] \qquad \text{Eq.(2.58)}$$

$$s_u = s_{u,ref}\,(\frac{v/D}{(v/D)_{ref}})^{\beta} \qquad \text{Eq.(2.59)}$$

where $(v/D)_{ref}$ in this instance is calculated using the T-bar penetration velocity, 0.8 in/s (20 mm/s), and diameter d of the bar, 1 inch (25.4 mm).

Sheahan et al. (1996) suggested λ is between 0.01 to 0.6 based on vane shear tests with rotation rate from 0.06°/min to 3000°/min, and 0.17 for strain rate with 0.0014% to 670% in triaxial compression tests. Biscontin and Pestana (2001) suggested β in the range from 0.05 to 0.1 based on vane shear tests. Chung et al. (2006) proposed β for 0.05 to 0.07 and Lehane et al. (2009) suggested 0.06 to 0.08 from T-bar and ball penetrometer tests. Peuchen and Mayne (2007) used 0.75 ± 0.025 for β and Abelev and Valent (2009) suggested 0.05 to 0.1 from vane shear tests. The wide range of back-calculated strain rate parameters indicates that back-calculating strain rate effects in clay is difficult. As shown in Figure 2.59, O'Loughlin et al. (2013) back calculated λ and β versus v_{av}/d_{eff} (the averaged velocity during penetration over the effective diameter) based on centrifuge tests with DPA (Figure 2.59). He reported that the range of λ is from 0.2 to 1.0 while β is from 0.06 to 0.17 if v_{av}/d_{eff} is in the range of 500 to 4250 s^{-1}. The strain rate parameter of λ with 0.2 to 1.0 implies that the undrained shear strength increases 20%-100%. Gaudin et al. (2013) back calculated β ranging from 0.16 to 0.19 based on centrifuge tests with OMNI-Max anchor in overconsolidated kaolin clay and calcareous silts (Figure 2.60)

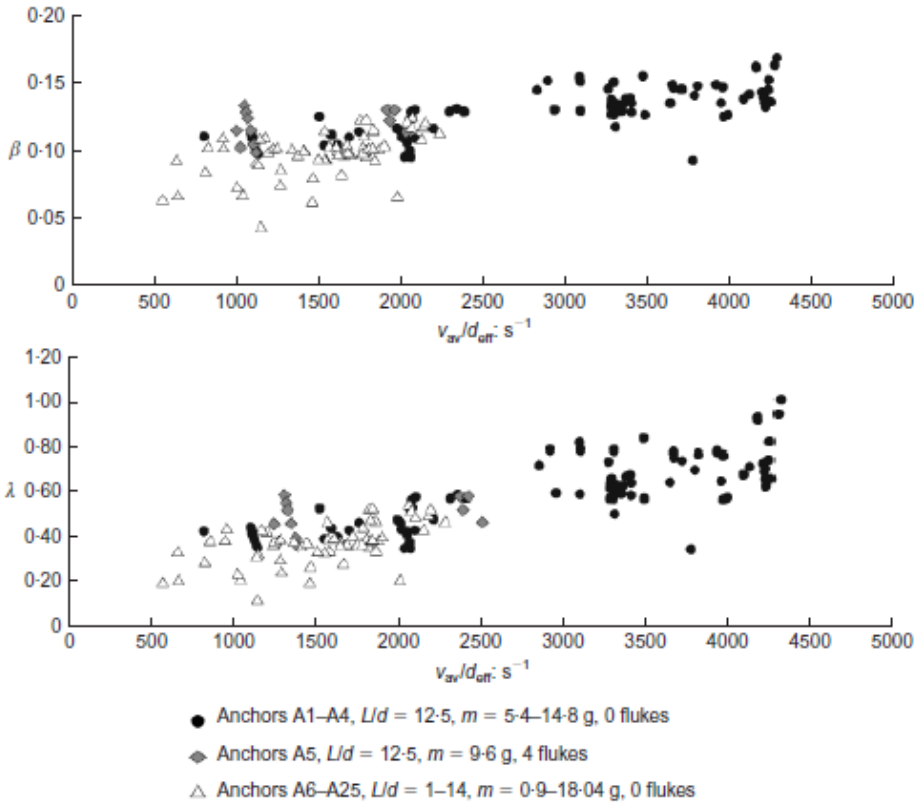

Figure 2.59. Back-Calculated Strain-Rate Parameters (O'Loughlin et al., 2013)

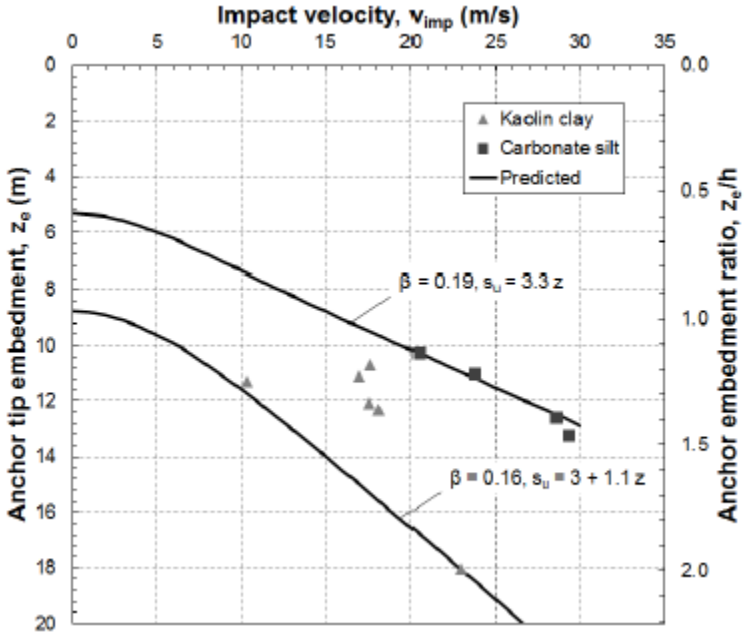

Figure 2.60. Comparison of Measured and Predicted Tip Embedment (Gaudin et al., 2013)

Additionally, it is acknowledged that the rate effect for the shearing mechanism is higher than it caused by the bearing mechanism (Dayal et al., 1975; Einav and Randolph, 2006; Zhu and Randolph, 2011; Steiner et al., 2014; Chow et al., 2014). Einav and Randolph (2006) derived a relationship to express the strain rate effect for bearing and shearing in the following form:

$$R_f = (n\frac{\dot{\gamma}}{\dot{\gamma}_{ref}})^{\beta} \qquad \text{Eq.(2.60)}$$

where n is 1 for bearing (Zhu and Randolph 2011) and is $2(\frac{n_1}{\beta} + n_1 - 2)$ for shearing resistance; $\dot{\gamma}$ is v/d, and $\dot{\gamma}_{ref}$ is v/d, which is 0.8 s^{-1} for a T-bar test.

Einav and Randolph (2006) explained the reason that the rate effect by bearing and shearing mechanism is different by an example of axial or torsional loading of a pile (Figure 2.61). The strain rate for the circular cross section at tip can be expressed as the velocity over the diameter of a pile, v/d; however, the strain rate effect at the cylindrical surface circumscribing a pile is the velocity over the thickness of shear band, v/t. In the assumption that soil exhibits strain-softening, the thickness of shear band, t, is with width equivalent to the width with a couple of soil particles, which is small compared with the diameter of pile. This difference implies that normalizing velocity to the pile diameter can reflect the strain rate effect by bearing (as shown in Equations 2.58 and 2.59), however, cannot reflect the strain rate effect by shearing mechanism. Thus, a new term to account the different strain rate effect (or different width of shear band) is proposed by Einav and Randolph (2006) as shown in Equation 2.60.

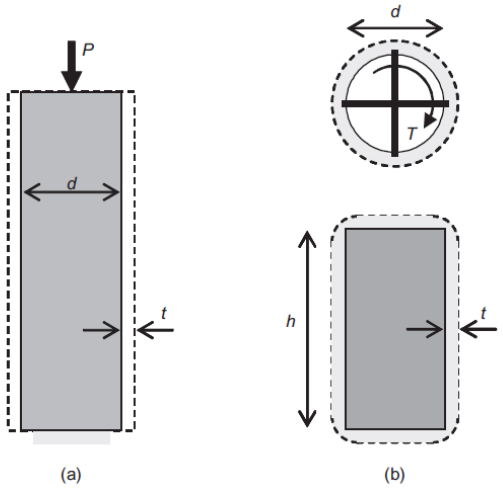

Figure 2.61. Schematic of Cylindrical Shear Bands: (a) Pile Under Axial Loading; (b) Van Undergoing Torsion (Einav and Randolph, 2006)

2.5 Scale Effect in Anchor Performance

It is expensive to perform anchors tests with a full-sized anchor. The scaled model anchor is easier and economical to test. However, to extrapolate the results from scaled model anchor to the behavior of full scale, the scale relationship needs to be well established to accuratly predict real behavior of the full-sized anchor.

Craig (1994) showed that the principles of similarity (Table 2.8) can be applied to extrapolate the scaled model anchor results. If the fluke length of prototype anchor is x times longer than the scaled model anchor such as $L_1/L_2 = x$, then the difference between weights of two anchor is x^3, the difference of area is x^2 and stresses due to anchor weight vary by x. For a drag embedment anchor, as discussed in Section 2.4.1.1, the drag embedment depth of drag anchor depends on the drag distance; thus, if the drag distance is sclaed in the ratio of x, then the penetration depth is also scaled with the ratio of x. Craig (1994) showed that the anchor capacity at shackle with differnet sizes can be expressed as in Equation 2.61

$$T_s = s_u N_c \text{ (f B L)} \qquad \text{Eq. (2.61)}$$

where s_u is the undrained shear strength

N_c is the bearing capacity factor

f is a shape factor

B is the maximum anchor width

L is the maximum anchor length

It can be see that in Equation 2.61, if the charateristic lengths of two anchors have a ratio of x, then the B and L are each scaled by x, which leads to the capacity is scaled with x^2 for the same undrained shear strength. Furthermore, if the undrained shear strength increases linearly with depth and the anchor penetration below the mudline is proportional to the charactersitc length, then the ratio of the capacities of the anchors will be proportional to x^3. Thus, the anchor efficiency (anchor capacity over anchor weight) is independent on the anchor size, and the capacity of scaled model anchor results in normally consolidated profiel can be scaled up to the prototype anchor with x times larger fluke length.

Table 2.8 Scale Relationship Related to Weight

Property	Model	Prototype	Related to Weight
Length	L	n	$W^{1/3}$
Fluke Area	A	n^2	$W^{2/3}$
Weight	W	n^3	W
Penetration	P	n	$W^{1/3}$
Moment	M	n^4	$W^{4/3}$
Moment of Inertia	I	n^4	$W^{4/3}$
Section Modulus	S	n^3	W
Bending Stress	M/S	$n^4/ n^3=n$	$W^{1/3}$
Shear Strength	F/A	$n^3/ n^2=n$	$W^{1/3}$

Unlike the capacity, the displacement required to mobilize the capacity will not necessarily scale up similarly with anchor size. When anchor moves in the soil, the soil mobilized around anchor fluke fails both in in-plane shearing (parallel to anchor fluke) and bearing (normal to anchor fluke). The dispalcement parallel to anchor fluke is dependent on the geometry of the shear band and nearly independent of the size of the anchor, while the displacement to mobilize the bearing capcity is approximately proportional to the anchor size (characteristic anchor length). Therefore, the R_{nt} term for a drag embedment anchor (Figure 2.54), and therefore the trajectory, is not simply scaled by ratio of the sizes between two anchors. Likewise for free-fall penetration, the strain rate enhanced by the high velocity from anchor is not simply scaled by the ratio between the characteristic length of two anchors. As discussed in Section 2.4.2.4.3, effect of strain rate on the side of anchor (strain rate by shearing mechanism) is higher than the effect of strain rate on the tip of anchor (strain rate by bearing mechanism).

Finally, for the free-fall anchor, if the ratio of charateristic length between two anchors is x, then ratio of area to resist soil shearing force is x^2 and the weight ratio between two anchors is x^3. Thus, the weight over area ratio, which governs the free-fall penetration (Eq.(2.46)), varies with the charateristic length ratio beween the two anchors, x. For exmaple, for a model anchor with a scale of 1:50 compared to a full-size anchor, then the weight over area ratio for the full-size anchor is 50 times greater than that for the model anchor.

2.6 Conclusion

This chapter reviewed offshore structures, mooring systems, and offshore anchors for deepwater. The recent physical tests including field tests and laboratory scaled model tests for reviewed anchors were briefly summarized. Next, the prediction models for drag anchors and the dynamically installed anchor are reviewed. From the literature review, there are limited studies in the following four aspects:

- Experimental results for drag embedment anchors and dynamically embedded anchors, both at model scale and field scale, in the layered soil profiles.
- Analytical prediction models for anchors in layer soil profiles.
- Experimental results to separate strain rate effects for anchors mobilizing both bearing and shearing mechanisms.
- Understanding about how tests on model anchors will scale up to full-sized anchors concerning the trajectory of drag embedment anchors and the free-fall penetration of dynamically embedded anchors.

Chapter 3. Test Facility

3.1 Introduction

This chapter presents the test facilities and equipment used in this study. Detailed descriptions of the facilities and equipment can be found in El-Sherbiny R. (2005) and Huang Y. (2015).

Figure 3.1. Test Facilities in Pickle Research Campus

3.2 Soil Tests Beds

The test bed in this study are built with the Gulf of Mexico Clay. The test bed with a single layer includes constant undrained shear strength profile and linearly increasing shear strength profile with remolded or overconsolidated Gulf of Mexico Clay. The test bed with layered soil profile with a stronger soil layer interbedded into soft soil, where the undrained shear strength, the thickness, and depth of stronger layer varies in each layered soil test bed.

3.2.1 Gulf of Mexico Clay

Soil used in this study are the marine clay from Gulf of Mexico (GoM). The soil index properties of GoM clay are shown in Table 3.1. We used the mixer (Figure 3.2) to mix the soil with saline water with 35 gram of sea salt per litter of fresh water. Horan (2012) reported that this saline concentration is comparable with that in ocean water. The mixer consists of a drill and a steel paddle. The torque capacity of the drill is 900 round per minute which is capable to reconstitute GoM soil with shear strength ranging from 0 to 90 psf. The paddle is with 28-inch long rod and 12-inch wide paddle in front. The paddle with slightly bended horizontal part helps to move soil when mixing.

Table 3.1. Soil Index of Gulf of Mexico Clay

Soil Index	
Liquid Limit	105%
Plasticity Limit	62%
Specific Gravity	2.75

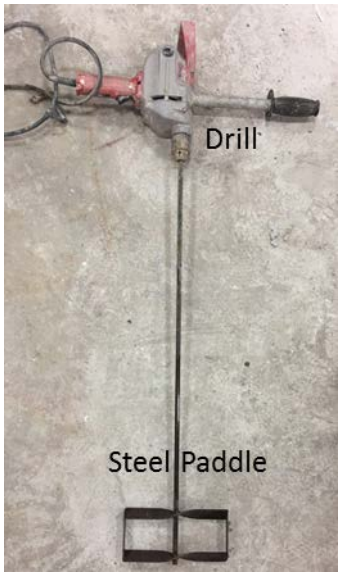

Figure 3.2 Soil Mixer

3.2.2 Preparation of Tests Beds

We prepare soil test bed with single layer in the thermoplastic tank shown in Figure 3.3. This tank is with dimensions of 4 feet in length, 2 feet in width and 2 feet in height. In this tank, we prepared the remolded soil test bed (sensitivity = 1) and the tests beds with sensitivity greater than 1. For the remolded test bed, we followed the method developed by Lee (2008). In this method, he first established relationship between the remolded undrained shear strength depending on water content (Figure 3.4). Next, he employed this relastionhip to control the undrained strength by mixing soil to a target water content, then constructed a desired shear strength profile versus depth by placing the mixed soil into tank. For the test bed with sensitivity greater than 1, we first prepare the remolded test bed, and then waiting remolded soil consolidating by self weight for a couple days or weeks depends on how much sensitivity is targeted for. If a higher sensitivity is desired, we will wait for a longer period.

Figure 3.3. Thermoplastic Tank for Preparing Soil Tests Beds

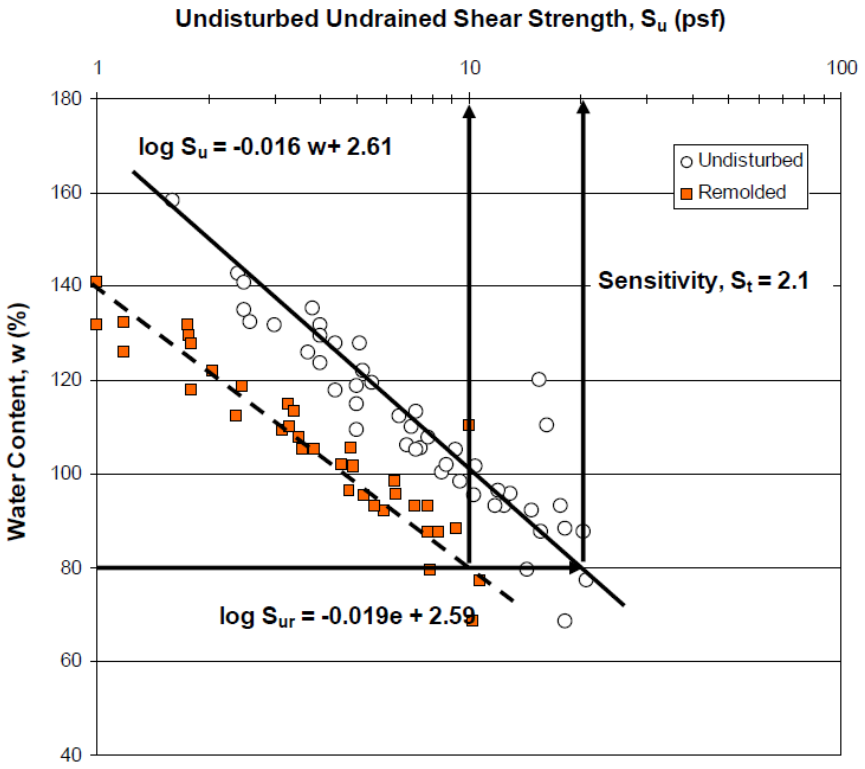

Figure 3.4. Relationship Between the Undrained Shear Strength and Water Content

The test bed with layered soil profile (a stronger layer interbedded within soft soil) are constructed by starting with preparing stronger soil. The stronger soil is prepared by drying GoM clay in small buckets (Figure 3.5) first, then remolded by the mixer. After remolding, we prepare stronger soil layer by making stronger soil into small patches at desired thickness. Then we place those small patches with same thickness into the thermoplastic tank contains soft soil, and bind those small patches together. If there exist gaps between the binding patches, we fill them by inserting stronger soil in. The test bed with stronger layer interbedded within soft soil are finalized by covering stronger layer with soft soil. The thickness of soft soil on top of strong layer depends on the desired depth of stronger layer.

Figure 3.5. Soil Buckets for Stronger Layer

3.2.3 Shear Strength Characterization

After preparing tests beds, we used T-bar (El-Sherbiny, 2005) to characterize the shear strength of soil tests beds. The T-bar (shown in Figure 3.6) is 4-in long and 1-in diameter acrylic rod. As shown in Figure 3.6, during T-bar tests, the T-bar is mounted on the loading rod with 3/8-inch diameter, and pushed into soil test bed by additional weights (5 to 6 pieces of 2.5-lb weights). The other end of loading rod is connected to load cell to measure the resistance from T-bar and loading rod.

First, we insert T-bar together with the loading rod into soil test bed and measure the resistance on the T-bar and rod from soil resistance. The T-bar test is displacement-controlled with the constant loading rate of 0.8 in/sec (20 mm/s). After T-bar tests, the loading rod is inserted into the test bed with the same loading rate at the same location, the soil resistance on the loading rod is measured. We follow the equation to determine undrained shear strength

$$S_u = \frac{F_{total} - F_{rod}}{N_c \times A} \quad \text{Eq.(3.1)}$$

where F_{total} is the load measured from test with T-bar attached to loading rod

F_{rod} is the load measured from test with the loading rod

A is the projected area of T-bar in the loading direction (1 inch × 4 inch)

N_c is the bearing capacity factor, 10.5 (Stewart and Randolph, 1994)

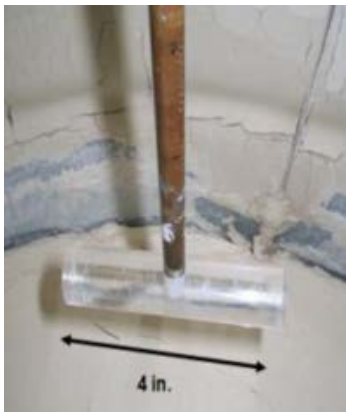

Figure 3.6. T-bar (El-Sherbiny, 2005)

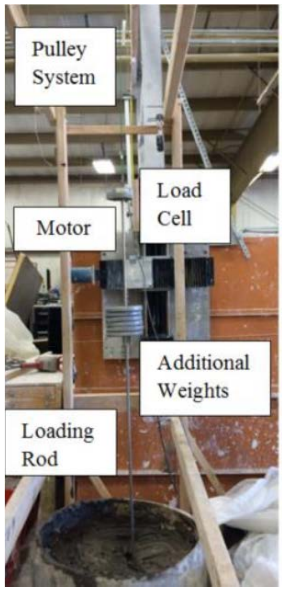

Figure 3.7. T-bar Tests (Gerkus, 2016)

If soil test bed constructed by remolded soil, then three cycles of T-bar test at same location are sufficient to determine undrained shear strength. The shear strength profile from three cycles of T-bar tests results in the same undrained shear strength (Figure 3.8). If soil test bed constructed by soil with sensitivity, then we perform six cycles of T-bar tests at same location (Figure 3.9). The sensitivity is determined by the undrained strength from the first cycle divided by the one from the last cycle. If soil test bed is with a layered soil profile, then the T-bar tests are performed at three different location in test bed. Then the undrained shear strength of soil profile is determined by averaging out the three tests (Figure 3.10). The strain effect can also be assessed by performing T-bar Tests, but with a different loading rate. An example of shear strength profile at different loading rate is shown in Figure 3.10. From Figure 3.10, the shear strength is first determined at the undrained loading rate 0.8 in/sec, and T-bar tests are performed with loading rate at 1.6 in/sec, 3.2 in/sec, 4.8 in/sec, 6.4 in/sec, and 8 in/sec. The shear strength at 1.6 in/sec is not enhanced a lot compared with the shear strength obtained at the normal undrained loading rate (0.8 in/sec); but enhanced obviously with the increase of loading rate when the rate is higher than 3.2 in/sec.

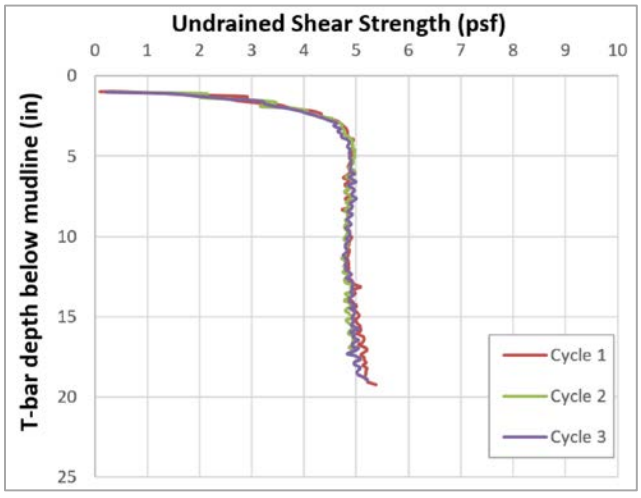

Figure 3.8. Example T-bar Tests in Remolded Soil Test Bed (Gerkus, 2016)

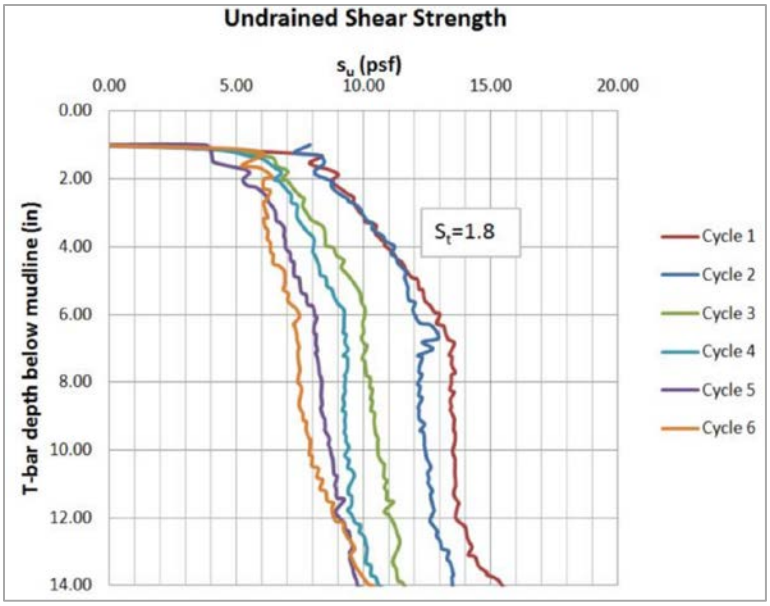

Figure 3.9. Example T-bar Tests in Test Bed of Soil with Sensitivity (Gerkus, 2016)

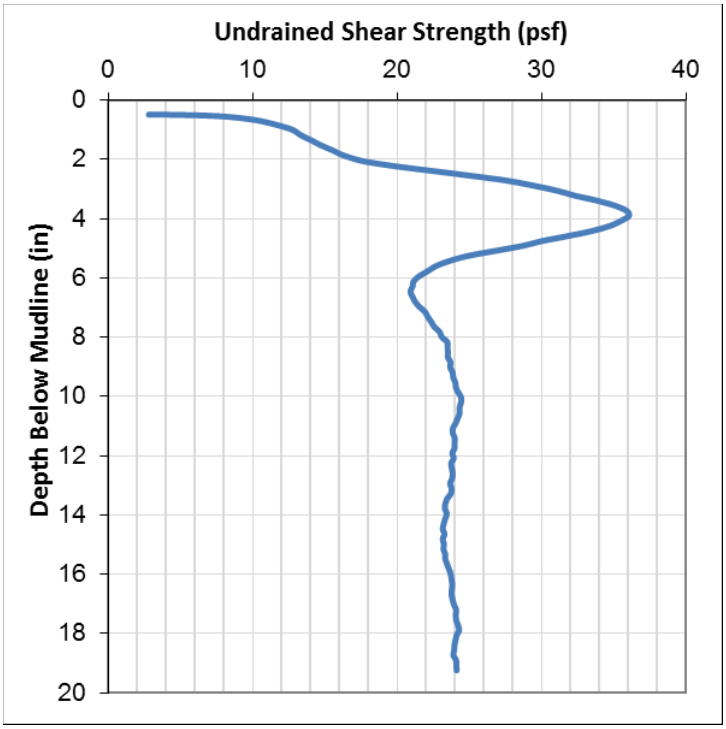

Figure 3.10. Example of Undrained Shear Strength Profile of Layered Soil Profile

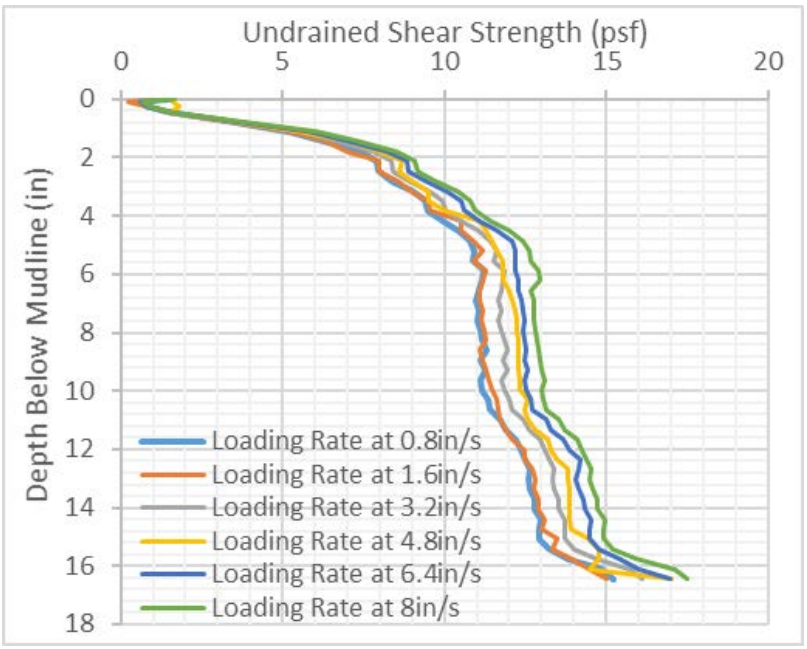

Figure 3.11. Example of Undrained Shear Strength Profile at Different Loading Rate

3.3 Loading Frame

Loading frame (Figure 3.12) consists two parts, the aluminum loading frame and the extended wooden arm. The aluminum loading frame was built by El-Sherbiny R. (2005), and with dimensions of 5 ft in width and 4.7 ft in height. This aluminum loading frame was installed on the top of the orange tank built by Lee (2008) and it is capable to slide to any location on the orange tank, which makes it possible to apply load at any location in soil tank. The extended 5-ft long wooden frame was built to transfer loading line to the area of thermoplastic tank.

Figure 3.12. Loading Frame

3.4 Stepper Motor

We employ the stepper motor (Superior Electric SLO-SYN MH112-ff-206) to provide displacement of loading line at constant rate. As shown in Figure 3.13, the maximum loading rate that motor can supply is 50 RPS (round per second), which is equivalent to 18.89 in/s for line displacement. The loading rate we apply for T-bar test corresponding to the undrained loading condition is 0.8 in/s (127 RPM). The motor was mounted on an aluminum plate attached to the loading frame on the orange tank and hang on the side of orange tank (Figure 3.14).

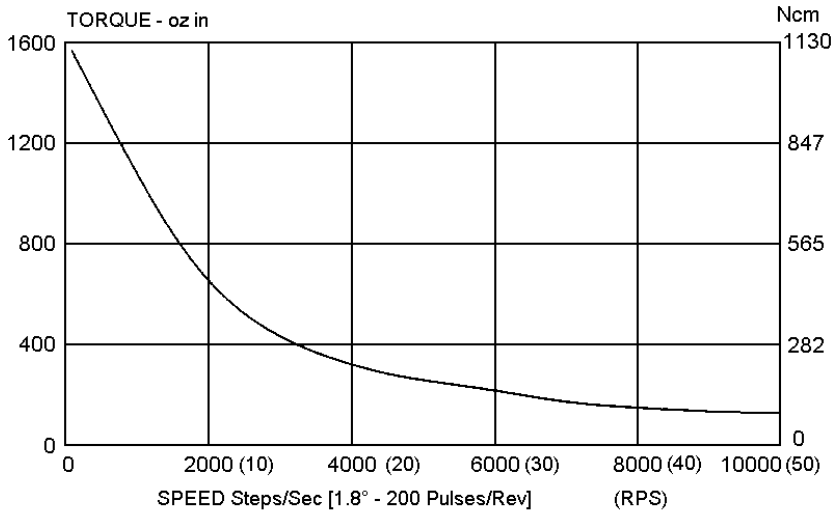

Figure 3.13. Torque versus Speed Curve of Stepper Motor

3.5 Loading Device

The loading device is shown in Figure 3.14. There are four main components, two stepper motors (one for horizontal displacement and one for vertical displacement), two linear actuators, two translator drivers, and one computer controller card. For the vertical displacement of motor, the total travelling distance of motor is 12.5 inches. A pulley with ratio of 3.25 was installed on the extended frame (Figure 3.15), which extends the total travelling distance of loading line to 40.63 inch (12.5 inch × 3.25). The linear actuators transform rotational motor displacement to a linear one (El-Sherbiny R., 2005). The translator drivers provide current to motivate the movement of motor. The movement of motor is controlled by a data acquisition system (more details in Section 3.8) using a National Instruments (NI) motion controller card.

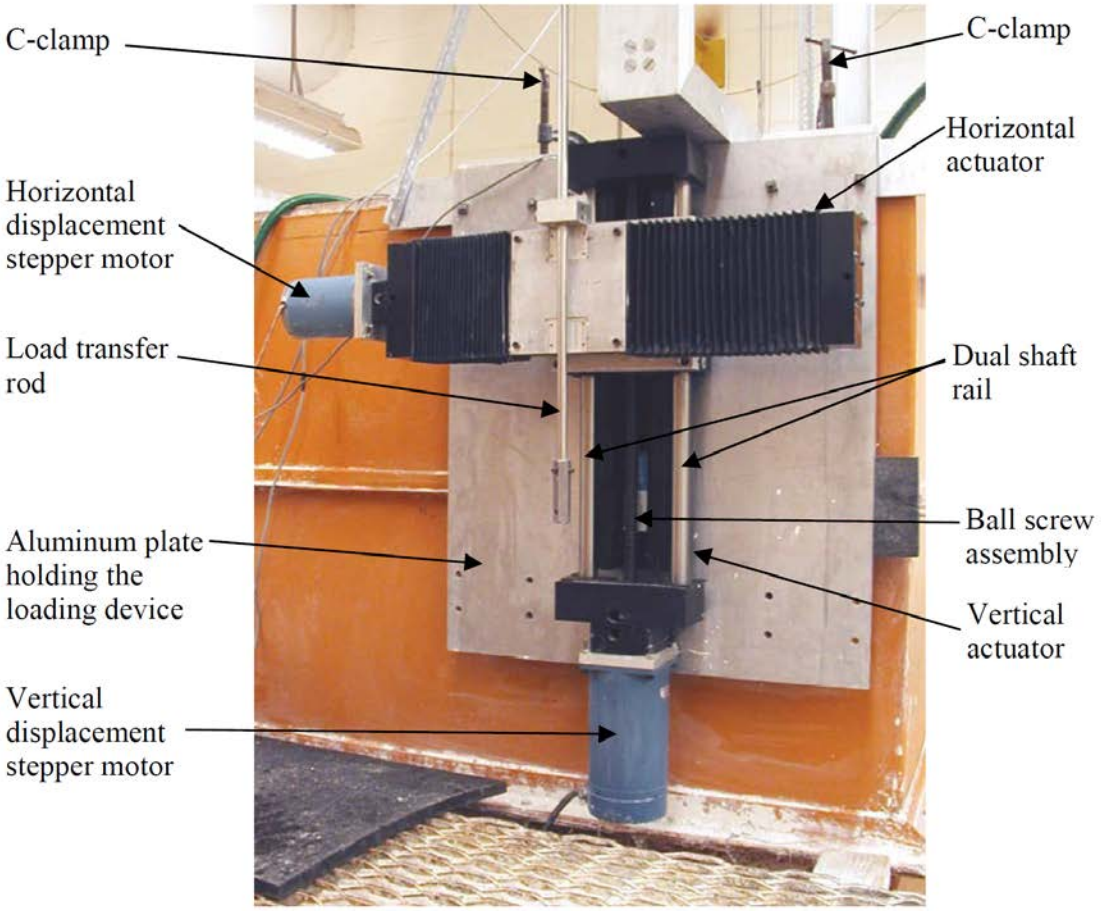

Figure 3.14. Stepper Motor (Huang, 2015)

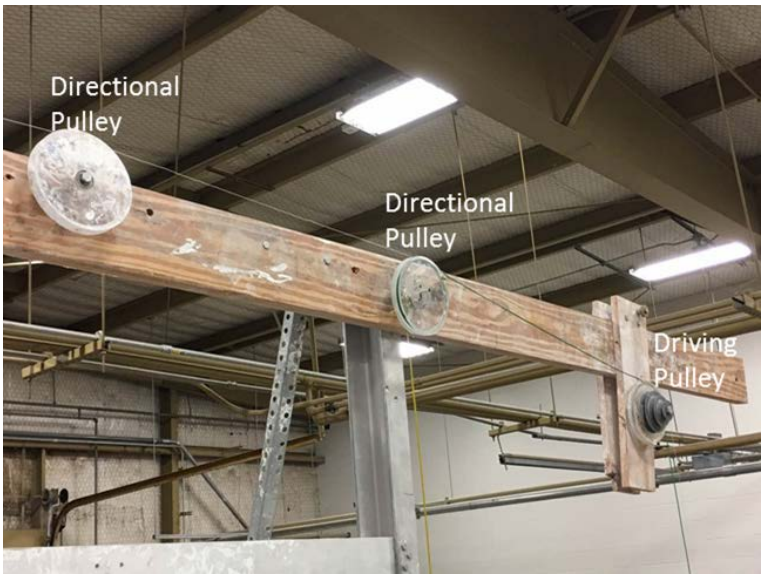

Figure 3.15. Pulley on the Extended Frame

3.6 Load Cell

A load cell (Figure 3.16) with 200-lb capacity (LeBow Products Inc.) is used to measure load resistance in drag embedment tests and T-bar tests. One side of load cell is connected to loading line around the pulley, and the other side of load cell connected with loading line during drag embedment tests or the loading rod during T-bar tests. If a compressive force is measured by the load cell, then a positive voltage reading is registered into the data acquisition system. If a tensile force is applied to the load cell, then a negative reading is recorded. This voltage output is linearly proportional to the magnitude of force. The force is calculated by Equation 3.2

$$F = A \times (\mathrm{V} - \mathrm{B}) \qquad \text{Eq.(3.2)}$$

where F is the force based on the voltage output

A is a calibration factor

V is the output voltage

B is the voltage reading corresponding with no load attached to the load cell

The load cell is calibrated occasionally. The most two sets of calibrated parameters are listed in Table 3.2.

Table 3.2. Calibration Parameter of Load Cell

Date	A	B
2015 Nov 14th	17.586	1.755
2017 Jan 10th	15.586	1.335

Figure 3.16. Load Cell

3.7 Linear Displacement Transducer

As shown in Figure 3.17, a linear motion transducer (LMT) is used to record loading line displacement in T-bar and drag embedment tests. The LMT consists of the sensor (MTS ® Temposonic ®) and a track for the sensor to slide on. The sensor is connected to the objects we want to measure by a fishing line. We choose fishing line since the friction of line on directional pulley can be minimized. When measuring displacement of T-bar or anchor during tests, the corresponding position of sensor on the track can be converted to the displacement of T-bar or anchor. Besides the track, a steel tape is installed for checking displacement reading. The total travelling distance for the sensor is 78 inches.

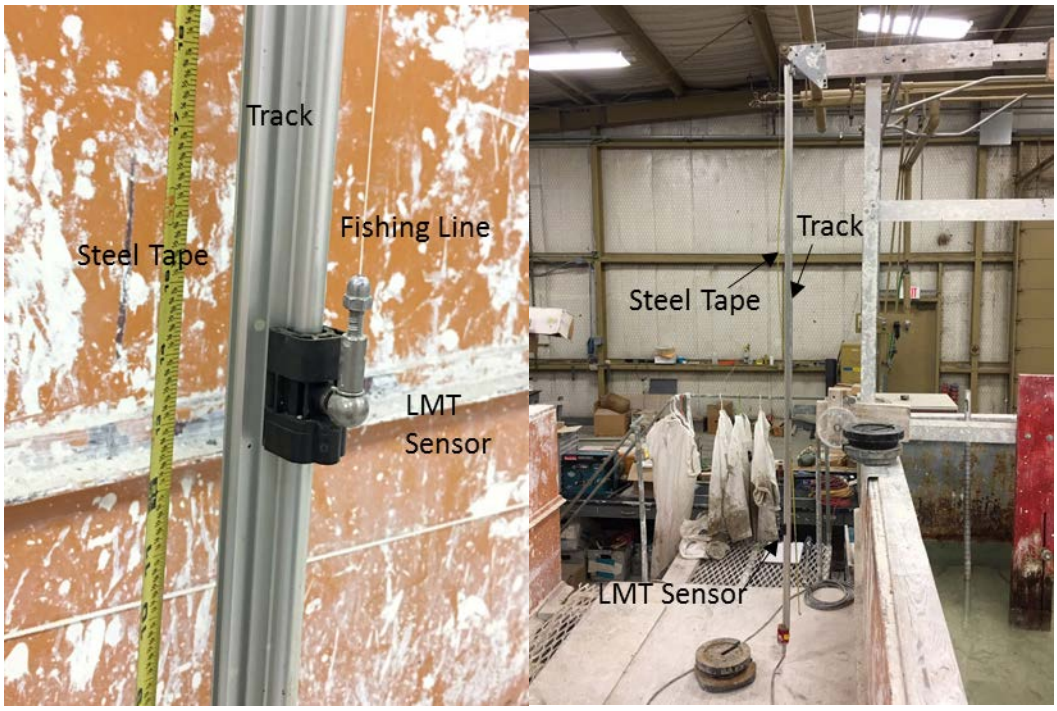

Figure 3.17. Linear Motion Transducer (LMT)

3.8 Data Acquisition and Motion Control Program

Huang (2015) updated the LabVIEW user interface which records data from the Data Acquisition (DAQ) hardware (Figure 3.18) and motion control card. This interface can record measurements of load from load cell, the displacement from stepper motor, and line displacement from linear motion transducer. The user interface is shown in Figure 3.19. The controlling panel (Figure 3.20) is used for starting and ending the command to record data and write into txt file into the specified file path set by user in the file path dialog. The calibration area (Figure 3.21) is for inputs of calibration factors which convert voltage signals from load cell, LMT, and LVDT into the real load and displacements. The output of load from load cell, the displacement from LMT and the displacement from LVDT with respect with time can be seen at the left side of user

interface. The load-displacement curve (LVDT) and load-displacement curve (LMT) will be updated in real time with the progress of testing.

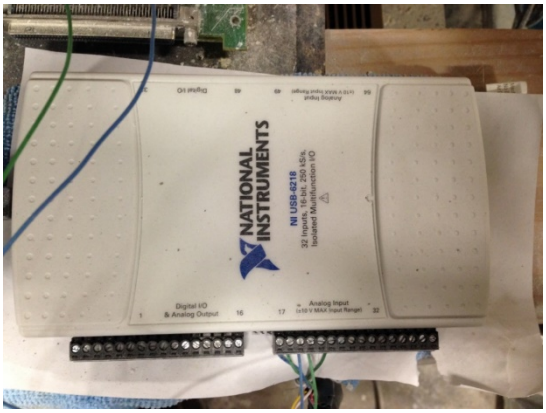

Figure 3.18. Data Acquisition Hardware

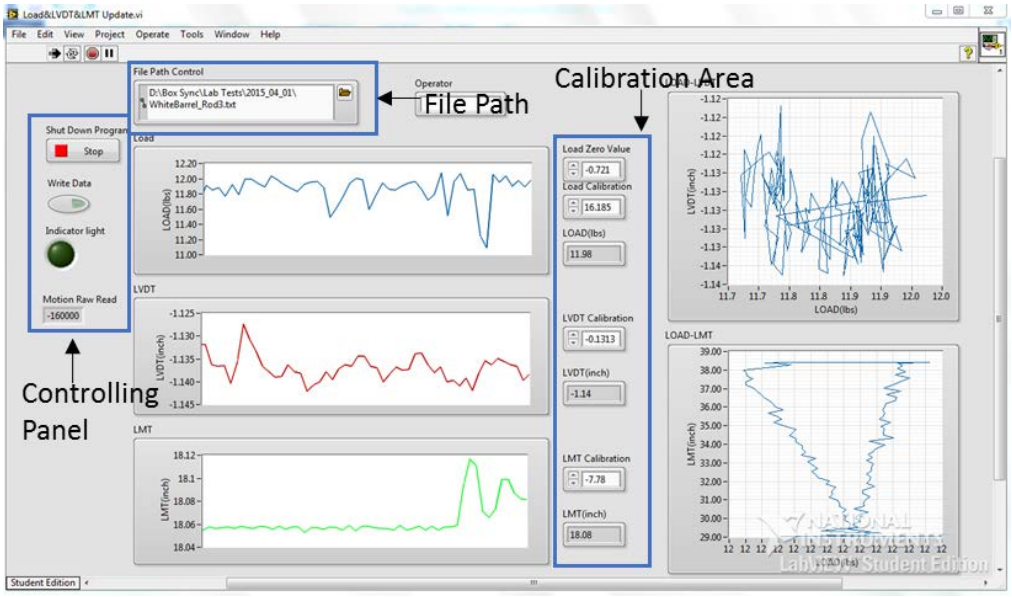

Figure 3.19. LabVIEW User Interface (Huang, 2015)

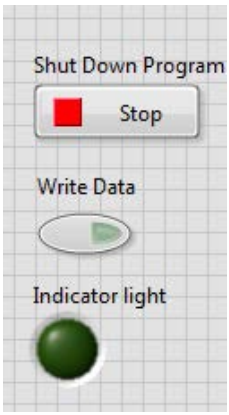

Figure 3.20. Control Panel in LabVIEW Interface

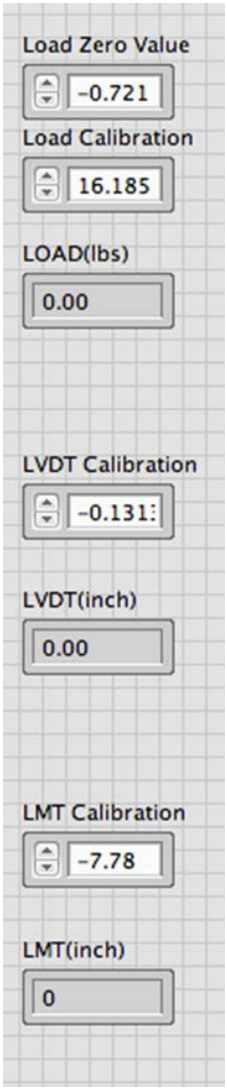

Figure 3.21. Calibration Area in LabVIEW Interface

3.9 Magnetometer

The Polhemus magnetometer (model number is Patriot P/N 4A0520-01, S/N 256B00086) is used to measure six-degree-of-freedom (position: x, y and z; orientation: yaw, pitch, and roll) of anchor motion in soil. The magnetometer package includes a sensor, a source, and electronic unit (Figure 3.22). The source emits the electromagnetic field, and identify the location and orientation of the sensor through the electromagnetic field. A software, PiMgr, developed by Polhemus is used for receiving the data from the source while watching the anchor movement movie during tests. An example of the user interface in PiMgr is shown in Figure 3.23. There are six columns of data shown in the upper part in the interface, and they are x, y, z, yaw, pitch, and roll from the first column to the sixth. Since the drag embedment anchor is designed to start with the orientation of 40° pitch from the horizontal, therefore the pitch reading from the fifth column is used for direction of placing the anchor at the beginning of test.

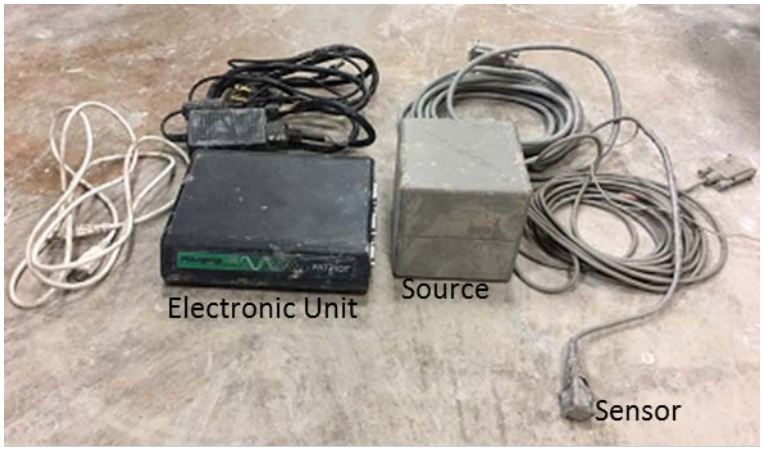

Figure 3.22. Polhemus Magnetometer

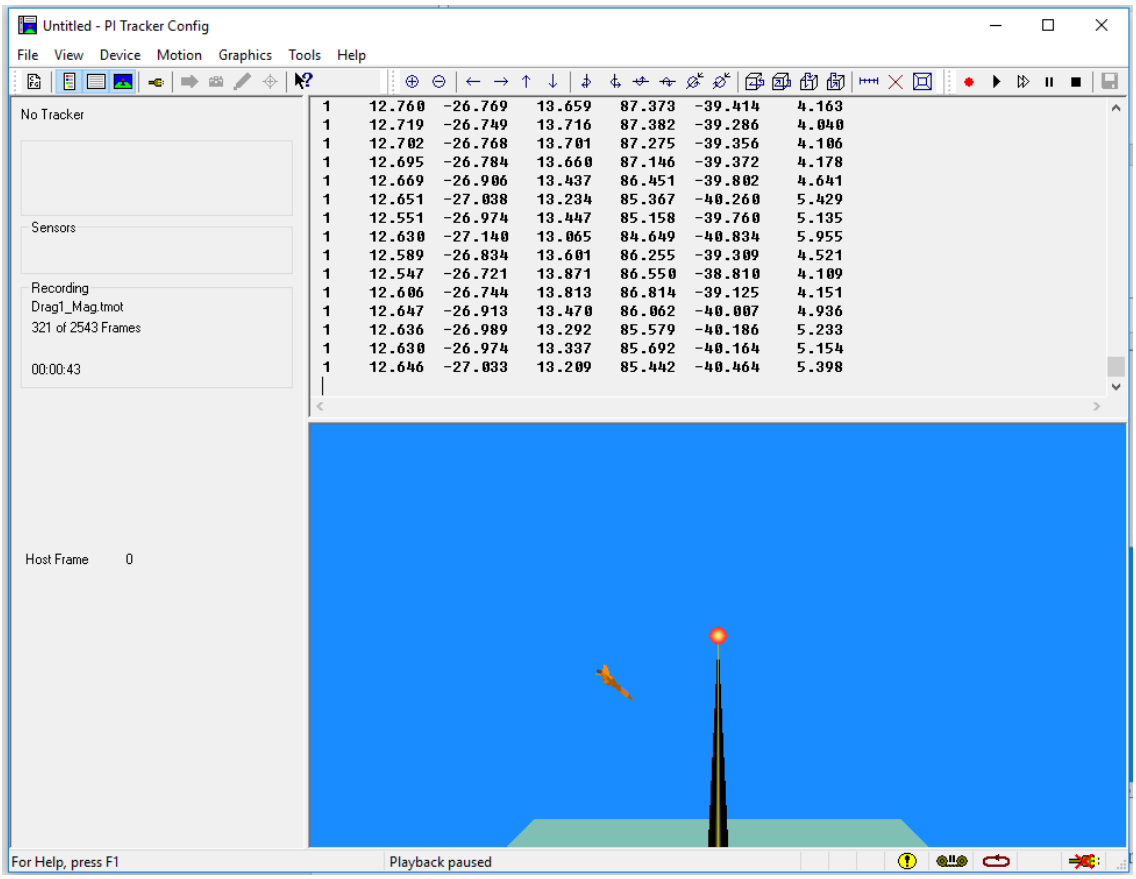

Figure 3.23. PiMgr User Interface

The output of six-degree-of-freedom data from magnetometer is with respect to real time (Figure 3.24). Then the outputs of y and z are combined to plot anchor trajectory, and the pitch and y are used to plot pitch angle of anchor along horizontal drag (Figure 3.25).

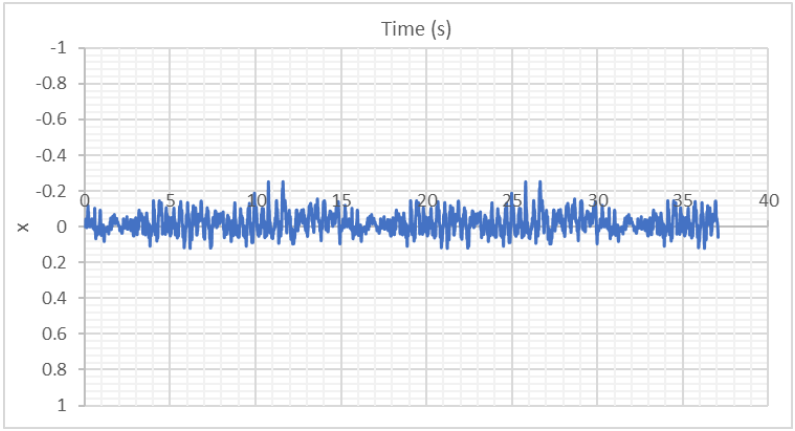

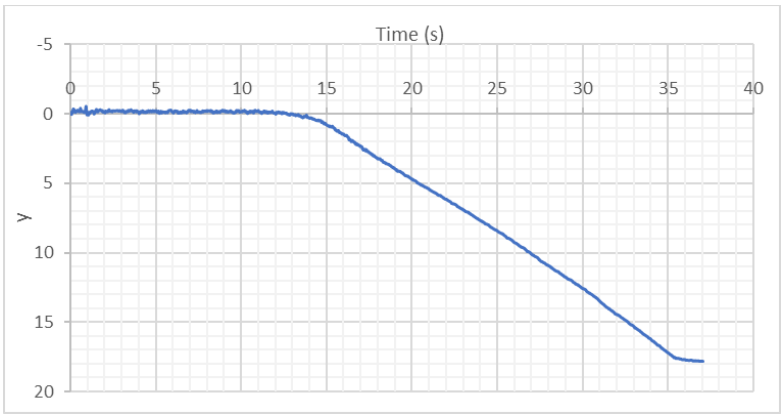
Time (s)
-5
0
5
10
15
20
25
30
35
40
y

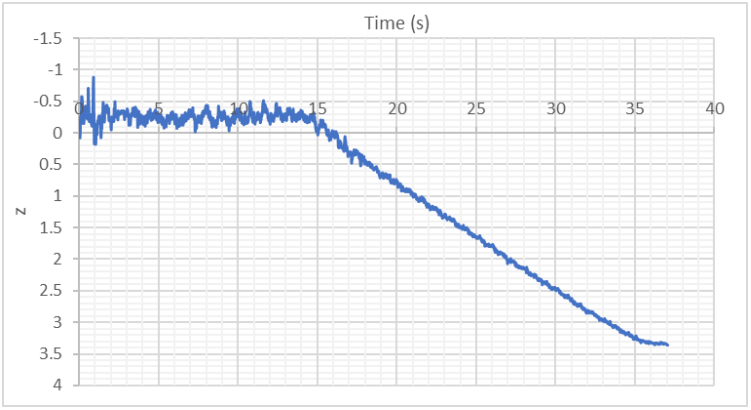
Time (s)
-1.5
-1
-0.5
0
0.5
1
1.5
2
2.5
3
3.5
4
z

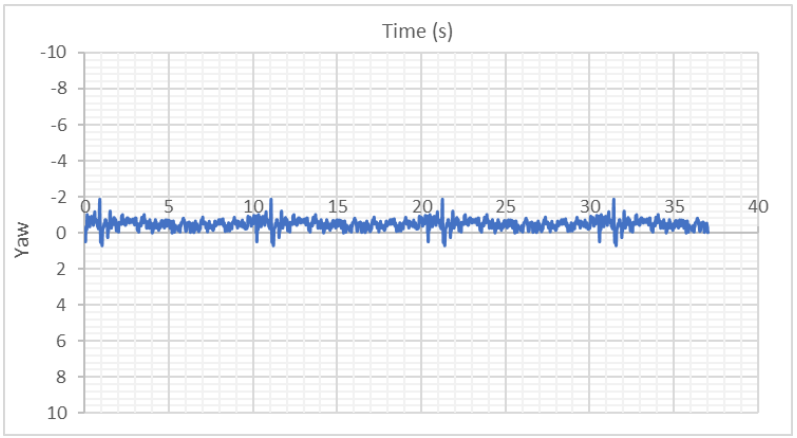
Time (s)
-10
-8
-6
-4
-2
0
2
4
6
8
10
Yaw

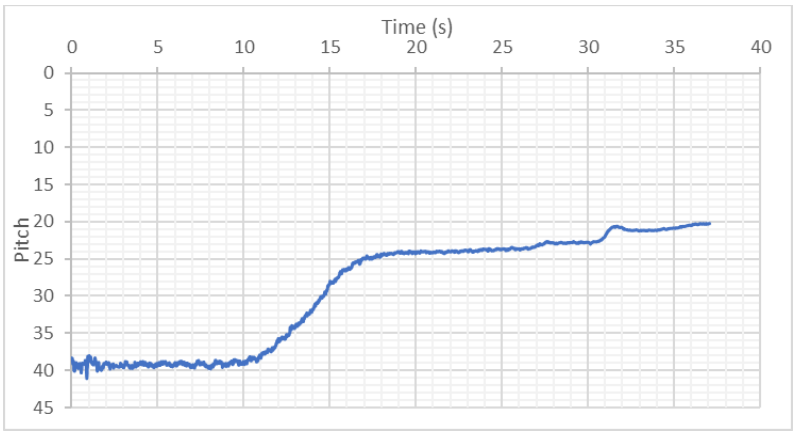

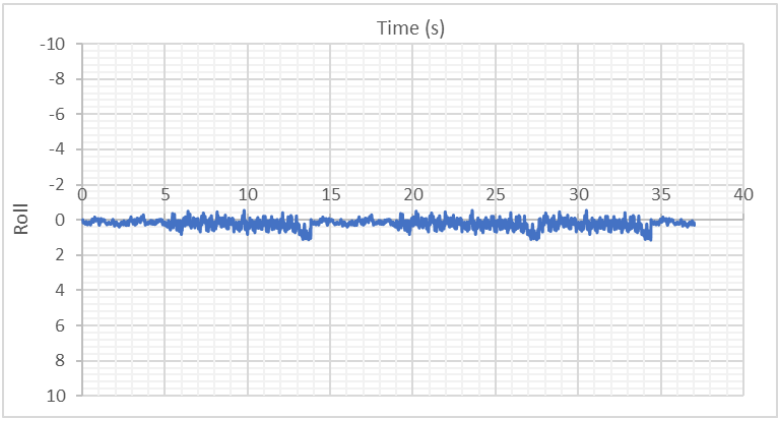

Figure 3.24. Output from Magnetometer

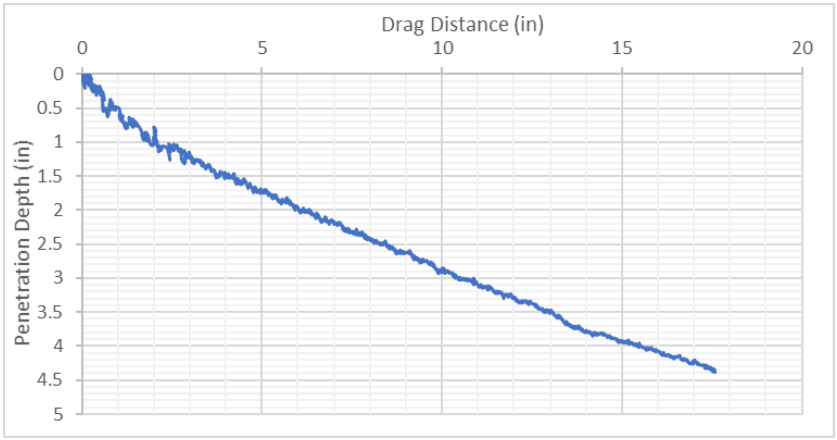

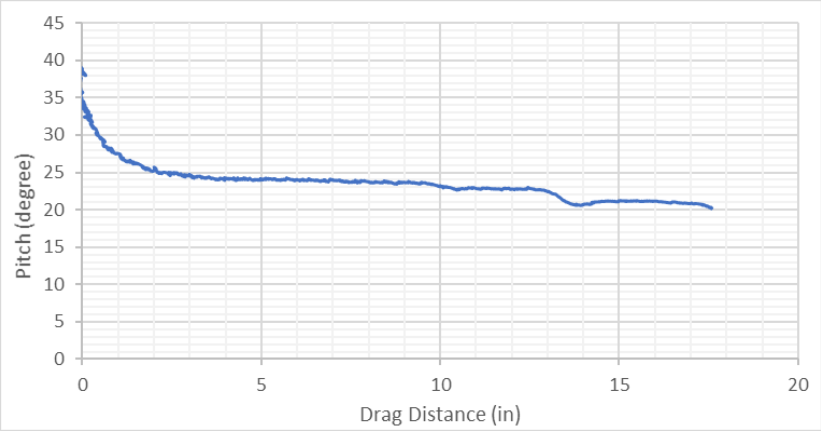

Figure 3.25. Trajectory and Pitch Versus Horizontal Drag

To receive good signal with tdhe least noise from the sensor and the source, we need to be cautious when placing the electronic unit, the source and the sensor. The electronic unit should be at least 2 ft from other magnetic or electromagnetic field. In the testing, since the motor is switched on for dragging anchor and computer is on for controlling motor movement and recording data, thus electromagnetic fields occur around the motor and the computer. These electromagnetic fields cause electromagnetic interference on the source and the sensor which leads to a noise on data received at PiMgr user interface. To avoid this electromagnetic interference, we place the electronic unit at least 2 ft away and the source at least 5 ft away from the computer and the motor. To achieve better data with the least noise, the source and the sensor should be close to each other.

3.10 Scaled Model Anchors

3.10.1 Drag Embedment Anchor

We employed the scaled anchor model used in a previous MMS project (Aubeny et al., 2011). This generic model anchor (Figure 3.26) made with acrylic has a scale factor of 1:30 to the full-

scale anchor that was designed by Delmar Industries, Inc. The generic model anchor has a fluke with a length of 3.625 inch, a width of 5.270 inch and a thickness of 0.1 inch. For a typical commercial anchor, the ratio of fluke length over fluke thickness ranges from 5 to 30 (29 for the model anchor), and the ratio of fluke width to the fluke length is 1 to 2 (1.5 for the model anchor). A 2.9-inch long shank is fixed to the fluke with a fluke-shank angle with 50 degrees. Normally the fluke angle is within 30° to 50° (DNV, 2000), the anchor with a lower fluke-shank angle is recommended for sand or relatively stiff clay, while a higher angle is for soft clay deposit. It may be appropriate to install anchor with an intermediate angle in layered soil. A small hole on the top end of shank represents padeye of commercial anchor. For the commercial anchor (Vryhof, 2015), as shown in Figure 2.4, anchor line and padeye of anchor is connected by shackle. However, for the drag embedment test with model anchor, we directly attach anchor line to the padeye. The weight of anchor is 0.072 lbs and the volume is 1.81 in^3. Figure 3.27 and Table 3.3 summarize the projected area of anchor in different plane.

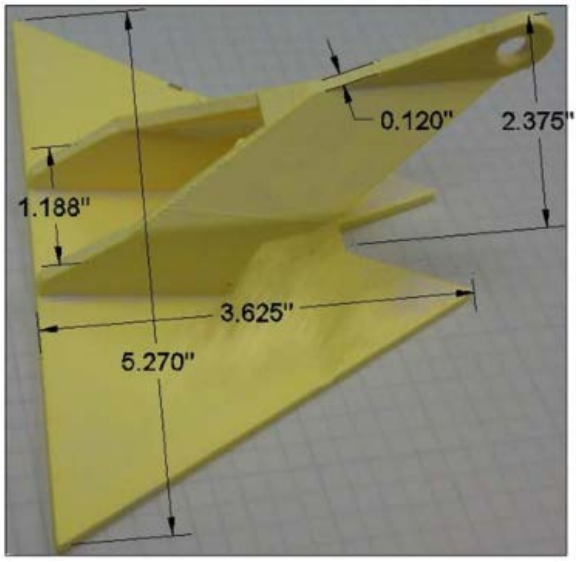

Figure 3.26. Scaled Generic Model Drag Embedment Anchor (McCarthy, 2011)

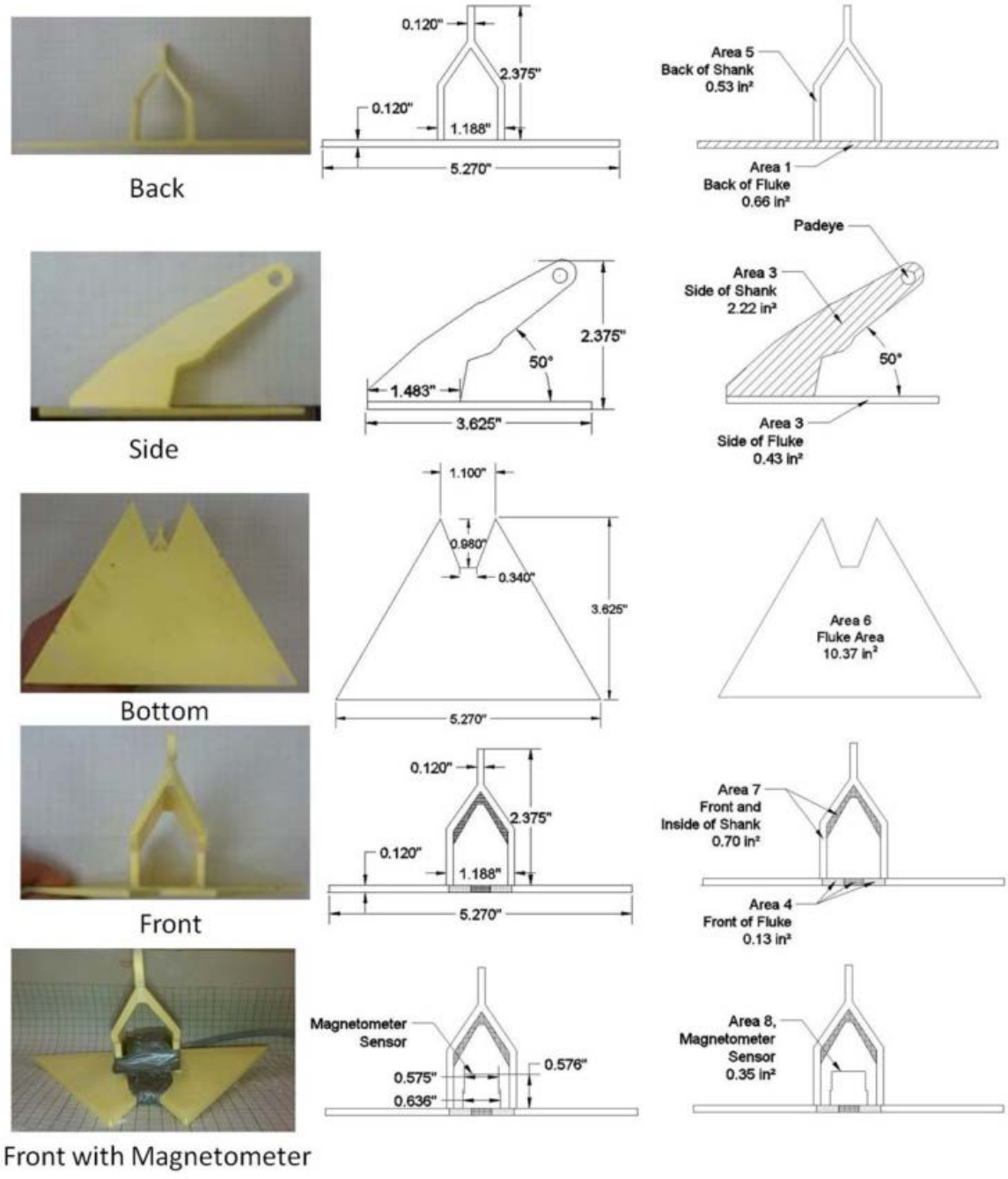

Figure 3.27. Bottom, Side, Front and Back Perspectives of Anchor with Dimensions and Projected Areas (McCarthy, 2011)

Table 3.3. Summary of Actual and Projected Areas of Fluke and Shank (McCarthy, 2011)

	Area 1	Area 2	Area 3	Area 4	Area 5	Area 6	Area 7	Area 8
	Back of Fluke (in^2)	Side of Fluke (in^2)	Side of Shank (in^2)	Front of Fluke (in^2)	Back of Shank (in^2)	Fluke Area (in^2)	Front and Inside of Shank (in^2)	Magnetometer Sensor (in^2)
Projected Area	0.66	0.43	2.22	0.13	0.53	10.37	0.70	0.35
Actual Area		0.52		0.30	0.80		2.99	

To perform drag embedment tests in piggy-back configuration, we need two more anchors. Thus, we replicate this anchor by drawing the anchor in AutoCAD first and then printing it in 3-D printer. To extrapolate the model anchor behavior to the prototype anchor, a larger anchor (Figure 3.29) with fluke length 1.5 times longer than the anchor shown in Figure 3.26 is printed and tested in GoM clay.

Figure 3.28. Scaled Anchors in Different Sizes

3.10.2 Flying Wing Anchor®

The Speedy Flying Wing Anchor® is used for free-fall penetration tests in this study. The flying anchor with shank opened (left in Figure 3.29) and shank closed (right in Figure 3.29). The flying wing anchor® has two plates, the front and back plate connected by two beams. There are four pieces of triangular fins attached at the back plate, and two oval fins at the edges of back plate. The shank is attached at the beams. The dimensions for the printed flying wing anchor is shown in Figure 3.30. The front plate area is 12 in^2, and the back plate is 17.28 in^2. A 6.55-inch long shank is closed during the free-fall penetration process, and is opened before the drag embedment process triggered by the increased load demand. The weight of the printed anchor is 0.2 lbs.

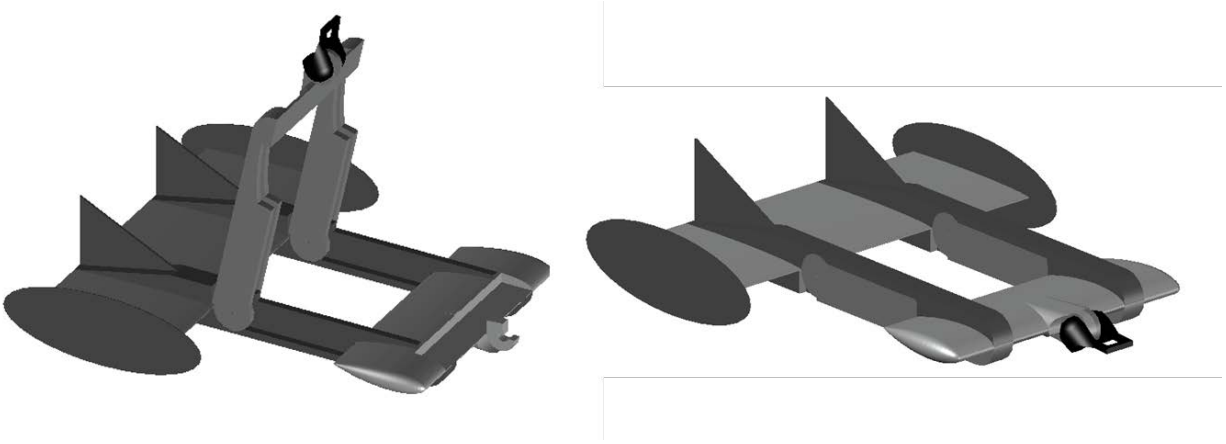

Figure 3.29. Scaled Model Flying Wing Anchor® (Left: Shank Opened; Right: Shank Closed)

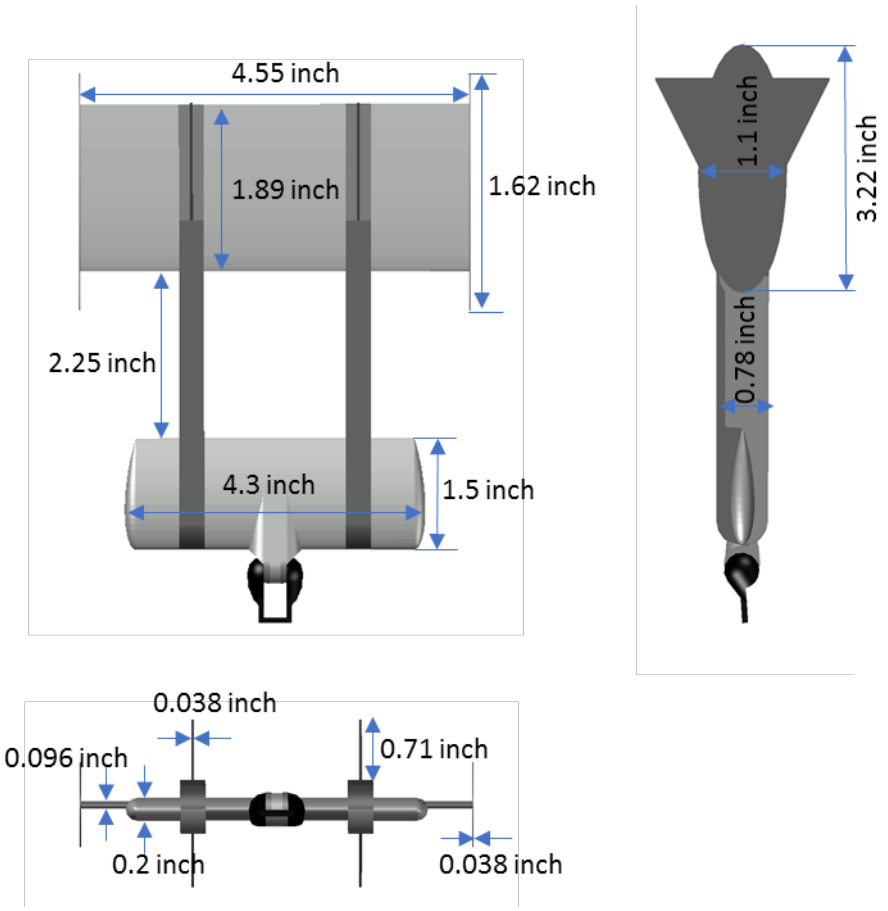

Figure 3.30. Dimensions of scaled Flying Wing Anchor®

3.11 Conclusions

The test facilities are reviewed in this chapter. The tests beds with Gulf of Mexico clay are prepared by remolding at established water contents. Thermoplastic tank is used for tests beds for drag embedment anchor, and the barrel is for the tests beds for Flying Wing anchor. The capacity of anchors and the soil resistance in tests are measured by the load cell. The anchor trajectory and orientation are tracked by magnetometer.

Chapter 4. Pure Loading Tests

4.1 Introduction

This chapter studies the non-dimensional yield capacity factor for the generic model of a drag embedment anchor and the larger model with a characteristic length 50% greater. The non-dimensional yield capacity is measured experimentally through pure loading tests. The scaled drag embedment anchor is tested under pure loading conditions to study the non-dimensional yield capacity factor. These factors for drag embedment anchors are applied to the predicted trajectory and capacity for the drag embedment tests Chapter 5.

4.2 Theoretical Non-Dimensional Yield Capacity Factor

The theoretical pure bearing and shearing factor are calculated by the limit-analysis relationship originally developed by (Murff, 1994) for shallow foundations. Murff (2005) and Yang et. al. (2008) adapted this relationship for shallow foundations to plate anchors. The plastic yield surface of a foundation or an anchor shows the combination of normal, shear and moment loads that causes foundation failure (O'Neil et al., 2003). N_{nmax} (Equation 4.1), N_{tmax} (Equation 4.2) and N_{mmax} (Equation 4.3) are the bearing capacity factors under conditions of pure axial, shearing and rorational loading.

$$N_{n\,max} = 3\pi + 2 + \frac{t_f}{L_f}\left(\alpha + \frac{1+\alpha}{\sqrt{2}}\right) \quad \text{Eq.(4.1)}$$

$$N_{t\,max} = 2\left(\alpha + N_{tip}\,\frac{t_f}{L_f}\right) \approx 2\,\alpha + 15\frac{t_f}{L_f} \quad \text{Eq.(4.2)}$$

$$N_{m\,max} = \frac{\pi}{2}\left(1 + \left(\frac{t_f}{L_f}\right)^2\right) \quad \text{Eq.(4.3)}$$

4.3 Experimental Non-Dimensional Yield Capacity Factor

To study the anchor behavior when it is loaded in the six degrees of freedom, we need to perform pure loading tests for each degree of freedom by restricting anchor movement in a single degree of freedom and measure anchor capacity. The six degrees of freedom are linear and rotational displacements in x, y, and z direction. The three components of anchor movement in x, y, and z axis is defined as bearing, in-plane shearing, and out-of-plane shearing loading. As shown in Figure 4.1, the three rotational components are roll (rotate around x axis), pitch (rotate around y), and yaw (around z axis). Among these six capacity factors, we measure three important capacity factors to understand the anchor behavior in drag embedment tests. The capacity factor in bearing (Figure 4.2), in-plane shearing (Figure 4.3), and rotational in pitch direction (Figure 4.4). We load anchor at the same rate (0.8inch/sec) of T-bar penetration rate, which is the rate corresponding with undrained condition. For each capacity factor, we compare the experimental measurement with the theoretical results.

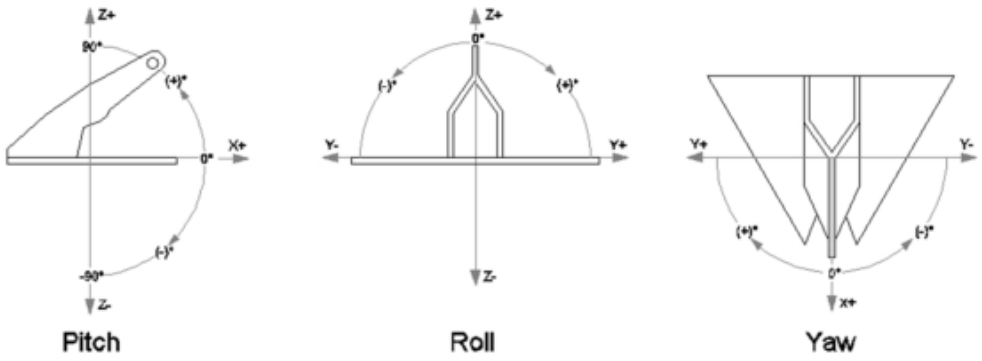

Figure 4.1. Orientation Sign Convention (McCarthy, 2011)

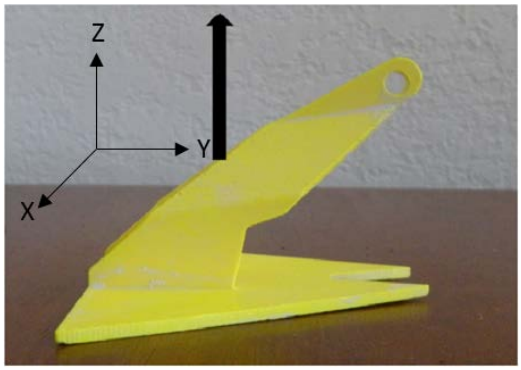

Figure 4.2. Anchor in Bearing Direction (Ganjoo, 2010)

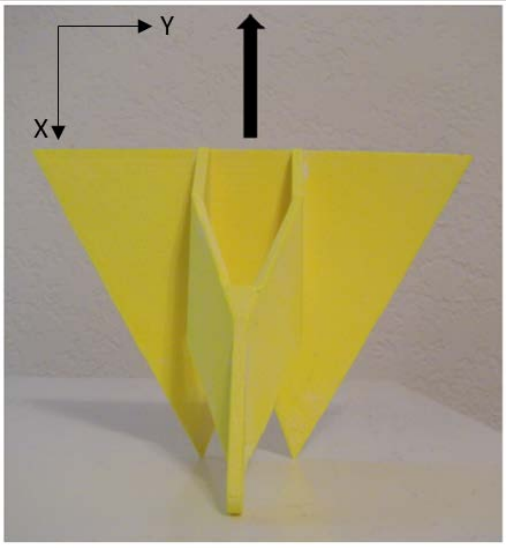

Figure 4.3. Anchor in In-Plane Shearing direction (Ganjoo, 2010)

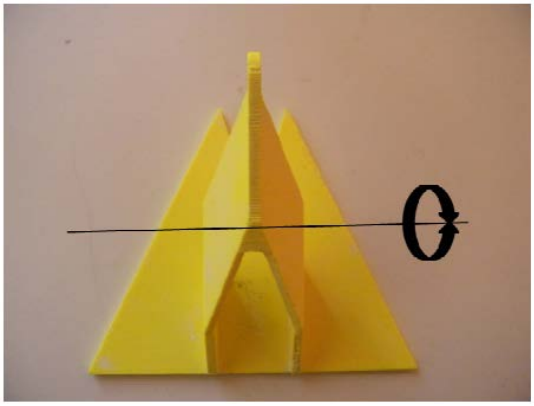

Figure 4.4. Anchor in Pure Pitching Rotational Direction (Ganjoo, 2010)

4.3.1 Pure Bearing Factor

4.3.1.1 Pure Bearing Test Procedure

Pure normal loading tests are performed by attaching the loading line to the center of gravity of the anchor, which makes the loading line perpendicular with the fluke when the loading line is in tension. To find center of gravity of anchor, it is hung by a wire at different locations. If the fluke of the anchor remains parallel to the ground level, then the location of connection is assumed as the center of gravity of the anchor. For normal loading configuration, a plastic tie is attached to the anchor and can be used to connect to a loading line as shown in Figure 4.5. The loading line is tied at the center of gravity found previously.

To perform pure loading test, first, we remove the soil above the desired embedment depth, then we place the anchor in the normal loading configuration, and next place the removed soil back to embed the anchor. This wish-in place method helps us to control the location and configuration of the anchor. The embedment depth is at least 10 inches below the surface of the test bed, which enables the anchor to travel at least 2 fluke lengths before being pulled out.

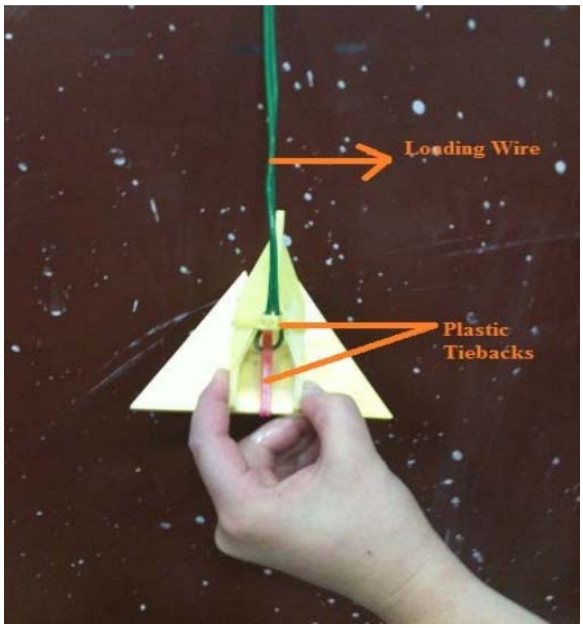

Figure 4.5. Anchor Suspended by Wire Using Plastic Ties to Find the Center of Gravity for Normal Loading Configuration (McCarthy, 2011)

4.3.1.2 Experimental Pure Bearing Factor

We have the following equation to calculate the pure normal bearing factor. The results of the normalized bearing factors for the generic anchor are shown in Table 4.1. One example of pure bearing tests results for generic anchor and larger anchor are shown in Figure 4.6 and Figure 4.7, respectively.

$$N_{nmax} = \frac{F_{rod+anchor} - F_{rod} - W'_{anchor}}{S_u \cdot A_f} \qquad \text{Eq.(4.4)}$$

where $F_{rod+anchor}$ = resistance normal force of the anchor with the rod

F_{rod} = resistance shear force of the separate tests on the rod

W'_{anchor} = submerged weight of the anchor

S_u = undrained shear strength

A_f = area of fluke

Table 4.1. Example of Normalized Bearing Factors for the Generic Model Anchor (Ganjoo, 2010)

Test ID	Approximated Su (psf)	F_{max}-W'$_{anchor}$ (lbs)	N_P
2010.02.19_B_pullout1	18.9	14.4	12.2
2010.02.19_B_pullout2	18.3	13.6	11.9
2010.02.19_B_pullout3	18.2	11.9	10.5
2010.06.17_B_pullout1	11.6	8.2	11.4
2010.06.17_B_pullout2	11.6	8.2	11.4
2010.06.17_B_pullout3	11.6	8.3	11.5

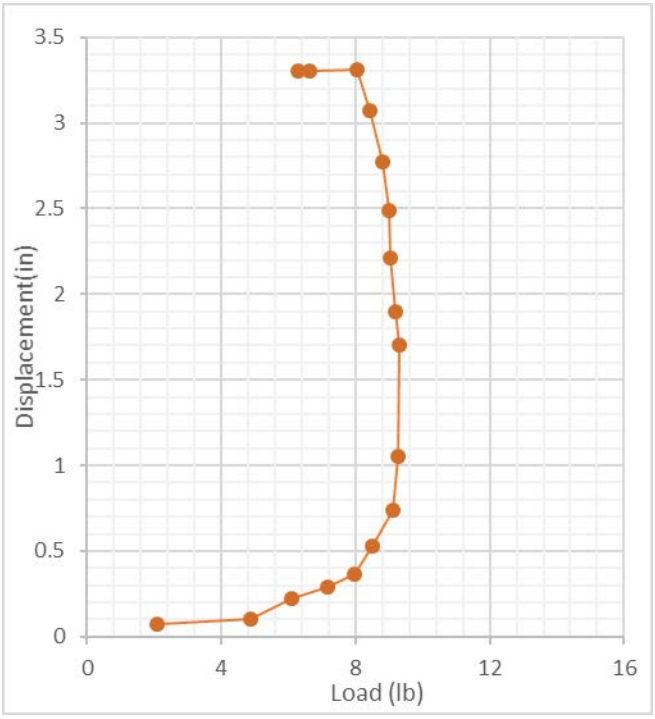

Figure 4.6. Example of Test Result from Pure Bearing Test for the Generic Model Anchor

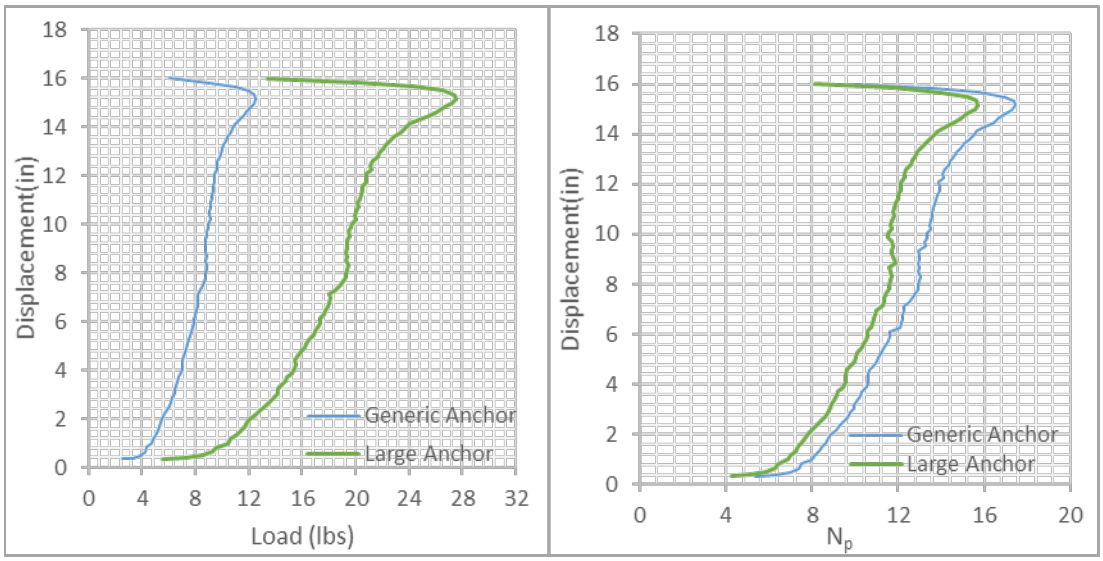

Figure 4.7. Example of Tests Results from Pure Bearing Tests with Anchors in Different Sizes

4.3.2 Pure In-Plane Shearing Factor

4.3.2.1 Pure In-plane Shearing Test Procedure

The tangential motion of the anchor is controlled by the in-plane shearing factor. The pure in-plane shearing factor can be determined by in-plane shear loading tests. In in-plane shear loading, a force is applied parallel to the fluke (Figure 4.8). In the test, the anchor is attached to the insertion rod by a wire. The anchor is then inserted into soil to 10 inches below the surface of the soil with a constant loading rate at 0.8 inch/sec. The rod friction is measured by removing the anchor at the tip of rod and inserting the rod itself to the soil bed. Since the magnetometer is attached to the anchor during drag embedment tests, the in-plane shearing factor of the anchor with and without magnetometer attached are performed separately. This helps us to quantify how the magnetometer impacts the anchor behavior during the drag tests.

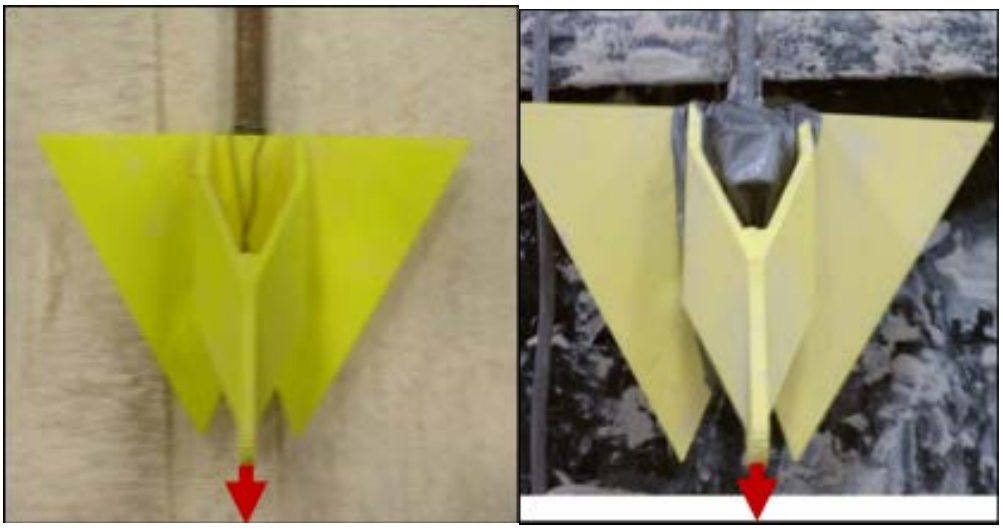

Figure 4.8 In-plane Shear Test Orientation (Left: Anchor Itself and Right: With Magnetometer) (McCarthy, 2011)

4.3.2.2 Experimental Pure In-Plane Shearing Factor

We have the following equation to calculate the pure shearing factor, and the results are shown in Table 4.2. One example of pure shearing tests results for generic anchor and larger anchor are shown in Figure 4.9 and Figure 4.10, respectively.

$$N_{tmax} = \frac{F_{rod+anchor} - F_{rod} - W'_{anchor}}{S_u \cdot A_f} \qquad \text{Eq.(4.5)}$$

where $F_{rod+anchor}$ = resistance normal force of the anchor with the rod

F_{rod} = resistance shear force of the separate tests on the rod

W'_{anchor} = submerged weight of the anchor

S_u = undrained shear strength

A_f = area of fluke

Table 4.2. Example of Normalized In-Plane Shearing Factors for the Generic Model Anchor (McCarthy, 2011)

Anchor or Anchor with Sensor	Clean (First Test) or Soil Adhered (Subsequent Test)	Load Correction	Number of Tests	Average Bearing Factor
Anchor	Clean	None	2	4.31
Anchor	Soil Adhered	None	4	4.41
With sensor attached	Clean	Corrected for Sensor Cord	1*	4.31
With sensor attached	Soil Adhered	Corrected for Sensor Cord	4	4.49

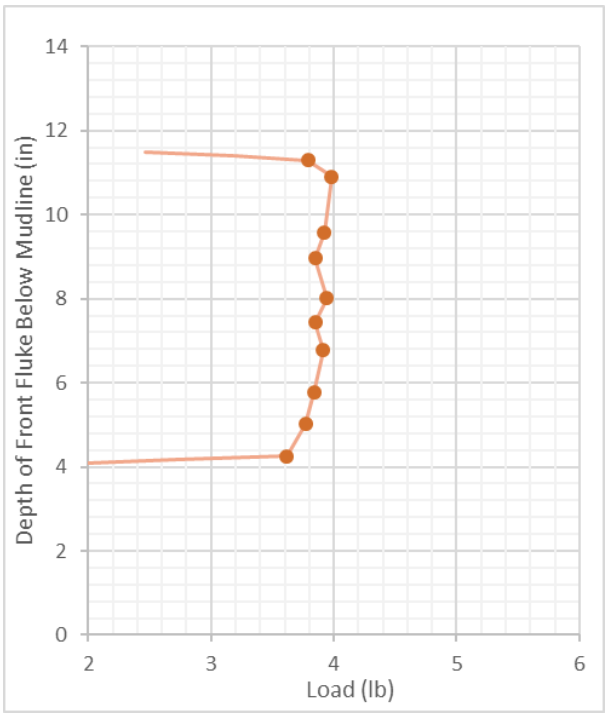

Figure 4.9. Example of Test Result from Pure In-Plane Shearing Test for the Generic Model Anchor

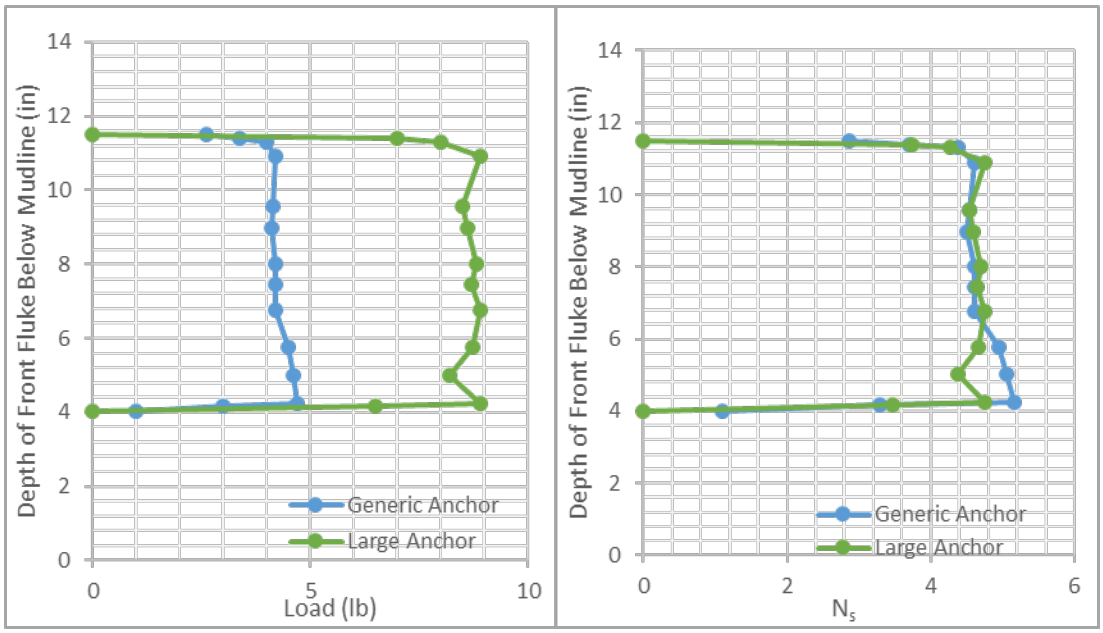

Figure 4.10 Example of Test Results from Pure In-Plane Shearing Tests with Anchors in Different Sizes

4.3.3 Pure Rotational Pitching Factor

4.3.3.1 Pure Rotation in Pitch Test Procedure

A threaded rod with two steel plate attached to each side (Figure 4.11) is designed to test the anchor in pure rotational resistance of pitch. The steel plate is 3 inches by 0.5 inches, and drilled with two holes with a diameter of 0.25 inches. These holes prevent anchor movement relative to the threaded rod in rotational motion. We attach the anchor to the steel plates and the threaded rod with plastic ties (Figure 4.12). After attaching the anchor, it is placed into the soil test bed 10 inches below the surface of soil.

4.3.3.2 Experimental Pure Rotational Pitching Factor

We calculate the normalized pitch rotation factor by the following equation, and results are shown in Table 4.3

$$N_{mmax} = \frac{M_{rod+anchor} - M_{rod}}{S_u \cdot A_f \cdot L_f} \qquad \text{Eq.(4.6)}$$

where $M_{rod+anchor}$ = resistance moment force of the anchor with the rod

M_{rod} = resistance moment force of the separate tests on the rod

W'_{anchor} = submerged weight of the anchor

S_u = undrained shear strength

A_f = area of fluke

L_f = length of fluke

Moment is calculated by the following equation

$$M = F_{drive} \cdot r \qquad \text{Eq.(4.7)}$$

where F_{drive} = the force to rotate the anchor

r = radius of the pulley

Figure 4.11. Steel Plate Attached to Threaded Rod (Ganjoo, 2010)

Figure 4.12. Connection of Threaded Rod to The Anchor for Pitch Rotation Testing (Ganjoo, 2010)

Table 4.3. Example of Normalized Pitch Rotation Factors for the Generic Model Anchor (Ganjoo, 2010)

Test ID	Approximated S_u (psf)	Moment (Mmax) (in-lbs)	$N_{m,p}$ (square fluke)	$N_{m,p}$ per unit width (ft)
2010.06.11_B_pitch_1	11.40	5.26	2.46	0.62
2010.06.11_B_pitch_2	11.40	5.18	2.42	0.61
2010.06.11_B_pitch_3	11.40	5.13	2.40	0.60
2010.06.11_B_pitch_4	11.40	5.12	2.40	0.60
2010.06.11_B_pitch_5	11.40	5.08	2.38	0.59
2010.06.11_B_pitch_6	11.40	5.10	2.39	0.60

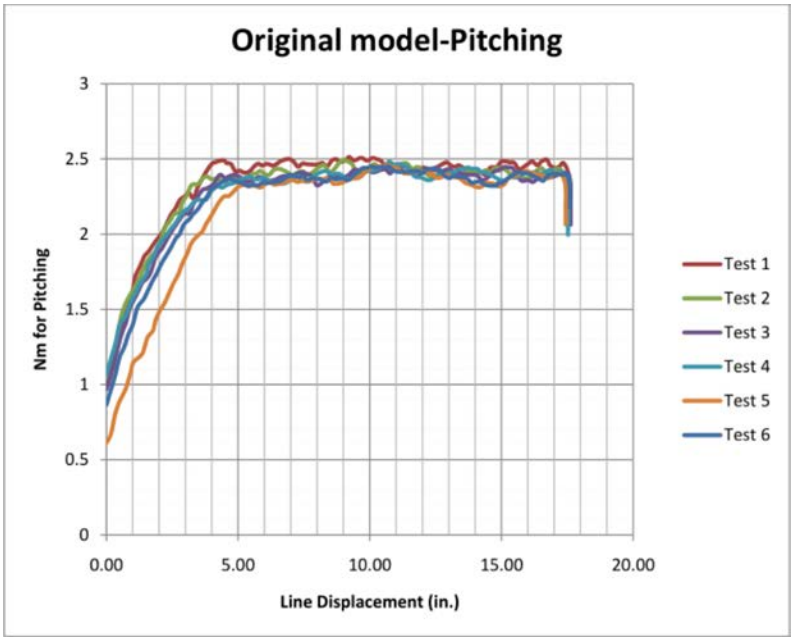

Figure 4.13. Example of Test Result of Pure Rotational in Pitch Direction for the Generic Model Anchor (Ganjoo, 2010)

4.4 Theoretical and Experimental Results of Non-Dimensional Yield Capacity Factor

4.4.1 Results for the Generic Model Anchor

The experimental and theoretical non-dimensional capacity factors for the generic model are summarized in Table 4.4. The theoretical pure normal, shearing, and pitch rotational factor are calculated by Equation 4.1, 4.2, and 4.3, respectively. The experimental N_p, 11, is close to the analytical one, 12. For the pure shear loading factor, the experimental measured N_s is 4.5, which is higher than the 2.9 obtained by the analytical model. The reason for this smaller N_s from theoretical model is that the shank is not involved for calculating the shearing factor, however, the surface area on the shank contributes shearing resistance. By calibrating the theoretical N_s, the thickness of the anchor is changed from 0.12 inch to 0.336 inch in the input in Equation 4.2 to obtain the same theoretical N_s as the experimental measurement.

Table 4.4. Measured Results for Non-Dimensional Bearing Capacity Factors

Bearing Capacity Factor	Measured Value	Theoretical Value
Pure normal loading factor, N_p	11	12
Pure shear loading factor, N_s	4.5	2.9
Pure pitch rotation factor, N_m	2.4	1.6

4.4.2 Results for the Larger Model Anchor

For the large anchor, the pure normal loading factor and shear loading factor are experimentally determined by following the producers in Section 4.3.1.1 and 4.3.2.1, and the results are summarized in Table 4.5. As a comparison, the theoretical N_p and N_s are calculated by Equation 4.1 and 4.2, and are shown in Table 4.5. From Table 4.5, it can be seen that the pure bearing and

pure in-plane shearing factor for different anchors are close. The larger anchor is measured to have a slightly smaller N_p and a slightly larger N_s compared with the generic anchor. From the test results, it can be concluded that the non-dimensional yield capacity factor for prototype anchor can be measured by using a scaled model anchor.

The measured N_p is close to the theoretical value, however, the in-plane shearing loading factor from experimental measurement (4.5) is higher than the theoretical values (2.9). The reason that the experimental measurement is higher than the theoretical ones is the same as discussed in Section 4.4.1, the shearing surface on the shank is not included when calculating the theoretical N_s. To calibrate, the thickness of fluke is increased from the real thickness, 0.18 inches, to 0.504 inches, which makes the shearing area higher.

Table 4.5. Measured Results for Non-Dimensional Bearing Capacity Factors

Bearing Capacity Factor	Measured Value	Theoretical Value
Pure normal loading factor, N_p	10.6	12
Pure shear loading factor, N_s	4.5	2.9

4.5 Conclusions

This chapter presents the test results of anchor capacity under pure loading. Tests on the pure normal and pure in-plane shearing capacity factors on the model drag embedment anchors lead to the following conclusions:

- For the generic model anchor, the experimental pure bearing capacity is 11, compared with 12 from plasticity-based analysis; the in-plane shearing capacity is 4.5 from experimental measurement, and 2.9 from analytical model.
- As Expected, the increase of 50% in the characteristic length has no impact on the bearing factors. For the larger model anchor, the experimental pure bearing capacity is 10.6 and the in-plane shearing capacity is 4.5; the theoretical bearing and in-plane shearing is 12 and 2.9, respectively. The theoretical pure bearing and pure in-plane shearing factor for the larger anchor is the same as the generic anchor.
- The theoretical in-plane shearing capacity factor for either the generic model anchor or the large anchor is calibrated by increasing the fluke thickness (0.12 inches to 0.34 inches for the generic anchor, 0.18 inches to 0.50 inches for the large anchor) since the increased part of fluke thickness counts for the shank area which is not involved for N_s calculation.

The calibrated non-dimensional yield capacity factor will be applied to the anchor trajectory and capacity prediction in Chapter 5.

Chapter 5. Drag Embedment Tests with a Single Anchor

5.1 Introduction

This chapter presents the experimental and analytical results for a single drag embedment anchor in single layer soil profile (constant and linearly increasing shear strength profile) and layered soil profiles. In constant shear strength profile, anchor parameters (equilibrium bearing capacity factor and ratio of displacement normal to displacement parallel to fluke) are first experimentally determined from drag embedment tests. Additionally, these two anchor parameters together with the non-dimensional yield capacity factors in Chapter 4 are applied to calibrate an analytical model, and the calibrated analytical model is applied to compare the tests results from linearly increasing shear strength profile and layered soil profiles. In linearly increasing shear strength profiles, two sizes of anchor are tested for extrapolating scaled model anchor tests results to predict prototype anchor behavior.

5.2 Drag Embedment Tests in a Single Layer

This section presents the drag embedment tests results with two different sizes of anchor in a single layer soil profile. First, the analytical model for anchor capacity, trajectory and orientation is presented. Next, based on the analytical model results, the experimental tests are designed. The experimental tests with the generic anchor in constant and linearly increasing shearing strength profile are presented first, and the experimental tests with a larger size anchor are presented for the purpose of understand how to extrapolate model anchor tests to real size anchor.

5.2.1 Analytical Model for Drag Embedment Anchor in a Single Layer

5.2.1.1 Theoretical Equilibrium Bearing Capacity Factor, N_e

The parameters in the prediction model are illustrated in Figure 5.1. The anchor in the prediction model is simplified into a rectangular fluke of length L_f with a cylindrical shank of length L_s. The fluke-shank angle is θ_{fs}. The tension, T_a with a line angle of θ_a, is at the shackle point and a corresponding tension, T_0 with an angle of θ_0, is at the mudline. The shank has an angle with θ_s, and $\theta_{as} = \theta_a - \theta_s$ is the angle of the anchor line force T_a (F) relative to anchor shank. The pitch angle of the anchor is designated as θ_f. (Aubeny and Chi, 2010).

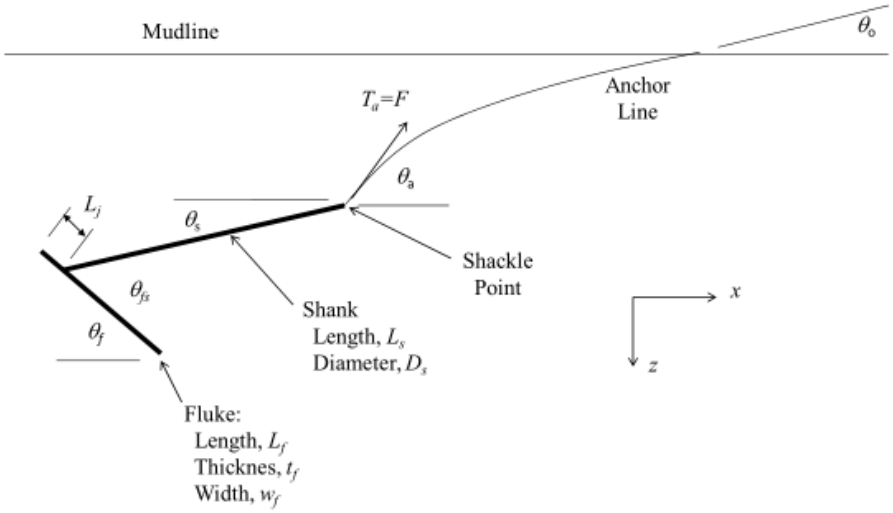

Figure 5.1. Anchor Definition Illustration (Aubeny and Chi, 2010)

Aubeny and Chi (2010) calculates the theoretical equilibrium bearing capacity factor by:

$$f = \left(\frac{|c_1|N_e}{N_{n,max}}\right)^q + \left[\left(\frac{|c_3|N_e}{N_{m,max}}\right)^m + \left(\frac{|c_2|N_e}{N_{t,max}}\right)^n\right]^{1/p} - 1 \qquad \text{Eq.(5.1)}$$

where N_e is the equilibrium bearing capacity factor

N_{nmax} is pure normal bearing factor (Equation 4.1)

N_{tmax} is the pure tangential factor (Equation 4.2)

N_{mmax} is the pure rotational factor (Equation 4.3)

m, n, p and q are the interaction coefficients for plasticity solutions and values proposed by Murff (2005) are used to model the interaction between the anchor and soil during drag embedment loading in this study (Table 5.1).

Table 5.1 Interaction Coefficients for Fluke with $L_f/t_f = 7$

Interaction factor	Murff (2005)	Yang et al. (2008)
m	1.56	1.40
n	4.19	3.49
p	1.57	1.31
q	4.43	1.14

$c_1 = \sin(\theta_{as} + \theta_{fs})$

$c_1 = \cos(\theta_{as} + \theta_{fs})$

$c_3 = \sin(\theta_{as} + \theta_{fs}) \left[\frac{L_j}{L_f} + \frac{L_s}{L_f}\cos\theta_{fs} - \frac{1}{2}\right] - \cos(\theta_{as} + \theta_{fs}) \sin\theta_{fs} \frac{L_s}{L_f}$

The yeild function in this study is preposed by Rasulo and Aubeny (2017) and they simplify Equation 5.1 into Equation 5.2 by vanishing moment term since the moment on anchor fluke is small when anchor is in equilibrium condition where the equialibrium capacity factor is calculated

$$f = \left(\frac{|c_1|N_e}{N_{n,max}}\right)^q + \left[\left(\frac{|c_2|N_e}{N_{t,max}}\right)^n\right]^{1/p} - 1 \qquad \text{Eq. (5.2)}$$

where $c_1 = \sin(\theta_{fs})$

$c_2 = \cos(\theta_{fs})$

From Equation 5.2, N_e can be calculated by taking the root of $f(N_e) = 0$.

The equilibrium bearing capacity factor is important for capacity estimation. A comparison example with different N_e for drag embedment anchor is shown in Figure 5.2. From Figure 5.2, a higher equilibrium capacity factor leads to a higher anchor capacity factor. The meaning of equilibrium bearing capacity on the yield surface will be discussed in Section 5.2.1.3.

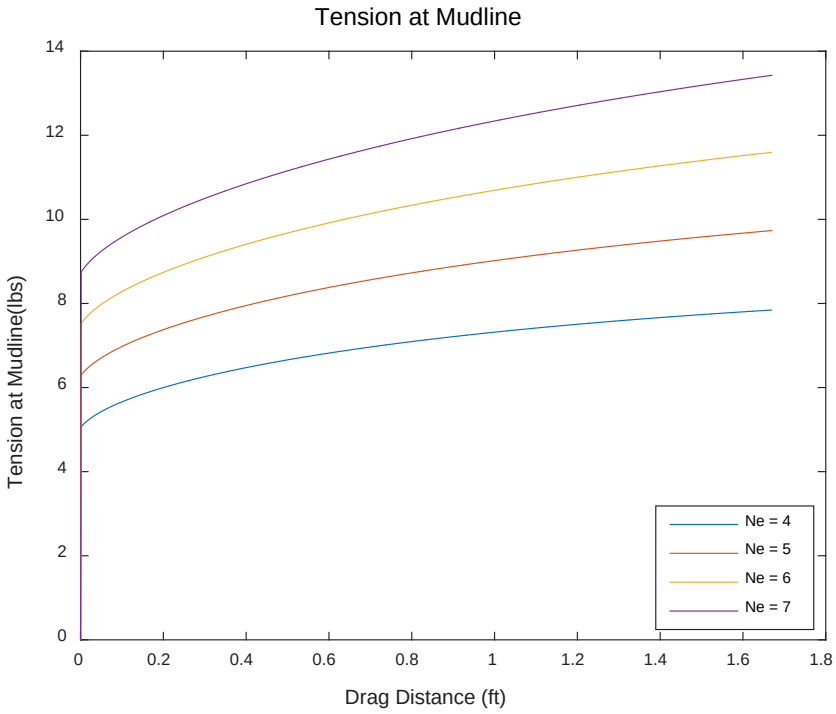

Figure 5.2. Capacity with Different N_e

5.2.1.2 Theoretical Ratio of Displacement Normal to Displacement Parallel to Fluke

Aubeny and Chi (2010) calculates the ratio of normal to tangential motion (R_{nt}) by:

$$R_{nt} = \frac{\left(\frac{N_{t,max}}{N_{n,max}}\right)\left(\frac{pq}{n}\right)}{\left[\left(\left|\frac{N_m}{N_{m,max}}\right|\right)^m + \left(\left|\frac{N_t}{N_{t,max}}\right|\right)^n\right]^{\left(\frac{1}{p}\right)-1}} \frac{\left(\left|\frac{N_n}{N_{n,max}}\right|\right)^{q-1}}{\left(\left|\frac{N_t}{N_{t,max}}\right|\right)^{n-1}} \qquad \text{Eq.(5.3)}$$

Rasulo and Aubeny (2017) simplifies Equation 5.3 into Equation 5.4 by making the moment term is equal to 0 since there is no rotation around fluke when anchor is in equilibrium.

$$R_{nt} = \frac{\left(\frac{N_{t,max}}{N_{n,max}}\right)\left(\frac{pq}{n}\right)}{\left[\left(\left|\frac{N_t}{N_{t,max}}\right|\right)^n\right]^{\left(\frac{1}{p}\right)-1}} \frac{\left(\left|\frac{N_n}{N_{n,max}}\right|\right)^{q-1}}{\left(\left|\frac{N_t}{N_{t,max}}\right|\right)^{n-1}} \quad \text{Eq. (5.4)}$$

Equation 5.4 can be further modified with N_e as shown in below

$$R_{nt} = \frac{\left(\frac{N_{t,max}}{N_{n,max}}\right)\left(\frac{pq}{n}\right)}{\left[\left(\left|\frac{N_e c_2}{N_{t,max}}\right|\right)^n\right]^{\left(\frac{1}{p}\right)-1}} \frac{\left(\left|\frac{N_e c_1}{N_{n,max}}\right|\right)^{q-1}}{\left(\left|\frac{N_t}{N_{t,max}}\right|\right)^{n-1}} \quad \text{Eq. (5.5)}$$

Therefore, if N_e is obtained from Equation 5.2, then R_{nt} can be calculated by Equation 5.5.

The R_{nt} controls the direction of anchor movement. If an anchor moves a certain displacement parallel to fluke, a higher R_{nt} makes anchor moves more in the direction normal to fluke, which makes anchor move towards to soil surface. In comparison, anchor with a lower R_{nt} moves less in the direction normal to fluke at a certain displacement parallel to fluke, that is, anchor dives deeper into soil. The R_{nt} directly influence anchor trajectory (Figure 5.3), trajectory with smaller R_{nt} is steeper than the trajectory with a higher R_{nt}. The meaning of R_{nt} on the yield surface will be discussed in Section 5.2.1.3.

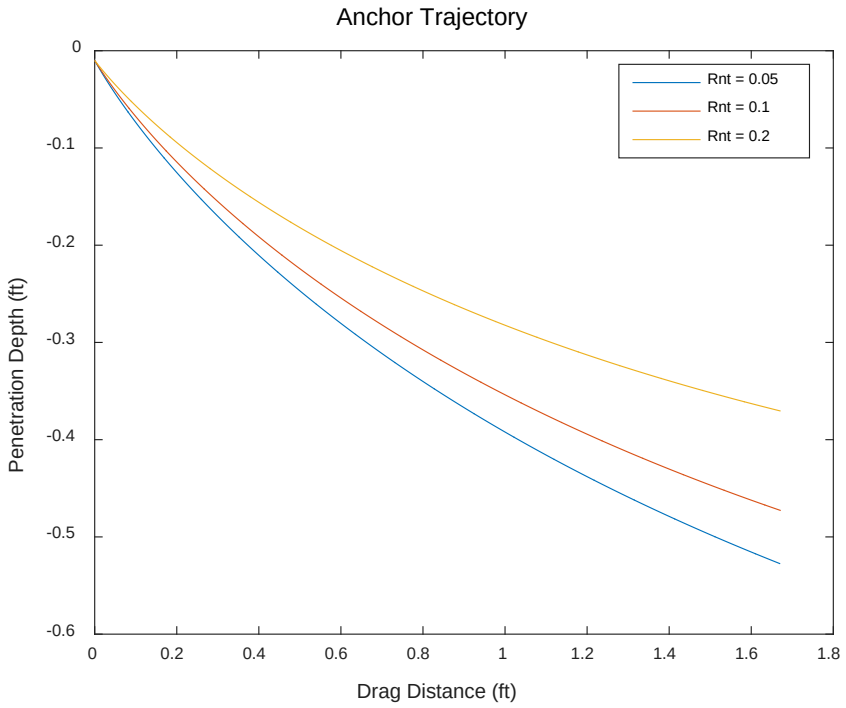

Figure 5.3. Trajectory with Different R_{nt}

5.2.1.3 Yield Surface

The yield surface is proposed by O'Neil et al. (2003) to describe soil-anchor interaction under combined loading (vertical load V, moment M, and lateral H). The yield surface is plotted based on the calculated results from Equation 5.2. An example of yield surface with different combination of R_{nt} and N_e is shown in Figure 5.4. The orange yield surface is with the R_{nt} with 0.2 and N_e with 6.1, and the blue yield surface is with the R_{nt} with 0.02 and N_e with 6.6. The Ne represents the distance between the origin to the point on the yield surface. Therefore, a larger N_e leads to a larger yield surface (blue yield surface is larger than the orange one as shown in Figure 5.4). The R_{nt} represents the tangential slope at the point where N_e touches yield surface. Therefore, a higher R_{nt} means a flatter angle (orange yield surface has a flatter angle compared with blue one as shown in Figure 5.4). In terms of anchor movement, at a certain displacement parallel to fluke

(Δs), a higher R_{nt} means anchor moves more in the normal to the fluke direction (Δn) compared with that anchor with a smaller R_{nt}.

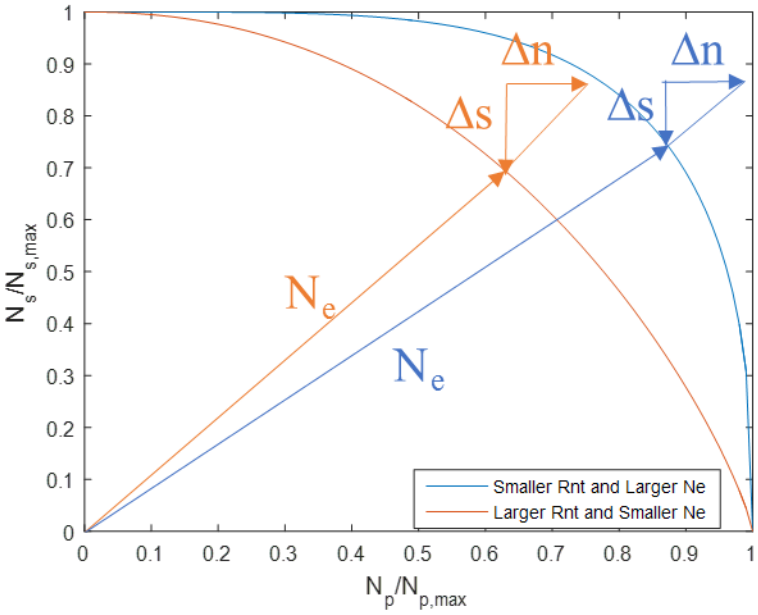

Figure 5.4. Comparison of Yield Surfaces with Different R_{nt} and N_e

5.2.1.4 Algorithm for Trajectory Prediction

The algorithm by Aubeny and Chi (2010) for in-plane drag embedment trajectory in a single layer is used to calculate the trajectory and the load capacity of the anchor.

The trajectory algorithm is presented below:

1. Advance the padeye at current coordinate (x, z) a small distance Δs in the direction of the fluke oriented at an angle θ_{f1} from horizontal. An increment Δs = 0.024 inch produced satisfactory convergence in this study.
2. Compute the corresponding increment of drag distance, Δs, parallel to fluke.

Then, the displacement normal to fluke is $\Delta n = R_{nt}\,\Delta s$.

$$\Delta z = \Delta s \sin\theta_{f1} - \Delta n \cos\theta_{f1} \qquad \text{Eq.(5.6)}$$

$$\Delta x = \Delta s \cos\theta_{f1} + \Delta n \sin\theta_{f1} \qquad \text{Eq.(5.7)}$$

3. Calculate the normalized depth $\hat{z}$ and normalized depth increment

$$\hat{z} = z/b \qquad \text{Eq.(5.8)}$$

$$d\hat{z} = dz/b \qquad \text{Eq.(5.9)}$$

where b is the anchor line or chain diameter

4. Compute the tension at the shackle by Equation 5.10

$$\hat{T}_a = T_a/S_{ua}b^2 = N_e A_f/b^2 \qquad \text{Eq.(5.10)}$$

where N_e is equilibrium capacity factor, and A_f is the fluke area.

5. Compute the line angle at the shackle by rearranging Equation 5.11 into Equation 5.12

$$T_a(\theta_a^2 - \theta_0^2)/2 = z\,E_n\,N_c\,b\,(S_{u0} + k\,z/2) \qquad \text{Eq.(5.11)}$$

$$\theta_a = \sqrt{2\,z\,E_n\,N_c\,b\,\frac{S_{uaverage}}{T_a} + \theta_0^2} \qquad \text{Eq.(5.12)}$$

θ_0 = anchor line angle at the mudline

Nc = bearing factor for anchor line

En = multiplier for anchor lines comprised of chains (1 is for anchor wire, and 2.5 for anchor chain)

k = soil shear strength increase per unit increase in depth

6. Calculate the increment of line angle at the shackle $d\theta_a$

$$d\theta_a = \frac{1}{\theta_a}\left[\frac{E_n N_c}{T_a^*} - \frac{\theta_a^2 - \theta_0^2}{2\left(\frac{1}{\eta} + \hat{z}\right)}\right] d\hat{z} \qquad \text{Eq.(5.13)}$$

where η = strength gradient parameter = $b\,k / s_{u0}$

7. Calculate the tension at the mud line

$$T_0 = T_a \exp[\mu (\theta_a - \theta_0)] \qquad \text{Eq.(5.14)}$$

where μ is the relative magnitude of tangential to normal unit force acting on the anchor line, which is typically is in the range of 0.4-0.6.

8. Update the fluke angle $\theta_f = \theta_{f1}$, and padeye coordinates (x, z)

Repeat step 1 to step 8 until the anchor reaches its ultimate embedment. At the ultimate embedment, the pitch of the anchor will become zero and there will be no further embedment. The capacity will be constant when the anchor reaches ultimate embedment (Aubeny et al., 2008).

5.2.2 Generic Drag Embedment Anchor in a Single Layer Soil Profile

5.2.2.1 Experimental Design

This section studies the analytical model in Section 5.2.1.4, and obtains the test bed characteristics such as the soil strength (undrained shear strength at mudline and the shear strength gradient) and anchor line thickness. Based on these information, the load cell capacity described in Section 3.6 is checked to ensure it will have the range needed to measure anchor capacity. Also, the magnetometer described in Section 3.9 is checked to ensure it is capable to cover the range of trajectory and orientation of drag embedment anchor.

5.2.2.1.1 Effect of Shear Strength at Mudline

In the constant shear strength profile, drag embedment anchor capacity, trajectory and orientation in terms of pitch are checked by analytical model. An example results with the shear strength at 16 psf, 18 psf, and 20 psf are shown in Figure 5.5 to Figure 5.7. From the capacities

shown in Figure 5.5, as the shear strength increases, the capacity is expected to increase. From the trajectories in Figure 5.6, the final penetration depth is independent on the shear strength in the constant shear strength profile. Figure 5.7 shows that the orientation is also independent on the shear strength in the constant shear strength profile.

From the capacities shown in Figure 5.5, it can be estimated that the maximum load from drag embedment tests in constant shear strength profile (S_u up to 50) is in range of the capacity of load cell. The horizontal displacement from trajectory is up to 20 inches and the vertical displacement is up to 4 inches which are in the range of magnetometer measurement. The pitch ranges from 40° to 20° is also in the measurable range by magnetometer.

Table 5.2. Input for Effect of Shear Strength at Mudline

Soil Parameter	
Su at mudline	16 or 18 or 20 psf
k	0 psf/ft
Anchor and Anchor line	
Anchor line	0.22 inch
Anchor initially embedment	0.12 inch
Initial pitch angle (fluke to horizontal)	40°

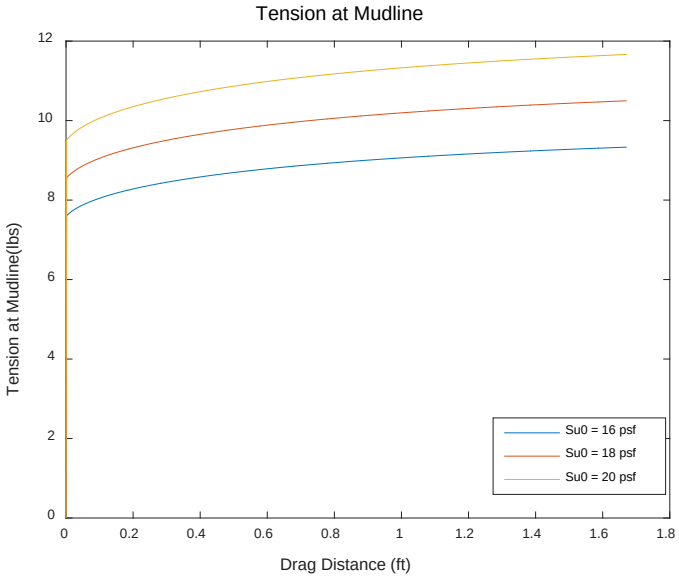

Figure 5.5. Anchor Capacity (Effect of Shear Strength at Mudline)

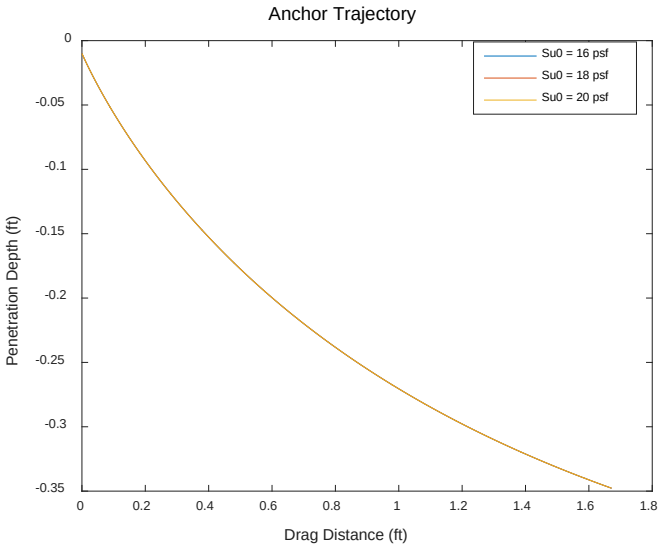

Figure 5.6. Anchor Trajectory (Effect of Shear Strength at Mudline)

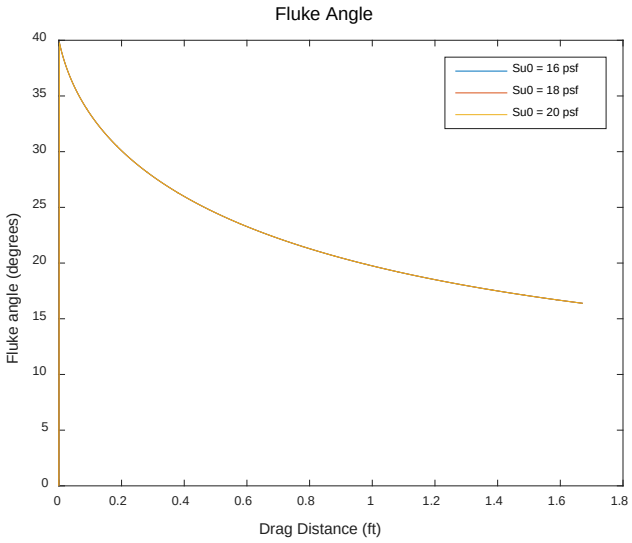

Figure 5.7. Anchor Pitch (Effect of Shear Strength at Mudline)

5.2.2.1.2 Effect of Shear Strength Gradient

The capacity (Figure 5.8), trajectory (Figure 5.9), and orientation (Figure 5.10) of drag embedment anchor is checked in the linearly increasing shear strength profile with a gradient of 6 psf/ft and 10 psf/ft. From Figure 5.8, the capacity is expected to increase with the increase of the shear strength gradient. Figure 5.9 shows that the higher shear strength gradient leads to a deeper penetration. Figure 5.10 shows that anchor pitches slightly less in the shear strength profile with a higher shear strength gradient.

From the capacity results, it can be estimated that the load cell is capable to measure the capacity in the linearly increasing shear strength profile. From the trajectory and pitch results, it can be concluded that the magnetometer is capable to track anchor displacement and rotation during drag tests.

Table 5.3. Input for Effect of Shear Strength Gradient at Mudline

Soil Parameter	
Su at mudline	16 psf
k	0 or 6 or 10 psf/ft
Anchor and Anchor line	
Anchor line	0.22 inch
Anchor initially embedment	0.12 inch
Initial pitch angle (fluke to horizontal)	40°

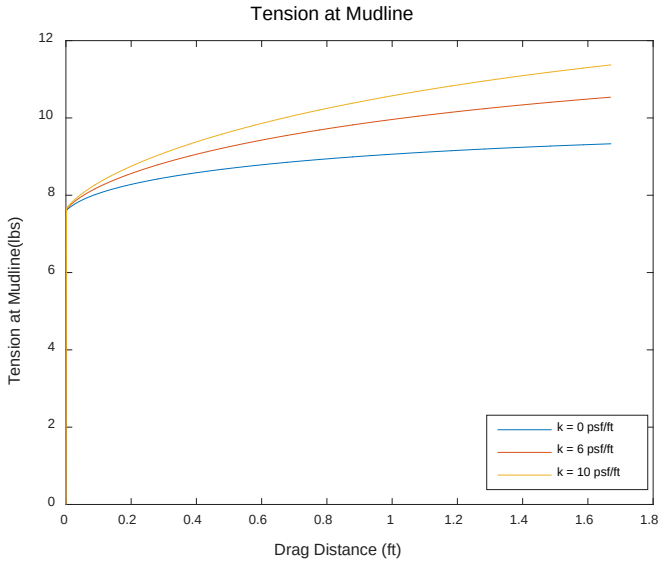

Figure 5.8. Anchor Capacity (Effect of Shear Strength Gradient)

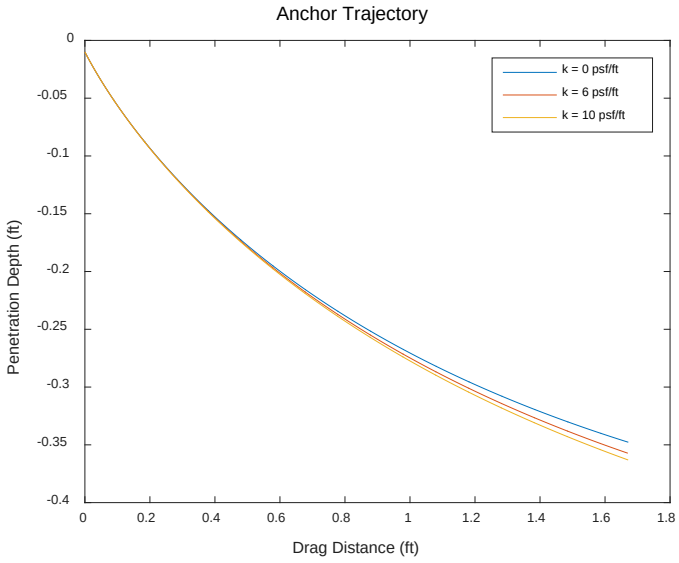

Figure 5.9. Anchor Trajectory (Effect of Shear Strength Gradient)

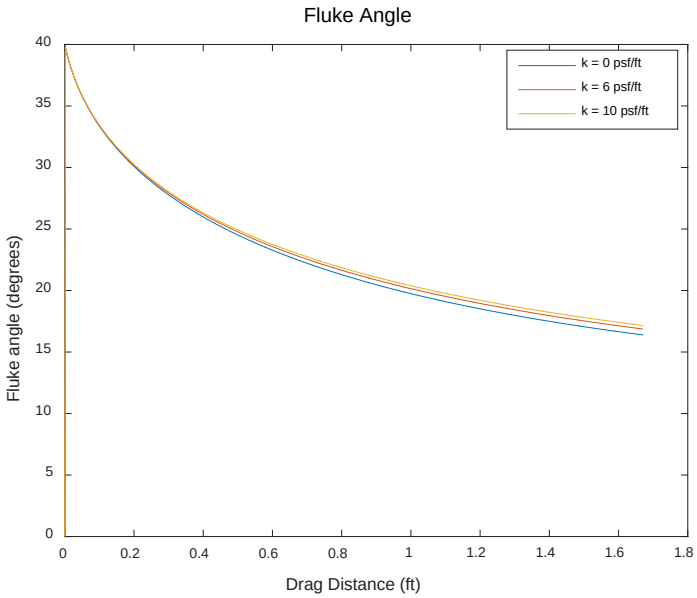

Figure 5.10. Anchor Pitch (Effect of Shear Strength Gradient)

5.2.2.1.3 Effect of Anchor Line Thickness

In the linearly increasing shear strength profile with gradient of 6 psft/ft and 16 psf at the surface at mudline, drag embedment anchor with different line thickness (0.05 inch and 0.22 inch) is checked in terms of its capacity, trajectory, and pitch. The 0.22 inch thickness line is selected since the industry standard ratio for fluke area over square of line thickness is around 200, and 0.22 inch thickness yields the ratio at 216. The line thickness of 0.05 inch is selected since the line is thin enough to influence anchor behavior, which minimizes the lines effect on the anchor pitch. Figure 5.11 shows the capacities with different line attached, a thicker line leads to a higher capacity. Figure 5.12 shows the trajectories with different line thickness. Figure 5.13 shows the orientation with different line thickness. It can be seen that the line thickness has impact the trajectory and orientation.

Table 5.4. Input for Effect of Anchor Line Thickness

Soil Parameter	
Su at mudline	16 psf
k	6 psf/ft
Anchor and Anchor line	
Anchor line	0.05 or 0.22 inch
Anchor initially embedment	0.12 inch
Initial pitch angle (fluke to horizontal)	40°

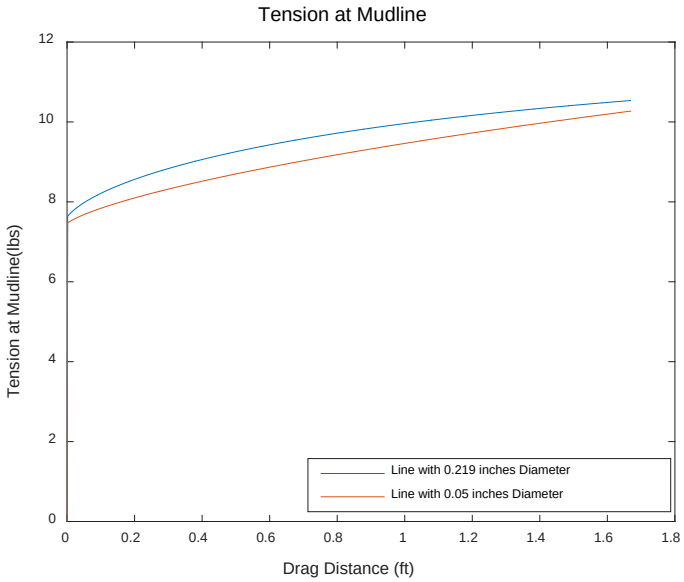

Figure 5.11. Anchor Capacity (Effect of Anchor Line Thickness)

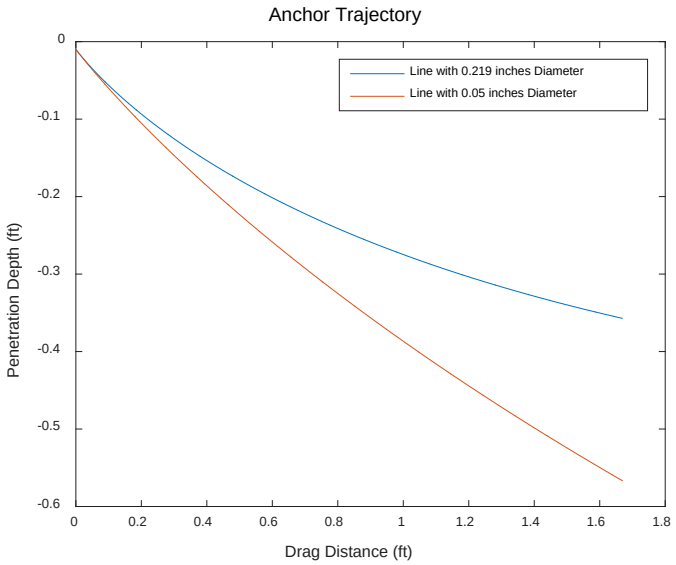

Figure 5.12. Anchor Trajectory (Effect of Anchor Line Thickness)

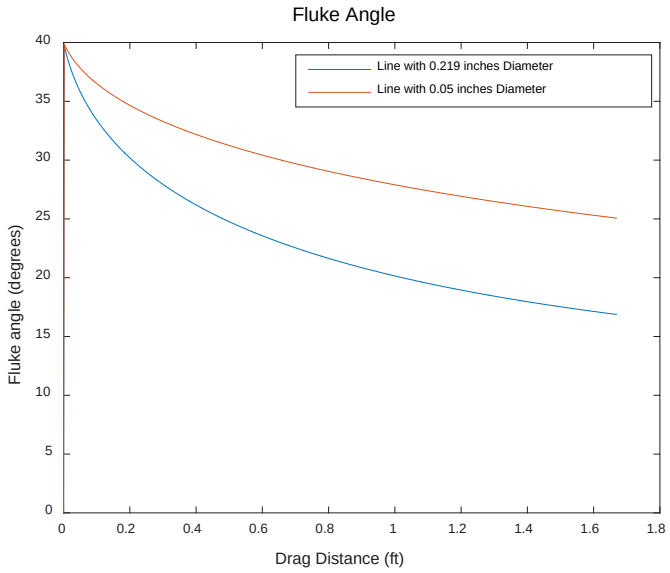

Figure 5.13. Anchor Pitch (Effect of Anchor Line Thickness)

5.2.2.2 Test Setup

Drag embedment tests are conducted by applying a load to the scale model. In the drag tests, the trajectory and capacity of the scaled model anchor is measured. The anchor is attached to the load cell with different sizes of loading lines. Drag tests are performed in a single layer soil test with either a constant shear strength profile or linearly increasing shear strength profiles. The pulley is installed at mudline to provide zero line angle and is located approximately 43 inches away from the starting point of the test. Additionally, the magnetometer sensor is attached to the anchor to track the location and orientation of the anchor throughout the test. The magnetometer source is located on top of the thermos-plastic tank (Figure 5.14).

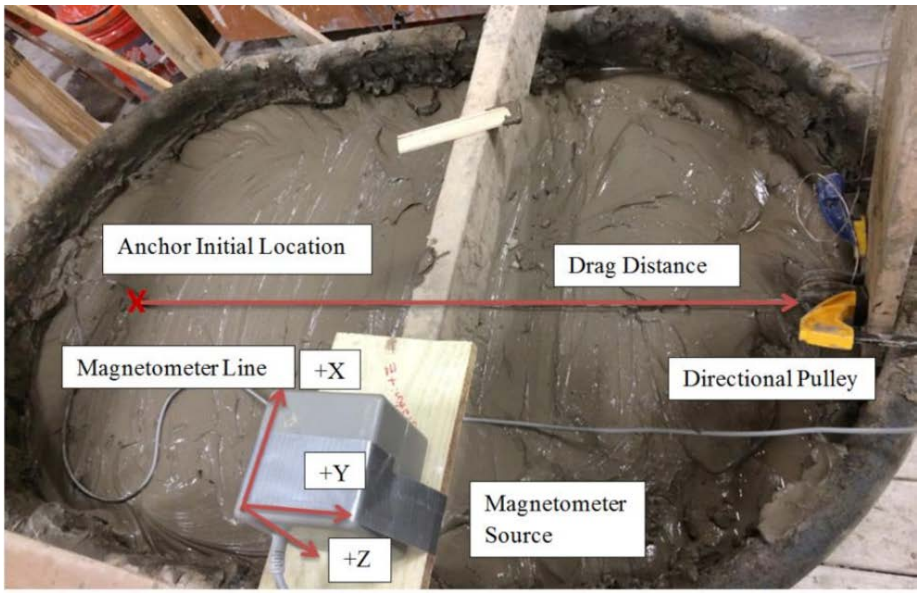

Figure 5.14. Picture of In-Plane Drag Embedment Test in Thermo-Plastic Tank (Gerkus, 2016)

Based on the study of analytical model in Section 5.2.2.1, the following two tests bed with a single layer soil profile is proposed. Table 5.5 summarizes the tests in a single layer. We perform drag tests in a constant shear strength profile and a linearly increasing shear strength profile. The constant shear strength profile is with shear strength 16 psf at the mudline, and slightly increases 6 psf per ft. Since the maximum penetration depth by drag embedment anchor is 4.5 inch, thus the increase of shear strength along depth is trivial. For the linearly increasing shear strength profile, the shear strength at mudline is 13.57 psf, and the shear strength gradient is 9.11 psf/ft.

Table 5.5. Summary of Tests in a Single Layer Soil Profile

Case 1 Constant Shear Strength	Su at mudline	16 psf
	Su gradient	6 psf/ft
	Sensitivity of soft layer	1
	Stiff Layer Thickness	0 inch
	Stiff Layer Depth from Mudline	0 inch
	Shear strength ratio of stiff layer over soft	0
Case 2 Linearly Increasing Shear Strength	Su at mudline	13.57 psf
	Su gradient	9.11 psf/ft
	Sensitivity of soft layer	1
	Stiff Layer Thickness	0 inch
	Stiff Layer Depth from Mudline	0 inch
	Shear strength ratio of stiff layer over soft	0

5.2.2.3 Experimental and Analytical Results

5.2.2.3.1 Experimental Equilibrium Bearing Capacity Factor, N_e

When the anchor is in equilibrium condition in drag tests, a dimensionless factor, N_e, can be determined. For tests in a linearly increasing undrained shear strength profile, the equilibrium bearing factor (N_e) is calculated at the end of test, that is determined by the holding capacity and the shear strength corresponding with the final embedment depth. For tests in a uniform undrained shear strength profile, the load used to determine the equilibrium bearing capacity factor is load averaged throughout the drag test with the neglect of load within the first couple inches of drag.

$$N_e = \frac{T_a}{S_u \cdot A_f} \qquad \text{Eq.(5.15)}$$

where N_e = Equilibrium bearing factor

T_a = Tension measured at the load cell

S_u = Undrained shear strength at the fluke

A_f = Area of fluke

The experimental N_e is derived based on the anchor capacity (Figure 5.15) in constant shear strength profile. The experimental N_e is calculated based on Equation 5.15. An example of N_e determined from the drag tests in the constant shear strength profile is shown in Figure 5.16. The N_e is about 6.2 after the first 6 inches of drag distance.

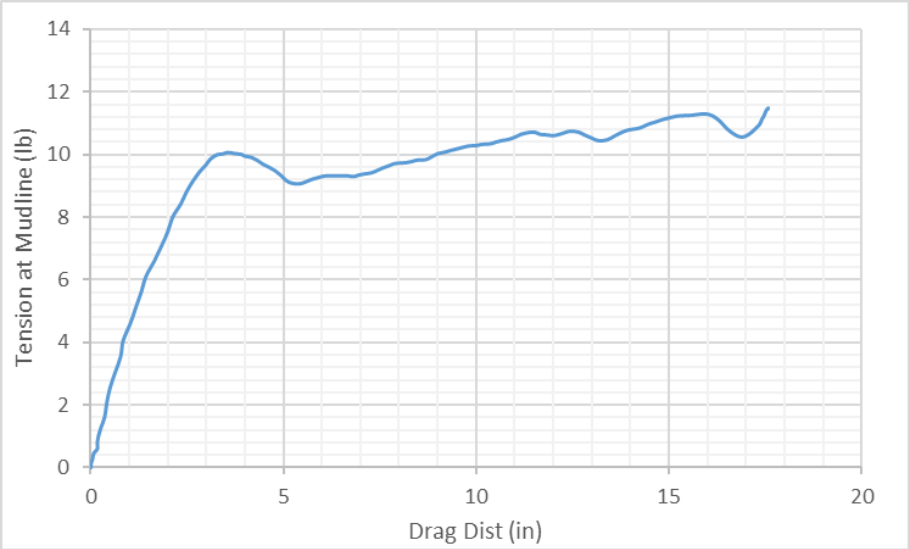

Figure 5.15. Test Result of Anchor Capacity for Calibrating Equilibrium Capacity Factor, N_e

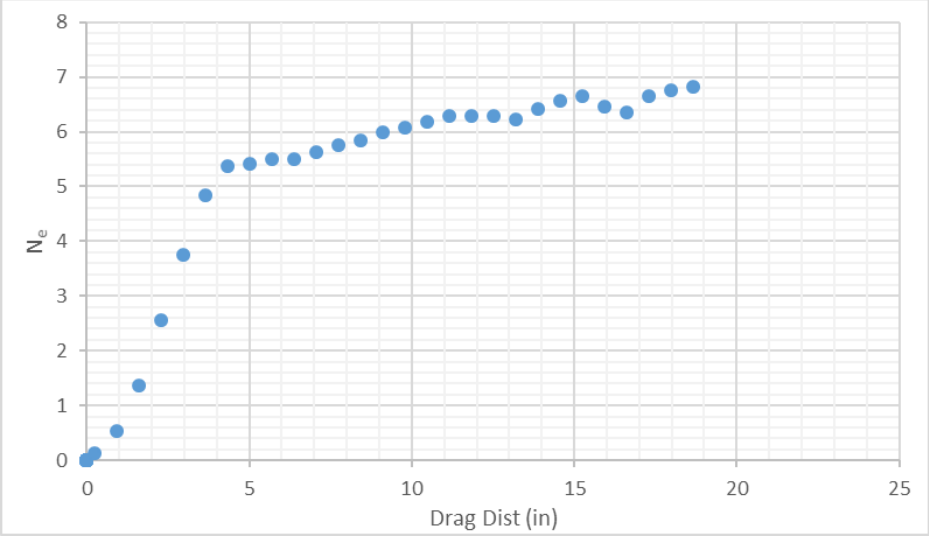

Figure 5.16. Example of Experimental Equilibrium Bearing Capacity Factor

5.2.2.3.2 Experimental Displacement Normal to Displacement Parallel to the Fluke (R_{nt})

The ratio of the change in displacement normal to the fluke (Δn) to the change in displacement parallel to the fluke (Δt) is usually small for a commercial DEA (Aubeny and Chi, 2010). This parameter can be calculated from the drag tests in the constant shear strength profile with sensitivity of 1 and applied to the predictive model. The experimental determination of this ratio is using the difference of horizontal and vertical displacements between two readings from a magnetometer from which Δx and Δz can be calculated. Afterwards, combining the corresponding pitch angle θ_f of the anchor with Δx and Δz, the Δn and Δt can be calculated by Equation 5.16 and 5.17

$$\Delta n = \Delta x \cdot \sin\theta_f - \Delta z \cdot \cos\theta_f \qquad \text{Eq.(5.16)}$$

$$\Delta t = \Delta x \cdot \cos\theta_f + \Delta z \cdot \sin\theta_f \qquad \text{Eq.(5.17)}$$

The experimental R_{nt} is obtained from the anchor trajectory (Figure 5.17) and pitch angle along the horizontal drag (Figure 5.18) in constant shear strength profile. First, the horizontal and vertical displacement of anchor is calculated based on the reading from magnetometer and then Δn and Δt. is obtained by using Equation 5.16 and Equation 5.17. The R_{nt} is then simply the ratio of Δn/Δt. Testing with the magnetometer indicated that the value of Δn/Δt is typically 0.2 after 1-3 fluke length of drag distance (Figure 5.19). This ratio is used in the evaluation of in-plane drag behavior in the predictive model.

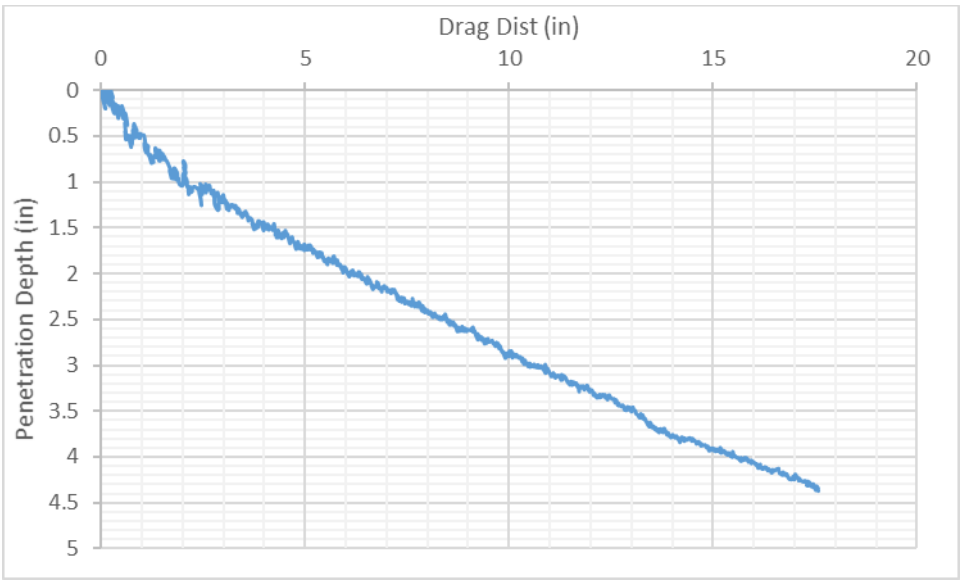

Figure 5.17. Test Result of Anchor Trajectory for Calibrating Experimental Displacement Normal to Displacement Parallel to Fluke R_{nt}

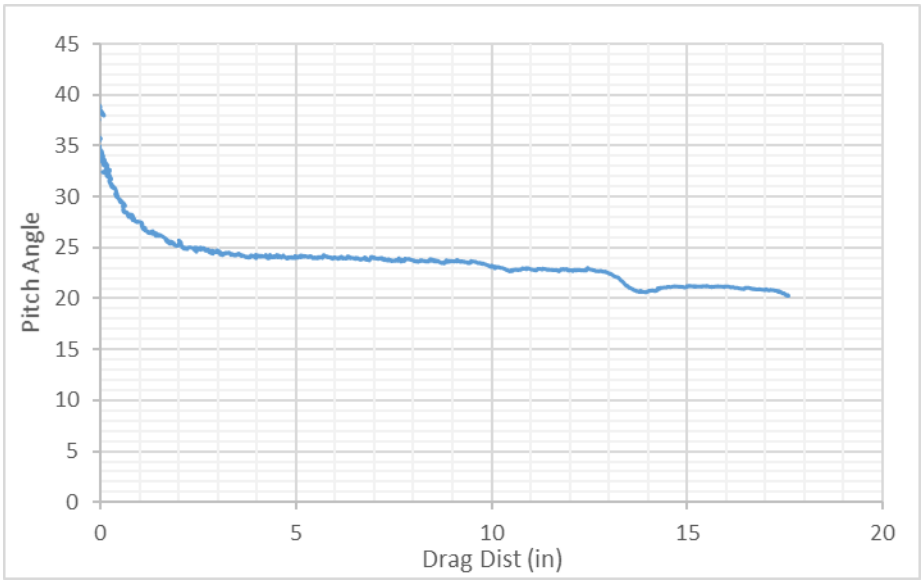

Figure 5.18. Test Result of Anchor Pitch for Calibrating Experimental Displacement Normal to Displacement Parallel to Fluke R_{nt}

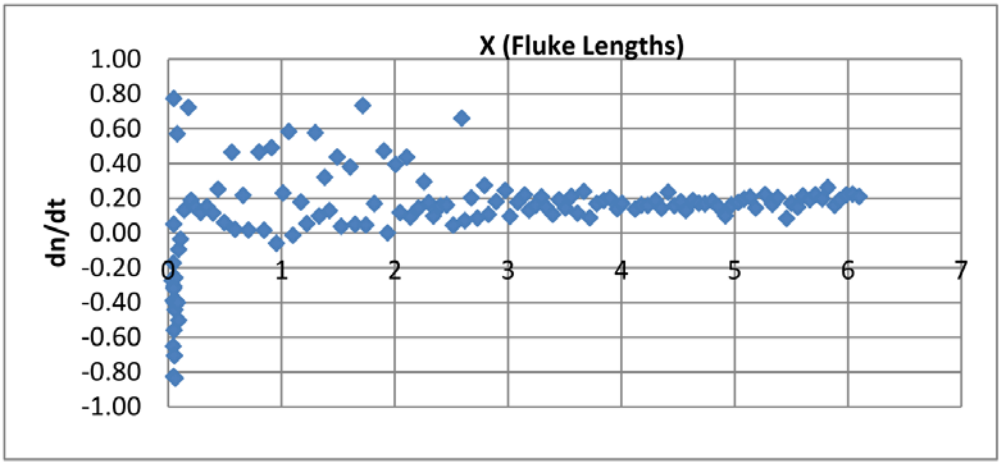

Figure 5.19. Example of Experimental Δn/Δt Throughout Drag Distance

5.2.2.3.3 Calibrated Yield Surface Based on Experimental Results

Table 5.6 presents the equilibrium bearing capacity factor and the ratio of the normal to shear movement. Table 5.7 summarizes the interaction coefficients for the yield surface before and after calibration based on the N_e and R_{nt} presented in Table 5.6. The yield surfaces with different sets of interaction coefficients are shown in Figure 5.20. The yield surface is calibrated by changing the n/p ratio and q in Eq. 5.2 to make the equilibrium bearing capacity factor and ratio of normal to shear movement in theoretical values close to the experiment values.

Table 5.6.The Equilibrium Bearing Capacity Factor, N_e, and the Ratio of the Normal to Shear Movement Ratio, R_{nt}

	Equilibrium bearing capacity factor, Ne	Ratio of the normal to shear movement, R_{nt}
Theoretical Results Before Calibration	4.3	0.05
Theoretical Results After Calibration (Experimental Results)	6.2	0.2

Table 5.7. Exponents in the Yield Function

Characteristics of Yield Surface	Calibrated Values based on Drag Tests	Theoretical Values based on FEM Work
n/p	1.23	2.67
q	2.2	4.43

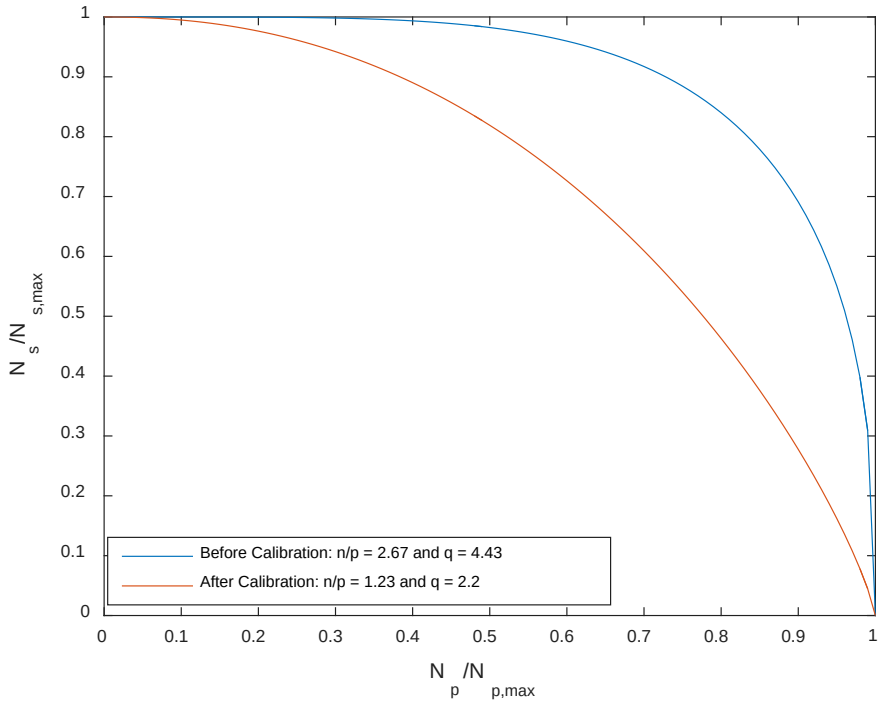

Figure 5.20. Comparison between yield surfaces with different parameters

5.2.2.3.4 Drag Embedment Tests Results

Based on the drag embedment test results in the constant shear strength profile in case 1, together with the pure loading tests results in Section 4.3.1 and Section 4.3.2, the equilibrium bearing capacity factor (N_e) and displacement normal to parallel to the fluke (R_{nt}) in Section 5.2.2.3.3, we calibrated the prediction model. The parameters we calibrate is pure in-plane

shearing factor (N_s), displacement normal to parallel to the fluke (R_{nt}), and equilibrium bearing capacity factor (N_e). The pure in-plane shearing factor (N_s) is calibrated based on the pure in-plane shearing tests. Before calibration, N_s by theoretical plasticity is 2.9. After calibration by increasing the thickness of plate from 0.12 inches to 0.336 inches, the theoretical N_s matches the experimental measured 4.47. The R_{nt} and N_e is calibrated based on the drag embedment tests in constant shear strength profile. N_e is experimentally obtained from normalizing the load with anchor fluke area and undrained shear strength. R_{nt} is calculated based on anchor trajectory extracted from magnetometer reading (Section 5.2.2.3.2). The theoretical N_e and R_{nt} is calibrated to match experimental ones by changing n/p ratio and q from 2.67 and 4.43 to 1.23 and 2.2, thus the N_e and R_{nt} is changed from 4.3 and 0.05 to 6.2 and 0.2. The results of prediction results between the before and after calibration are shown Figure 5.21 and Figure 5.22. Figure 5.21 shows the capacity, trajectory, and pitch in a constant shear strength profile, and Figure 5.22 shows the tests results in a linearly increasing shear strength. From those two comparisons, it can be seen that the predicted capacity with the calibrated model can better predict the anchor capacity in either the constant shear strength and linearly increasing shear strength profile since the N_e is increased from 4.3 to 6.2. Comparing the original and the calibrate trajectory, it can be seen that the original model predicts a shallow penetration depth, however, the calibrated model can better predict the trajectory. For the pitch prediction, the calibrated model can better match with the measured pitch, but still is not capable for the flat pitch during the first inches drag.

Figure 5.23 and Figure 5.24 present the calibrated model compared with all experimental results in constant and linearly increasing shear strength profile. It can be seen that the variability between the experimental results and calibrated prediction still exists, but in a reasonable range.

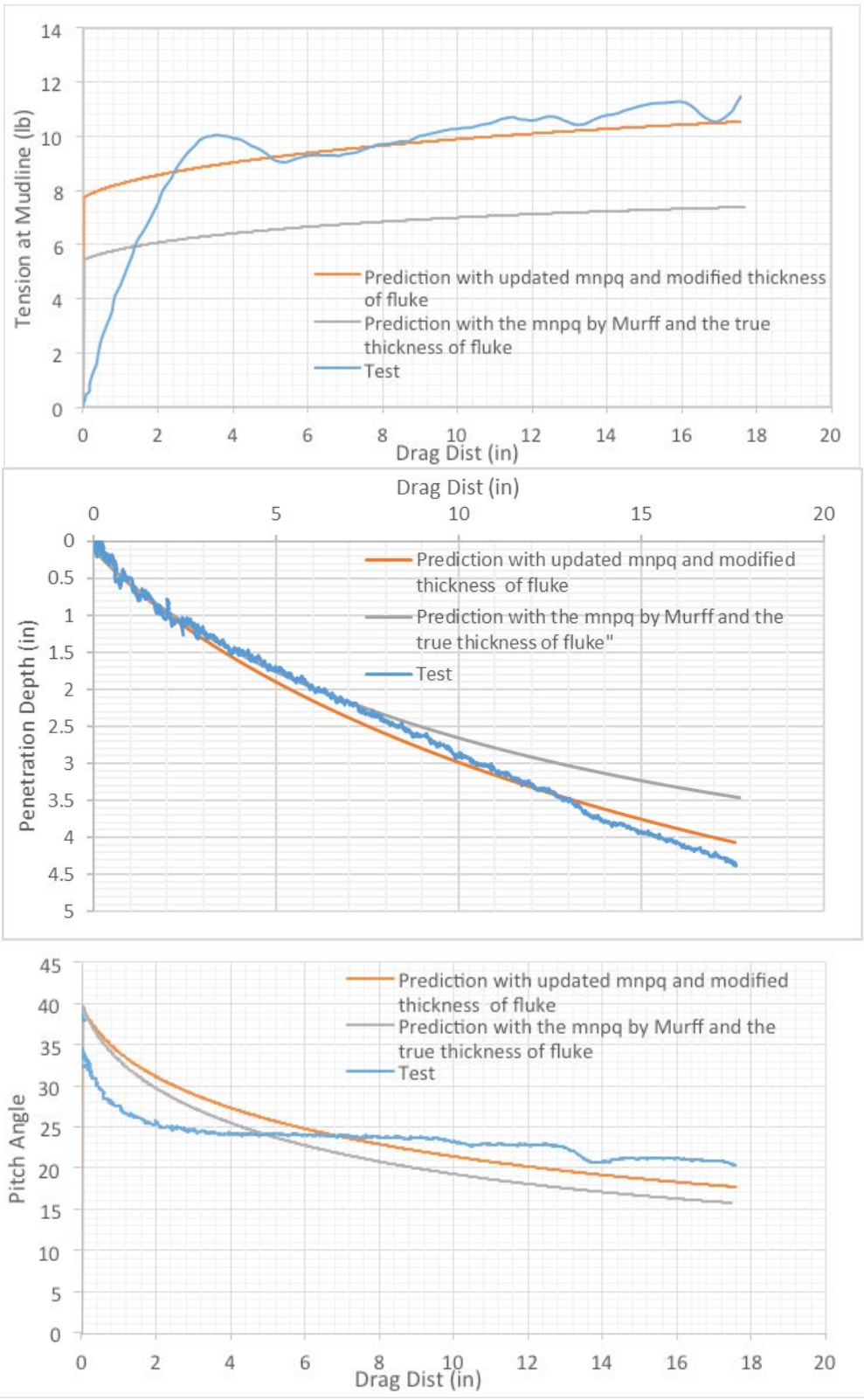

Figure 5.21. Comparison of Experimental Results with Predictions for Constant Undrained Shear Strength with Depth (Case 1)

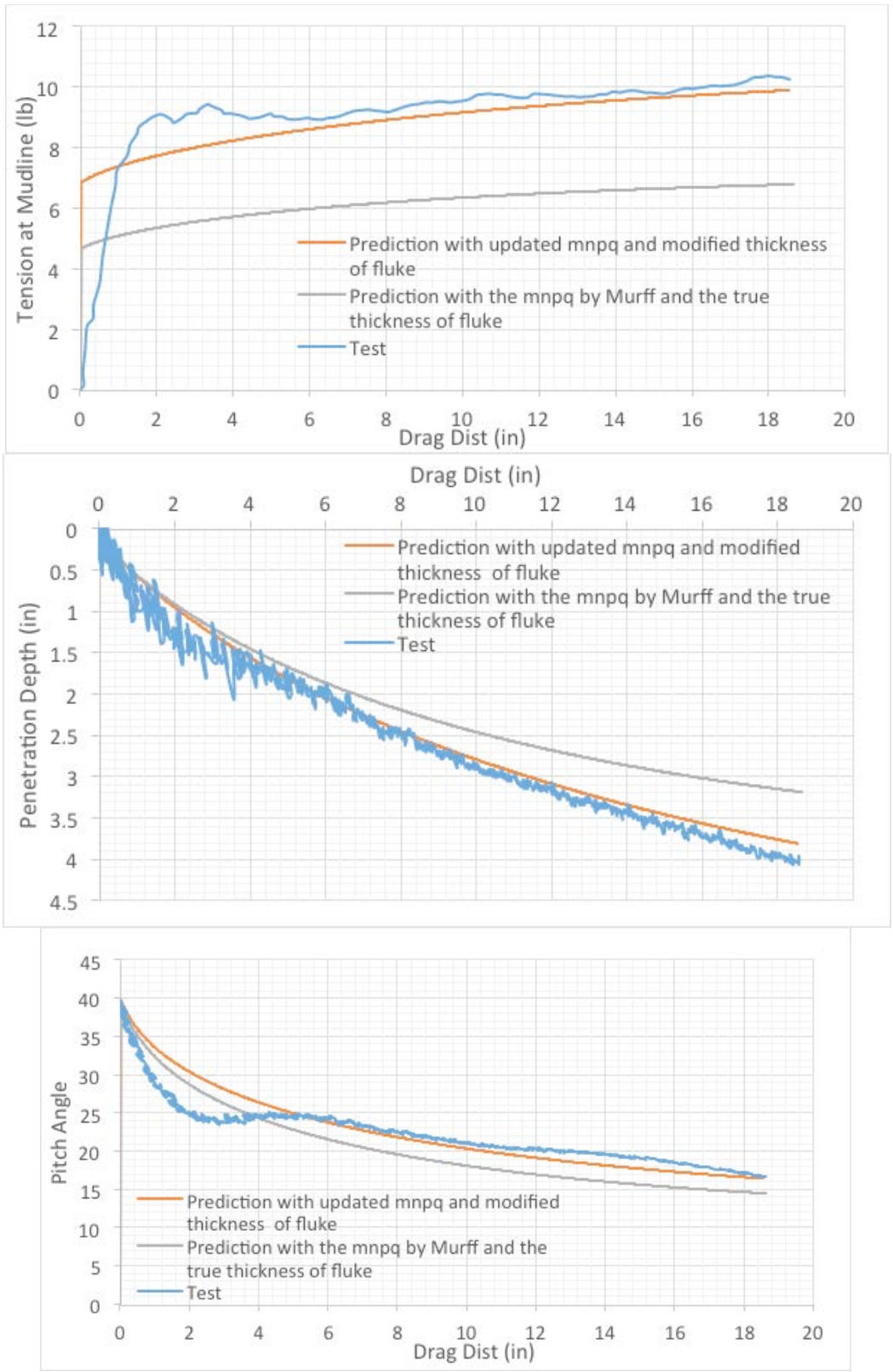

Figure 5.22. Comparison of Experimental Results with Predictions for Linearly Increasing Undrained Shear Strength with Depth (Case 2)

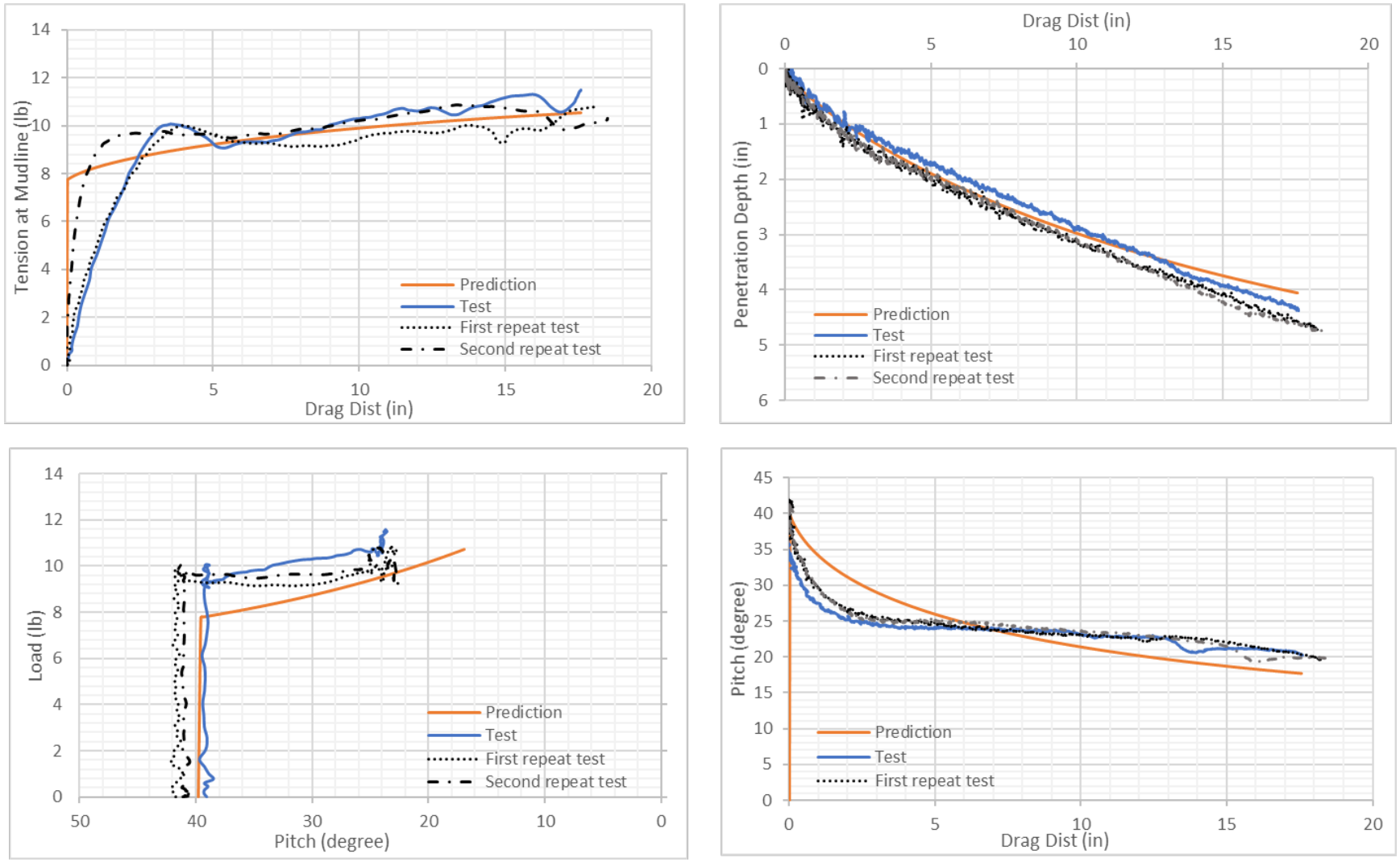

Figure 5.23. Drag Embedment Test Results for Single Layer with Constant Strength (Soil Profile 1)

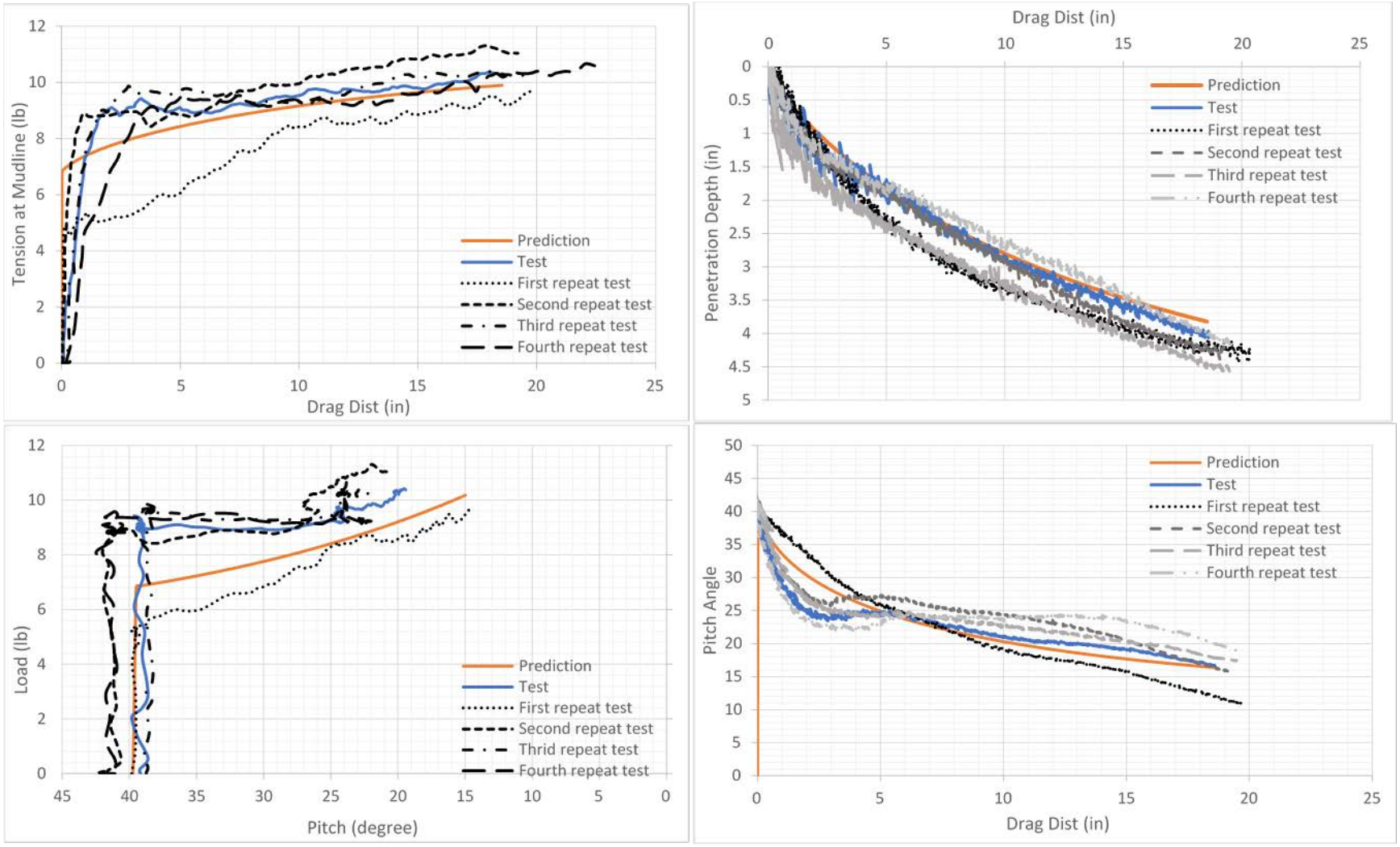

Figure 5.24. Drag Embedment Test Results for Single Layer with Linearly Increasing Strength (Soil Profile 2)

5.2.3 Extrapolate Generic Drag Embedment Anchor Results

To extrapolate the tests results to the prototype sized anchor, it is necessary to understand which anchor property is scalable and which is not. A larger size anchor with fluke length 1.5 longer than the generic anchor is printed and dragged in the same soil test bed as the generic anchor.

5.2.3.1 Experimental Design

By the analytical model in Section 5.2.1 with different input of fluke area, the capacity (Figure 5.25), trajectory (Figure 5.26), and pitch (Figure 5.27) are obtained with different size of fluke. Figure 5.25 shows that a larger size anchor is expected to have a higher capacity. Figure 5.26 shows that a larger size anchor can penetrate deeper. Figure 5.27 shows that a larger size anchor pitches more when penetrating into soil. The capacity by the larger size anchor is still in the capacity range of load cell. The range of displacement and pitch by the larger size anchor is also in the range of magnetometer capable to measure.

Table 5.8. Input for Different Sizes of Anchor Fluke

Soil Parameter	
Su at mudline	10 psf
K	5.6 psf/ft
Anchor and Anchor line	
Anchor line	0.22 or 0.32inch
Anchor Fluke Area	10 in^2 or 22 in^2
Anchor initially embedment	0.12 inch
Initial pitch angle (fluke to horizontal)	40°

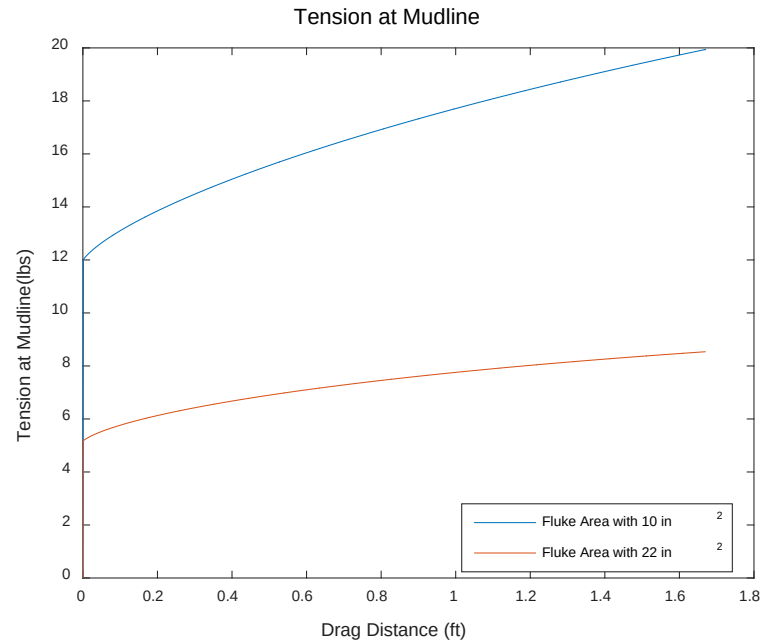

Figure 5.25. Capacity from Different Sizes of Anchor Fluke

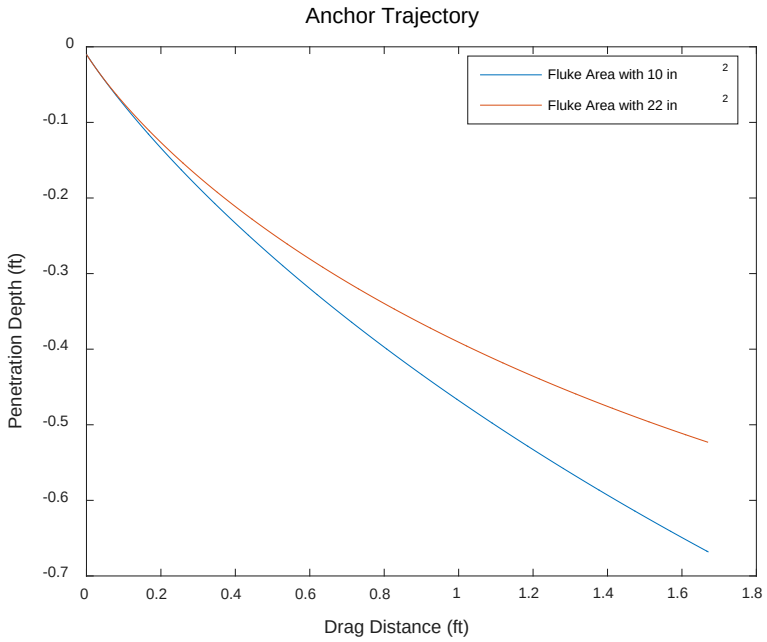

Figure 5.26. Trajectory from Different Sizes of Anchor Fluke

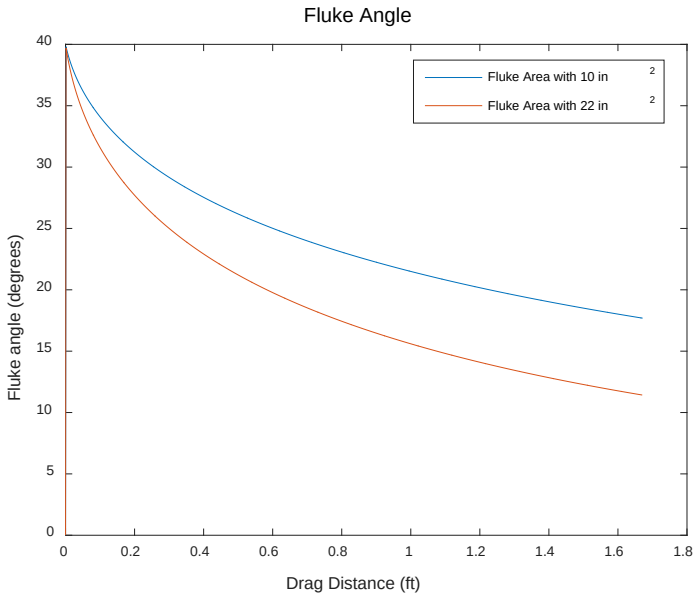

Figure 5.27. Pitch from Different Sizes of Anchor Fluke

5.2.3.2 Test Setup

In the experiment tests to study how to extrapolate model anchor tests results to prototype anchor, two different sizes of anchors are printed. The characteristic length of the larger anchor is 1.5 times longer than the generic anchor. Both anchors are tested in the same soil test bed (Figure 5.28). The anchors are connected to the appropriate size of loading line for drag embedment tests. The line thickness for each anchor is chosen based on the area of fluke by keep the ratio of area over square of line thickness as constant at 216 (same as the industry standards). The basic property of anchor and anchor line thickness in different sizes are summarized in Table 5.9. For the drag embedment tests with large size anchor, the magnetometer is also attached to track the trajectory and orientation. The drag embedment test procedure for the large size anchor is the same as described in Section 5.2.2.2.

Table 5.9. Comparison of Geometric Properties of Anchor in Different Sizes

	Fluke Area (in^2)	Fluke Length (in)	Thickness of Fluke (in)	Line Thickness (in)
Generic Anchor	10.37	3.6	0.120	0.22
Larger Anchor	22.45	5.3	0.186	0.32

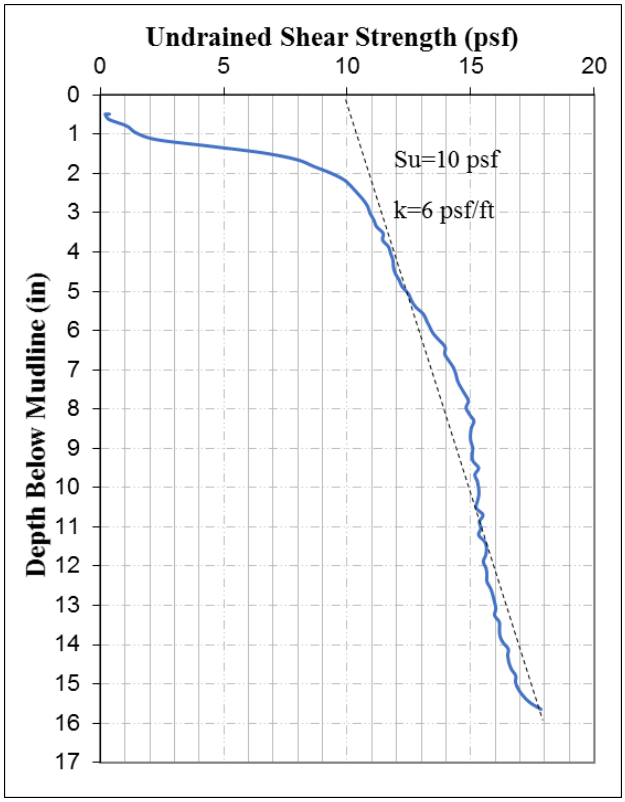

Figure 5.28. Undrained Shear Strength Profile for Drag Embedment Test with Anchor in Different Sizes

5.2.3.3 Experimental and Analytical Results

5.2.3.3.1 N_e, R_{nt} and Yield Surface

The N_e is back-calculated from the load reading and R_{nt} is calculated from the magnetometer reading. Based on the N_e and R_{nt} together with N_p and N_s from pure loading tests (Section 4.4.2), the yield surface is calibrated following the same procedure as for the

generic anchor in Section 5.2.2.3.3. The comparison between the yield surface between the generic anchor and large anchor is shown in Figure 5.29. From Figure 5.29, we can see that the large anchor has more flat yield surface, which is close to the reported yield surface by commercial anchor. From the N_e results from anchors in different sizes, it can be concluded that capacity is dependent on the size of anchor and is scalable with the area (characteristic length) ratio of two anchors. The R_{nt} for anchor in different sizes cannot be simply scaled by the ratio of the sizes between two anchors. For example, the fluke length ratio between the two anchors is 1.47 (5.3÷3.6=1.47), and the area ratio between the larger and the generic anchor is 2.167 (22.45÷10.37=2.167) which is close to the square of length ratio (1.47^2 = 2.1609). The ratio of R_{nt} between the larger anchor is 0.25. Since the shearing displacement is independent on the size of anchor, thus, the ratio of Δs between two anchors is 1. The ratio of R_{nt} together with Δs implies that the ratio of Δn between the two anchor is 0.25, which means that if two anchors both move in the direction parallel to the fluke, the displacement normal to fluke for the larger anchor is 0.25 of the displacement normal to fluke for the generic anchor.

Table 5.10. N_e and R_{nt} for Different Size Anchor

	N_e	R_{nt}
Generic Anchor	6.2	0.2
Larger Anchor	6.2	0.05

The theoretical N_e and R_{nt} is calculated by equation 5.2 and 5.5 in Section 5.2.1.1 and 5.2.1.2. To match the theoretical N_e and R_{nt} to experimental measurements, the n/p and q are changed. However, for the larger size anchor, with n/p and q are changed only once, it is hard to get N_e and R_{nt} to match experimental results at the same time. For example, ifN_e

matches with experimental measurement of 6.2 when n/p is 1.23 and q is 4.3, then R_{nt} is 0.12. If R_{nt} matches with experimental measurement of 0.05 when n/p = 2.67 and q is 3.87, then N_e is 6.9. The best fit results can be achieved by compensating accuracy for both parameters with n/p = 2.1 and q = 3.2, and gives N_e = 6.8 and R_{nt} = 0.08. The yield surfaces corresponding with different sets of interaction coefficient are shown in Figure 5.29, Figure 5.30 and Figure 5.31. Figure 5.29 shows that the R_{nt} for the larger anchor matches with experimental measurements, 0.05, however, N_e is 6.9; it shows that the slope for the larger anchor is steeper than the generic anchor since the R_{nt} is smaller for the larger anchor. However, the N_e is quite different for both anchors, which is contrast with the experimental results that the N_e for both anchors are the same. Figure 5.30 show that N_e for the larger anchor has agreement with experimental results of 6.2, however, the R_{nt} is 0.12 which is different from 0.05 measured in the lab. Figure 5.30 shows that the N_e for both anchors are the same. Figure 5.31 shows the best fit for experimental results.

Table 5.11. Interaction Coefficient in the Yield Surface for Different Size Anchor

	Generic Anchor	Large Anchor (R_{nt} Matches with Test)	Large Anchor (N_e Matches with Test)	Large Anchor (Best Fit with Test)
n/p	1.23	2.67	1.23	2.1
q	2.2	3.87	4.3	3.2

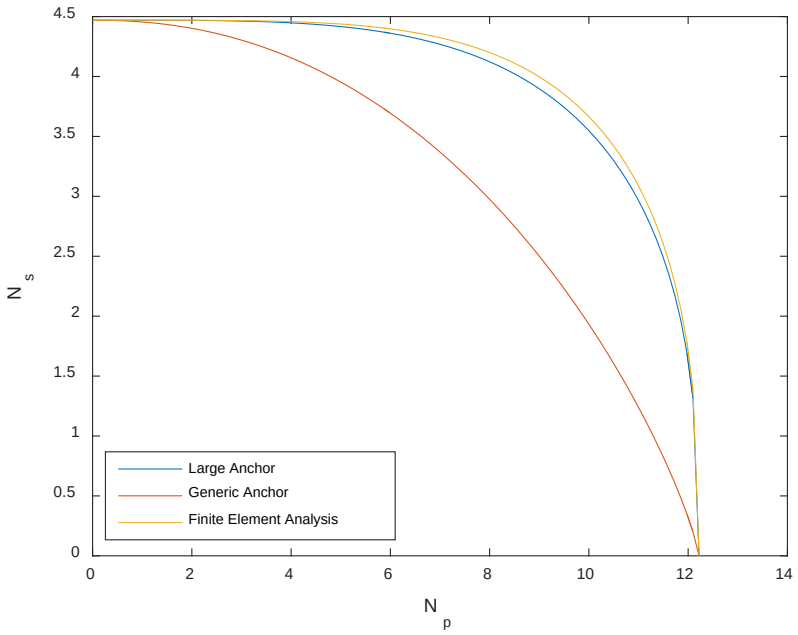

Figure 5.29. Comparison of Yield Surface between Large and Generic Anchor (R_{nt} matches Experimental Measurements)

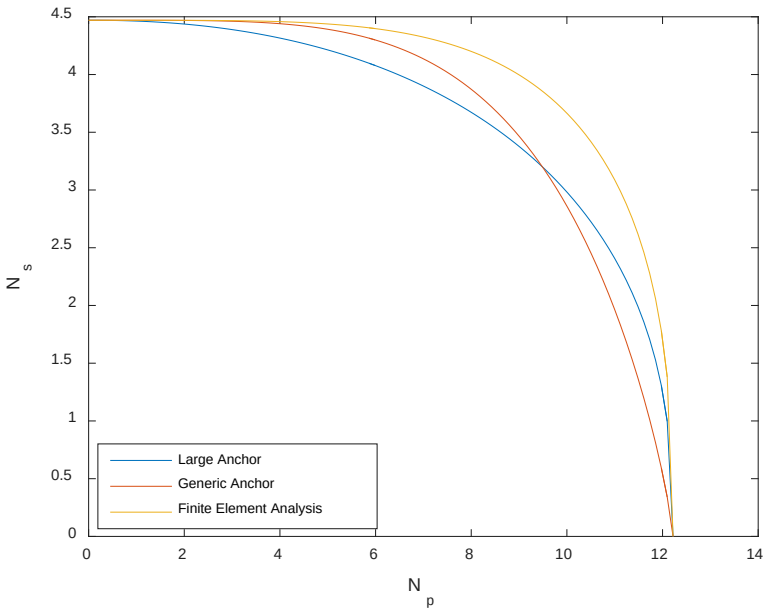

Figure 5.30. Comparison of Yield Surface between Large and Generic Anchor (N_e matches Experimental Measurements)

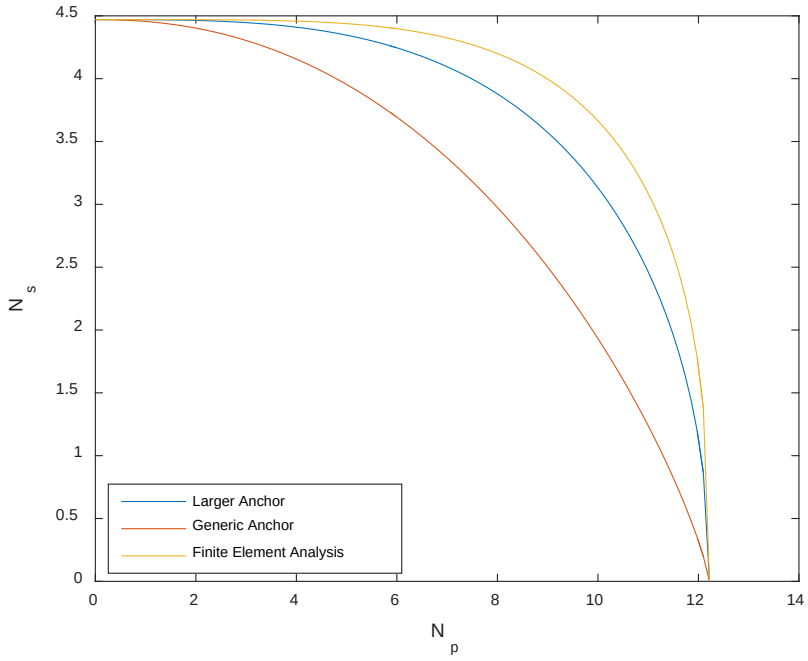

Figure 5.31. Comparison of Yield Surface Between Large and Generic Anchor (N_e and R_{nt} Best-fitted with Experimental Results)

5.2.3.3.2 Drag Embedment Tests

A comparison of load, trajectory and pitch versus horizontal drag are shown in Figure 5.29, Figure 5.32 and Figure 5.33, respectively. In addition, the prediction model described in Section 5.2.1.4 is capable to catch the characteristic of load-displacement curve for the generic and large anchor. Figure 5.33 shows that the measured trajectory matches well with the predicted trajectory after calibrating the prediction model for each size of anchor. Figure 5.34 shows that the pitch angle is not influenced by the size of anchor. All the tests results are shown in Appendix B.

From Figure 5.29 and Table 5.12, it can be seen that the load is proportional to the ratio of area between two anchors. The area ratio between two anchors is 2.16, and the load

ratio between the two anchor is 2.28, which implies that the capacity can be scaled to the ratio of area between two anchors. The penetration depth ratio is 1.4 and the fluke length ratio between two anchors is 1.47, which implies that the penetration depth may be scaled by the ratio fluke length.

Table 5.12. Ratio of Geometry, Load, Penetration Depth Between Two Anchors

Fluke Length Ratio	Area Ratio	Load Ratio	Penetration Depth Ratio
1.47	2.12	2.28	1.4

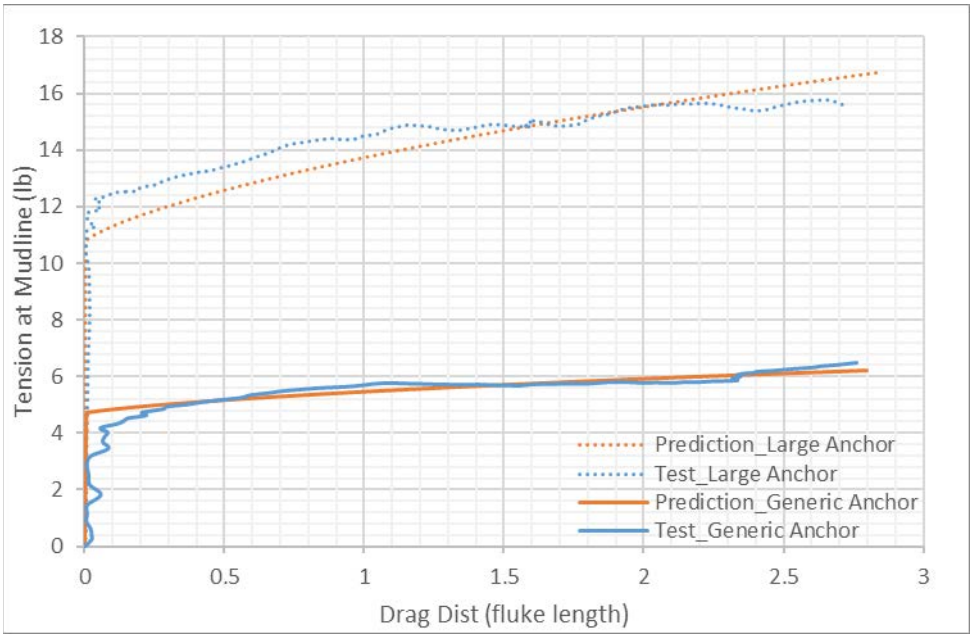

Figure 5.32. Comparison of Tension at Mudline for Anchor in Different Sizes

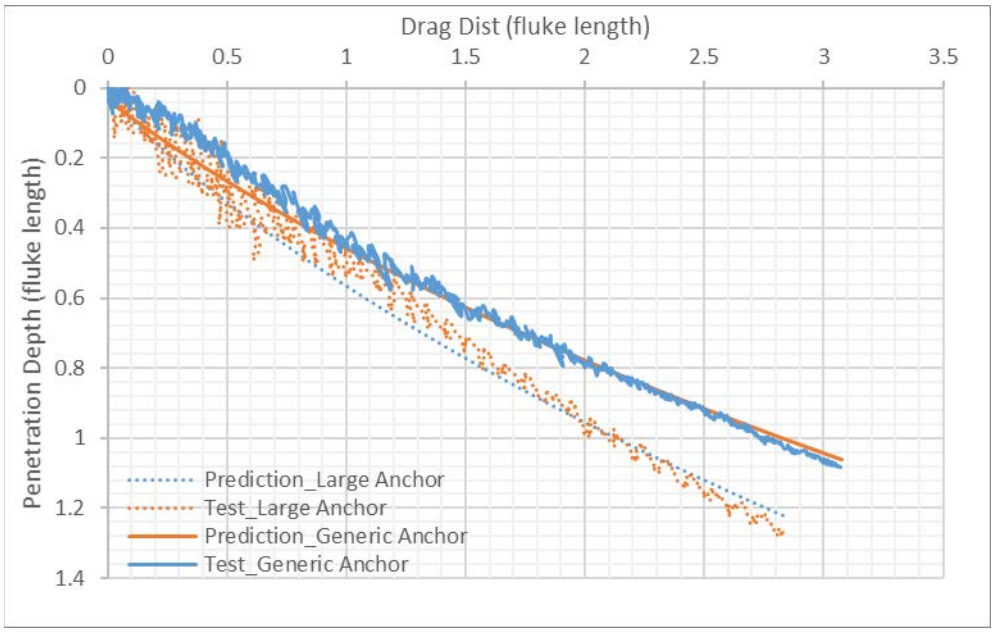

Figure 5.33. Comparison of Trajectory for Anchor in Different Sizes

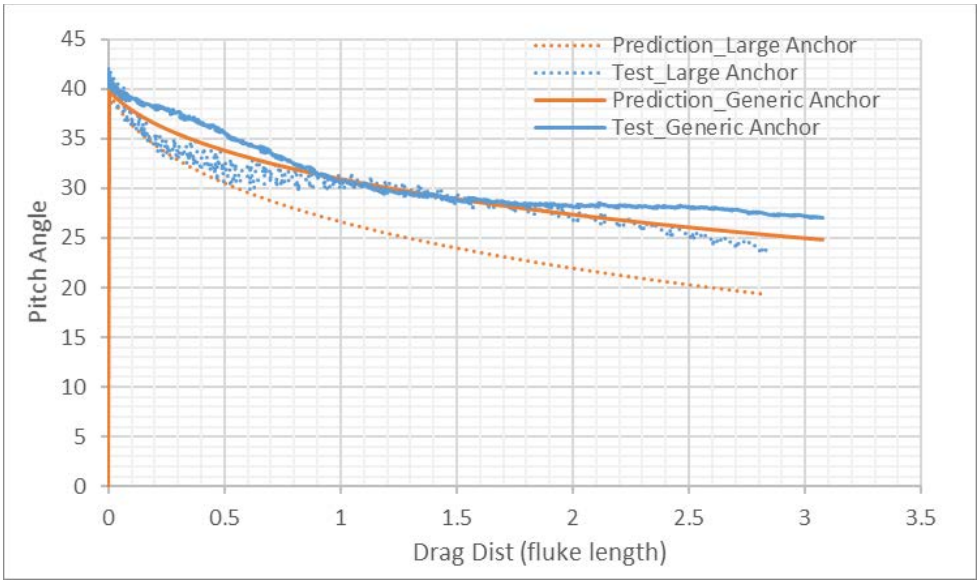

Figure 5.34. Comparison of Pitch for Anchor in Different Sizes

5.3 Drag Embedment Tests in Layered Soil Profiles

5.3.1 Analytical Model

The prediction model for the drag embedment tests in a layered soil profile is developed based on the prediction of anchor in a single layer in Section 5.2.1.4. An immediate issue that arises in predicting anchor trajectory and load in layered soil is how anchor and anchor line behave when hitting a stiff layer. That is, to quantify the effect of stiff layer on the non-dimensional bearing factors and the fluke angle, fluke-line angle.

When the fluke of the anchor hits a stiff layer, as shown in Figure 5.35, the shear resistance and the center of rotational resistance shifts towards the front of the anchor. Compared with anchors in a soft soil layer only, a higher pressure from a stiff layer is applied to the tip of anchor. This higher pressure at the tip makes the anchor pitch forward as shown in Figure 5.36. Additionally, as the anchor pitches forward, the line angle at the shackle also changes compared with that anchor is in the soft soil only.

The additional resistance from a stiff layer is considered by including the multipliers on the normal bearing factor and the tangential bearing factor.

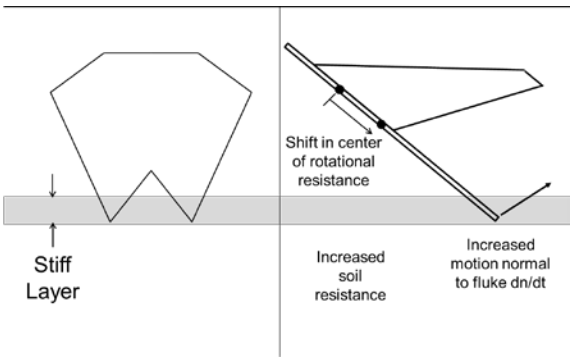

Figure 5.35. Anchor Fluke Hits Stiff Layer (Rasulo and Aubeny, 2017)

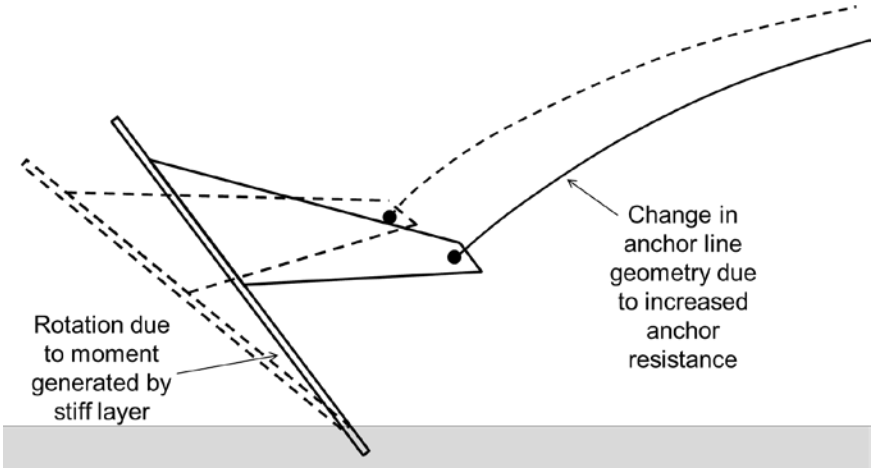

Figure 5.36. Anchor Rotation and Anchor Line Reconfiguration When Anchor Hits Stiff Layer (Rasulo and Aubeny, 2017)

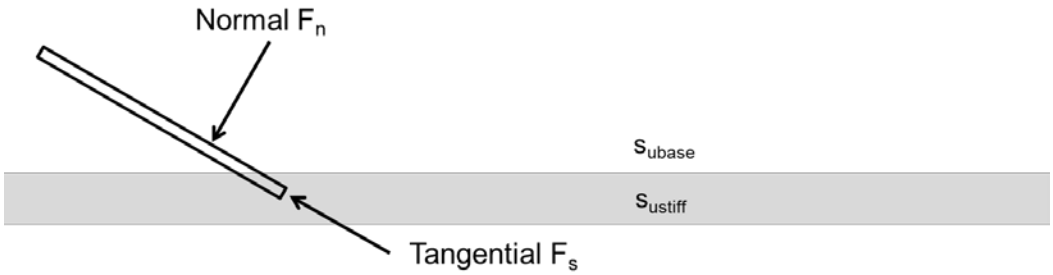

Figure 5.37 Normal and Tangential Bearing Resistance When Anchor Hits Stiff Layer (Rasulo and Aubeny, 2017)

The Normal Bearing resistance force shown in Figure 5.37 is calculated by Eq.5.18, and the shearing resistance force is calculated by Eq. 5.19.

$$F_n = s_u A_f N_p M_n \qquad \text{Eq.(5.18)}$$

$$F_s = s_u A_f N_s M_s \qquad \text{Eq.(5.19)}$$

where s_u = base soil strength

A_f = fluke area

N_p = normal bearing factor (experimentally determined by Equation 4.4 or determined by Equation 4.1 from plasticity analysis)

N_s = tangential bearing factor (experimentally determined by Equation 4.5 or determined by Equation 4.2 from plasticity analysis)

M_n and M_s = multipliers for stiff layer effect shown in Figure 5.38, which is a function of (A_{stiff}/A_f, s_{ustiff}/s_{ubase})

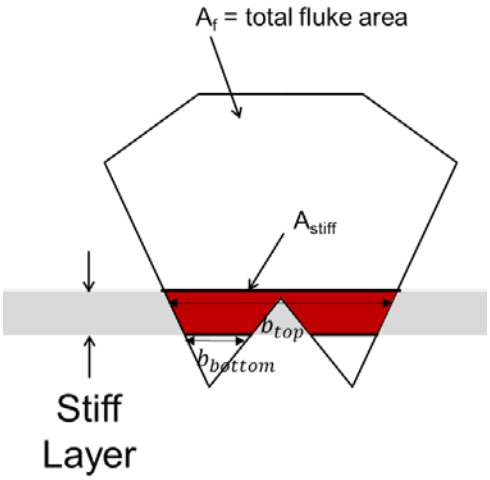

Figure 5.38. Bearing Factor Multipliers

First, the ratio of the shear strength of the stiff layer over the shear strength of the soil layer needed to be determined. Then the area in the stiff layer can be multiplied by this ratio. That is, the fluke in the stiff layer is enlarged by the shear strength ratio, S_{uratio}. An enhanced fluke area can be calculated by involving the enlarged area in a stiff layer. Then the multiplier for the bearing factor and shearing factor can be determined.

$$M_n = \frac{A_{enhanced}}{A_{real}} \quad \text{Eq.(5.20)}$$

To determine the multiplier for the shearing factor, the width of the top and bottom of the fluke in a stiff layer needs to be determined first, which is designated as b_{top} and b_{bottom} in Figure 5.38. Additionally, the maximum width of the fluke in the stiff layer, b_{max}, is needed for the shearing factor multiplier.

$$M_s = 1 + \frac{b_{top} - b_{bot}}{bmax} \frac{(Suratio - 1)}{2} \quad \text{Eq.(5.21)}$$

The prediction model for anchors in a layered soil profile is the same as in a single layer soil except applying the multipliers to bearing and shearing factors, respectively when the anchor is in a stiff layer. In addition, a line multiplier ranging from 1 to 1.22, depending on the depth of line, will be applied to the line resistance if the anchor line is in the stiff layer.

5.3.2 Experimental Design

This section studies the analytical model in 5.3.1. From the study of analytical model, the effect by the characteristics of stiff layer such as the shear strength, depth, and thickness is evaluated as a guide to experimentally construct soils tests beds which are at the threshold anchor can or cannot penetrate into stiff layer.

5.3.2.1 Effect of Shear Strength of Stiff Layer

Table 5.13 summarizes the soil parameters for sensitivity analysis of shear strength of stiff layer. A 1 inch thickness stiff layer interbedded into the constant shear strength profile with 12 psf, and the shear strength is 24 psf, 36 psf or 48 psf.

The capacity (Figure 5.39), trajectory (Figure 5.40), and orientation (Figure 5.41) of drag embedment anchor is checked. From Figure 5.39, the capacity is expected to increase with the increase of the shear strength of stiff layer. Figure 5.40 shows that it is less possible for anchor to penetrate into the stiff layer with higher shear strength. In the shear strength profile with 24 psf, anchor can penetrate into the stiff layer, however, anchor canno penetrate into stiff layer with shear strength at 36 psf and 48 psf. Figure 5.10 shows that anchor pitches slightly less in the shear strength profile with a lower shear strength gradient.

From the capacity results, it can be estimated that the load cell is capable to measure the capacity. From the trajectory and pitch results, it can be concluded that the magnetometer is capable to track anchor displacement and rotation during drag tests.

Table 5.13. Input for Effect of Stiff Layer Shear Strength

Soil Parameter	
Su at mudline	12 psf
k	0 psf/ft
Stiff Layer Thickness	1 inch
Stiff Layer Depth from Mudline	3 inch
Shear strength ratio of stiff layer over soft layer	2 (24 psf) or 3 (36 psf) or 4 (48 psf)
Anchor and Anchor line	
Anchor line	0.22 inches
Anchor initially embedment	0.6 inches
Initial line angle at mudline	0°
Initial pitch angle (fluke to horizontal)	40°

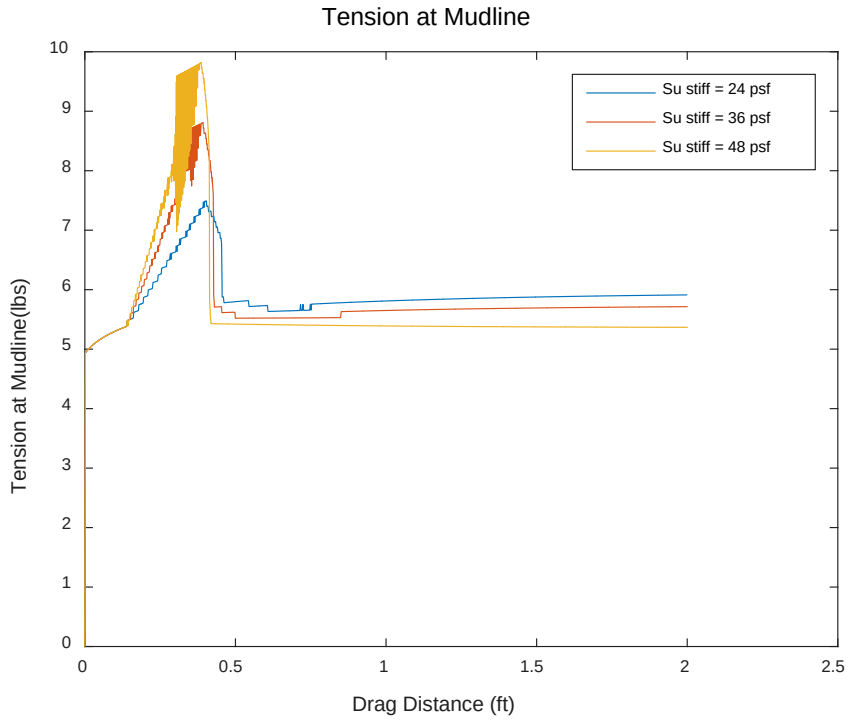

Figure 5.39. Anchor Capacity (Effect of Stiff Layer Shear Strength)

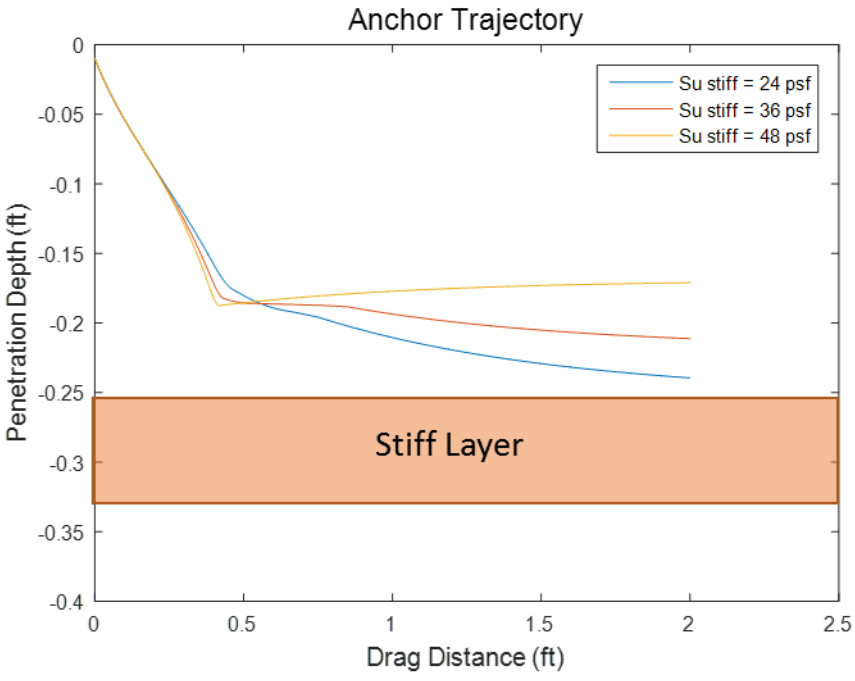

Figure 5.40. Anchor Trajectory (Effect of Stiff Layer Shear Strength)

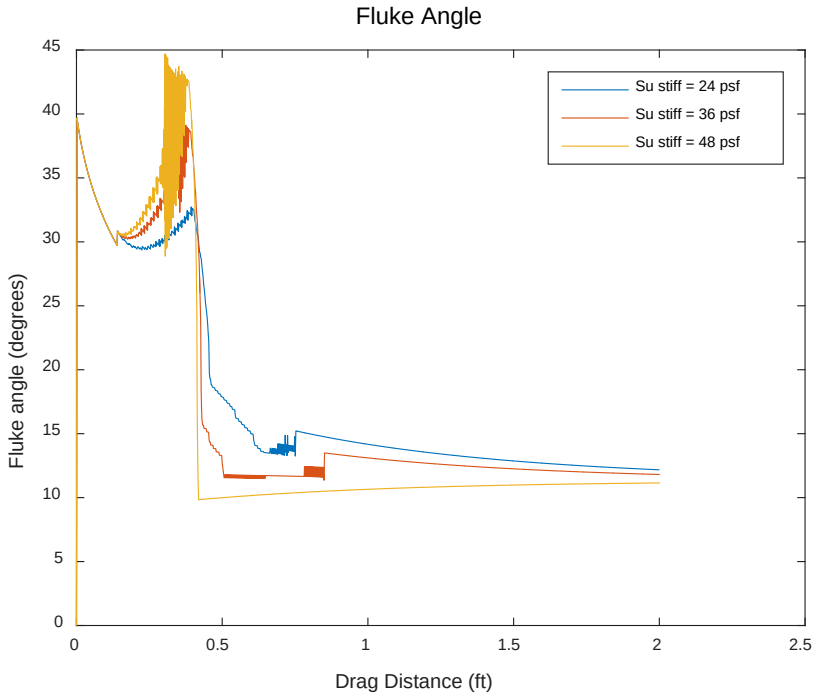

Figure 5.41. Anchor Pitch (Effect of Stiff Layer Shear Strength)

5.3.2.2 Effect of Thickness of Stiff Layer

Table 5.14 summarizes the soil parameters for sensitivity analysis of shear strength of stiff layer. A 3-in thick stiff layer with 24 psf shear strength interbedded into the constant shear strength profile with 12 psf, and the shear strength is 1 inch or 1.5 inches or 2 inches.

The capacity (Figure 5.42), trajectory (Figure 5.43), and orientation (Figure 5.44) of drag embedment anchor is checked. From Figure 5.42, the capacity is independent with the thickness of stiff layer. Figure 5.43 shows that the thickness does not impact the fact that anchor can or cannot penetrate into stiff layer, but affect that anchor can or cannot penetrate through the stiff layer. For the thinnest stiff layer (1 inch), anchor can penetrate through the stiff layer, however for the thicker layers (3 inches), anchor only can penetrate into but not through. Figure 5.10 shows that anchor pitches the same way in shear strength profile with different thicknesses when approaching into stiff layer, however, the pitch

angel is the different in shear strength profile with different thicknesses when anchor is in stiff layer.

Table 5.14. Input for Effect of Stiff Layer Thickness

Soil Parameter	
Su at mudline	12 psf
k	0 psf/ft
Stiff Layer Thickness	1 or 1.5 or 2 inch
Stiff Layer Depth from Mudline	3 inch
Shear strength ratio of stiff layer over soft layer	2 (24 psf)
Anchor and Anchor line	
Anchor line	0.22 inches
Anchor initially embedment	0.6 inches
Initial line angle at mudline	0°
Initial pitch angle (fluke to horizontal)	40°

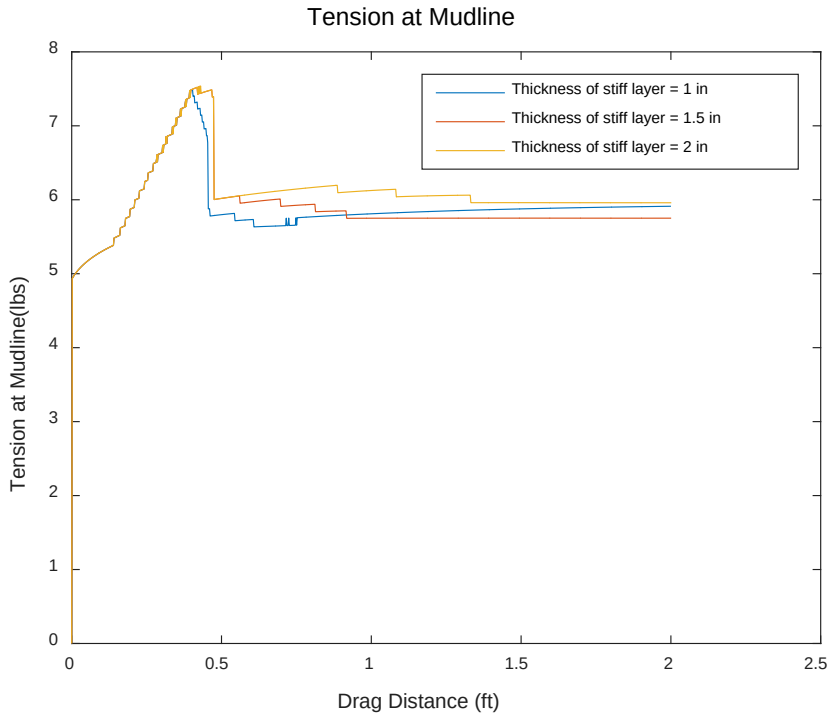

Figure 5.42. Anchor Capacity (Effect of Stiff Layer Thickness)

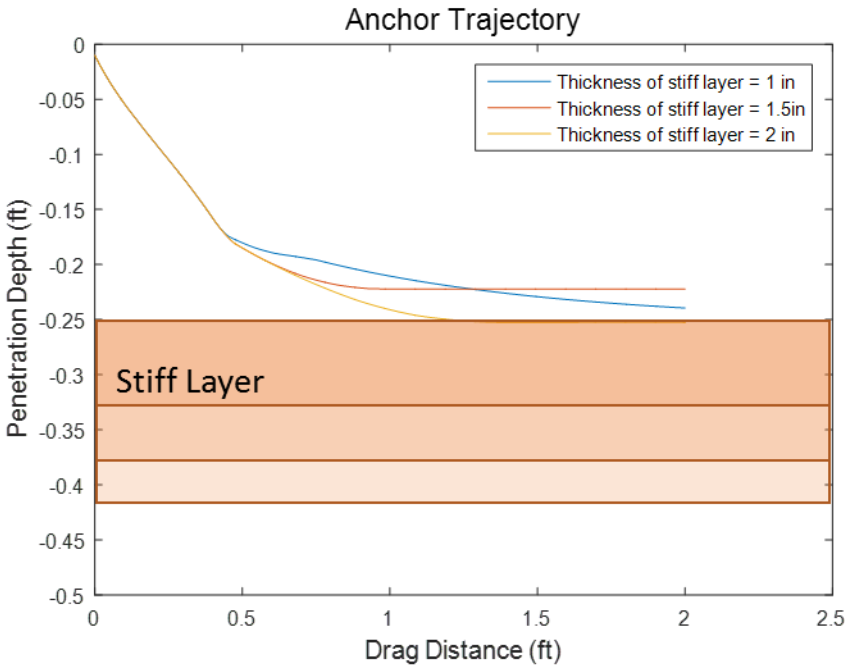

Figure 5.43. Anchor Trajectory (Effect of Stiff Layer Thickness)

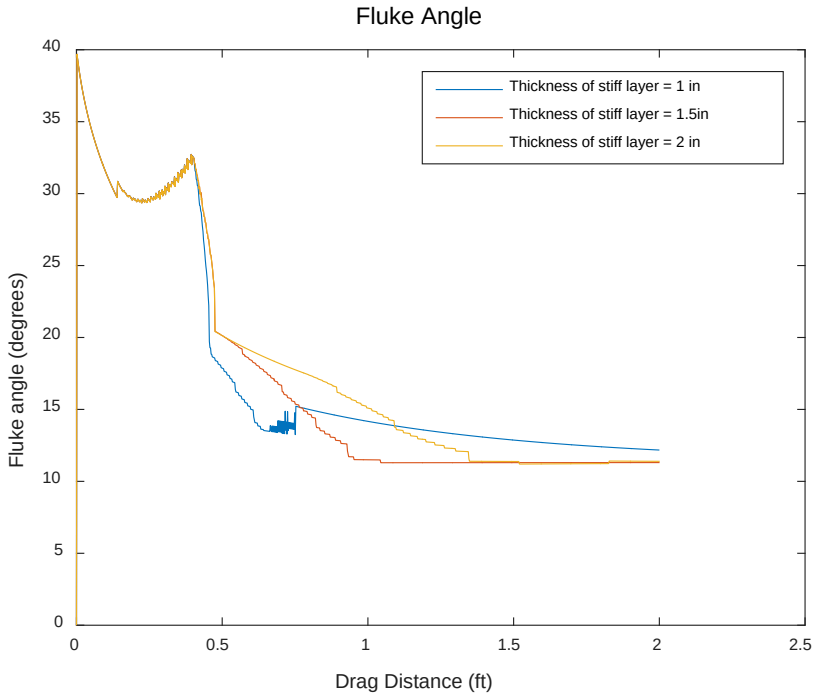

Figure 5.44. Anchor Pitch (Effect of Stiff Layer Thickness)

5.3.2.3 Effect of Stiff Layer Depth

Table 5.15 summarizes the soil characteristics for the sensitivity analysis of stiff layer depth. The shear strength of soft soil is 13 psf and increasing with the gradient of 8.21 psf/ft. The 1-in thick stiff layer starts at 3 or 4 or 5 inches below mudline. The shear strength of stiff layer is 39 psf.

From Figure 5.45, the soil resistance increases with the increase of depth of stiff layer. From Figure 5.46, the trajectory shows that the anchor cannot penetrate into the stiff layer deeper than 3 inches (1 fluke length).

Table 5.15. Input for Effect of Stiff Layer Depth

Soil Parameter	
Su at mudline	13 psf
k	8.2 psf/ft
Stiff Layer Thickness	1 inch
Stiff Layer Depth from Mudline	3 or 4 or 5 inch
Shear strength ratio of stiff layer over soft layer	3
Anchor and Anchor line	
Anchor line	0.22 inches
Anchor initially embedment	0.6 inch
Initial line angle at mudline	0°
Initial pitch angle (fluke to horizontal)	40°

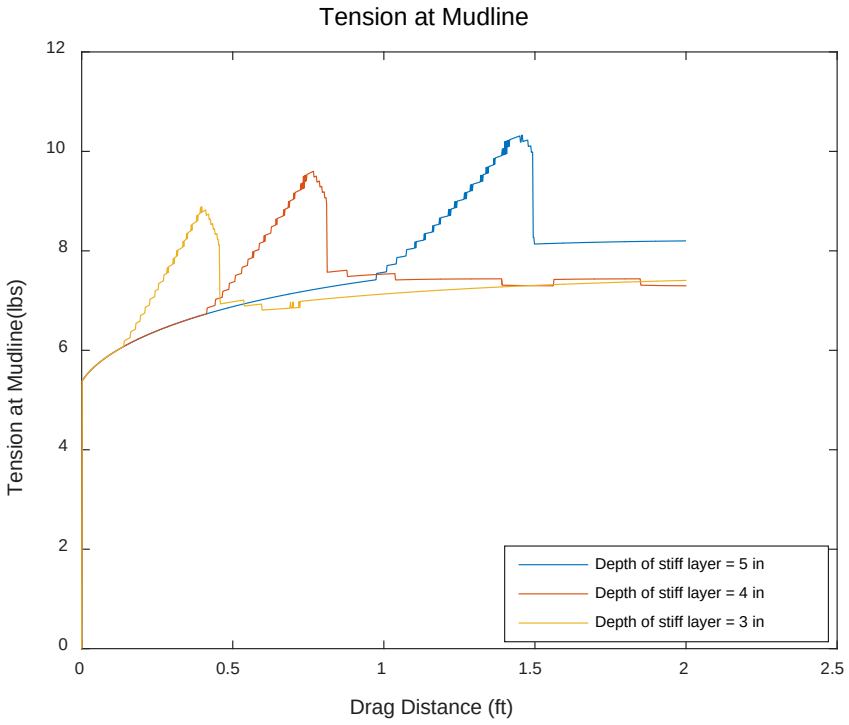

Figure 5.45. Anchor Capacity (Effect of Stiff Layer Depth)

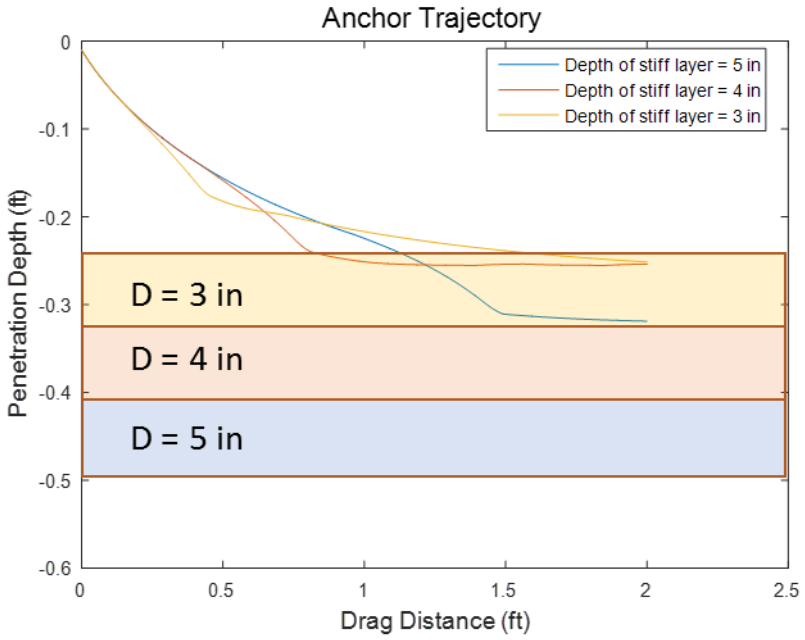

Figure 5.46. Anchor Trajectory (Effect of Stiff Layer Depth)

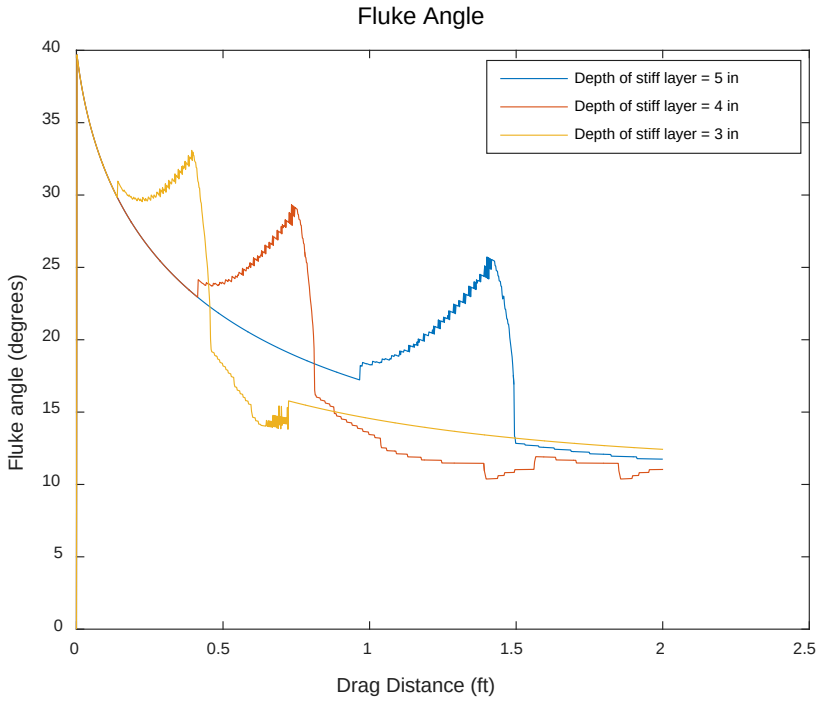

Figure 5.47. Anchor Pitch (Effect of Stiff Layer Depth)

5.3.2.4 Effect of Anchor Line Thickness

Table 5.16 summarizes the soil parameters for sensitivity analysis of shear strength of stiff layer. A 1-in thick stiff layer with 24 psf shear strength interbedded into the constant shear strength profile with 12 psf. The thin anchor line is 0.05 inch and the thick line is 0.218 inch.

The capacity (Figure 5.48), trajectory (Figure 5.49), and orientation (Figure 5.50) of drag embedment anchor is checked. From Figure 5.48, the capacity increases with the increase of line thickness. Figure 5.49 shows that the thickness line impacts that anchor can or cannot penetrate into stiff layer. Figure 5.50 shows that anchor pitches less with the thin line attached compared with thick line attached.

Table 5.16. Input for Effect of Anchor Line Thickness

Soil Parameter	
Su at mudline	12 psf
k	0 psf/ft
Stiff Layer Thickness	1 inch
Stiff Layer Depth from Mudline	3 inch
Shear strength ratio of stiff layer over soft layer	2 (24 psf)
Anchor and Anchor line	
Anchor line	0.05 or 0.218 inch
Anchor initially embedment	0.6 inch
Initial line angle at mudline	0°
Initial pitch angle (fluke to horizontal)	40°

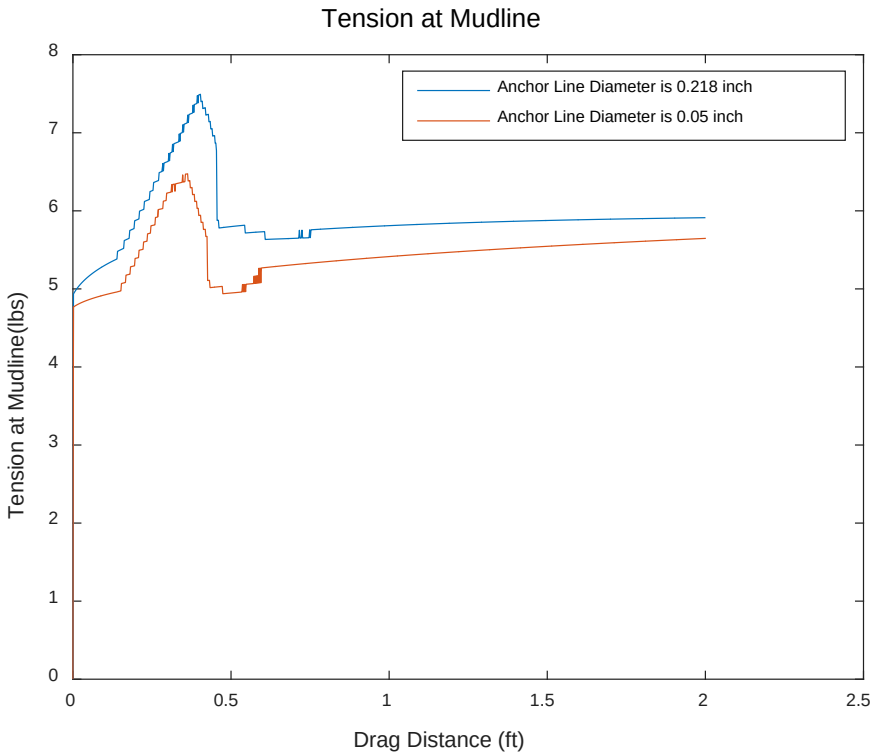

Figure 5.48. Anchor Capacity (Effect of Anchor Line Thickness)

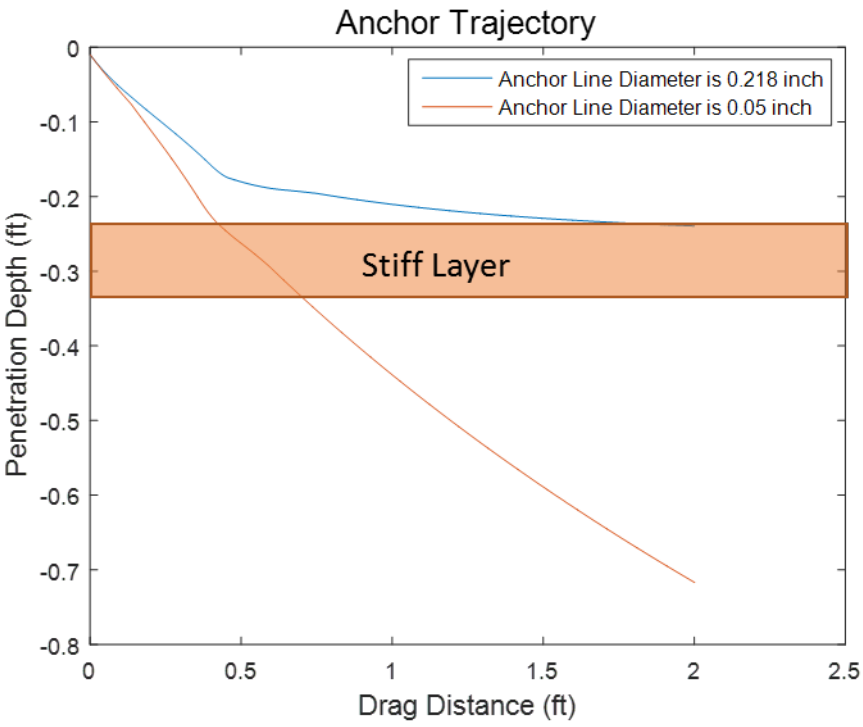

Figure 5.49. Anchor Trajectory (Effect of Anchor Line Thickness)

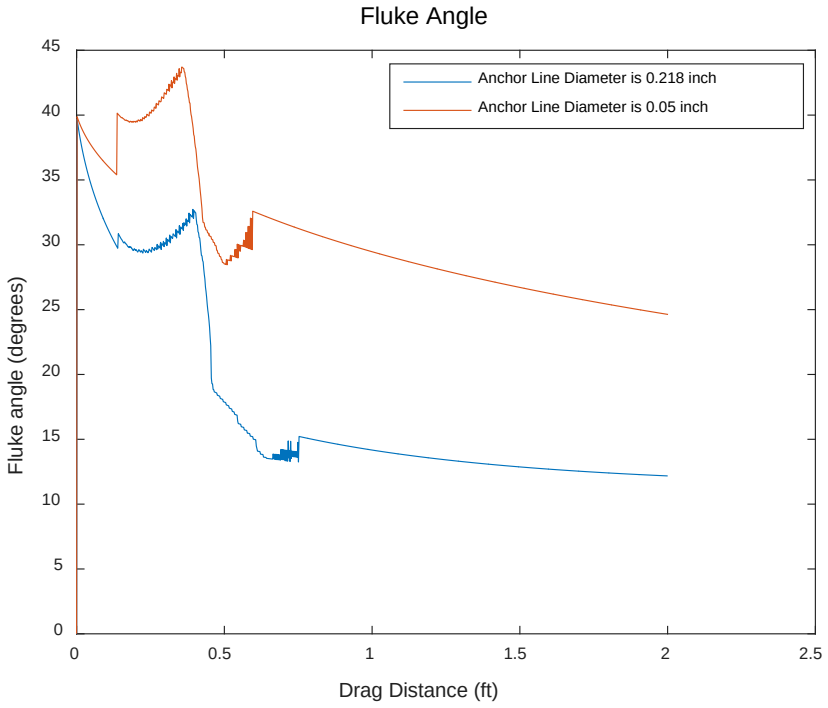

Figure 5.50. Anchor Pitch (Effect of Anchor Line Thickness)

5.3.3 Tests Setup

The drag embedment tests setup is the same as the drag embedment anchor in a single layer as described in Section 5.2.3.2 except that test bed preparation is slightly different. The clay layer with relative higher shear strength is prepared by drying the GoM clay in a soil bucket 1.6 feet in diameter and 2.6 feet in height to a desired undrained shear strength. The strength of the dried GoM clay is characterized by T-bar tests before being placed into thermoplastic tank. Then the stratified soil profile can be prepared by removing the top couple inches of soft clay in the thermoplastic tank placing stiff clay and covering the tank with removed soft soil.

Table 5.17 summarizes the soil strength characteristics of soft and stiff soil in layered soil profile in six cases including the shear strength of soft soil at mudline, shear strength gradient of soft soil, stiff layer thickness, stiff layer depth, and the shear strength ratio of stiff layer over surrounding soft soil. The thickness of stiff layer ranges from 1 inches to 4 inches. The depth of stiff layer ranges from 3 inches to 4 inches. The shear strength ratio of stiff layer over surrounding soft soil ranges from 1.4 to 5. The soft soil in case 3, 4, and 5 are with sensitivity with 1.6, and in case 7, 8, and 9 are remolded soil. The shear strength of soft soil at mudline ranges from 10 psf to 14 psf, and the shear strength gradient is between 0 psf/ft to 13.34 psf/ft.

In the first column in Table 5.17, the expectation of that anchor can or cannot penetrate into or through the stiff layer is listed. It should be noticed that this expectation is based on the predicted trajectory from the calibrated model instead of the original model.

Table 5.17. Summary of Tests in Layered Soil Profiles

Case 3 Stiff Layer – Anchor Expected to Penetrate Through Stiff Layer based on Prediction Model	Su at mudline	14 psf
	Su gradient	6.3 psf/ft
	Sensitivity of soft layer	1.6
	Stiff Layer Thickness	1 inch
	Stiff Layer Depth from Mudline	3 inches
	Shear strength ratio of stiff layer over soft	2.2
Case 4 Stiff Layer - Anchor Expected to Penetrate Through Stiff Layer based on Prediction Model	Su at mudline	14 psf
	Su gradient	6.3 psf/ft
	Sensitivity of soft layer	1.6
	Stiff Layer Thickness	1 inch
	Stiff Layer Depth from Mudline	4 inches
	Shear strength ratio of stiff layer over soft	2.2
Case 5 Stiff Layer – Anchor Expected to Penetrate into but not Through Stiff Layer based on Prediction Model	Su at mudline	16 psf
	Su gradient	0 psf/ft
	Sensitivity of soft layer	1.6
	Stiff Layer Thickness	4 inches
	Stiff Layer Depth from Mudline	3 inches
	Shear strength ratio of stiff layer over soft	1.4
Case 6 Stiff Layer – Anchor Expected to Penetrate into Stiff Layer based on Prediction Model	Su at mudline	10 psf
	Su gradient	13.4 psf/ft
	Sensitivity of soft layer	1
	Stiff Layer Thickness	1 inch
	Stiff Layer Depth from Mudline	3 inches
	Shear strength ratio of stiff layer over soft	2
Case 7 Stiff Layer – Anchor Expected to Not Penetrate into Stiff Layer based on Prediction Model	Su at mudline	13 psf
	Su gradient	6.3 psf/ft
	Sensitivity of soft layer	1
	Stiff Layer Thickness	5 inches
	Stiff Layer Depth from Mudline	4 inches
	Shear strength ratio of stiff layer over soft	5
Case 8 Stiff Layer – Anchor Expected to Penetrate into but not Through Stiff Layer based on Prediction Model	Su at mudline	14 psf
	Su gradient	8.2 psf/ft
	Sensitivity of soft layer	1
	Stiff Layer Thickness	2 inches
	Stiff Layer Depth from Mudline	4 inches
	Shear strength ratio of stiff layer over soft	2.4

5.3.4 Experimental and Analytical Results

From Figure 5.51, the calibrated model can better predict the capacity, trajectory and pitch of anchor in layered soil profile. It should be noted that the calibrated model is only calibrated once based on the test results in constant shear strength profile, and directly applied to the cases in layered soil profile. Figure 5.52 shows the comparison between the calibrated prediction model with the experimental results in case 5. The variability between the prediction model and experimental results still exist but that they generally match well, thus the calibrated model is applied to evaluate the ability of anchor in layered soil profile before constructing soil tests beds, and is checked with experimental results after testing in the corresponding soil profile.

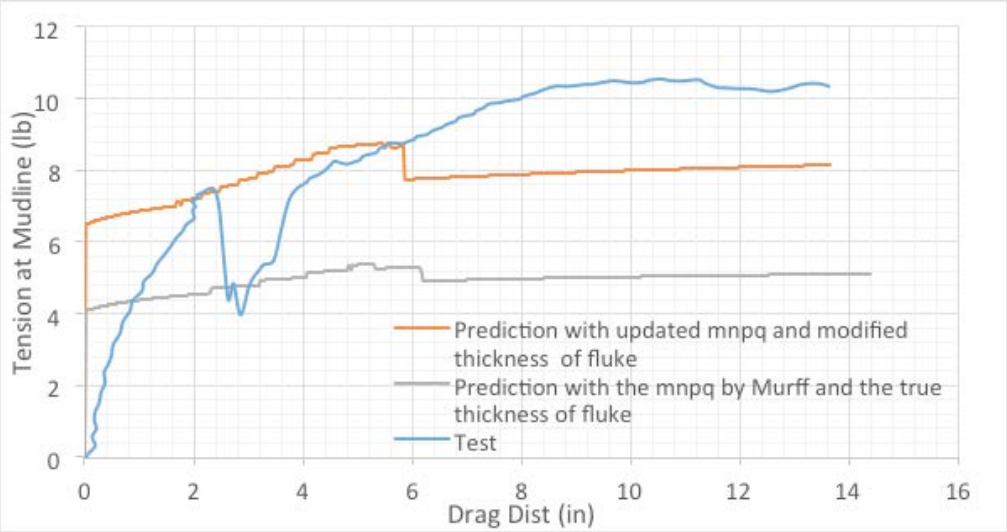

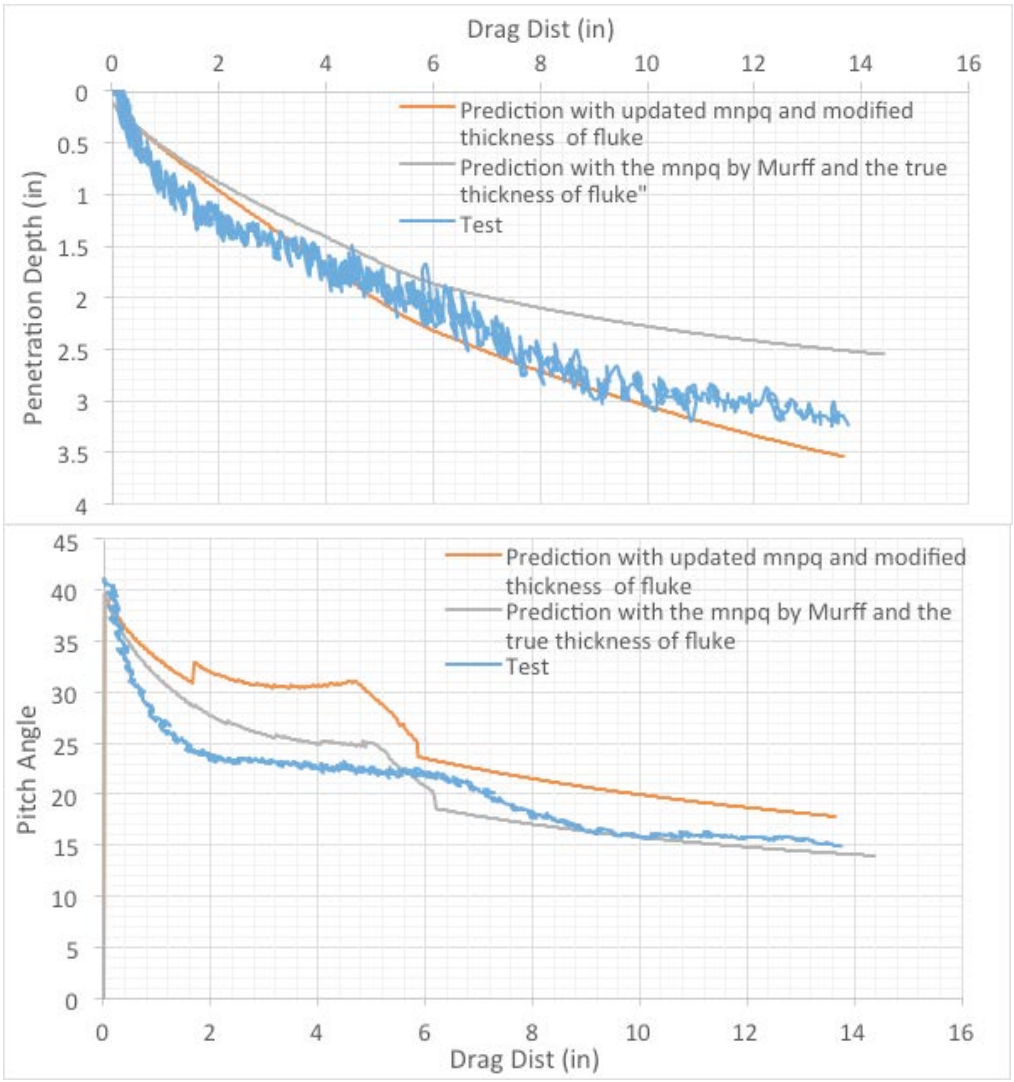

Figure 5.51. Comparison of experimental results with predictions for a relatively weak layer (Case 5)

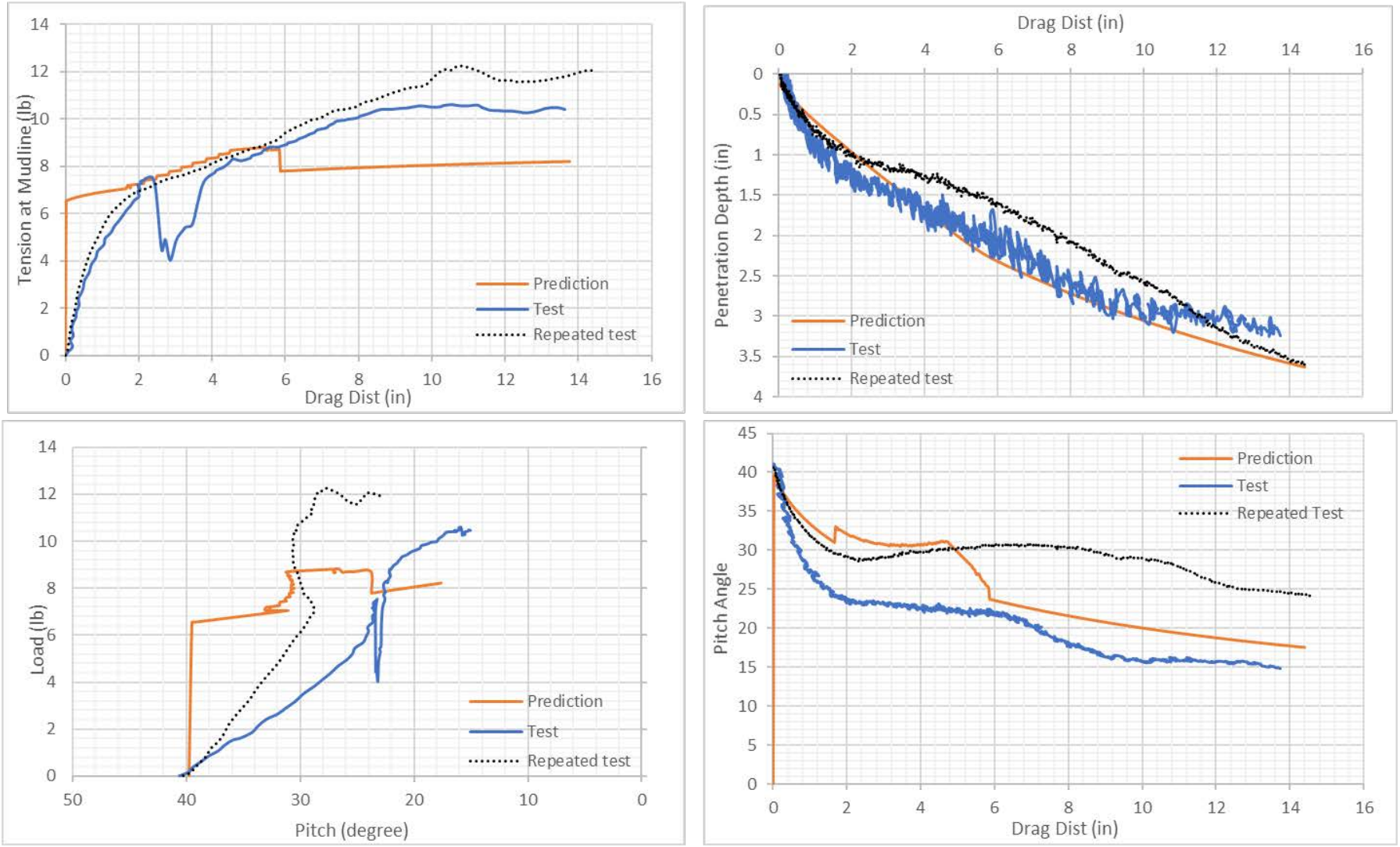

Figure 5.52. Drag embedment test results for layered soil profile (Soil Profile 5)

Table 5.18 to Table 5.20 summarizes comparison on capacity, penetration depth and pitch when anchor hitting stiff layer and at the point where the maximum difference between analytical and experimental results exist.

From Table 5.18, it can be seen that the analytical model is capable to predict the capacity when anchor hitting stiff layer generally within 20% difference. However, comparing the normalized horizontal drag distance (marked x_fluke length) when hitting stiff layer, the analytical model predict anchor hits stiff layer with more horizontal drag distance compared with experimental measurement, which implies that anchor hits stiff layer earlier experimentally than analytically. The maximum difference between the analytical and experimental capacity exist either before hitting stiff layer or at the end of drag tests. This makes consistent with the previous conclusion (anchor hits stiff layer earlier in experiement) and experimental capacity is higher than analytical since anchor already hits stiff layer.

Table 5.19 summarizes the penetration depth when anchor hits stiff layer and the maximum difference on penetration depth between experimental and analytical results. Generally, the analytical penetration depth is 30% deeper than the experimental ones when hitting stiff layer. This also makes consistent with the capacity observation that anchor experimentally feels stiff layer earlier than in the analytical prediction. Due to the early exposure to enhanced shear strength from stiff layer, experimentally anchor penetrates less than predicted by analytical model. The maximum difference between analytical and experimental penetration exist mostly at the end of drag tests. Since the analytical model predicts less and lagged resistance therefore anchor is more possible to penetrate into stiff layer. However, in the same case, experimentally anchor cannot penetrate into stiff layer.

This discrepancy makes a difference on the final penetration between analytical and experimental results.

Table 5.20 summarizes the pitch angle when anchor hitting stiff layer and the maximum difference on pitch between experimental and analytical results. First, from the normalized horizontal drag distance (x fluke length), it shows that experimentally anchor hits stiff layer earlier than analytical results. Second, in case 3, 4 and 8, the analytical model predicts shallower pitch angle when hitting stiff layer than experimental measurement. The maximum difference between analytical and experimental pitch exists after around one fluke length drag anchor penetrates stiff layer or at the end of drag. At the point where after around one fluke length drag after penetrate stiff layer, the analytical model predicts anchor flattened, however, the anchor is still pitching forward experimentally. At the end of drag, analytical model predicts that anchor penetrates through stiff layer and continues the trajectory in soft soil and with a flattened pitch. However, experimentally pitch angle is still steep and anchor slides on top of stiff layer.

Table 5.18. Difference between the Experimental and Analytical Capacity

		Encounter the Stiff					Maximum Difference				
		Prediction		Experiment		Load Difference	Prediction		Experiment		Load Difference
		x (Fluke Length)	Load	x (Fluke Length)	Load		x (Fluke Length)	Load	x (Fluke Length)	Load	
Case 3	Test	0.5	8.8	0.3	8.0	9%	0.5	8.8	0.5	8.8	0%
	Repeat 1	0.5	8.8	1.1	7.5	15%	0.5	8.8	1.9	9.0	-2%
	Repeat 2	0.5	8.8	0.3	7.0	20%	0.5	8.8	0.5	6.8	23%
Case 4	Test	1.4	9.2	1.4	7.8	15%	1.4	9.4	1.4	7.8	17%
	Repeat 1	1.4	9.2	1.4	8.0	13%	3.6	9.6	3.6	7.2	25%
Case 5	Test	1.4	8.8	0.5	7.8	11%	3.7	8.0	3.7	10.8	-35%
	Repeat 1	1.4	8.8	1.4	8.8	0%	3.9	8.0	3.9	12.0	-50%
Case 6	Test	1.4	7.5	1.4	5.5	27%	1.4	7.5	1.4	5.5	27%
	Repeat 1	1.4	7.5	0.8	7.5	0%	0.8	6.0	0.8	7.5	-25%
	Repeat 2	1.4	7.5	0.8	3.5	53%	1.4	7.5	0.8	3.5	53%
	Repeat 3	1.4	7.5	1.4	5.0	33%	1.4	7.5	1.4	5.0	33%
	Repeat 4	1.4	7.5	0.8	7.5	0%	5.2	6.0	5.2	3.0	50%
	Repeat 5	1.4	7.5	1.1	6.0	20%	4.8	6.0	4.8	4.8	20%

Table 5.18. Difference between the Experimental and Analytical Capacity (Continued)

Case 7	Test	2.2	15.0	3.8	15.0	0%	3.8	8.0	3.8	15.0	-88%
	Repeat 1	2.2	15.0	3.4	12.0	20%	2.2	15.0	2.2	8.0	47%
	Repeat 2	2.2	15.0	2.2	10.0	33%	3.8	8.0	3.8	14.0	-75%
	Repeat 3	2.2	15.0	2.2	18.0	-20%	2.7	9.0	2.7	15.0	-67%
	Repeat 4	2.2	15.0	1.9	14.0	7%	2.7	9.0	2.7	14.0	-56%
Case 8	Test	2.5	10.8	3.0	10.8	0%	6.8	8.8	6.8	5.2	41%
	Repeat 1	2.5	10.8	1.1	10.0	7%	1.4	7.2	1.4	10.0	-39%
	Repeat 2	2.5	10.8	0.5	12.0	-11%	0.5	6.4	0.5	12.0	-88%
	Repeat 3	2.5	10.8	2.1	13.0	-20%	2.1	9.0	2.1	13.0	-44%
	Repeat 4	2.5	10.8	2.1	12.0	-11%	6.0	8.8	6.0	5.6	36%

Table 5.19. Difference between the Experimental and Analytical Penetration Depth

		Encounter the Stiff					Maximum Difference				
		Prediction		Experiment		Difference on z	Prediction		Experiment		Difference on z
		x (Fluke Length)	z (Fluke Length)	x (Fluke Length)	z (Fluke Length)		x (Fluke Length)	z (Fluke Length)	x (Fluke Length)	z (Fluke Length)	
Case 3	Test	0.3	0.8	0.3	0.8	0%	2.7	0.7	2.7	0.5	20%
	Repeat 1	0.5	0.8	1.1	0.3	67%	2.2	1.4	2.2	0.3	80%
	Repeat 2	0.5	1.0	0.3	0.4	57%	3.5	1.5	3.5	0.8	45%
Case 4	Test	1.4	1.2	1.4	1.2	0%	1.9	1.1	1.9	1.4	-25%
	Repeat 1	1.4	1.4	1.4	0.7	50%	2.7	0.8	2.7	1.9	-133%
Case 5	Test	1.4	1.2	0.5	0.8	33%	3.6	1.6	3.6	1.5	8%
	Repeat 1	1.4	1.2	1.4	1.1	11%	1.9	1.4	1.9	1.2	10%
Case 6	Test	1.4	1.2	1.4	1.0	22%	1.4	1.2	1.4	1.0	22%
	Repeat 1	1.4	1.2	0.8	0.8	33%	3.8	1.4	3.8	0.5	60%
	Repeat 2	1.4	1.2	0.7	1.0	22%	4.9	1.5	4.9	0.8	45%
	Repeat 3	1.4	1.2	1.4	0.8	33%	4.9	1.5	4.9	0.5	64%
	Repeat 4	1.4	1.2	0.8	0.8	33%	4.9	1.5	4.9	0.0	100%
	Repeat 5	1.4	1.2	1.1	0.8	33%	4.8	1.5	4.8	0.5	64%

Table 5.19. Difference between the Experimental and Analytical Penetration Depth (Continued)

Case 7	Test	2.2	1.4	3.8	1.4	0%	5.2	1.6	5.2	1.1	33%
	Repeat 1	2.2	1.4	3.4	0.9	34%	4.4	1.6	4.4	1.1	33%
	Repeat 2	2.2	1.4	2.2	1.1	20%	3.8	1.6	3.8	1.4	17%
	Repeat 3	2.2	1.4	2.2	0.8	40%	4.9	0.5	4.9	1.6	-200%
	Repeat 4	2.2	1.4	1.9	1.0	30%	5.8	1.6	5.8	0.8	50%
Case 8	Test	2.5	1.5	3.0	1.4	9%	4.1	1.6	4.1	1.2	25%
	Repeat 1	2.5	1.5	1.1	1.1	27%	4.7	1.6	4.7	2.3	-42%
	Repeat 2	2.5	1.5	0.5	0.8	45%	5.5	1.6	5.5	1.1	33%
	Repeat 3	2.5	1.5	2.1	1.1	27%	2.1	1.5	2.1	1.1	27%
	Repeat 4	2.5	1.5	2.1	1.0	36%	6.0	2.4	6.0	1.5	36%

Table 5.20. Difference between the Experimental and Analytical Pitch

		Encounter the Stiff					Maximum Difference				
		Prediction		Experiment		Pitch Difference	Prediction		Experiment		Pitch Difference
		x (Fluke Length)	Pitch	x (Fluke Length)	Pitch		x (Fluke Length)	Pitch	x (Fluke Length)	Pitch	
Case 3	Test	0.3	38.0	0.3	30.0	21%	2.7	18.0	2.7	28.0	-56%
	Repeat 1	1.1	22.0	1.1	38.0	-73%	1.6	20.0	1.6	52.0	-160%
	Repeat 2	0.5	40.0	0.3	47.5	-19%	3.4	17.5	3.4	42.5	-143%
Case 4	Test	1.4	40.0	1.4	35.0	13%	1.9	25.0	1.9	35.0	-40%
	Repeat 1	1.4	40.0	1.4	50.0	-25%	2.2	24.0	2.2	52.0	-117%
Case 5	Test	1.4	30.0	0.5	23.0	23%	1.4	31.0	1.4	23.0	26%
	Repeat 1	1.4	30.0	1.4	30.0	0%	2.2	22.0	2.2	30.0	-36%
Case 6	Test	1.4	33.0	1.4	33.0	0%	1.9	14.0	1.9	33.0	-136%
	Repeat 1	1.4	33.0	0.8	30.0	9%	1.9	14.0	1.9	33.0	-136%
	Repeat 2	1.4	33.0	0.8	26.0	21%	2.7	15.0	2.7	35.0	-133%
	Repeat 3	1.4	33.0	1.4	30.0	9%	4.9	12.5	4.9	32.0	-156%
	Repeat 4	1.4	33.0	0.8	32.0	3%	4.9	12.5	4.9	-30.0	340%
	Repeat 5	1.4	33.0	1.1	35.0	-6%	2.2	15.0	2.2	32.0	-113%

Table 5.20. Difference between the Experimental and Analytical Pitch (Continued)

Case 7	Test	2.2	43.0	3.8	35.0	19%	5.2	13.0	5.2	27.0	-108%
	Repeat 1	2.2	43.0	3.4	40.0	7%	4.4	14.0	4.4	35.0	-150%
	Repeat 2	2.2	43.0	2.2	27.0	37%	2.5	43.0	2.5	27.0	37%
	Repeat 3	2.2	43.0	2.2	35.0	19%	2.7	16.0	2.7	35.0	-119%
	Repeat 4	2.2	43.0	1.9	37.0	14%	3.6	15.0	3.6	46.0	-207%
Case 8	Test	2.5	21.0	3.0	45.0	-114%	4.1	13.0	4.1	45.0	-246%
	Repeat 1	2.5	21.0	1.1	40.0	-90%	2.5	40.0	2.5	20.0	50%
	Repeat 2	2.5	21.0	0.5	47.0	-124%	5.5	11.0	5.5	43.0	-291%
	Repeat 3	2.5	21.0	2.1	47.0	-124%	2.1	20.0	2.1	47.0	-135%
	Repeat 4	2.5	21.0	2.1	3.5	83%	6.0	6.0	6.0	3.5	42%

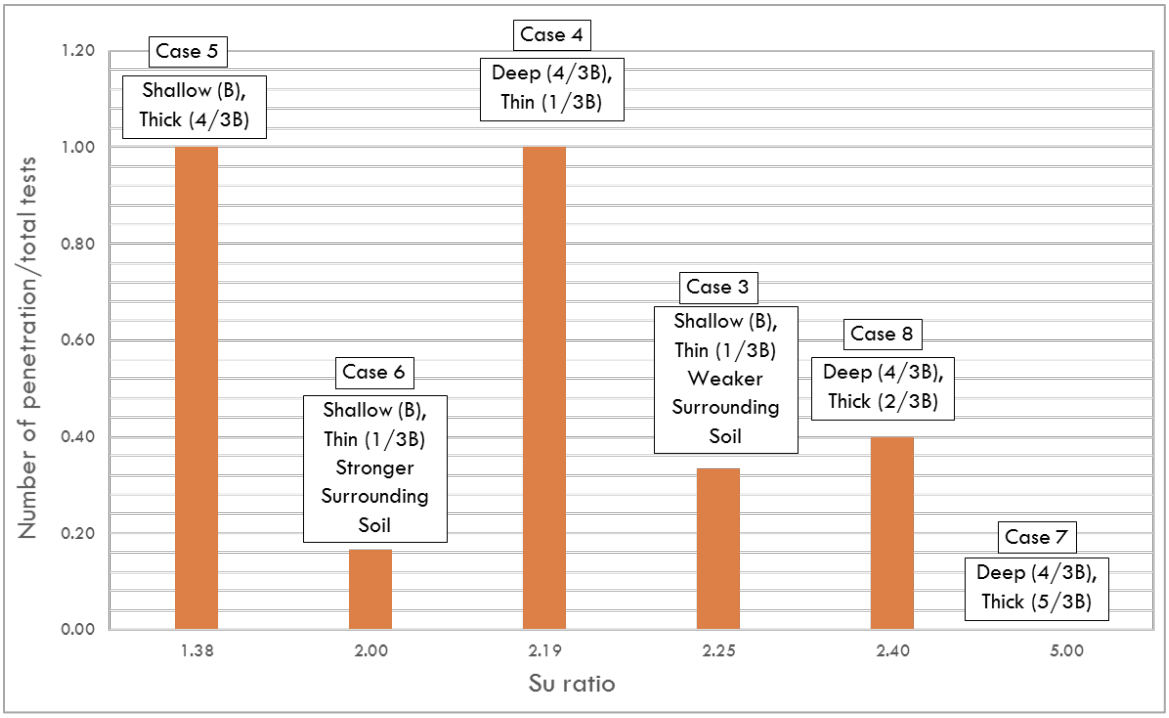

Figure 5.53. Percentage of Tests in Which Stiff Layer Was Penetrated Versus the Undrained Strength Ratio for The Stiff Layer Compared to the Surrounding Soil

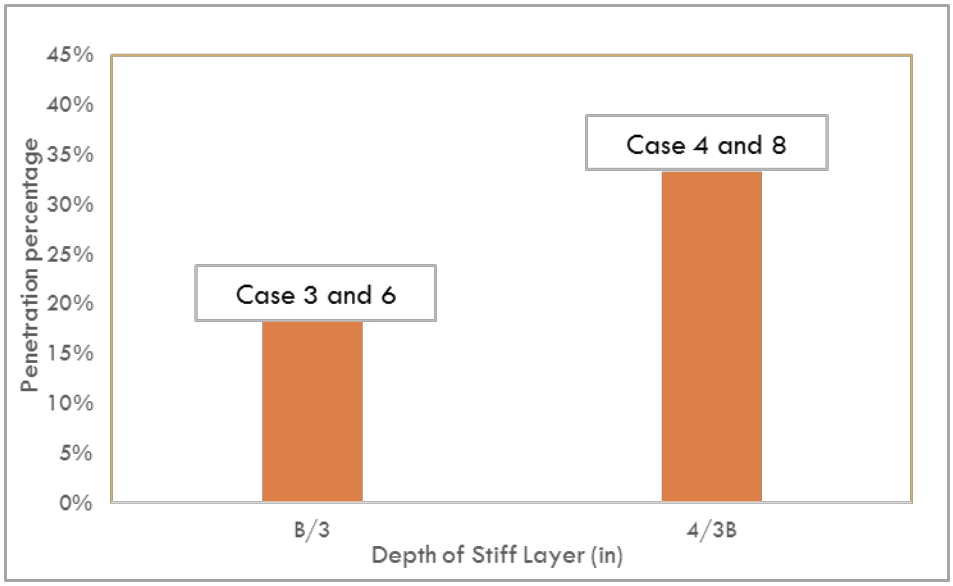

Figure 5.54. Percentage of Tests in Which Stiff Layer Was Penetrated Versus Depth of Stiff Layer

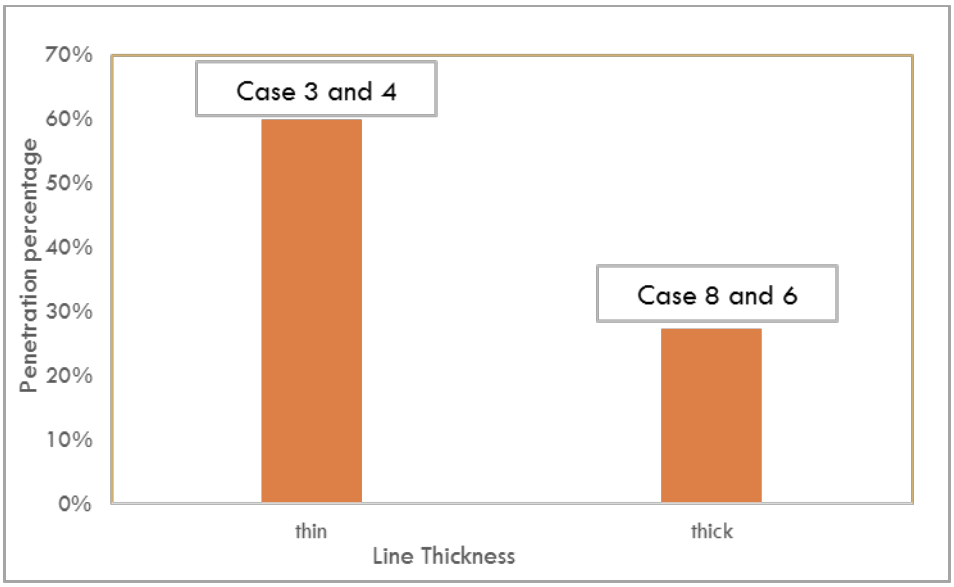

Figure 5.55. Percentage of Tests in Which Stiff Layer Was Penetrated Versus Anchor Line Thickness

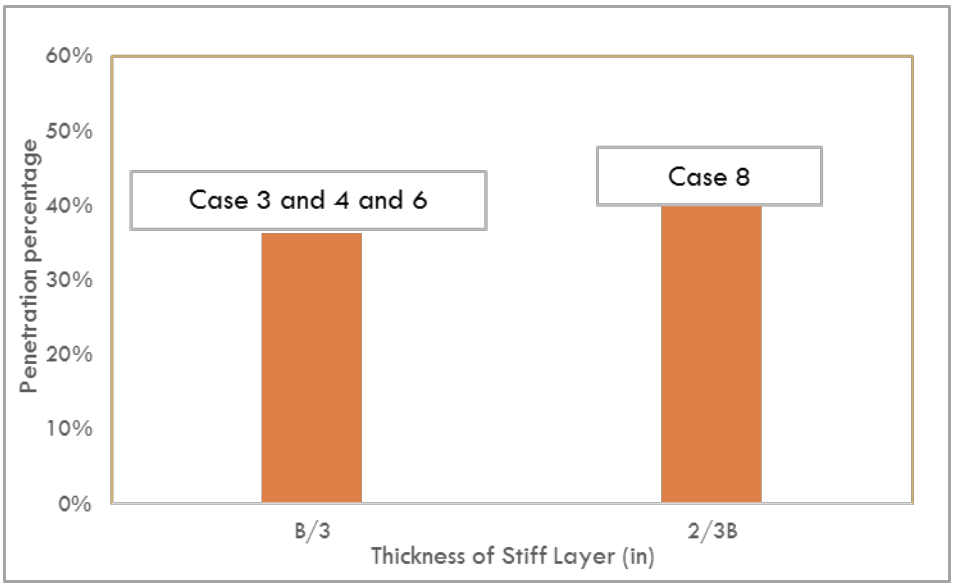

Figure 5.56. Percentage of Tests in Which Stiff Layer Was Penetrated Versus Thickness of Stiff Layer

As shown in Figure 5.52, the calibrated model can generally match with experimental results, but there is slight difference on trajectory (final penetration depth) which makes discrepancy between the experimentally and theoretically that if anchor can or cannot penetrate into or through the stiff layer. In the same test bed where anchor is expected to penetrate into or through the stiff layer by the calibrated model, but experimental results may not match the analytical expectation in every test. Figure 5.53 summarizes the number of penetration over the total tests. Combining Table 5.17 and Figure 5.53, we can summarize that:

- For the stiff layer with lowest and highest undrained shear strength, the prediction model matches with every experimental test (case 5 and case 7 in Figure 5.53).
    - When the anchor is expected to penetrate into the stiff layer in case 5 based on the calibrated model, the anchor penetrates into the stiff layer in every test. In this case, the undrained shear strength of stiff layer is 22 psf, and the thickness is 4 inches, the depth is 3 inches. One example test compared with calibrate model is shown in Figure 5.59, from which the experimental measured capacity agrees well with the predicted one, the experimental and analytical trajectory matches well, the measured pitch is slightly flattened than the predicted one. The rest of tests results in case 5 are shown in Appendix A, and they all match well with analytical results that anchor penetrates into the stiff layer.
    - When the anchor is not expected to penetrate into the stiff layer in case 7, the anchor in every test cannot penetrate into the stiff layer. In this

case, the shear strength of stiff layer is 76 psf, and the thickness is 2 inches, and starting at 4 inches below mudline. An example of the comparison between the analytical and experimental results of capacity, trajectory, and pitch is shown in Figure 5.61. The rest of tests are shown in Appendix A. From Figure 5.61, the calibrated and experimental results match generally well, and either the analytical or experimental results show the anchor cannot penetrate into the stiff layer.

- For a Su ratio with 2 to 2.4, anchor can or cannot penetrate into stiff layer does not highly depends on the shear strength ratio between the stiff layer over surrounding soil, however, it depends on the depth of stiff layer and the thickness of anchor line (Figure 5.54 and Figure 5.55) and does not depend on stiff layer thickness (Figure 5.56). From Figure 5.53, it can be seen that there is no clear trend that anchor is less possible to penetrate into stiff layer with the increase of shear strength. This implies that within the shear strength ratio range between 2 and 4, the shear strength ratio may not be the determinant for anchor to penetrate or not into stiff layer. Figure 5.54 summarizes the percentage of anchor penetrates into stiff layer with the depth of stiff layer, and it shows that a lead to a less percentage to penetrate. Figure 5.55 shows that a thinner anchor line makes anchor more possibility to penetrate into stiff layer. Figure 5.56 shows that the thickness of stiff layer is not the key variable to determine anchor can or cannot to penetrate into stiff layer. In summary, the depth of stiff layer and anchor line thickness are two factors to influence anchor to penetrate into stiff layer, which implies that anchor can or cannot penetrate

into stiff layer is the pitch angle when approaching stiff layer. If the pitch angle is relative steep, then it is likely to for anchor to slide on the surface of stiff layer. Otherwise, the anchor with a relatively flattened pitch can penetrate into stiff layer. Thus, the thin anchor line helps anchor pitch downward compared with the thick line which makes a steeper angle at the shackle. On the other hand, if the depth of stiff layer is relatively deeper, then the pitch of anchor has already flattened when touching the stiff layer since pitch generally decreases with the horizontal drag distance.

- It is easier for anchor to penetrate into the stiff layer with deeper depth compared with the case with shallower depth. Comparing case 4 and case 8 with case 6 and case 3 in Figure 5.53, the percentage of penetration numbers over total tests for the cases with deeper stiff layer (case 4 and case 8) is higher than the cases with shallower stiff layer (case 3 and case 6).
- If the depth of stiff layer is the same, then it is easier for anchor to penetrate into stiff layer with a thinner anchor line attached. Comparing the case 8 (thick anchor line) with case 4 (thin anchor line), case 6 (thick anchor line) and case 3 (thin anchor line), the number of penetration over total tests is higher for the cases with thin anchor line. For example, with the stiff layer at shallower depth (case 3 and case 6), the thick anchor line (case 6) has one test out of 6 tests for anchor penetrating into stiff layer, while the thin line (case 3) has two test out of 6 tests for anchor penetrating into stiff layer; with the stiff layer at deeper depth

(case 4 and case 8), the anchor with a thin line (case 4) penetrates into stiff layer in every test while anchor with a thick line (case 8) penetrates into stiff layer twice out of 5 times.

- When the behavior in the experiment matches the predicated behavior (either penetrating or not penetrating the stiff layer), the experimental results are generally in good agreement with the predictions for the load and trajectory (Figure 5.57 to Figure 5.62).
- The anchor and the T-bar are both affected by the stiff layer before penetrating it (Figure 5.57 to Figure 5.62). The orange block represents the real stiff layer thickness and depth in undrained shear strength versus depth plot and trajectory plot, while the gray block represents the stiff layer felt by the T-bar and anchor. From the undrained shear strength profiles in Figure 5.57 to Figure 5.62, the undrained shear strength increases before the T-bar touching the stiff layer, and the soil resistance decreases gradually when the T-bar back to the soft soil.
- The anchor tends to pitch forward (stand up vertically or rotate in the opposite direction of the flattening it typically exhibits) when it hits the stronger layer. This effect is most significant with the shallower stiff layers. Figure 5.63 shows an example of trajectory and pitch from case 3 with stiff layer at a shallower depth, and Figure 5.64 shows an example of trajectory and pitch from case 8 with stiff layer at a deeper depth. Comparing pitches in Figure 5.63 and Figure 5.64, the anchor stands up more vertically in the case with a shallower stiff layer.

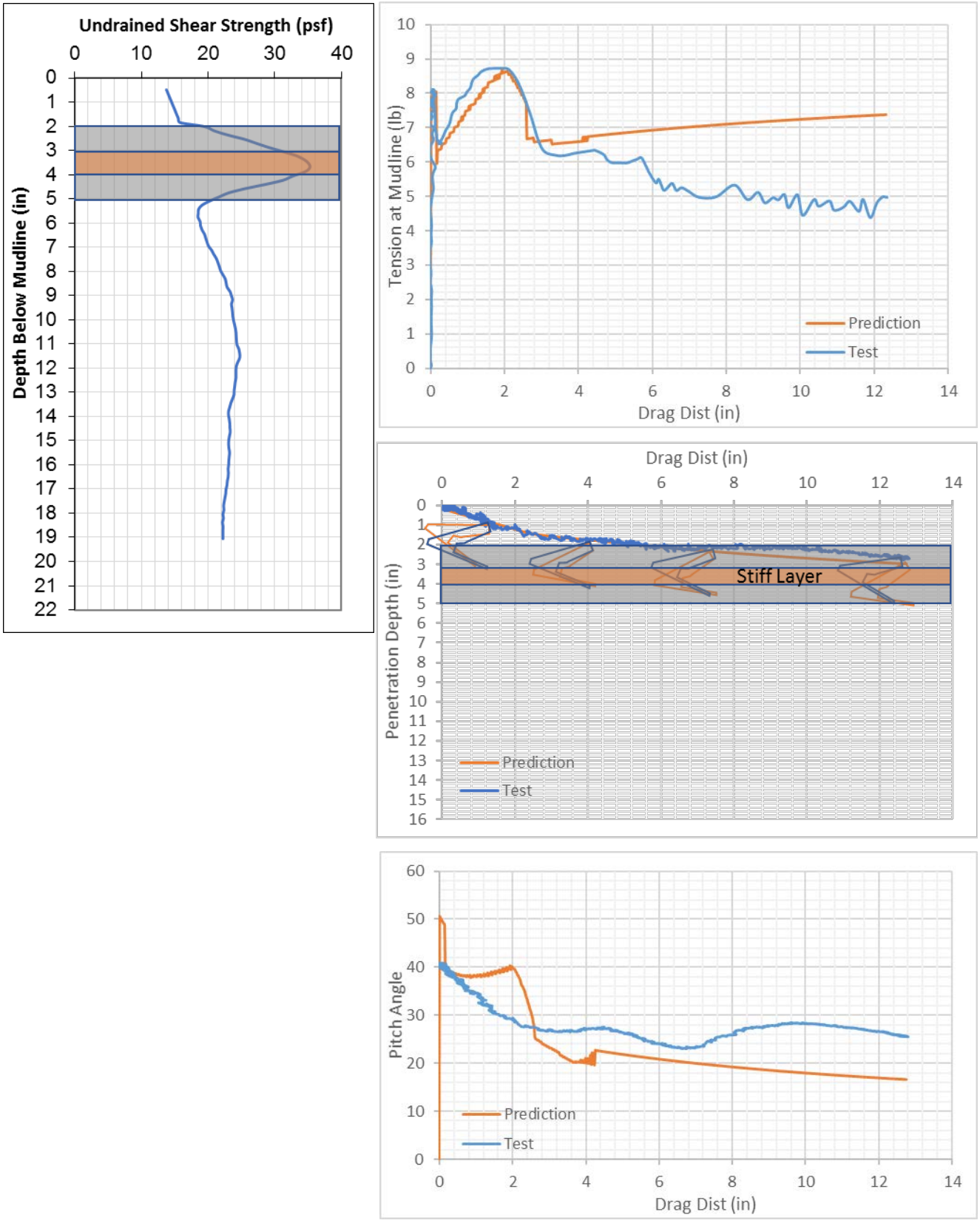

Figure 5.57 Drag embedment test results in Case 3

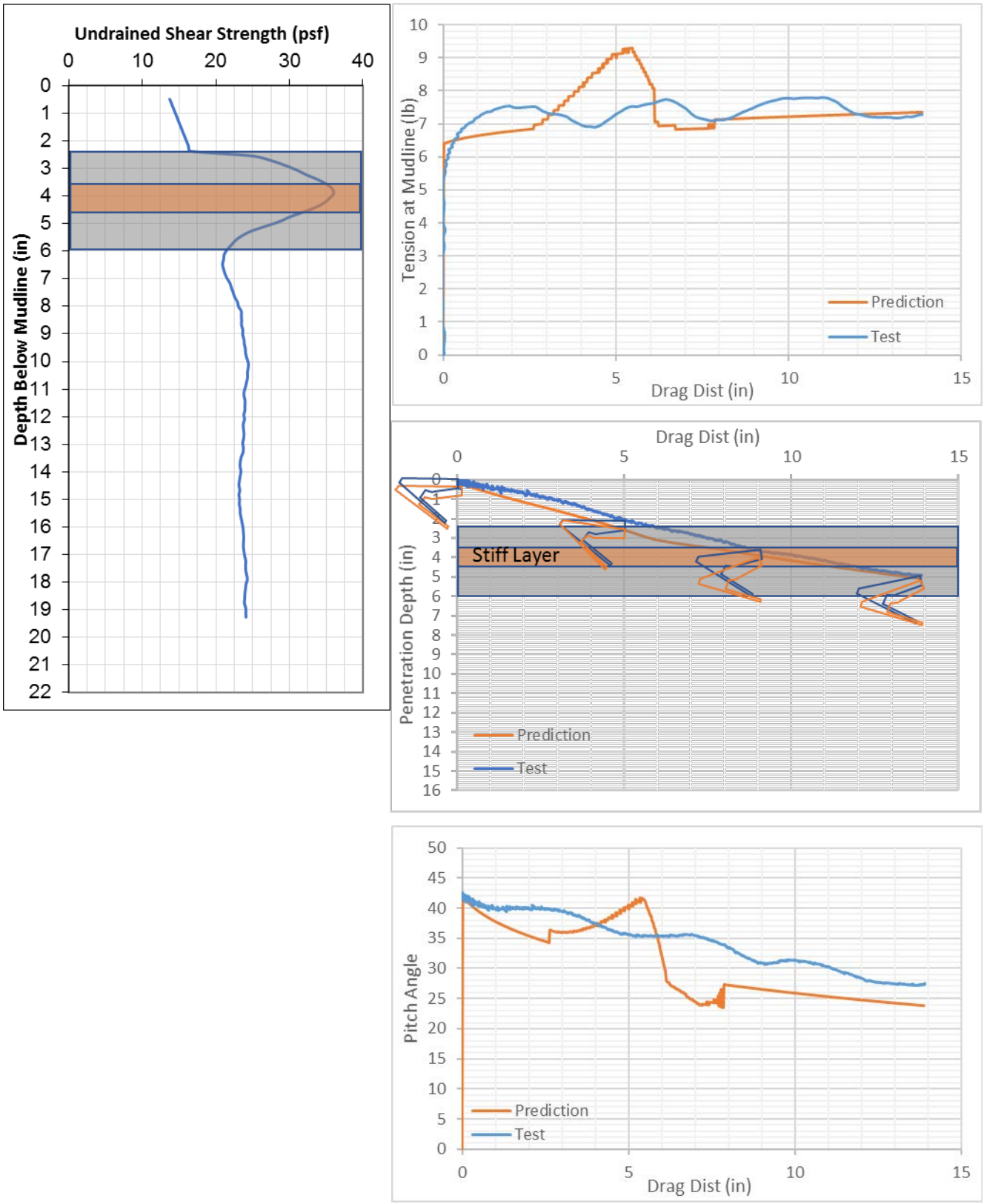

Figure 5.58. Drag embedment test results in Case 4

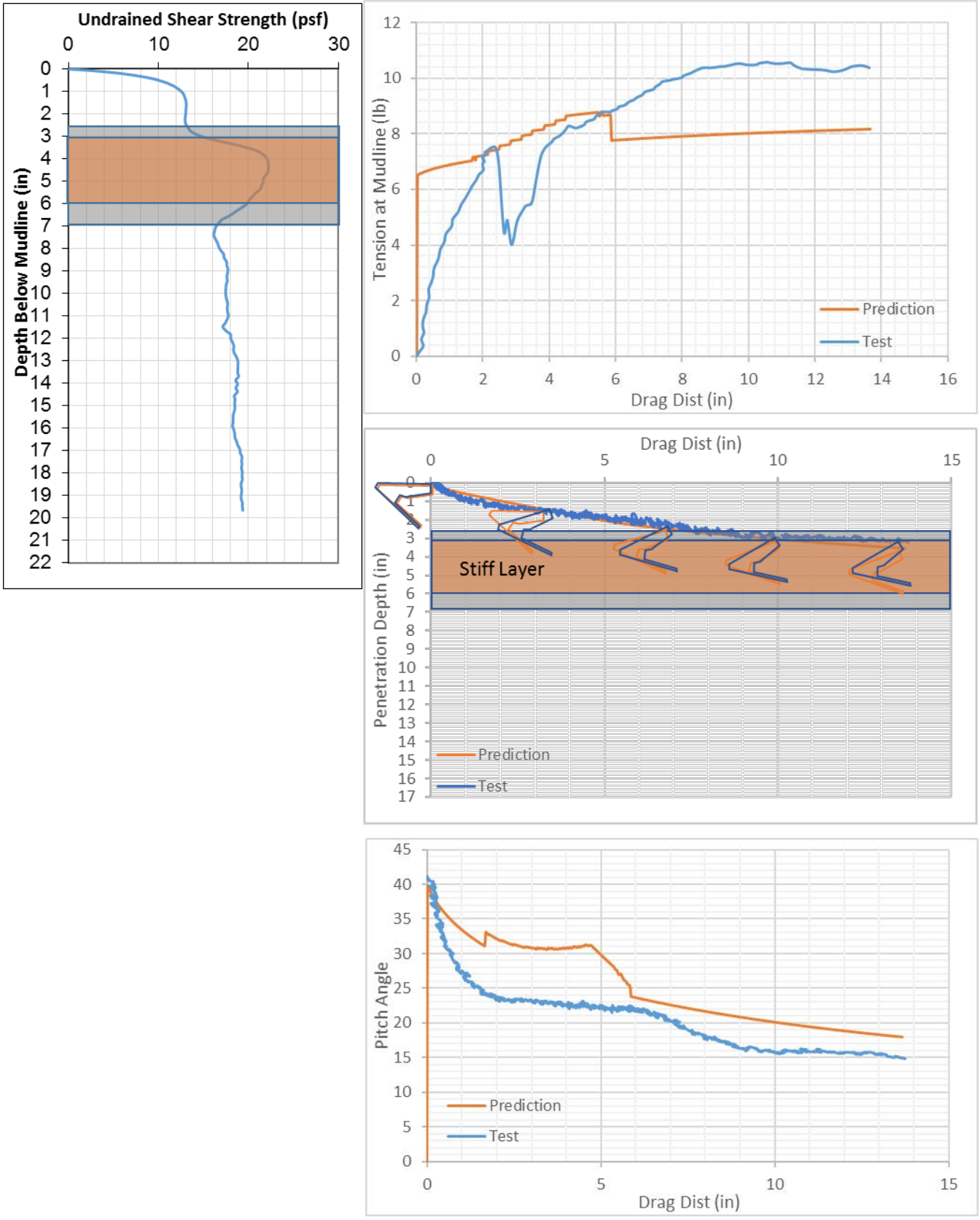

Figure 5.59. Drag embedment test results in Case 5

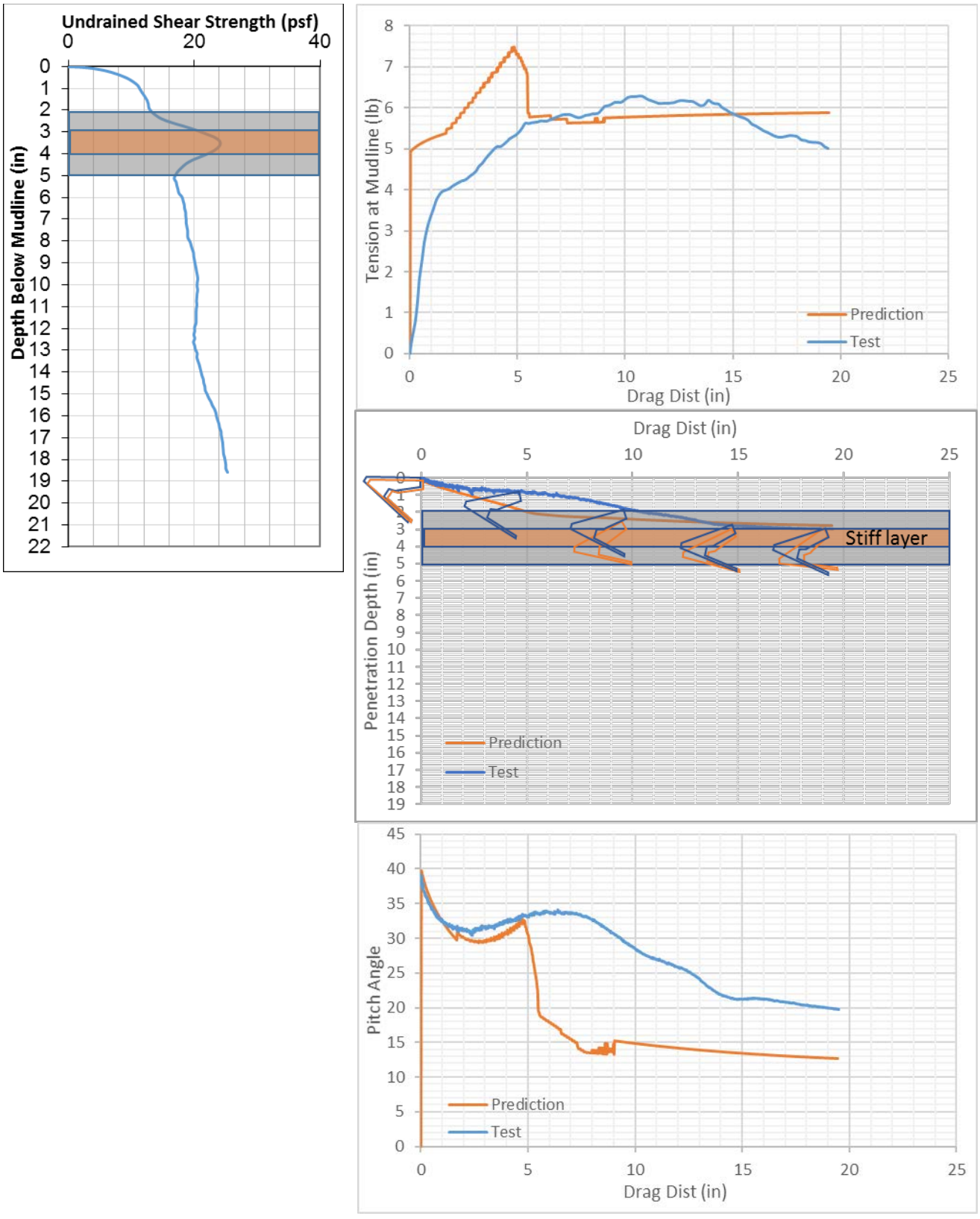

Figure 5.60. Drag embedment test results in Case 6

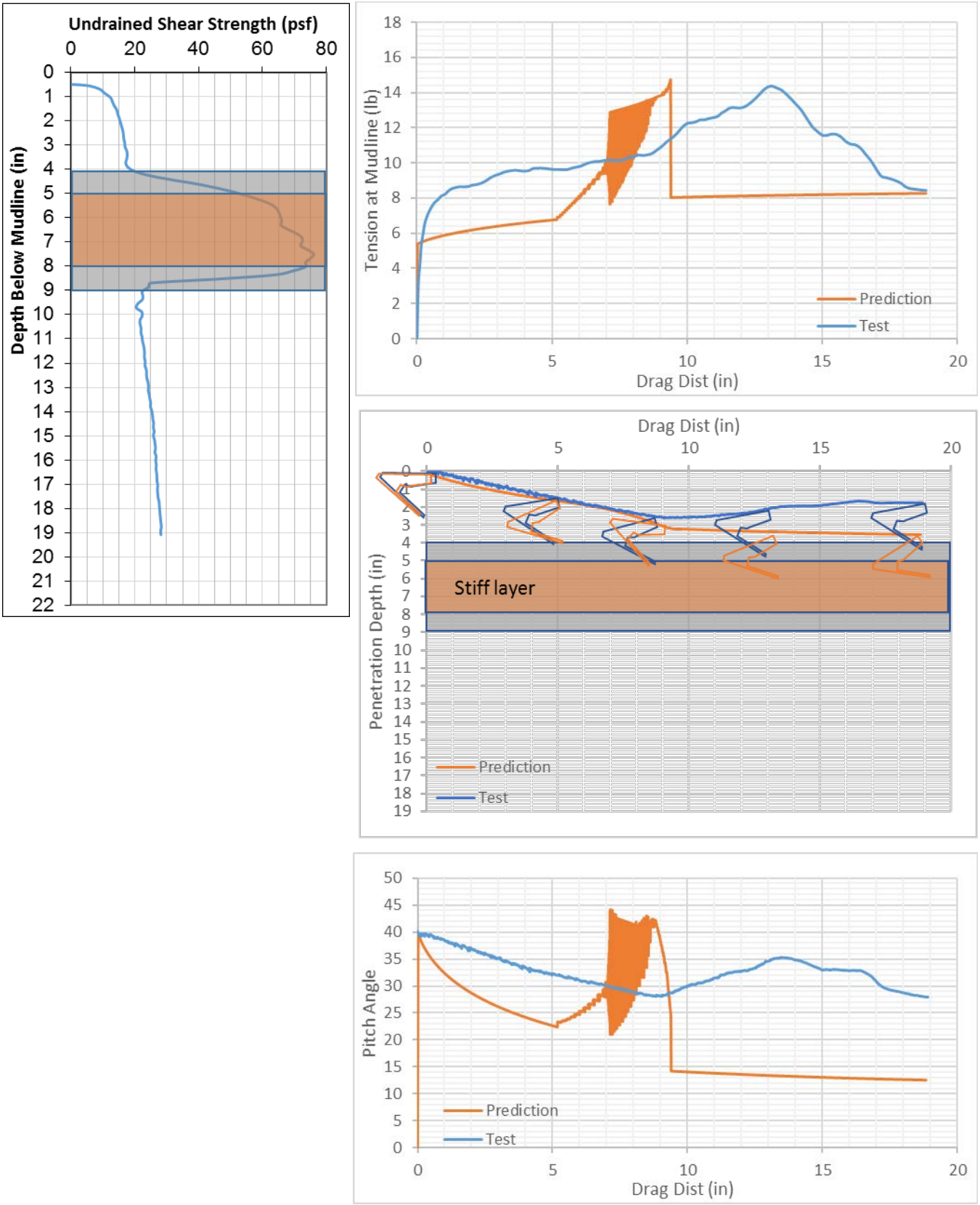

Figure 5.61. Drag Embedment Test Results in Case 7

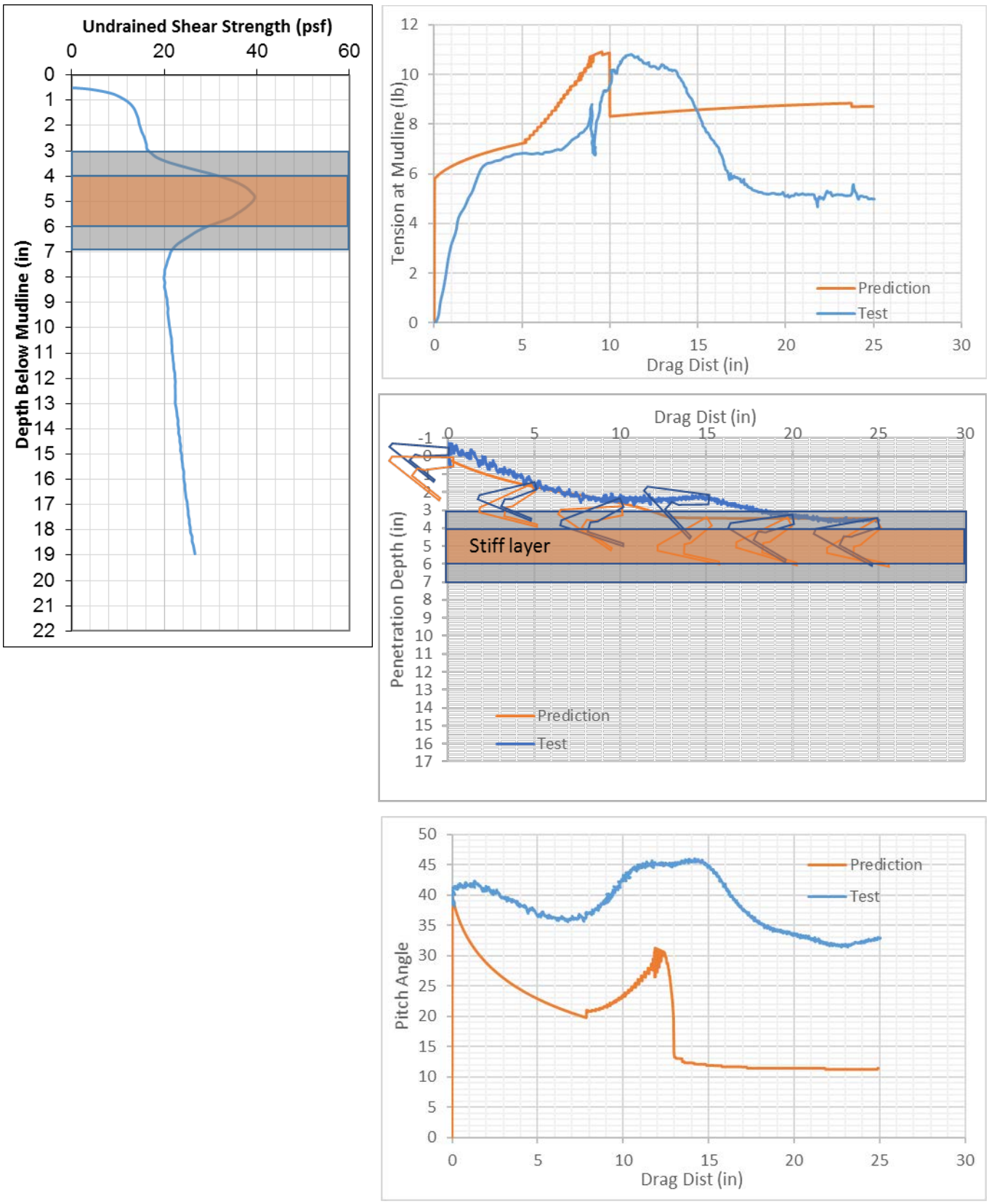

Figure 5.62. Drag Embedment Test Results in Case 8

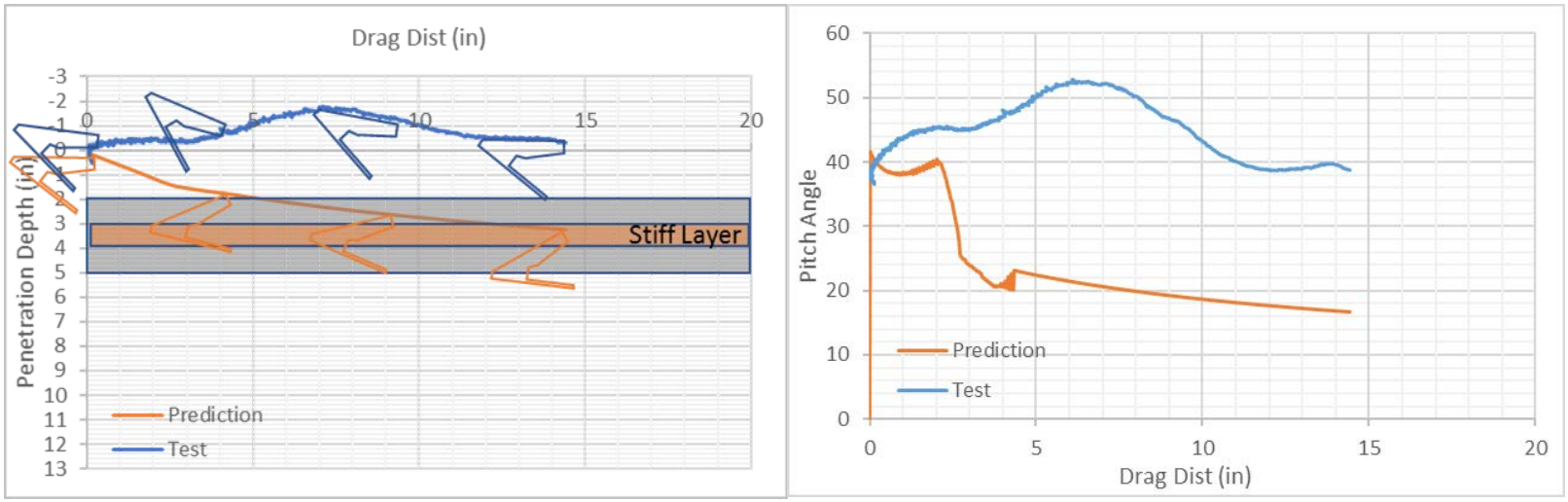

Figure 5.63. Example of Anchor Pitching Forward from Case 3

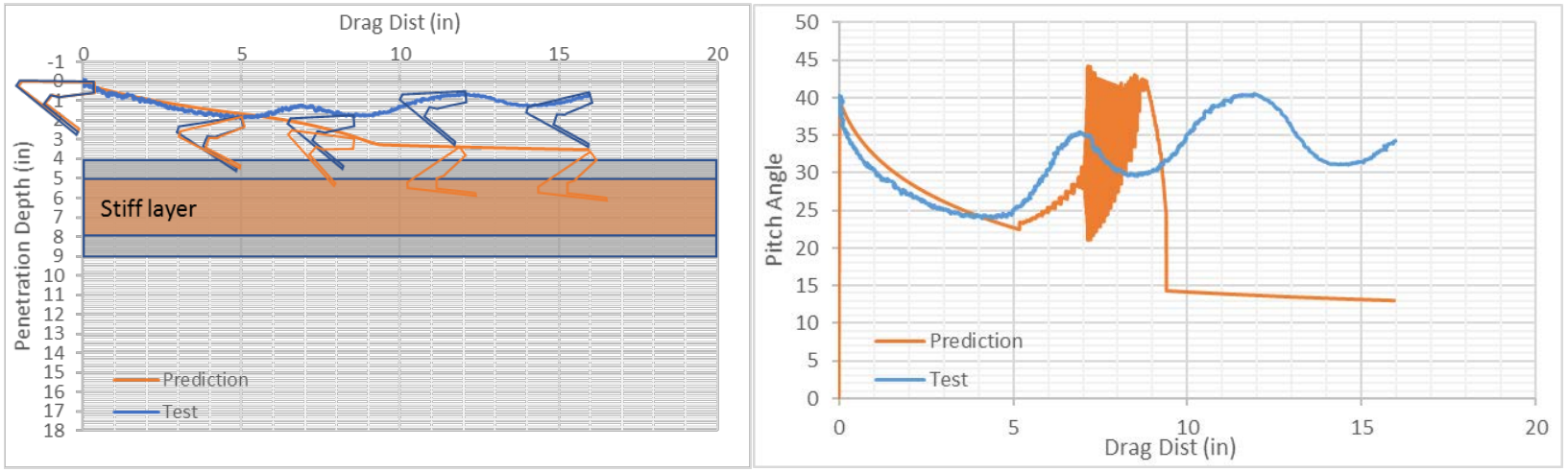

Figure 5.64. Example of Anchor Pitching Forward from Case 7

5.3.5 Updated Analytical Model

From previous comparison, the prediction model did not include the effect that the T-bar and anchor experiences the stiff layer earlier before touching the stiff layer lagging after leaving the stiff layer. In the updated prediction model, this effect is included. The comparison between the shear strength is shown in Figure 5.65. The updated prediction model adds a linear ramp above and below the stiff layer. In that ramp region above stiff layer, the multiplier is stepped up linearly from 1 at the beginning of the ramp to the stiff layer multiplier at the boundary of the stiff layer. In the same way, a linear ramp below stiff layer, the multiplier is equal to the stiff layer multiplier and reduce to 1 when back to soft layer. This linear ramp models the effect that T-bar and anchor feels stiff layer earlier before penetrating and lagging after leaving stiff layer. All the comparison between the original prediction, the experimental results and updated prediction are shown in Appendix C.

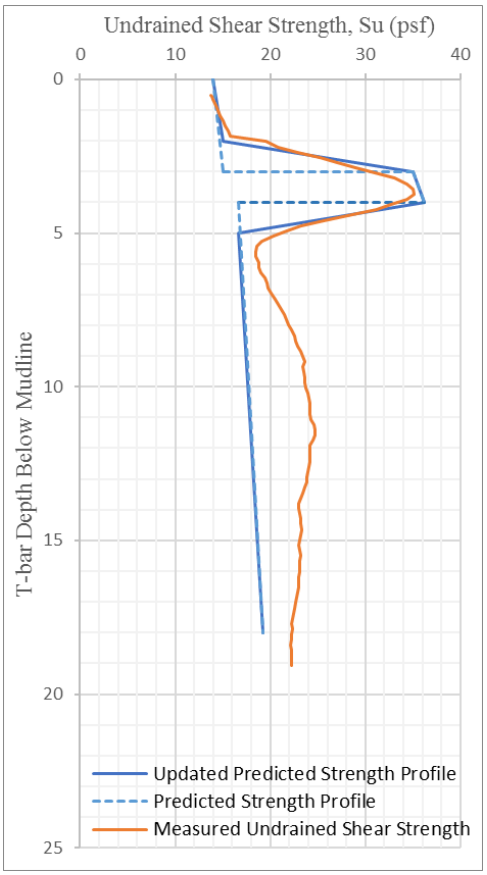

Figure 5.65. Shear Strength Comparison Between the Primary and Updated Model

5.3.5.1 Updated Analytical Capacity

The peak capacity from both prediction models are similar. However, the capacity curve by the updated prediction has two features different from that by the original prediction model. First, load gradually increases when the anchor approaches to stiff layer and gradually decreases when anchor breaks stiff layer and back to soft layer. Second, the capacity by the updated prediction model tends to predict higher load than that from original prediction after its peak. Figure 5.66 shows an example of capacity comparison from case 4. The curve by the original model has a sharp increase and decrease when anchor penetrates and leaves the stiff layer. In comparison, the peak load by the updated

prediction moderately reaches its peak and then decreases. After the peak load, the updated predicted capacity is slightly higher than the original prediction.

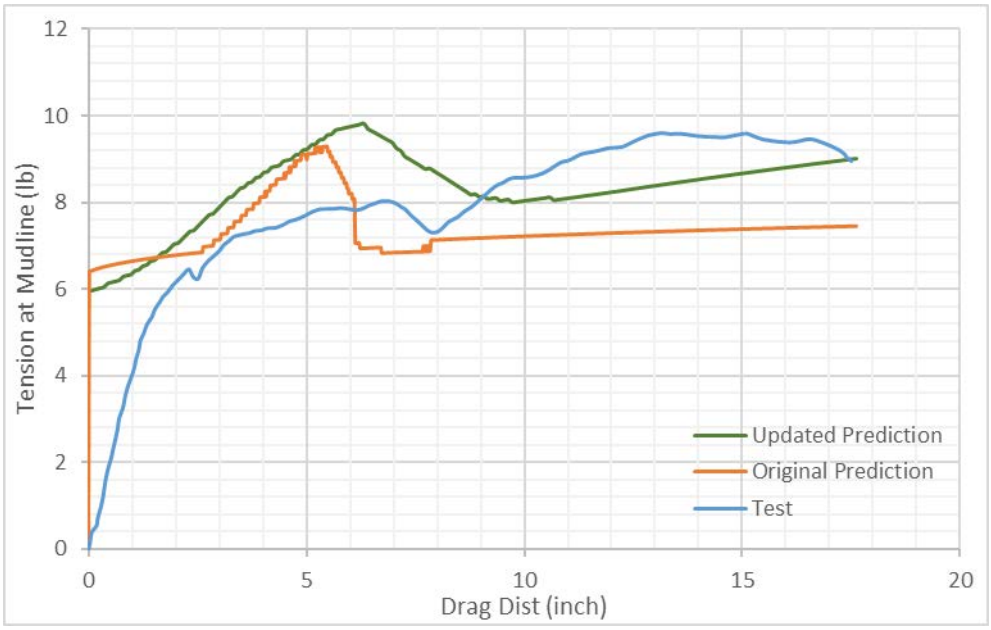

Figure 5.66. Example of Capacity Comparison between Updated and Original Prediction for Case 4

The updated prediction has a similar trend as the original prediction as shown above in Figure 5.66. However, in the cases where the shear strength ratio of the stiff layer over surrounding soft soil is higher than 2.4, instead of having an obvious drop in load-displacement curve after the peak, load keeps slightly increasing. Figure 5.67 and Figure 5.68 show an example of load-displacement curves from case 7 and case 8 with shear strength ratio of 5 and 2.4, respectively. From these two examples, we can see that the updated prediction model predicts the capacity still slightly increases after the sharp increase.

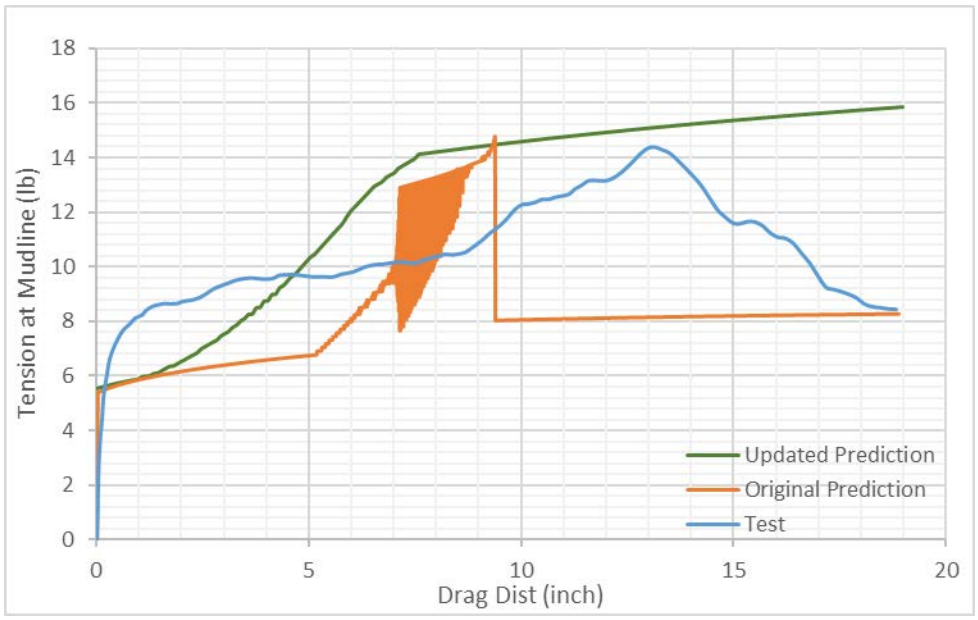

Figure 5.67. Example of Capacity Comparison between Updated and Original Prediction for Case 7

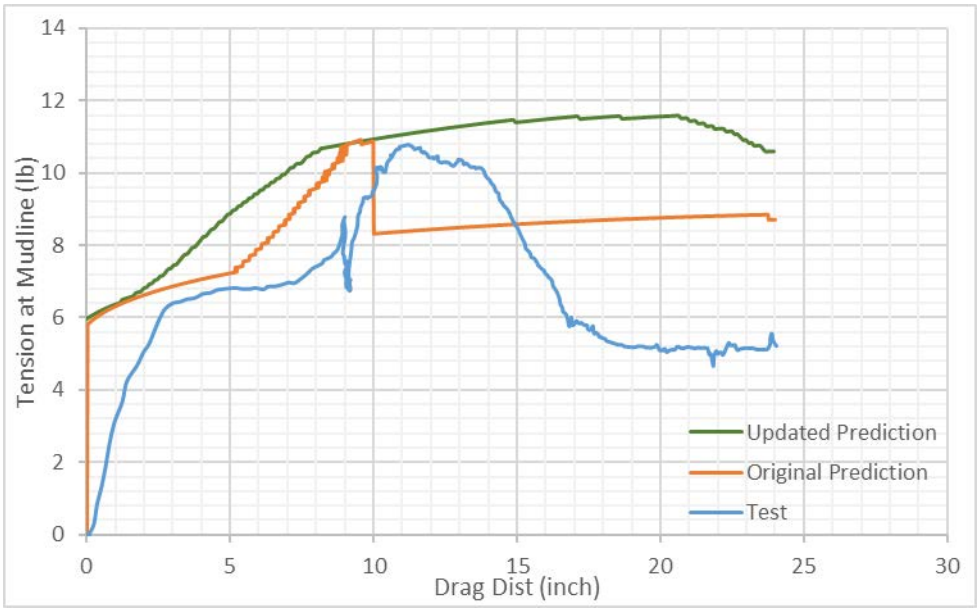

Figure 5.68. Example of Capacity Comparison between Updated and Original Prediction for Case 8

The characteristics of load-displacement curves by the updated model are summarized below:

- If the shear strength ratio of stiff layer over the surrounding soft soil is lower than 2, then the updated prediction model predicts the similar capacity as the original model. Both predictions have an obvious peak load, but the updated prediction model predicts higher peak load and higher capacity after the peak than the original prediction. The slightly higher capacity is because of the introduce of linear ramp representing the effect that the anchor or the T-bar experiences higher resistance before reaching and after leaving stiff layer. This linear ramp extends the thickness of stiff layer and increases the shear resistance from stiff layer.
- If the shear strength ratio is higher than 2.4, the load-displacement curve by the updated prediction model has no obvious peak compared with the original model. Instead, the updated model predict that capacity keeps increasing after reaching stiff layer.
- From the above two characteristics, we can conclude that the updated model with linear ramp above and below actual stiff layer is capable to capture the effect of elevated resistance before anchor touching and after anchor leaving stiff layer.

5.3.5.2 Updated Analytical Trajectory

The updated prediction model predicts a similar trajectory of anchor in layered soil profile. There are three examples shown below from different cases to show the similarity between the original model and the updated model.

The original model can predict the anchor trajectory well when the stiff layer is relatively deeper and anchor is expected to penetrate through stiff layer. However, when the stiff layer is shallower, the prediction trajectory has few agreements with the measured trajectory. In the cases with shallower stiff layer, the original prediction model predicts anchor can penetrate into stiff layer, but experimentally, anchor pitches forward and slides on top of stiff layer.

There is no obvious improvement on trajectory prediction with the updated model with a linear ramp in shear strength profile. Figure 5.69 to Figure 5.72 show three comparison example between the original and the updated prediction from different cases. Figure 5.69 shows an example from case 4 where anchor is expected to penetrate into the stiff layer and anchor penetrates into stiff layer experimental in every test. In this case with the stiff layer is relatively deeper, the updated and the original prediction agrees well with the experimental trajectory. Figure 5.70 and Figure 5.71 show another example of case with a relatively deep stiff layer. In this case, anchor is analytically expected to penetrate into stiff layer either by the original and the updated model, however, it only penetrates into stiff layer two times out of five trials experimentally. The experimental result in Figure 5.70 shows anchor penetrates into stiff layer and matches well with both predictions. In comparison, Figure 5.71 shows that anchor does not penetrate into stiff layer, however, both prediction model predict that anchor penetrates into stiff layer. Figure 5.72 shows an

example of that stiff layer is relatively shallower. In this case, anchor pitches forward and slide on the top of stiff layer, however, both analytical model predict anchor can penetrate and have a similar predicted trajectory.

In summary, the updated prediction model

- Predicts a similar final penetration depth as the original prediction model
- Still cannot capture that anchor pitching forward when hitting a shallower stiff layer.

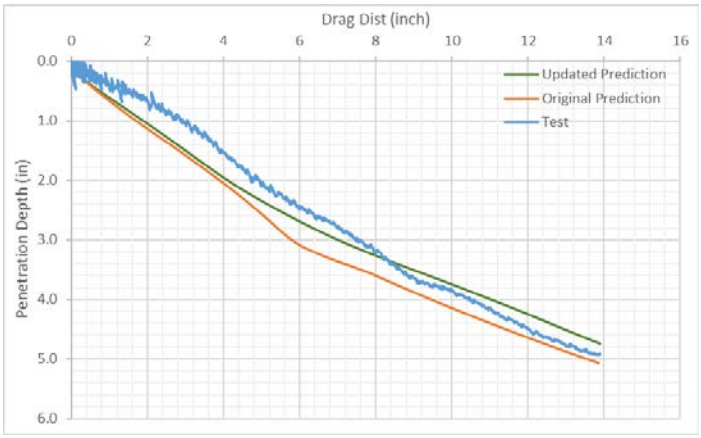

Figure 5.69. Example of Trajectory from Case 4

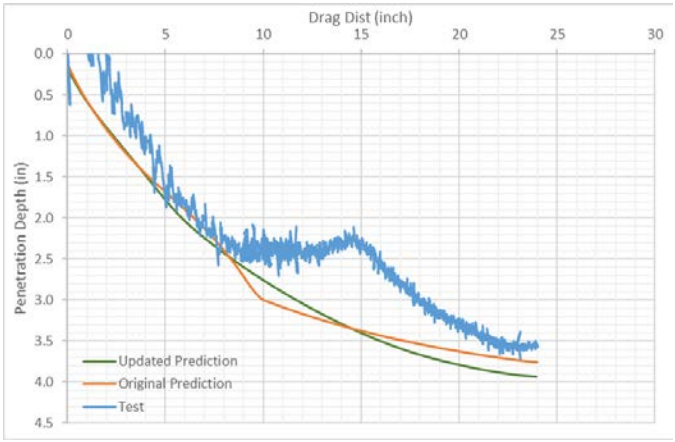

Figure 5.70. Example of Trajectory from Case 8 (Penetrate into Stiff Layer)

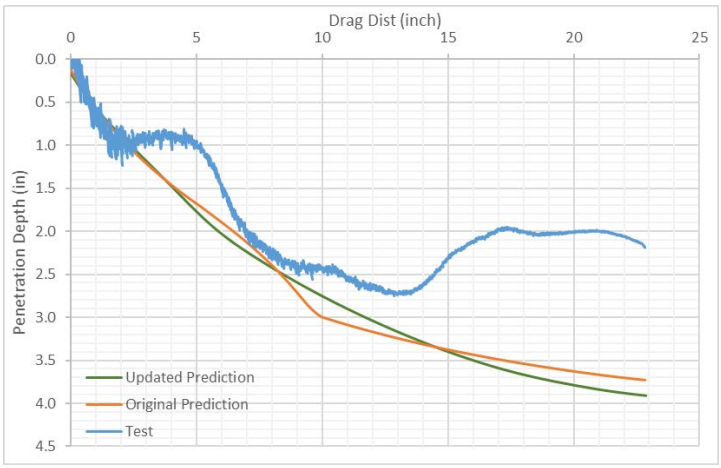

Figure 5.71. Example of Trajectory from Case 8 (Not Penetrate into Stiff Layer)

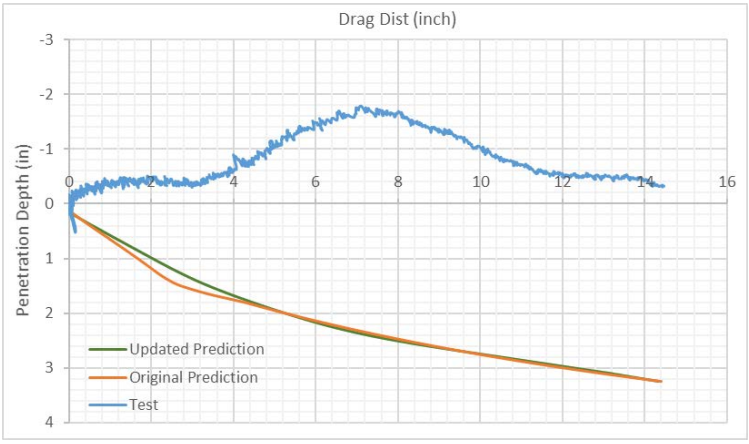

Figure 5.72. Example of Trajectory from Case 3

5.3.5.3 Updated Analytical Pitch

The pitch angle along horizontal dragging distance by the original prediction model has an obvious increase and decrease. In contrast, the pitch by the updated prediction model generally decreases with horizontal drag.

Figure 5.73 and Figure 5.74 show two examples of pitch angle along drag distance from two cases. Figure 5.73 shows the pitch angle in the test anchor penetrates into stiff

layer, and the corresponding trajectory is shown in Figure 5.69. In this case, the pitch angle by the original model has an obvious jump in the horizontal drag, however, the pitch by the updated prediction has similar trend as the measured pitch, that is, pitch angle decreases with horizontal drag. Figure 5.74 shows the pitch-drag curve from one test in case 8, and the corresponding trajectory is shown in Figure 5.71. In this particular test, anchor pitches forward when encounters stiff layer and continues sliding with the pitch first touches the stiff layer, thus the measured pitch increases first then keeps at a relative constant. However, neither the updated prediction nor the original model predicts the relative constant pitch.

In summary, the pitch by the updated model

- Has no sharp increase and decrease
- Better predicts the measured pitch with the case where the measured pitch gradually decreases with the horizontal drag
- Still does not capture the standing up and sliding features when anchor paws on top of stiff layer

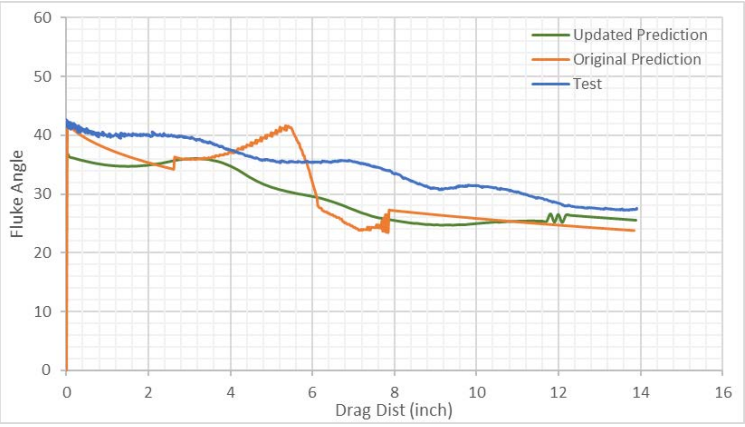

Figure 5.73. Example of Pitch-Drag from Case 4

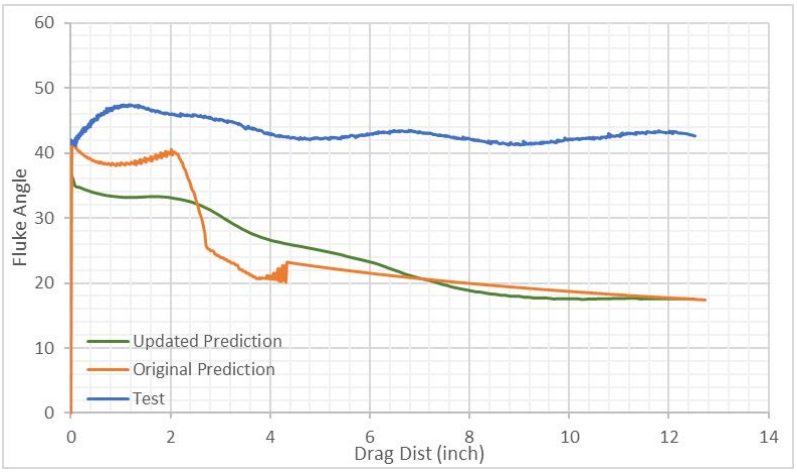

Figure 5.74. Example of Pitch-Drag from Case 8

5.4 Conclusion

This chapter summarizes the experimental results of the generic drag embedment anchor in constant undrained shear strength profile with sensitivity of 1, linearly increasing undrained shear strength profile with sensitivity of 1.6, and a variety of layered undrained shear strength profiles. In the linearly increasing shearing strength profile, a larger anchor with fluke length of 1.5 times longer than the generic one is tested. The following conclusions are drawn based on the measured results and the predicted results using the plasticity model.

For the generic anchor in a single layer:

- The prediction model is calibrated using the experimental results from soils with the simplest profiles (no layer or a relatively weak layer) by changing n/p ratio, q (based on the trajectory) and the thickness of anchor fluke (based on the measured resistance to in-plane shear). The variability between the

experimental results and the calibrated analytical prediction is generally consistent and repeatable. The measured equilibrium capacity is 6.2, and the R_{nt} is 0.2. The equilibrium capacity from plasticity-based analysis is 4.3 and R_{nt} is 0.05 with interaction coefficient with n/p = 2.67 and q = 4.43. In order to make the predicted R_{nt} and N_e matches with the experimental measurement, the n/p is changed into 1.23 and q into 2.2.

To extrapolate scaled model anchor results based on the larger anchor in the linearly increasing shear strength profile:

- The larger size anchor is stable and dives deeper as expected. The measured capacity and trajectory for the larger size anchor matches well with the predicted results by the calibrated prediction model.
- The R_{nt} for the large size anchor is 0.05, and the N_e is 6.2. Therefore, R_{nt} is related to the model scale, but N_e is independent on the model scale. However, the theoretical R_{nt} for and the N_e for the larger anchor cannot be matched with experimental results at the same time with changing n/p and q once. The interaction coefficient for the larger anchor at best-fit is that n/p of 2.1, and q of 3.2. The yield surface from larger anchor is different from the one for generic anchor, which implies that the soil surrounding different size anchor yields differently. The yield surface for tested larger size anchor is close to the yield surface for prototype anchor.
- The ratio of capacity between two anchors is the same as the area ratio, and the ratio of penetration depth between two anchors it close to the fluke length ratio. This result implies that when extrapolating scale model results, the capacity can

be scaled by the ratio of area, and the trajectory may be scaled by the ratio of fluke length.

For the generic anchor in layered soil profiles:

- For the tests with the stiff layer being the weakest (Case 5 – undrained shear strength of layer is 1.38 times the undrained shear strength of surrounding soil), the anchor was predicted to penetrate and did penetrate in every test (Fig. 4).
- For the tests with the stiff layer having an undrained shear strength about five times the undrained shear strength of the surrounding soil (Case 7), the anchor was not predicted to penetrate and did not penetrate the stiff layer (Fig. 4).
- For the tests with the stiff layer having an undrained shear strength about twice the undrained shear strength of the surrounding soil (Cases 3, 4, 6 and 8), the anchor was predicted to penetrate the stiff layer but did consistently only for the case in which the layer was the deepest and the thinnest – Case 4.
- When the behavior in the experiment matches the behavior predicted (either penetrating or not penetrating the stiff layer), the experimental results are in generally good agreement with the predictions for the load and trajectory.
- The anchor and the T-bar are both affected by the stiff layer before penetrating it. The estimated capacity from updated prediction with adding ramps above and below stiff layer is capable to catch this effect.

Chapter 6. Drag Embedment Tests of Tandem System Anchor

6.1 Introduction

The tandem (piggy-back) anchor system concept involves attaching two drag embedment anchor or vertically loaded anchors together to achieve higher capacity than a single anchor. Walker (1983) performed drag embedment tests in cohsionless soil by connecting two Navmoor anchors with 1/20 scale and found that tandem system anchor has twice higher than a single anchor. Taylor (1987) validated this conclusion with field tests in soft mud. In this study, to further understanding of tandem system anchor, drag embedmnet tests are performed the drag embedment tests with varying the attachment point of piggy-back anchor, the thickness of tailing and the spacing between two anchors. Additionally, drag embedment tests with a single anchor are performed in the same test bed for comparison. Furthermore, the tests results are used to calibrate and validate an analytical prediction.

6.2 Analytical Model

The prediction model for piggy-back configuration is developed by Aubeny (2017). This prediction model is capacble to predict the capacity, trajectory and pitch angle for piggy-back anchor system in which the second anchor is attached to the back of the fluke of first anchor. The prediction model allows slacks between the first anchor and second anchor. The prediction model uses the padeye of anchor as the reference point when calculating embedment depth for each anchor. It is assumed that the first anchor is pre-embedded at mudline with pitch angle of 45° (shank is horizontally placed at mudline). The

second anchor is also pre-embedded deeper than at the mudlineThe initial orientation and location of the first anchor is assumed that At each point along the predicted embedment depth, the fluke angles (θ_{f1} and θ_{f2}) during embedment are calculated. During the drag embedment process, the anchor system behavior is controlled by the fluke-shank angles θ_{af0}, and the pitch, θ_{af1}. The variables used in the prediction model are schematically described in Figure 6.1 and Figure 6.2.

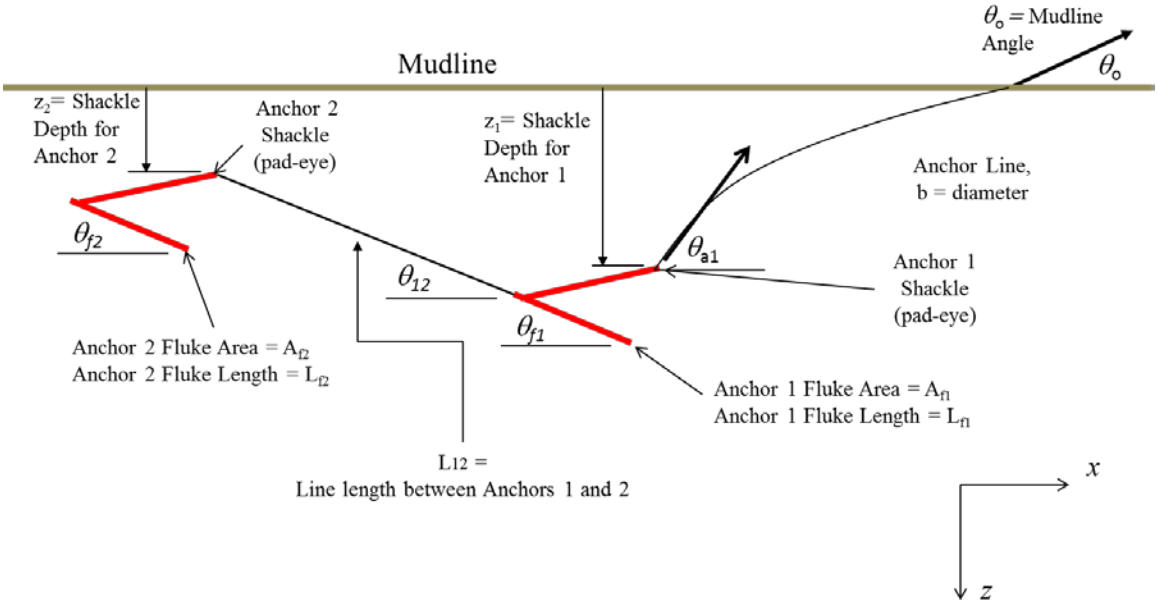

Figure 6.1. Geometric Description of the Piggyback Anchor System (Aubeny, 2017)

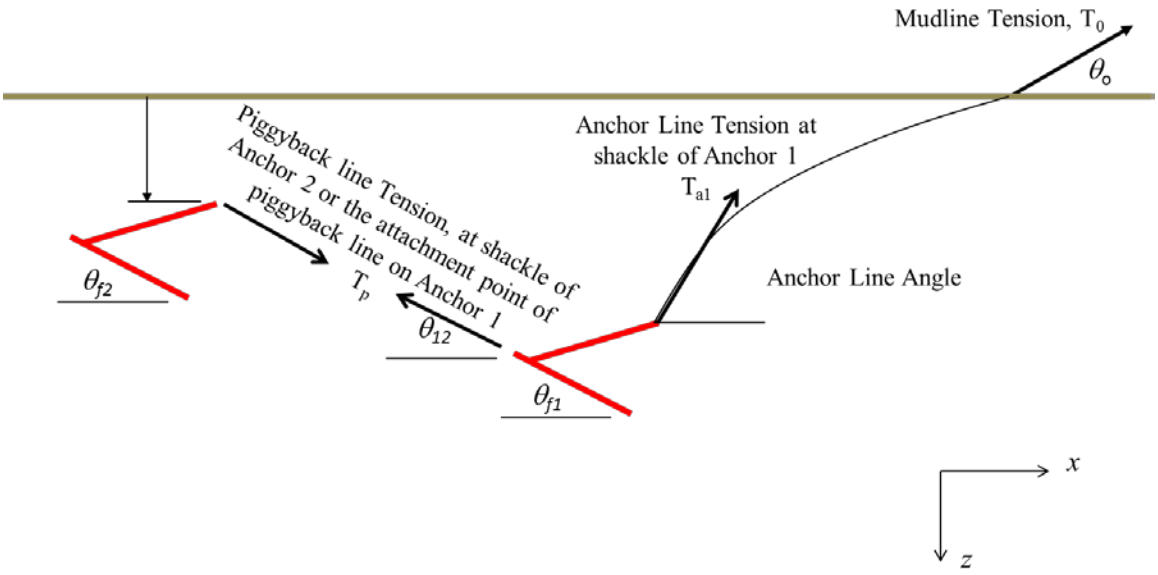

Figure 6.2. Tension Description of the Piggyback Anchor System Lines (Aubeny, 2017)

The line angle at shackle of the first anchor at the beginning can be determined by

$$\theta_{a1} = \sqrt{\frac{2\,E_n N_c\, b\, z_1}{T_{a1}}\left(s_{u0} + \frac{k z_1}{2}\right) + {\theta_0}^2} \qquad \text{Eq.(6.1)}$$

where E_n — Multiplier to be applied to chain diameter

N_c – Bearing factor for Anchor line;

b – Anchor line diameter

k – Strength gradient.

z_1 – Depth from mudline to shackle of Anchor 1.

θ_0– line angle at the mudline

And the fluke angle of the first anchor can be calculated as

$$\theta_{f1} = \theta_{af1} - \theta_{a1} \quad \text{Eq.(6.2)}$$

where θ_{f1} – Anchor fluke angle with respect to the horizontal plane

θ_{af1} – Line Angle parallel to anchor fluke

For the second anchor, the line angle at shackle is

$$\theta_{12} = \tan^{-1}\left(\frac{z_b - z_2}{x_b - x_2}\right) \quad \text{Eq.(6.3)}$$

where z_b – Depth from mudline to connection of piggyback line at back of Anchor 1.

x_b – Distance from reference to connection of piggyback line at back of Anchor 1.

z_2 – Depth from mudline to shackle of Anchor 2.

x_2 – Distance from reference to shackle of Anchor 2.

The fluke angle of the second anchor is

$$\theta_{f2} = \theta_{a02} + \theta_{12} \quad \text{Eq.(6.4)}$$

where θ_{12} – Piggyback line angle with respect to the horizontal plane.

θ_{f2} – Anchor fluke angle with respect to the horizontal plane

θ_{a02} – Angle the resistance force makes with the anchor fluke

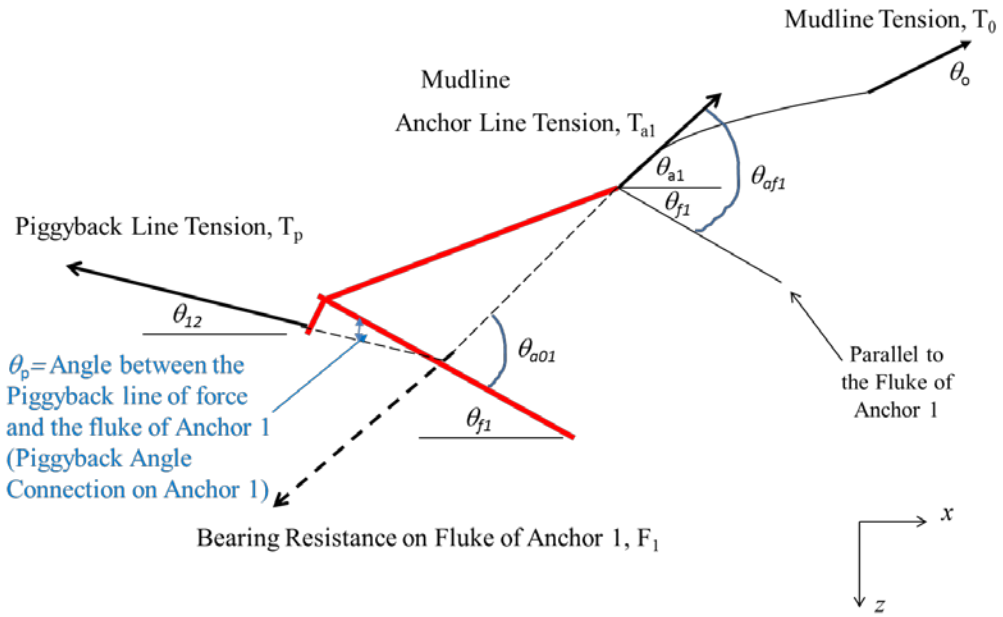

Figure 6.3. Sketch of the First Anchor in Tension (Aubeny, 2017)

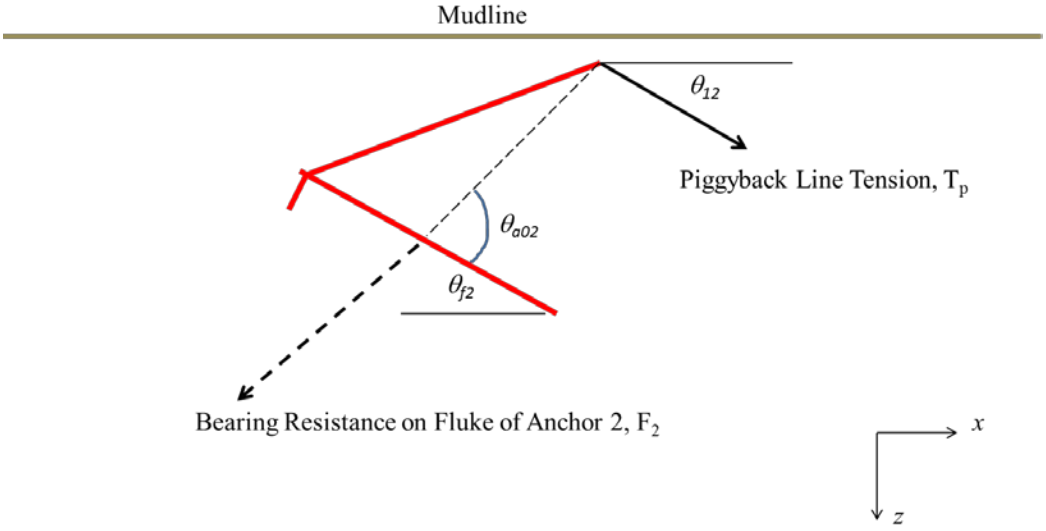

Figure 6.4. Sketch of the Second Anchor in Tension (Aubeny, 2017)

When both anchors start diving and reach equilibrium point, the bearing force acting on the fluke of the first anchor and the line angle relative to its fluke:

$$F_1 = N_{e1}\, s_{ua1}\, A_{f1} \qquad \text{Eq.(6.5)}$$

$$\theta_{af1} = \frac{F_1 \sin(\theta_{a01}) + T_p \sin(\theta_p)}{F_1\, cos(\theta_{a01}) + T_p\, cos(\theta_p)} \qquad \text{Eq.(6.6)}$$

where N_e is the equilibrium bearing capacity factor

F_1 – Anchor 1 bearing resistance of fluke

T_p – Piggyback line Tension at connection point on back of Anchor 1

θ_p – Angle of the Piggyback line tension with respect to fluke of Anchor 1

If the trailing line connects piggy-back anchor is slack, the anchor line tension of piggyback system at the shackle of the first anchor

$$T_{a1} = \frac{F_1 \cos(\theta_{a01}) + T_p\, cos(\theta_p)}{cos(\theta_{af1})} \qquad \text{Eq.(6.7)}$$

If the trailing line in tension, the line tension at the connection point at the first anchor

$$\begin{cases} T_p = T_{a2} = F_2 = N_{e2}\, s_{ua2} A_{f2} & if\ Z_b > Z_2 \\ T_p = F_2 \exp[\,\mu\,(\theta_{a1} - \theta_{12})] & if\ Z_b < Z_2 \end{cases} \qquad \text{Eq.(6.8)}$$

For the trajectory prediction, the horizontal and vertical movement of each anchor is calculated for each increment. The sketch of increment for each anchor is shown in Figure 6.5.

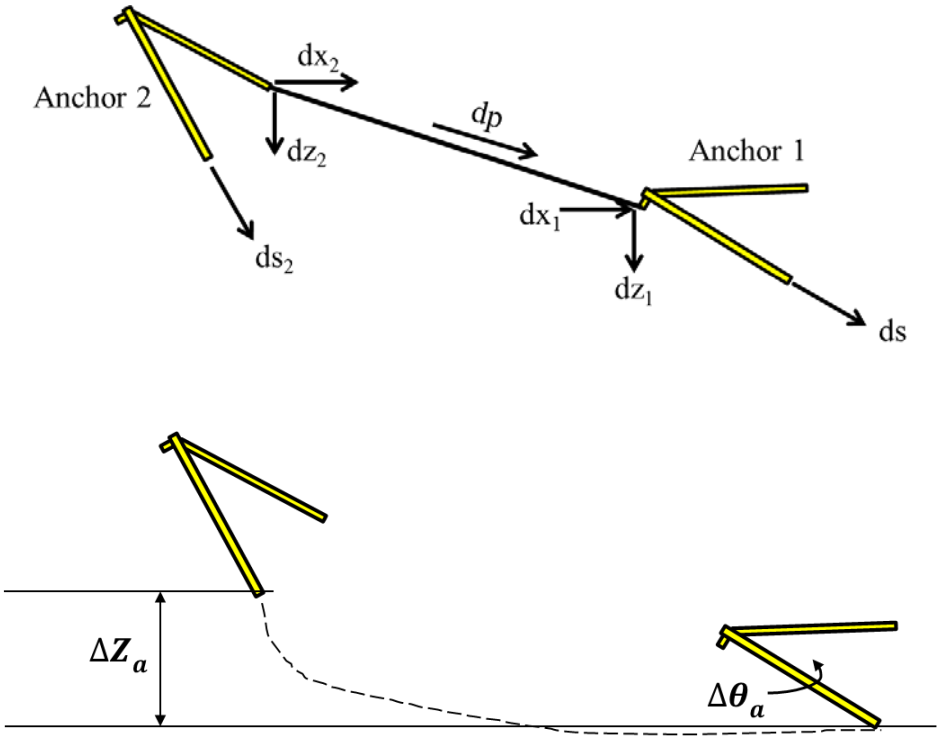

Figure 6.5. Evolution of Anchor (Aubeny, 2017)

For the first anchor, the horizontal and vertical movement as well as the movement parallel to the fluke

$$dx_1 = ds_1\ (\cos\theta_{f1}\ + \frac{dn}{dt}\ \sin\theta_{f1}) \qquad \text{Eq.(6.9)}$$

$$dz_1 = ds_1\ (\sin\theta_{f1}\ - \frac{dn}{dt}\ \cos\theta_{f1}) \qquad \text{Eq.(6.10)}$$

$$dp = dx_1\ \cos\theta_{12}\ + dz_1\ \sin\theta_{12} \qquad \text{Eq.(6.11)}$$

where θ_{12} – Piggyback line angle with respect to the horizontal plane.

For the first anchor, the movement parallel to the fluke, the horizontal and vertical movement is

$$\begin{cases} ds_2 = \dfrac{dp}{\cos(\theta_{f2} - \theta_{12})} & if\ Z_b > Z_2 \\ ds_2 = \dfrac{dp}{\cos(\theta_{f2} + \theta_{12})} & if\ Z_b < Z_2 \end{cases} \quad \text{Eq.(6.12)}$$

$$dx_2 = ds_2\ (\cos\theta_{f2}\ + \frac{dn}{dt}\ \sin\theta_{f2}) \quad \text{Eq.(6.13)}$$

$$dz_2 = ds_2\ (\sin\theta_{f2}\ - \frac{dn}{dt}\ \cos\theta_{f2}) \quad \text{Eq.(6.14)}$$

When the embedment occurs, the evolution equation for the first and second anchor is,

$$\frac{d\theta_{a1}}{dz_1} = \frac{1}{T_{a1}\theta_{a1}}\left[(E_n N_c b s_{ua1}) - \left(\frac{{\theta_{a1}}^2}{2}\frac{\cos\theta_{a01}}{\cos\theta_{af1}} N_{e1} A_{f1} k\right) - \left(\frac{{\theta_{a1}}^2}{2}\frac{\cos\theta_p}{\cos\theta_{af1}} N_{e2} A_{f2} k \frac{dz_{a2}}{dz_{a1}}\right)\right] \quad \text{Eq.(6.15)}$$

$$\frac{d\theta_{a2}}{dz_2} = \frac{\dfrac{(E_n N_c b s_{ua2})}{T_{a2}} - \dfrac{K({\theta_{a2}}^2 - {\theta_{12}}^2)}{2\, s_{ua2}}}{\theta_{a2} + \dfrac{1}{T_{a2}}\ (E_n N_c b^2 s_{uab} \dfrac{dZ_b}{d\theta_{a2}})} \quad \text{Eq.(6.16)}$$

6.3 Test Setup

The piggy-back tests setup is the same as the drag embedment tests with a single anchor (Figure 6.6). The magnetometer source is placed on the frame of small thermos-plastic tank. A directional pulley is installed at one side of tank, while two anchors are connected and placed at the other side of tank. On each anchor, a magnetometer sensor is attached. The second anchor is attached to the padeye (Figure 6.7) or back of the fluke (Figure 6.8) of the front anchor by a tailing line thickness of 0.05 inch or 0.19 inch (Figure 6.9). When the piggy-back anchor is attached to the back of the fluke of front anchor, a rope with 0.05 inch thickness is wrapped around the shank and fluke of the front anchor to provide an

attachment in the middle of back fluke for the piggy-back anchor. The tailing line with 0.19-inch thickness is achieved by wrapping the 0.05-inch thickness tailing line with the magnetometer line by duct tape (Figure 6.9).

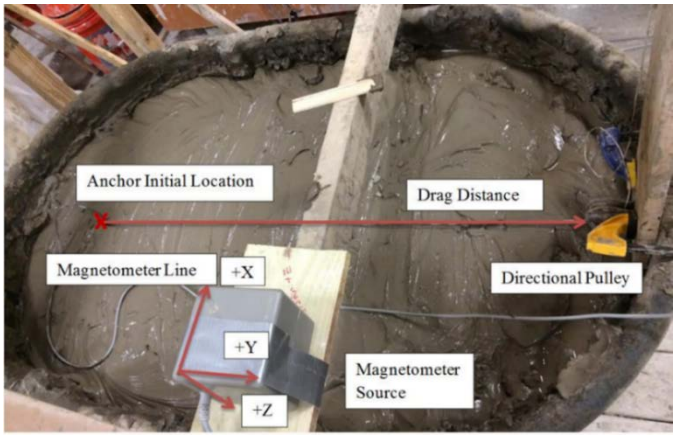

Figure 6.6. Piggy-Back Test Setup (Gerkus, 2016)

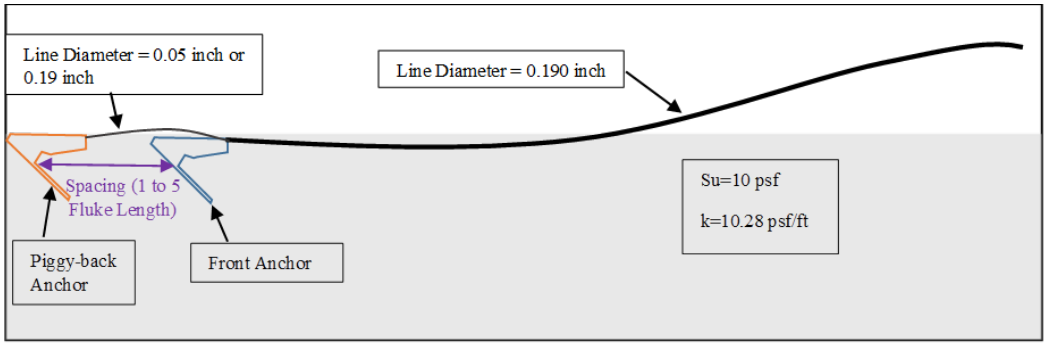

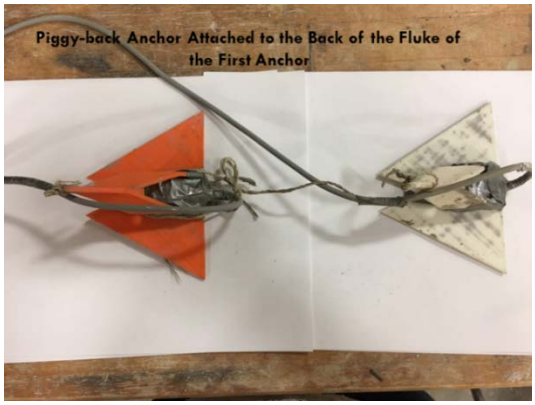

Figure 6.7. Piggy-back Anchor Attached to the Back of Front Anchor

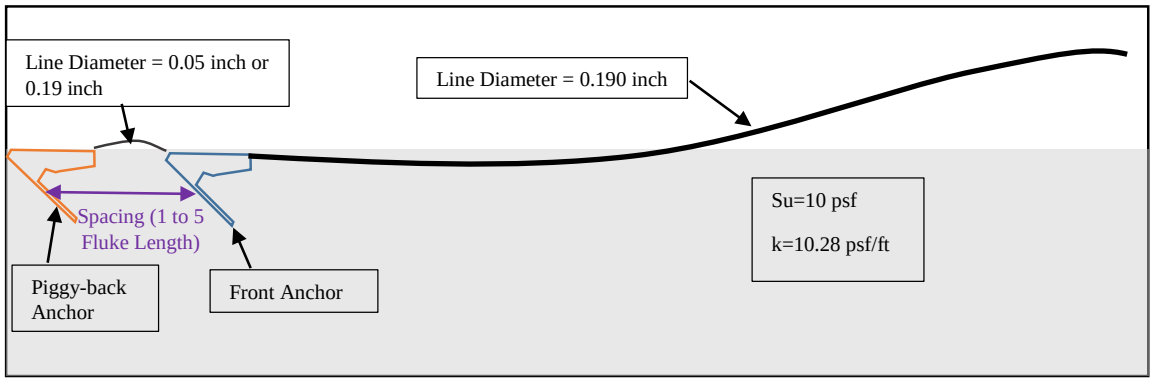

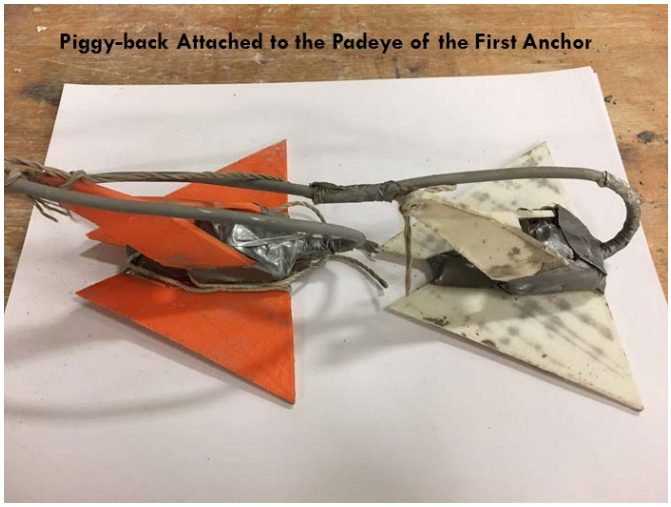

Figure 6.8. Piggy-back Anchor Attached to the Padeye of Front Anchor

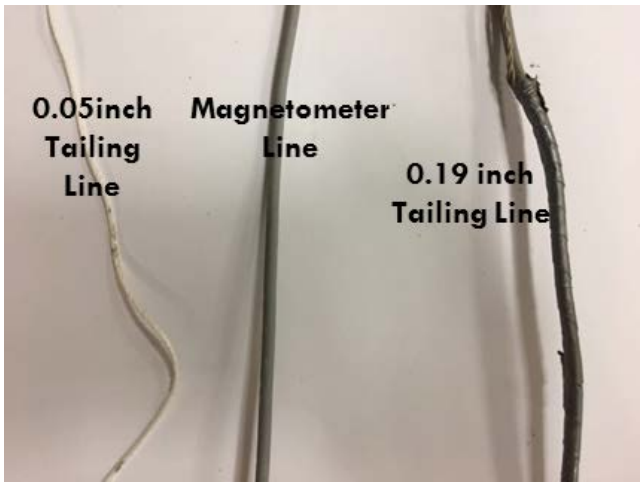

Figure 6.9. Piggy-back Line Thickness

The soil test bed for drag embedment test with piggy-back anchor is normally consolidated shear strength profile with the shear strength at the mudline 10 psf and the shear strength increasing gradient is 10 psf/ft. For comparison purpose, a series of drag embedment tests of a single anchor is also tested in this soil test bed. In this set of single anchor test, we also perform tests with a thin loading line with 0.05-inch thickness and a thick loading line with 0.19-inch thickness.

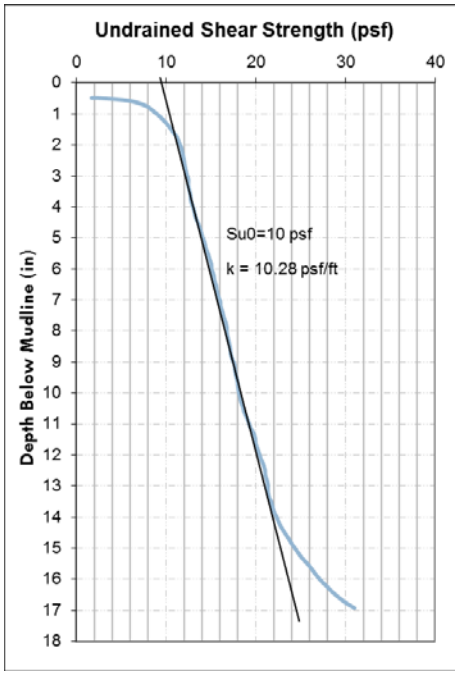

Figure 6.10. Shear Strength Profile of Piggy-back Tests

Except varying the tailing line thickness and the attachment point of piggy-back anchor, we also change the spacing between two anchors. The range of spacing between two anchors are from 1.2 fluke length (5 inch) to 5 fluke length (18 inch). The tests setup in different anchor configurations are summarized in Table 6.1.

Table 6.1. Piggy-Back Anchor Tests Summary

	The Second Anchor Connected to the First Anchor's	Line Thickness (inch)	Spacing (Fluke Length)	Number of Tests Performed
Case 1	Padeye	0.19	1.16	3
Case 2	Back of the Fluke	0.19	1.77	2
Case 3	Padeye	0.19	1.81	3
Case 4	Padeye	0.05	1.38	2
Case 5	Back of the Fluke	0.19	2.87	3
Case 6	Back of the Fluke	0.05	3.14	3
Case 7	Padeye	0.19	2.28	4
Case 8	Padeye	0.05	3.18	1
Case 9	Back of the Fluke	0.19	3.39	3
Case 10	Back of the Fluke	0.05	4.03	2
Case 11	Padeye	0.05	4.24	4
Case 12	Back of the Fluke	0.19	5.39	3
Case 13	Back of the Fluke	0.05	4.2	2
Case 14	Padeye	0.05	1.9	3
Case 15	Padeye	0.19	3.78	3
Case 16	Padeye	0.19	4.95	3

6.4 Experimental Results of Tandem System Anchor Compared with a Single Anchor

All the drag embedment tests results of piggy-back anchor are shown in this section in a format of comparing with a single anchor including its capacity, embedment depth, and the pitch angle along horizontal drag.

The tests results shown in Figure 6.12 are the measured capacity of piggy-back anchor compared with capacity of a single anchor. The capacity plotted in Figure 6.12 is the maximum load measured within a certain drag distance. Thus, for some cases, the anchor capacity can be higher with further horizontal drag distance since the anchor can penetrate deeper with a longer drag. It also should be noticed that the horizontal drag distance for each case are different because of the limitation from length of soil tank. That is, a short spacing between two anchor results in more space for anchor travelling along the tank; otherwise, a long spacing between the two anchors leaves an insufficient horizontal drag distance for anchors. Because of the different drag distance for each case, when the measured capacity of piggy-back anchor compared with the capacity of a single anchor, the single anchor capacity is chosen based on the horizontal drag distance of piggy-back anchor from that case compared with. In details, we take the maximum measured load from the single anchor corresponding with the horizontal drag distance of the piggy-back anchor in the case we compare with.

When comparing the penetration depth and pitch angle of front anchor and second anchor from tandem system to a single anchor, the penetration depth and pitch angle from the single anchor is also selected based on the horizontal drag distance of tandem system

we compare with. The ratio of embedment depth from front or second anchor over a single anchor is shown in Figure 6.13, and the ratio of pitch angle is shown in Figure 6.11. Figure 6.14 and Figure 6.15 show the embedment depth and pitch angle ratio of piggy-back anchor over a single anchor within the same drag distance. The minimum drag distance in all cases are 7 inches. These two graphs are plotted by cutting the embedment depth and pitch angle versus horizontal drag curves at 7 inches for the cases where the horizontal drag distance is longer than 7 inches.

The following conclusions are obtained based on the measured results of piggy-back anchors and a single anchor (Figure 6.11 and Figure 6.13)

Pitch angle of piggy-back configuration:

- For the tests with the second anchor attached to the padeye of the front anchor, the second anchor has higher pitch angle compared with a single anchor and the front anchor at the end of test. This high pitch angle indicates that the second anchor has potential to dive deeper with further drag (Figure 6.11). When the second anchor attached to the padeye of the front anchor with a shorter spacing (less than 3 fluke length), the thick line restricts the front anchor pitching forward when dragging, thus we see the front anchor has lower pitch angle compared with a single anchor. However, the front anchor still has lower pitch angle even two anchors are further apart (spacing between the two anchors are from 3-fluke length to 5-fluke length). This can be explained by that the front anchor is too close to the directional pulley, thus a steep angle at the mudline for the front anchor forms which restricts the front anchor dive deeper and pitch

forward. This limitation can be improved with performing piggy-back anchor testing in the larger tank.

- The restriction from tailing line to the front anchor becomes less when the tailing line thickness is 0.05 inch. From the top right graph in Figure 6.11, the pitch angle of front anchor is higher compared with those cases shown in the top left graph where the thick tailing line is used.
- For the tests the second anchor attached to the back of fluke of the front anchor, the restriction of trailing line on the front anchor becomes less. The second anchor is still in a pitching forward position at the end of test, which indicates that the second anchor can dive deeper with further drag. Generally, the second anchor has higher pitch angle than the front anchor either with thick or thin tailing line.

Total capacity of piggy-back configuration:

- For the tests with the second anchor attached to the padeye of the first anchor, the total capacity of piggy-back configuration increases with the increase of spacing between the front anchor and the second anchor, and can achieve twice higher capacity than a single anchor provided that the spacing between two anchors are at least fluke length (Figure 6.12).
- For the tests with the second anchor attached to the back of fluke of the first anchor, the total capacity of piggy-back configuration slightly increases with the increase of spacing between the front anchor and the second anchor (Figure 6.12).

- Due to the limitation of length of soil tank, for each test, the maximum horizontal drag distance is achieved. Since at the end of test, the second anchor is still in pitching position (Figure 6.11), thus a higher capacity can be achieved with a further drag distance since the second anchor can dive deeper.

Embedment depth of piggy-back configuration:

- For the tests with the second anchor attached to the padeye of the first anchor, the second anchor can penetrate deeper than the first anchor, and deeper than the embedment depth of a single anchor. The first anchor can penetrate deeper than a single anchor if the trailing line is thick and the spacing between two anchors are greater than 1.5 times the fluke length (Figure 6.13).
- For the tests with the second anchor attached to the back of fluke of the first anchor, the second anchor can penetrate deeper than the first anchor and a single anchor (Figure 6.13).
- Since the second anchor is still in the pitching position, thus it can dive deeper if a further drag distance is provided. It is also possible for the first anchor to dive deeper if we perform the drag embedment test in a larger tank where the directional pulley is further away from the front anchor which provides a less steep mudline angle to the front anchor and thus it can dive deeper (Figure 6.11). This also can be approved by comparing Figure 6.11 Figure 6.15, together with Figure 6.13 and Figure 6.14. Figure 6.11 and Figure 6.13 show the results of embedment depth and pitch from each case, while Figure 6.13 and Figure 6.14 show the embedment depth and pitch at the same drag distance of 7 inches, which is shorter drag distance for the most of cases. Comparing Figure 6.11

and Figure 6.15, we can see that both anchor flatten itself with further drag, and correspondingly they dive deeper.

All the comparison between experimental results with tandem system anchor and single anchor are shown in Appendix D.

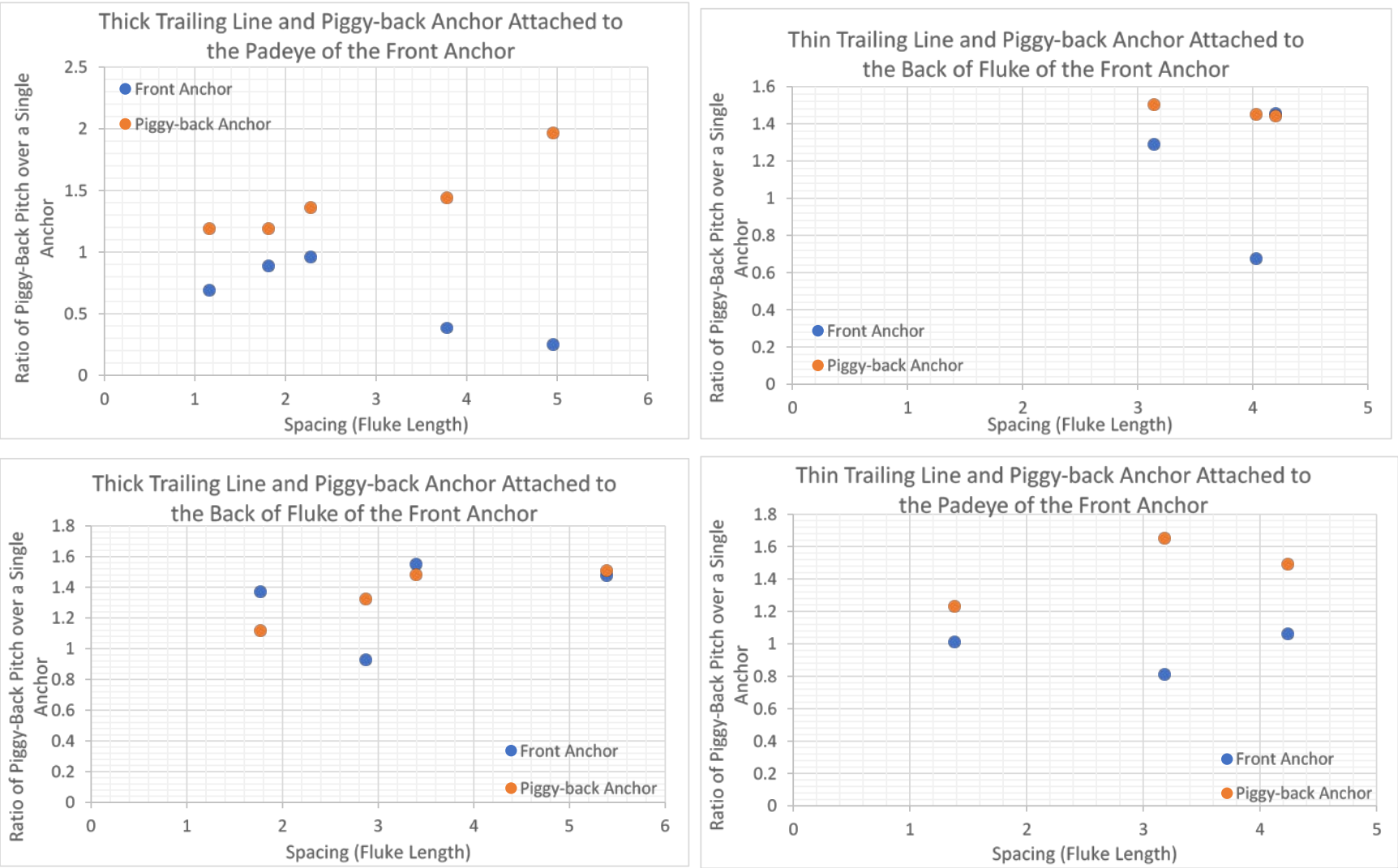

Figure 6.11. Pitch Angle Ratio of Piggy-Back over a Single Anchor

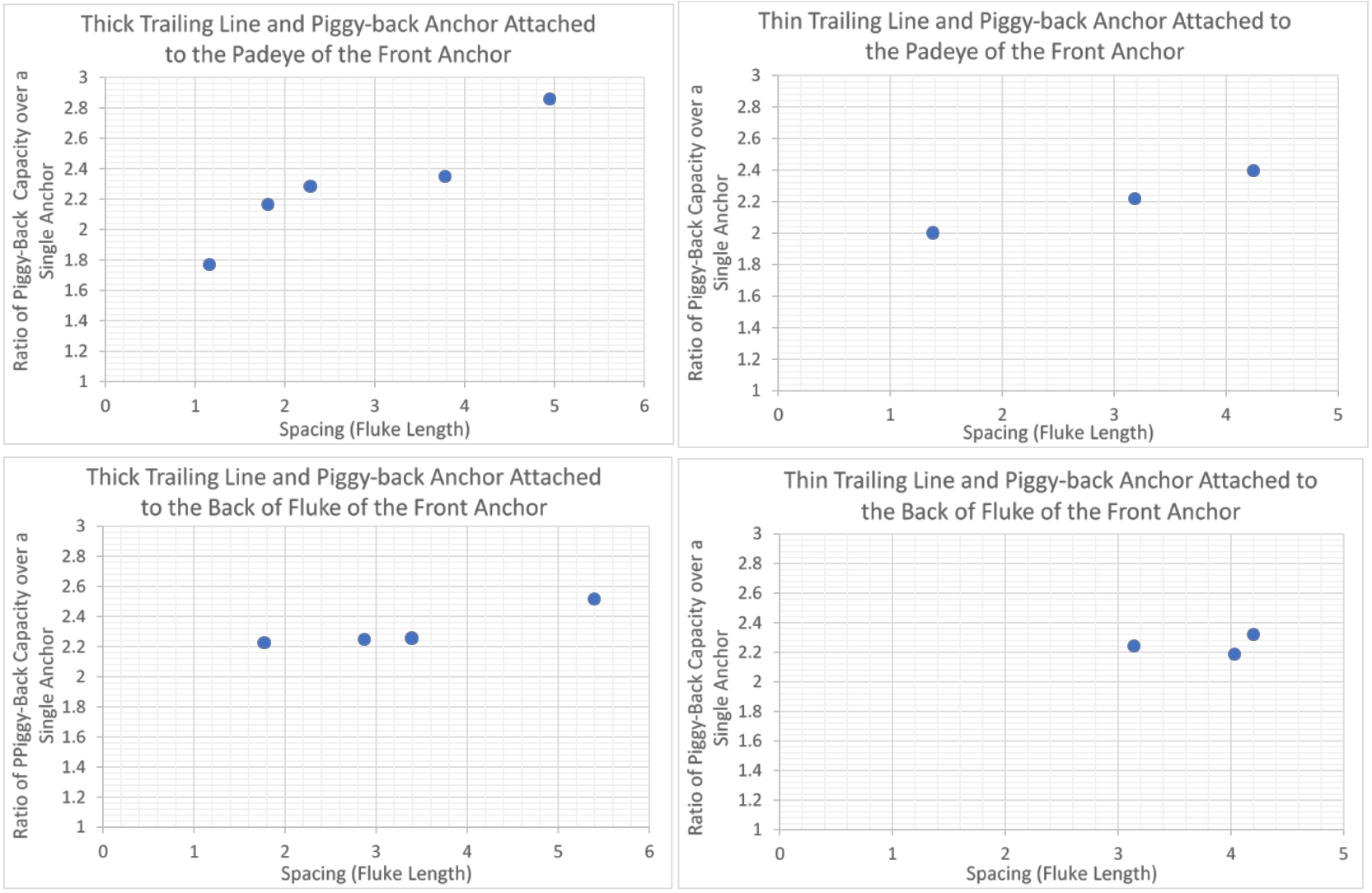

Figure 6.12. Capacity Ratio of Piggy-Back over a Single Anchor

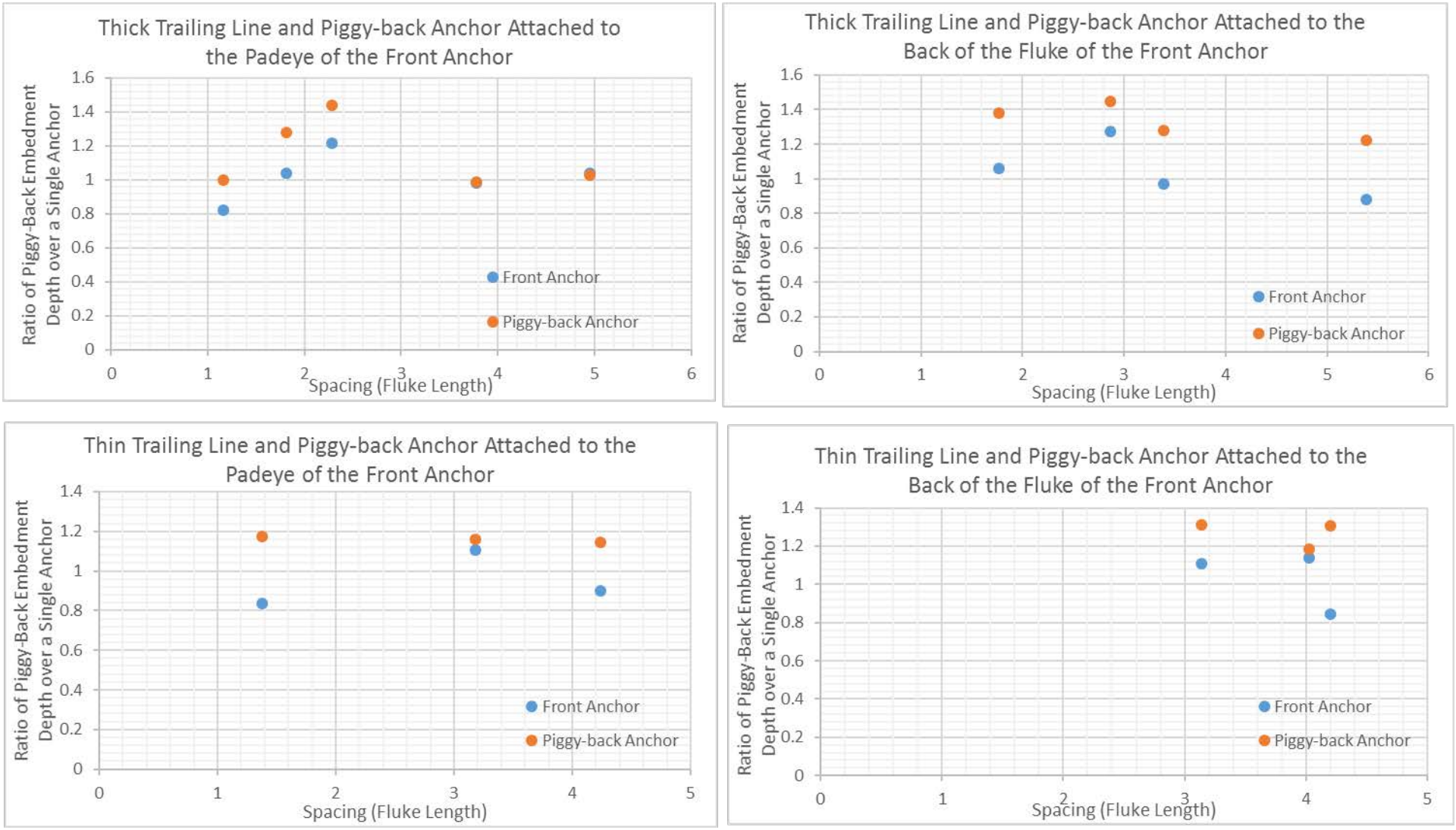

Figure 6.13. Embedment Depth Ratio of Piggy-Back over a Single Anchor

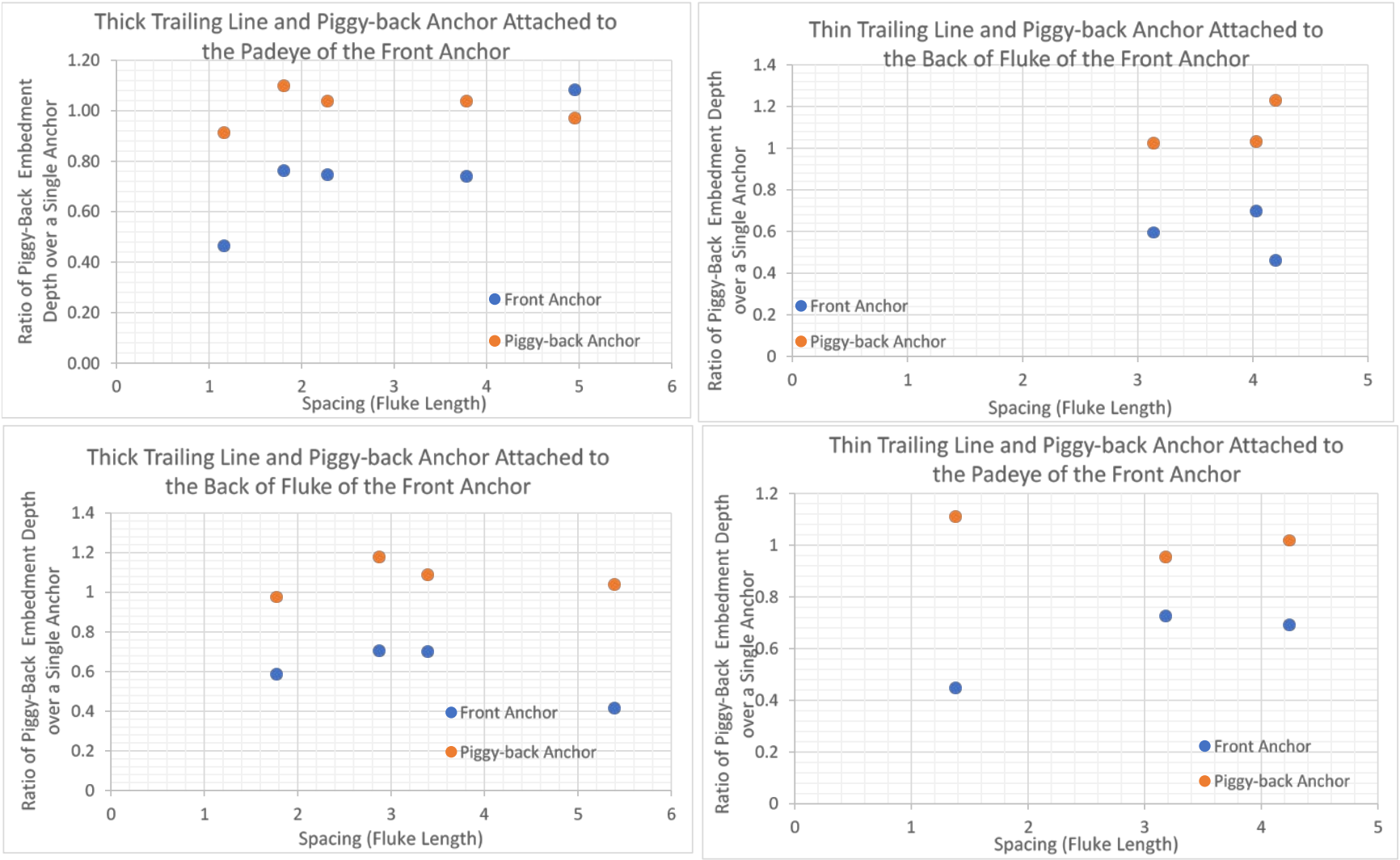

Figure 6.14. Embedment Depth Ratio of Piggy-Back over a Single Anchor Embedment Depth at the Same Drag Distance

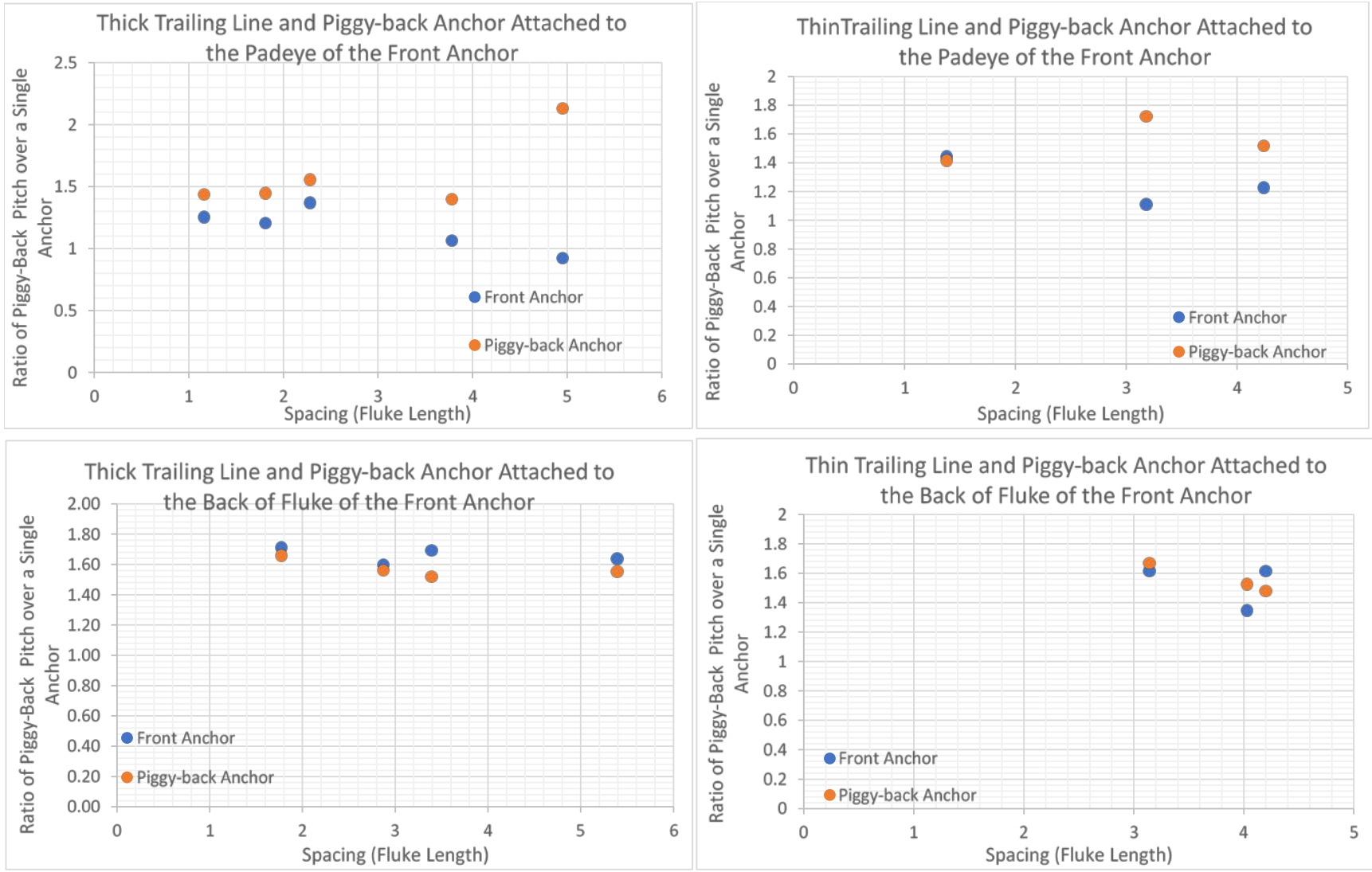

Figure 6.15. Pitch Angle Ratio of Piggy-Back over a Single Anchor Embedment Depth at the Same Drag Distance

6.4.1 Effect of Spacing

From Figure 6.12, with the increase of spacing, the higher capacity can be attained if the second anchor is attached to the padeye of front anchor. Spacing has no obvious impact on total capacity of piggy-back configuration when the second anchor is attached to the back of the fluke of front anchor.

6.4.2 Effect of Line Thickness

Before discussing the line effect on the penetration of front and second anchor, the tests results are replotted by plotting cases with same test setup except the line thickness is different. The results of front anchor embedment depth are shown in Figure 6.16 and Figure 6.18, and the results of second anchor are shown in Figure 6.17 and Figure 6.19. If the second anchor is attached to the padeye of the front anchor, the front anchor and the second anchor generally embed deeper with the thin tailing line. The test data enclosed by the blue circled and yellow circle in Figure 6.16 and Figure 6.17 indicate that the thinner tailing line makes the front and the second anchor dive deeper, however, the test data in orange circle shows that only the second anchor dives deeper with thinner tailing line. If the second anchor attached to the back of fluke of front anchor, the thinner tailing line still makes the anchor dives deeper. From Figure 6.18 and Figure 6.19, when the second anchor is attached to the back of fluke of front anchor, the test results in yellow circle and orange circle show that the thinner line makes anchor penetrate deeper if the spacing between two anchors is larger than 3-fluke length. A thinner line makes the anchor dives deeper since the thin line leads to a higher pitch angle during horizontal drag, thus the resistance from bearing on the fluke is less which is easier for anchor to dive deeper.

An example of trajectory either with thick line or thin line is shown in Figure 6.20 and Figure 6.21. Figure 6.20 presents the front anchor dives into 4.37 inches while the second anchor dives 6.04 inches with the thick line connecting both anchors. In comparison, Figure 6.21 shows that the front anchor dives 6.33 inches and the second anchor dives 6.16 inches with a thick tailing line connecting two anchors. The spacing between two anchors are 1.77 and 1.9 fluke length, respectively; and the attachment point are the same for two anchors.

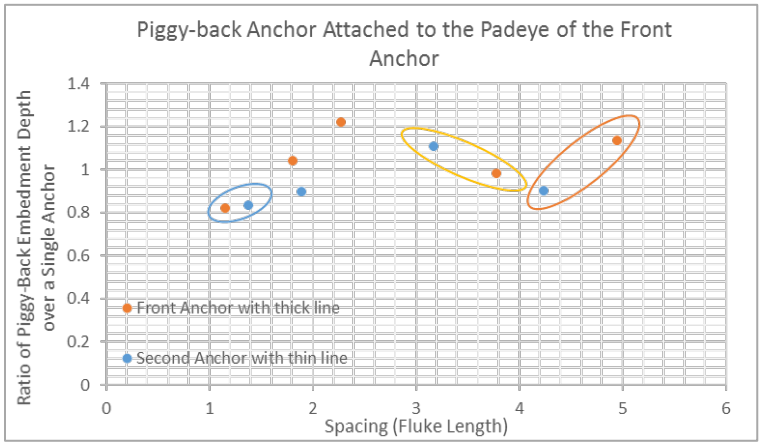

Figure 6.16. Line Effect – Front Anchor Results from Cases of Padeye as Attachment Point

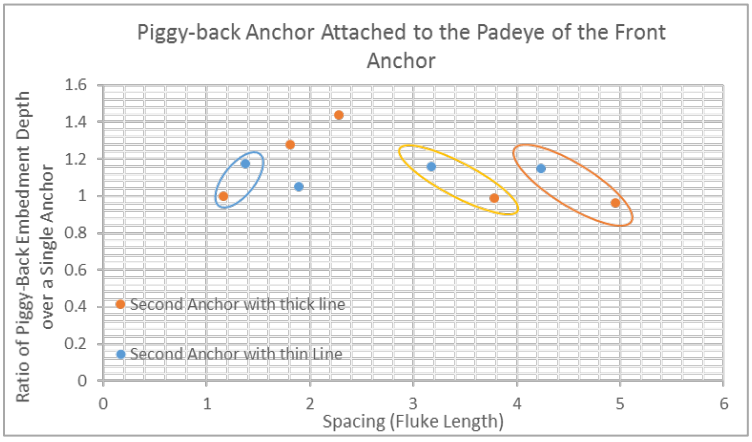

Figure 6.17. Line Effect – Second Anchor Results from Cases of Padeye as Attachment Point

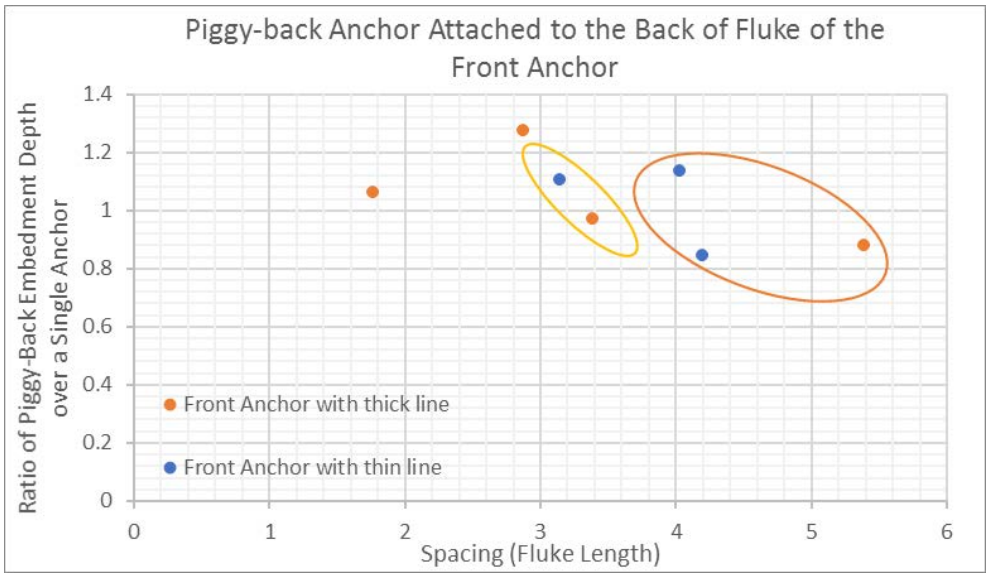

Figure 6.18. Line Effect – Front Anchor Results from Cases of Back of Fluke as Attachment Point

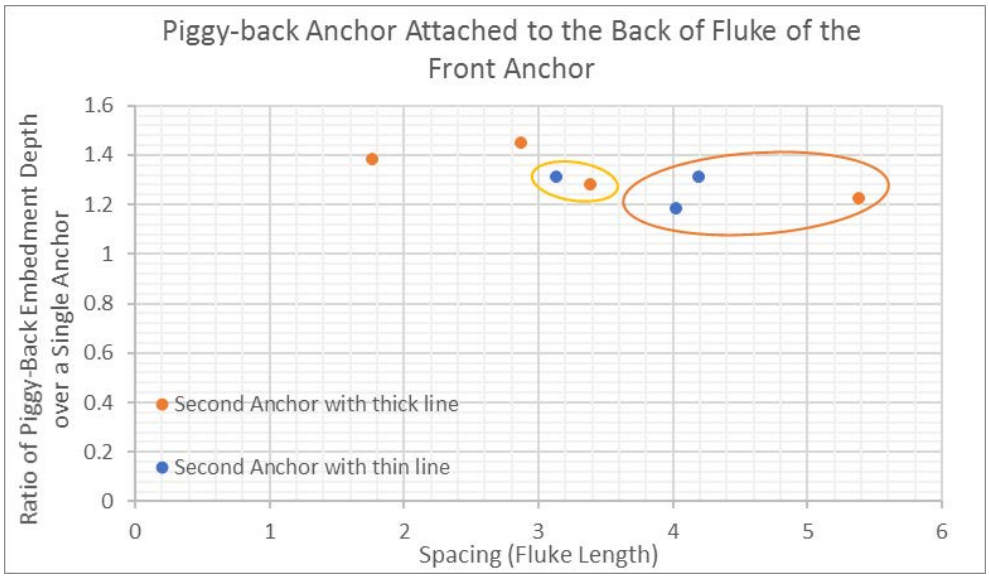

Figure 6.19. Line Effect – Second Anchor Results from Cases of Back of Fluke as Attachment Point

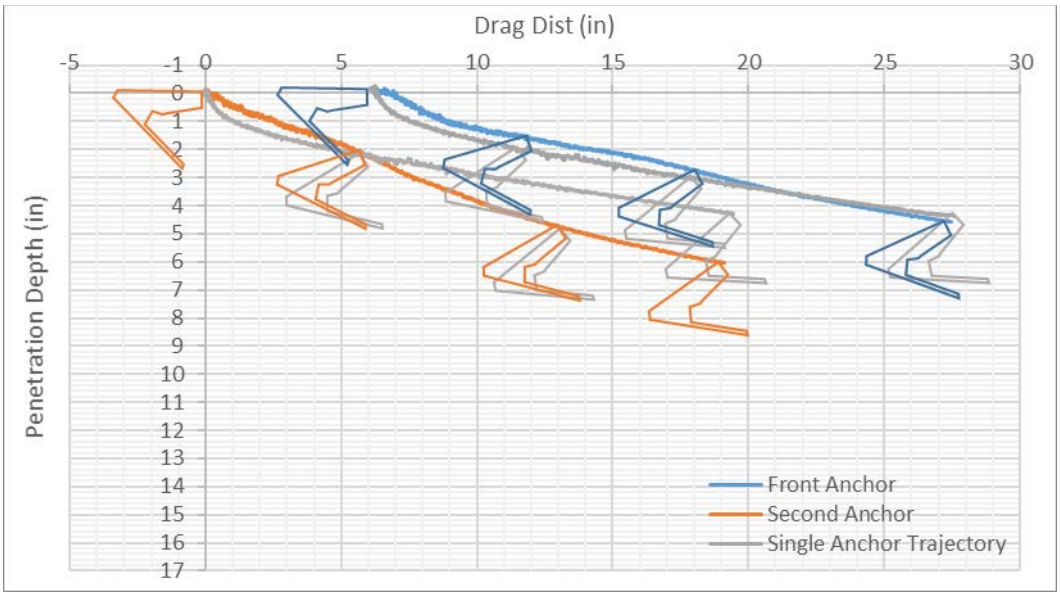

Figure 6.20. Trajectory from Case 2 (thick tailing line)

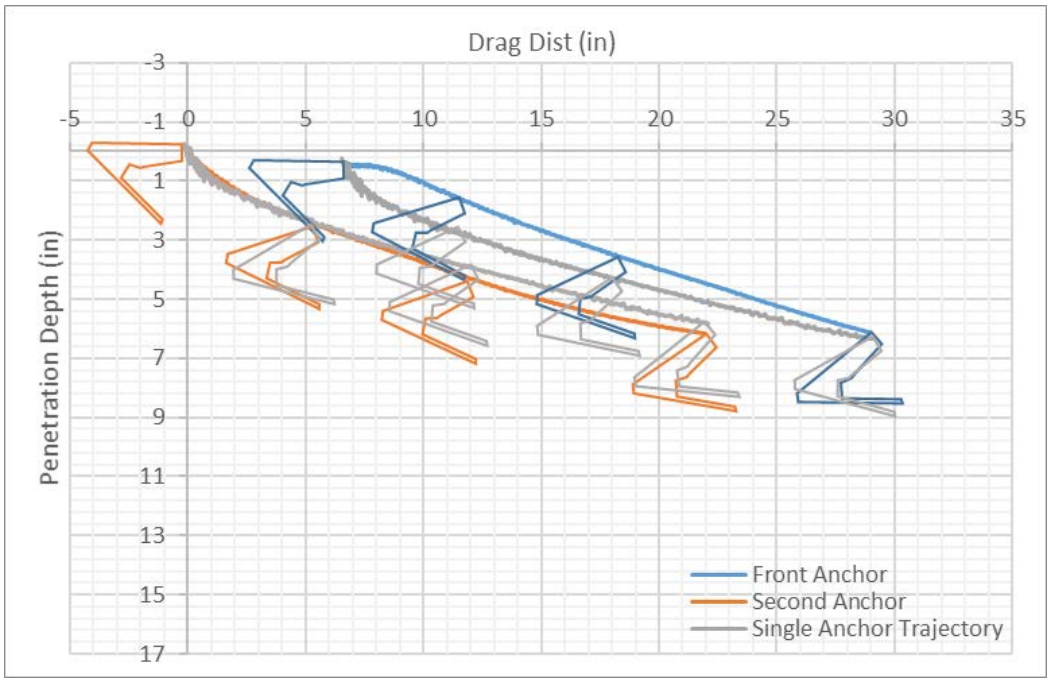

Figure 6.21. Trajectory from Case 14 (thin tailing line)

6.4.3 Effect of Attachment Point

Figure 6.22 to Figure 6.25 show the pitch angle ratio of either the front anchor or the second anchor over a single anchor. From Figure 6.22 and Figure 6.23, it can be concluded that attaching the second anchor to the back of fluke restricts less for the front anchor pitching forward. From Figure 6.24 and Figure 6.25, the attachment point has no obvious effect on the pitch angle of the second anchor.

Figure 6.26 to Figure 6.29 presents the comparisons of effect of padeye or tail on embedment depth. Figure 6.26 and Figure 6.27 shows the results of front anchor, the front anchor dives deeper with the second anchor attached to the back of fluke of the front anchor. This makes good agreement with the pitch angle shown in Figure 6.22 and Figure 6.23. Since the front anchor is in a relative steep pitch angle, thus it has less bearing resistance on the fluke and can dive deeper. From Figure 6.28 and Figure 6.29, the second anchor dives deeper when attached to the back of fluke of the front anchor.

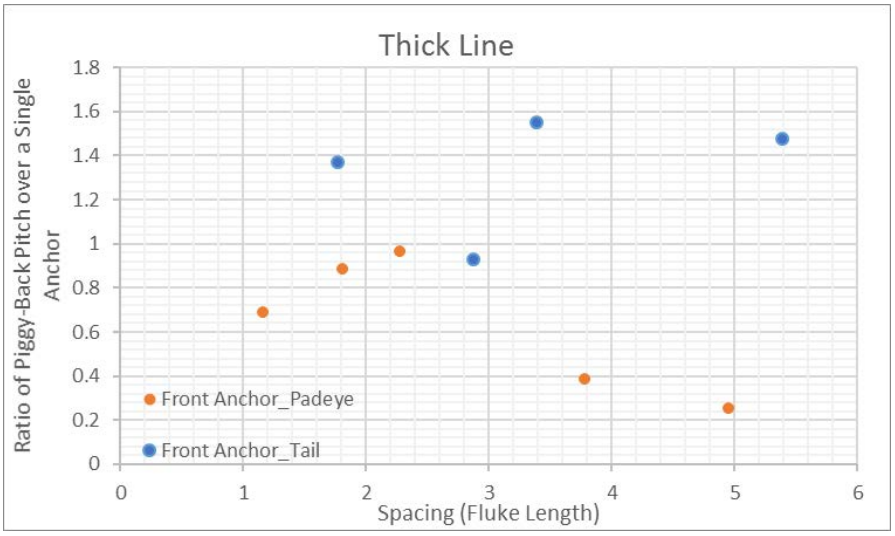

Figure 6.22. Pitch Ratio of Front Anchor with Thick Tailing Line

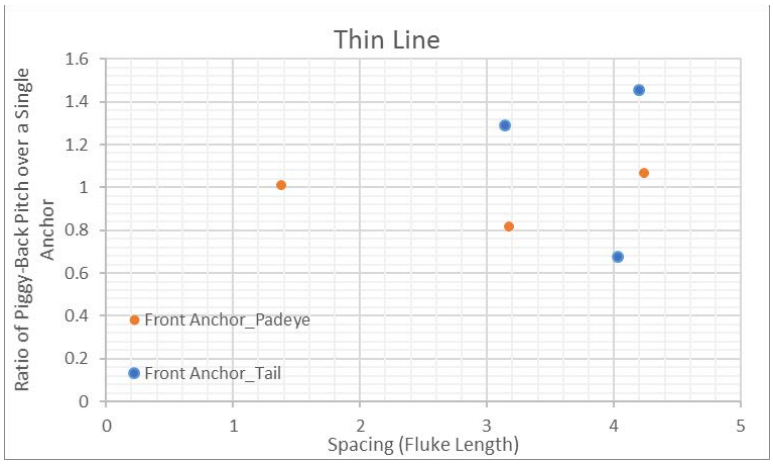

Figure 6.23. Pitch Ratio of Front Anchor with Thin Tailing Line

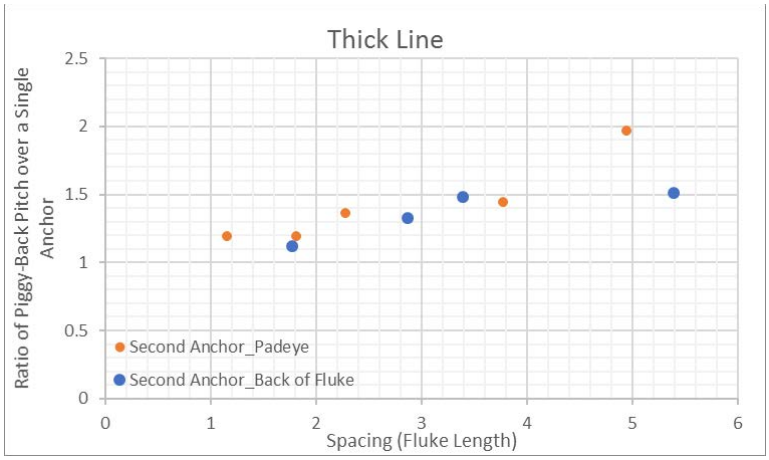

Figure 6.24. Pitch Ratio of Second Anchor with Thick Tailing Line

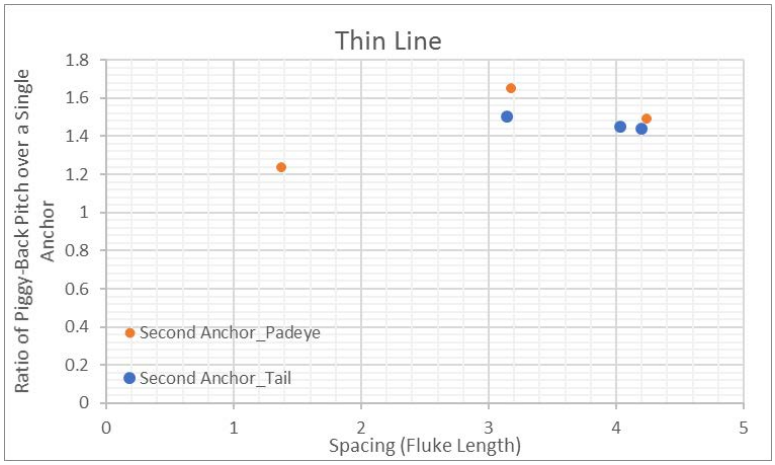

Figure 6.25. Pitch Ratio of Second Anchor with Thin Tailing Line

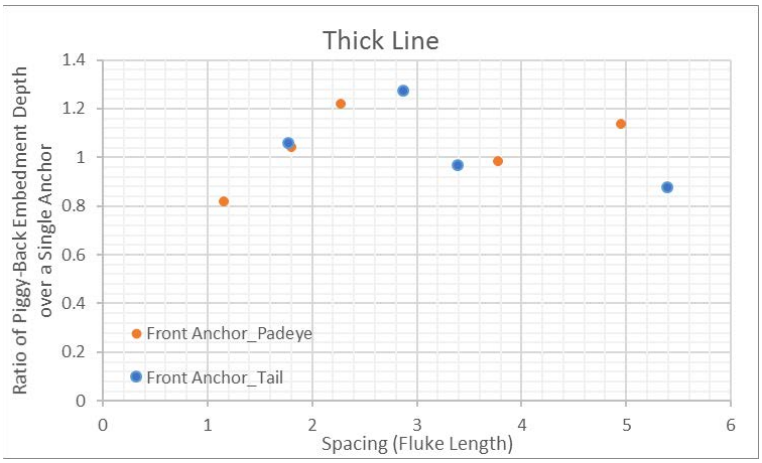

Figure 6.26.Embedment Ratio of Front Anchor with Thick Tailing Line

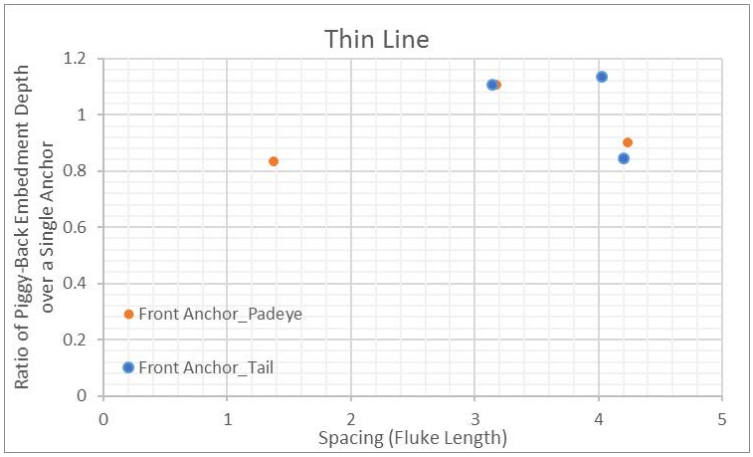

Figure 6.27. Embedment Ratio of Front Anchor with Thin Tailing Line

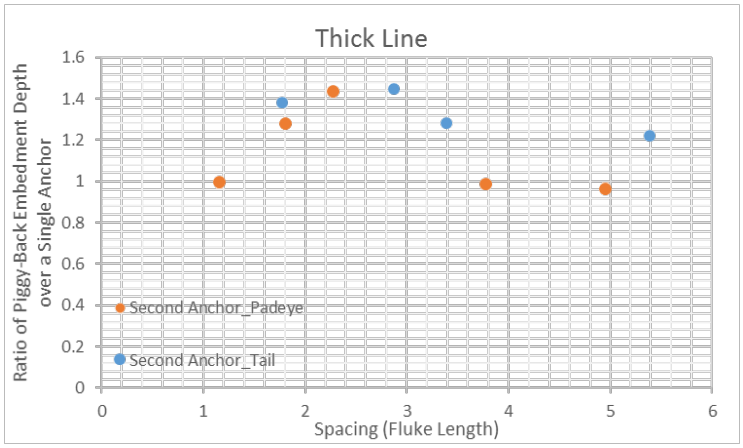

Figure 6.28. Embedment Ratio of Second Anchor with Thick Tailing Line

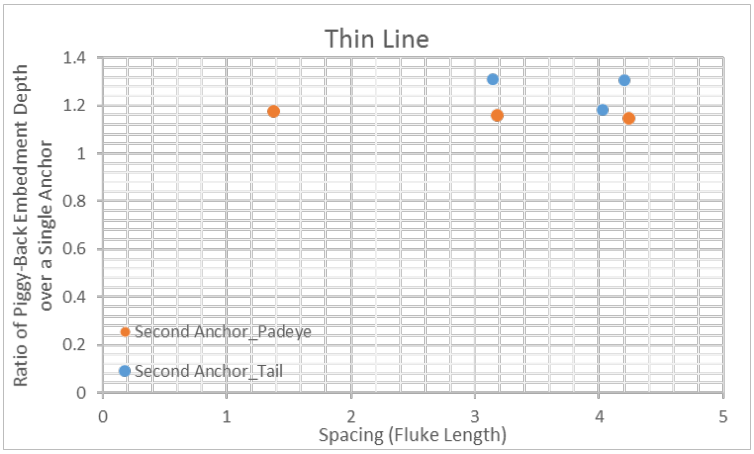

Figure 6.29. Embedment Ratio of Second Anchor with Thin Tailing Line

6.5 Experimental Results of Tandem System Anchor Compared with Analytical Results

To calibrate the prediction model for piggy-back tests, we changed the equilibrium capacity factor and the ratio of normal to tangential motion to make the analytical prediction results matches. The N_e and R_{nt} in each case are summarized in Table 6.2. From Table 6.2, we can see that the N_e and R_{nt} for piggy-back configuration is different from those obtained from drag embedment tests for a single anchor. It is reasonable since the yield surface for each anchor in piggy-back configurations interacts compared with the yield surface for a single anchor. This can be also confirmed by comparing anchor trajectory and pitch with substituting N_e and R_{nt} from a single anchor and N_e and R_{nt} for piggy-back anchor. An example of capacity, trajectory, and pitch with different sets of N_e and R_{nt} are shown in Figure 6.30. From Figure 6.30, the capacity with N_e and R_{nt} from a single anchor is smaller than the capacity with N_e and R_{nt} for piggy-back configuration. Additionally, the predicted trajectory with N_e and R_{nt} is not capable to match with the

measured trajectory. The impact by N_e and R_{nt} on the pitch is not obvious compared with the influence on load and trajectory.

Table 6.2. Summary of N_e and R_{nt} for Piggy-back Prediction Model

			First Anchor		Second Anchor	
	Spacing	Line Thickness	N_e	R_{nt}	N_e	R_{nt}
Case 2	1.77	Thick	5.4	0.02	5.4	0.02
Case 5	2.87	Thick	6.2	0.01	6.2	0.07
Case 6	3.14	Thin	7	0.01	7	0.2
Case 9	3.39	Thick	7.2	0.05	7.2	0.4
Case 10	4.03	Thin	7.1	0.015	7.1	0.4
Case 12	5.39	Thick	7.5	0.03	7.5	0.2
Case 13	4.2	Thin	8	0.1	8	0.3

Figure 6.31 plots the N_e from piggy-back prediction versus spacing, it can be concluded that the further spacing leads to a higher N_e, which implies that a further spacing result in a higher total capacity of tandem system. A straight line with N_e for single anchor of 6.2 is plotted in the Figure 6.31, it can be seen that if the spacing between the two anchor is less than 2-fluke length, than the N_e is smaller than a single anchor, which coincide with the experimental measured capacity that is smaller than twice of a single anchor. All the comparison between the experimental and analytical results of capacity, trajectory, and pitch are shown in Appendix E.

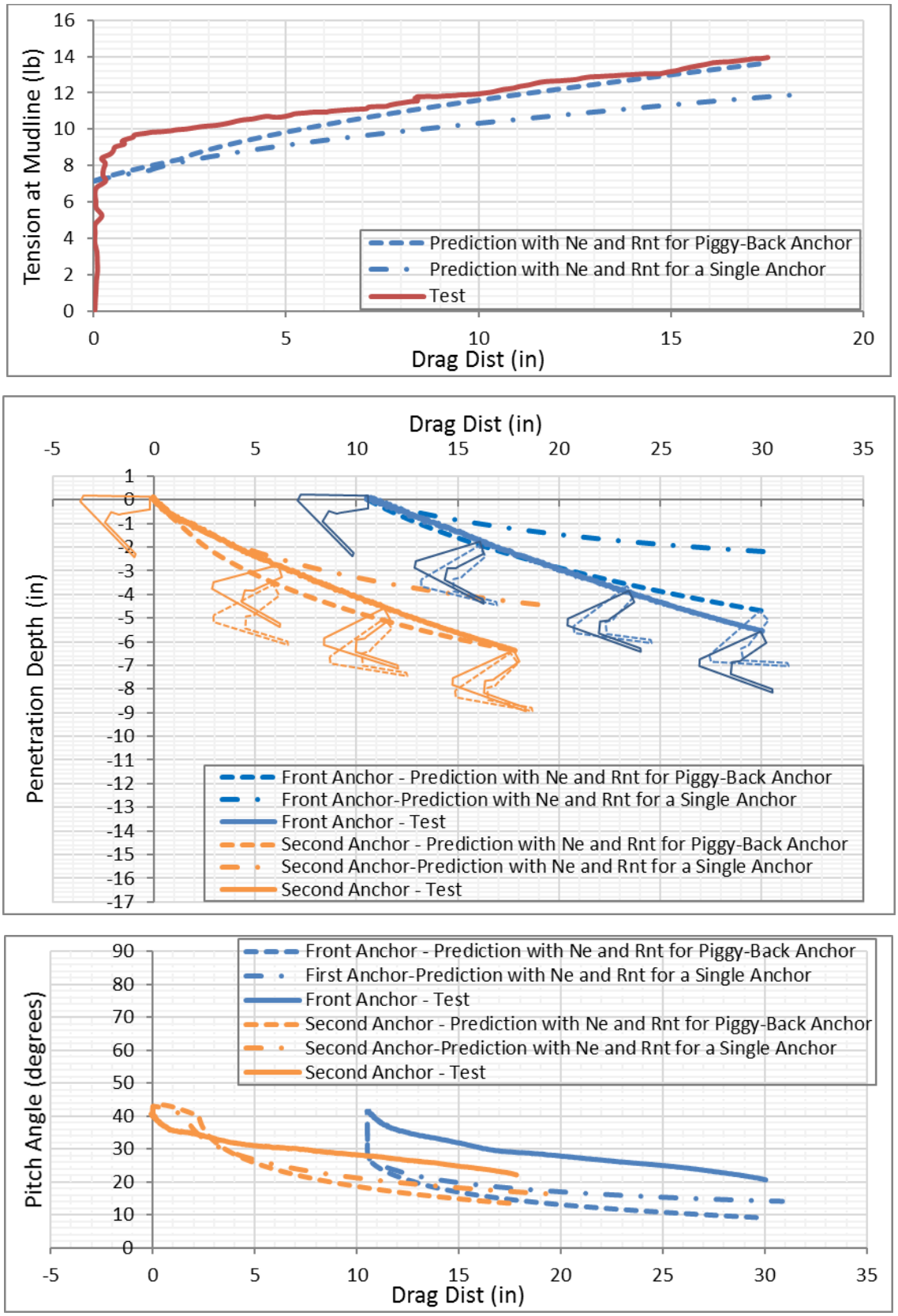

Figure 6.30. Example Comparison of Prediction with Different N_e and R_{nt}

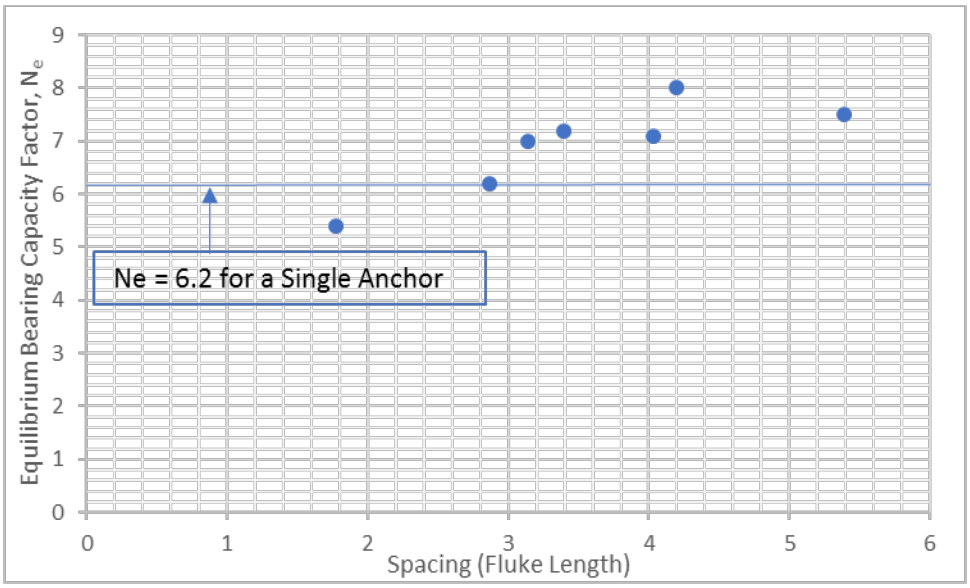

Figure 6.31. Equilibrium Bearing Capacity for Prediction Model

6.6 Conclusion

This chapter explores the tandem system anchor behavior in normally consolidated soil profile. Two sets of testing configuration of two different line attachment points for the piggy-back anchor are studied: one at the padeye of the front anchor and one at the back of the fluke of the front anchor. A variety of spacings between the piggy-back anchor and the front anchor, ranging from one fluke lengths to five fluke lengths, and two different line thicknesses for the trailing line attaching the piggy-back anchor to the front anchor are considered. For every test bed with piggy-back anchor tests, drag test with a single anchor are performed for comparison.

The following conclusions can be drawn from the test results:

- For both attachment points, the total capacity of the piggy-back configuration tends to increase with increasing spacing between the front anchor and the piggy-back anchor.
- For both attachment points, the total capacity of the piggy-back configuration is greater than twice the capacity of a single anchor provided that the spacing between the anchors is at least two fluke lengths.
- The piggy-back anchor is able to dive deeper than both the front anchor and a single anchor. It is also possible for the front anchor to dive deeper than a single anchor.
- For the tests with the second anchor attached to the back of fluke of the front anchor, the experimental results are compared with analytical results. The analytical results reasonably agree with the experimental results after calibrating by changing equilibrium bearing capacity factor and ratio of normal to tangential movement.

Chapter 7. Free-Fall Penetration Tests of Flying Wing Anchor®

7.1 Introduction

This chapter studies Flying Wing Anchor® free-fall penetration in constant shear strength profile and a layered soil profile. The undrained shear strength is increased by high velocity from anchor travelling through soil, thus the strain rate effect is studied first by performing T-bar tests as well as pure normal and pure in-plane shearing tests with a thin steel plate at different loading rates. The strain rate parameters, β and λ, from this series of pure loading tests are applied into the analytical model to predict the impact velocity and embedment depth of Flying Wing Anchor® in constant shear strength profile and layered profiles. From the experimental and analytical results, the potential application of Flying Wing Anchor® in layered soil profiles is assessed.

7.2 Strain Rate Effect

As discussed in Section 2.4.2.4.3, the wide range of velocity during the free-fall penetration tests either in the laboratory or in the field increases the soil strength. This increased undrained shear strength is accounted by R_f based on the shear strain rate. Additionally, the strain rate effect is acknowledged that the rate effects for the shearing mechanism is higher than it caused by the bearing mechanism (Dayal et al., 1975; Steiner et al., 2014). The objectives of exploring strain rate effect in this section are:

- to characterize the rate effect with T-bar tests at different loading rate

- to experimentally quantify the strain rate effect in bearing and shearing mechanism experimentally and compared with the typical formulation (semi-logarithmic and power-law).
- to apply the appropriate strain rate effect results from the above to the trajectory prediction of Flying Wing Anchor® in GoM clay.

7.2.1 Strain Rate Effect Test Setup

The rate effect on different mechanism (bearing and shearing) is explored by performing the pure loading tests on a 0.1-inch thick circular pate with a 4-inch diameter. The surface area is 12.57 in^2, and side area is 1.26 in^2. Therefore, when placing the steel plate horizontally (right one in Figure 7.1), the bearing area is 12.57 in^2 while the shearing area 1.26 in^2; in comparison, when placing the steel plate vertically (left in Figure 7.1), the shearing area is 1.26 in^2 while the bearing area 12.57 in^2. The shearing area is small compared with bearing area in normal loading tests, and the bearing area is small compared with shearing area in pure shearing tests. Therefore, bearing mechanism and shearing mechanism are separated in either the pure normal or shearing loading tests. The pure bearing tests are carried out for quantifying the strain rate effect on bearing resistance, while the in-plane shearing tests are performed for assessing the strain rate effect on the shearing resistance.

Different loading rate is selected based on the velocity range from free-fall penetration tests. The maximum impact velocity obtained from the free fall penetration tests is 247 in/s, and the effective diameter of Speedy Flying Wing anchor® is 2.5 inch. Thus,

maximum v/d from the free penetration tests is 99 s^{-1}, which is three orders of magnitude compared to T-bar tests in undrained loading conditions (0.8 s^{-1}). There are two limitations on the maximum loading rate in pure loading tests to study rate effect, one is the capacity of motor, and the other one is depth of soil bed. For the capacity of motor, as discussed in Section 3.4, the maximum loading rate can be provided by stepper motor is 50 RPS (Figure 3.13) which is 18.95 in/s. The soil depth in test bed limits maximum loading rate since the loading system reaches the setting travelling distance (soil depth) first and then motor already stops moving even if the setting speed has not been reached. In details, the motor accelerates from zero to the speed set on the LabVIEW control panel while moving towards to the set position (corresponding to the travelling distance of loading rod in soil). The motor stops when reaching the set position. Since the travelling distance for motor accelerating from zero to the set speed is longer than the soil depth, thus the speed has not been reached however the set distance has already been reached then the motor stops. After a couple of trial tests in the deepest soil bed can be performed with GoM, the maximum speed is 21.17 RPS (8 in/s), which cover two orders of magnitude.

Figure 7.1. Pure Loading Test on the Circular Plate

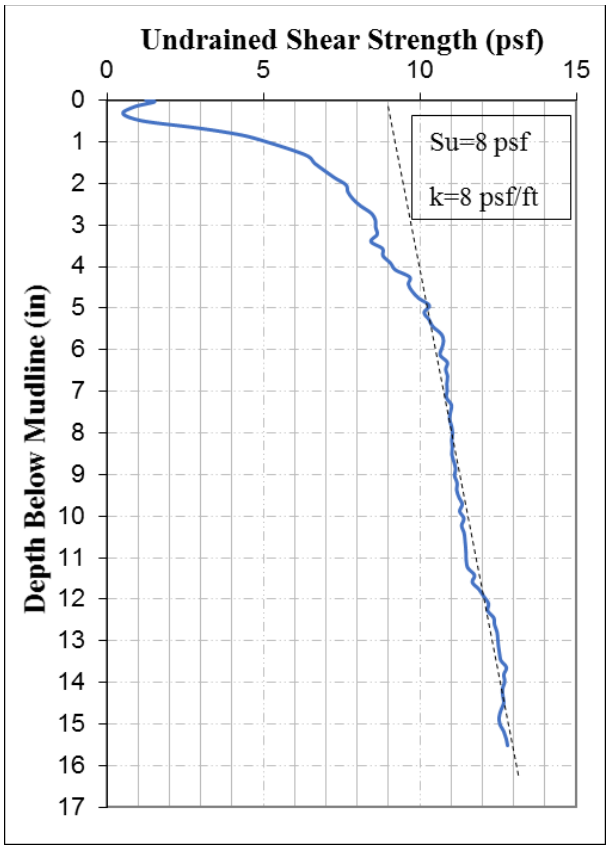

Figure 7.2. Undrained Shear Strength Profile for Pure Loading Tests at Different Rate

7.2.2 Experimental and Theoretical Results

7.2.2.1 T-bar Tests at Different Loading Rate

The T-bar Tests are performed at different loading rate (0.8 in/s, 1.6 in/s, 3.2 in/s, 4.8 in/s, 6.4 in/s and 8 in/s), and the R_f is obtained based on the ratio of measured soil resistance at different loading rate over the resistance corresponding with 0.8 in/s (shown as black circle in Figure 7.3 and Figure 7.4). The R_f is generally formulated using either semi-logarithmic or power-law functions (Biscontin and Pestana, 2001), and can be expressed as

$$R_f = 1 + \lambda \log\left(\frac{\dot{\gamma}}{\dot{\gamma}_{ref}}\right) \quad \text{Eq.(7.1)}$$

$$R_f = \left(\frac{\dot{\gamma}}{\dot{\gamma}_{ref}}\right)^{\beta} \quad \text{Eq.(7.2)}$$

where $\dot{\gamma}_{ref}$ is the reference strain rate at loading rate corresponding with undrained condition (0.8 in/s), and β and λ are strain rate parameters for semi-logarithmic and power-law function, respectively. To best fit the experimental R_f from T-bar tests in this study, the β and λ is 0.05 and 0.12, respectively.

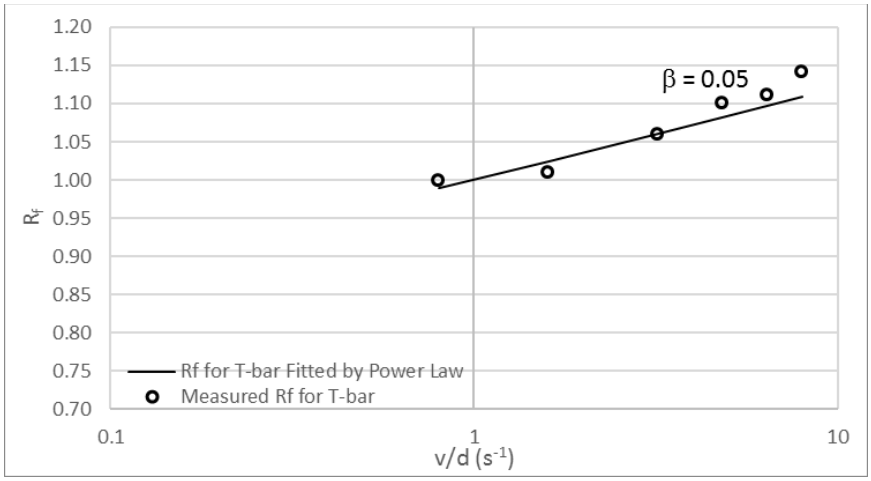

Figure 7.3. T-bar at Different Rates Fitted by Power-Law Function

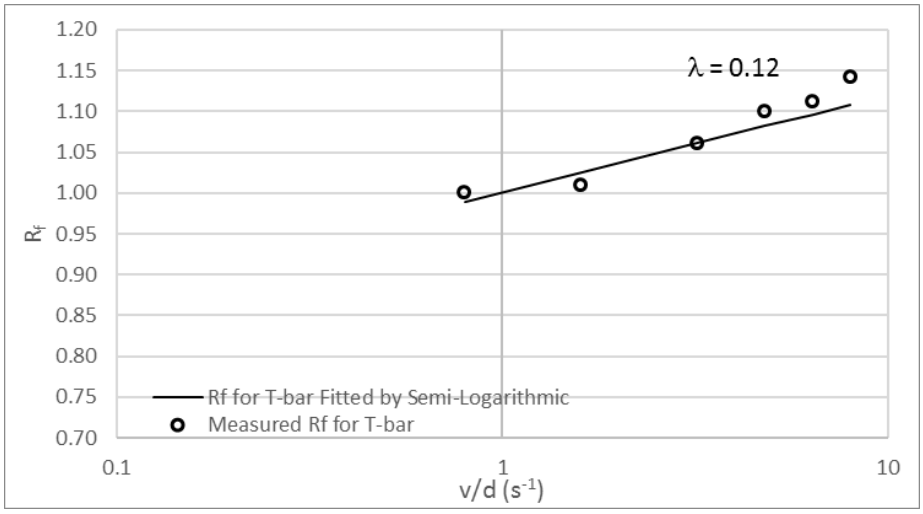

Figure 7.4. T-bar at Different Rates Fitted by Semi-Logarithmic Function

7.2.2.2 Pure Loading Tests with Plate at Different Loading Rate

7.2.2.2.1 Pure Bearing Tests with Plate at Different Loading Rate

The pure loading tests with the circular plate (0.1-inch thick circular plate with a 4-inch diameter) are performed at 0.8 in/s, 1.6 in/s, 3.2 in/s, 4.8 in/s, 6.4 in/s and 8 in/s, and the R_f is obtained based on the ratio of measured soil resistance at different loading rate over the resistance corresponding with 0.8 in/s. The pure normal loading tests results are shown in Table 7.1, and the pure shearing tests results are shown in Table 7.2.

The pure normal capacity factor at 0.8 in/s us measured as 11.97, which is close to the simplified theoretical pure loading threshold by Gerkus (2016) shown below

$$N_{normal} = 12.5 + 4\times(1/S_t) \times (t/B) \qquad \text{Eq.(7.3)}$$

$$N_{normal} = 12.5 + 4\times(1/1) \times (0.1/4) = 12.6$$

One set of tests results at different loading rate is shown in Figure 7.5. As shown in Table 7.1 and Figure 7.5, the measured N_p increases with the increasing loading rate, and this increasing trend is more obvious when loading rate higher than 4.8 in/s.

Table 7.1. N_p at Different Rate

		N_p			
Velocity (in/s)	v/d (s^{-1})	Test 1	Test 2	Test 3	Average
0.8	0.2	12.52	11.73	11.65	11.97
1.6	0.4	11.93	12.08	12.03	12.01
3.2	0.8	11.83	12.10	12.22	12.05
4.8	1.2	14.18	13.18	12.81	13.39
6.4	1.6	13.29	13.32	13.59	13.40
8	2	13.79	13.88	13.71	13.79

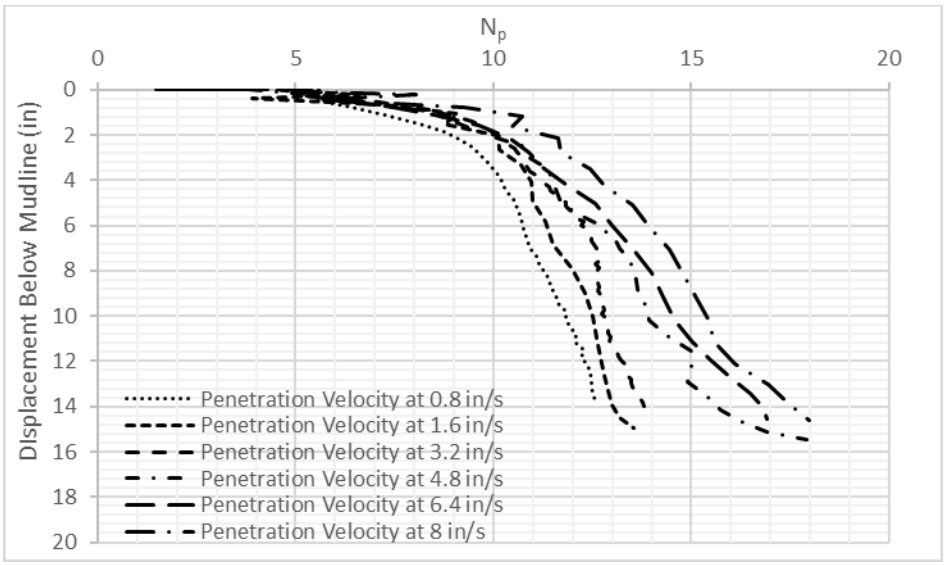

Figure 7.5. Example of Pure Normal Loading Tests at Different Rate

As shown in Figure 7.6, the R_f obtained from pure bearing tests are fitted with power-law function and compared with the R_f from T-bar fitted with power-law function. The R_f is plotted against $(v/d)/(v/d)_{ref}$ where the $(v/d)_{ref}$ is 0.8 s^{-1} (the reference velocity of 0.8 in/s with 1-in diameter of T-bar). The β with 0.05 is obtained by fitting T-bar tests at different loading rate as shown in Figure 7.2 in Section 7.2.2.1 and Figure 7.6 shown below. Since the soil failure around T-bar penetration tests and around pure bearing tests is bearing mechanism, so the strain rate parameter of β with 0.05 is first applied to R_f obtained from pure bearing tests. However, as shown in Figure 7.6, the R_f curve of β with 0.05 cannot fit the whole range but only cover the part with $(v/d)/(v/d)_{ref}$ lower than 1 (corresponding with velocity lower than 3.2 in/sec). The β with 0.15 is fitted for the R_f from pure bearing loading tests, and can fit well with the range over $(v/d)/(v/d)_{ref}$ higher than 1 (corresponding with velocity lower than 3.2 in/sec). As discussed in Section 7.2.1, the maximum v/d from free-fall penetration tests with Flying Wing Anchor® is 99 s^{-1}, thus the fitting results at the

higher velocity range is more suitable for the condition for Flying Wing Anchor®. Therefore, the β with 0.15 is more suitable for the strain rate effect condition for Flying Wing Anchor®.

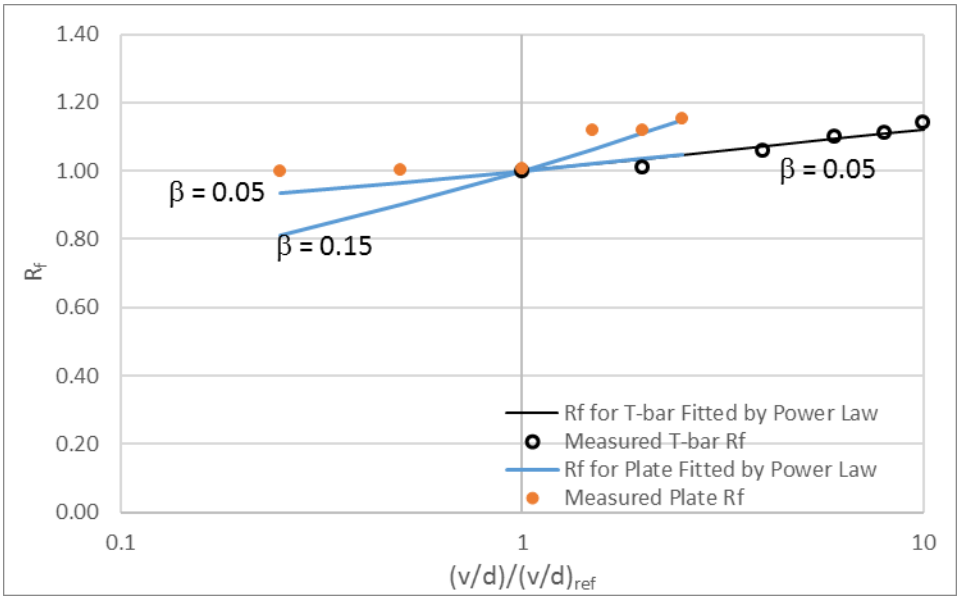

Figure 7.6. Comparison of R_f from Pure Bearing Tests and T-bar Tests Fitted with Power-Law Function

The similar fitting process is performed with employing semi-logarithmic function to fit the R_f from pure bearing tests. First, the strain rate parameter λ with 0.12 from fitting R_f obtained from T-bar tests is applied to the semi-logarithmic function with R_f from pure bearing tests, as shown in Figure 7.7. However, the λ with 0.12 with only can fit the velocity range up to 3.2 in/s which is $(v/d)/(v/d)_{ref}$ with 1. Then the semi-logarithmic function of λ with 0.35 is plotted and fit the velocity range higher than 3.2 in/s.

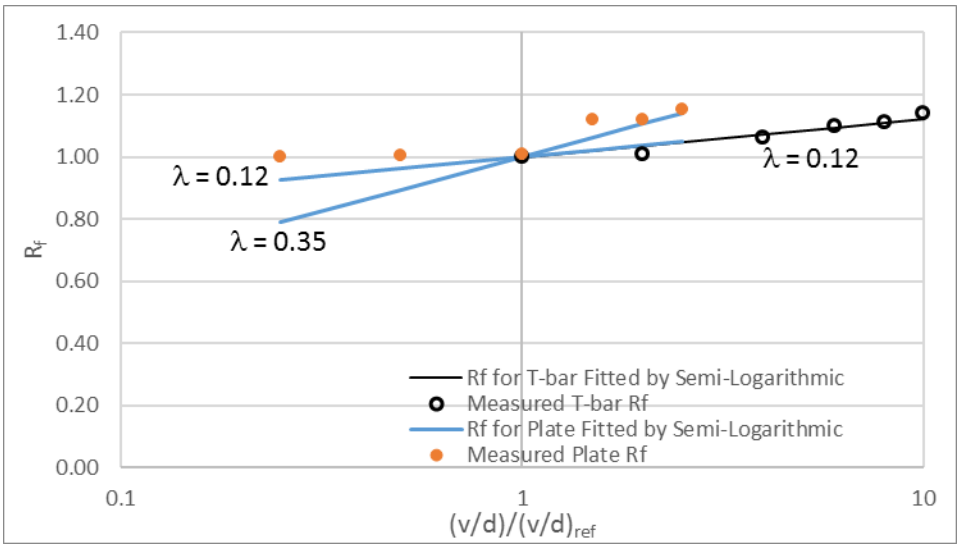

Figure 7.7. R_f from Pure Bearing Tests and T-bar Tests Fitted with Semi-Logarithmic Function

In summary, the soil failure mechanism in pure bearing tests and T-bar is pure bearing. However, the theoretical R_f with strain rate parameter (β with 0.05 and λ with 0.12) obtained from T-bar can only cover the lower velocity range for the R_f from the pure bearing tests with plate. A higher strain rate parameter (β with 0.15 and λ with 0.35) is employed to fit the higher velocity range, and is suitable with the strain rate condition for the free-fall penetration tests with Flying Wing Anchor® (a higher range of v/d than tested with plate and T-bar).

7.2.2.2.2 Pure In-Plane Shearing Tests with Plate at Different Loading Rate

The pure shearing capacity factor at 0.8 in/s is measured as 2.568, which is close to the simplified theoretical pure loading threshold by Gerkus (2016) shown below

$$N_{shear} = 2\times(1/S_t) + 2 \times 7.5 \times (t/B) \qquad \text{Eq.(7.4)}$$

$$N_{shear} = 2\times(1/1) + 2 \times 7.5 \times (0.1/4) = 2.375$$

One set of tests results at different loading rate is shown in Figure 7.8. As shown in Table 7.2 and Figure 7.8, the measured N_s increases with the increasing loading rate. In contrast from the trend of N_p with loading rate, the N_s increases as the rate increases.

Table 7.2. N_s at Different Rate

		Ns			
Velocity (in/s)	v/d (s^{-1})	Test 1	Test 2	Test 3	Average
0.8	0.2	2.64	2.53	2.52	2.56
1.6	0.4	2.64	2.63	2.59	2.62
3.2	0.8	2.87	3.00	2.93	2.93
4.8	1.2	3.23	3.43	3.21	3.29
6.4	1.6	3.28	3.34	3.36	3.33
8	2	3.56	3.51	3.48	3.52

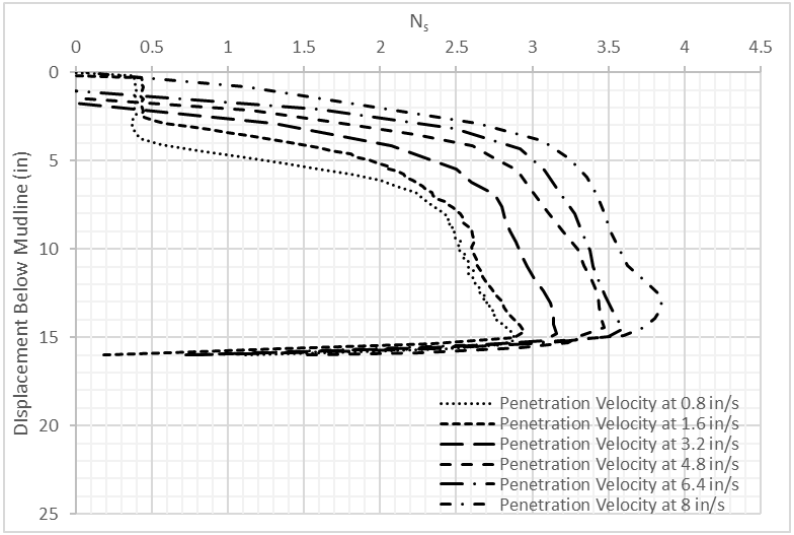

Figure 7.8. Example of Pure In-Plane Shearing Loading Tests at Different Rate

As shown in Figure 7.9, the R_f obtained from pure in-plane shearing tests are fitted with power-law function and plotted against (v/v_{ref}) where the v_{ref} is 0.8 in/s. The β with 0.15 is fitted for the R_f from pure in-plane shearing loading tests, and can fit well with the entire tested velocity range. As shown in Figure 7.10, the R_f obtained from pure in-plane shearing tests are fitted with semi-logarithmic function, and the λ with 0.35 can fit well with the R_f in the entire tested velocity.

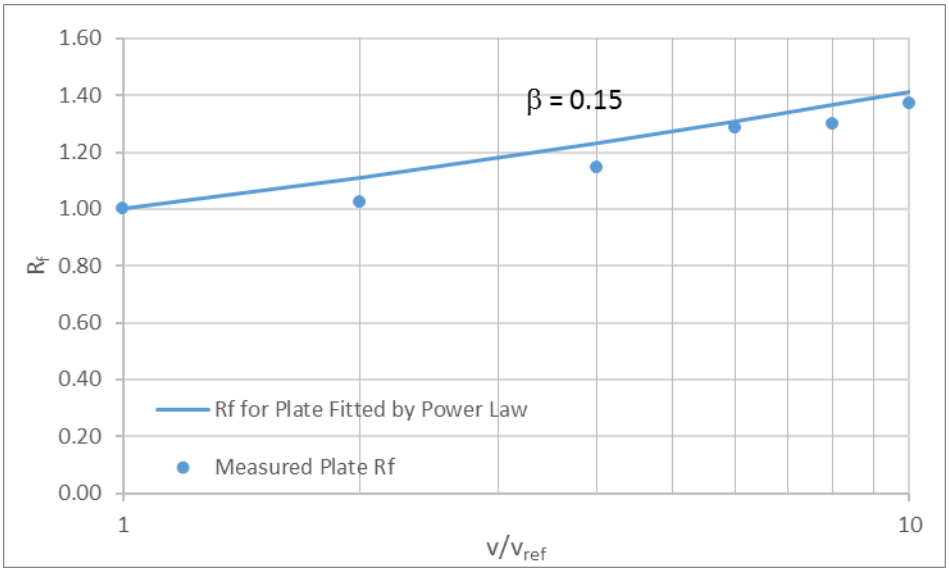

Figure 7.9. R_f from Pure In-Plane Tests Fitted with Power-Law Function

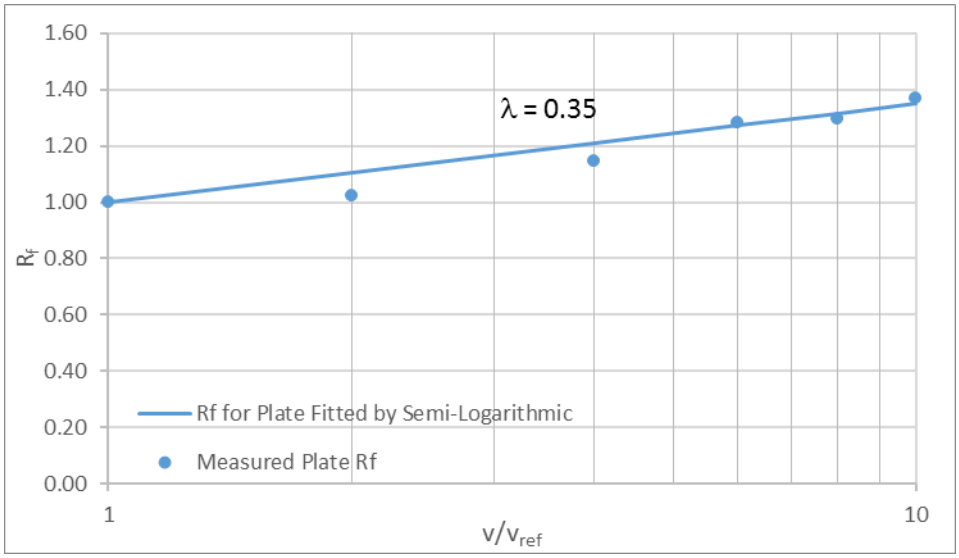

Figure 7.10. R_f from Pure In-Plane Tests Fitted with Semi-Logarithmic Function

7.2.2.2.3 Comparison of R_f from Bearing and Shearing Mechanism

The strain rate effect $R_{f,bear}$ and $R_{f,friction}$ obtained from plate are plotted in Figure 7.11 together with the R_f from T-bar. The tests results show that the $R_{f,friction}$ is higher than $R_{f,bear}$, which agrees well with the theoretical conclusion by Einav and Randolph (2006) and experimental results by Dayal et al. (1975) and Steiner, et al. (2014).

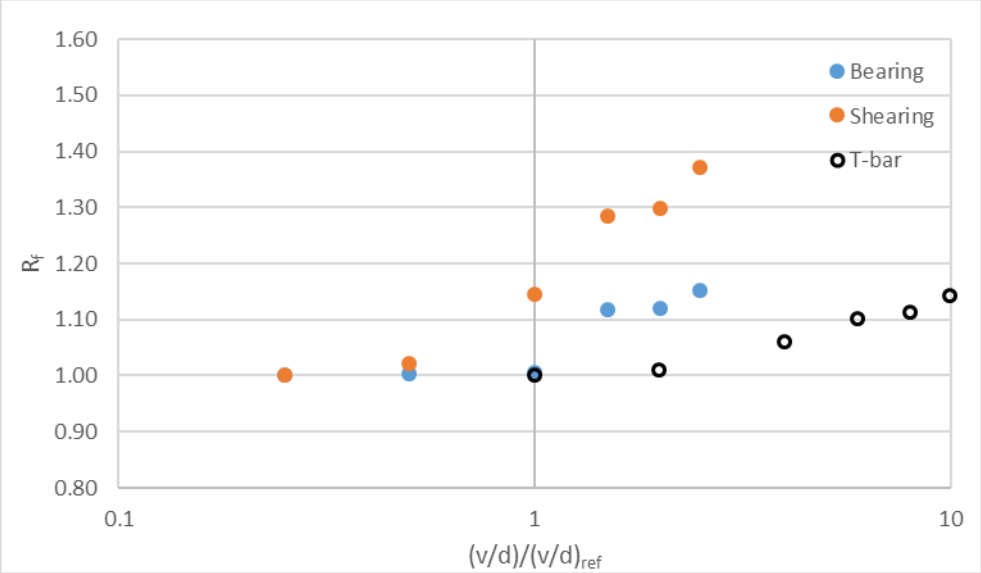

Figure 7.11. $R_{f,bear}$ and $R_{f,friction}$ Versus Different Loading Rate

7.2.3 Selected Strain Rate Parameter for Flying Wing Anchor®

The strain rate parameter β with 0.15 and λ with 0.35 is applied for the strain rate effect function for the prediction model of free-fall penetration tests with Flying Wing Anchor®. The strain rate effect for Flying Wing Anchor® penetrating into soil is mostly shearing since the shear surface contributes 87% among the total area (Gerkus, 2016). It should be

noted that the soil failure mechanism in pure bearing loading tests and T-bar tests are pure bearing. Thus, applying the strain rate effect of shearing mechanism from pure in-plane shearing tests is appropriate to the condition for Flying Wing Anchor®.

7.3 Free-Fall Penetration with Flying Wing Anchor® in a Single Layer

7.3.1 Analytical Model

The model applied in this study is the modified True's method discussed in Section 2.4.2.4. This is basically Newton's second law of motion with forces acting on the anchor in one-dimensional space varied with time and equates the submerged anchor mass and acceleration varied with time:

$$m' \frac{d^2z}{dt^2} = W' - R_f (F_{frict} + F_{bear}) - F_d \qquad \text{Eq.(7.5)}$$

where m' is the submerged anchor mass, z is anchor depth, t is time, W' is the submerged anchor weight, F_{frict} is frictional resistance along the soil anchor interface, F_{bear} is bearing resistance on the anchor tip and flukes, and F_d is drag resistance. The R_f term in Equation 7.5 accounts for the viscous enhancement of strength due to strain rate effects. Drag resistance is formulated as

$$F_d = \frac{1}{2} C_D \rho_s A_P v^2 \qquad \text{Eq.(7.6)}$$

where C_D is drag coefficient, ρ_s is soil density, A_P is projected area of anchor and v is anchor velocity.

Frictional and bearing resistances can be expressed in the form,

$$F_{frict} = \alpha\, s_u\, A_s \qquad \text{Eq.(7.7)}$$

$$F_{bear} = N_c\, s_u\, A_P \qquad \text{Eq.(7.8)}$$

where α is an interface friction ratio, N_c is the bearing capacity for the anchor tip or fluke and s_u is the undisturbed undrained shear strength for calculating F_{bear}, and remolded shear strength for calculating F_{frict}. The interface friction ratio, α, required for calculating the frictional resistance in Equation 7.7 is identical to that used in the estimation of frictional resistance on drive piles and suction caissons and may be estimated as the inverse of soil sensitivity. For the GoM clay in this study, the soil sensitivity is 1 since soil is remolded in each test which results in $\alpha = 1$. The capacity factor, N_c, in Equation 7.8 for calculating tip is similar to that used in the analysis of driven piles and suction installed caissons. American Petroleum Institute guidelines recommend $N_c = 9$ (American Petroleum Institute, 2002), O'Loughlin et al. (2009) suggested that $N_c = 12$, Gilbert et al. (2006) applied 17, Skempton (1951) proposed 7.5.

As discussed in Section 2.4.2.4.3 and Section 7.2, the high anchor penetration velocity results in an increase soil strength (Casagrande and Wilson, 1951; Graham et al., 1983; Sheahan et al., 1996). R_f is applied to quantify this enhanced shear strength by using either power-law or semi-logarithmic function (Biscontin and Pestana, 2001; Abelev and Valent, 2009; O'Loughlin et al., 2013). In this study, R_f is calculated in two different formulation, the power-law function (Equation 7.9) and semi-logarithmic function (Equation 7.10).

$$R_{f,bear} = \left(\frac{v/D}{(v/D)_{ref}}\right)^{\beta} \qquad \text{Eq.(7.9)}$$

$$R_f = 1 + \lambda \log\left(\frac{v/D}{(v/D)_{ref}}\right) \qquad \text{Eq.(7.10)}$$

7.3.2 Experimental Design

By performing sensitivity analysis with the analytical model in Section 7.3.1, the displacement range and velocity range from different release height and in different soil profiles is obtained. This displacement range and velocity range, the measuring facility (linear transducer or magnetometer) is chosen for the experimental tests.

7.3.2.1 Effect of Release Height

In the soil test bed with constant shear strength at 20 psf, Flying Wing Anchro® is released at 3 ft, 2 ft and 1ft. The maximum displacement is 3.5 ft and velocity range is up to 15 ft/sec. Based on the maximum velocity, the magnetometer is selected to track Flying Wing Anchor® motion during free-fall penetration. Since the weight of black sensor shown in Figure 3.17 is too small compared with the weight of Flying Wing Anchor®, thus when anchor impact soil surface and slows down, the momentum by sensor drives the sensor travels on the measuring track with the velocity before anchor impacts soil. Using LMT to track free-fall penetration tests with lower impact velocity won't raise this issue. Therefore, magnetometer is selected and attached to the anchor to measure displacement of anchor.

Table 7.3. Input for Effect of Release Height

Soil Parameter	
Su at mudline	20 psf
k	0 psf/ft
Anchor Parameter	
Anchor Weight	1.26 lbs
Model Parameter	
Drag Coefficient, C_D	0.05
Strain Rate Parameter, λ	0.35

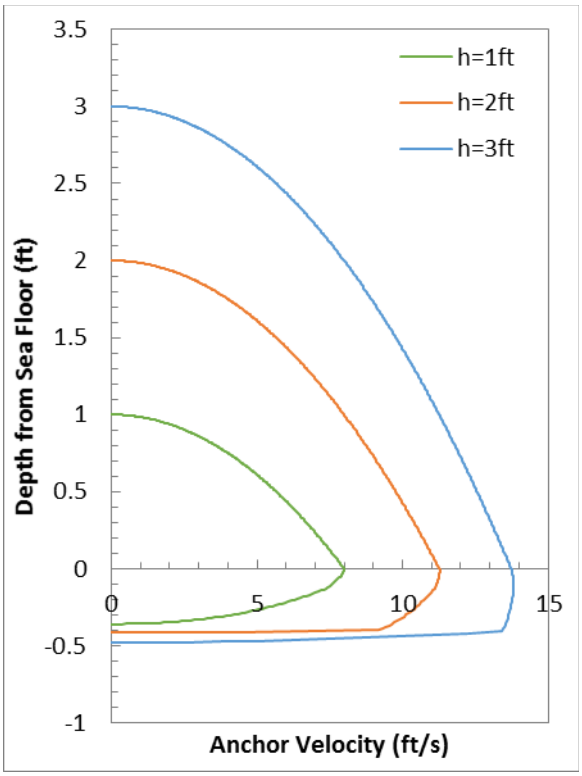

Figure 7.12. Impact Velocity versus Displacement (Effect of Release Height)

7.3.2.2 Effect of Shear Strength at Mudline

The left figure in Figure 7.13 is the whole displacement range, and the right one in Figure 7.13 shows the displacement below the mudline. The analytical model predicts that Flying Wing Anchor® penetrates slightly less in the constant shear strength profile with higher shear strength.

Table 7.4. Input for Effect of Shear Strength at Mudline

Soil Parameter	
Su at mudline	10 or 20 or 30 psf
k	0 psf/ft
Anchor Parameter	
Anchor Weight	1.26 lbs
Model Parameter	
Drag Coefficient, C_D	0.05
Strain Rate Parameter, λ	0.35

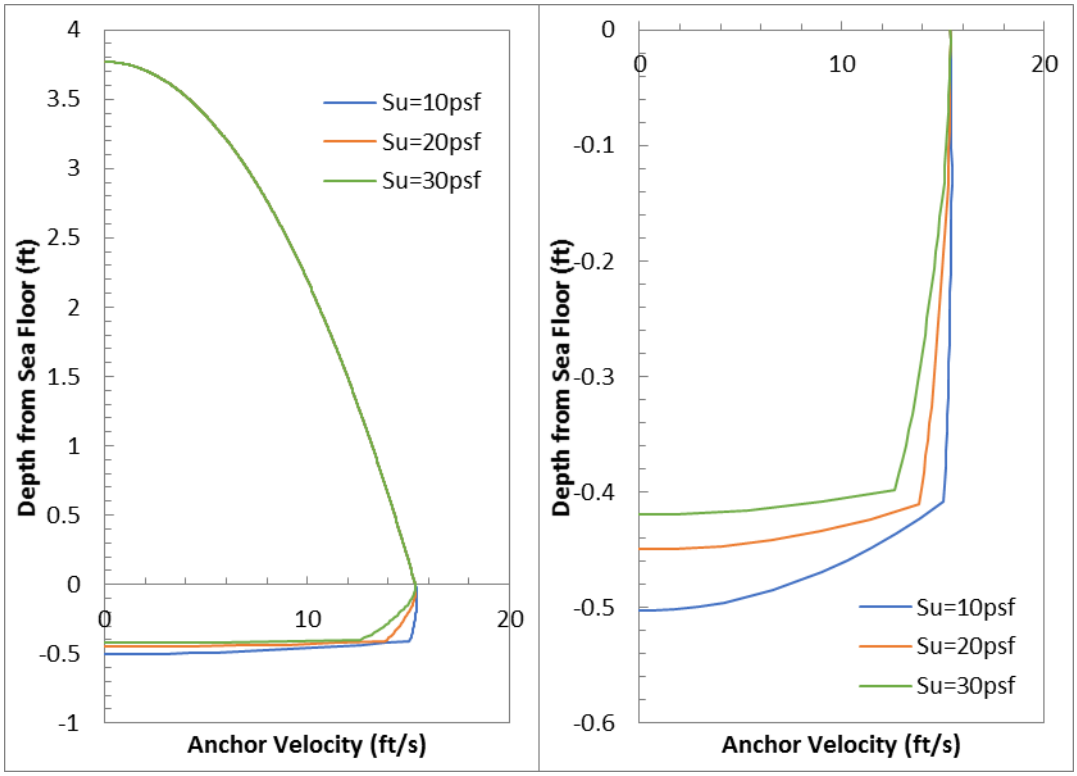

Figure 7.13. Impact Velocity versus Displacement (Effect of Shear Strength at Mudline)

7.3.2.3 Effect of Shear Strength Gradient

The left figure in Figure 7.14 is the whole displacement range, and the right one in Figure 7.14 shows the displacement below the mudline. The analytical model predicts that

Flying Wing Anchor® penetrates slightly less in the linearly increasing shear strength profile with higher gradient.

Table 7.5. Input for Effect of Shear Strength Gradient

Soil Parameter	
Su at mudline	10 psf
k	5 or 10 or 20 psf/ft
Anchor Parameter	
Anchor Weight	1.26 lbs
Model Parameter	
Drag Coefficient, C_D	0.05
Strain Rate Parameter, λ	0.35

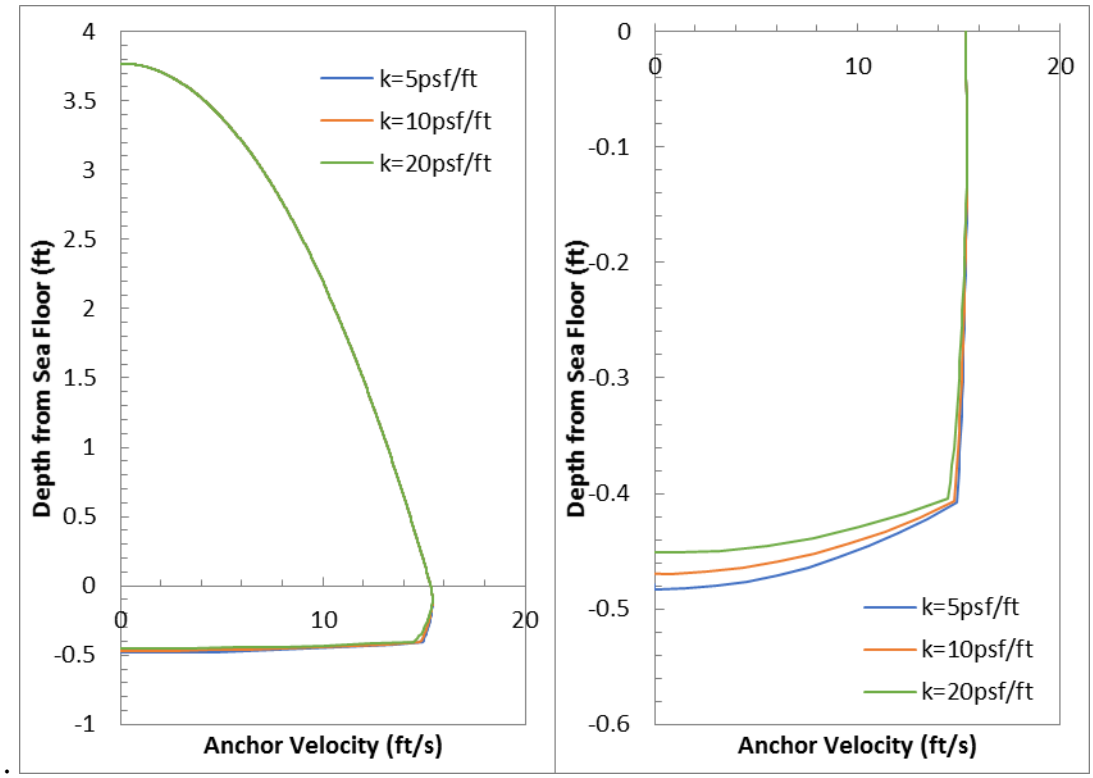

Figure 7.14. Impact Velocity versus Displacement (Effect of Shear Strength Gradient)

7.3.3 Test Setup

Due to the complex shape of Flying Wing anchor®, it is difficult to make Flying Wing anchor® in steel. The Speedy Flying Wing anchor® used in this study is printed by 3D printer. The printing material is ABS (Acrylonitrile Butadiene Styrene) with density of 1.05 g/cm^3. The weight of printed anchor is only 0.2 lbs, and the weight of anchor made with steel in the same volume of the printed anchor is 1.26 lbs. Thus, a steel plate is cut and attached to the rod with 0.25-inch diameter and 6-inch length. On the other side of the rod, the printed anchor is attached (Figure 7.15). The total weight including rod, nuts and washers to tighten steel plate as well as steel plate and anchor is 1.27 lbs, which is close to the weight of anchor made with steel in the size of the printed anchor. The magnetometer discussed in Section 3.9 is used to track displacement of anchor during tests and is taped on the surface of plate. The magnetometer is capable to measure displacement within 96 inches and record 60 readings per second. Due to the limitation of measured length, the maximum drop height is 4.25 ft above soil surface. On the top of the rod, a circular link is connected to enable a string line to be tied. This string goes around the pulley on the loading frame, so we can pull the other end of string on the ground to easily rise the anchor to the drop heights.

Figure 7.15. Flying Wing Anchor® for Free-Fall Penetration Tests

Figure 7.16. Free Penetration Test Set-up

The soil test bed for the free fall penetration tests with Flying Wing Anchor® is shown in Figure 7.17. The soil test bed is a relatively constant shear strength profile with undrained shear strength of 12.5 psf.

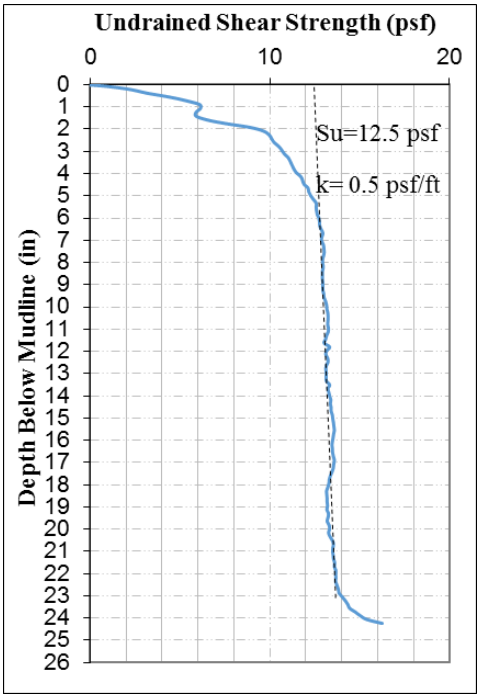

Figure 7.17. Shear Strength Profile for Free-Fall Penetration Test

7.3.4 The Experimental and Analytical Results

The free-fall penetration tests with Flying Wing Anchor ® are performed by releasing anchor attached with steel plate from 1.64 ft to 4.25 ft above the soil surface. The prediction model is calibrated by experimental tests. The calibrated parameters are the coefficient of drag, C_D, the bearing factor N_c, and the strain rate parameter β and λ as summarized in Table 7.6. The adopted C_D, 0.05, is obtained by fitting the predicted impact velocity with the experimental measurement. The bearing capacity at the tip of Flying Wing Anchor® is modelled as a deeply embedded strip footing with N_c = 7.5 by Skempton

(1951). The back-calculated strain rate parameter, β, in the power-law function is between 0.1 to 0.2. The β is close to the β from the pure in-plane shearing tests (0.15), are slightly higher than the β (0.05 to 0.1) obtained from vane shear tests (Biscontin and Pestana, 2001), higher than the β (0.05 to 0.07) obtained from T-bar penetrometer (Chung et al., 2006), and higher than the β (0.06 to 0.08) from T-ball penetrometer (Lehane et al., 2009). The back-calculated strain rate parameter, λ, in the semi-logarithmic strain rate function is between 0.2 to 0.5, which is in the typical range from λ (0.01 to 0.6) obtained from vane shear test (Sheahan et al., 1996) and in the range of back-calculated λ (0.2 to 1.0) from centrifuge tests with DPA (O'Loughlin et al., 2013). The embedment depth versus impact velocity shown in Figure 7.18 are normalized by the equivalent fluke width (square root of front plate of Flying Wing Anchor®, 2.54 inch for the scaled model anchor).

The prediction results are calculated by using the parameters listed in Table 7.6. The Figure 7.18 and Table 7.7 show the comparison between the analytical and experimental embedment depth and the impact velocity. Prediction with two different strain rate functions are evaluated by comparing with experimental results. As discussed in Section 7.3.1, the strain rate function includes the power-law function and the semi-logarithmic function. From Table 7.7, the predicted impact velocity is close to the experimental one. From Figure 7.18 and Table 7.7, the least square between the predicted and the experimental embedment depth is 0.867 and 0.87 for the prediction with power-law and semi-logarithmic function, respectively. The experimental embedment depth is slightly deeper than the predicted ones from strain rate effect modeled by semi-logarithmic function or power-law function. This slightly deeper embedment from experimental results may be due to the additional weight of magnetometer sensor and magnetometer line being part of

the anchor weight when being released from designated dropping height. This assumption is checked by changing the anchor weight in the prediction model by including the estimated magnetometer line and sensor weight. Figure 7.19 shows the predicted results with the real anchor weight and the weight of anchor together with line weight compared with the experimental result. The experimental embedment depth is 0.55 ft, and the predicted embedment depth with anchor weight only is 0.48 ft, in contrast with 0.53 ft from the prediction with anchor weight and magnetometer line weight. Thus, this weight difference is part of the reason that the prediction model underestimates embedment depth.

Table 7.6. Parameters in Prediction Model for a Single Layer

Parameter	Value
C_D	0.05
N_c	7.5
β	0.1~0.2
λ	0.2~0.5
α	1

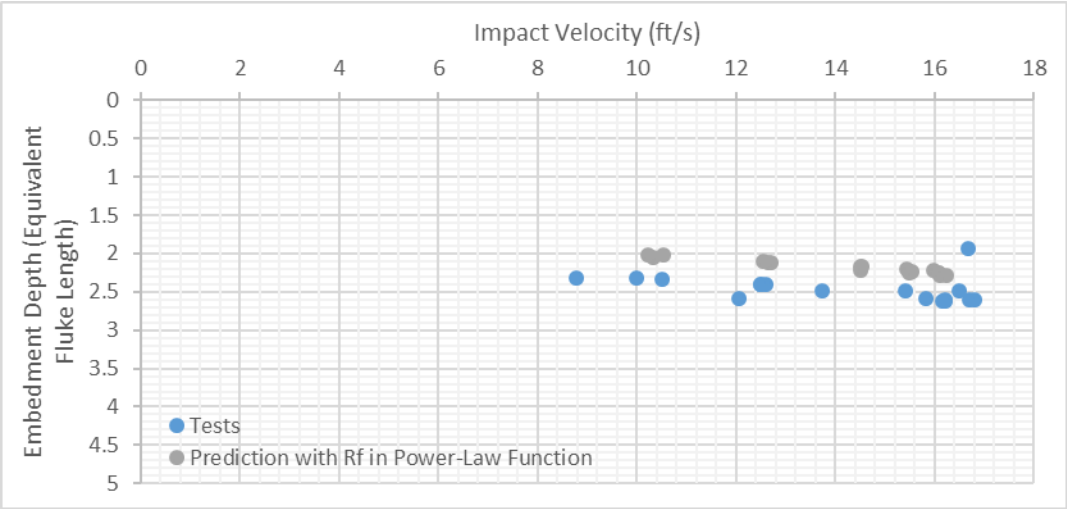

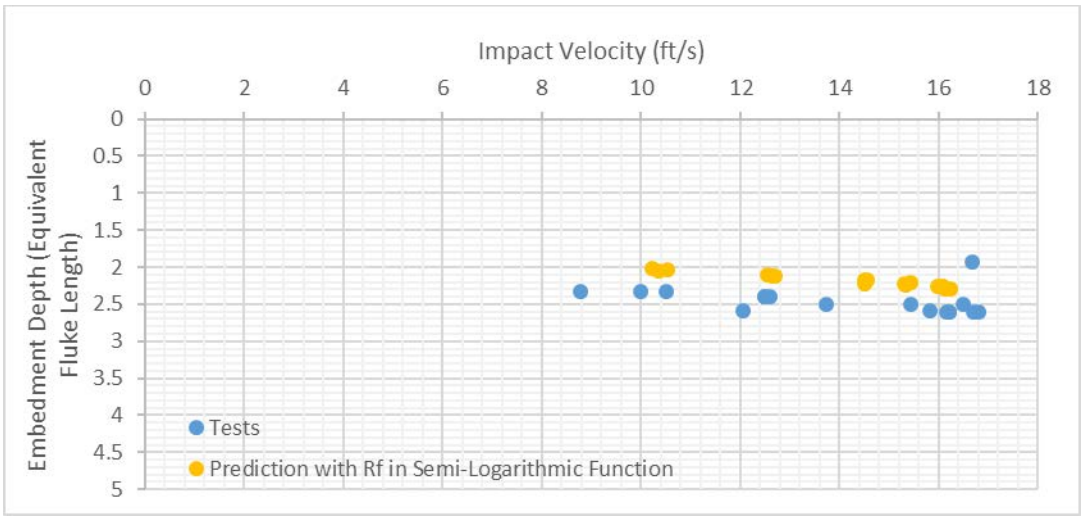

Figure 7.18. Experimental and Analytical Embedment Depth versus Impact Velocity

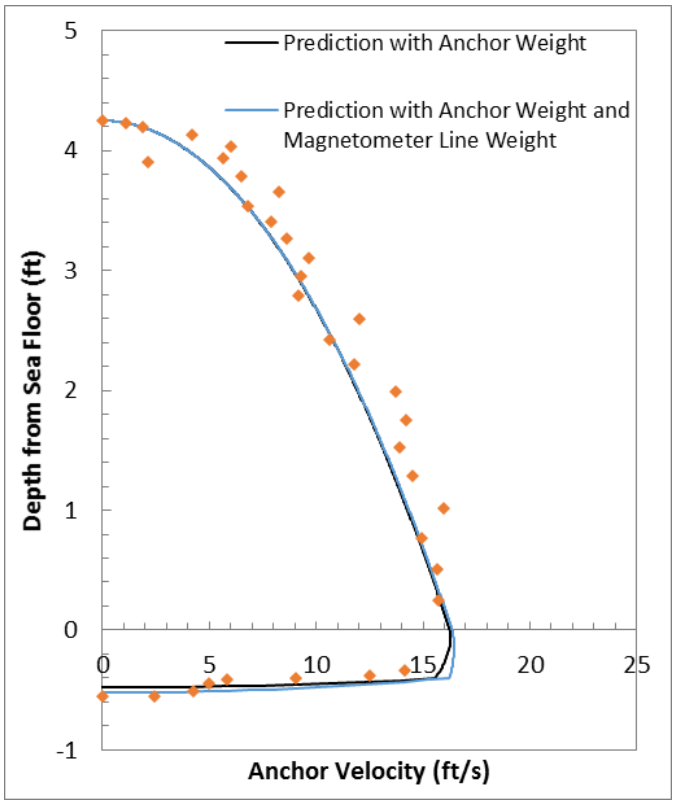

Figure 7.19. Comparison of Prediction between With and Without Magnetometer Line Weight

Table 7.7. Experimental and Analytical Embedment Depth and Impact Velocity

Test	Drop Height (ft)	Experiment v (ft/s)	Experiment Ztip (Equivalent Length)	R_f in Power-Law v (ft/s)	R_f in Power-Law Ztip (Equivalent Length)	R_f in Semi-Log v (ft/s)	R_f in Semi-Log Ztip (Equivalent Length)
1	4.17	16.80	2.61	16.09	2.26	16.09	2.26
2	4.18	16.16	2.61	16.12	2.28	16.12	2.29
3	4.10	16.20	2.61	15.97	2.21	15.97	2.26
4	4.17	16.71	2.61	16.09	2.26	16.09	2.27
5	4.25	16.20	2.61	16.24	2.28	16.24	2.29
6	3.36	16.50	2.49	14.51	2.17	14.51	2.18
7	3.37	15.43	2.49	14.51	2.21	14.51	2.22
8	3.38	13.73	2.50	14.54	2.16	14.54	2.17
9	2.57	12.50	2.40	12.70	2.11	12.70	2.12
10	2.54	12.60	2.40	12.64	2.11	12.64	2.12
11	2.50	12.50	2.40	12.55	2.11	12.55	2.11
12	1.75	10.50	2.33	10.53	2.03	10.53	2.03
13	1.69	8.78	2.33	10.34	2.04	10.34	2.05
14	1.65	10.00	2.33	10.21	2.02	10.21	2.02
17	3.81	15.83	2.59	15.43	2.20	15.43	2.21
18	3.75	16.67	1.93	15.49	2.26	15.30	2.23
19	3.77	12.05	2.59	15.55	2.23	15.33	2.24

A comparison example of experimental and analytical free-fall trajectory with three tests with different release height are shown in Table 7.8 to Table 7.10 and Figure 7.20 to Figure 7.22. From Figure 7.20 to Figure 7.22, the predicted results with different strain rate formulation generally have a good agreement with experimental results. Additionally, the predicted results by different R_f function is close to each other. All 19 tests results with prediction models can be found in Appendix F.

Table 7.8. Experimental and Analytical Impact Velocity and Embedment Depth (Drop 5)

	Impact v (ft/s)	Embedment D (L_f)	β	λ
Experiment	16.2	2.6	–	–
R_f in Power-Law	16.24	2.28	0.1	–
R_f in Semi-log	16.24	2.28	–	0.2

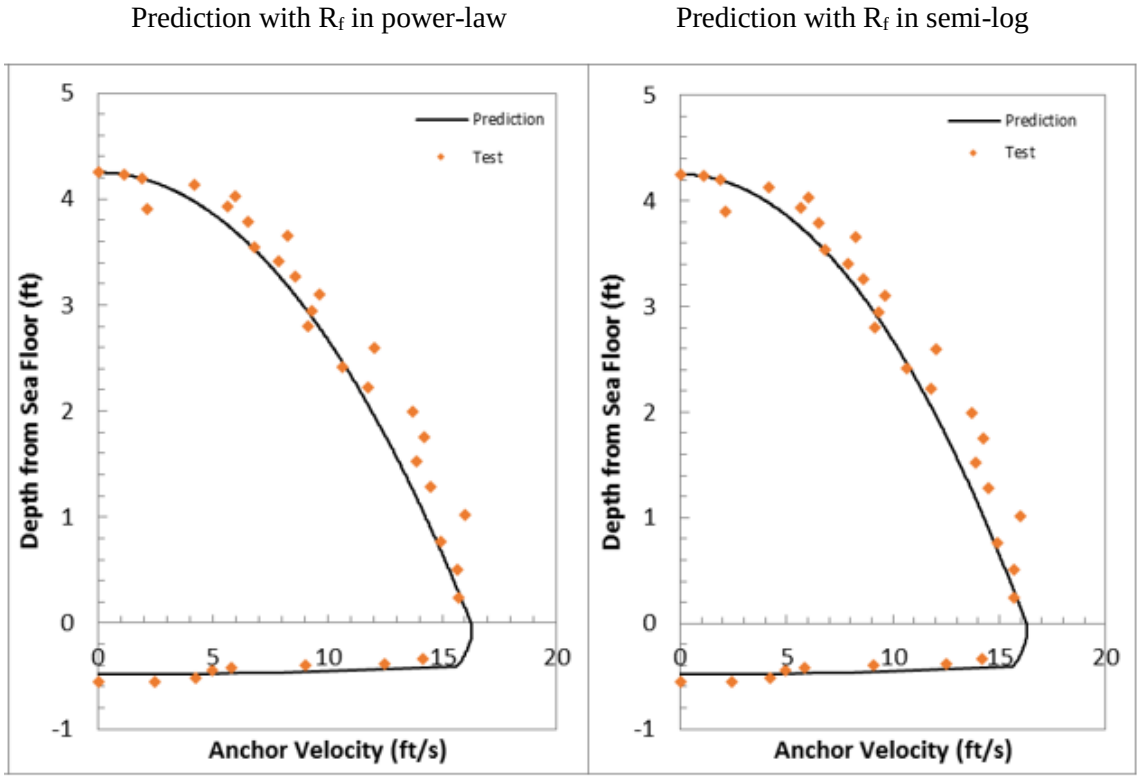

Figure 7.20. Experimental and Analytical Results of Flying Wing Anchor® in a Single Layer (Drop 5)

Table 7.9. Experimental and Analytical Impact Velocity and Embedment Depth (Drop 8)

	Impact v (ft/s)	Embedment D (L_f)	β	λ
Experiment	13.73	2.4950	–	–
R_f in Power-Law	14.54	2.1643	0.1	–
R_f in Semi-log	14.54	2.1697	–	0.2

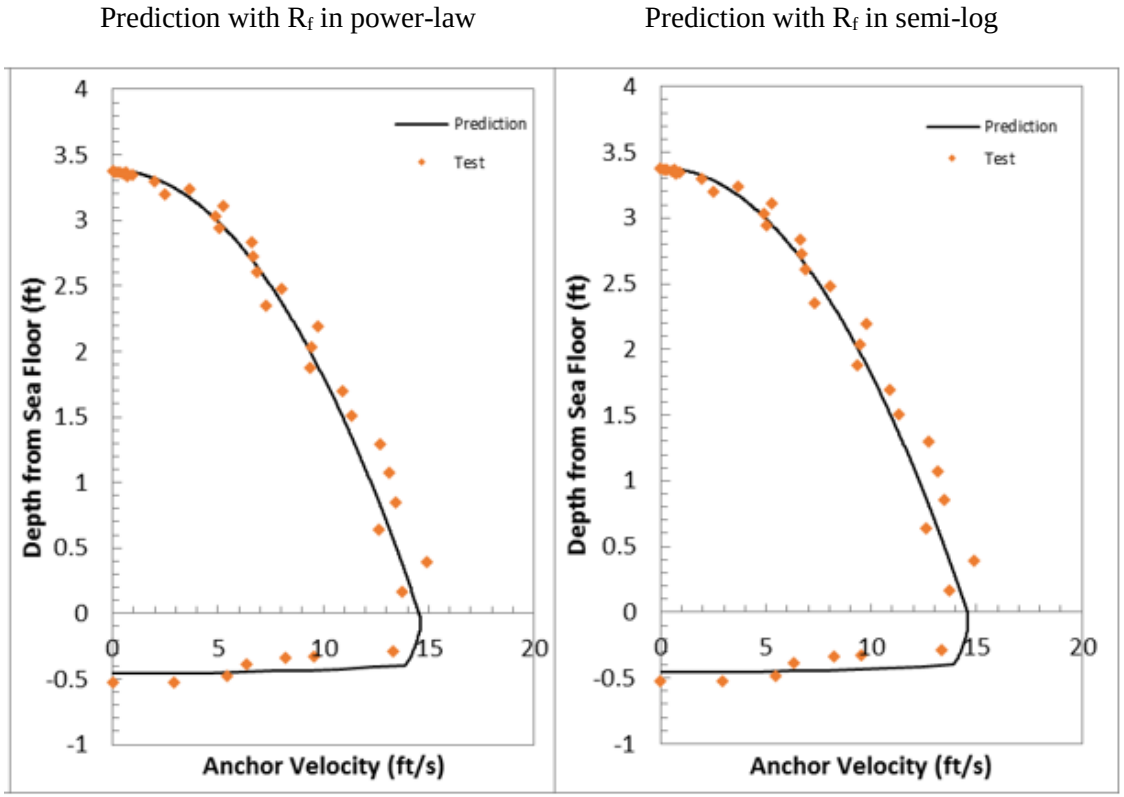

Figure 7.21. Experimental and Analytical Results of Flying Wing Anchor® in a Single Layer (Drop 8)

Table 7.10. Experimental and Analytical Impact Velocity and Embedment Depth (Drop 13)

	Impact v (ft/s)	Embedment D (L_f)	β	λ
Experiment	8.78	2.33	–	–
R_f in Power-Law	10.34	2.04	0.1	–
R_f in Semi-log	10.34	2.05	–	0.2

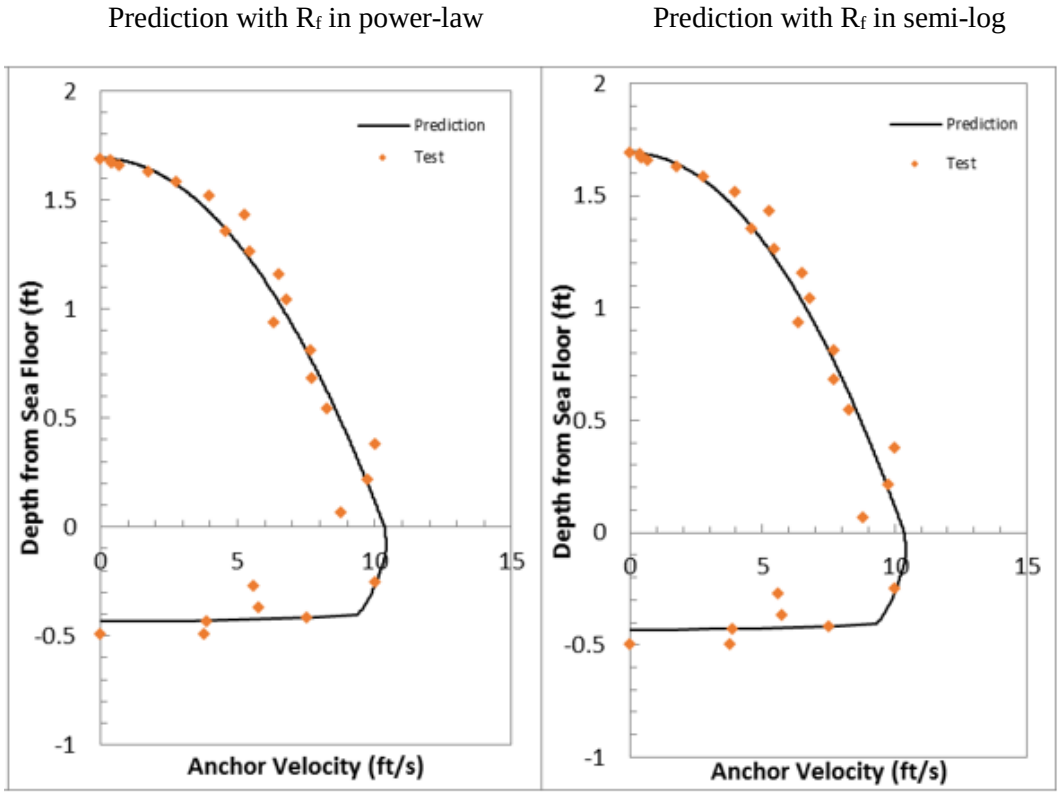

Figure 7.22. Experimental and Analytical Results of Flying Wing Anchor® in a Single Layer (Drop 13)

7.4 Extrapolate Results of Free-Fall Penetration with Flying Wing Anchor®

7.4.1 Experimental Design

This section performs sensitivity analysis with varying the weight over area ratio and release height. From Figure 7.21 and Table 7.7, a higher release height results in a deeper penetration. A heavier anchor is expected to penetrate deeper than a lighter anchor. The penetration depth is limited by the maximum soil depth that can be provided in the lab. Therefore, the sensitivity analysis in this section is for selecting a maximum weight can be attached on anchor and a maximum height for releasing anchor.

7.4.1.1 Effect of Weight Over Area Ratio

By increasing the ratio of weight over area as shown in Figure 7.23, the final penetration depth of anchor is increased. The maximum soil depth available in the lab is 30 inches (2.5 ft). Therefore, if the anchor is released at 1.7 ft above mudline in the constant shear strength profile with 10 psf, the maximum weight over area ratio should be less than 22. A ratio higher than 22 may results the anchor stopped by hitting test bed bottom instead of being stopped by the soil resistance. If the anchor with the ratio higher than 22 is intended to be tested, then a test bed with higher strength (higher than 10 psf) should be prepared.

Table 7.11. Input for Effect of Weigh Over Area Ratio

Soil Parameter	
Su at mudline	10 psf
k	0 psf/ft
Anchor Parameter	
Weight Over Area Ratio	4 or 8 or 15 or 22
Model Parameter	
Drag Coefficient, C_D	0.05
Strain Rate Parameter, λ	0.35

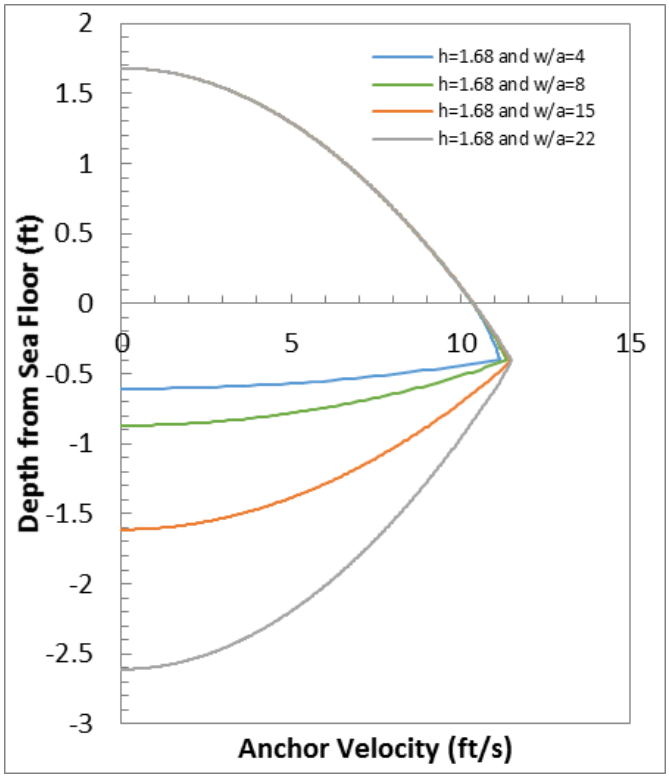

Figure 7.23. Impact Velocity versus Displacement (Effect of Weigh Over Area Ratio)

7.4.1.2 Effect of Release Height

The weight over area ratio of 22 is selected as the maximum w/a for extrapolating scaled Flying Wing Anchor® results to prototype as discussed in Section 7.4.1.1. This section studies that the maximum height for releasing anchor. As expected that a higher

release height results in a deeper penetration. Therefore, if performing free-fall test in the constant shear strength profile with 10 psf, the maximum release height at 1.5 ft is selected for the anchro with w/a ratio of 22 due to the limitation of soil depth.

Table 7.12. Input for Effect of Release Height with Weight Over Area Ratio with 22

Soil Parameter	
Su at mudline	10 psf
k	0 psf/ft
Anchor Parameter	
Weight Over Area Ratio	22
Model Parameter	
Drag Coefficient, C_D	0.05
Strain Rate Parameter, λ	0.35

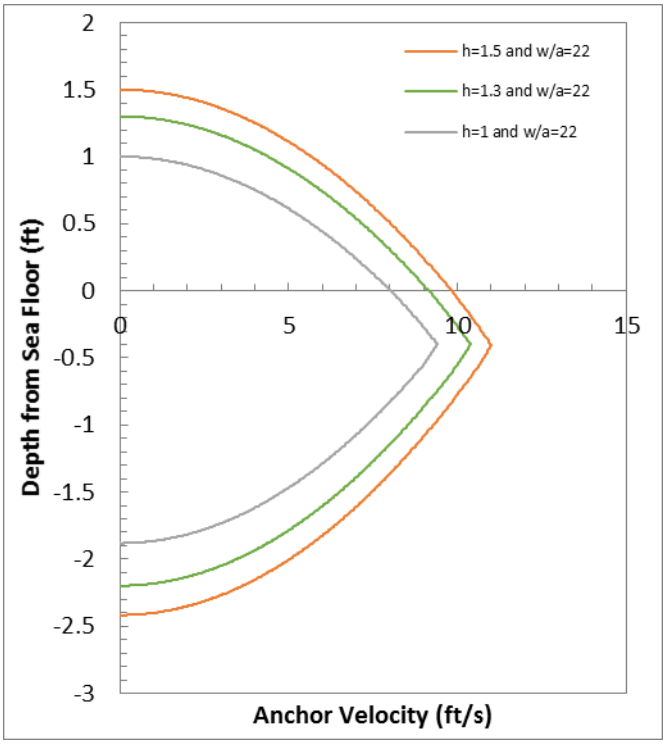

Figure 7.24. Impact Velocity versus Displacement (Effect of Release Height with Weight Over Area Ratio with 22)

7.4.2 Test Setup

In the tests to explore the scaling relationship of free penetration tests, the same size Speedy Flying Wing Anchor® will be used. The difference between each test is measured by attaching different weights on top of the anchor to present different size of anchor. As shown in Table 2.8, if the difference of weights between two anchors is x^3, then the difference between surface area of two anchor is x^2, and characteristic lengths of two anchor is x. Thus, the weight to area ratio of prototype anchor is x times greater than the scaled model anchor with 1:x scale. For example, the weight to area ratio of prototype anchor is 50 times greater than the 1:50 scaled Flying Wing Anchor® tested in Chapter 7. If the behavior of prototype anchor is tended to predict by extrapolating the measurement from scale model tests, the weight of area ratio is increased up to 50. As discussed in Section 7.3.2, the weight of prototype anchor is 1.27 lbs, additional 48 lbs weight should be added to simulate test condition for prototype anchor. However, due to the limitation of length of rod connecting the weights and anchor (preventing the attached weight on the top touches the soil surface when anchor travelling into soil bed), and the depth of soil test bed (preventing anchor being stopped by hitting bottom of soil barrel instead of being static by deacceleration from soil resistance), the maximum weight attached is 28 lbs, which provides the ratio of weight over area is 22 (28 lbs/1.27lbs = 22). By following the same test set up discussed in Section 7.3, the free-fall penetration for study scale effect is the same except: (1) attaching different weights on the top of anchor and; (2) using a longer rod (24 inches) to connect anchor and weights and; (3) using a PVC pipe as guide to preventing anchor together with rod and heavier weights (over 15 lbs) tilting when

impacting soil tests bed. The releasing height is selected at 1.7 ft above soil surface and remains the same for all tests with different weights attached.

Figure 7.25. Free-Fall Flying Wing Anchor® and Guide

7.4.3 The Experimental and Analytical Results

The soil test bed for scale effect study is the same as shown in Figure 7.17. An example of free-fall penetration tests with weight over area ratio higher than 1 is shown in Table 7.13 and Figure 7.26. The strain rate parameter, β with 0.15 λ with 0.35 is applied to the strain rate function R_f in the prediction model, which is consistent with the β and λ obtained in the pure in-plane shearing tests. All the tests results are shown in Appendix G. The experimental and analytical embedment depth and impact velocity with different weights attached are summarized in Table 7.14 and the results are plotted in Figure 7.27 with fitted prediction curve for extrapolating scaled model tests to prototype tests in the field. The fitted prediction curve can predict the embedment depth based on the weight to area ratio,

$$\text{Embedment Depth} = 0.4993 \times e^{0.08 \times Weight\ to\ Area\ Ratio} \qquad \text{Eq.(7.11)}$$

From the predicted equation, the prototype corresponds with weight to area ratio of 50 can penetrate 27 ft if being released at 1.7 ft above mudline. The equivalent fluke length of prototype anchor is 10 ft, which implies that the Flying Wing Anchor® can penetrate 2.7 fluke length when being dropped from 1.7 ft above mudline.

Table 7.13. Experimental and Analytical Impact Velocity and Embedment Depth with Flying Wing Anchor® with Weight to Area Ratio of 22.13

	Impact v (ft/s)	Embedment D (L_f)	β	λ	Weight of Area Ratio = 22.13
Experiment	12.01	7.89	–	–	
R_f in Power-Law	10.49	8.54	0.15	–	
R_f in Semi-log	10.49	8.47	–	0.35	

Prediction with R_f in power-law Prediction with R_f in semi-log

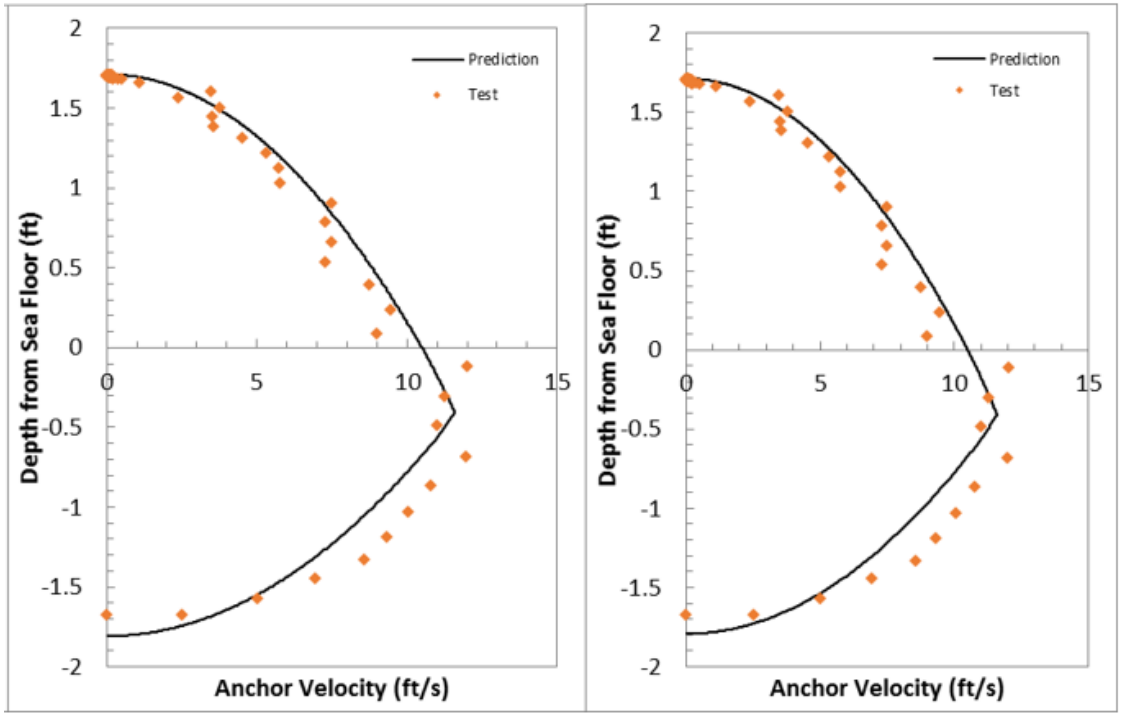

Figure 7.26. Experimental and Analytical Impact Velocity and Embedment Depth with Flying Wing Anchor® with Weight to Area Ratio of 22.13

Table 7.14. Experimental and Analytical Embedment Depth and Impact Velocity of Flying Wing Anchor® with Different Weight to Area Ratio

Test	Weight to Area Ratio	Drop Height (ft)	Experiment		R_f in Power-Law □		R_f in Semi-Log □	
			v (ft/s)	Z (Equivalent Length)	v (ft/s)	Z (Equivalent Length)	v (ft/s)	Z (Equivalent Length)
12	1.00	1.75	10.50	2.33	10.53	2.03	10.53	2.03
13	1.00	1.69	10.30	2.33	10.34	2.04	10.34	2.05
20	22.13	1.71	8.53	7.69	10.40	8.23	10.46	8.41
21	22.13	1.71	12.01	7.89	10.49	8.54	10.49	8.47
22	22.13	1.69	8.76	7.81	10.40	8.40	10.40	8.33
23	9.49	1.72	7.82	3.86	10.49	3.94	10.49	3.92
24	9.49	1.73	7.53	4.35	10.52	3.95	10.52	3.94
25	9.49	1.69	8.81	4.30	10.42	3.93	10.42	3.91
26	6.32	1.72	7.07	3.36	10.48	3.17	10.48	3.16
27	6.32	1.75	7.71	3.37	10.58	3.21	10.58	3.20
28	6.32	1.69	7.57	3.56	10.42	3.16	10.42	3.15

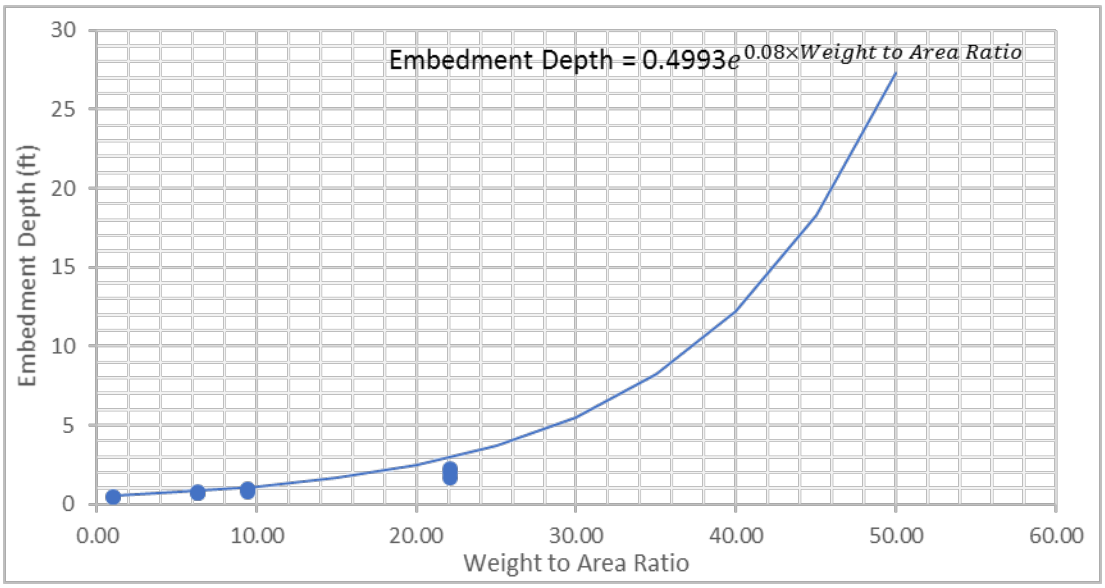

Figure 7.27. Extrapolate Scaled Model Anchor Embedment Depth to Prototype Anchor Embedment Depth

7.5 Free-Fall Penetration with Flying Wing Anchor ® in Layered Soil Profiles

This section presents the analytical and experimental results of Flying Wing Anchor® in layered soil profiles. The prediction model follows the same prediction as the free-fall penetration in a single layer but with a factor to account force enhancement from stiff layer. The comparison between analytical and experimental results are presented for each case in Appendix H.

7.5.1 Analytical Model of Free-Fall Penetration in Layered Soil Profile

The prediction model for the Flying Wing Anchor® in a layered soil profile is developed based on the prediction for Flying Wing Anchor® in a single layer described in

Section 7.3.1 and the prediction for DEA in layered soil described in Section 5.3.1. The prediction model for the anchor being released to reach the soil is followed the same prediction as the Flying Wing Anchor® in a single layer. As anchor impacts soil surface, the prediction still follows the same one as in a single layer for the part of anchor travels within soft soil layer. The stiff layer effect is evoked when the tip of anchor starts touching the stiff layer. The stiff layer effect is accounted by involving a multiplier in tip bearing capacity similarly in Equations 5.18 and 5.20. However, different from the multiplier for DEA in layered soil profiles which is a function of ratio of enhanced fluke area due to stiff layer over physical area and shear strength ratio of stiff layer and soft soil, the multiplier for Flying Wing Anchor® in free-fall penetration is only a function of shear strength ratio. Thus, the bearing force when anchor interacts with stiff layer is expressed as

$$F_{bear} = M_n N_c s_u A_P \qquad \text{Eq.(7.12)}$$

$$M_n = \frac{S_{u,stiff}}{S_{u,soft}} \qquad \text{Eq.(7.13)}$$

The strain effect enhanced by high velocity from anchor is accounted in the same power-law or semi-logarithmic functions as shown in Equations 7.9 and 7.10 for the part of anchor in the stiff layer.

7.5.2 Experimental Design

This section performs sensitivity analysis with the analytical model in Section 7.5.1, and studies the impact from characteristics of stiff layer such as depth, thickness and shear strength on the final penetration depth of Flying Wing Anchor®. These information guides constructing layere soil profiles in the lab.

7.5.2.1 Effect of Stiff Layer Depth

Figure 7.28 shows the impact velocity versus displacement in layered soil profile with stiff layer with shear strength of 20 psf and soft soil with shear strength of 10 psf. The 5-inch thick stiff layer starts at 1 or 2 or 3 inches. Figure 7.28 shows that the penetration depth in the soil profile with stiff layer at 2 inches is the same as in the one with stiff layer at 3 inches. This comparison implies that the stiff layer at 2 inches may be the threshold where anchor can or cannot penetrate into stiff layer from the release height from 4 inches. This assumption will be checked experimentally in Section 7.5.4.

Table 7.15. Input for Effect Stiff Layer Depth

Soil Parameter	
Su at mudline	10 psf
k	0 psf/ft
Stiff Layer Thickness	5 inch
Stiff Layer Depth from Mudline	1 or 2 or 3 inch
Shear strength ratio of stiff layer over soft layer	2
Anchor Parameter	
Anchor Weight	1.26 lbs
Model Parameter	
Drag Coefficient, C_D	0.05
Strain Rate Parameter, λ	0.35

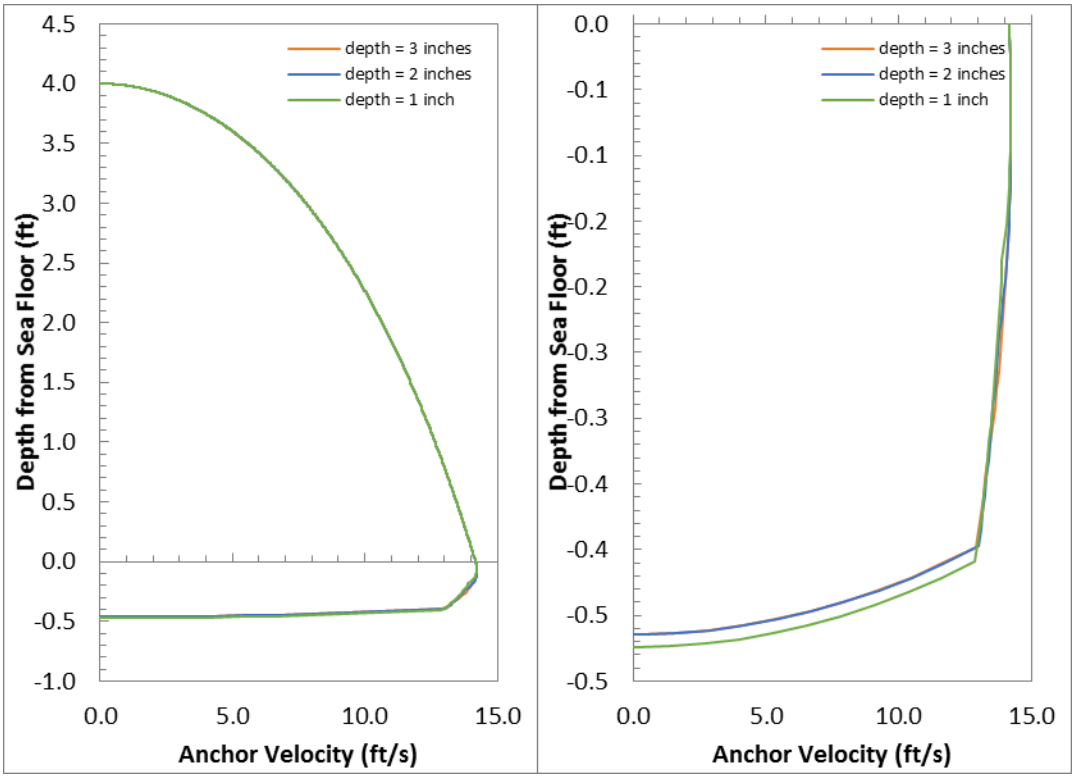

Figure 7.28. Impact Velocity versus Displacement (Effect of Stiff Layer Depth)

7.5.2.2 Effect of Stiff Layer Thickness

Figure 7.29 shows that the velocity versus displacement in layered soil profile with stiff layer with shear strength of 20 psf and soft soil with shear strength of 10 psf. The stiff layer starts at 1 inch below mudline with thickness of 1 or 2 or 3 inches. Figure 7.29 shows that the penetration depth in the soil profile with thicker stiff is less compared with the thinner stiff layer. This comparison implies that the anchor may penetrate into the stiff layers in all three cases. This assumption will be checked experimentally in Section 7.5.4.

Table 7.16. Input for Effect Stiff Layer Thickness

Soil Parameter	
Su at mudline	10 psf
k	0 psf/ft
Stiff Layer Thickness	3 or 2 or 1 inch
Stiff Layer Depth from Mudline	1 inch
Shear strength ratio of stiff layer over soft layer	2
Anchor Parameter	
Anchor Weight	1.26 lbs
Model Parameter	
Drag Coefficient, C_D	0.05
Strain Rate Parameter, λ	0.35

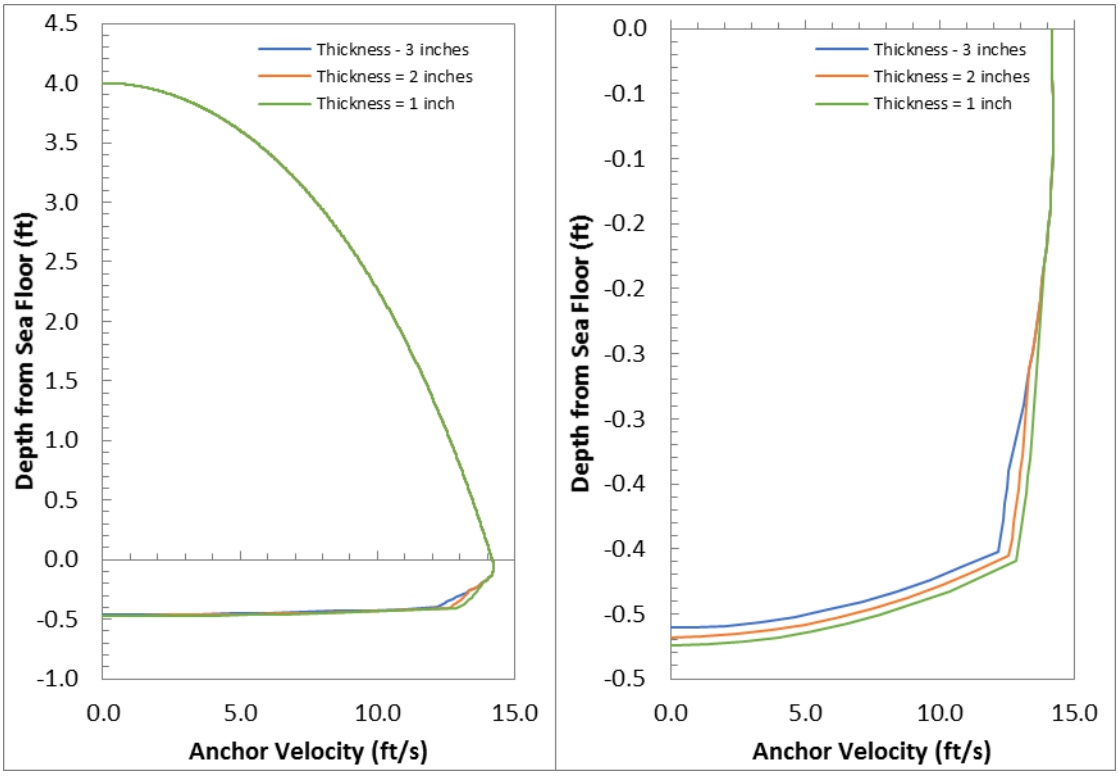

Figure 7.29. Impact Velocity versus Displacement (Effect of Stiff Layer Thickness)

7.5.2.3 Effect of Stiff Layer Shear Strength

Figure 7.30 shows that the velocity versus displacement in layered soil profile with stiff layer with shear strength of 20 or 30 or 40 psf and soft soil with shear strength of 10 psf. The stiff layer starts at 3 inch below mudline with thickness of 2 inches. Figure 7.30 shows that the penetration depth in the soil profile with stronger stiff is less compared with the weaker stiff layer. This comparison implies that the anchor may penetrate into the stiff layers in all three cases. This assumption will be checked experimentally in Section 7.5.4.

Table 7.17. Input for Effect Stiff Layer Shear Strength

Soil Parameter	
Su at mudline	10 psf
k	0 psf/ft
Stiff Layer Thickness	2 inch
Stiff Layer Depth from Mudline	3 inch
Shear strength ratio of stiff layer over soft layer	2 or 3 or 4
Anchor Parameter	
Anchor Weight	1.26 lbs
Model Parameter	
Drag Coefficient, C_D	0.05
Strain Rate Parameter, λ	0.35

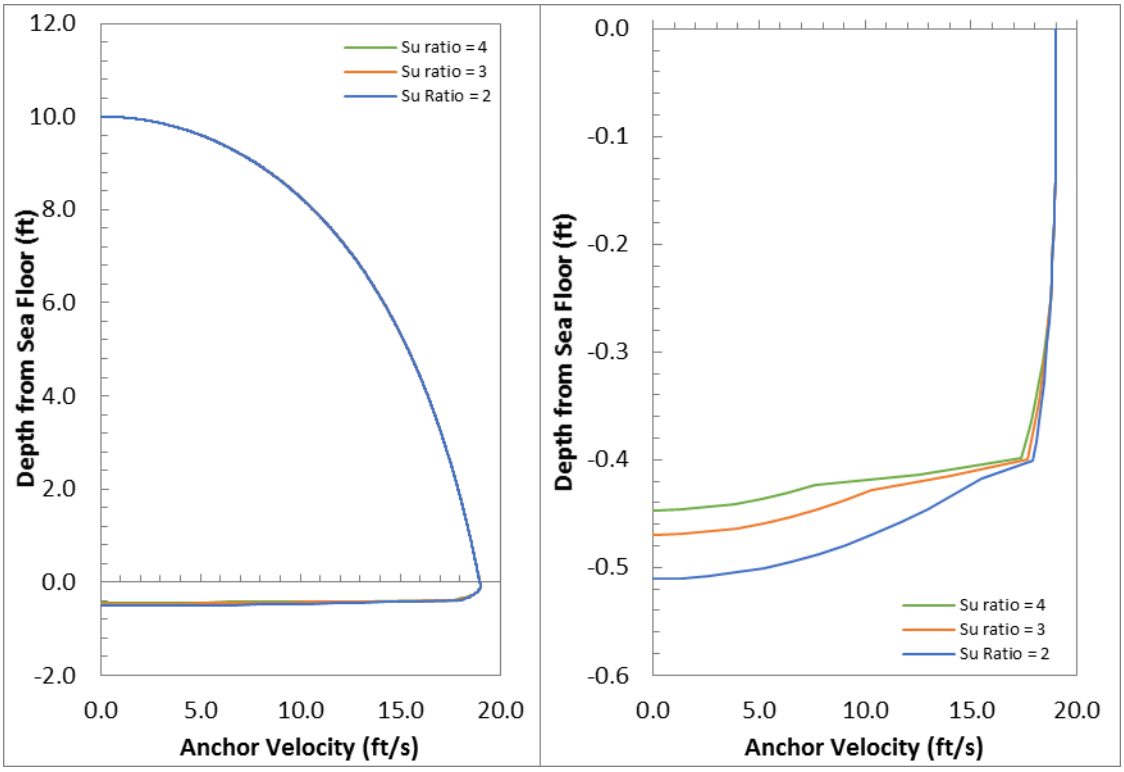

Figure 7.30. Impact Velocity versus Displacement (Effect of Stiff Layer Shear Strength)

7.5.3 Test Setup

The shear strength characteristics of soft and stiff layer are summarized in Table 7.18. The characteristics of stiff layers are similar to the stiff layers shown in Table 5.17. The

thickness of stiff layer is also 1 inch or 2 inches, and the shear strength ratio of stiff layer over soft layer ranges from 1.5 to 4. The difference of stiff layer profiles for DEA and Flying Wing Anchor® is the depth of stiff layer. For the tests with DEA in layered profiles, the depth of stiff layer ranges from 3 inches to 4 inches, and it is difficult for DEA to break through the shallower stiff layer. In contrast, for free-fall tests with Flying Wing Anchor® in layered soil profiles, the shallowest stiff layer starts at 1 inch below mudline. This shear strength profile with shallow stiff layer is prepared for explore the potential of Flying Wing Anchor® in the soil profiles where DEA cannot successfully embed. In the first column, after case designated number, the expectation of anchor can or cannot penetrate into or through stiff layer is listed. It should be noted that the listed penetration expectation is based on the drop height at 8 ft above soil surface, which means that the Flying Wing Anchor® has potential to penetrate through the stiff layers where being listed as not penetrate by releasing the anchor at a higher drop height. However, due to the limitation of effective length measurement by magnetometer, the maximum drop height is up to 8 ft in this study.

Table 7.18. Shear Strength Summary of Layered Soil Profile for Free-Fall Penetration Tests with Flying Wing Anchor®

Case 1 Stiff Layer – Anchor Expected to Penetrate Through Stiff Layer	Su at mudline	11 psf
	Su gradient	0 psf/ft
	Sensitivity of soft layer	1
	Stiff Layer Thickness	1 inch
	Stiff Layer Depth from Mudline	3 inches
	Shear strength ratio of stiff layer over soft	1.5

Table 7.18. Shear Strength Summary of Layered Soil Profile for Free-Fall Penetration Tests with Flying Wing Anchor® (Continued)

Case 2 Stiff Layer - Anchor Expected to Penetrate Through Stiff Layer	Su at mudline	13 psf
	Su gradient	0 psf/ft
	Sensitivity of soft layer	1
	Stiff Layer Thickness	1 inch
	Stiff Layer Depth from Mudline	1.5 inches
	Shear strength ratio of stiff layer over soft	2
Case 3 Stiff Layer – Anchor Expected to Penetrate into but not Through Stiff Layer	Su at mudline	13 psf
	Su gradient	0 psf/ft
	Sensitivity of soft layer	1
	Stiff Layer Thickness	1 inch
	Stiff Layer Depth from Mudline	2.5 inches
	Shear strength ratio of stiff layer over soft	3
Case 4 Stiff Layer – Anchor Expected to Penetrate through Stiff Layer	Su at mudline	13 psf
	Su gradient	0 psf/ft
	Sensitivity of soft layer	1
	Stiff Layer Thickness	1 inch
	Stiff Layer Depth from Mudline	3 inches
	Shear strength ratio of stiff layer over soft	2
Case 5 Stiff Layer – Anchor Expected to Penetrate Through Stiff Layer	Su at mudline	13 psf
	Su gradient	0 psf/ft
	Sensitivity of soft layer	1
	Stiff Layer Thickness	2 inches
	Stiff Layer Depth from Mudline	2.5 inches
	Shear strength ratio of stiff layer over soft	1.8
Case 6 Stiff Layer – Anchor Expected to Penetrate into but not Through Stiff Layer	Su at mudline	13 psf
	Su gradient	0 psf/ft
	Sensitivity of soft layer	1
	Stiff Layer Thickness	2 inches
	Stiff Layer Depth from Mudline	5 inches
	Shear strength ratio of stiff layer over soft	2
Case 7 Stiff Layer – Anchor Expected to Penetrate into but not Through Stiff Layer	Su at mudline	13 psf
	Su gradient	0 psf/ft
	Sensitivity of soft layer	1
	Stiff Layer Thickness	2 inches
	Stiff Layer Depth from Mudline	6 inches
	Shear strength ratio of stiff layer over soft	2

7.5.4 Experimental and Analytical Results

As summarized in Table 7.18, Flying Wing Anchor ® penetrates through the stiff layer in case 1, case 2, case 4, and case 5. The minimum release height enables anchor penetrates through the stiff layer is summarized in Figure 7.31. Table 7.19 to Table 7.26, and Figure 7.36 to Figure 7.42 summarize the impact velocity and embedment depth from tests and predictions with different strain rate effect functions. All the experimental and analytical results are shown in Appendix H

From these summaries, the conclusions for the Flying Wing Anchor® in layered soil profiles are:

- The Flying Wing Anchor® can penetrate into stiff layer in all layered soil profiles prepared in this study. For the cases with stiff layer at relative shallow depth (less than 1 effective fluke width or length), DEA slides on the top of stiff layer and pitch forward without diving deeper in the cases where stiff layer is one fluke length below the mudline, but FWA can penetrate into or through the stiff layer even less than 1fluke width. For the cases with stiff layer at relative deeper depth (more than 1 fluke length or width), DEA can penetrate through the stiff layer with a thin loading line. However, there is no line thickness restriction for FWA.
- For the cases FWA penetrates through the stiff layer:
    - When the thickness of stiff layer is less than half of the effective fluke width, the higher shear strength ratio requires higher release height for FWA to penetrate through stiff layer. Compare case 4 and case 1, the 1 inch stiff layer starts at 3 inches below mudline, the shear strength ratio

of stiff layer over surrounding soft soil is 2 and 1.5 for case 4 and 1, respectively; the impact velocity for FWA to penetrate through stiff layer is 15.79 ft/s and 15.22 ft/s respectively (Figure 7.31).

- When the thickness of stiff layer is less than half of the effective fluke width, the shallower depth of stiff layer requires higher release height for FWA to penetrate through the stiff layer. Compare case 2 and case 4, the shear strength ratio and thickness of stiff layer in these two cases are the same, but the depth of stiff layer is different, 1.5 inch for case 2, and 3 inches for case 4. From Figure 7.31, the minimum impact velocity for anchor penetrate through the stiff layer is 17.19 ft/s and 15.79 ft/s for case 2 and case 4, respectively. To penetrate a shallower stiff layer depth, it requires higher kinematic energy since the maximum velocity being achieved is below mudline (Figure 7.32), thus the anchor may reach the shallower stiff layer first before reaching its maximum velocity which lowers the kinematic energy input before reaches the stiff layer. To compensate the loss of velocity (kinematic energy) by early encountering stiff layer, a higher release height is required (Figure 7.31).
- A shallower stiff layer with thicker thickness may require higher release height to penetrate through compared with the case where a thinner stiff layer at a deeper depth. Comparing Case 5 and Case 1, the shear strength ratio in two cases are around 1.7, the depth of stiff layer is 2.5 inches and 3 inches, respectively, and the thickness of stiff layer is 2

inches and 1 inch, respectively; the minimum height for anchor penetrate through the stiff layer in case 5 and case 1 is 19.05 ft/s and 15.22 ft/s. This comparison leads to a conclusion that higher release height is required to penetrate a thicker stiff layer (Figure 7.31).

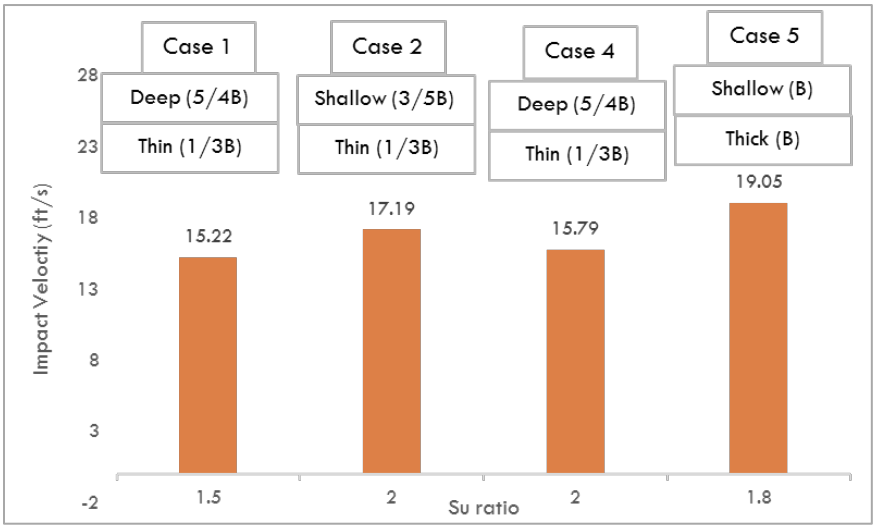

Figure 7.31. Minimum Release Height to Penetrate Through Stiff Layer

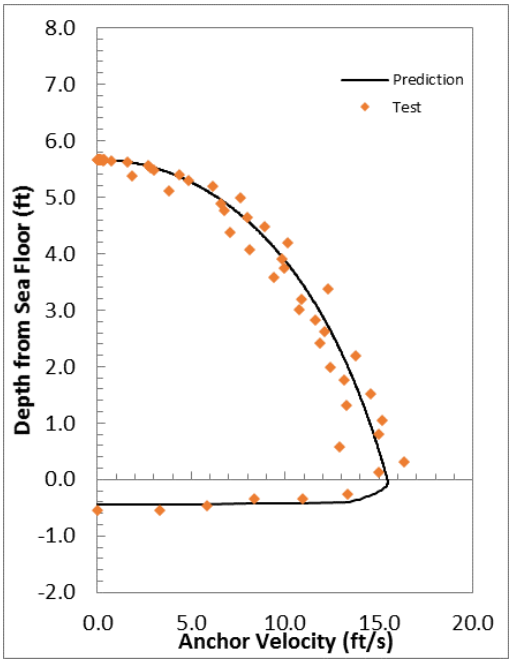

Figure 7.32. Example of Anchor Trajectory by Experimental and Analytical Results

- For the cases FWA model penetrates into the stiff layer but not through:
    - From Figure 7.33, the shear strength of stiff layer is over 3 (the undrained shear strength is 40 psf), the FWA model can penetrate into the stiff layer but not through the stiff layer. Comparing case 3 and case 5, the anchor can penetrate through the stiff layer in case 5, but only can penetrate into stiff layer in case 3. The depth of stiff layer is the same for two cases, the shear strength in case 3 is a stiffer thinner layer (1-inch thick with undrained shear strength of 42 psf), and in case 5 is a relative softer thicker layer (2-inch thick with undrained shear strength of 24 psf). The FWA model can penetrate through the thicker softer layer, but only into the thinner stiffer layer.
    - From Figure 7.34, the FWA model can only penetrate into but not through the deeper stiff layer (deeper than 1.5 fluke length). Compare case 5, case 6, and case 7; the shear strength ratio, the thickness of stiff layer is the same, but the depth of stiff layer in each case is different. The anchor can penetrate through the shallowest stiff layer (case 5), but only penetrate into but not through the deeper stiff layers (case 6 and case 7).

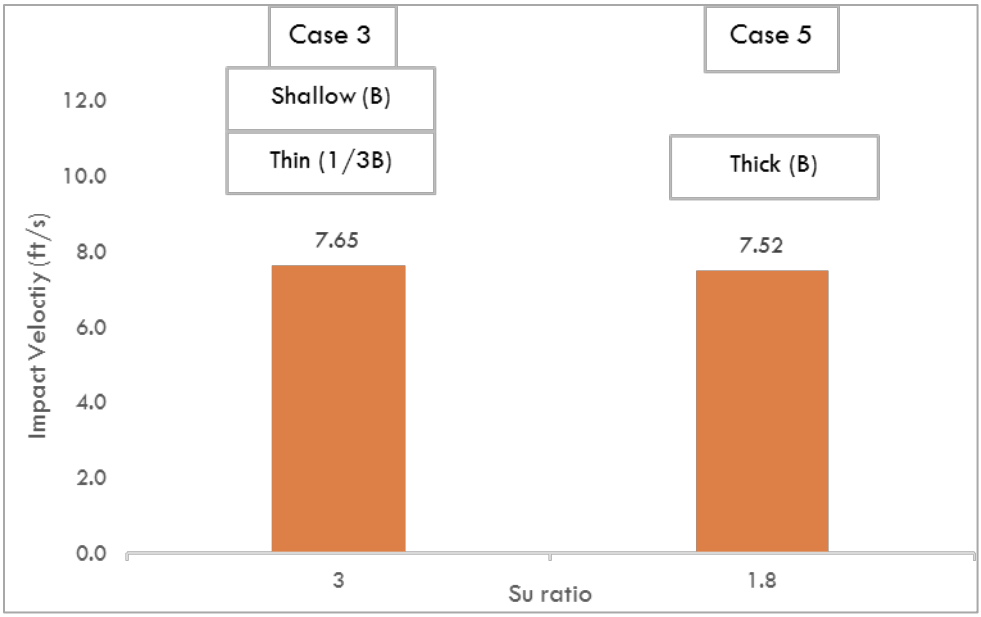

Figure 7.33. Comparison between Case 3 and Case 5

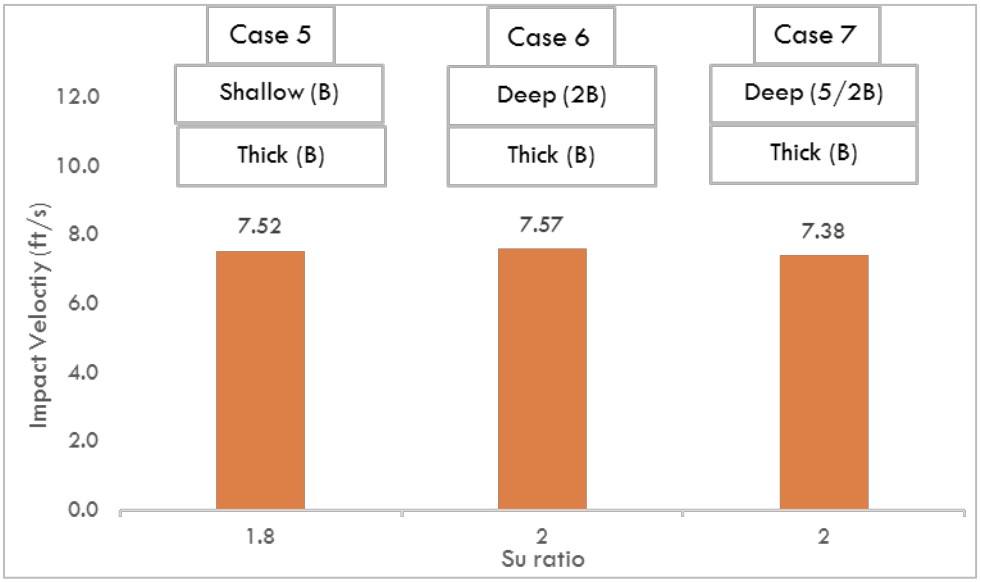

Figure 7.34. Comparison between Case 5, Case 6 and Case 7

- Comparing the predicted and experimental results including displacement-velocity curve, impact velocity, and embedment depth, we can conclude that
    - the displacement-velocity by the predictions with different strain rate functions yields similar results and all can match well with the

experimental results. One example is shown in Table 7.19 and Figure 7.35.

- the predicted embedment depth and velocity by analytical model with different strain rate function is close; however, the prediction model underestimates the final embedment depth (Table 7.20 to Table 7.26 and Figure 7.36 to Figure 7.42). For example, the prediction models predict the anchor can only penetrate into the stiff layer but not through for case 1, which is different from the experimental results that the anchor penetrates through the stiff layer. Additionally, the anchor can experimentally penetrate into the stiff layer in case 6 and case 7, but the prediction model predicts the anchor cannot penetrate into the stiff layer. The parameters used in the prediction model are the same as described in Table 7.6.

Table 7.19. Experimental and Analytical Impact Velocity and Embedment Depth (1st repeat in Case 1)

	Impact v (ft/s)	Embedment D (L_f)	β	λ
Experiment	15.41	2.95	–	–
R_f in Power-Law	15.41	2.03	0.1	–
R_f in Semi-log	15.41	2.07	–	0.2

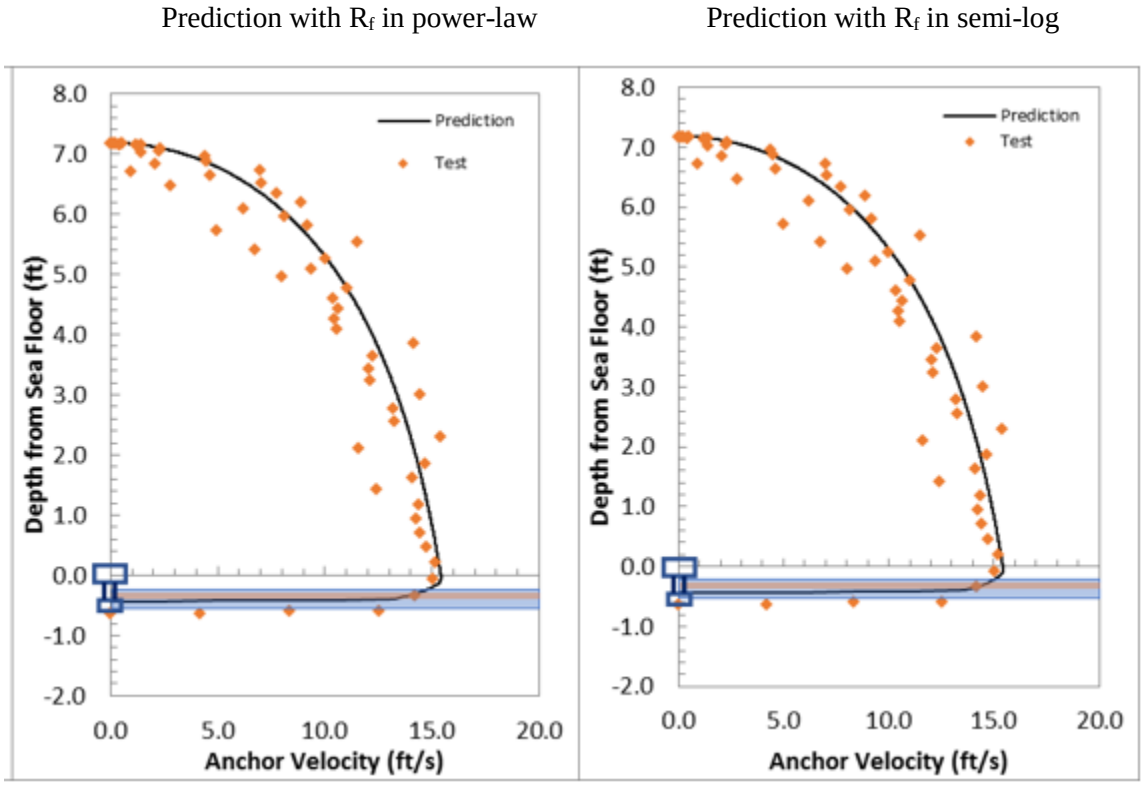

Figure 7.35. Comparison Between Predicted and Experimental Displacement-Impact Velocity Curve

Table 7.20 Experimental and Analytical Impact Velocity and Embedment Depth in Case 1

	Experimental Results				Prediction by Power-Law			Prediction by Semi-Logarithmic		
Test	h (ft)	z (ft)	v (ft/s)	Penetrate Through or Into	z (ft)	v (ft/s)	Penetrate Through or Into	z (ft)	v (ft/s)	Penetrate Through or Into
1	7.65	-0.67	16.54	Through	-0.47	17.66	Into	-0.48	17.66	Into
2	6.78	-0.63	16.85	Through	-0.47	17.03	Into	-0.47	17.03	Into
3	5.46	-0.59	16.67	Through	-0.46	15.86	Into	-0.46	15.86	Into
4	7.73	-0.67	19.05	Through	-0.48	17.72	Into	-0.48	17.72	Into
5	6.84	-0.63	16.87	Through	-0.47	17.08	Into	-0.47	17.08	Into
6	5.77	-0.59	16.00	Through	-0.46	16.16	Into	-0.46	16.16	Into

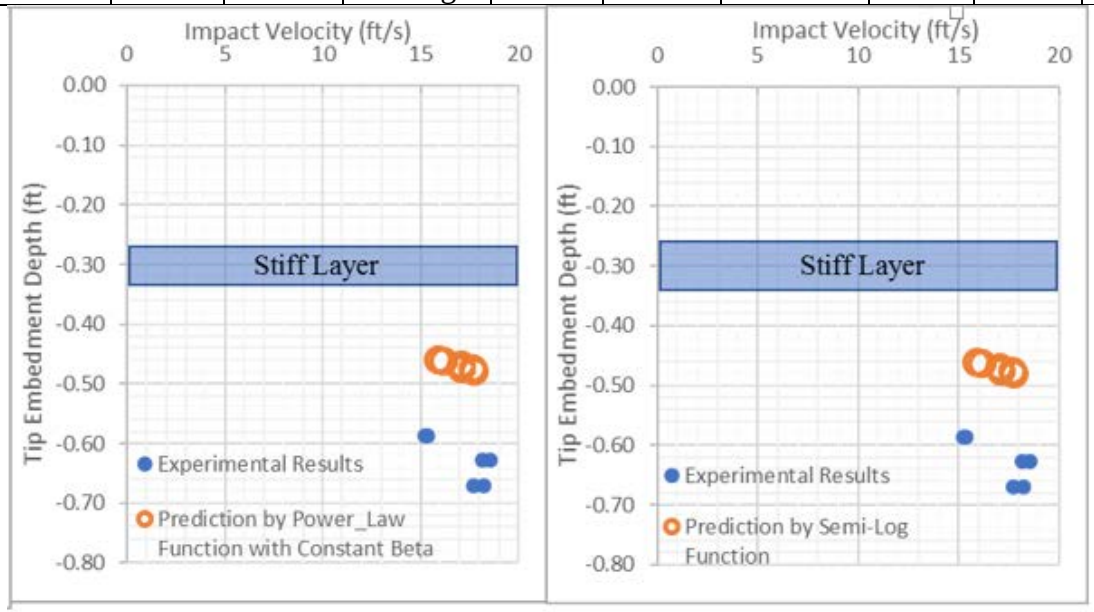

Figure 7.36. Experimental and Analytical Impact Velocity and Embedment Depth in Case 1

Table 7.21. Experimental and Analytical Impact Velocity and Embedment Depth in Case 2

	Experimental Results				Prediction by Power-Law			Prediction by Semi-Logarithmic		
Test	h (ft)	z (ft)	v (ft/s)	Penetrate Through or Into	z (ft)	v (ft/s)	Penetrate Through or Into	z (ft)	v (ft/s)	Penetrate Through or Into
1	7.88	-0.40	18.87	Into	-0.41	17.81	Into	-0.45	17.81	Through
2	6.93	-0.39	17.93	Into	-0.41	17.15	Into	-0.45	17.15	Through
3	6.14	-0.30	15.00	Into	-0.35	16.50	Into	-0.42	16.50	Into
4	7.88	-0.44	17.81	Through	-0.41	17.81	Into	-0.45	17.81	Through
5	7.01	-0.44	17.19	Through	-0.41	17.20	Into	-0.44	17.20	Through
6	6.16	-0.28	17.50	Into	-0.34	16.51	Into	-0.43	16.51	Through

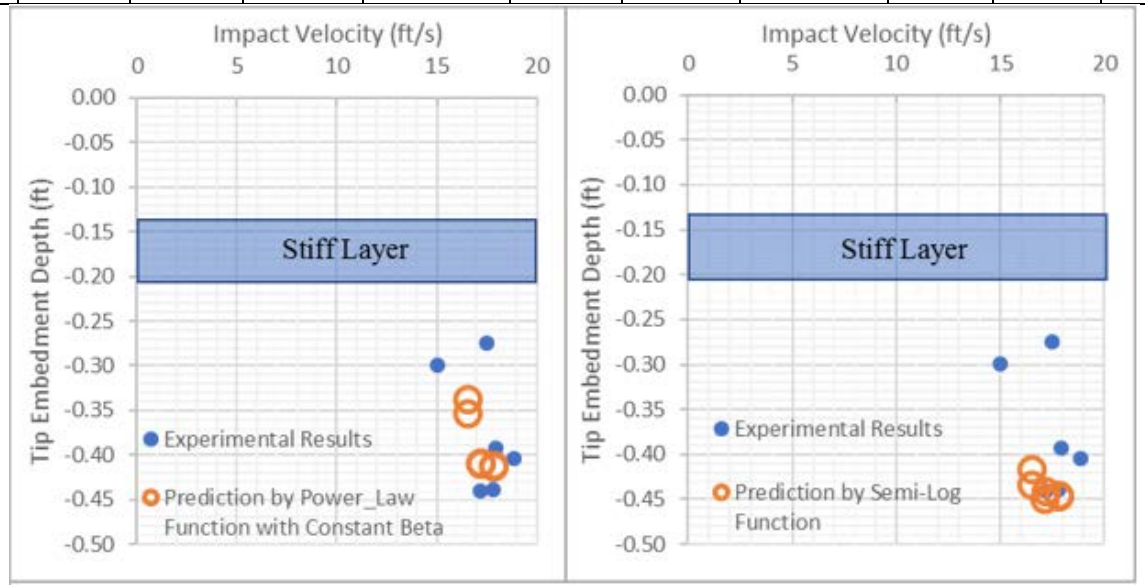

Figure 7.37. Experimental and Analytical Impact Velocity and Embedment Depth in Case 2

Table 7.22. Experimental and Analytical Impact Velocity and Embedment Depth in Case 3

	Experimental Results				Prediction by Power-Law			Prediction by Semi-Logarithmic		
Test	h (ft)	z (ft)	v (ft/s)	Penetrate Through or Into	z (ft)	v (ft/s)	Penetrate Through or Into	z (ft)	v (ft/s)	Penetrate Through or Into
7	7.60	-0.31	18.87	Into	-0.28	17.62	Into	-0.41	17.62	Into
8	6.83	-0.25	17.93	Into	-0.28	17.07	Into	-0.40	17.07	Into
9	6.04	-0.18	15.00	Not Into	-0.24	16.41	Into	-0.36	16.41	Into
10	7.65	-0.31	17.81	Into	-0.33	17.66	Into	-0.40	17.66	Into
12	6.93	-0.24	17.19	Into	-0.32	17.15	Into	-0.41	17.15	Into
13	6.23	-0.20	17.50	Not Into	-0.27	16.57	Into	-0.36	16.57	Into
11	6.97	-0.38	18.87	Into	-0.38	17.17	Into	-0.41	17.17	Into

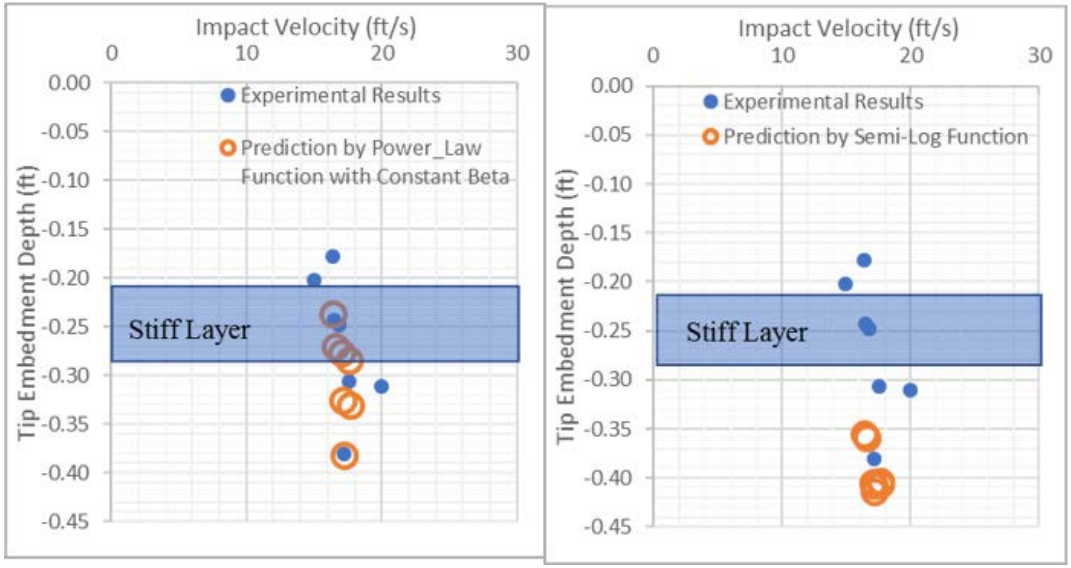

Figure 7.38. Experimental and Analytical Impact Velocity and Embedment Depth in Case 3

Table 7.23. Experimental and Analytical Impact Velocity and Embedment Depth in Case 4

	Experimental Results				Prediction by Power-Law			Prediction by Semi-Logarithmic		
Test	h (ft)	z (ft)	v (ft/s)	Penetrate Through or Into	z (ft)	v (ft/s)	Penetrate Through or Into	z (ft)	v (ft/s)	Penetrate Through or Into
4	7.06	-0.62	15.20	Through	-0.43	14.42	Into	-0.42	13.86	Into
5	6.24	-0.40	12.50	Into	-0.43	13.58	Into	-0.43	13.58	Into
6	5.50	-0.40	14.17	Into	-0.40	14.47	Into	-0.41	14.47	Into
7	7.19	-0.62	15.41	Through	-0.43	15.42	Into	-0.44	15.42	Into
8	6.12	-0.60	15.79	Through	-0.44	15.79	Into	-0.44	15.79	Into
9	5.66	-0.44	15.00	Into	-0.44	15.43	Into	-0.44	15.43	Into
10	6.35	-0.43	15.96	Into	-0.44	15.97	Into	-0.44	15.97	Into
11	6.66	-0.37	17.75	Into	-0.44	16.18	Into	-0.44	16.18	Into

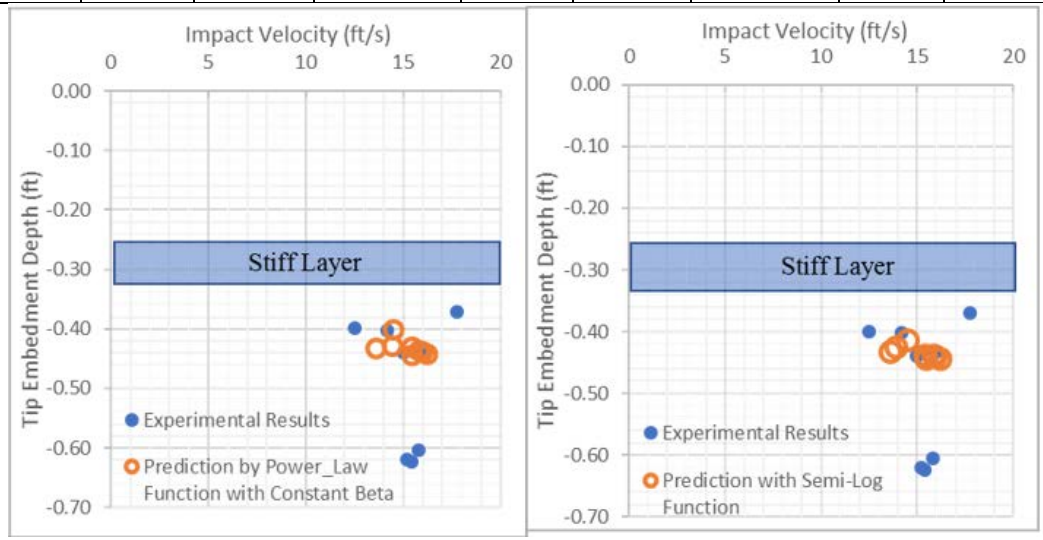

Figure 7.39. Experimental and Analytical Impact Velocity and Embedment Depth in Case 4

Table 7.24. Experimental and Analytical Impact Velocity and Embedment Depth in Case 5

	Experimental Results				Prediction by Power-Law			Prediction by Semi-Logarithmic		
Test	h (ft)	z (ft)	v (ft/s)	Penetrate Through or Into	z (ft)	v (ft/s)	Penetrate Through or Into	z (ft)	v (ft/s)	Penetrate Through or Into
7	7.58	-0.63	16.54	Through	-0.48	17.61	Into	-0.45	17.61	Into
9	6.66	-0.55	16.85	Into	-0.46	16.93	Into	-0.42	16.93	Into
10	5.73	-0.55	16.67	Into	-0.46	16.13	Into	-0.43	16.13	Into
13	7.52	-0.61	19.05	Through	-0.48	17.56	Into	-0.45	17.56	Into
11	6.58	-0.57	16.87	Into	-0.47	16.86	Into	-0.43	16.86	Into
12	5.61	-0.50	16.00	Into	-0.46	16.00	Into	-0.43	16.00	Into

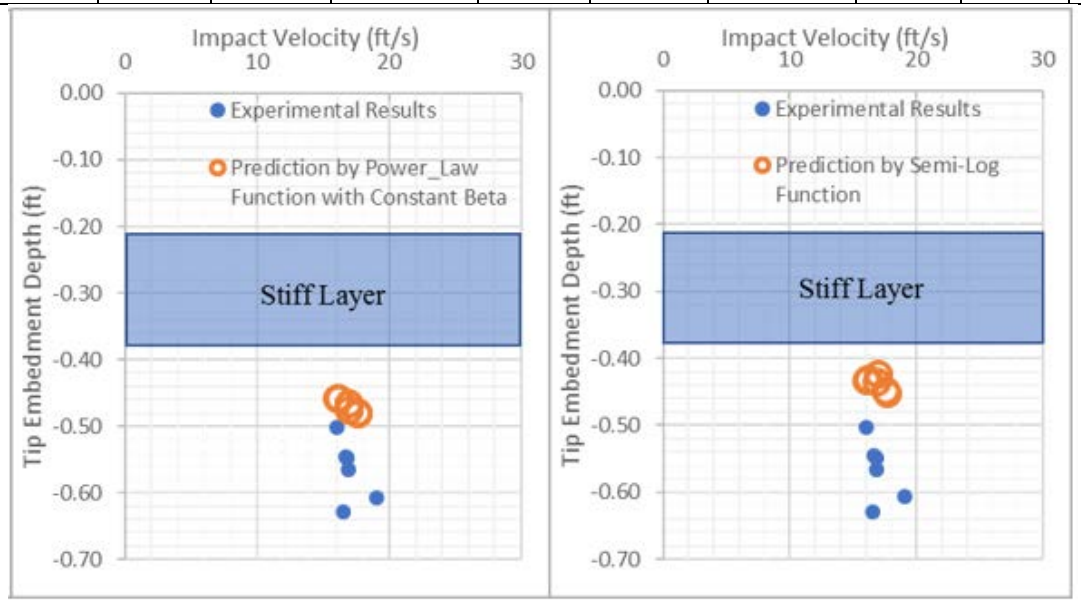

Figure 7.40. Experimental and Analytical Impact Velocity and Embedment Depth in Case 5

Table 7.25. Experimental and Analytical Impact Velocity and Embedment Depth in Case 6

	Experimental Results				Prediction by Power-Law			Prediction by Semi-Logarithmic		
Test	h (ft)	z (ft)	v (ft/s)	Penetrate Through or Into	z (ft)	v (ft/s)	Penetrate Through or Into	z (ft)	v (ft/s)	Penetrate Through or Into
1	7.32	-0.68	17.90	Into	-0.48	17.43	Into	-0.48	17.43	Into
2	6.63	-0.64	16.30	Into	-0.47	16.91	Into	-0.47	16.91	Into
3	6.54	-0.62	16.30	Into	-0.48	16.84	Into	-0.48	16.84	Into
6	7.57	-0.70	16.98	Into	-0.47	17.61	Into	-0.48	17.61	Into
5	6.55	-0.65	17.33	Into	-0.47	16.84	Into	-0.47	16.84	Into
4	5.70	-0.63	14.89	Into	-0.46	16.10	Into	-0.47	16.10	Into
7	7.66	-0.75	19.50	Through	-0.48	17.67	Into	-0.48	17.67	Into

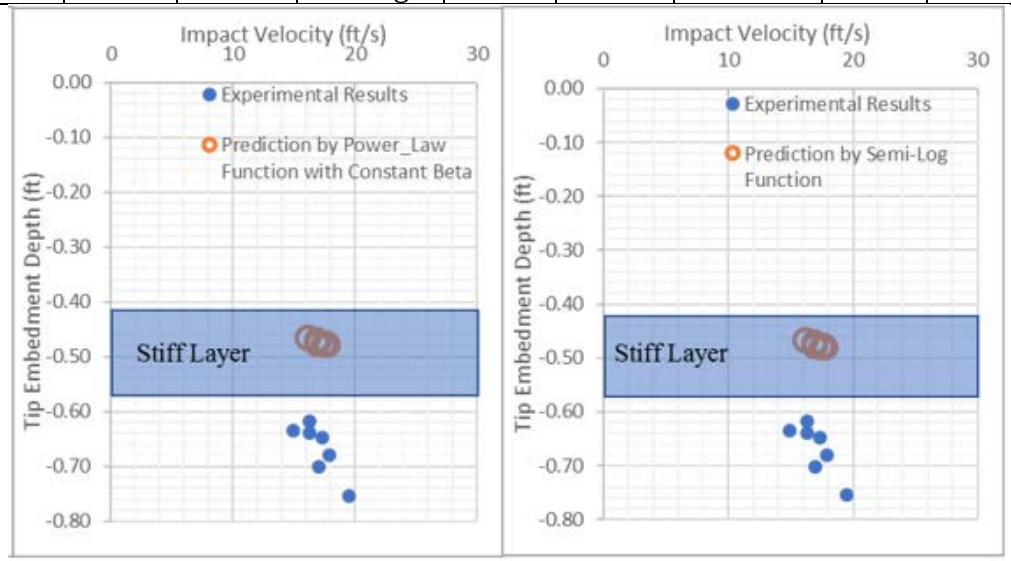

Figure 7.41. Experimental and Analytical Impact Velocity and Embedment Depth in Case 6

Table 7.26. Experimental and Analytical Impact Velocity and Embedment Depth in Case 7

	Experimental Results				Prediction by Power-Law			Prediction by Semi-Logarithmic		
Test	h (ft)	z (ft)	v (ft/s)	Penetrate Through or Into	z (ft)	v (ft/s)	Penetrate Through or Into	z (ft)	v (ft/s)	Penetrate Through or Into
8	7.34	-0.69	16.67	Into	-0.47	17.45	Not Into	-0.47	17.45	Not Into
9	6.37	-0.63	16.99	Into	-0.47	16.70	Not Into	-0.23	16.70	Not Into
10	5.73	-0.61	16.67	Into	-0.46	16.11	Not Into	-0.43	16.11	Not Into
14	7.38	-0.78	17.32	Into	-0.47	17.48	Not Into	-0.48	17.48	Not Into
13	6.83	-0.65	16.67	Into	-0.47	17.07	Not Into	-0.47	17.07	Not Into
11	5.75	-0.61	16.67	Into	-0.46	16.14	Not Into	-0.47	16.14	Not Into
12	6.62	-0.71	16.67	Into	-0.47	16.91	Not Into	-0.47	16.91	Not Into

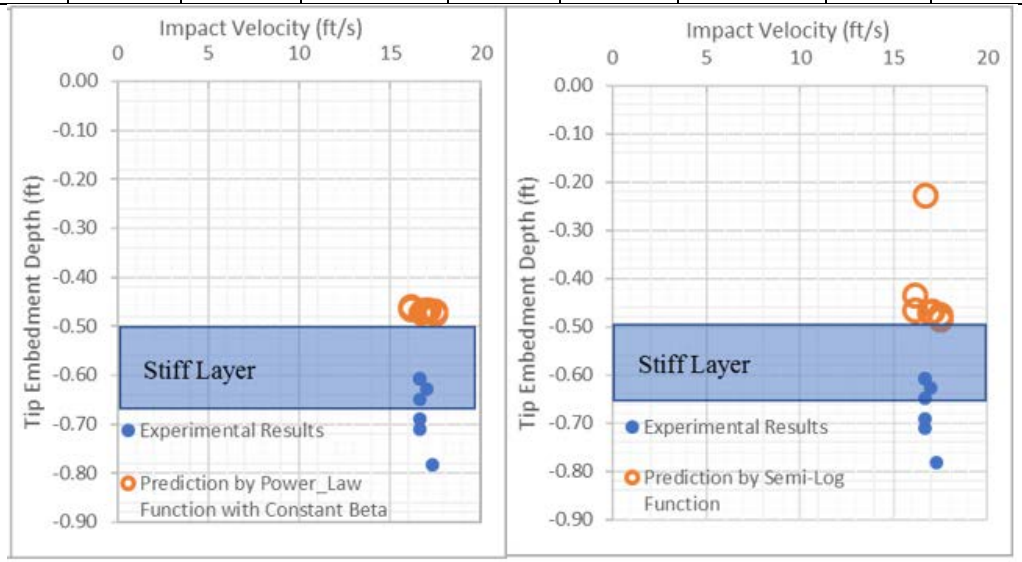

Figure 7.42. Experimental and Analytical Impact Velocity and Embedment Depth in Case 7

7.6 Conclusion

To investigate effects of strain rate in shearing versus bearing, T-bar tests and pure loading tests with a circular steel plate (0.1-in thick and 4-in diameter) in different orientations and at different loading rates are performed. From the tests result, the following conclusions can be obtained:

- The strain rate parameter obtained from T-bar tests at different loading rate is β equal to 0.05 for power-law function and λ equal to 0.12 for semi-logarithmic function.
- From the pure loading tests with the steel plate, the enhanced shear strength by increasing rate is in shearing is higher than in bearing. The shear strength starts being enhanced by bearing mechanism at the loading rate higher than 3.2 in/sec; however, the shear strength starts being enhanced by shearing mechanism at the loading rate higher than 0.8 in/sec. The maximum enhanced shear strength by bearing and shearing mechanism is 15% and 40%, respectively, and both are achieved at the loading rate with 8 in/sec.
- The strain rate parameters obtained from T-bar tests cannot fit the entire velocity range for pure bearing tests with steel plate, but only fit the lower velocity range. For the higher velocity range, the β with 0.15 and λ with 0.35 can better fit the tests results from pure bearing plate.
- The strain rate parameter for shearing mechanism is obtained by fitting pure in-plane shearing tests with thin steel plate, and the parameters are β with 0.15 in power-law function and λ with 0.35 for semi-logarithmic function. The strain rate parameter for power-law, β, and for semi-logarithmic, λ, is in the typical

range for strain rate parameters obtained from back-calculated β and λ from dynamically installed anchor tests.

- This strain rate parameter obtained from in-plane shearing tests are applied to the predict embedment depth for Flying Wing Anchor® since 87% area in Flying Wing Anchor acts as shearing surface.

From the free-fall penetration tests with Flying Wing Anchor®, the following conclusions are drawn:

- In the constant shear strength profile, the embedment depth from experiment and prediction matches well.
- In layered soil profiles, the Flying Wing Anchor® can penetrate through a shallow stiff layer that the DEA is unable to penetrate. Additionally, Flying Wing Anchor® can penetrate into the deeper stiff layer where DEA cannot penetrate. This finding implies that Flying Wing Anchor® is a possible solution for layered soil profiles in deepwater.

Based on free-fall penetration tests of the Flying Wing Anchor® with different ratios of the weight to surface area (up to 22), the test results match well with the prediction model. Therefore, this model can likely be used to predict the free-fall penetration for a full-sized anchor, which will have a weight to area ratio that is about twenty-two as large as what has thus far been tested.

Chapter 8. Conclusions and Future Works

8.1 Conclusions

Constructing foundations for offshore structures in deepwater can be a significant cost. Layered soil profiles are common and can further increase the cost of foundations by hampering installation and performance. This research focuses on experimental model testing of plate anchors installed by drag or free-fall in layered soil profile, with the goal to improve understanding of anchor performance and to capitalize on this improved understanding to improve the efficiency of anchors in layered soils.

Objective 1 is to further understanding of the drag trajectory and capacity for a plate anchor in layered soil profiles. The first conclusion is that the ratio of normal to tangential displacement is affected by model scale, with smaller ratios applying to larger anchors. Therefore, the prediction models calibrated with small-scale model tests can be adjusted to better predict full-scale performance. The second conclusion is that the equilibrium capacity factor is not dependent on model scale, therefore, the small scaled equilibrium can be applied to a larger size anchor with the same shape. The third conclusion is that the calibrated analytical model based on simplified plasticity theory can predict anchor capacity, trajectory and pitch in a non-layered soil profile (with remolded soil or soil with sensitivity), including constant and linearly increasing shear strength profiles. The fourth conclusion is that the calibrated analytical results match well with experimental results (capacity, trajectory and pitch) in the layered soil profile with shear strength ratio of stiff layer over surrounding soft soil less than 1.5 (anchor can penetrate into stiff layer) or greater than 5 (anchor cannot penetrate into stiff layer). The fifth conclusion is that the analytical model can predict capacity but cannot capture anchor trajectory and pitch when

the shear strength ratio for the layers is between 2 to 4. The analytical model predicts the anchor can penetrate into a stiff layer with shear strength between 2 to 4 times greater than the surrounding soil, however, only about half of the tests show that the anchor experimentally penetrates into stiff layer. The key factor in whether or not the anchor will penetrate the stiff layer is the pitch of the fluke as it approaches the layer; the pitch needs to be at about 30° for the best potential to penetrate. The sixth conclusion is that analytical model cannot capture anchor behavior in the layered soil profile with a stiff layer at a shallower depth. Experimentally, the anchor does not reach its equilibrium point before hitting the stiff layer and pitches forward as well as plowing on the top of stiff layer; however, the analytical model assumes the anchor is at the equilibrium point at the beginning and will follow the equilibrium trajectory and therefore to penetrate into stiff layer without pitching forward.

Objective 2 is to further understanding of the drag trajectory and capacity of tandem anchor systems. The first conclusion is that the total anchor capacity increases with an increase of spacing between the front anchor and the piggy-back anchor. The second conclusion is that the total capacity of the piggy-back configuration is greater than twice the capacity of a single anchor, provided that the spacing between the anchors is at least two fluke lengths. The third conclusion is that the piggy-back anchor is able to dive deeper than both the front anchor and a single anchor, and it is also possible for the front anchor to dive deeper than a single anchor. The practical conclusion is that a tandem anchor system can achieve higher capacity with less penetration compared with installing two anchors separately.

Objective 3 is to further understanding of the free-fall penetration trajectory and resistance of a dynamically embedded plate anchor in layered soil profiles. The first conclusion is that the strain rate effect from shearing is higher than that from bearing as measured from pure normal and pure in-plane shearing tests at loading rate from 0.8 in/sec to 8 in/sec. The strain rate parameters β equal to 0.15 (power law) and λ equal to 0.35 (semi-log law) from pure in-plane shearing tests with a steel plate is applied to the analytical model of free-fall penetration with Flying Wing Anchor®. The calibrated predication model with these strain rate parameters produces results similar to the test results, generally matching or slightly under-predicting the actual penetration in non-layered and layered soil profiles. The second conclusion is that in the layered soil profile, the ability to penetrate into and through the stiff layer increases with decreasing shear strength of the stiff layer, decreasing thickness of the stiff layer, increasing depth of the stiff layer, increasing impact velocity and increasing weight-to-area ratio for the anchor. For the model anchor, the anchor was able to penetrate through stiff layers with undrained shear strengths three times greater than the surrounding soil, depths to the top of the stiff layer as shallow as 1/3 fluke lengths, and thicknesses of the stiff layers as much as 5/6 fluke lengths.

Objective 4 is to develop and explore concepts to improve anchor performance in layered soil profiles. The first conclusion is that a conventional drag embedment anchor can penetrate through the stiff layer with shear strength 50% higher than the surrounding soil and cannot penetrate into the stiff layer with shear strength 5 times higher than the surrounding soil. The second conclusion is that it is less likely for a conventional drag embedment anchor to penetrate into a stiff layer with shear strength between 2 to 4 times

higher than the surrounding soil. Whether the anchor can or cannot penetrate into stiff layer with s_u ratio of 2 to 4 depends on the depth of stiff layer and the anchor line thickness. The drag embedment anchor is less likely to penetrate into the stiff layer at shallower depth (shallower than one fluke length) and being dragged with chain due to its steep pitch (around 50°). The third conclusion is that attaching two drag embedment anchor together to achieve a tandem anchor system can provide a capacity more than twice the capacity from a single anchor provided that the spacing between two anchors is at least two fluke lengths. The second anchor in tandem system can penetrate deeper than a single anchor and the front anchor. The fourth conclusion is that a dynamically embedded plate anchor can penetrate through the stiff layer with shear strength at least three times greater than the surrounding soft soil. The fifth conclusion is that one dynamically embedded anchor, the Flying Wing Anchor®, can penetrate through a shallow stiff layer (shallower than one fluke length) while a conventional drag embedment anchor will stand up on the surface of stiff layer and pitch forward without diving. If the terminal velocity can be achieved in the field, the Flying Wing Anchor® can readily penetrate through a stiff layer with a shear strength 3 times greater than the surrounding soil if the layer is one fluke-length thick and up to two fluke-lengths deep. For a stiff layer that is one fluke-length deep and 1/2 fluke-lengths thick, the Flying Wing Anchor® can penetrate the stiff layer even if its shear strength is 40 times greater than the surrounding soil. Based on above conclusion, it implies that Flying Wing Anchor® is possible solution for layered soil profiles in deepwater.

8.2 Recommended Future Work

The understanding for the drag embedment anchor in terms of capacities (pure bearing capacity, pure in-plane shearing capacity and pure rotational pitch capacity) can improved by involving shank into the plasticity based model. The analytical prediction model for the drag embedment anchor in layered soil profile can be further calibrated by involving a factor which can reduce pure rotational pitch capacity when anchor hits stiff layer and therefore it is more possible for anchor to rotate forward which is consistent with the experimental observations. The analytical model for tandem system anchors can be further improved by involving yield surface calculation for each anchor (which depends on the spacing between two anchor and interacts with each other when the spacing between two anchors is less than 2-fluke length). The strain rate effect on side shearing and bearing can be further understood by running pure in-plane shearing and bearing tests with different size of penetrometer to verify the conclusion obtained in current study. A larger Flying Wing Anchor® model can be tested in the free-fall penetration tests to verify the scale effect on extrapolation and to optimize Flying Wing Anchor® Design.

Appendices

Appendix A. Drag Embedment Tests with a Single Drag Embedment Anchor

Case 1

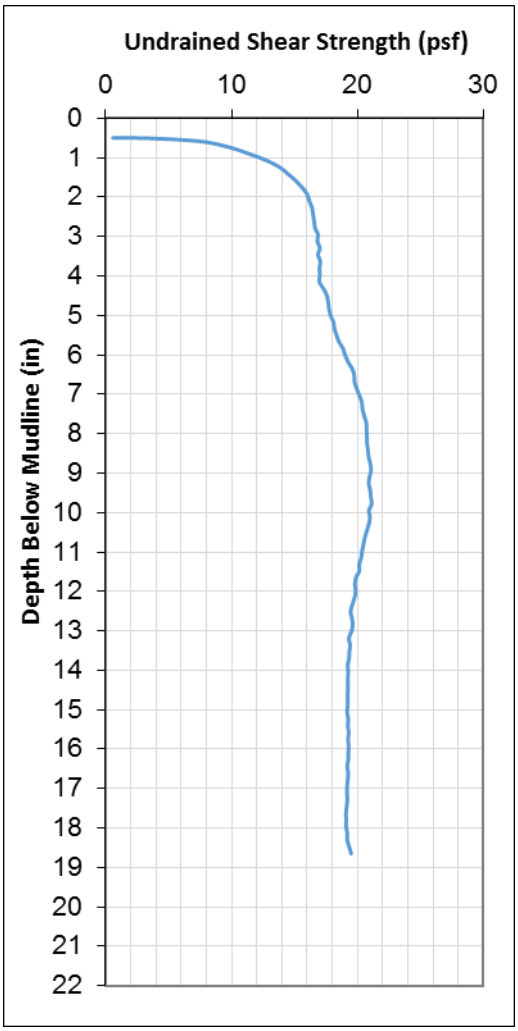

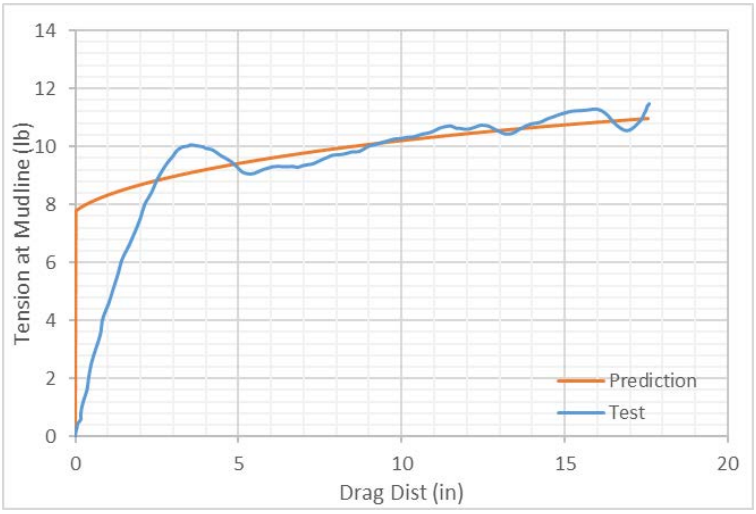

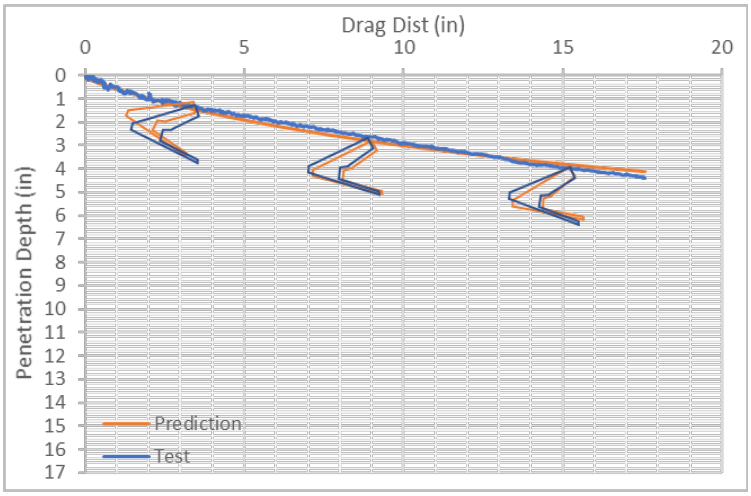

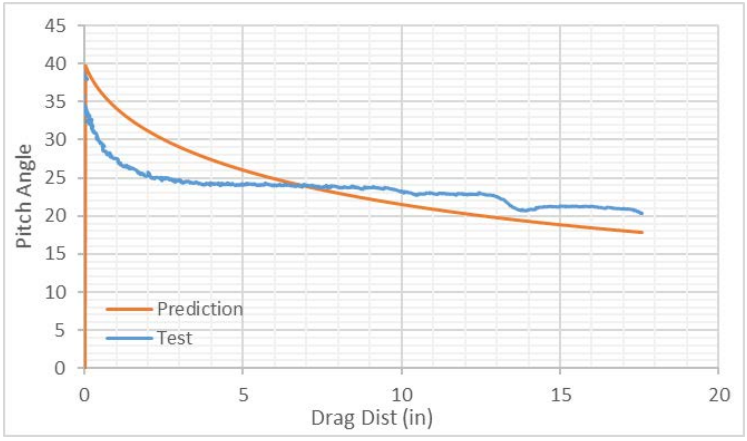

First repeat test in Case 1

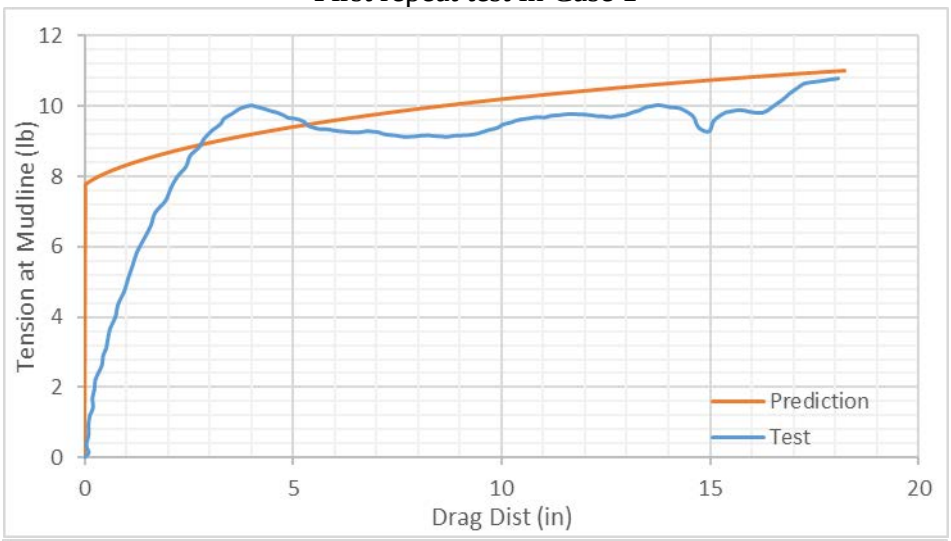

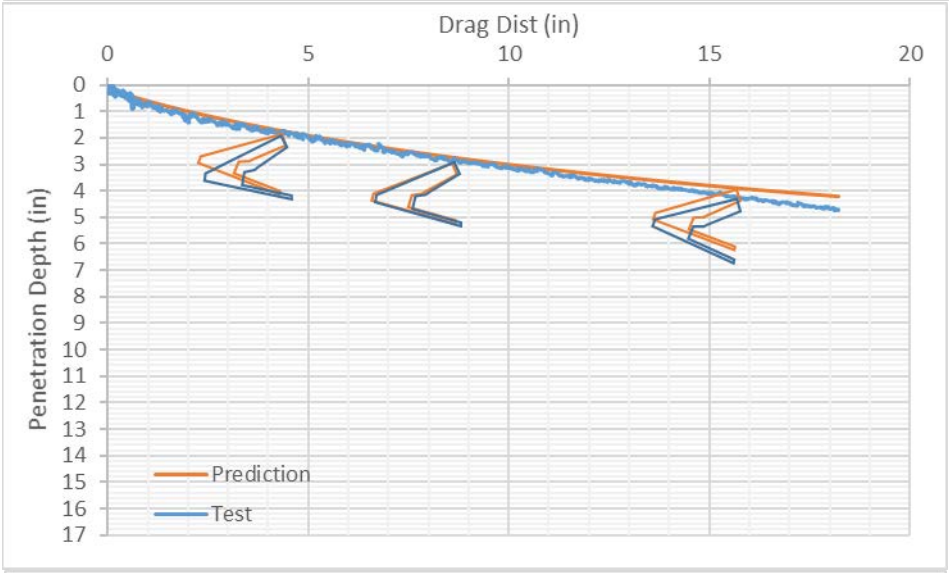

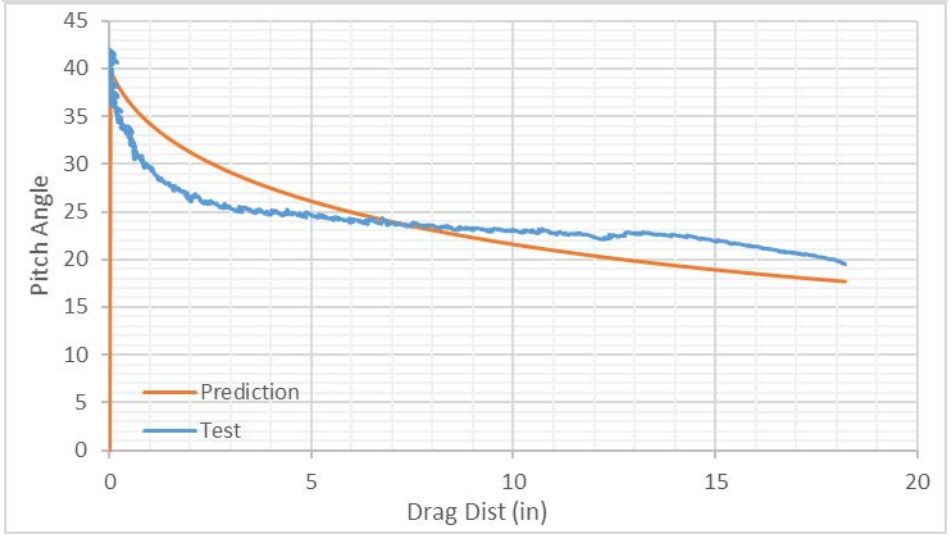

Second repeat test in Case 1

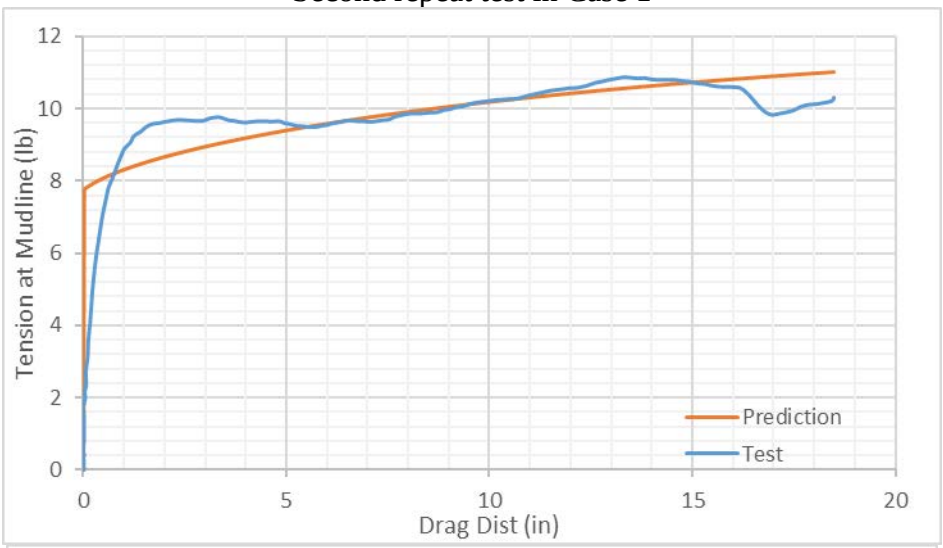

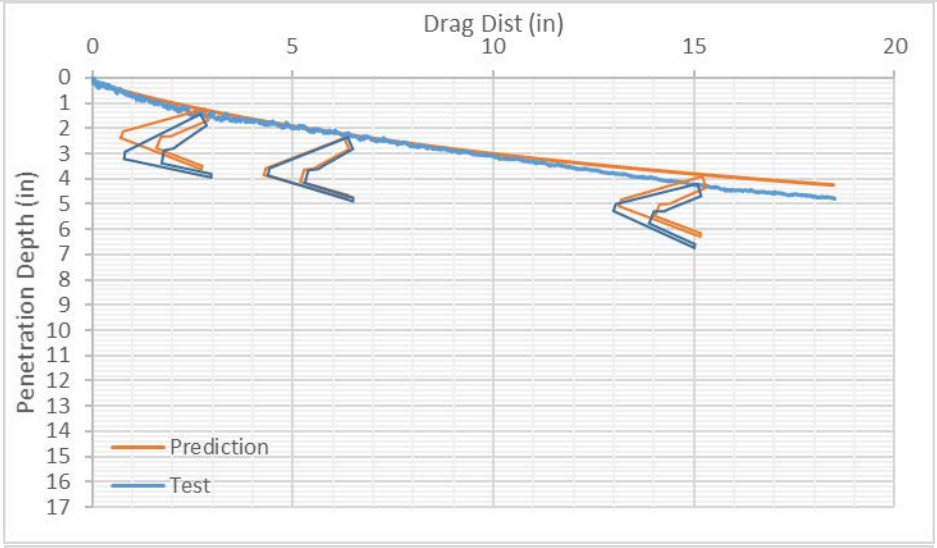

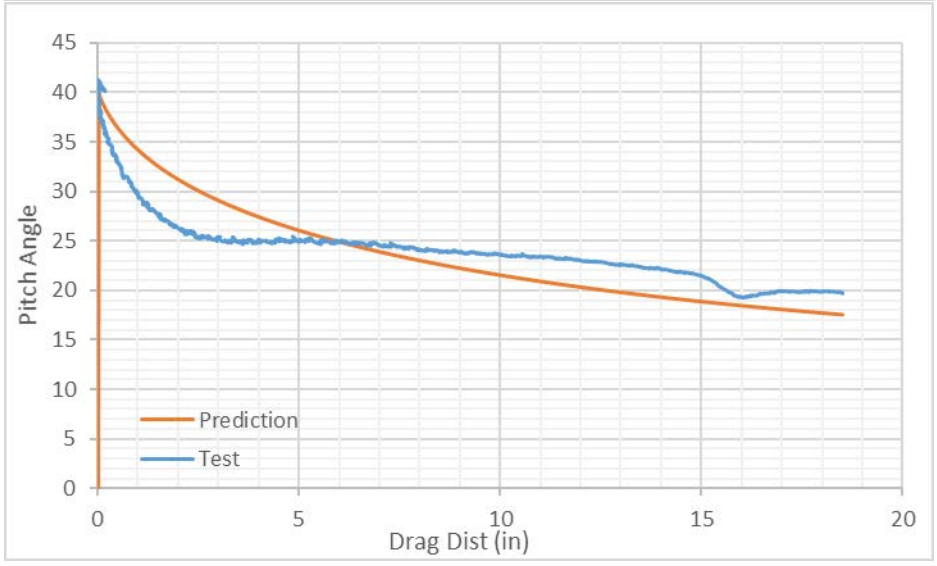

Case 2

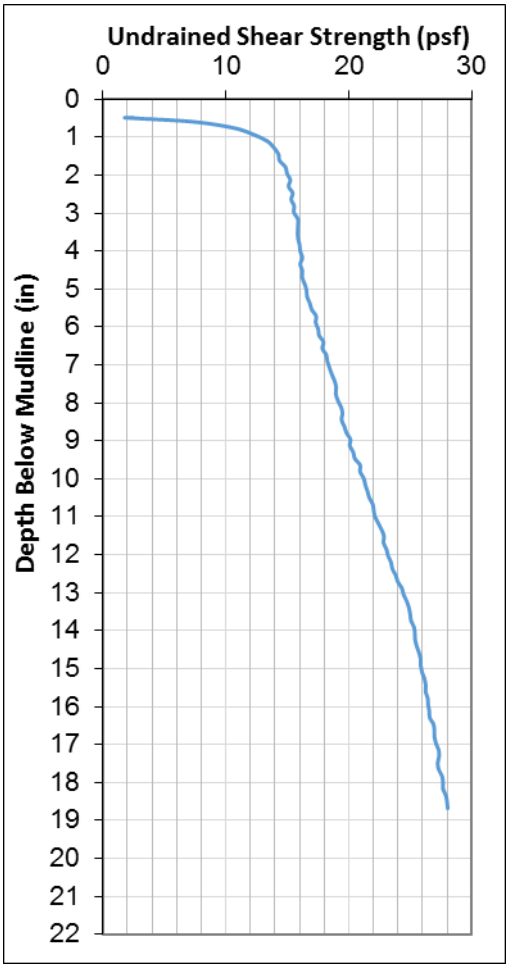
Undrained Shear Strength (psf)
0
10
20
30
Depth Below Mudline (in)
0
1
2
3
4
5
6
7
8
9
10
11
12
13
14
15
16
17
18
19
20
21
22

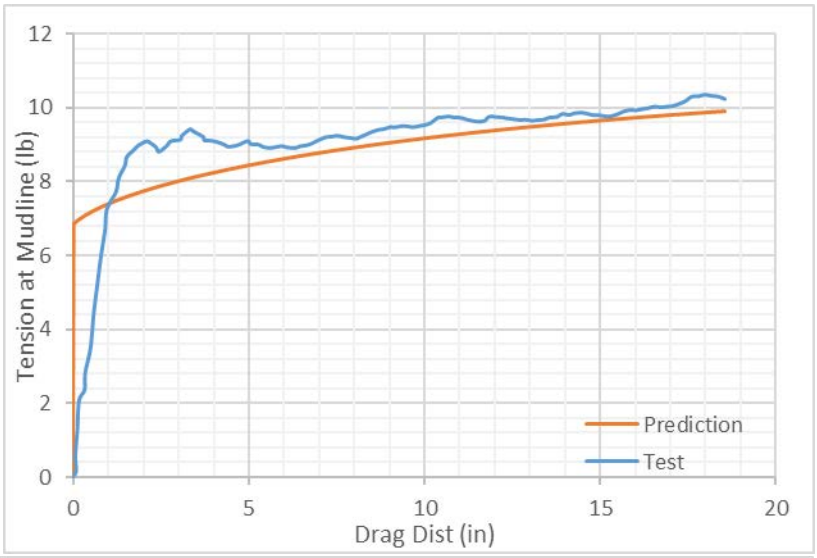
Tension at Mudline (lb)
0
2
4
6
8
10
12
0
5
10
15
20
Drag Dist (in)
Prediction
Test

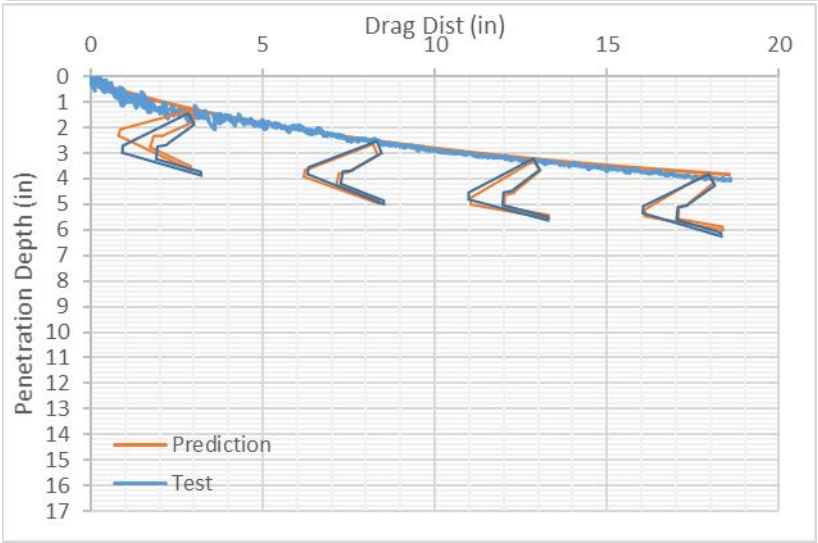
Drag Dist (in)
0
5
10
15
20
Penetration Depth (in)
0
1
2
3
4
5
6
7
8
9
10
11
12
13
14
15
16
17
Prediction
Test

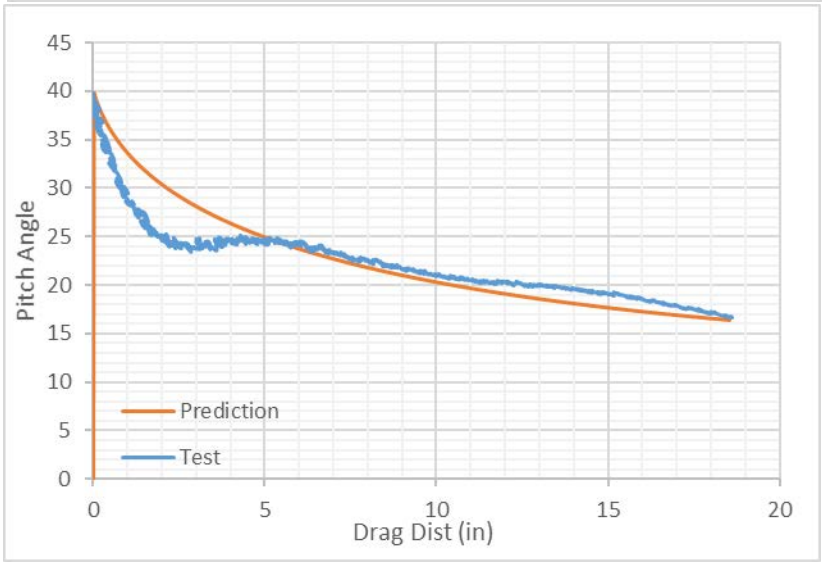
Pitch Angle
0
5
10
15
20
25
30
35
40
45
0
5
10
15
20
Drag Dist (in)
Prediction
Test

First Repeat Test in Case 2

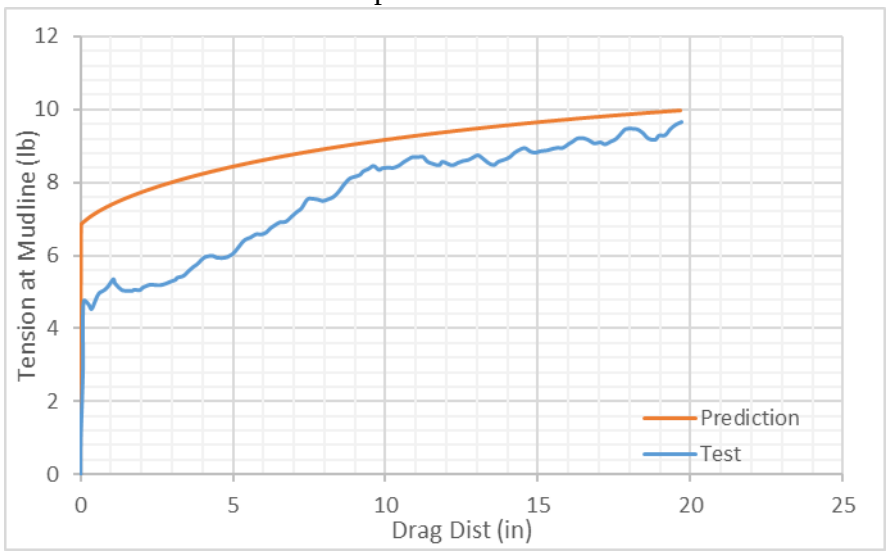

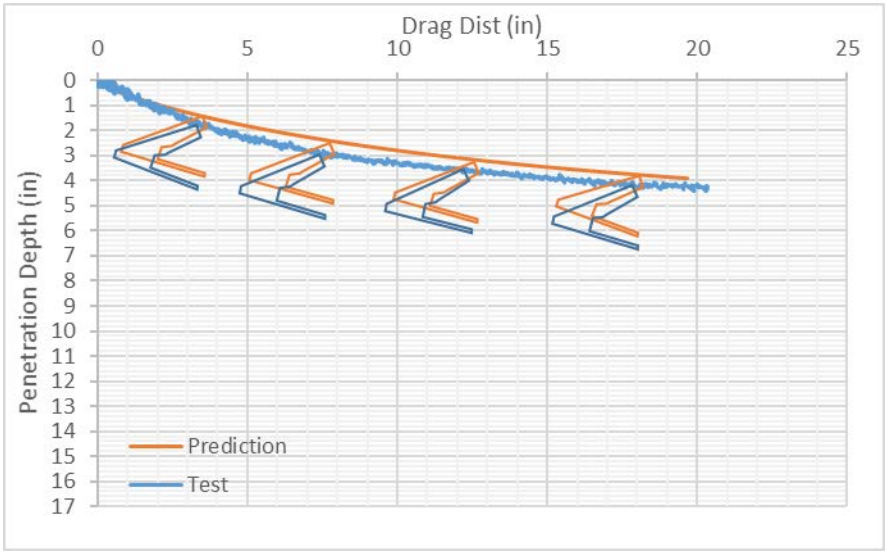

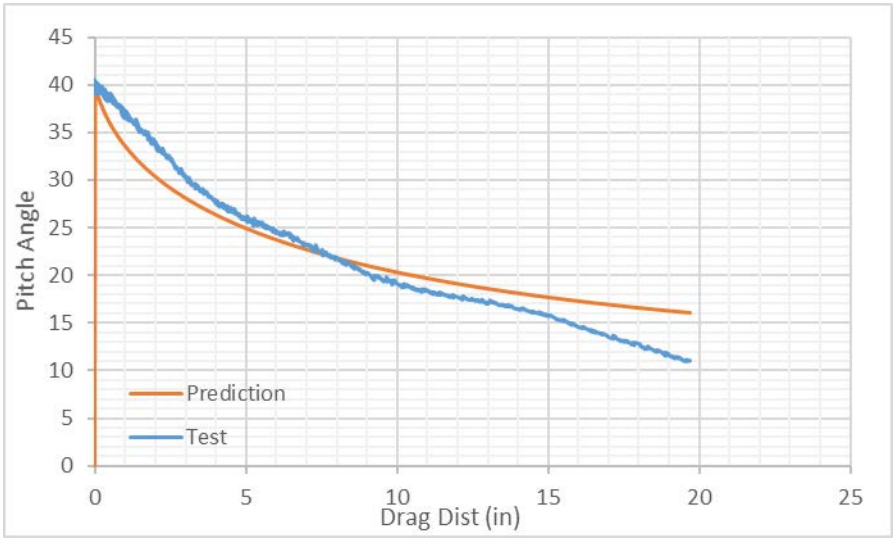

Second Repeat Test in Case 2

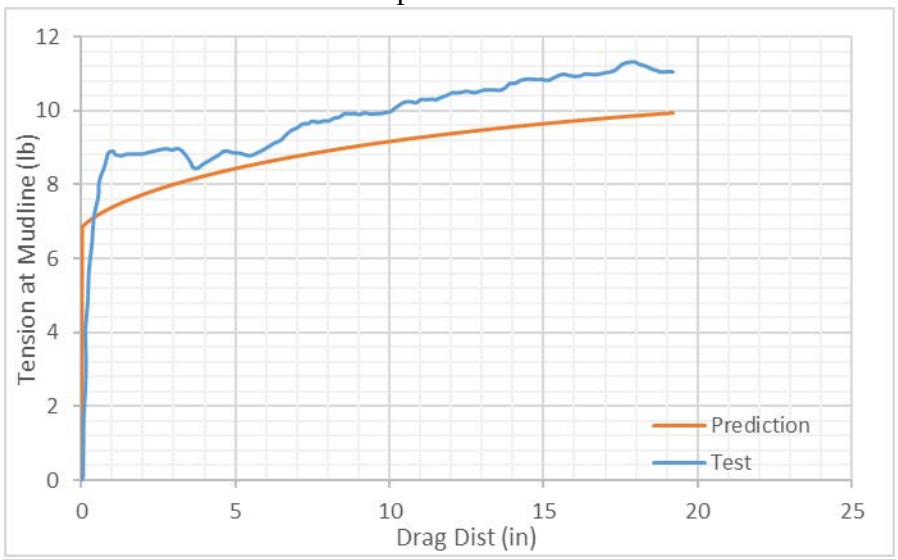

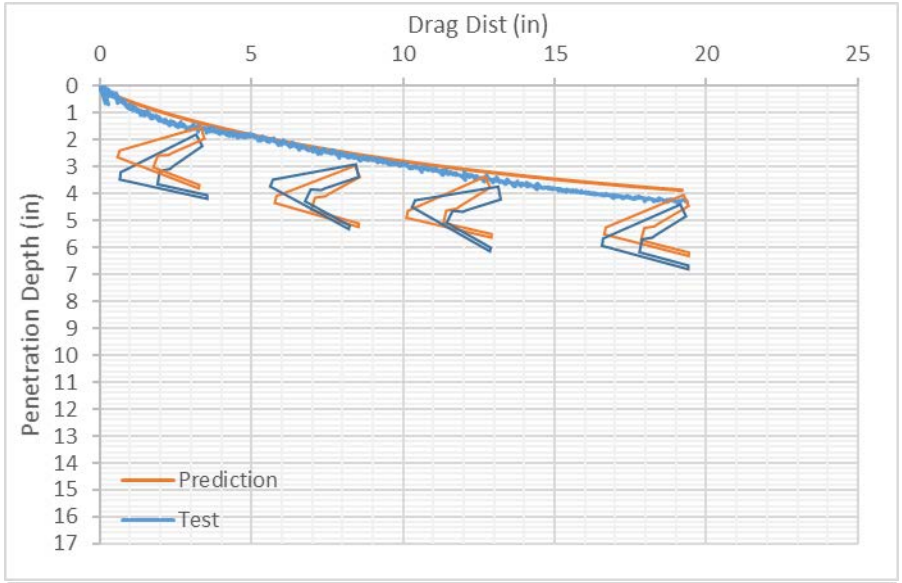

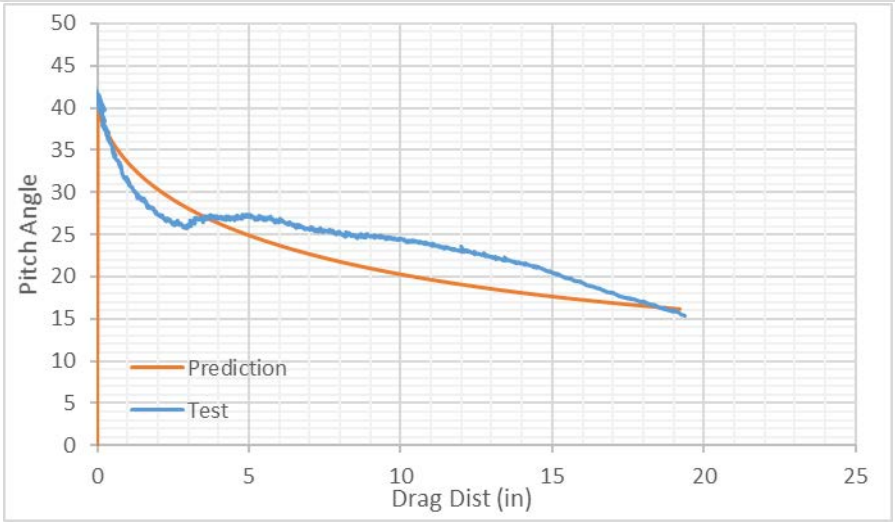

Third Repeat Test in Case 2

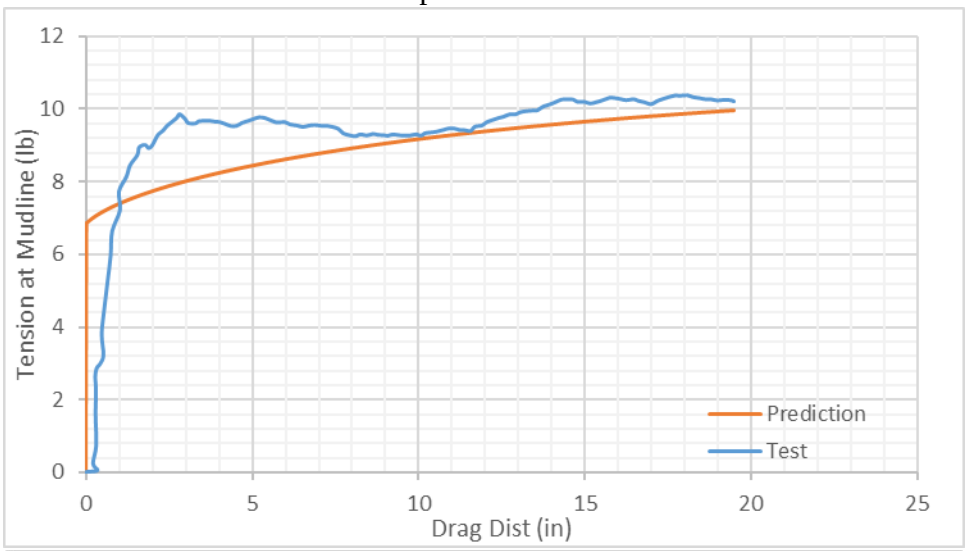

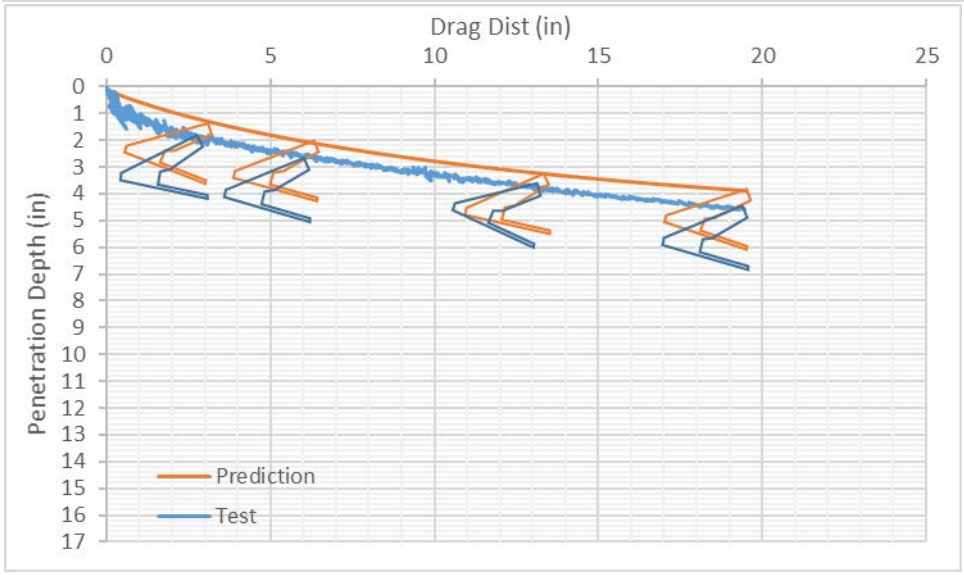

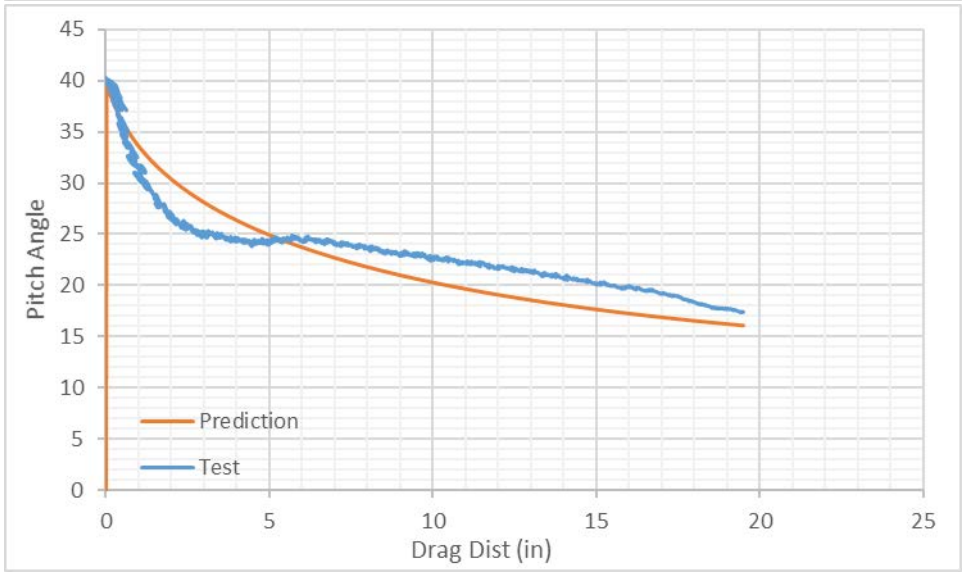

Forth Repeat Test in Case 2

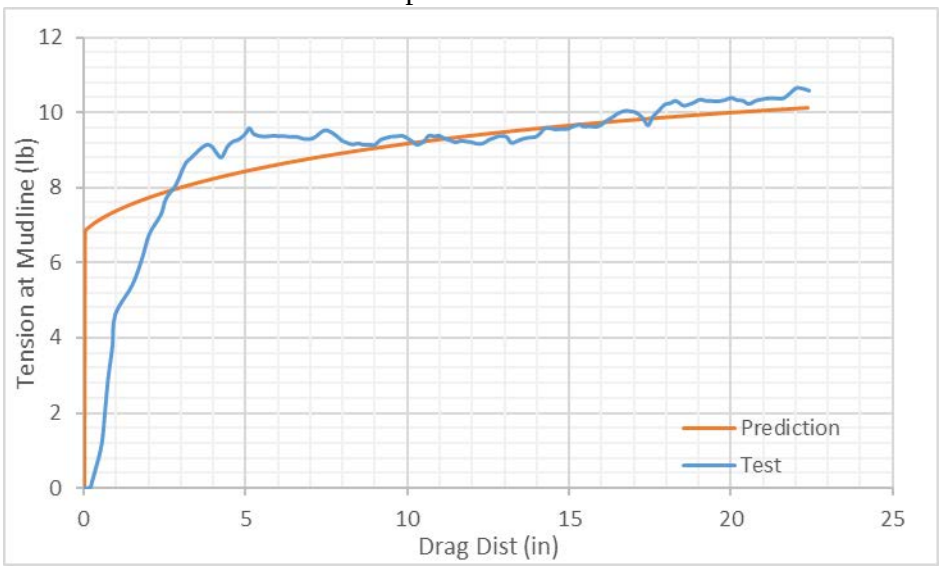

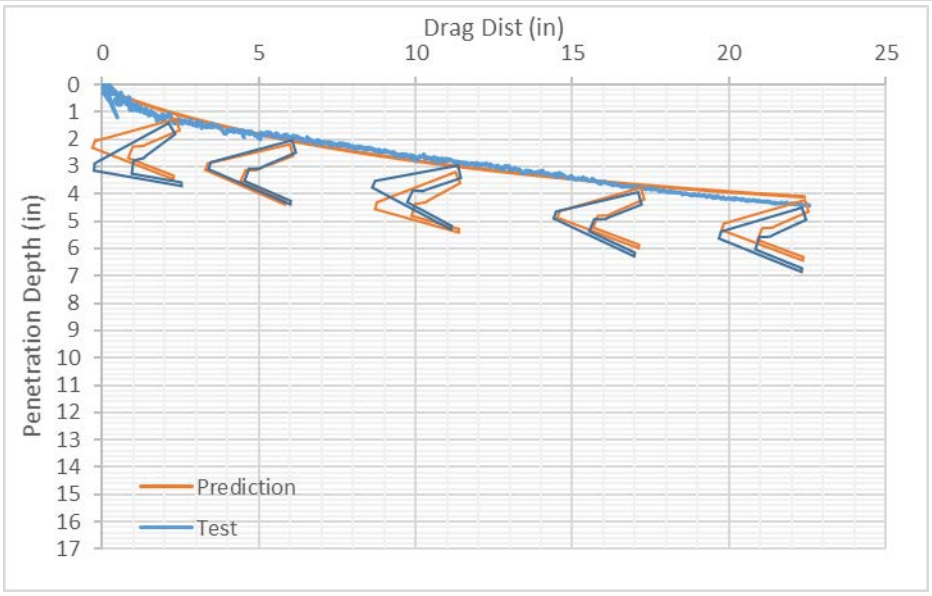

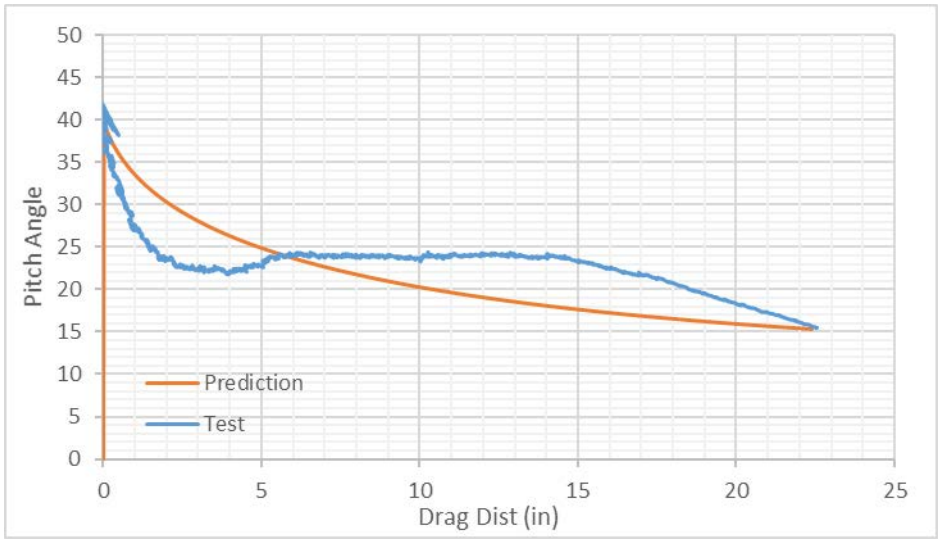

Case 3

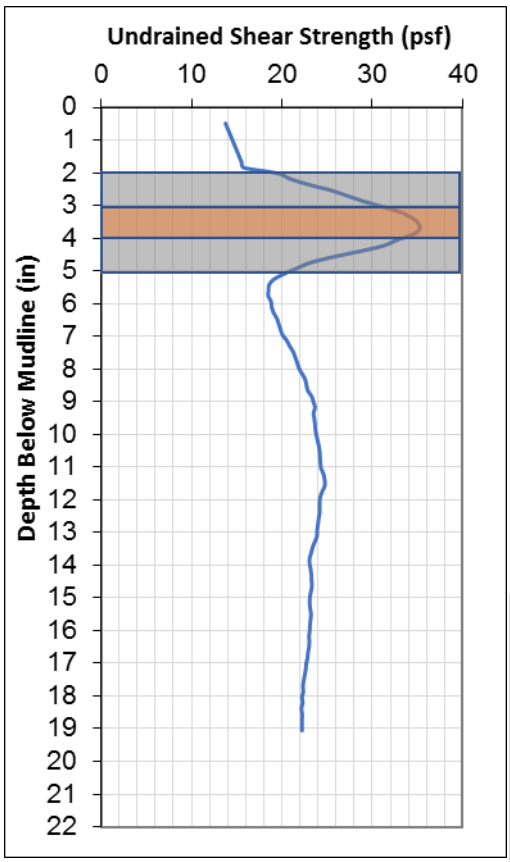
Undrained Shear Strength (psf)
0
10
20
30
40
Depth Below Mudline (in)
0
1
2
3
4
5
6
7
8
9
10
11
12
13
14
15
16
17
18
19
20
21
22

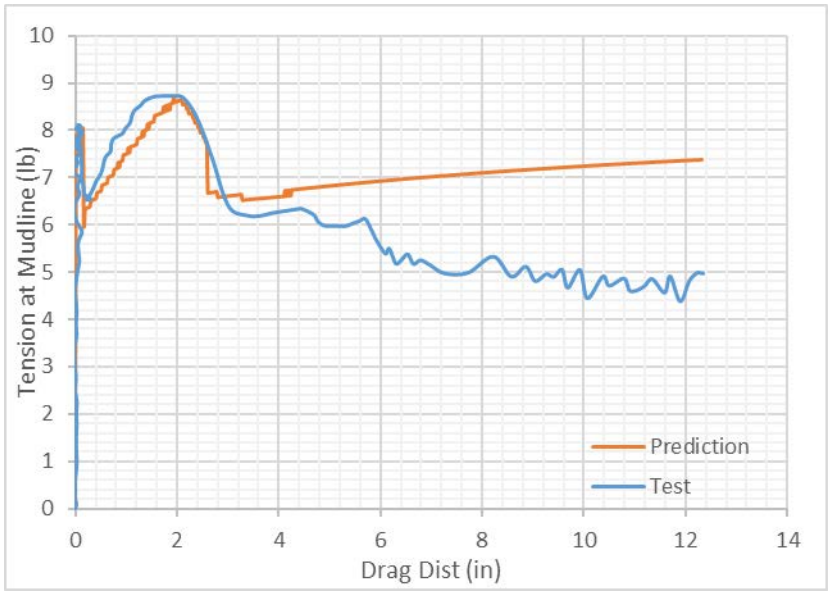
Tension at Mudline (lb)
0
1
2
3
4
5
6
7
8
9
10
0
2
4
6
8
10
12
14
Drag Dist (in)
Prediction
Test

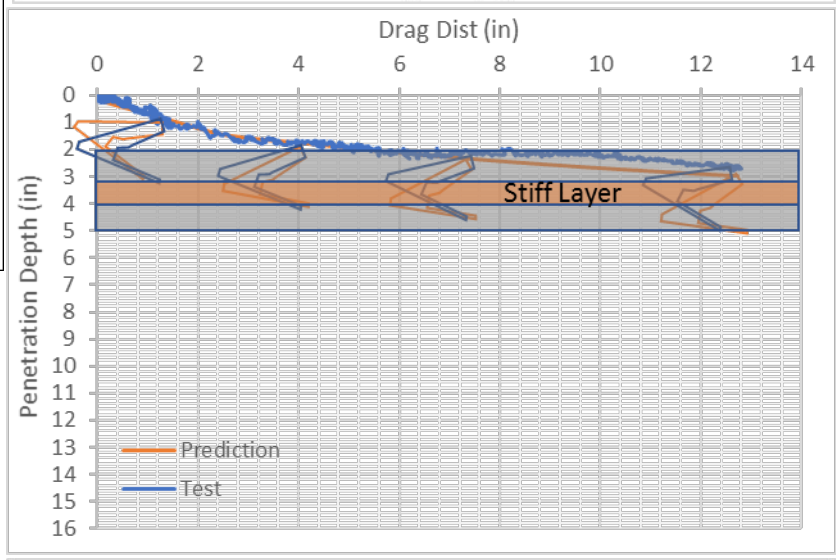
Drag Dist (in)
0
2
4
6
8
10
12
14
Penetration Depth (in)
0
1
2
3
4
5
6
7
8
9
10
11
12
13
14
15
16
Stiff Layer
Prediction
Test

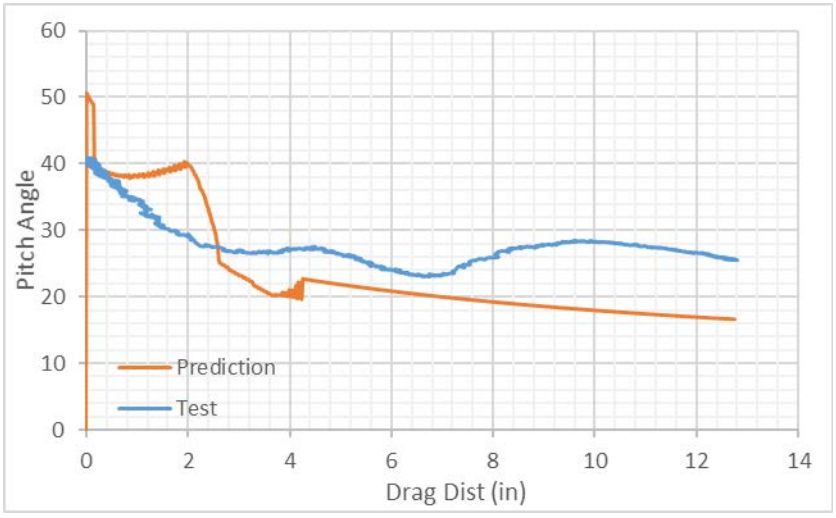
Pitch Angle
60
50
40
30
20
10
0
0
2
4
6
8
10
12
14
Drag Dist (in)
Prediction
Test

First Repeat Test in Case 3

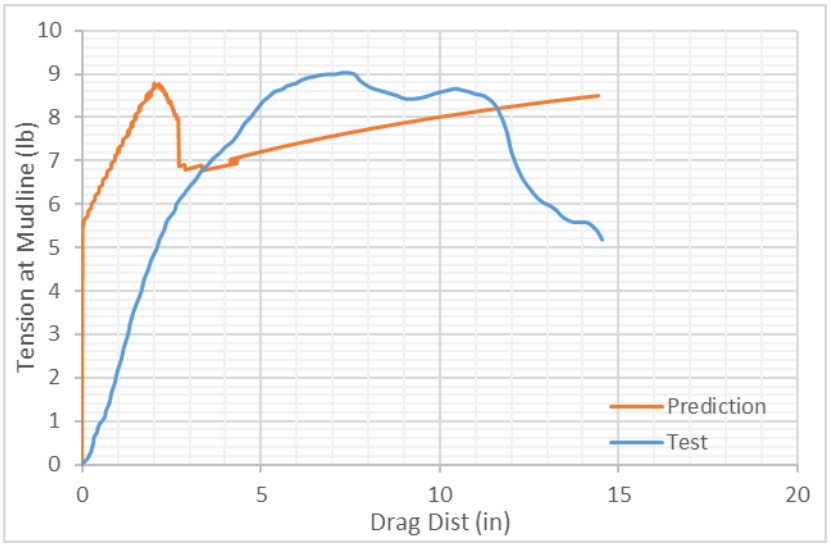

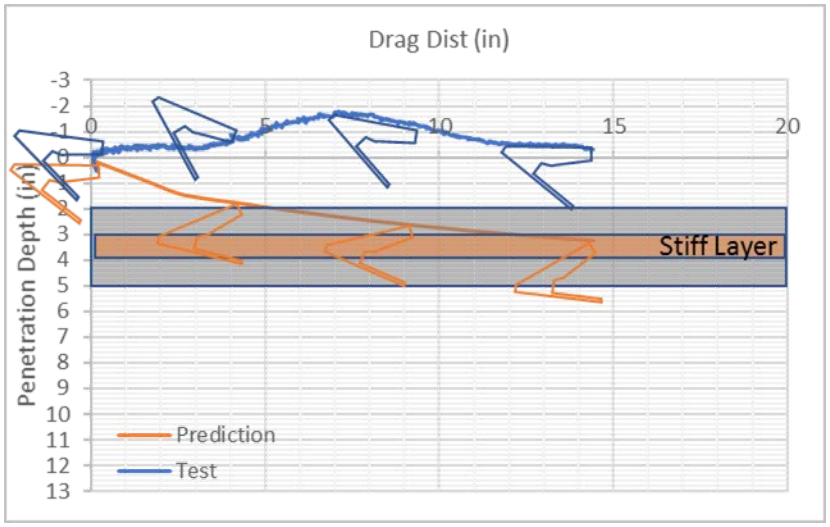

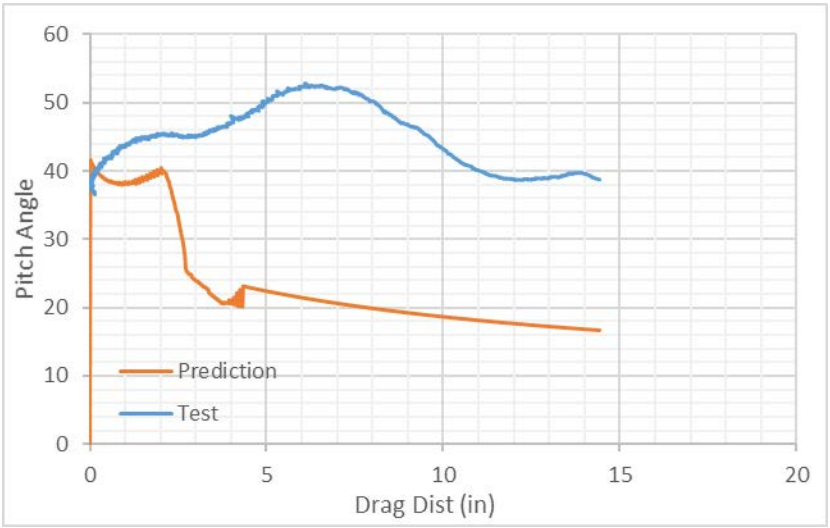

Second Repeat Test in Case 3

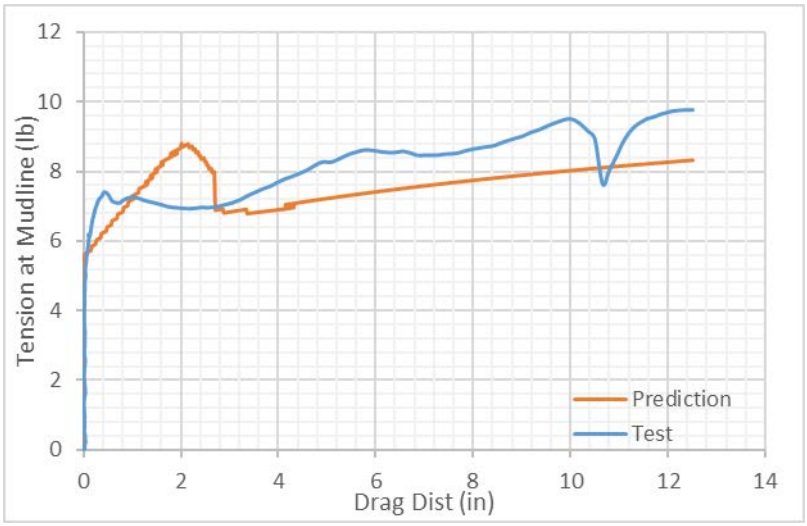

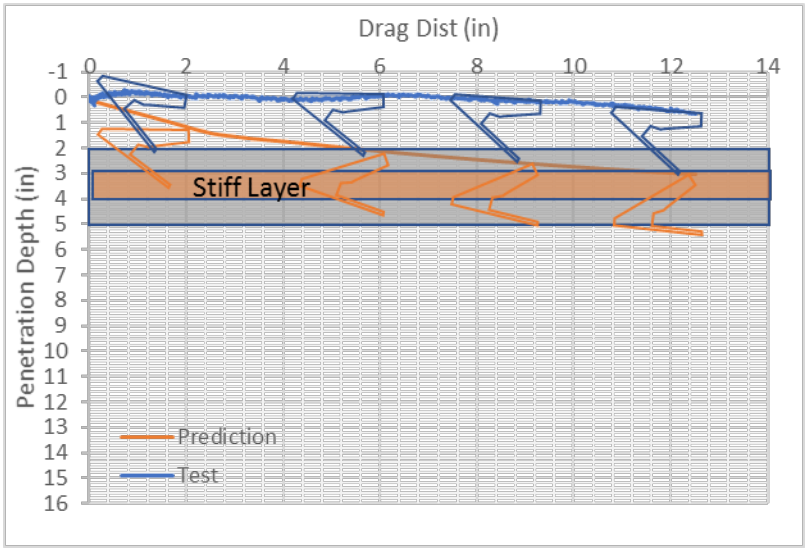

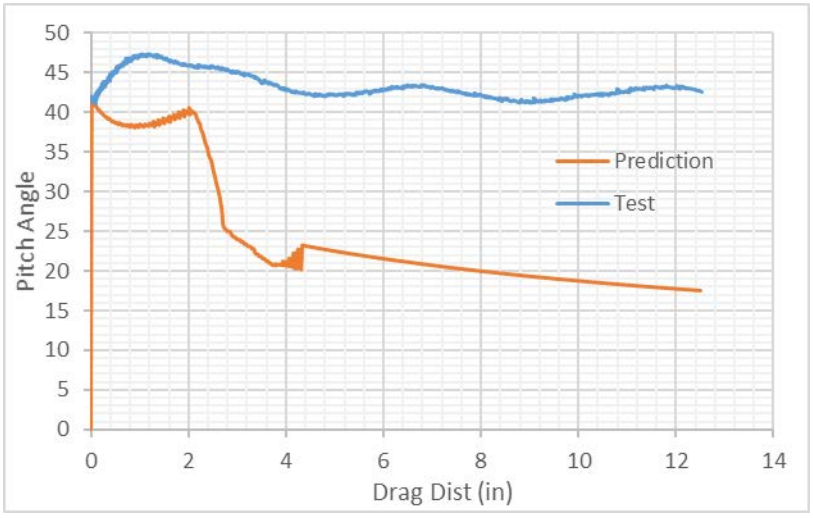

Case 4

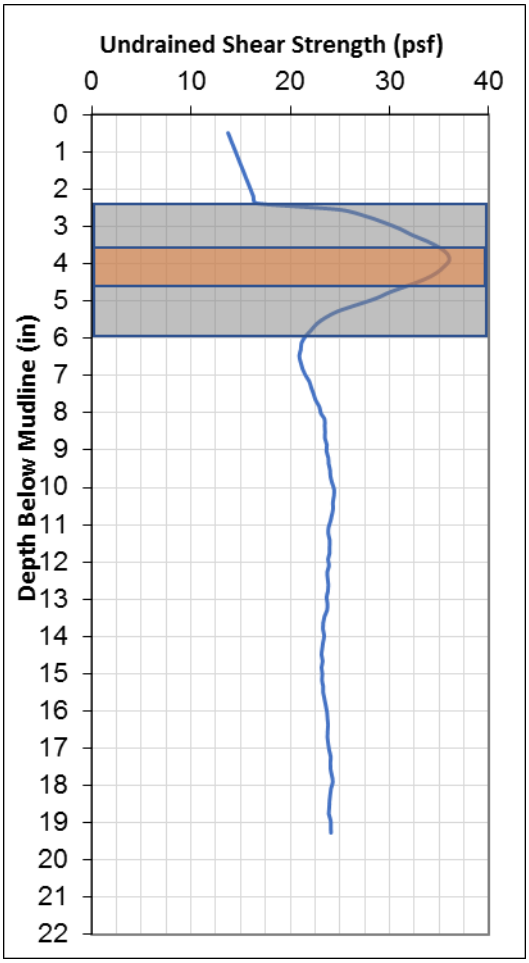
Undrained Shear Strength (psf)
0
10
20
30
40
Depth Below Mudline (in)
0
1
2
3
4
5
6
7
8
9
10
11
12
13
14
15
16
17
18
19
20
21
22

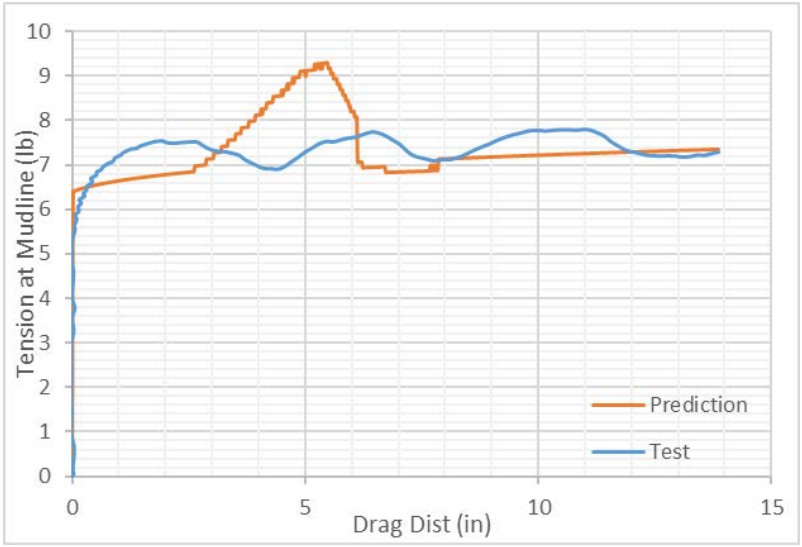
Tension at Mudline (lb)
0
1
2
3
4
5
6
7
8
9
10
Drag Dist (in)
0
5
10
15
Prediction
Test

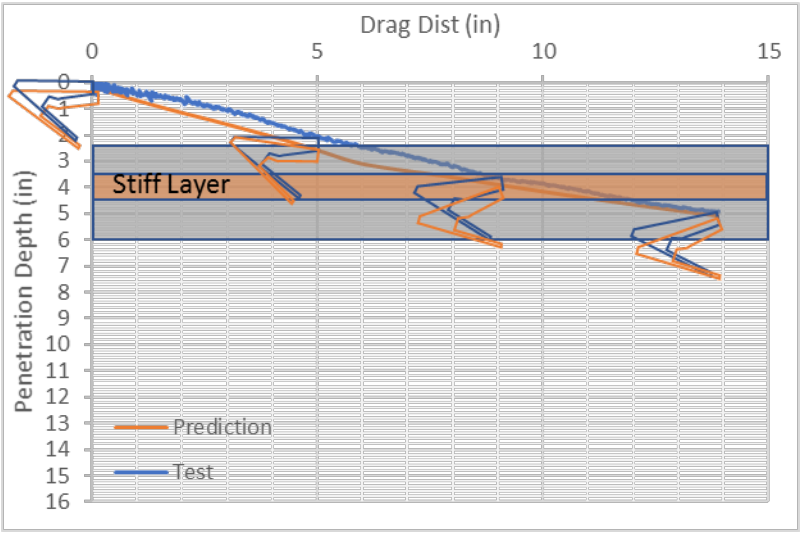
Drag Dist (in)
0
5
10
15
Penetration Depth (in)
Stiff Layer
Prediction
Test

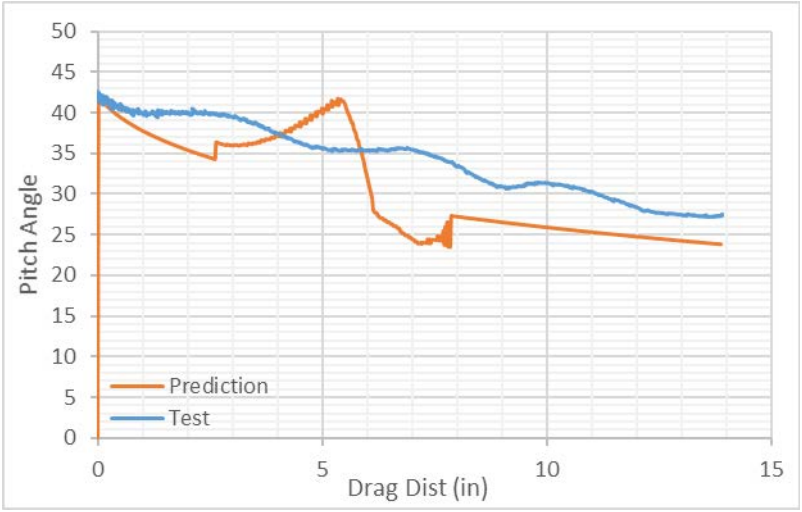
Pitch Angle
50
45
40
35
30
25
20
15
10
5
0
Prediction
Test
0
5
10
15
Drag Dist (in)

First Repeat Test in Case 4

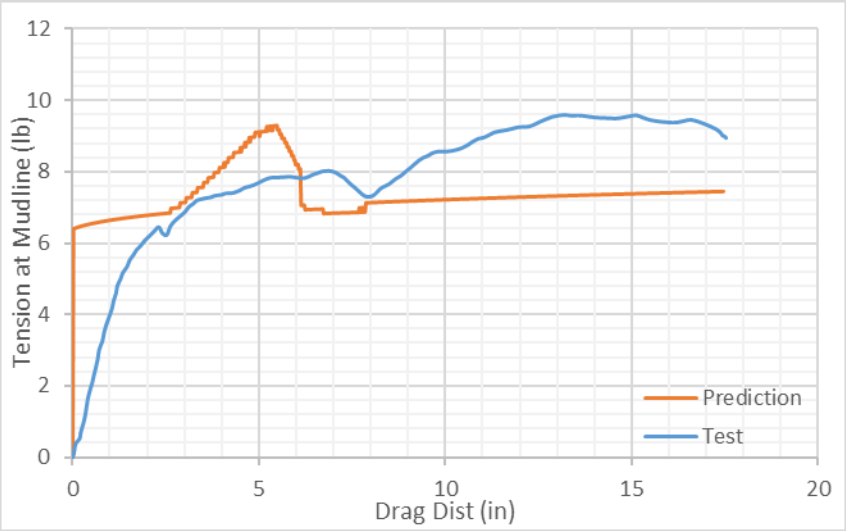

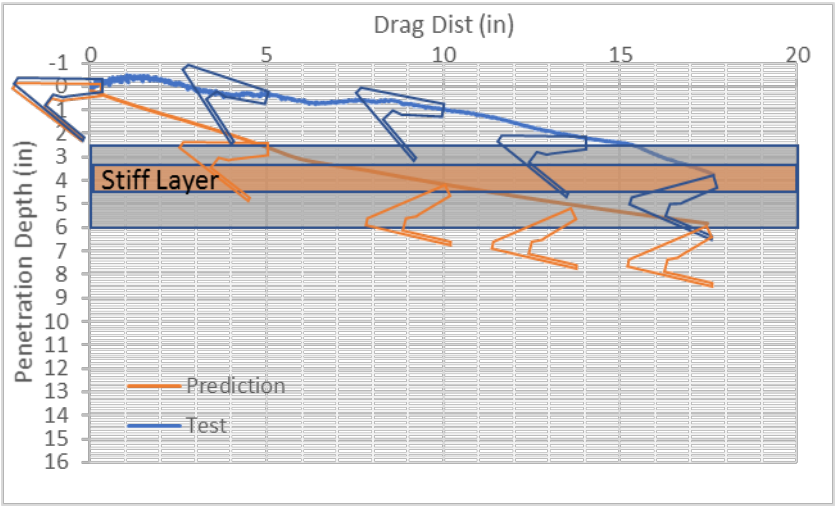

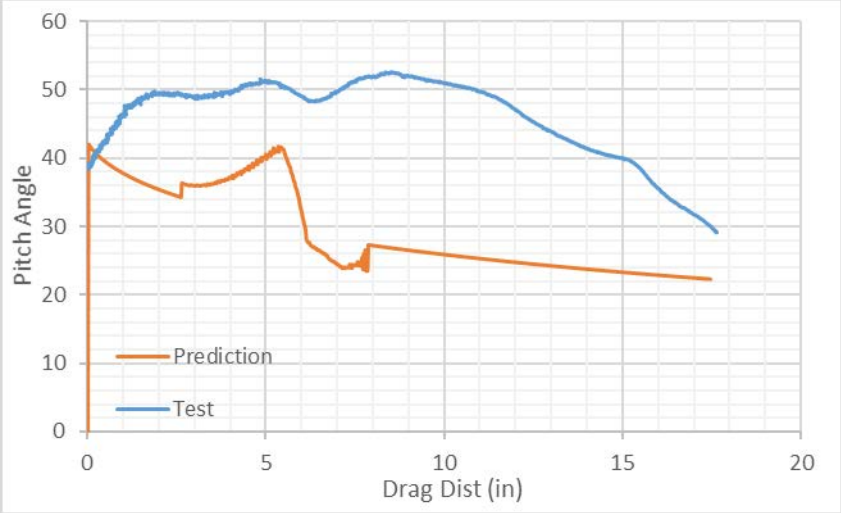

Case 5

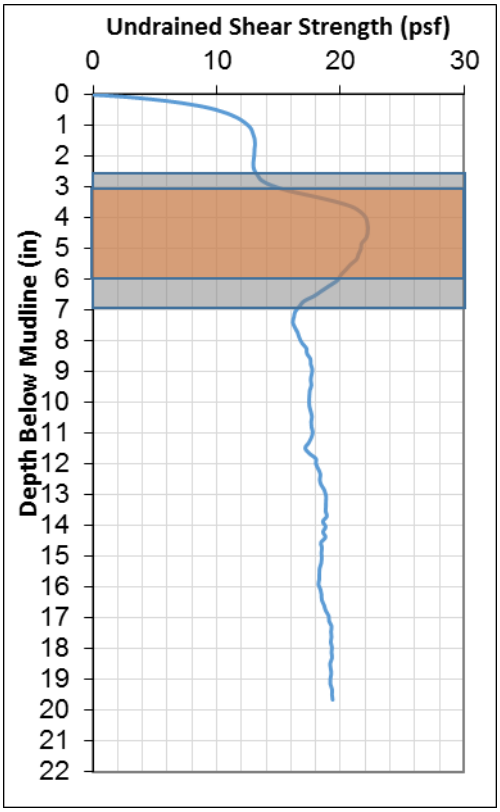
Undrained Shear Strength (psf)
0
10
20
30
Depth Below Mudline (in)
0
1
2
3
4
5
6
7
8
9
10
11
12
13
14
15
16
17
18
19
20
21
22

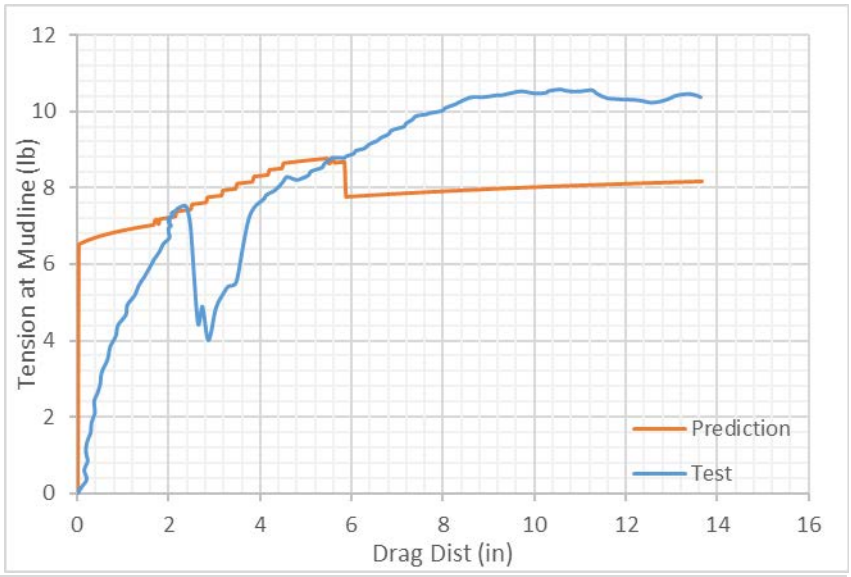
Tension at Mudline (lb)
0
2
4
6
8
10
12
Drag Dist (in)
0
2
4
6
8
10
12
14
16
Prediction
Test

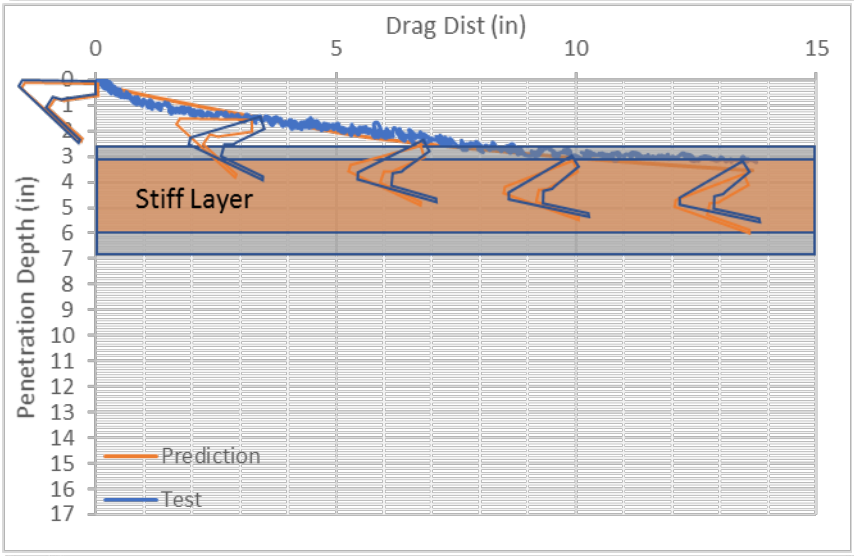
Drag Dist (in)
0
5
10
15
Penetration Depth (in)
Stiff Layer
Prediction
Test

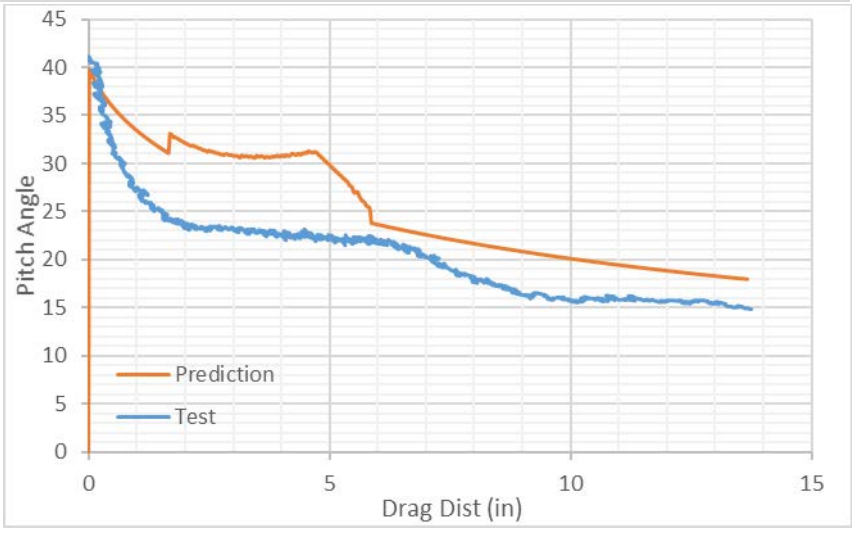
Pitch Angle
0
5
10
15
20
25
30
35
40
45
Drag Dist (in)
0
5
10
15
Prediction
Test

First Repeat Test in Case 5

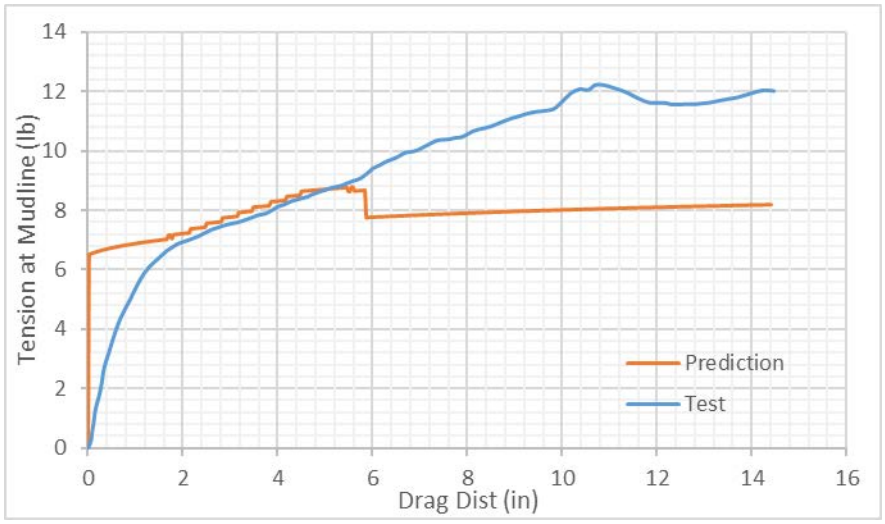

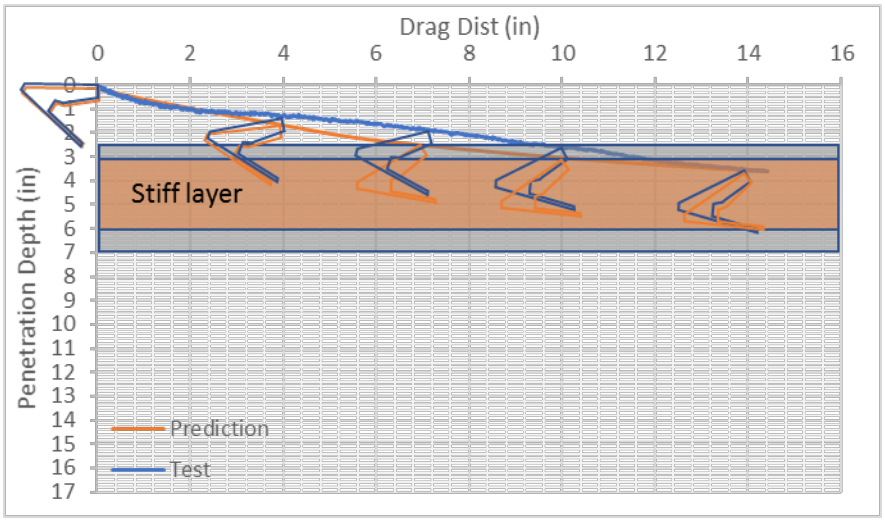

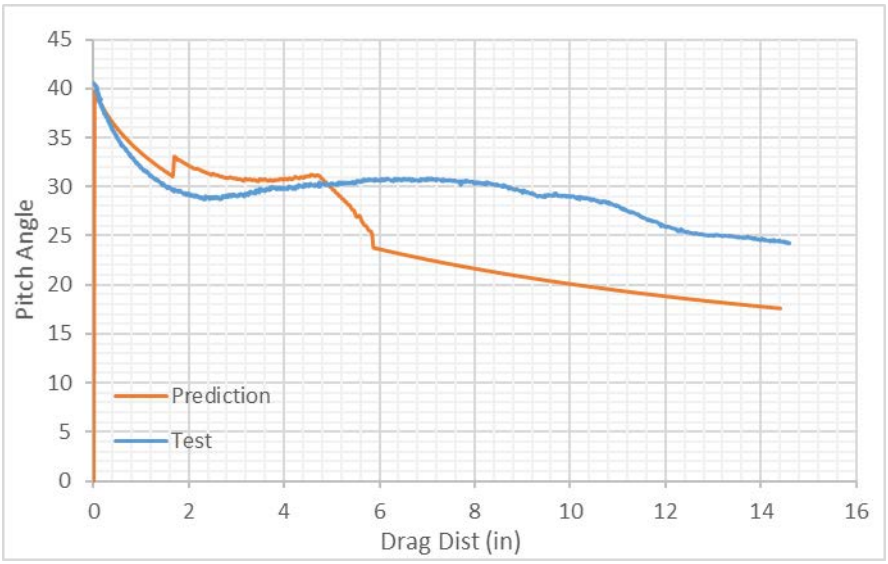

Case 6

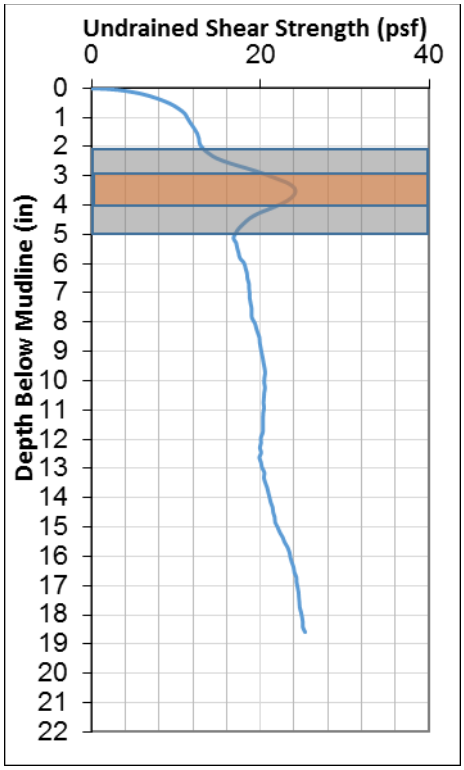
Undrained Shear Strength (psf)
0
20
40
Depth Below Mudline (in)
0
1
2
3
4
5
6
7
8
9
10
11
12
13
14
15
16
17
18
19
20
21
22

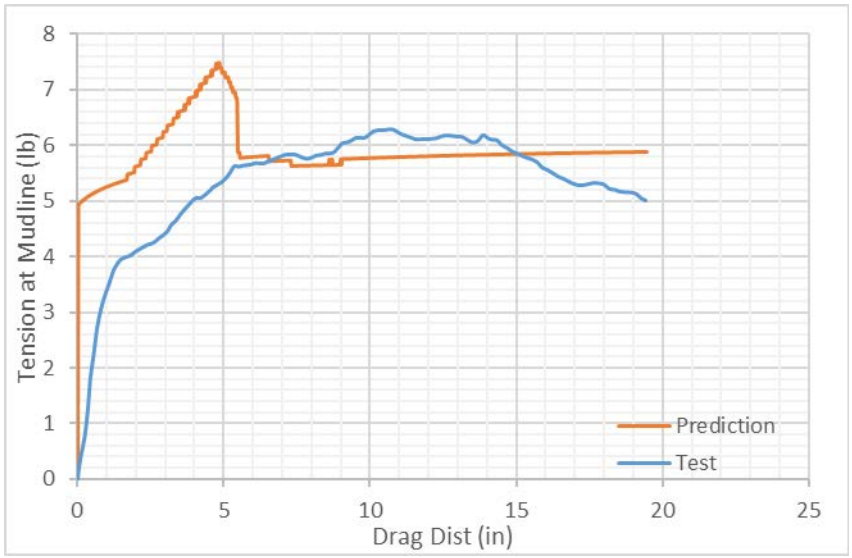
Tension at Mudline (lb)
0
1
2
3
4
5
6
7
8
0
5
10
15
20
25
Drag Dist (in)
Prediction
Test

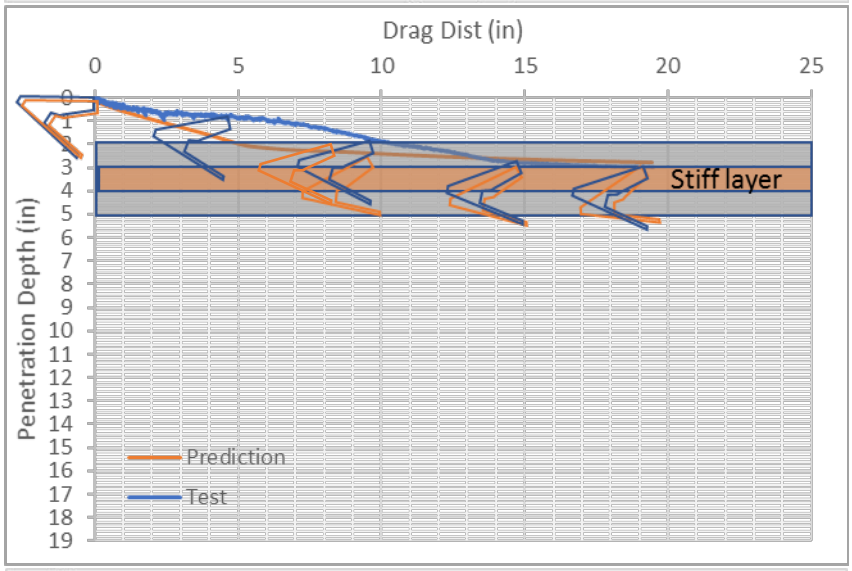
Drag Dist (in)
0
5
10
15
20
25
Penetration Depth (in)
0
1
2
3
4
5
6
7
8
9
10
11
12
13
14
15
16
17
18
19
Stiff layer
Prediction
Test

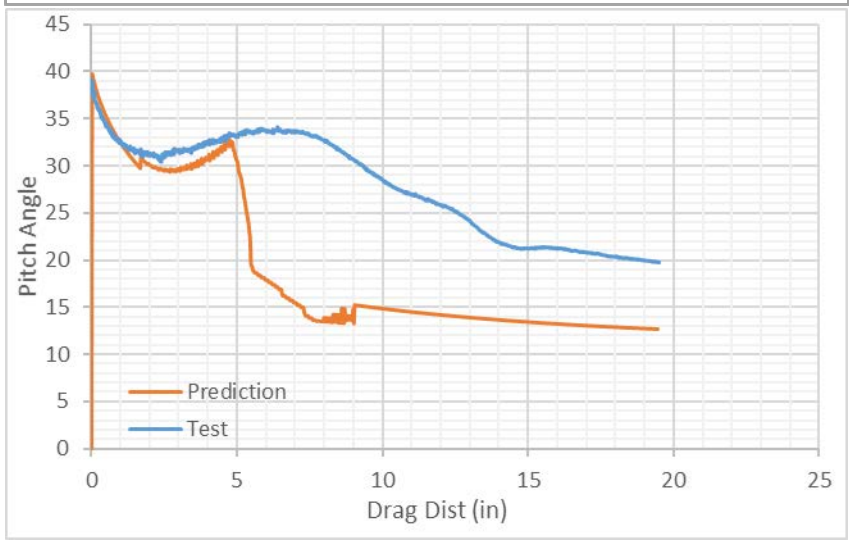
Pitch Angle
45
40
35
30
25
20
15
10
5
0
0
5
10
15
20
25
Drag Dist (in)
Prediction
Test

First Repeat Test in Case 6

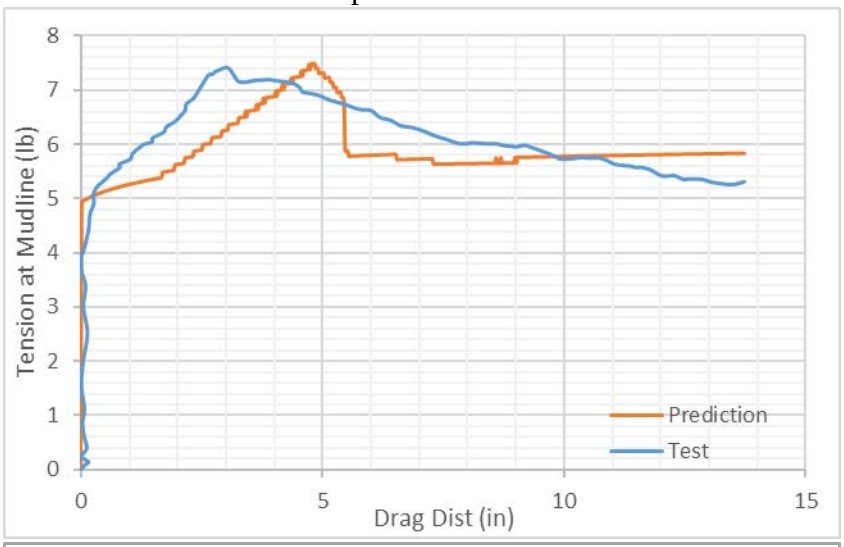

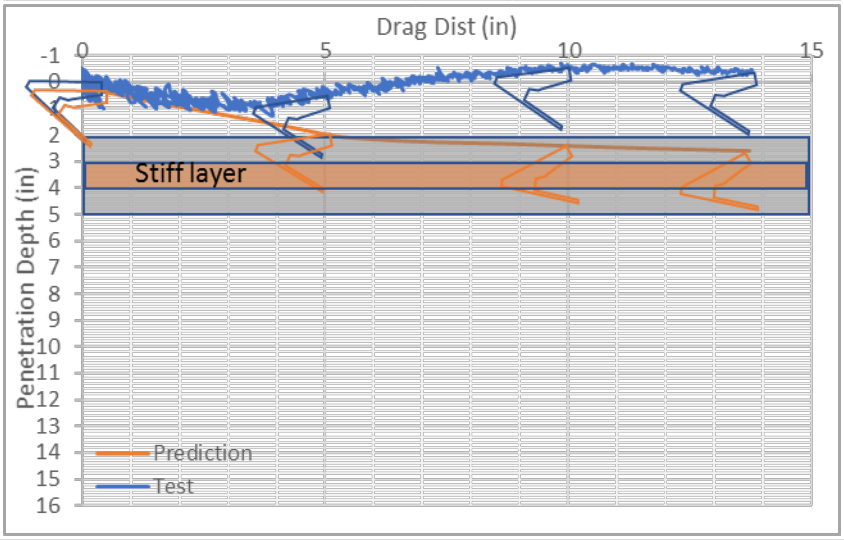

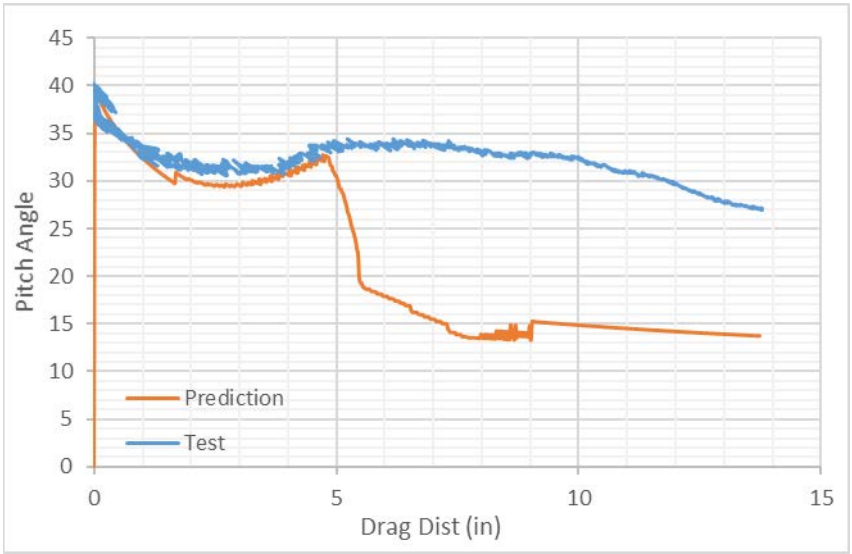

Second Repeat Test in Case 6

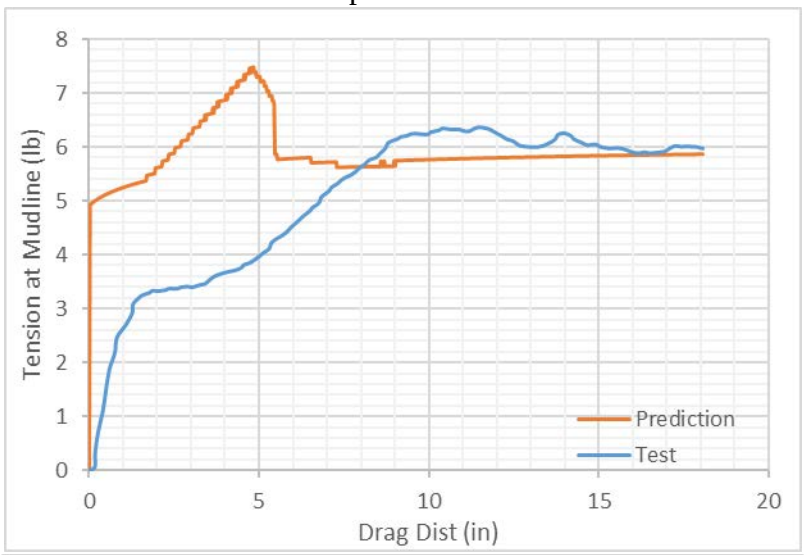

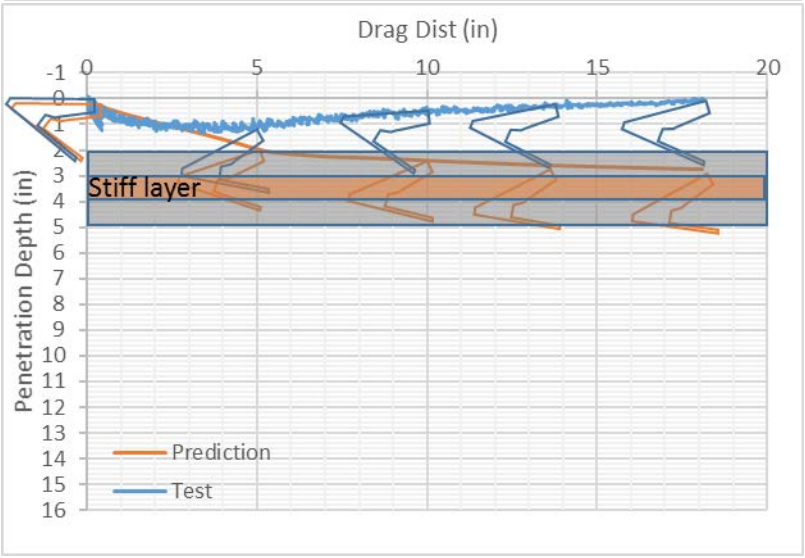

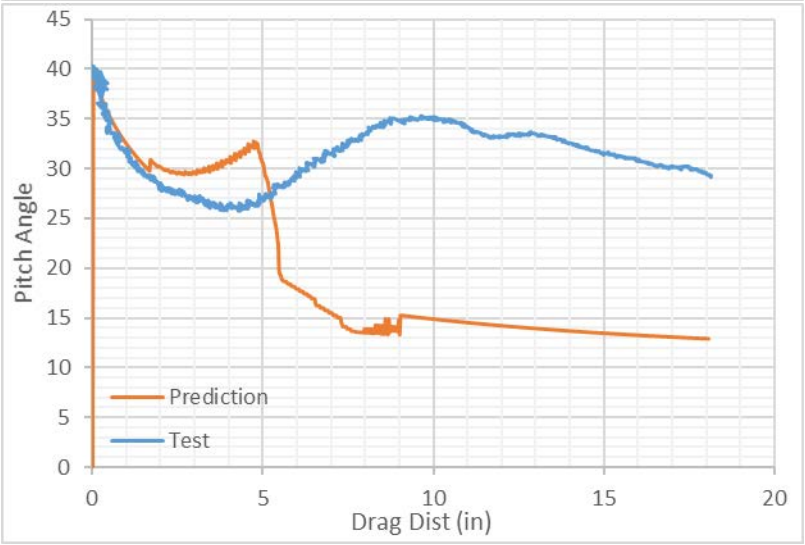

Third Repeat Test in Case 6

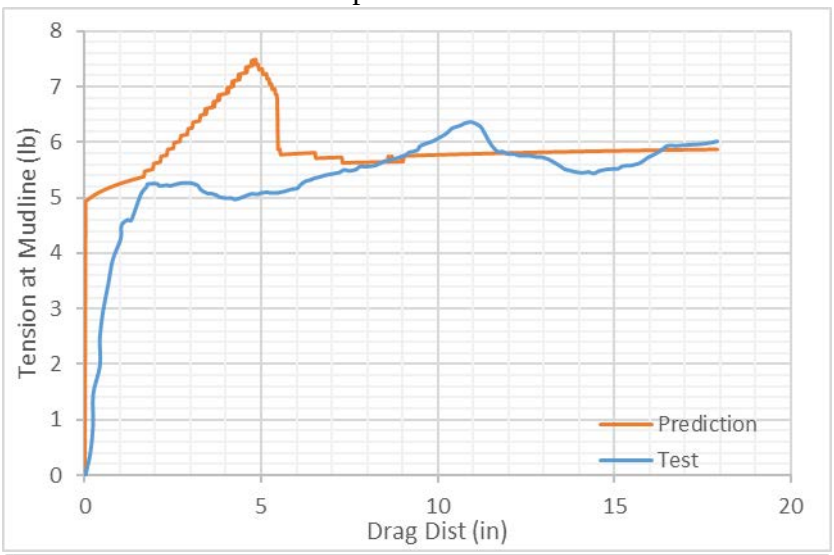

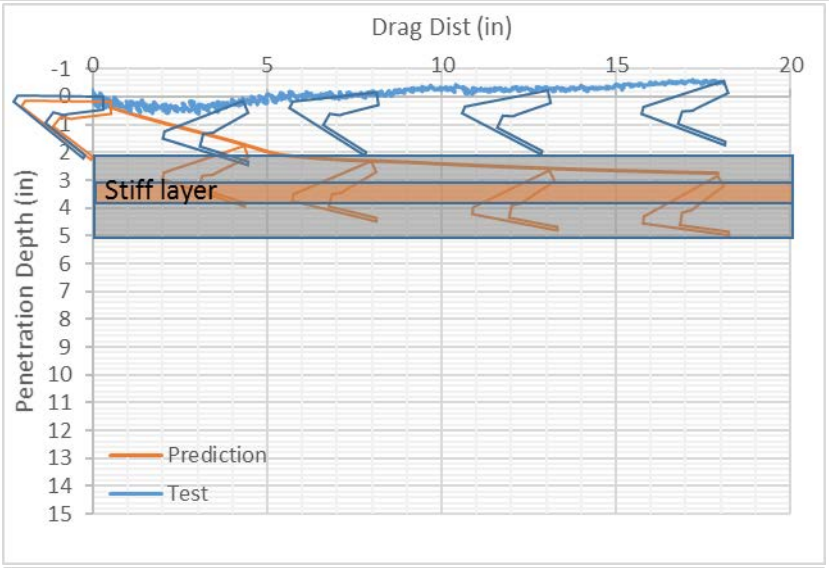

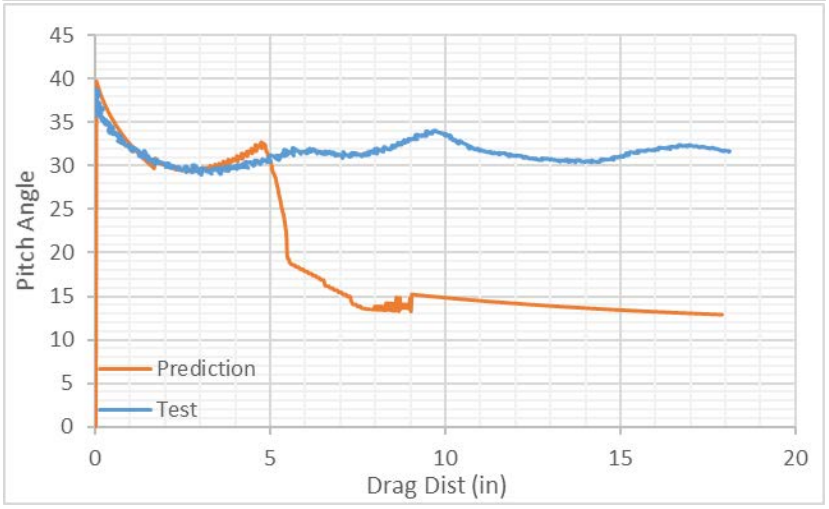

Fourth Repeat Test in Case 6

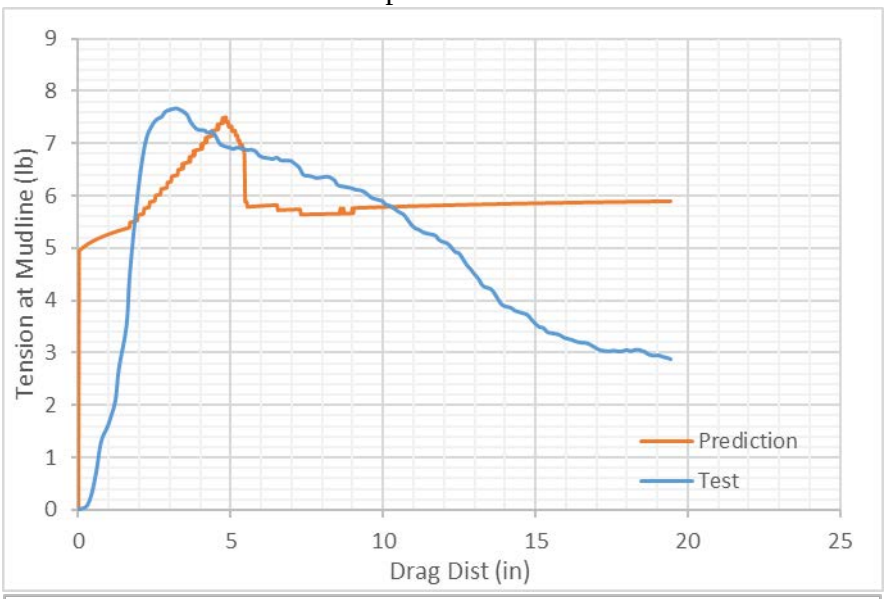

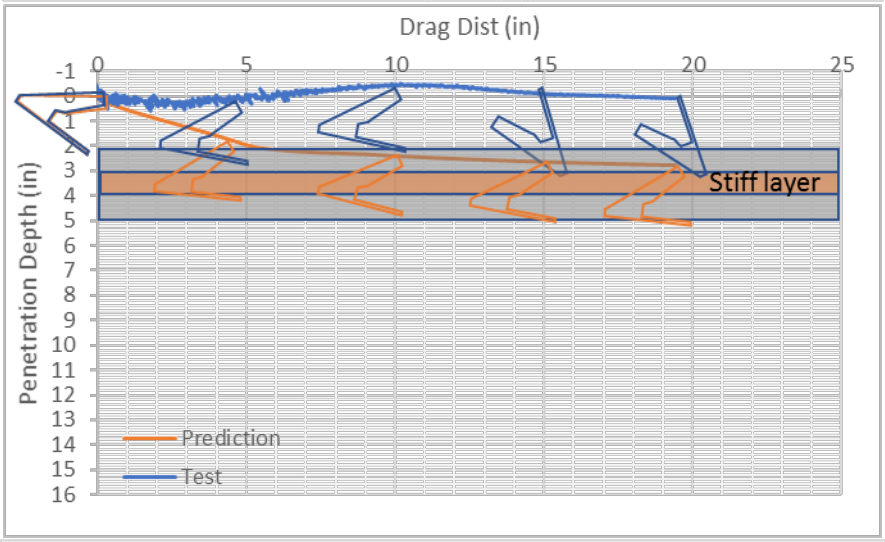

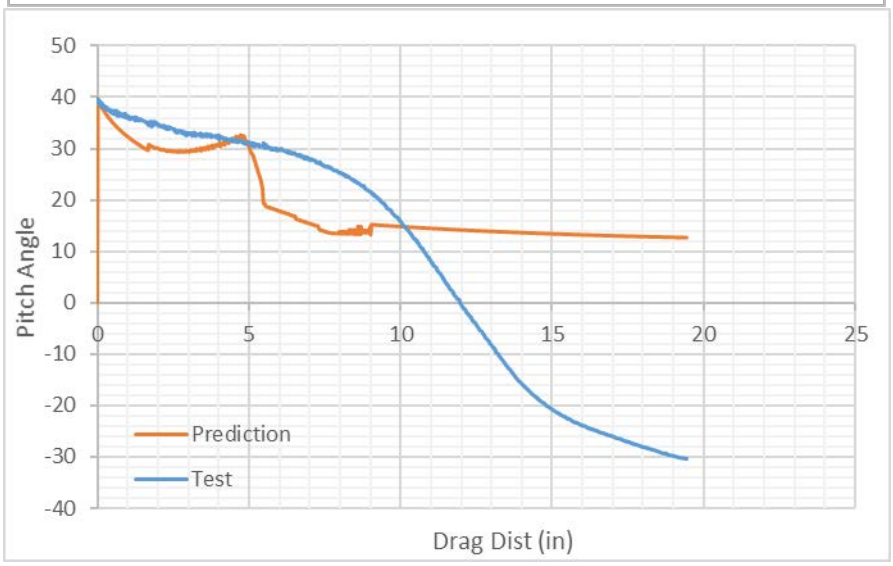

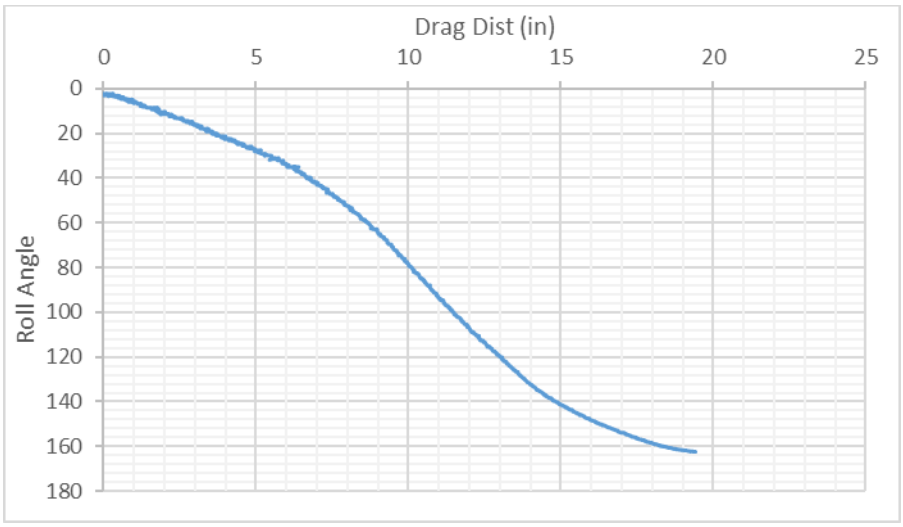
Drag Dist (in)
0
5
10
15
20
25
Roll Angle
0
20
40
60
80
100
120
140
160
180

Fifth Repeat Test in Case 6

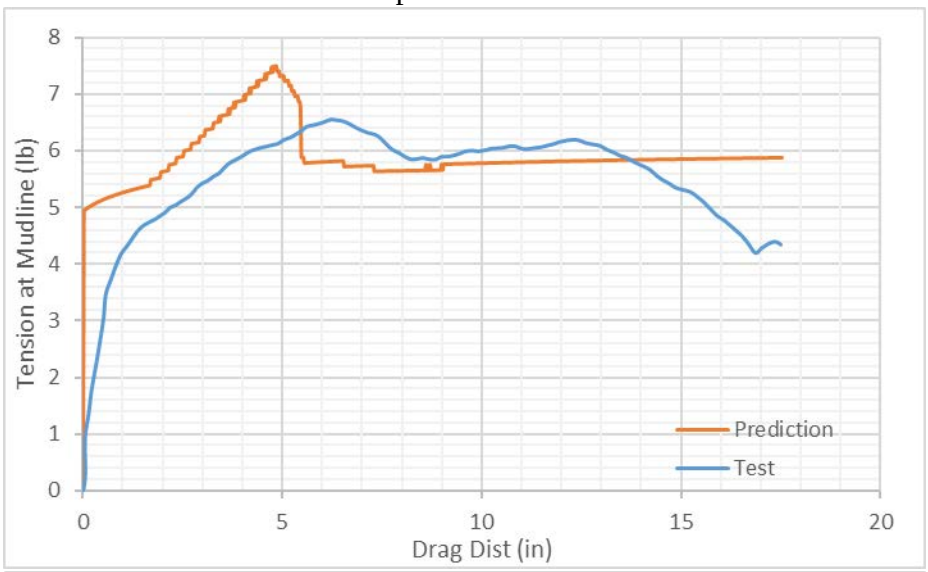

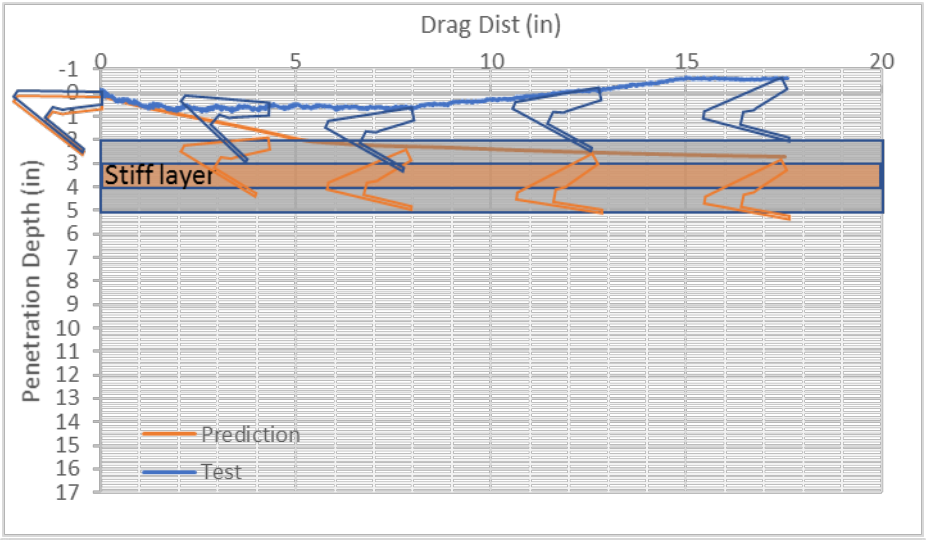

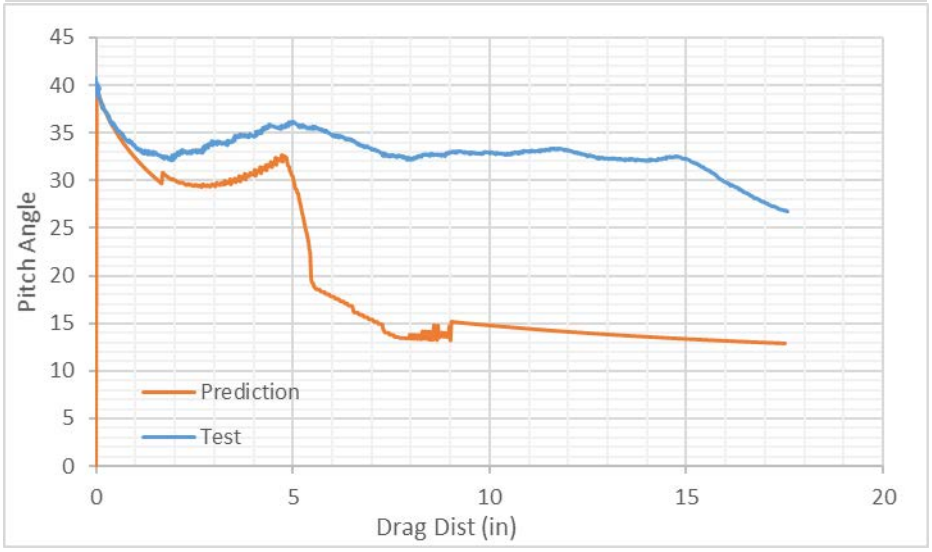

Case 7

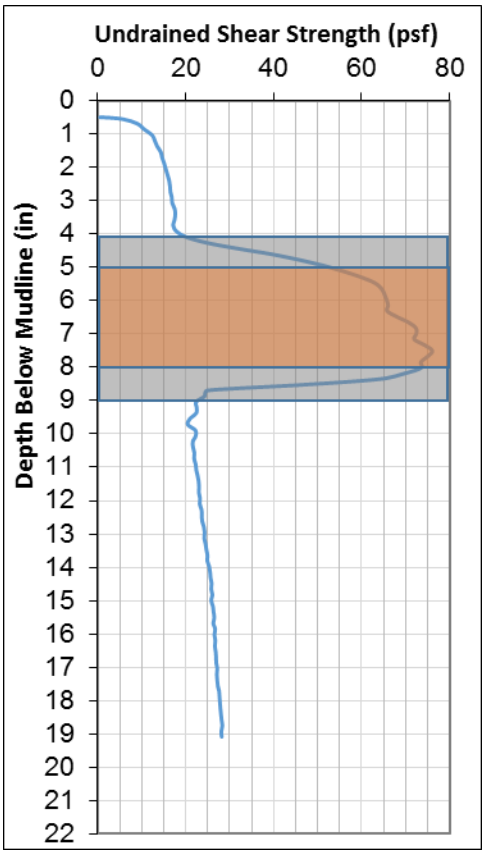
Undrained Shear Strength (psf)
0
20
40
60
80
Depth Below Mudline (in)
0
1
2
3
4
5
6
7
8
9
10
11
12
13
14
15
16
17
18
19
20
21
22

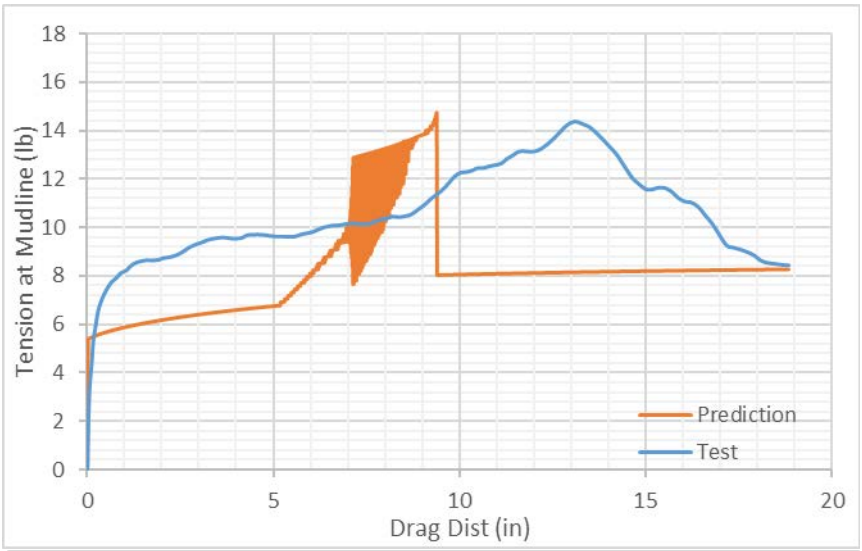
Tension at Mudline (lb)
0
2
4
6
8
10
12
14
16
18
0
5
10
15
20
Drag Dist (in)
Prediction
Test

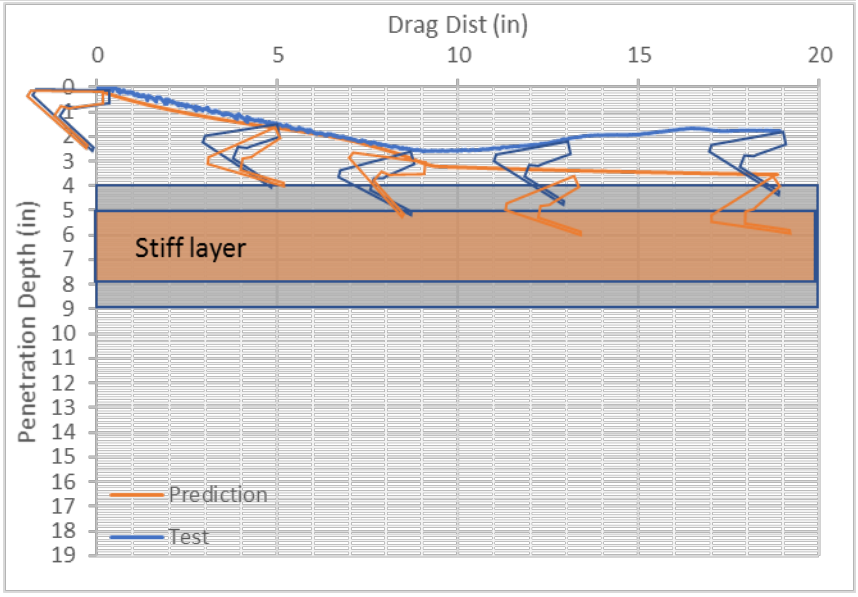
Drag Dist (in)
0
5
10
15
20
Penetration Depth (in)
Stiff layer
Prediction
Test

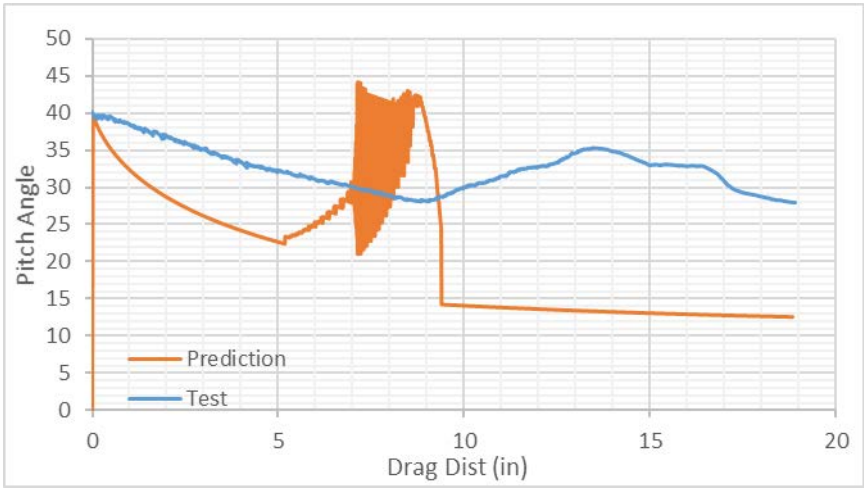
Pitch Angle
0
5
10
15
20
25
30
35
40
45
50
0
5
10
15
20
Drag Dist (in)
Prediction
Test

First Repeat Test in Case 7

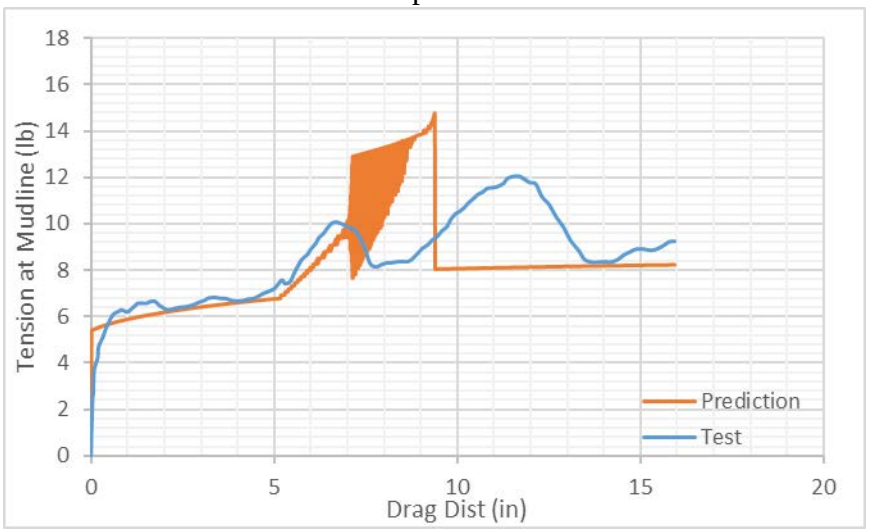

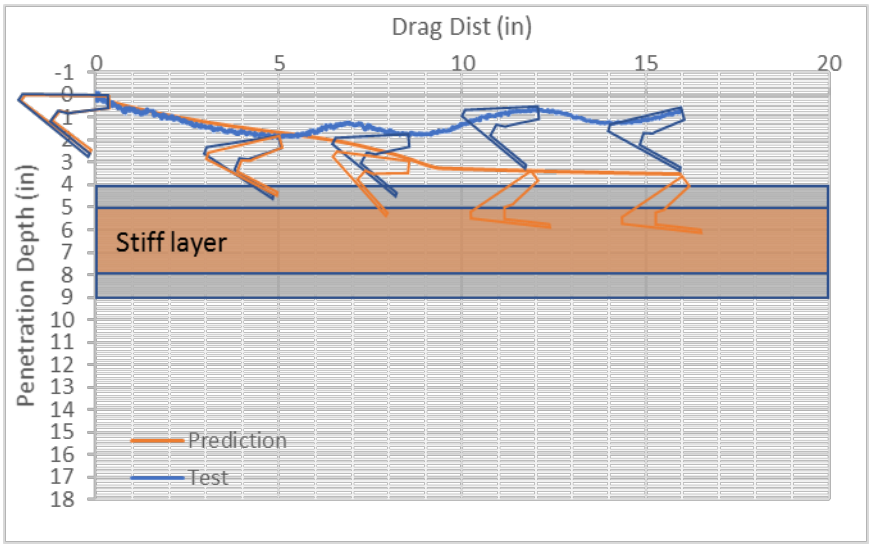

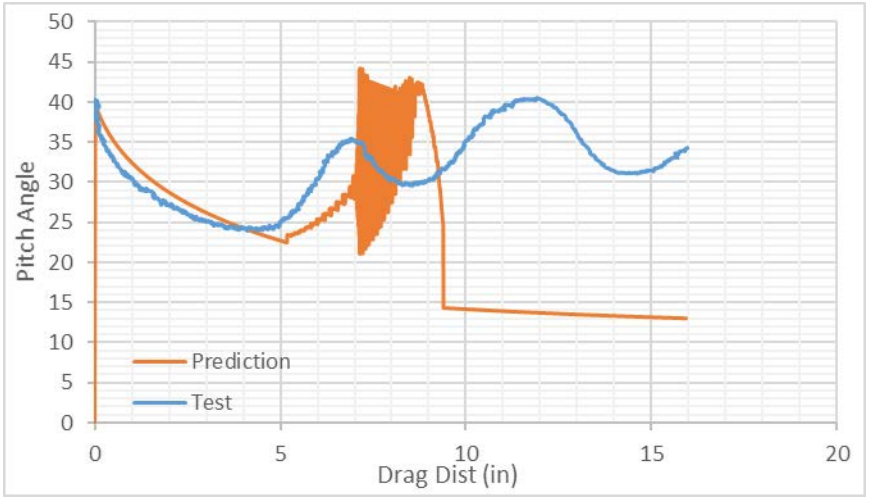

Second Repeat Test in Case 7

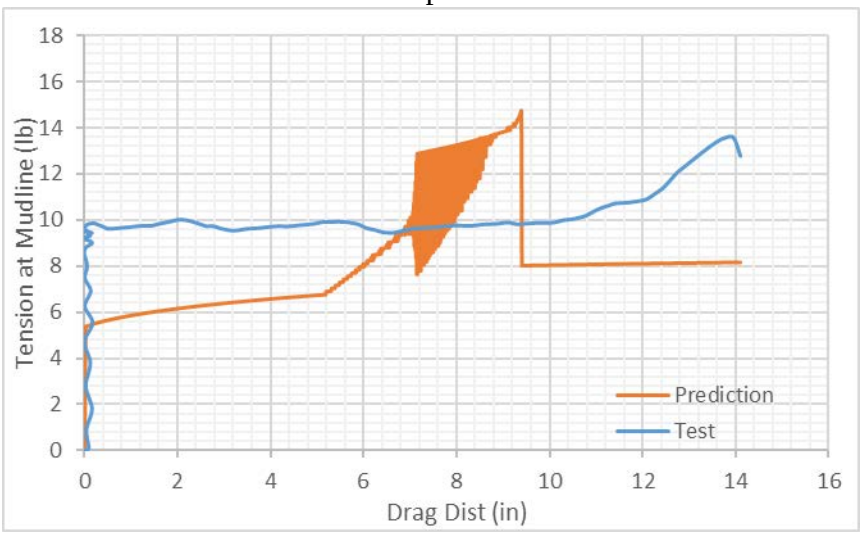

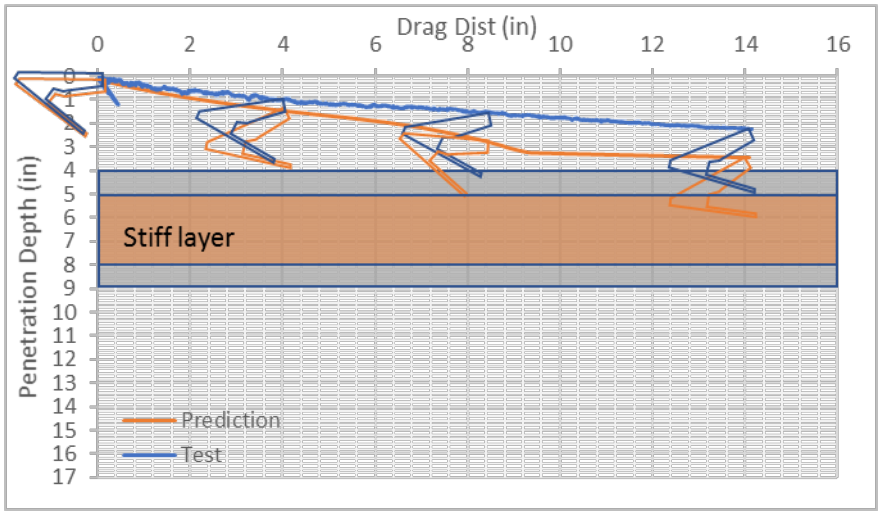

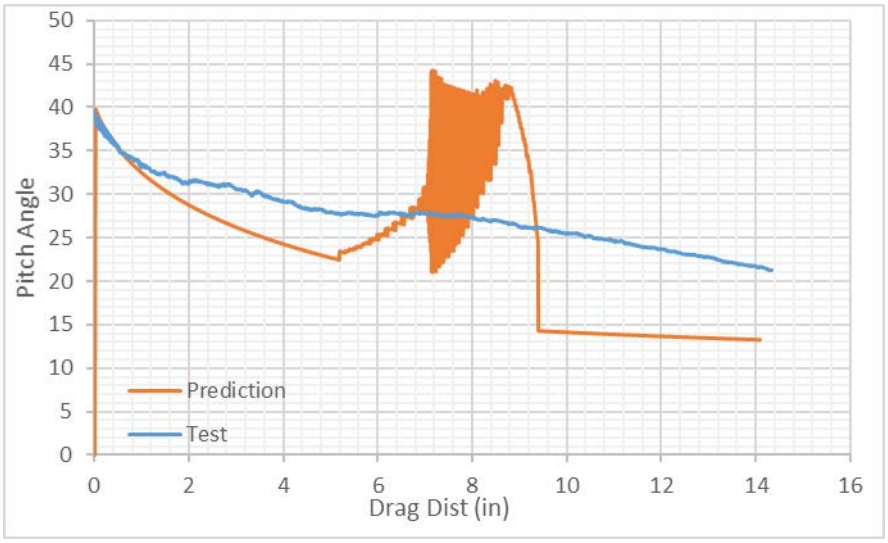

Third Repeat Test in Case 7

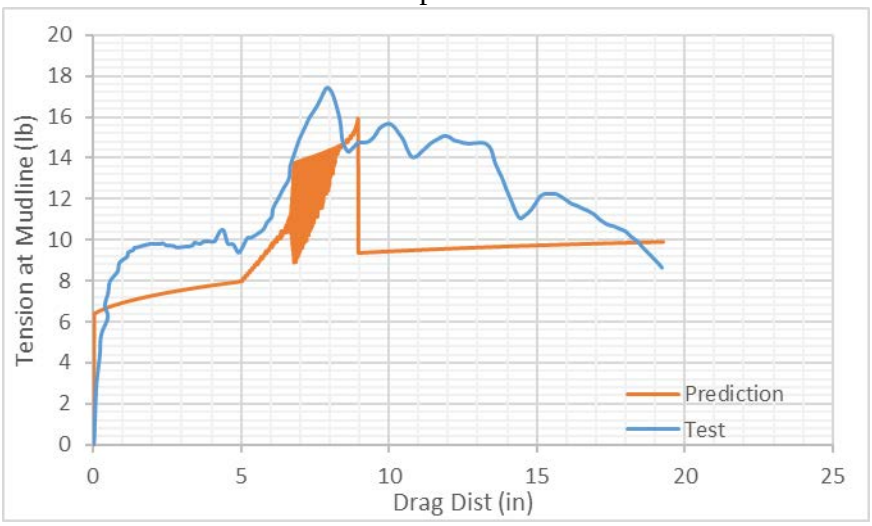

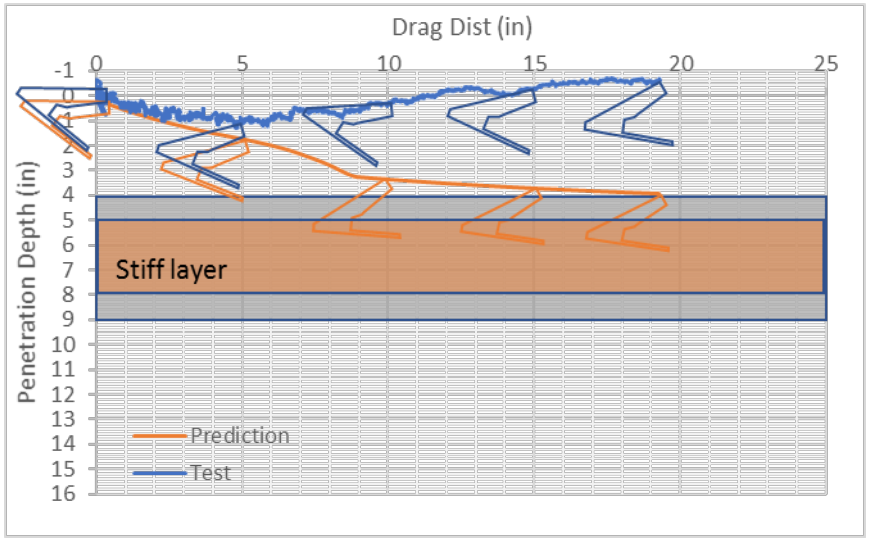

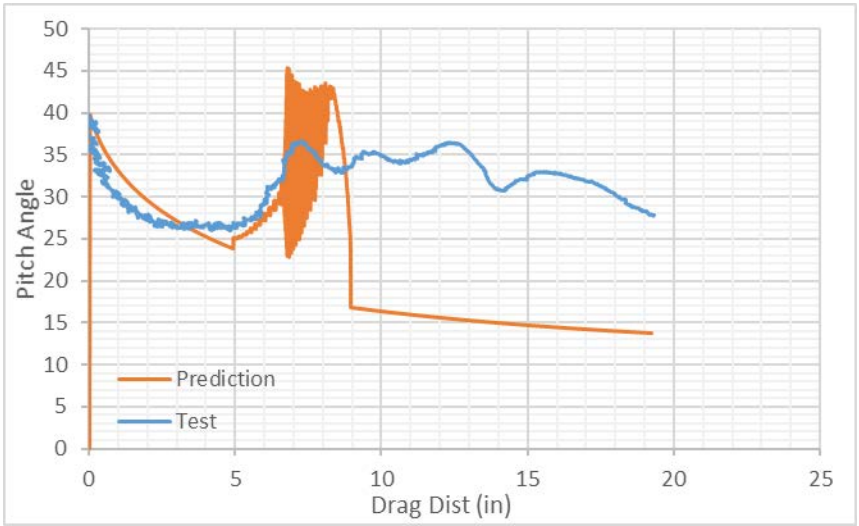

Fourth Repeat Test in Case 7

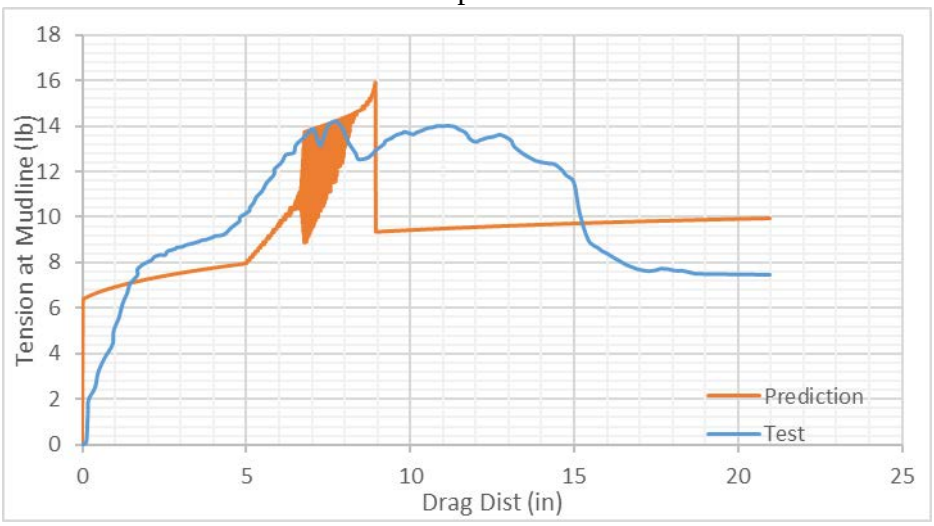

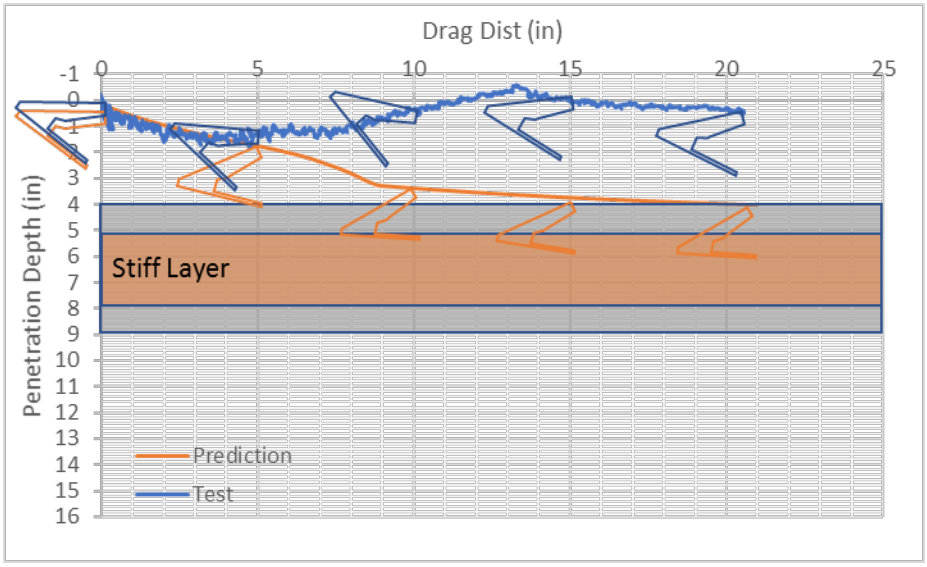

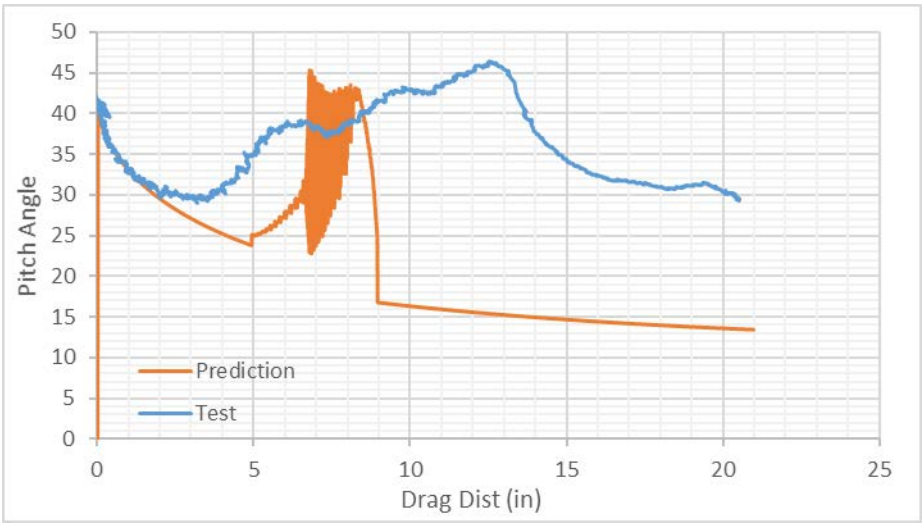

Case 8

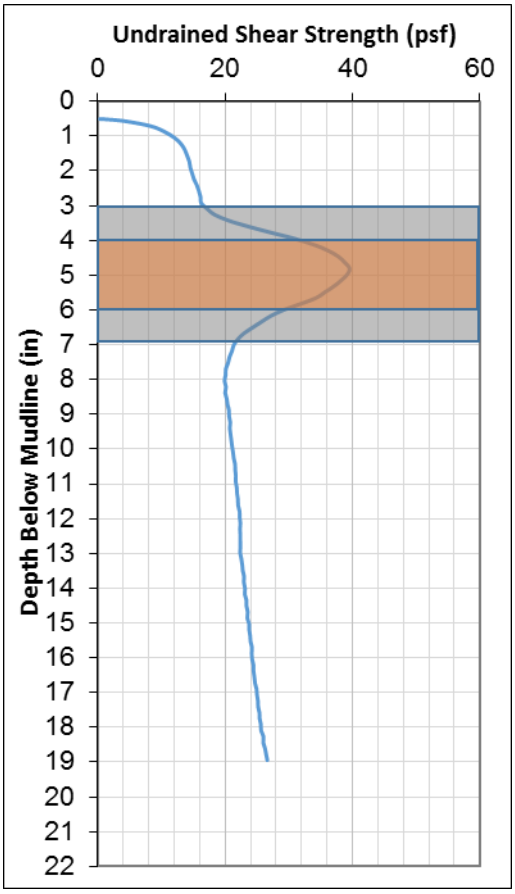
Undrained Shear Strength (psf)
0
20
40
60
Depth Below Mudline (in)

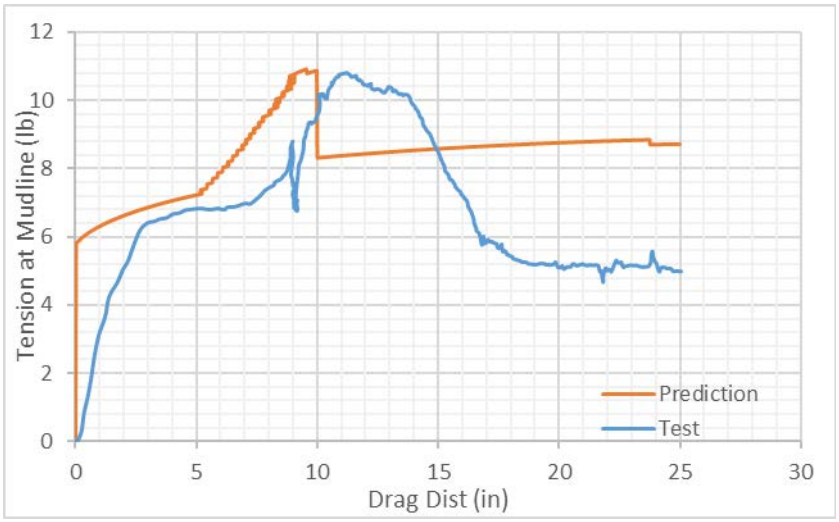
Tension at Mudline (lb)
Drag Dist (in)
Prediction
Test

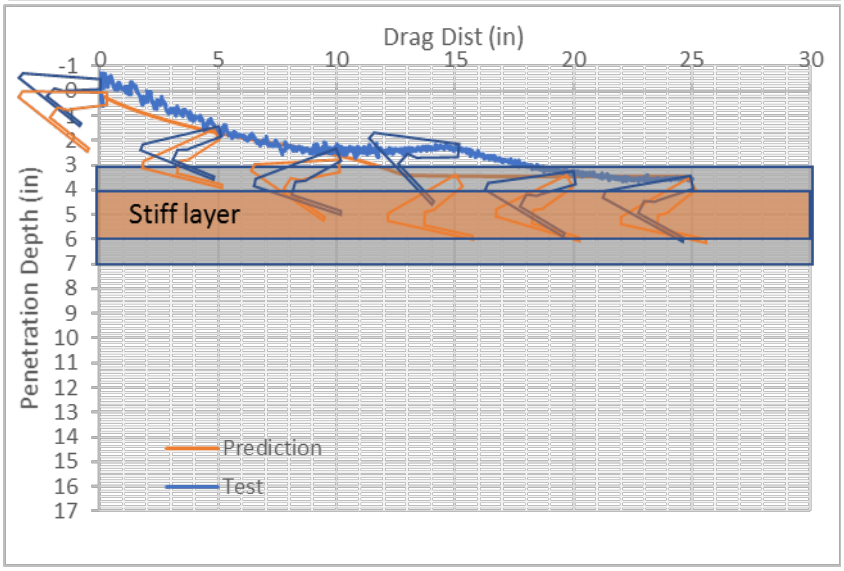
Drag Dist (in)
Penetration Depth (in)
Stiff layer
Prediction
Test

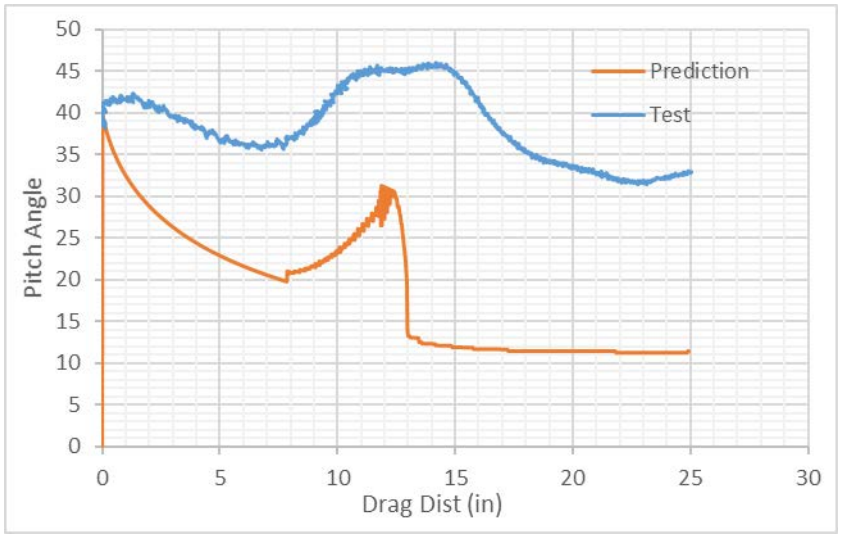
Pitch Angle
Drag Dist (in)
Prediction
Test

First Repeat Test in Case 8

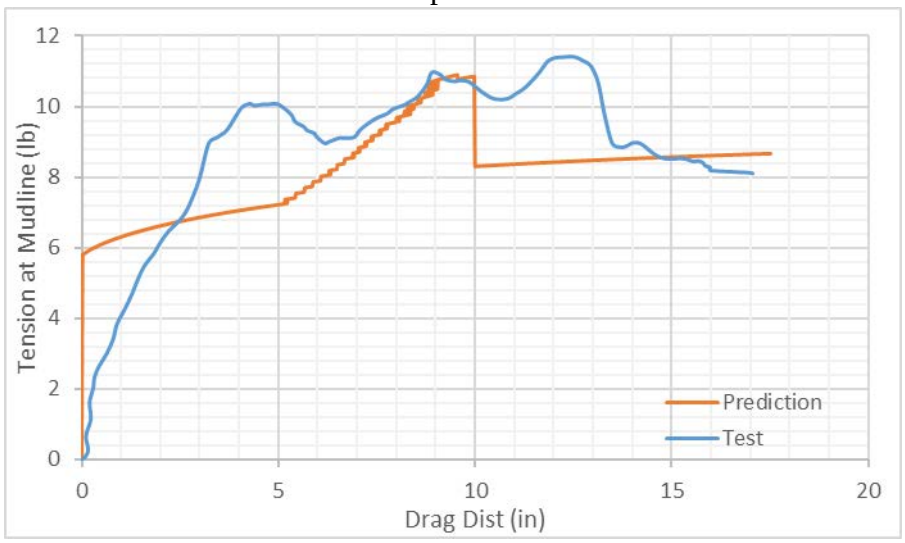

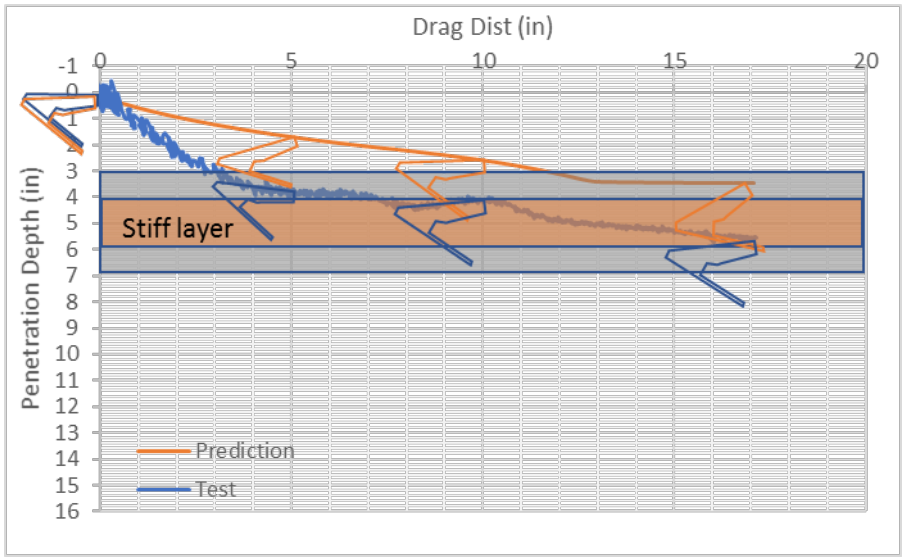

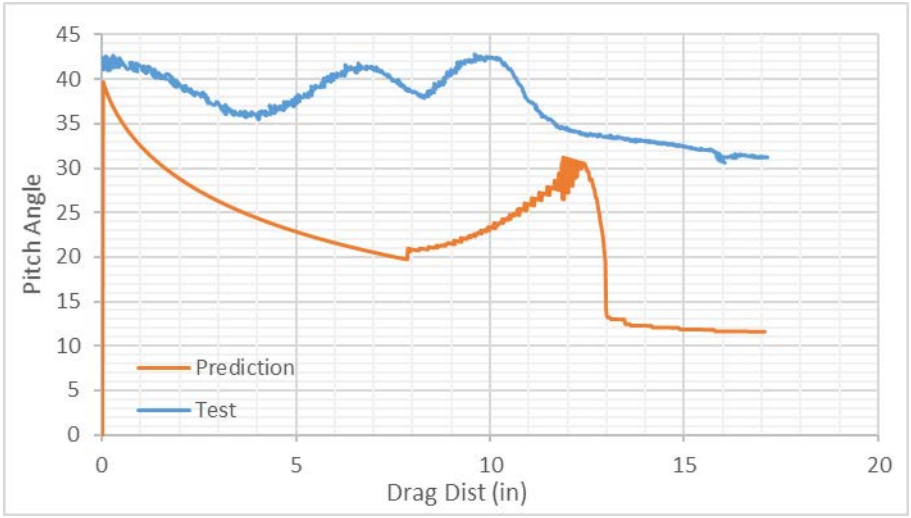

Second Repeat Test in Case 8

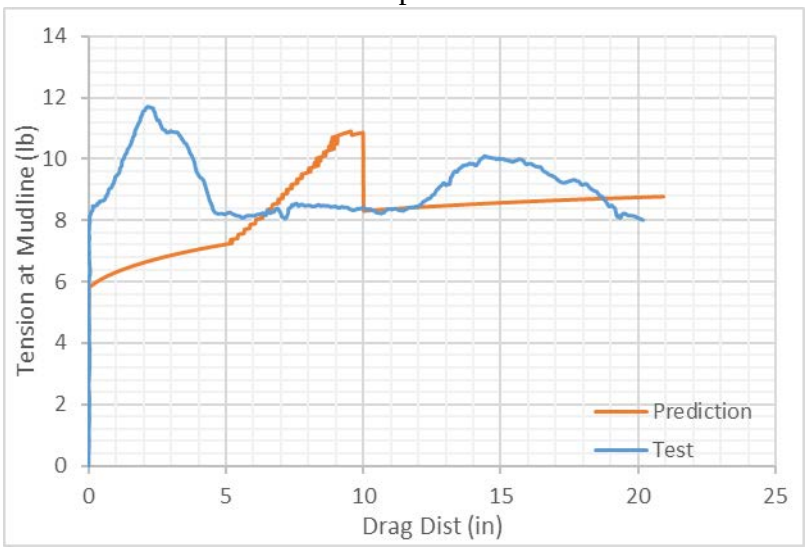

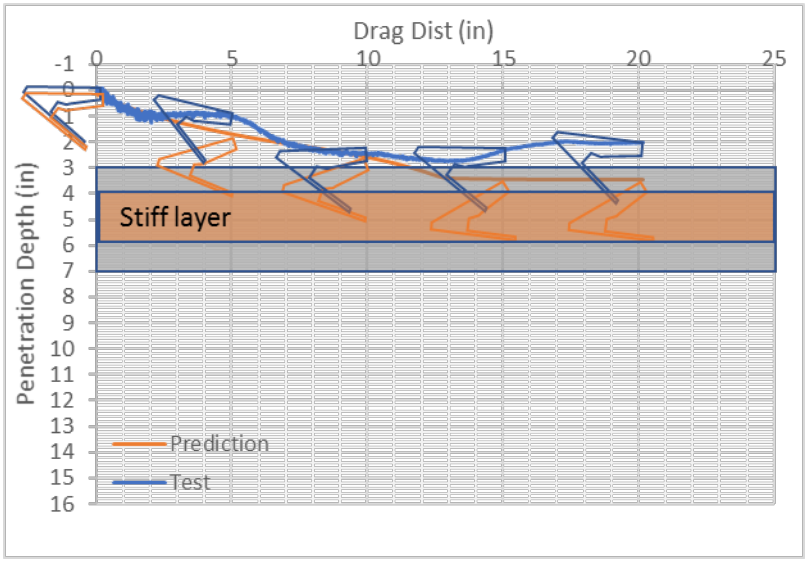

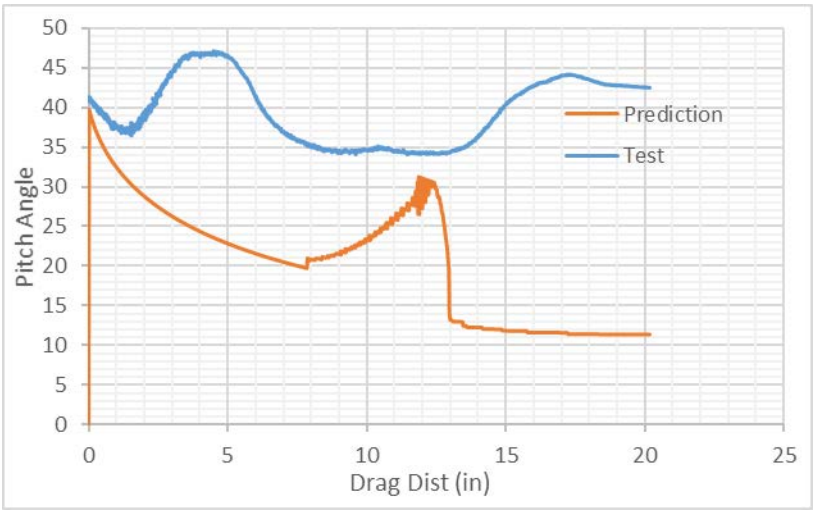

Third Repeat Test in Case 8

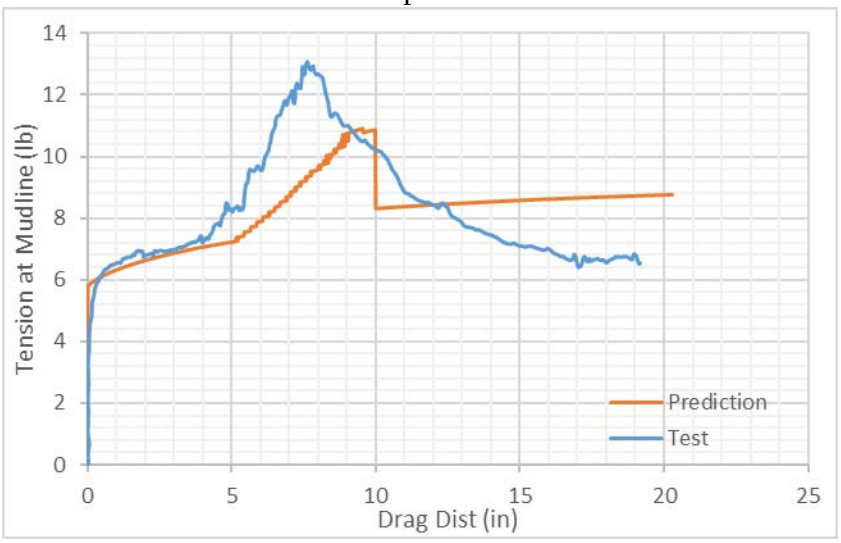

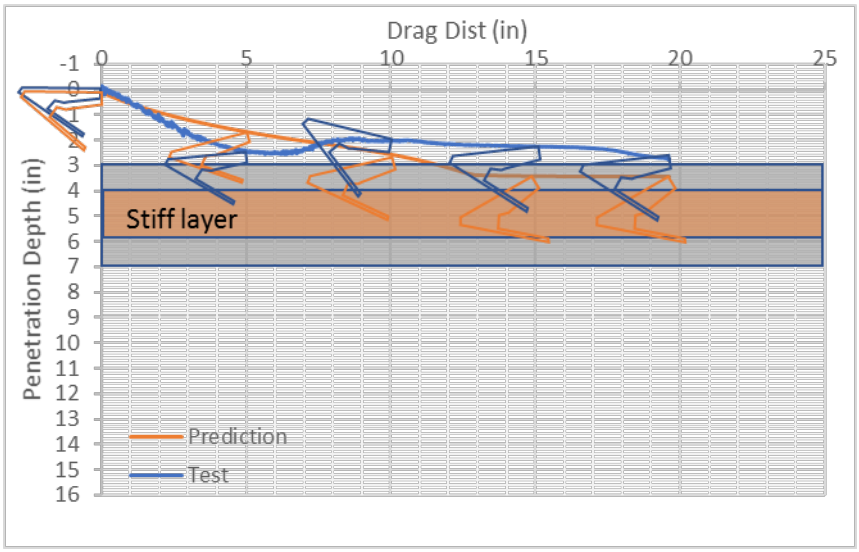

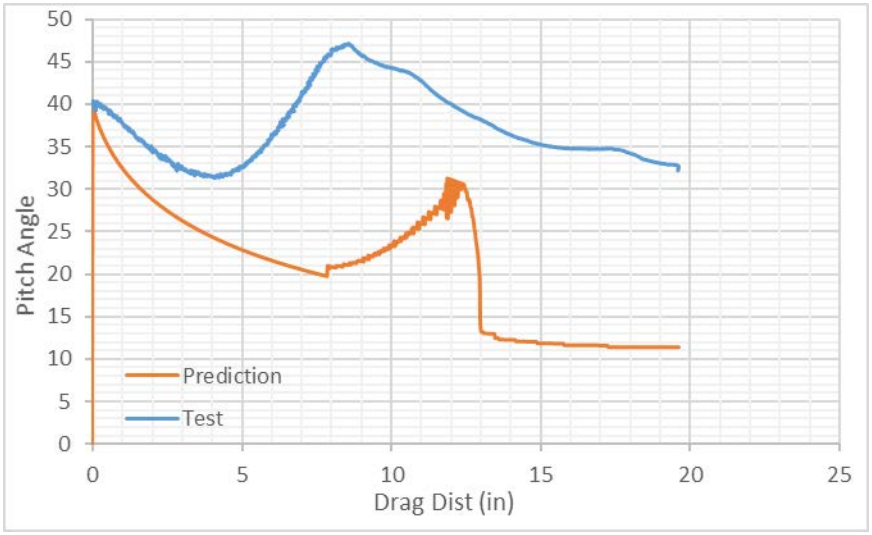

Fourth Repeat Test in Case 8

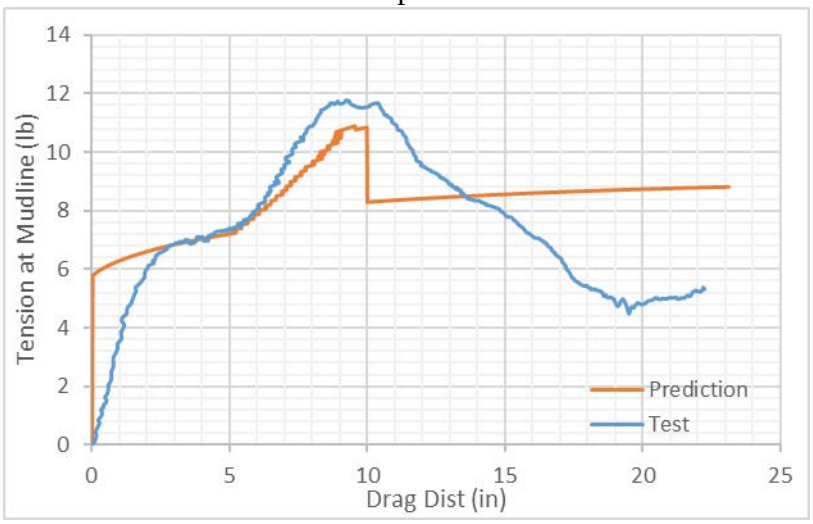

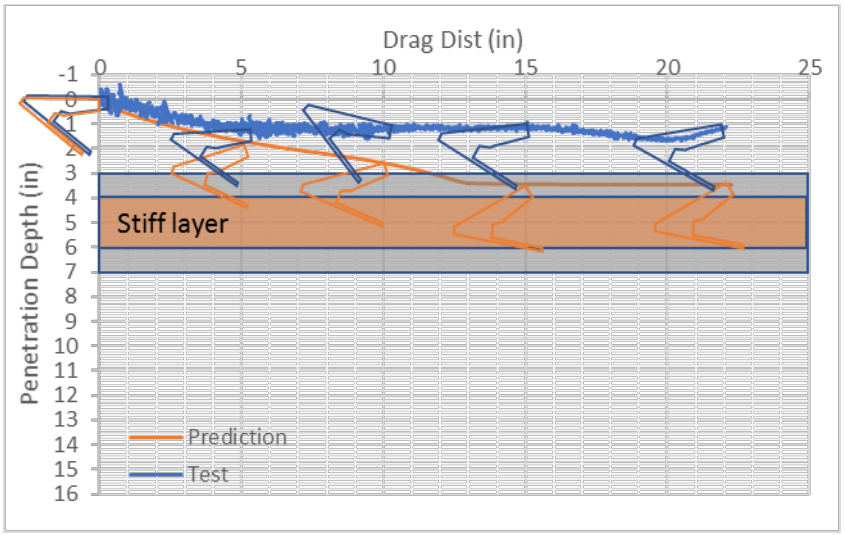

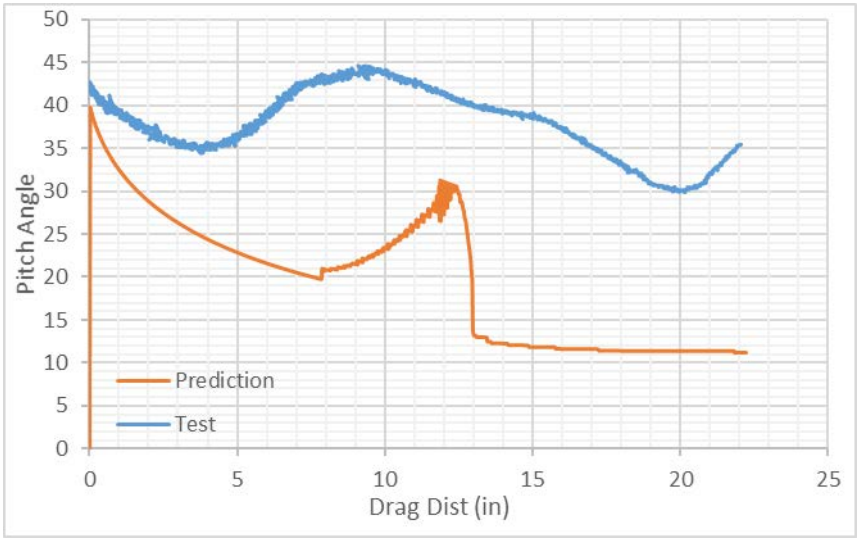

Appendix B. Drag Embedment Tests with Drag Embedment Anchor in Different Sizes

Generic Anchor Tests Results

First test

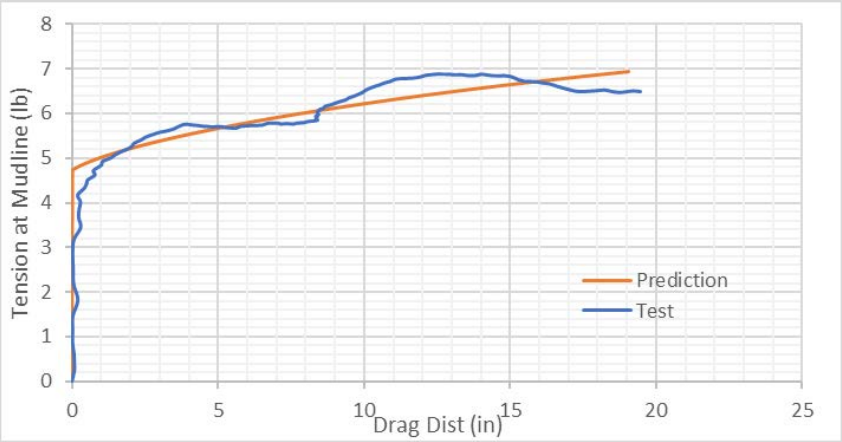

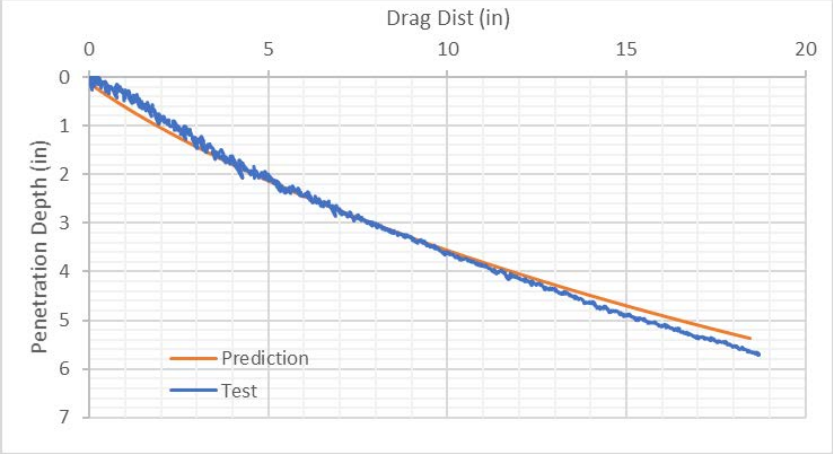

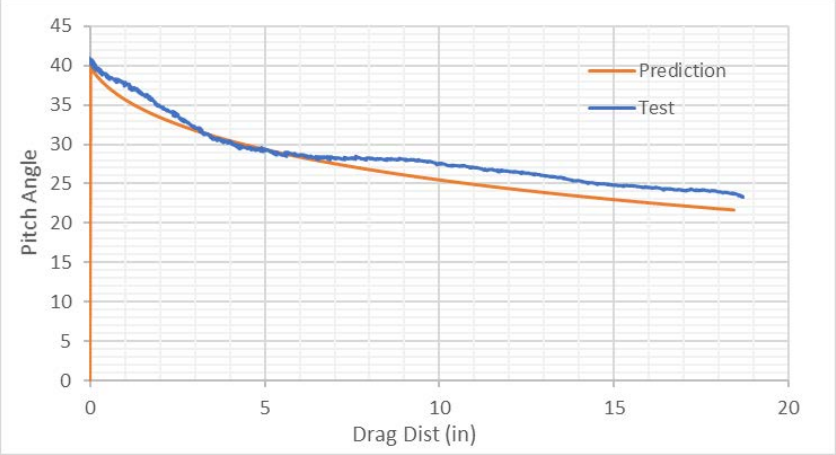

Generic Anchor Tests Results

First test

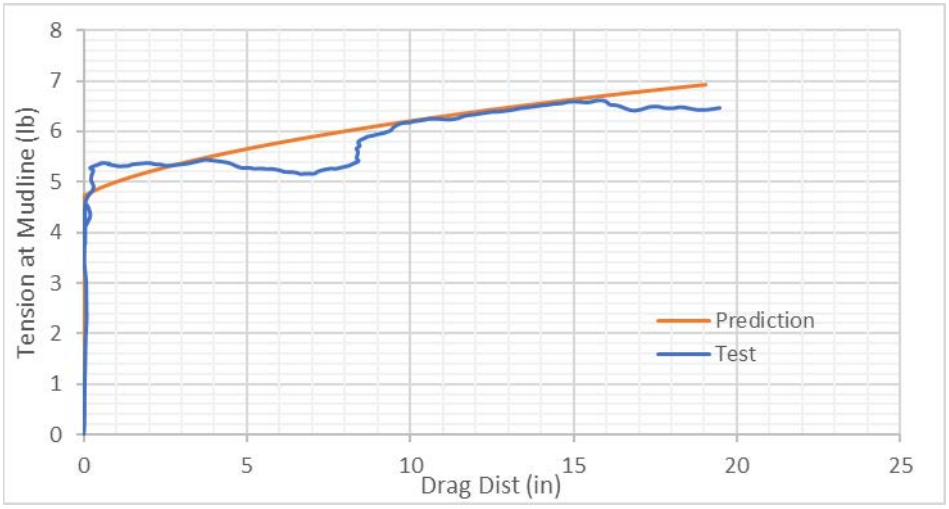

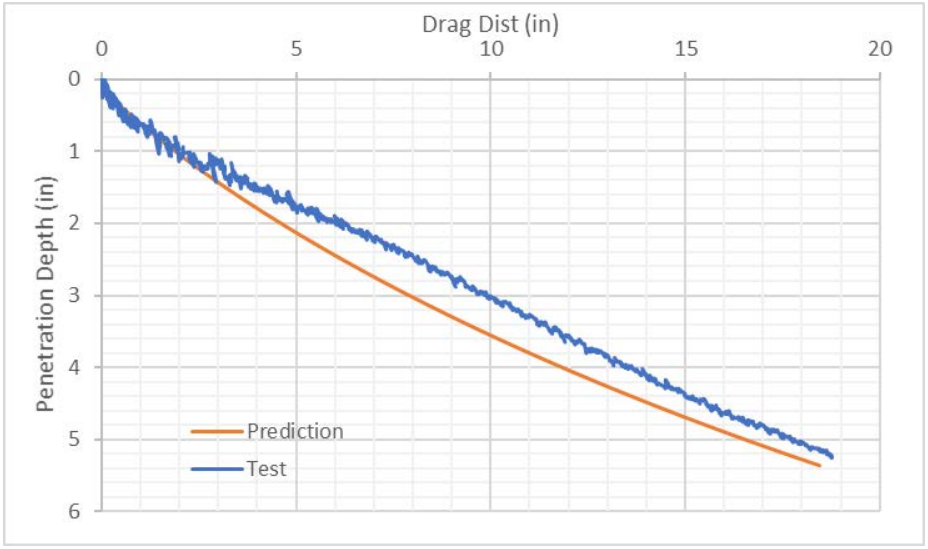

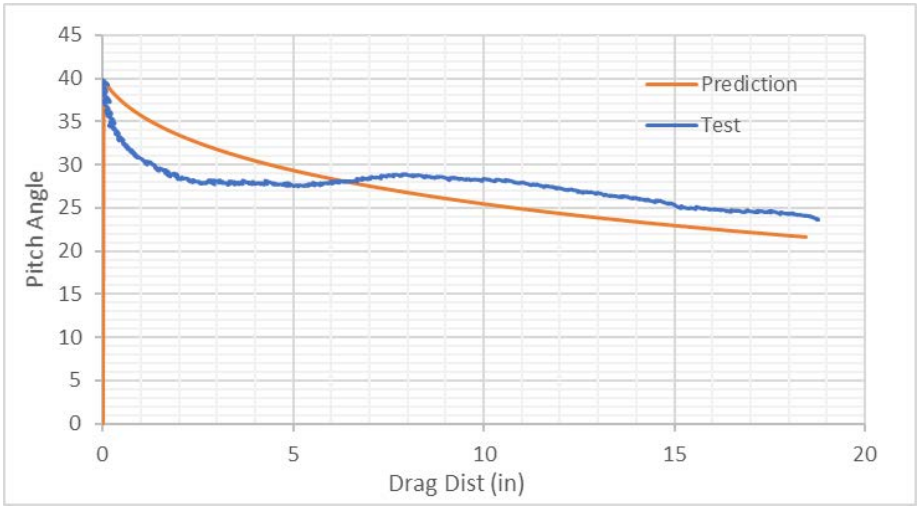

Generic Anchor Tests Results

Third test

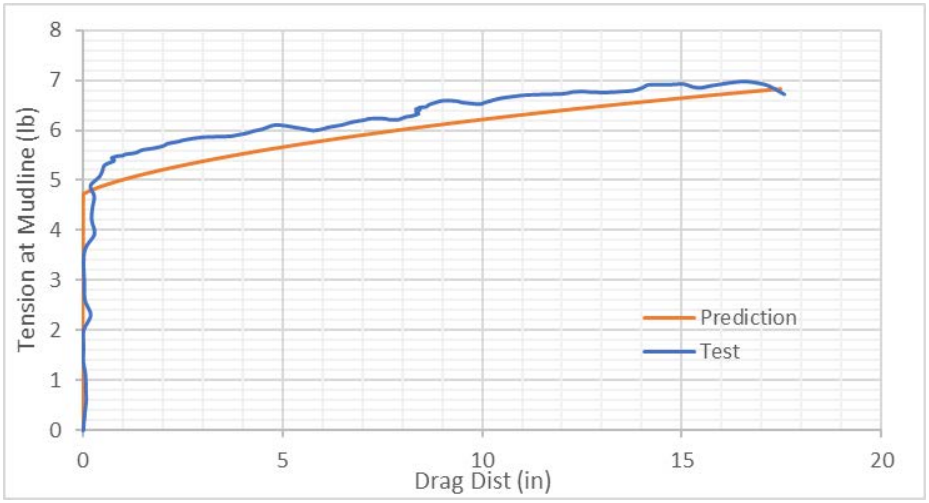

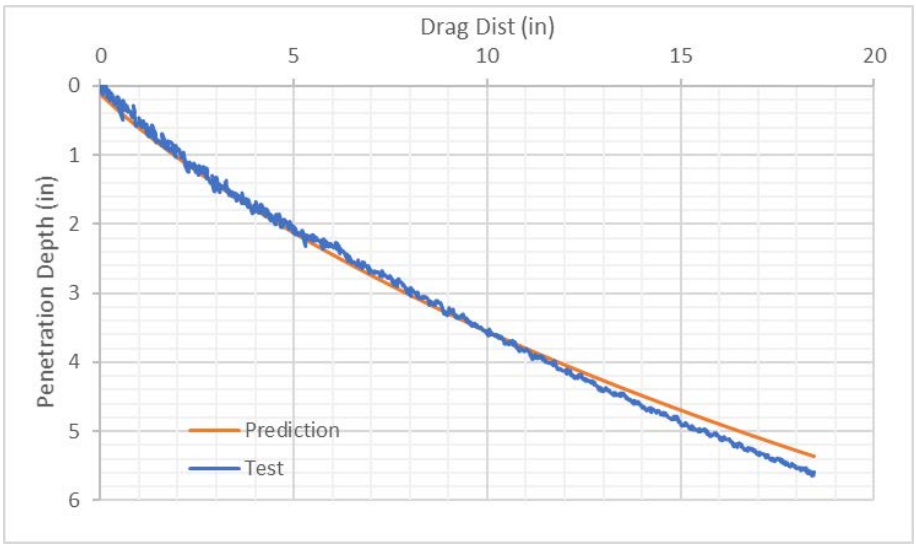

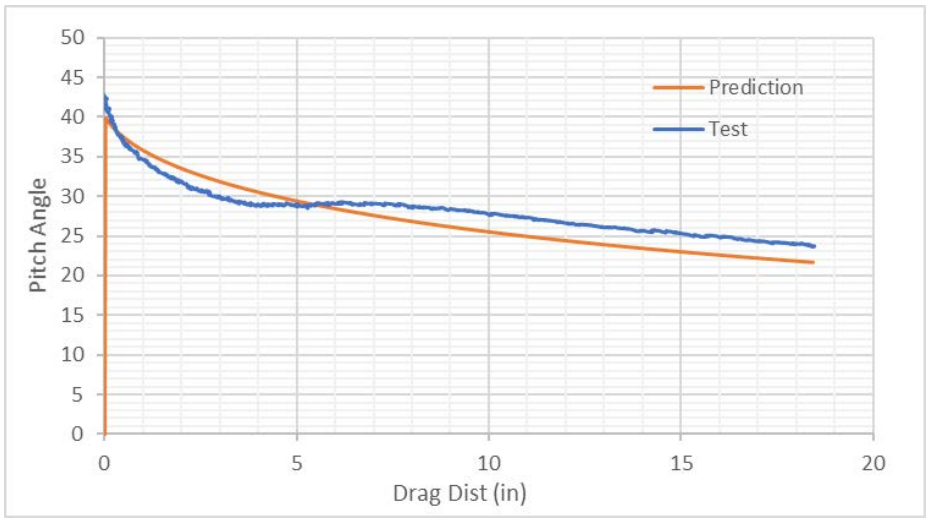

Larger Anchor Tests Results

First test

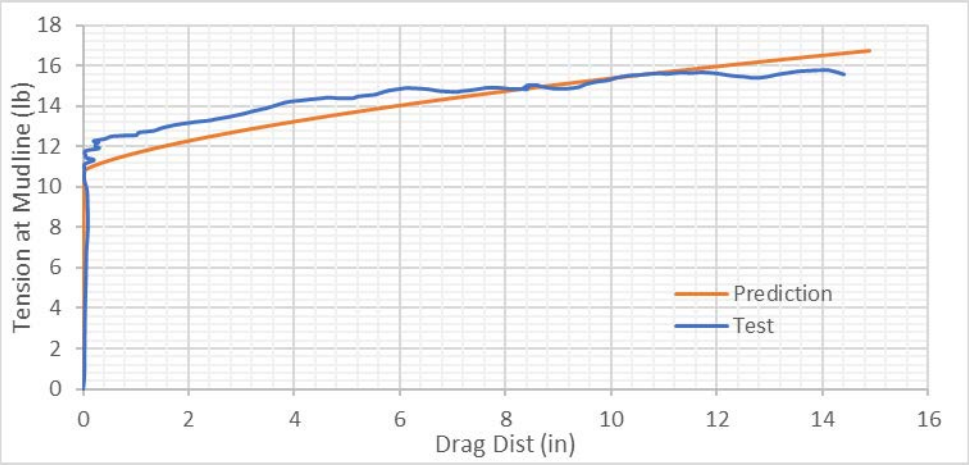

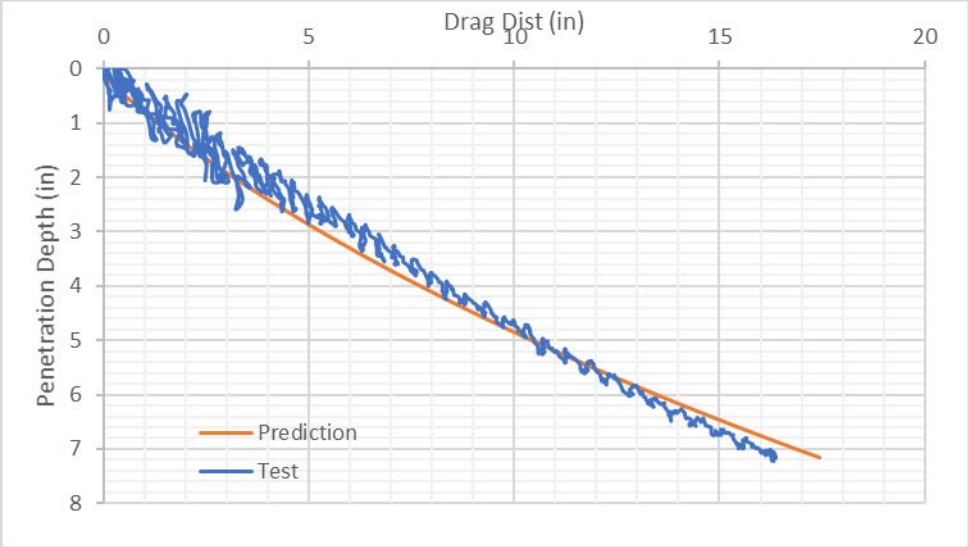

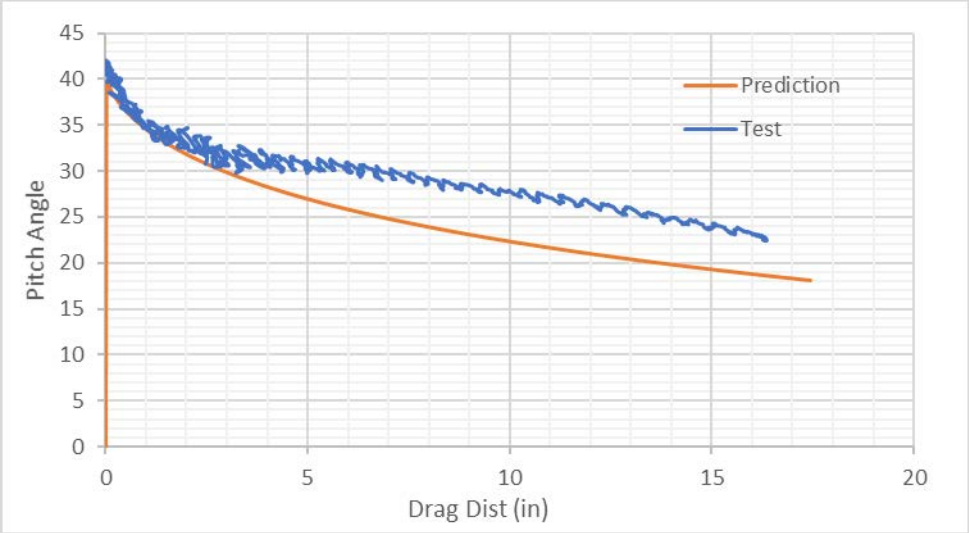

Larger Anchor Tests Results

Second test

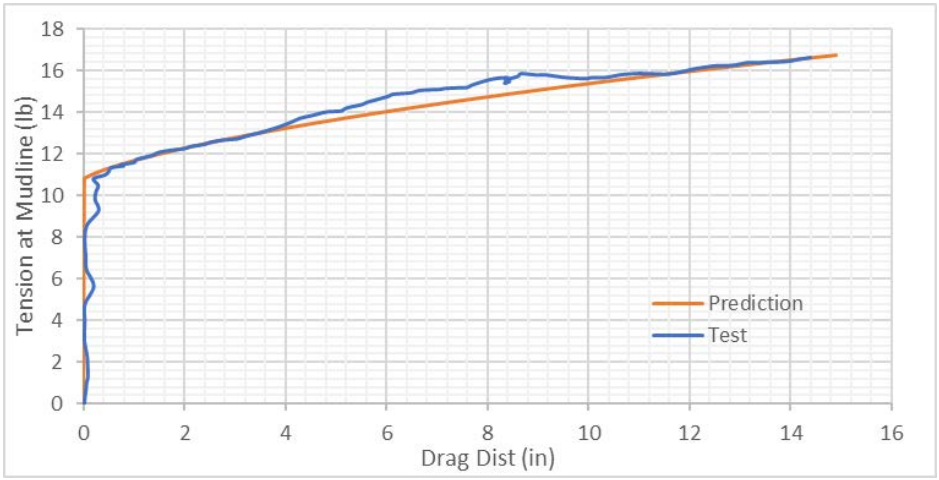

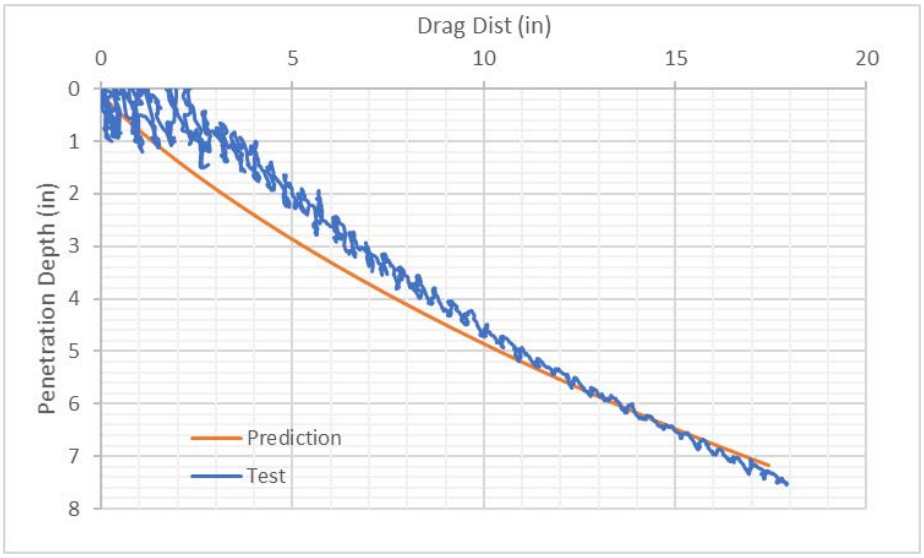

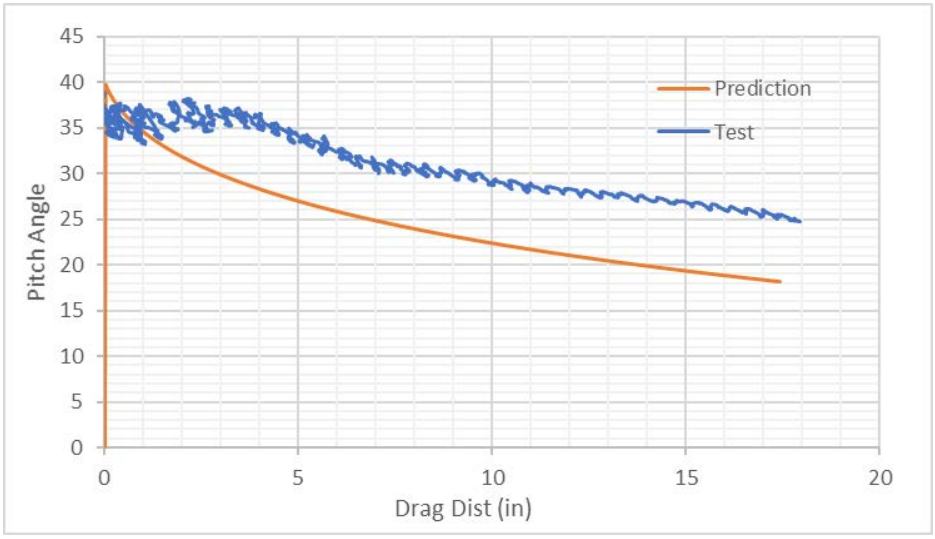

Larger Anchor Tests Results

Third test

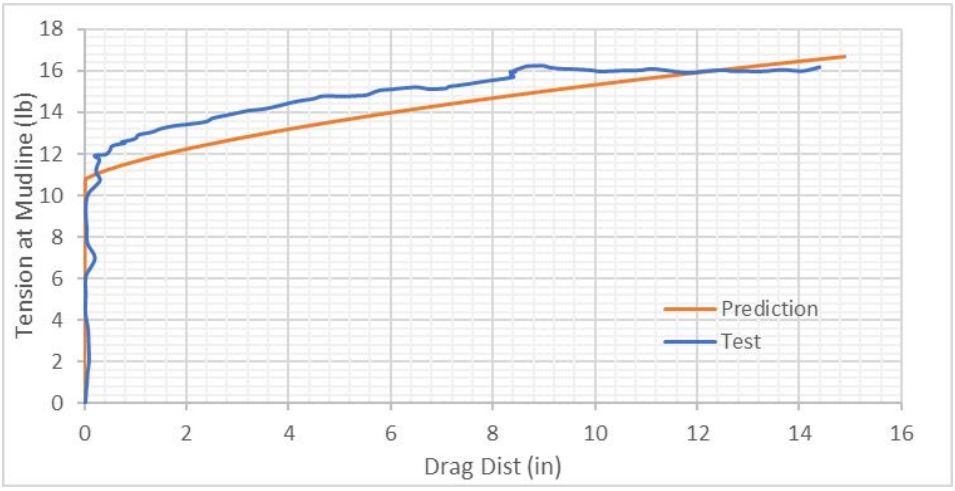

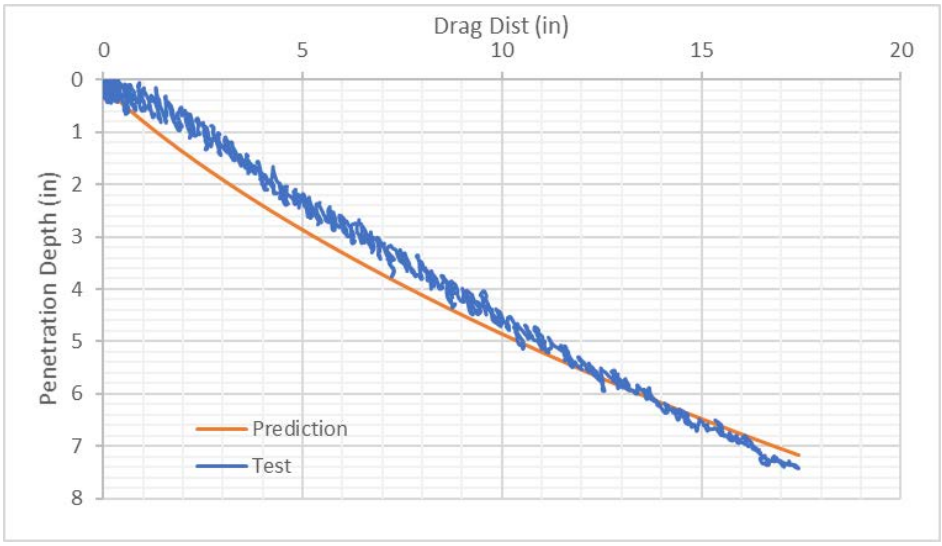

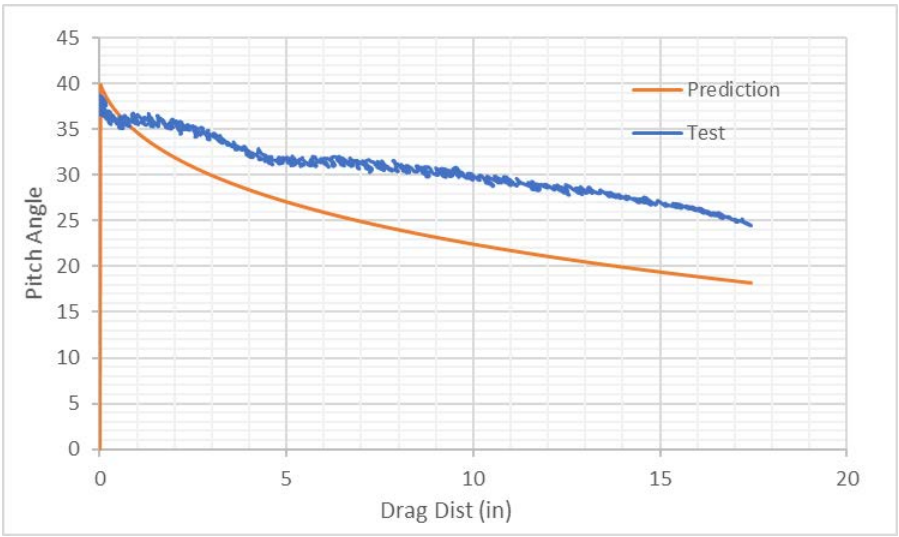

Appendix C. Comparison between the Updated and Original Prediction for Drag Embedment Anchor in Layered Soil Profile

Case 3

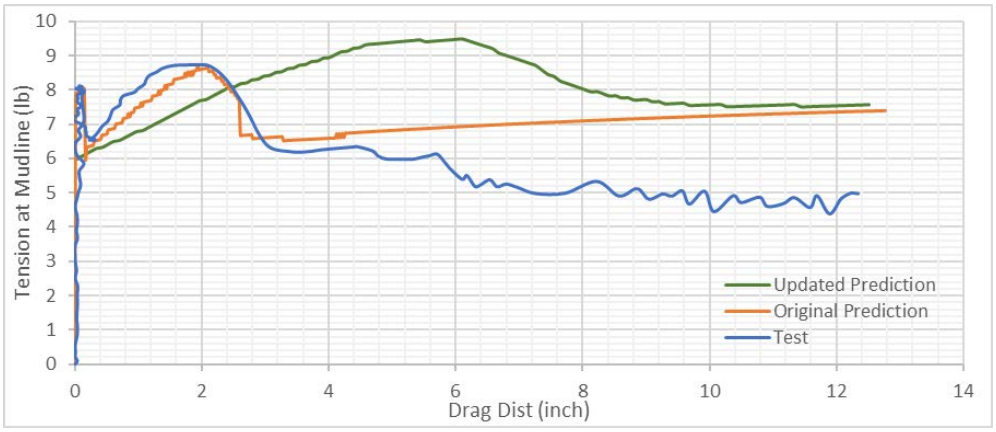

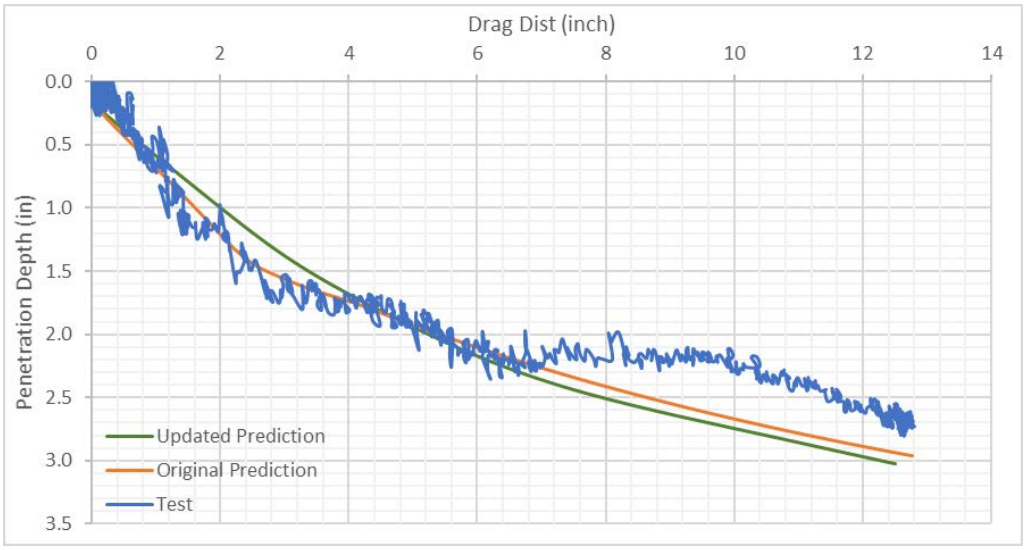

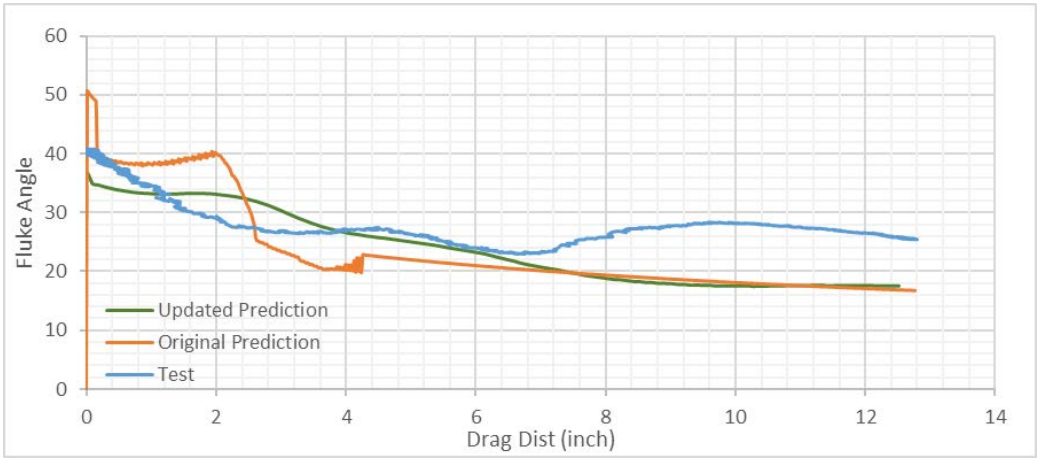

Case 3 First Repeat

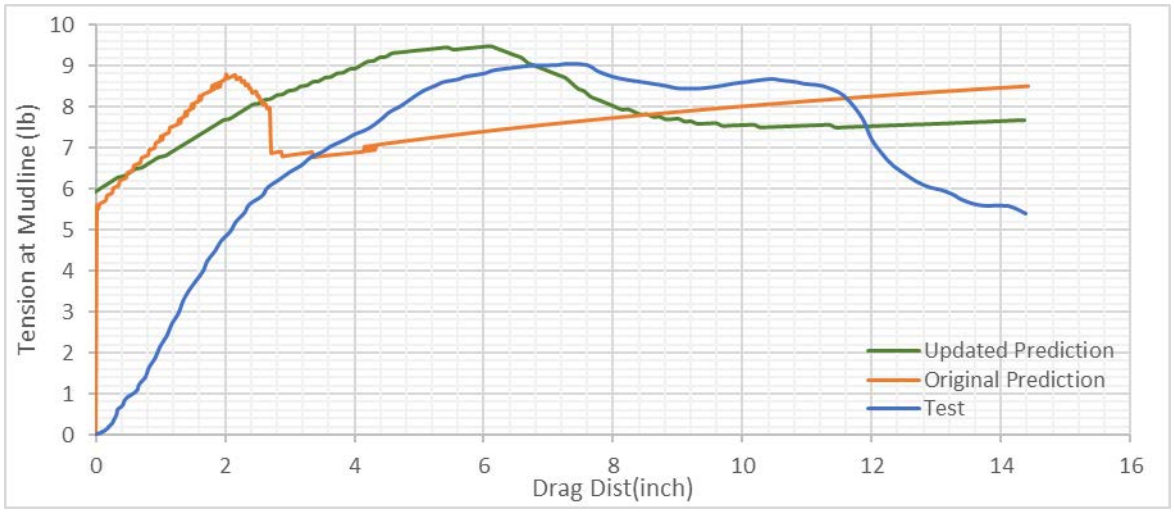

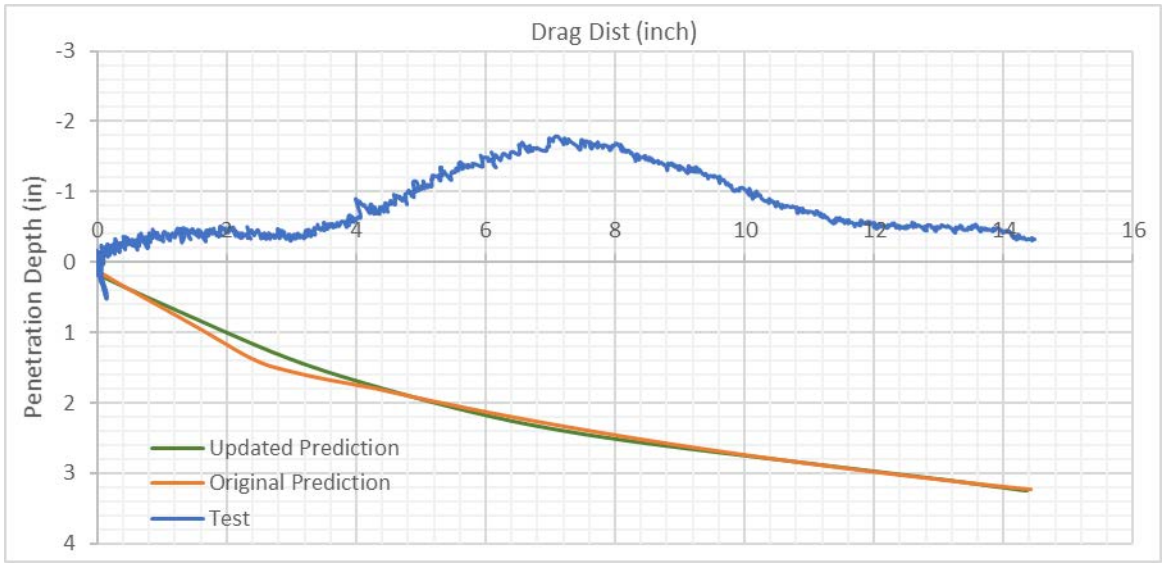

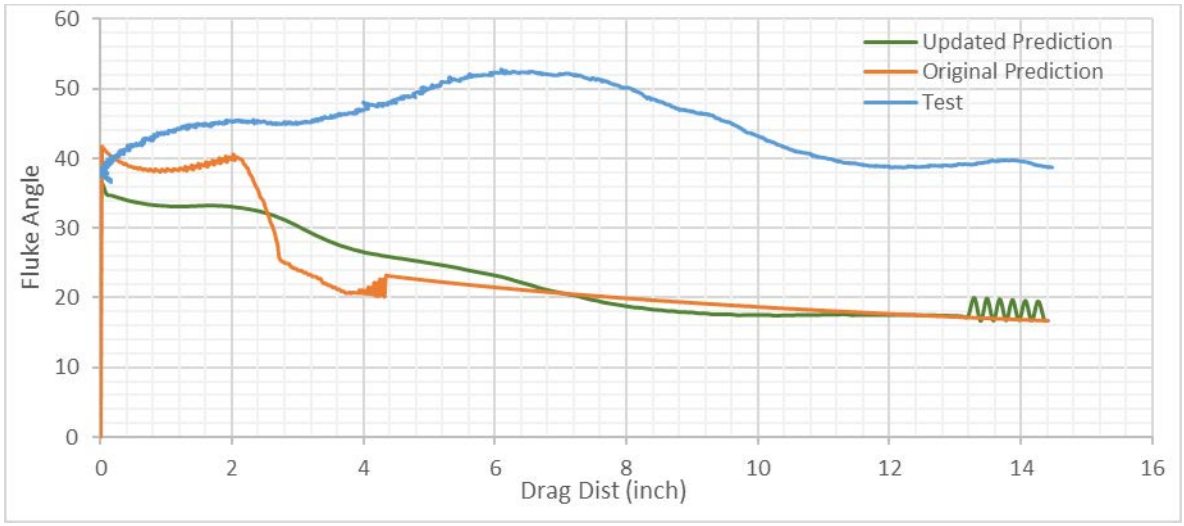

Case 3 Second Repeat

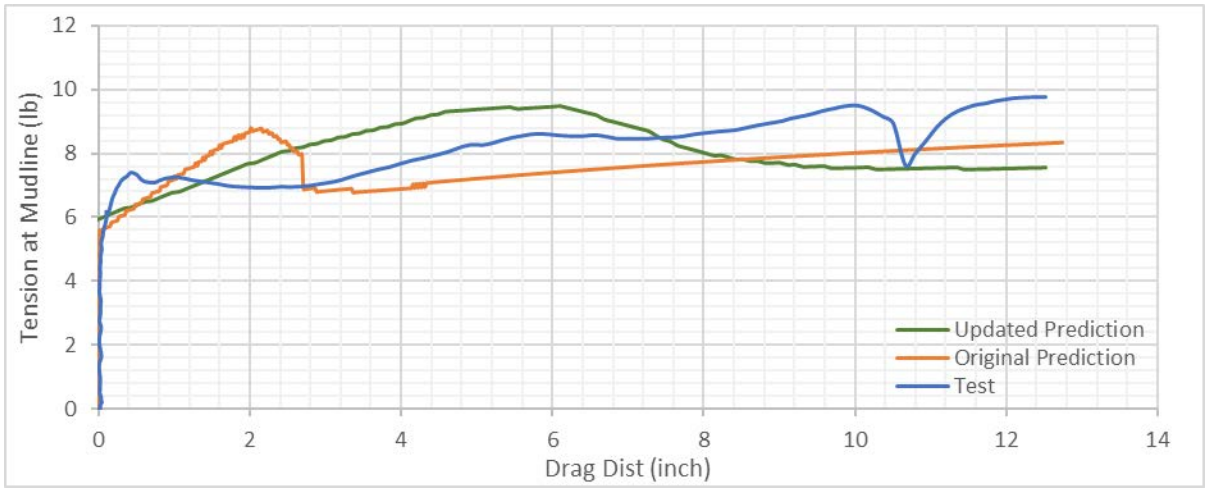

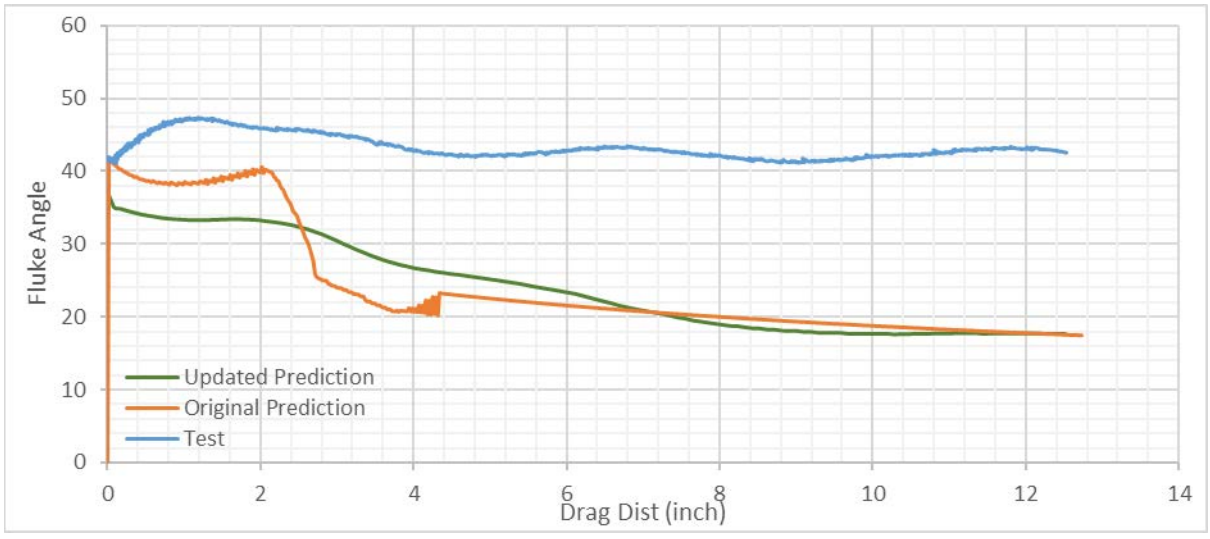

Case 4

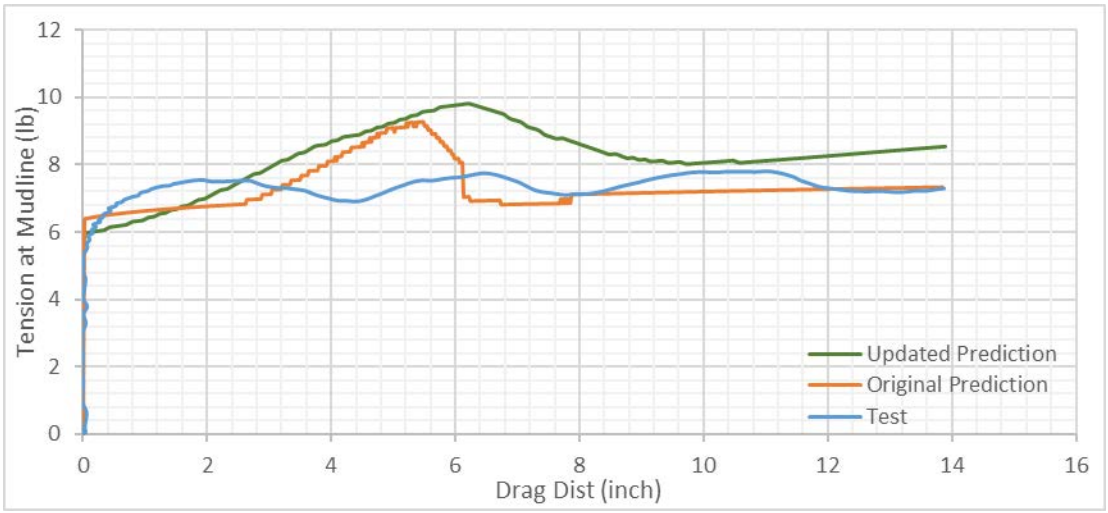
Tension at Mudline (lb)
Drag Dist (inch)
Updated Prediction
Original Prediction
Test

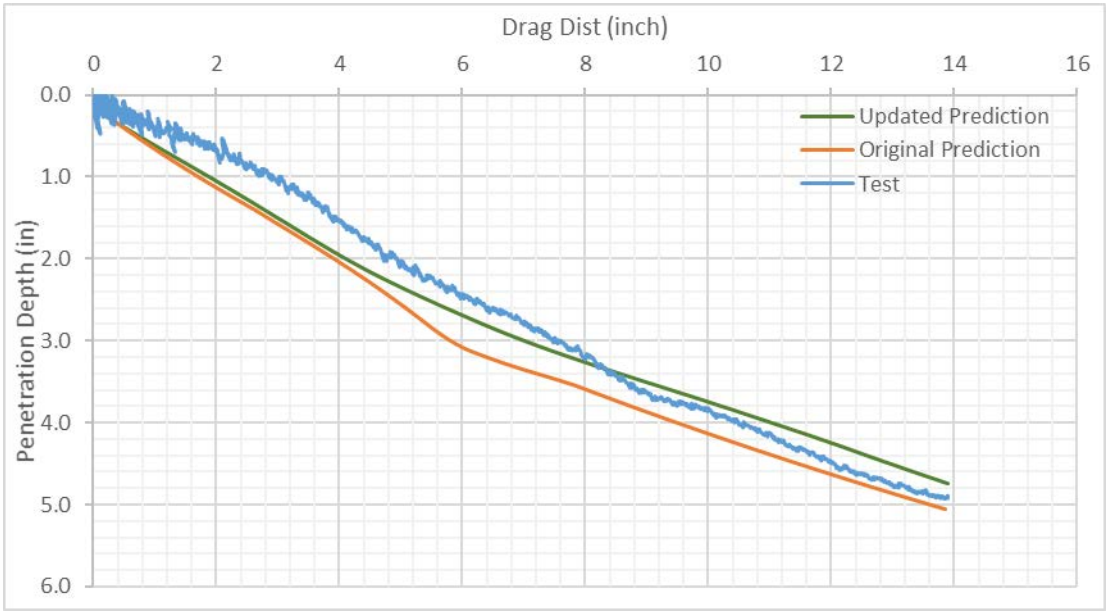
Drag Dist (inch)
Penetration Depth (in)
Updated Prediction
Original Prediction
Test

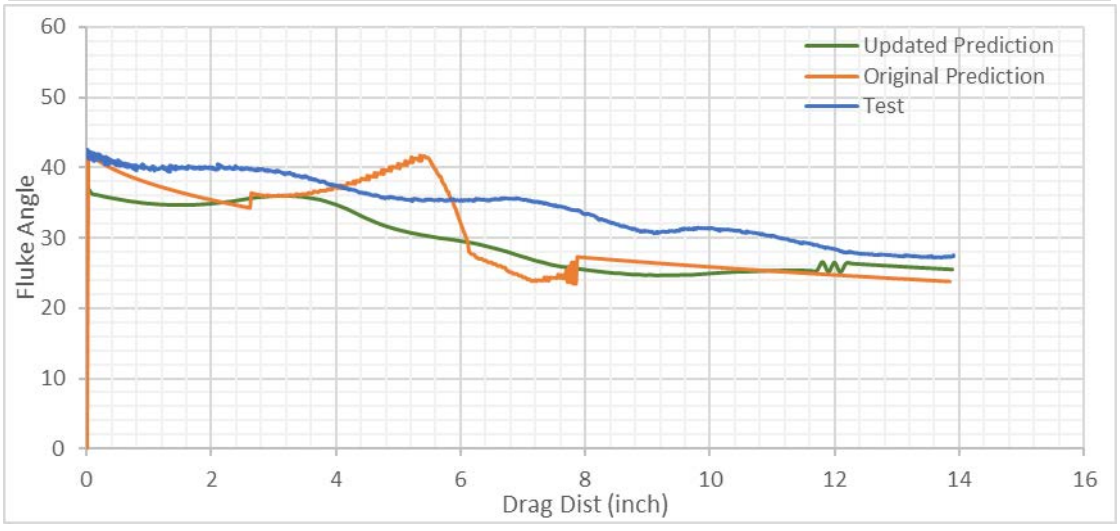
Fluke Angle
Drag Dist (inch)
Updated Prediction
Original Prediction
Test

Case 4 First Repeat

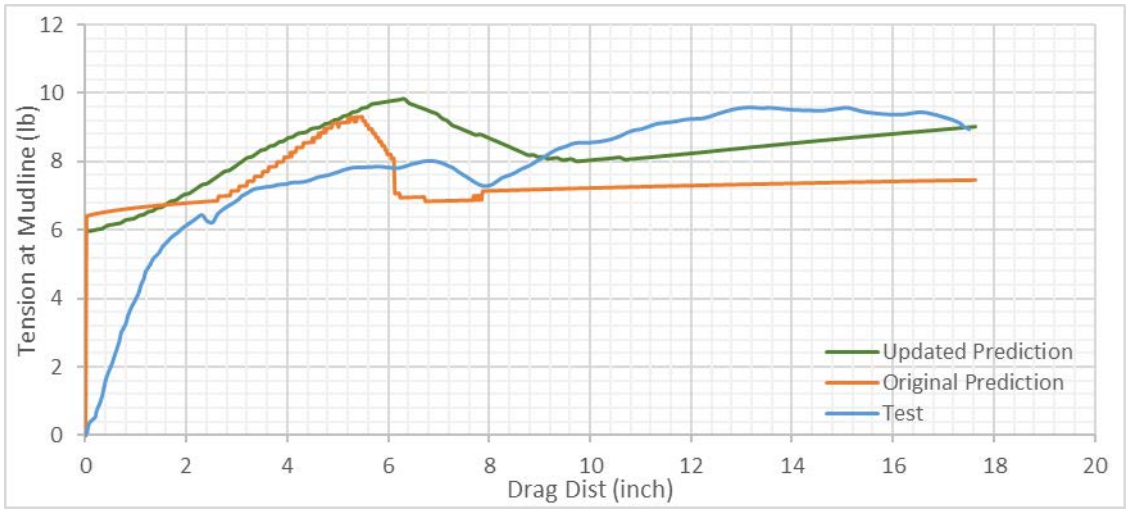

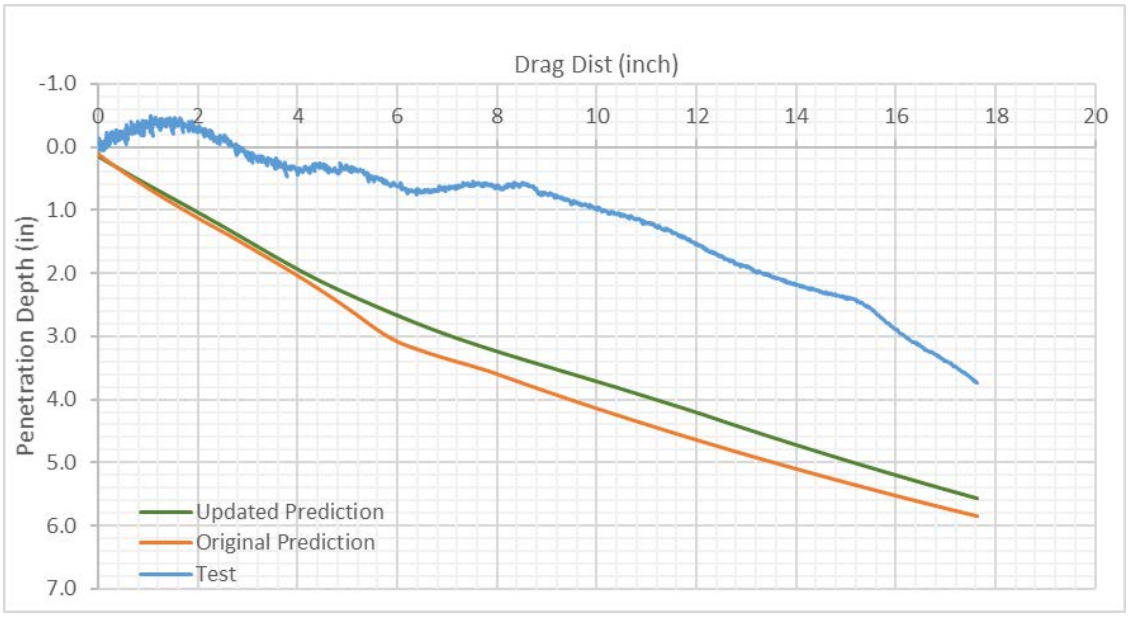

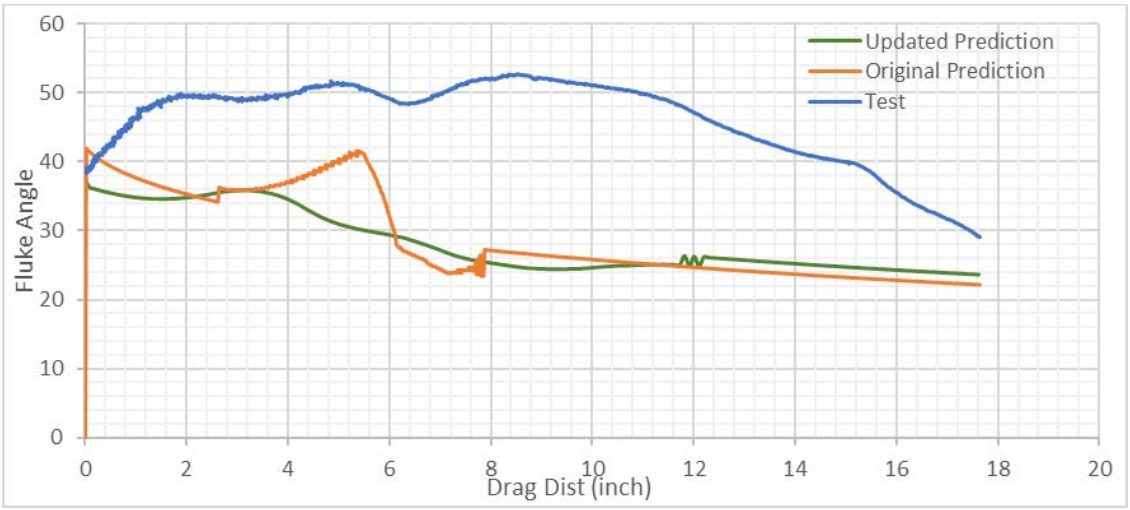

Case 5

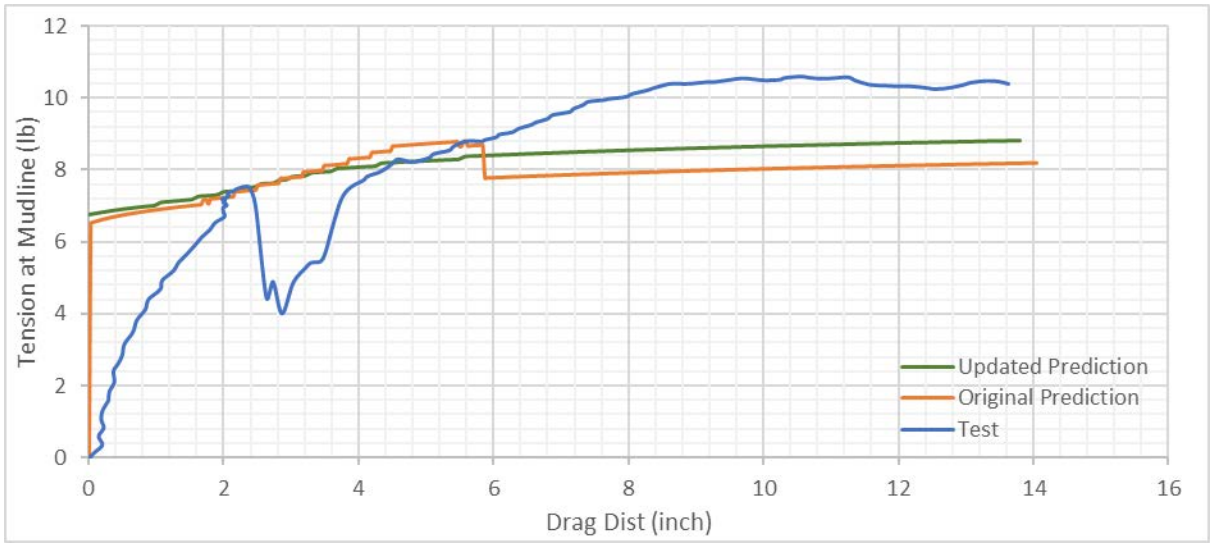
Tension at Mudline (lb)
Drag Dist (inch)
Updated Prediction
Original Prediction
Test

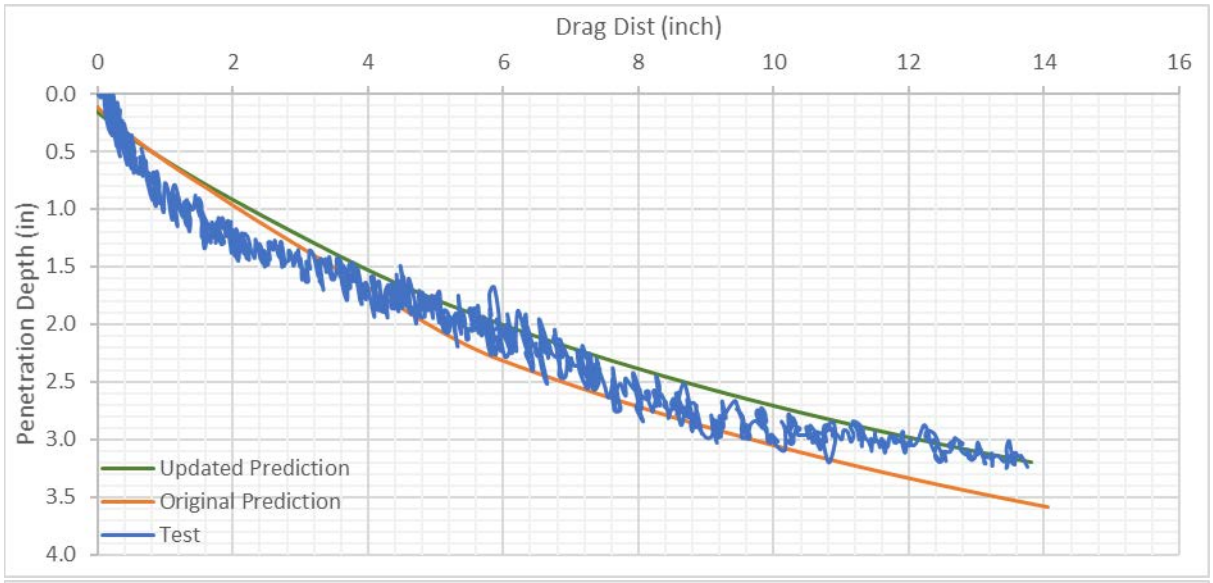
Drag Dist (inch)
Penetration Depth (in)
Updated Prediction
Original Prediction
Test

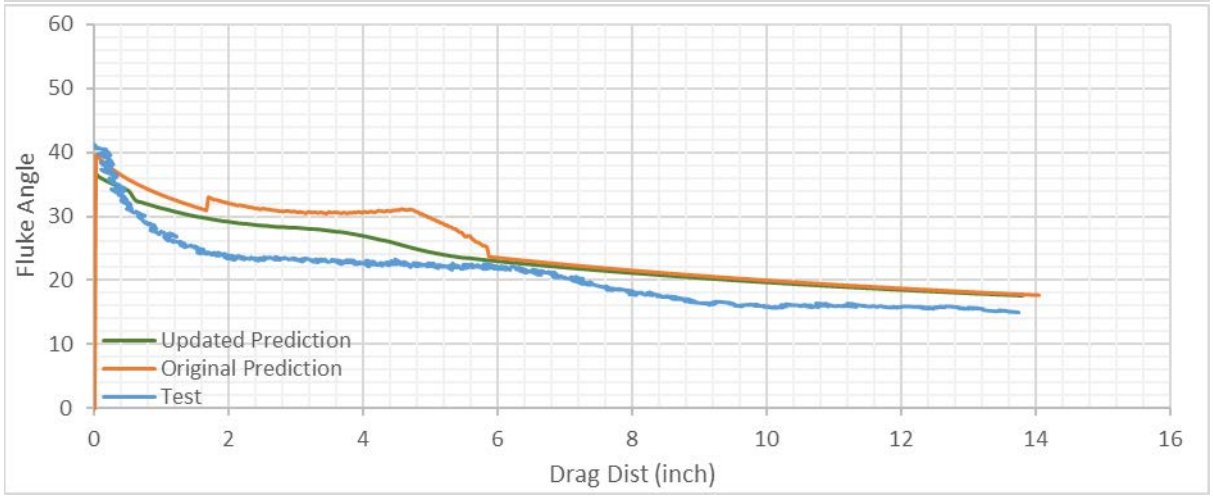
Fluke Angle
Drag Dist (inch)
Updated Prediction
Original Prediction
Test

Case 5 First Repeat

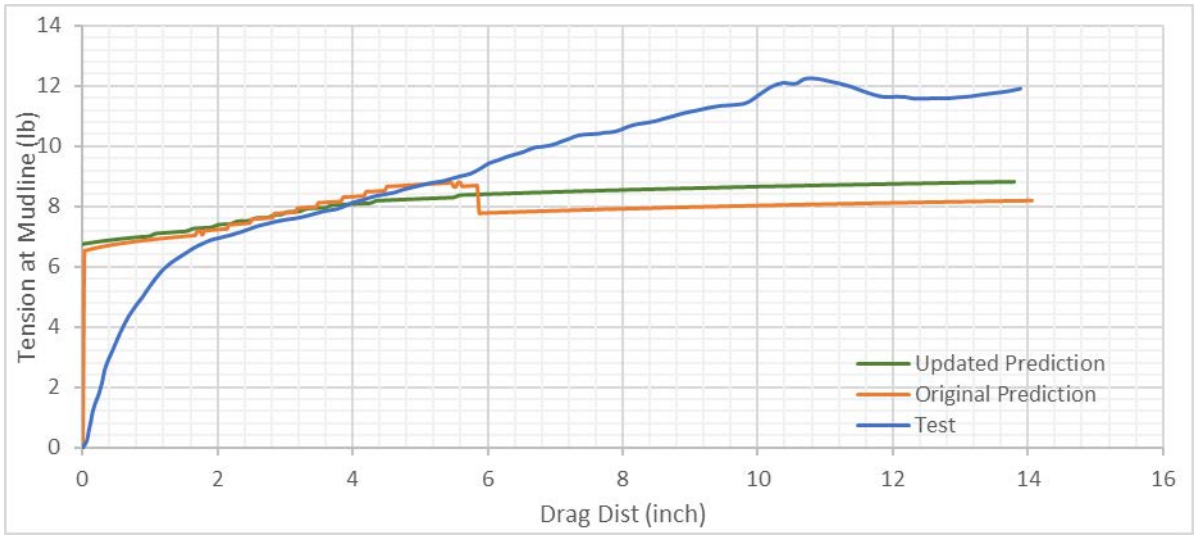

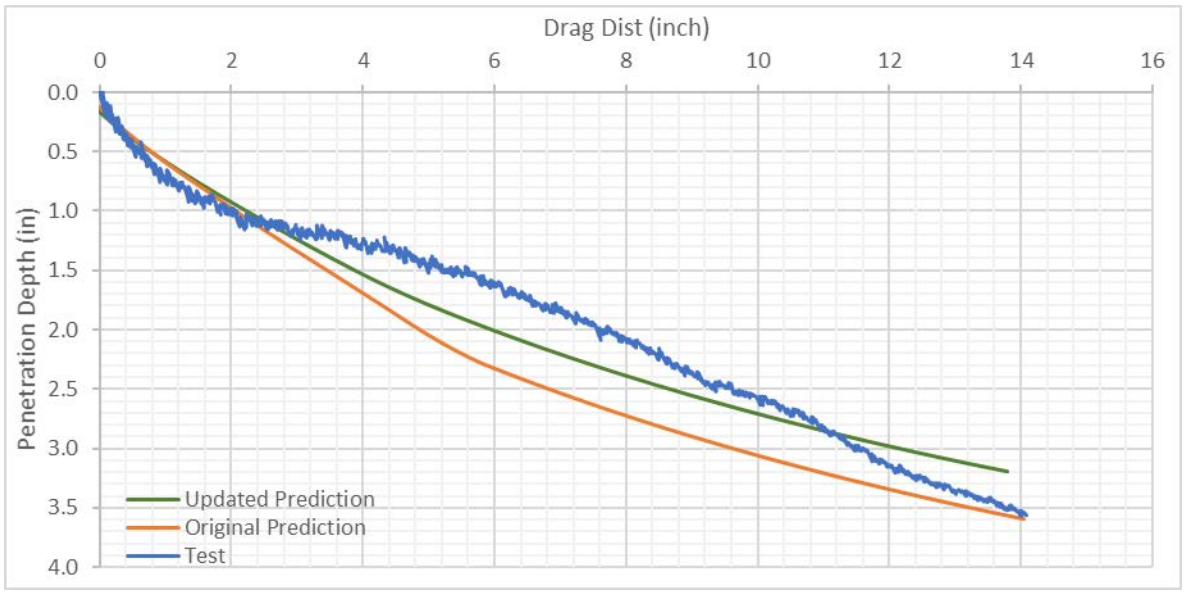

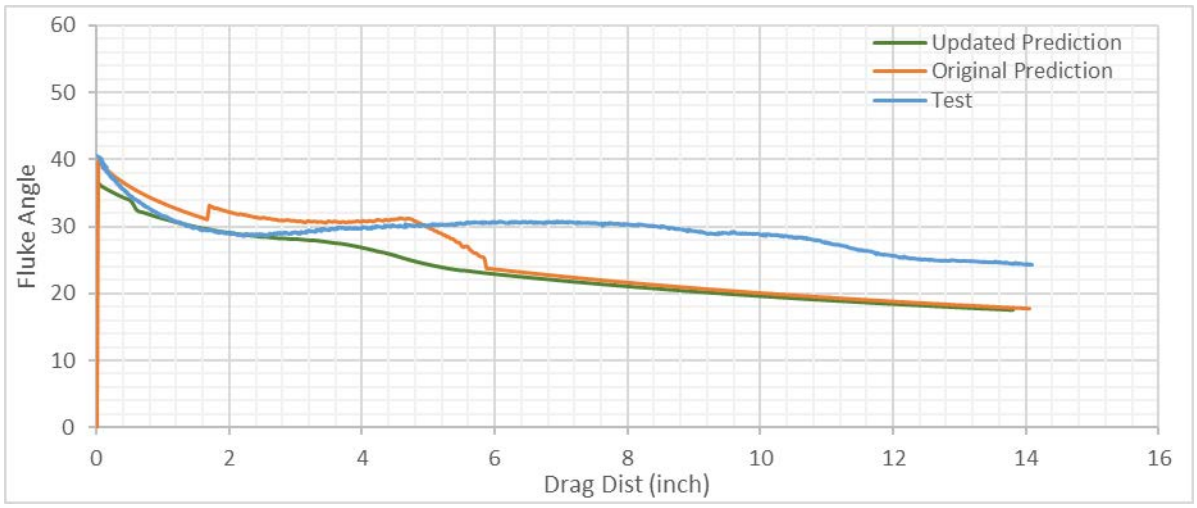

Case 6

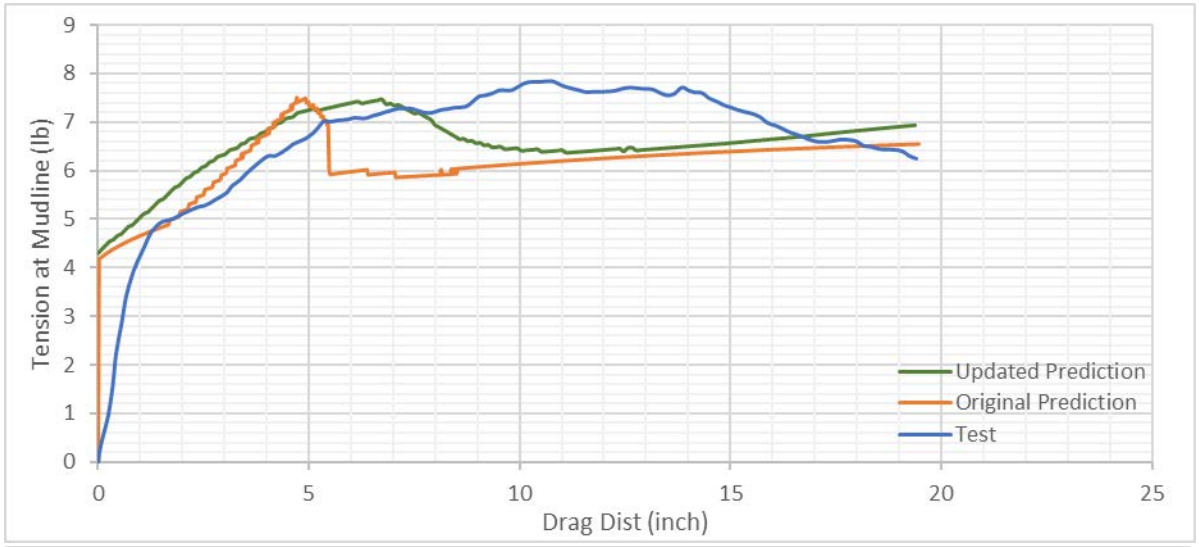
Tension at Mudline (lb)
Drag Dist (inch)
Updated Prediction
Original Prediction
Test

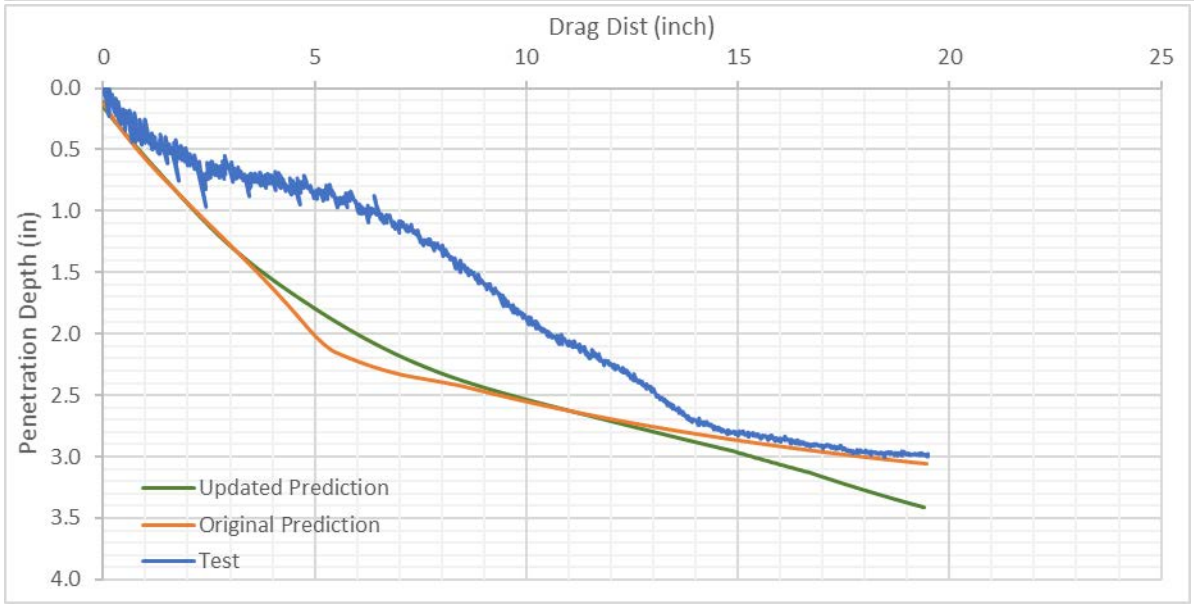
Drag Dist (inch)
Penetration Depth (in)
Updated Prediction
Original Prediction
Test

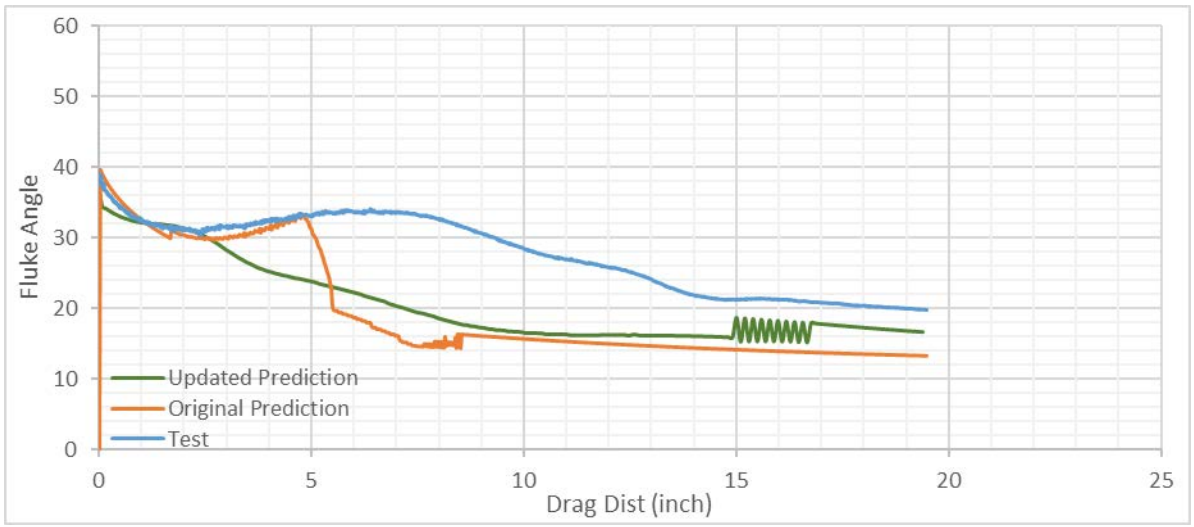
Fluke Angle
Drag Dist (inch)
Updated Prediction
Original Prediction
Test

Case 6 First Repeat

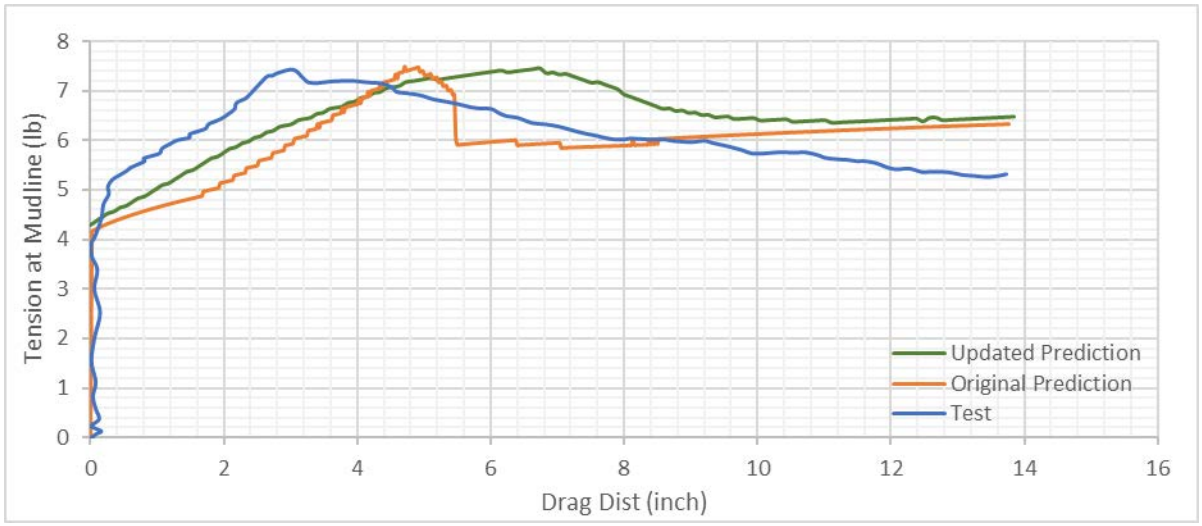

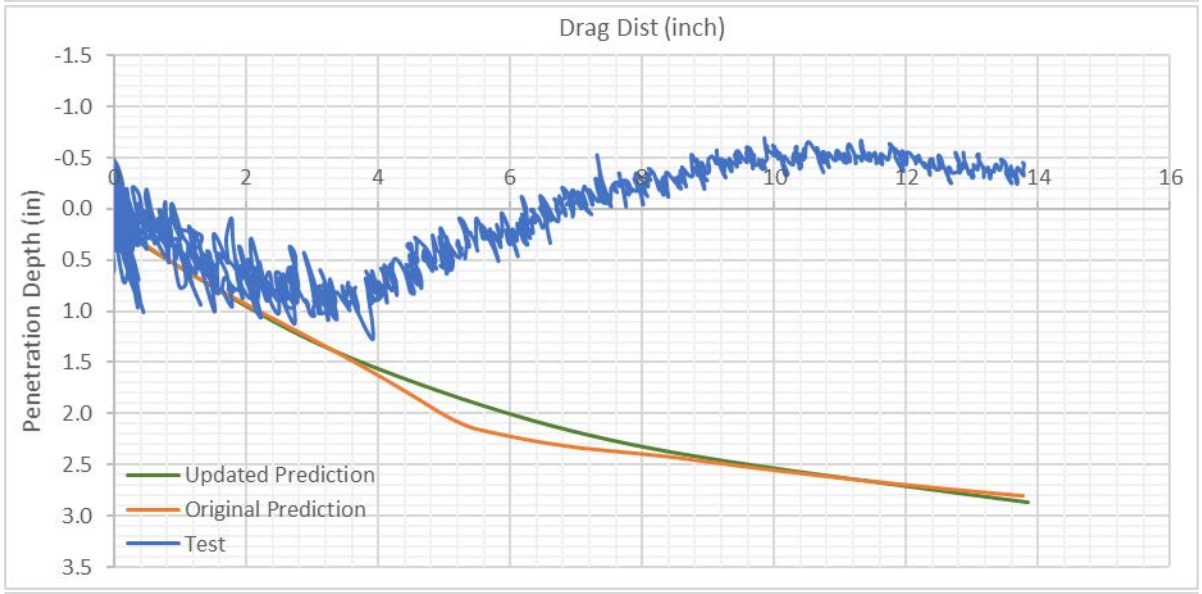

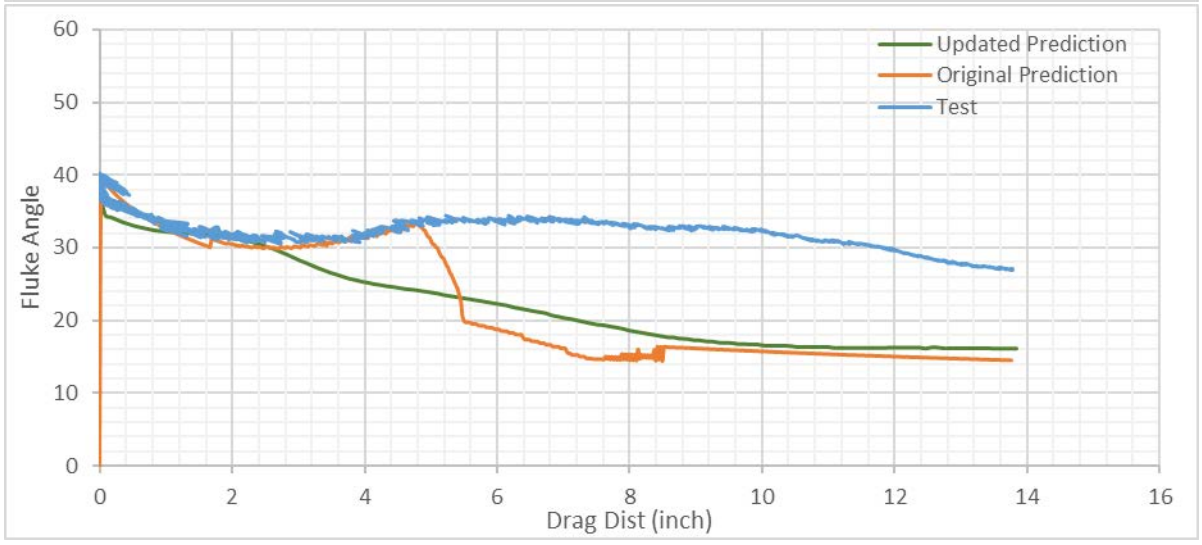

Case 6 Second Repeat

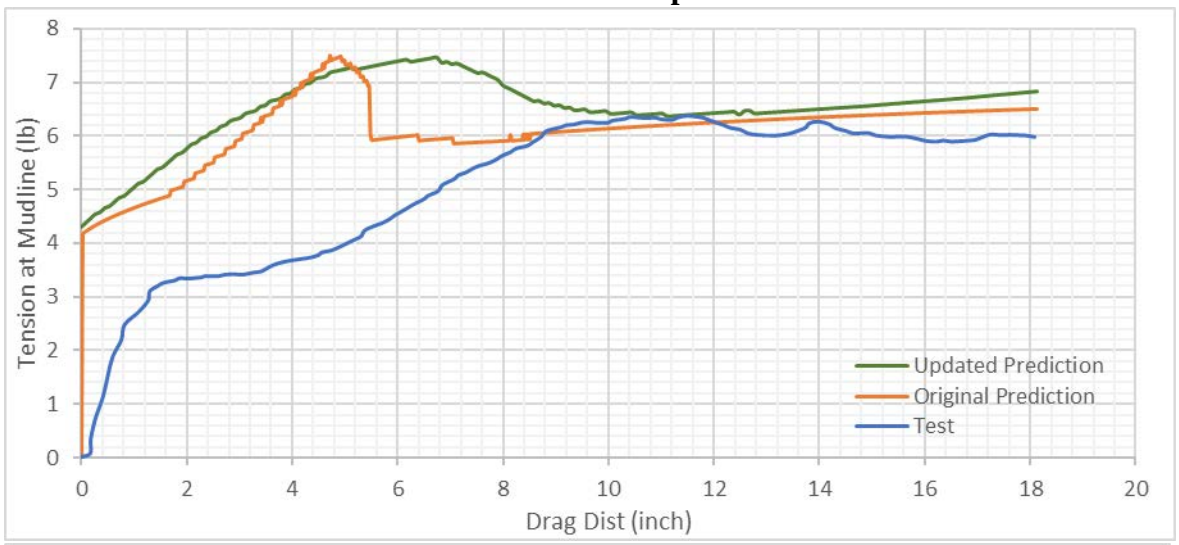

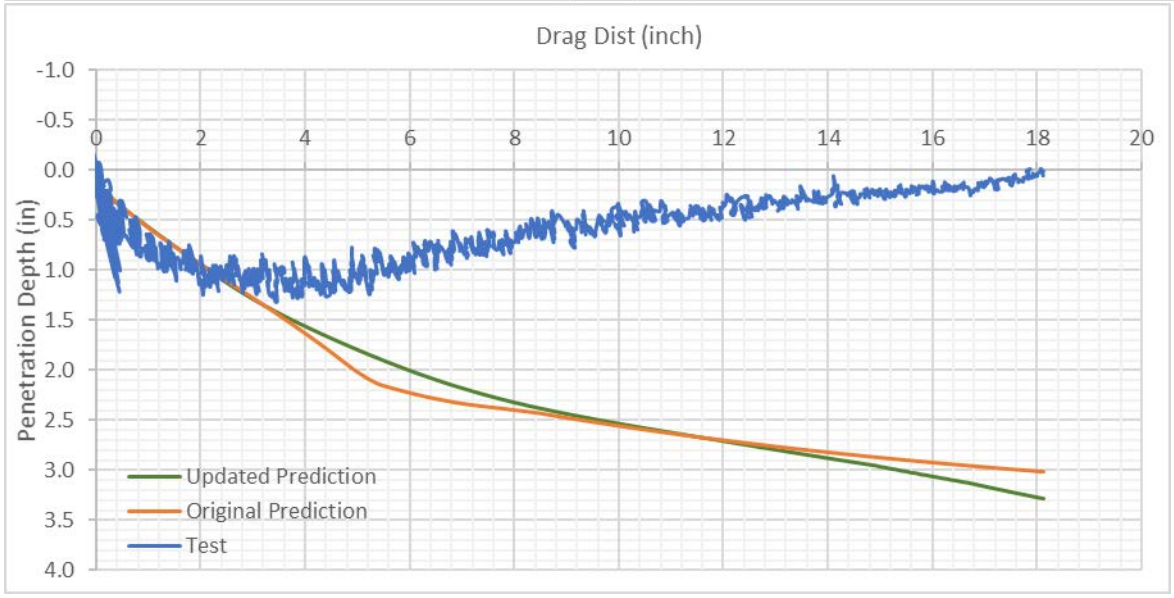

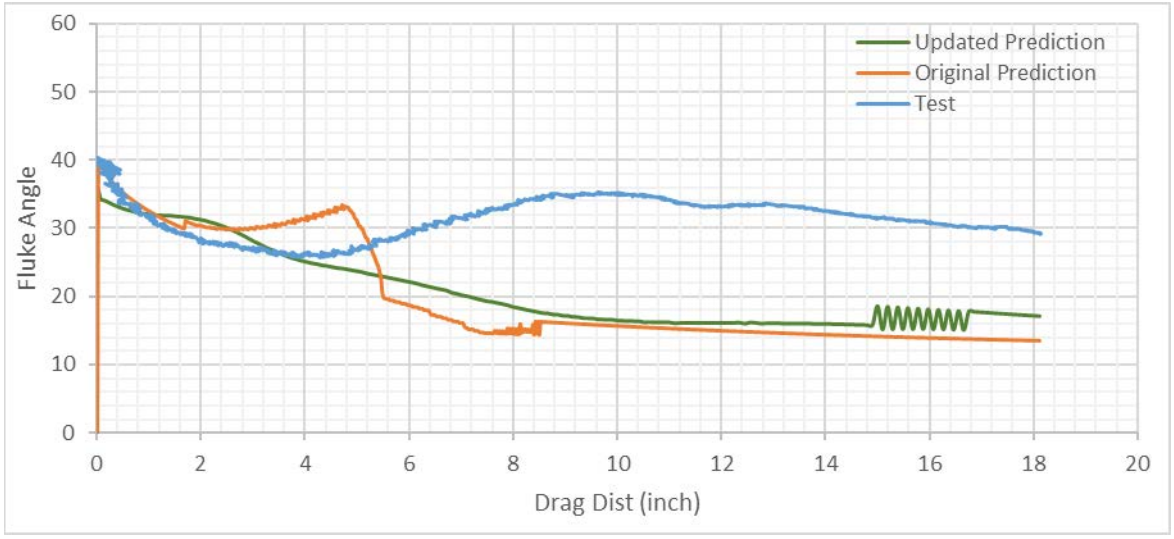

Case 6 Third Repeat

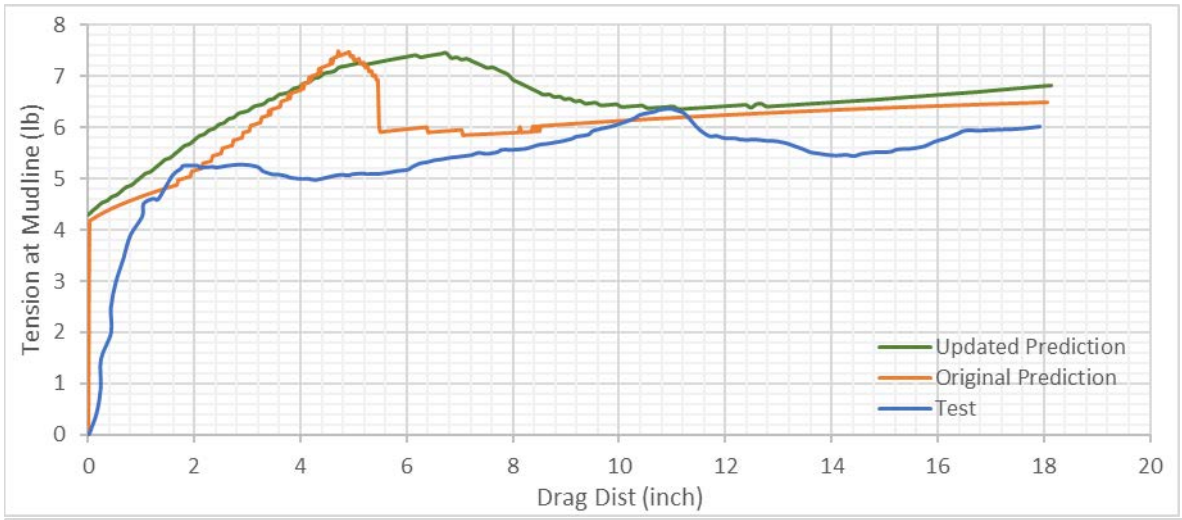

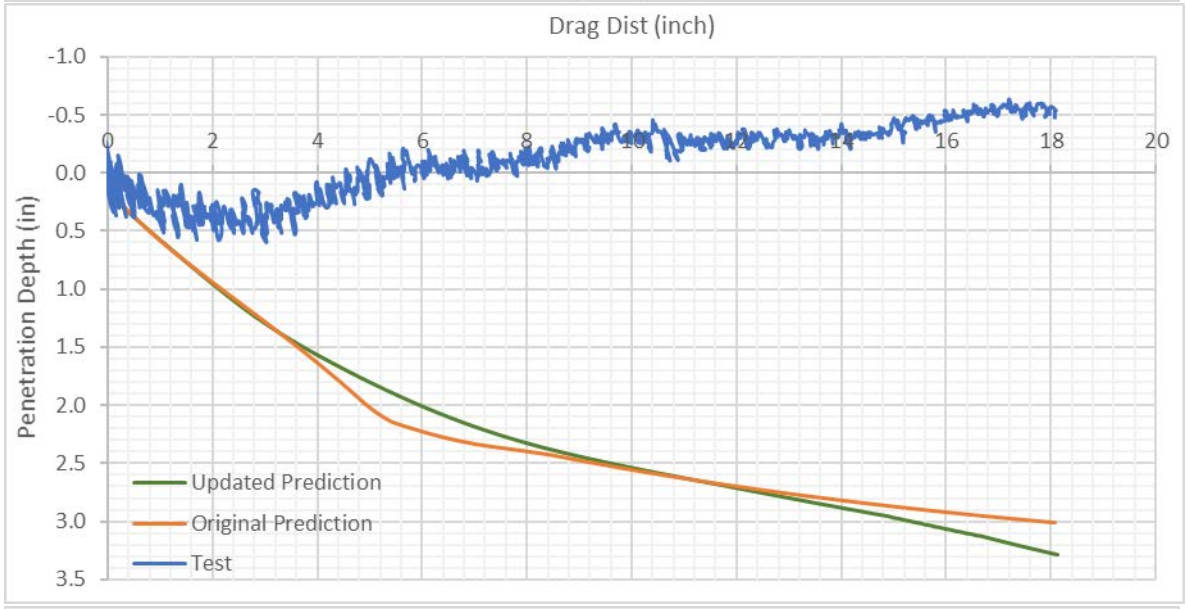

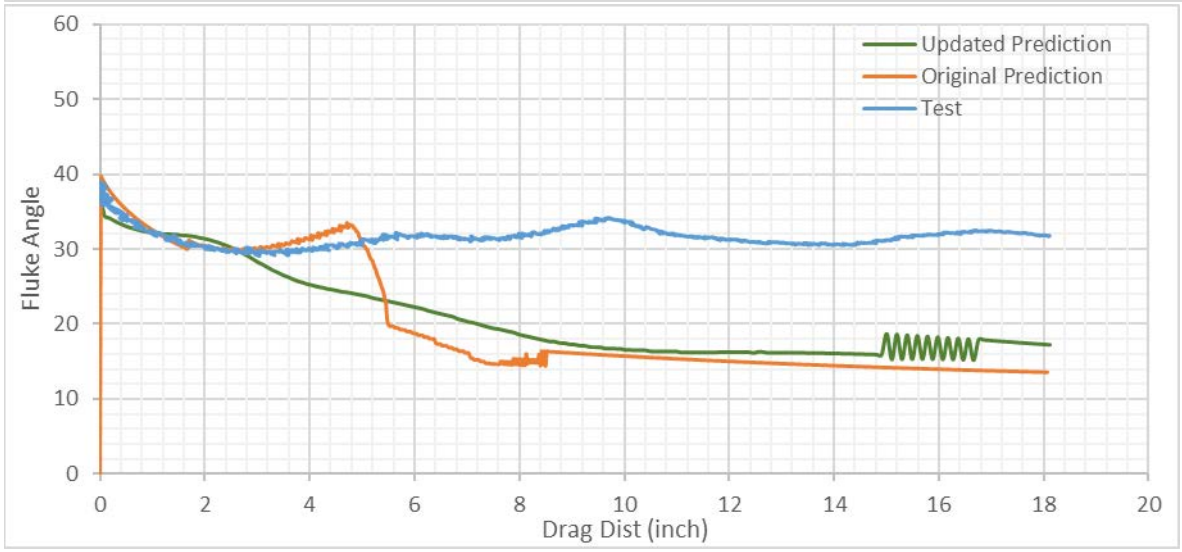

Case 6 Fourth Repeat

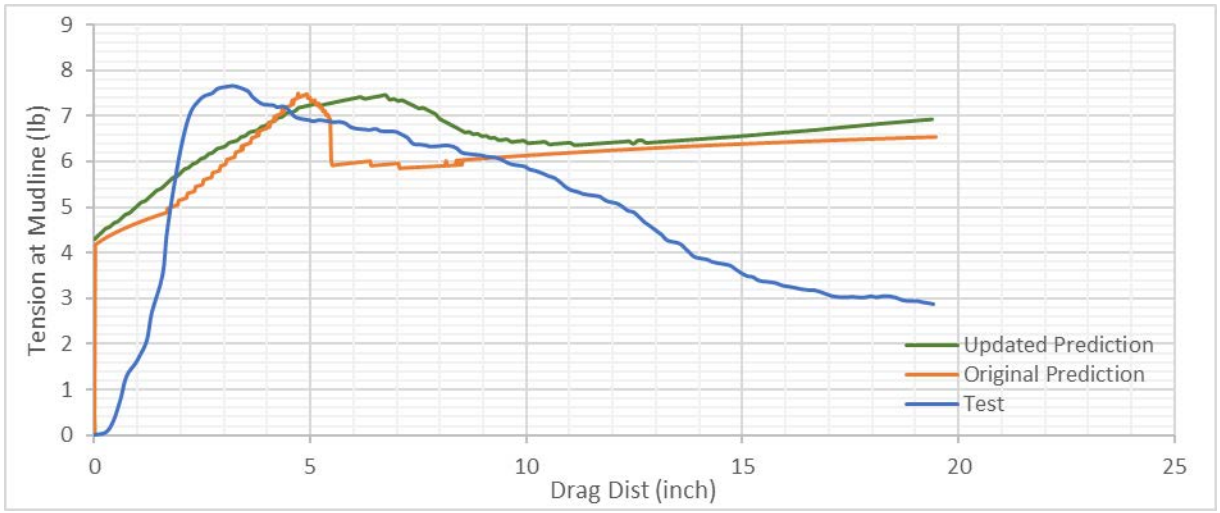

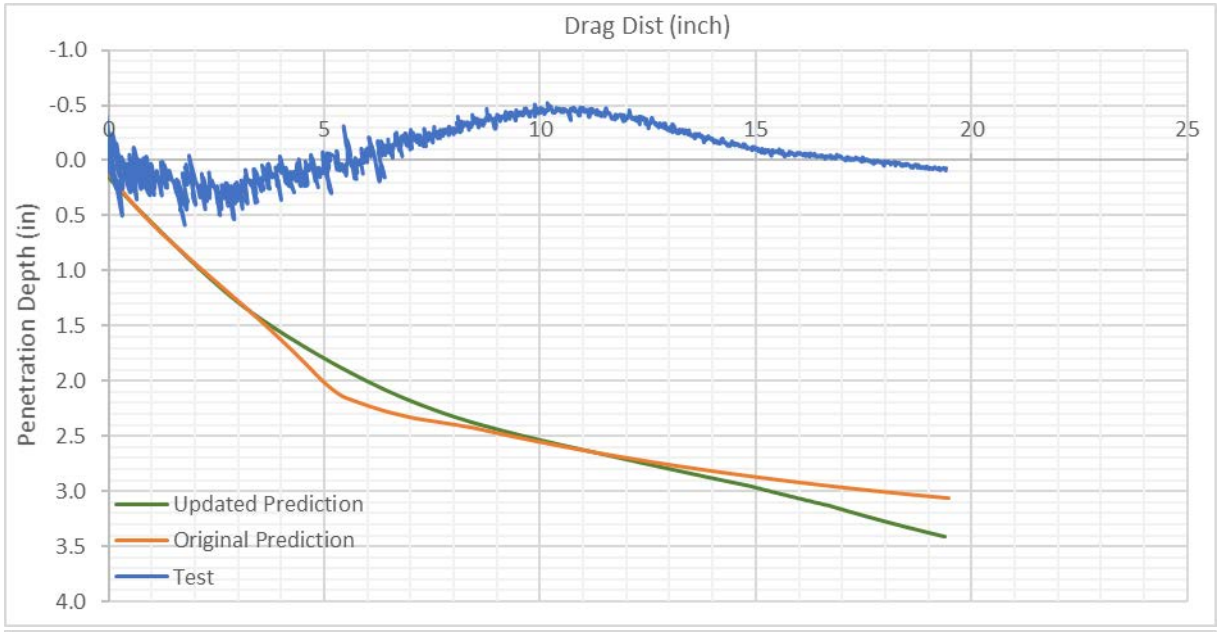

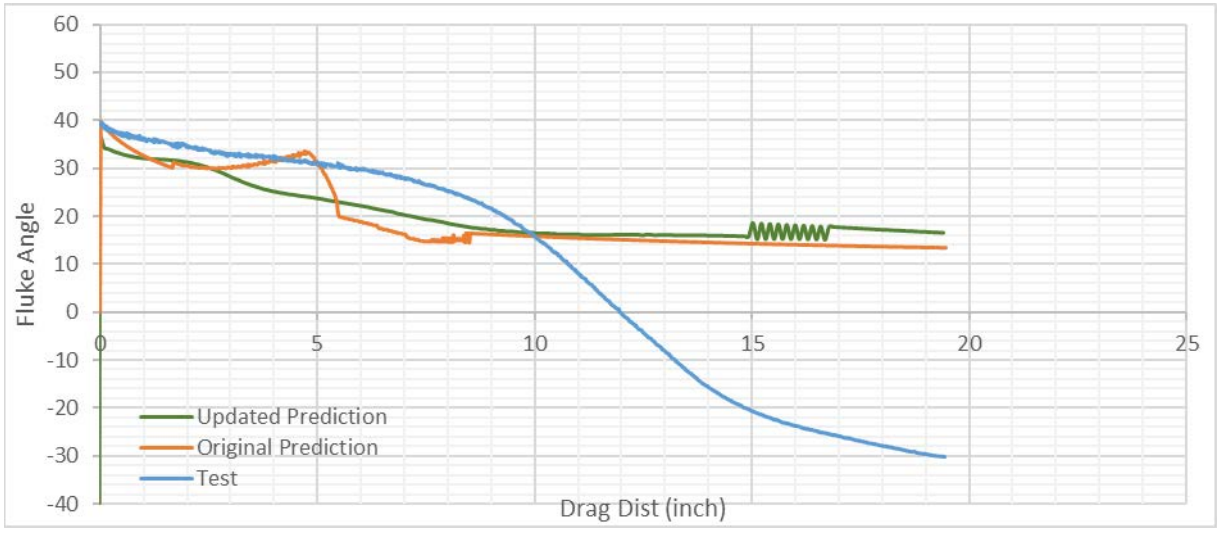

Case 6 Fifth Repeat

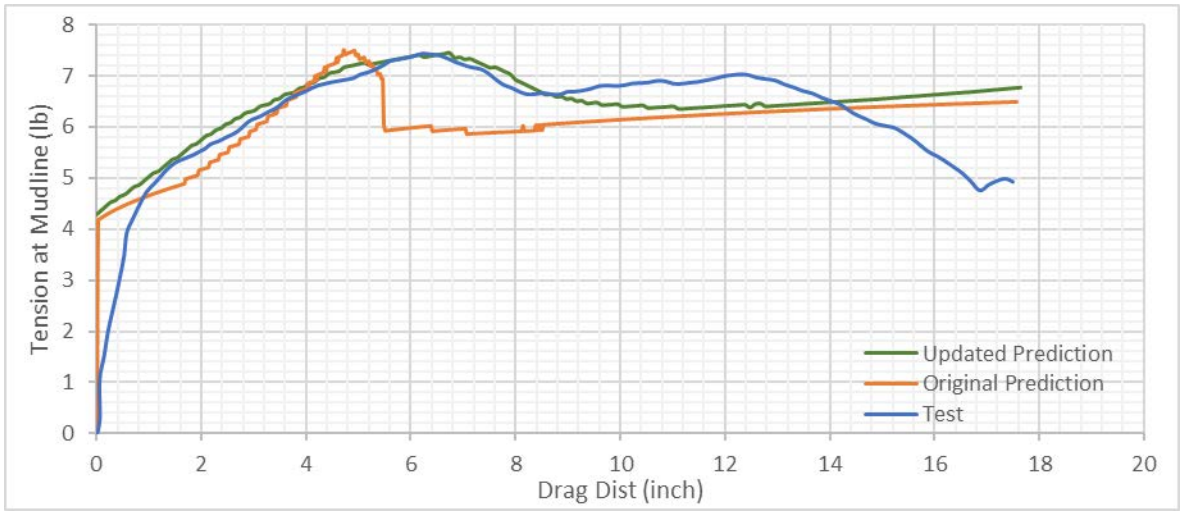

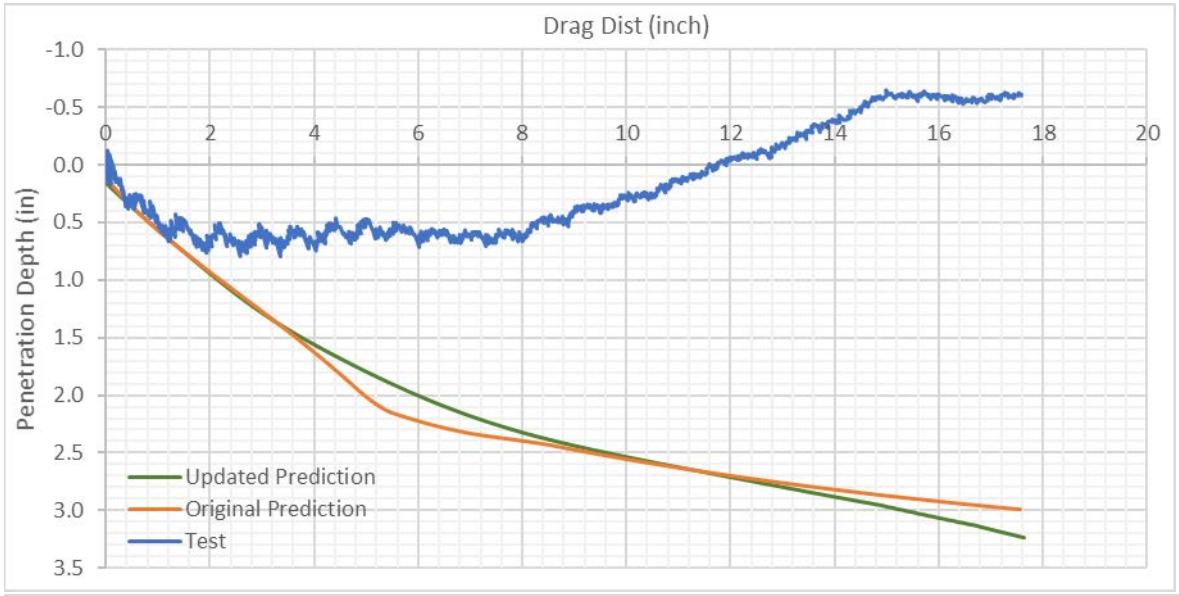

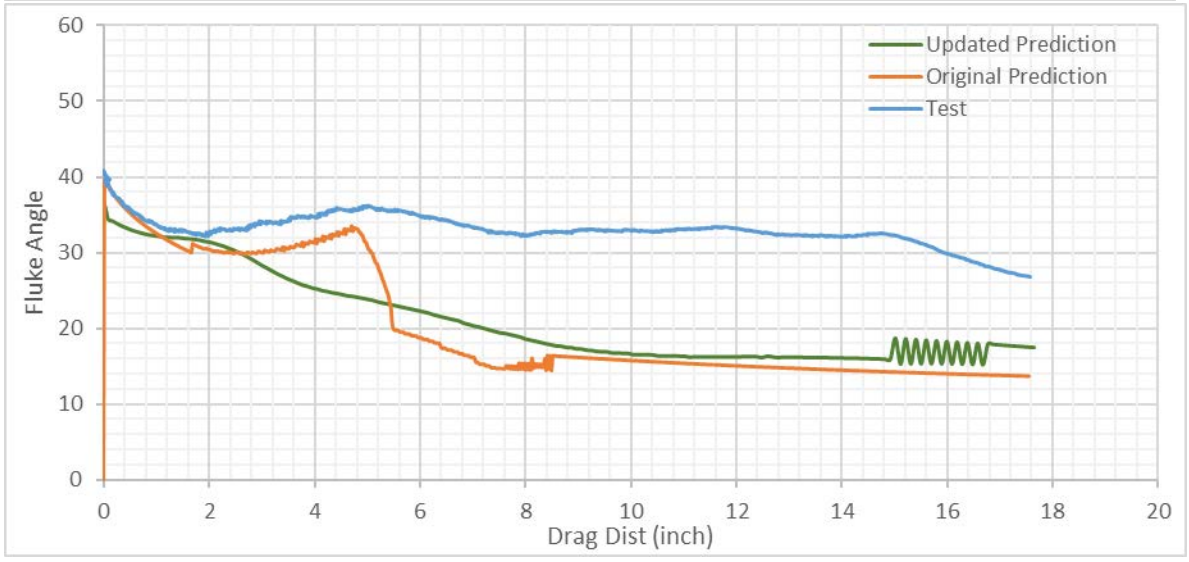

Case 7

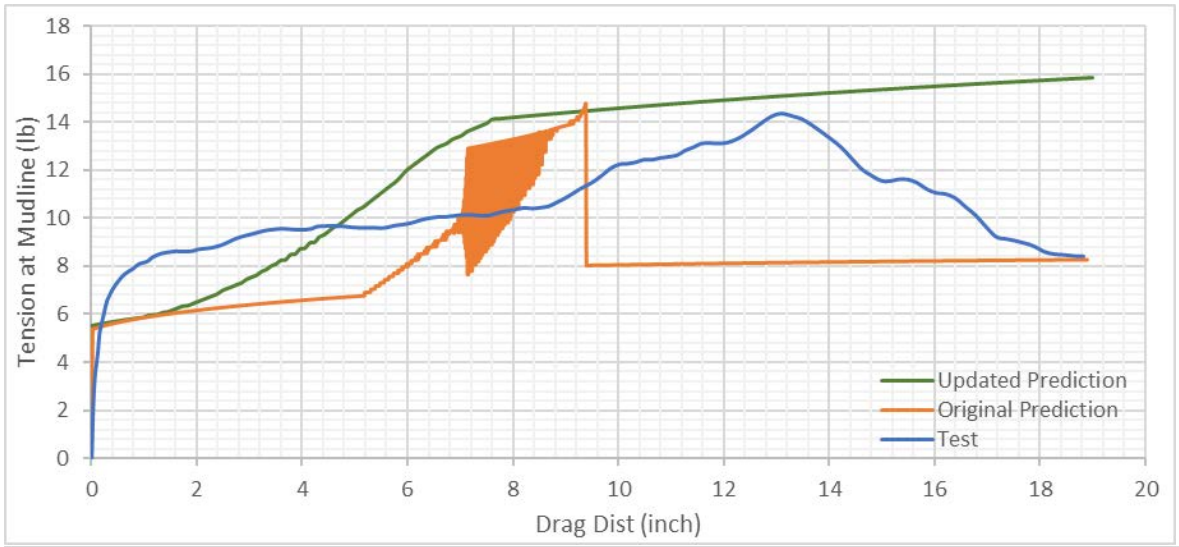
Tension at Mudline (lb)
Drag Dist (inch)
Updated Prediction
Original Prediction
Test

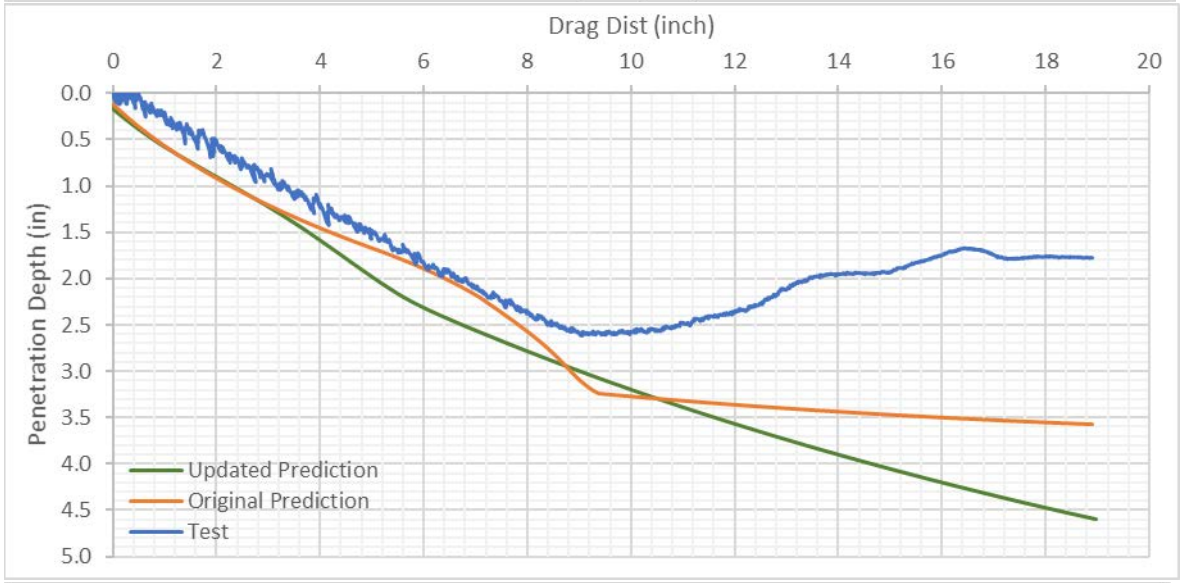
Drag Dist (inch)
Penetration Depth (in)
Updated Prediction
Original Prediction
Test

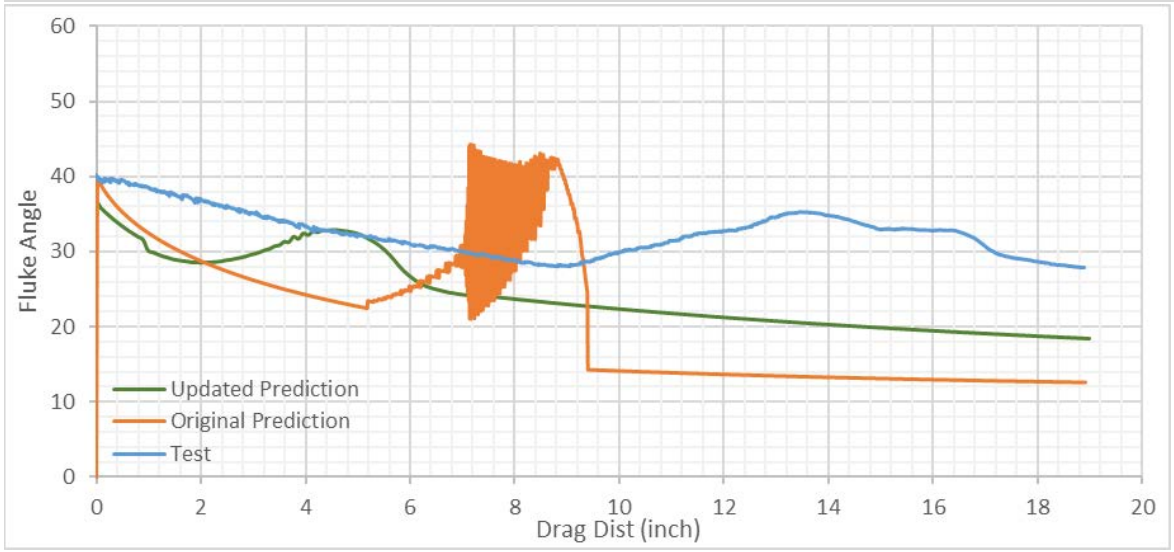
Fluke Angle
Drag Dist (inch)
Updated Prediction
Original Prediction
Test

Case 7 First Repeat

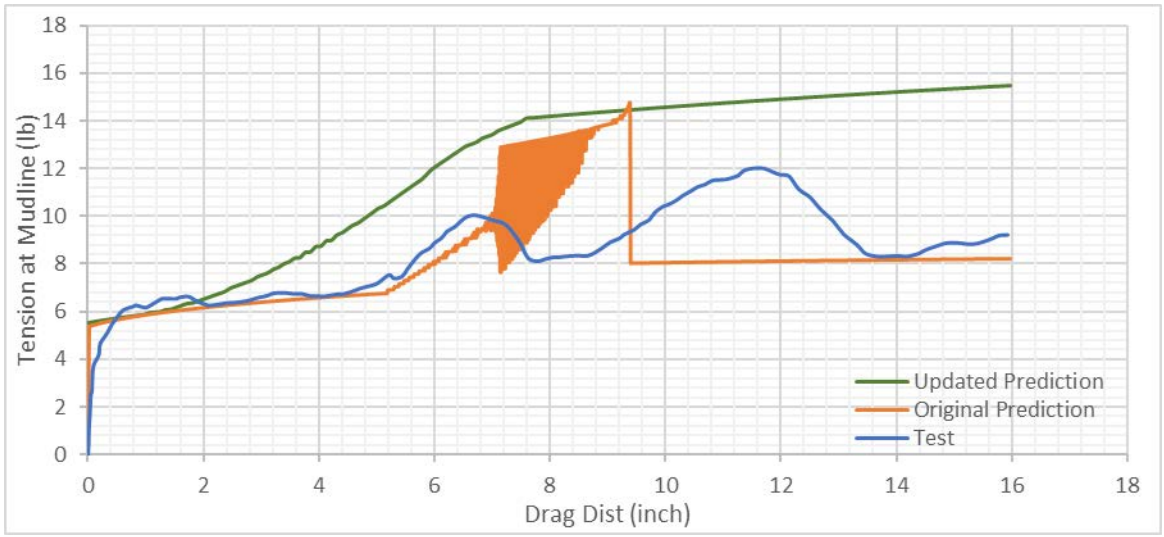

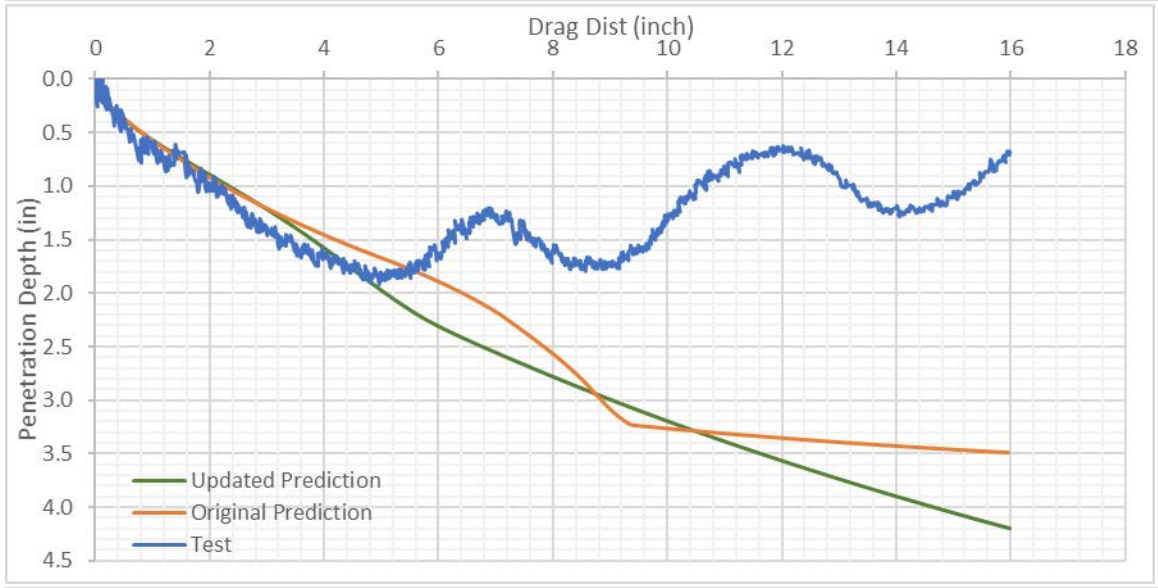

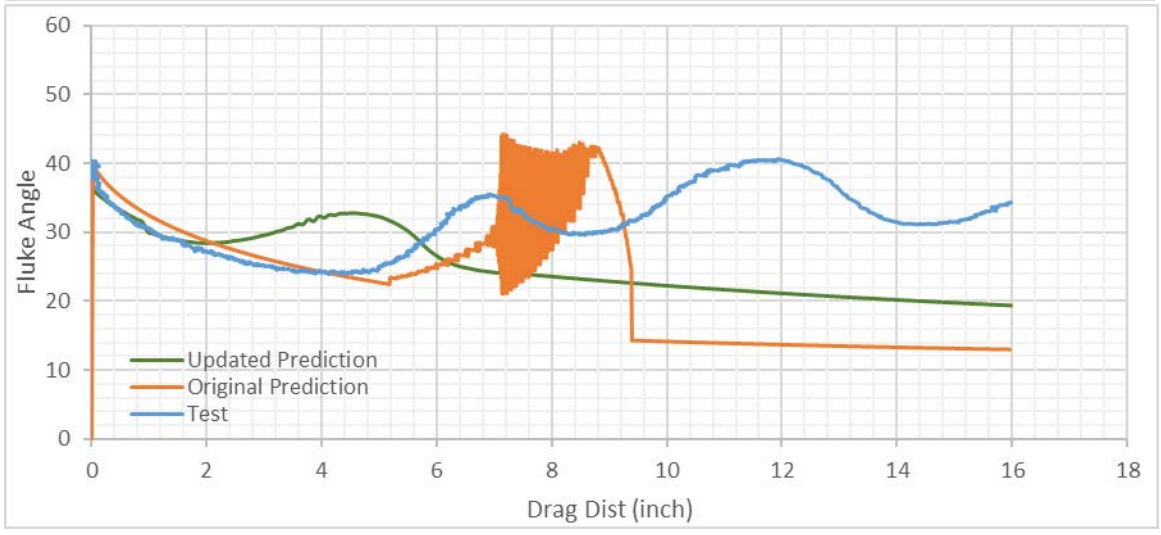

Case 7 Second Repeat

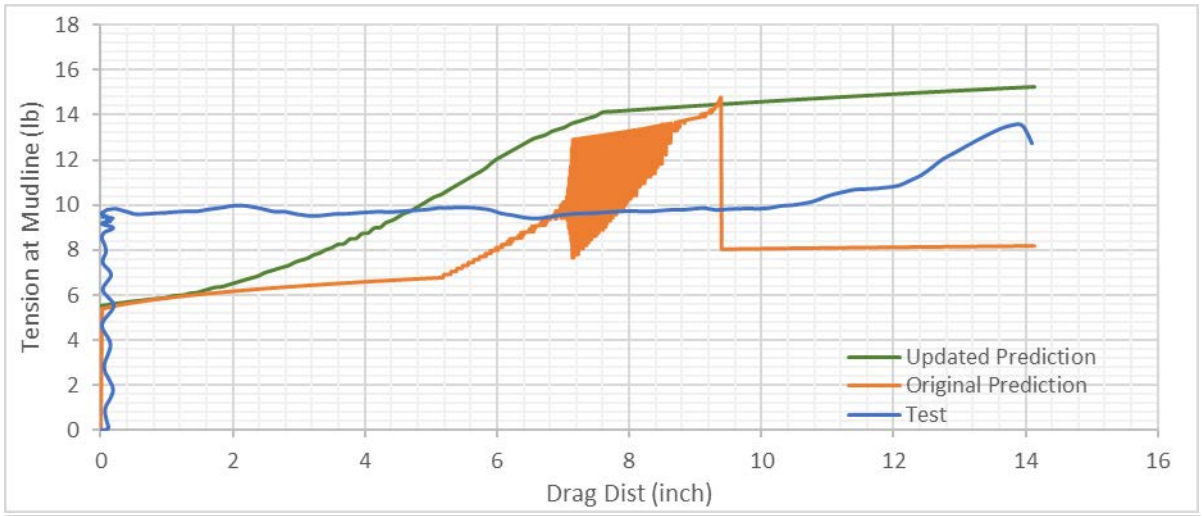

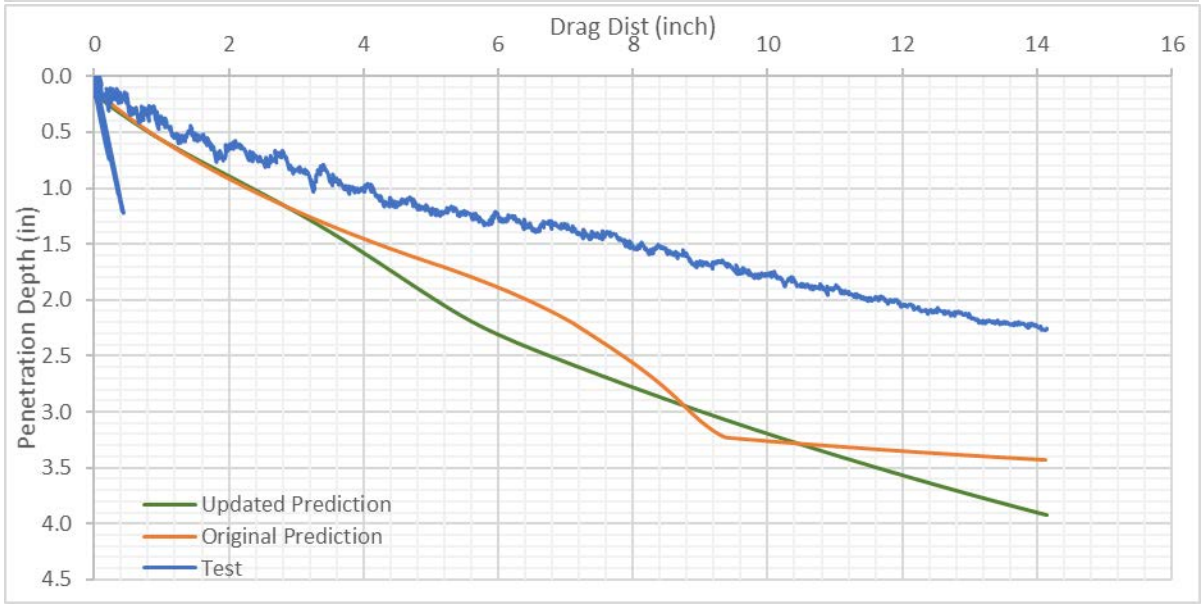

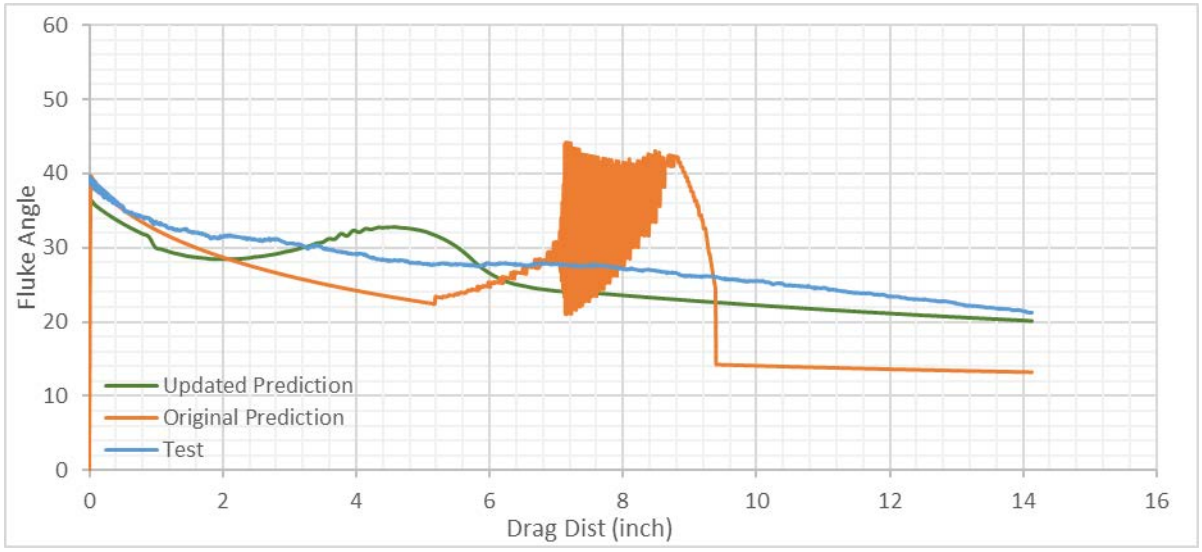

Case 7 Third Repeat

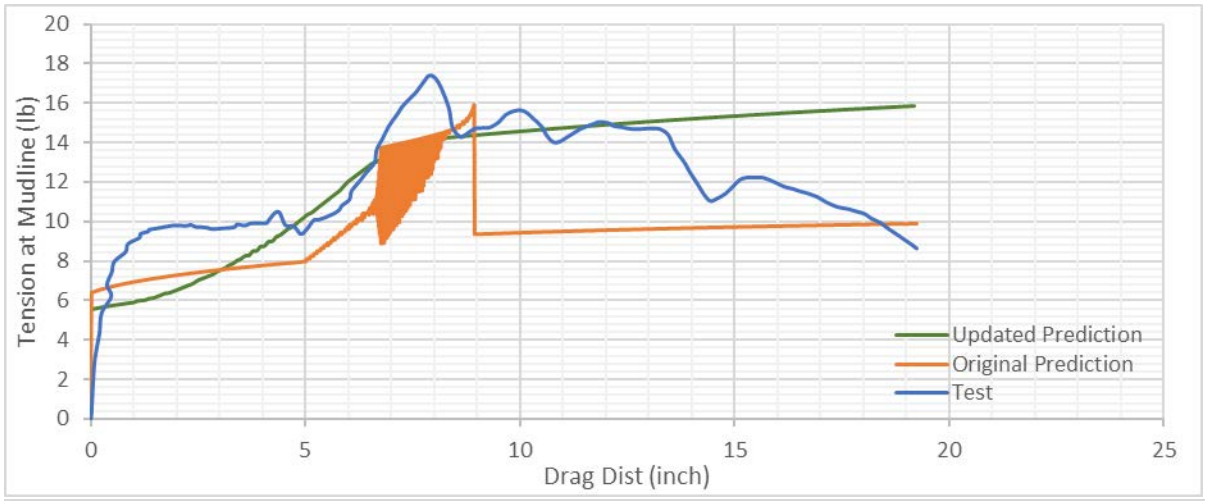

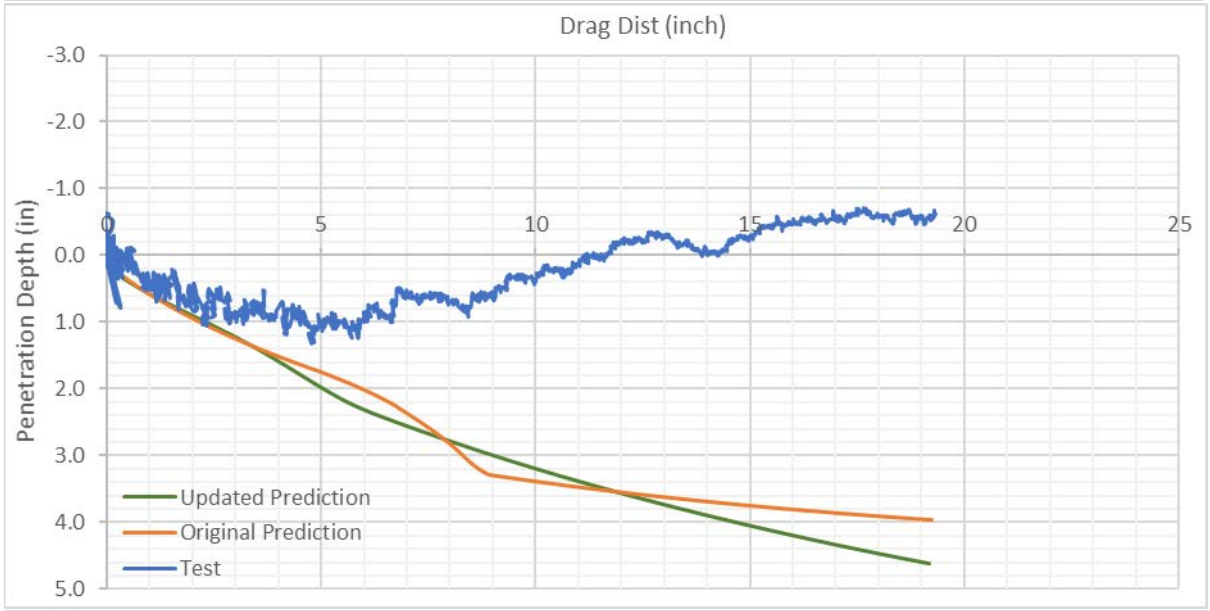

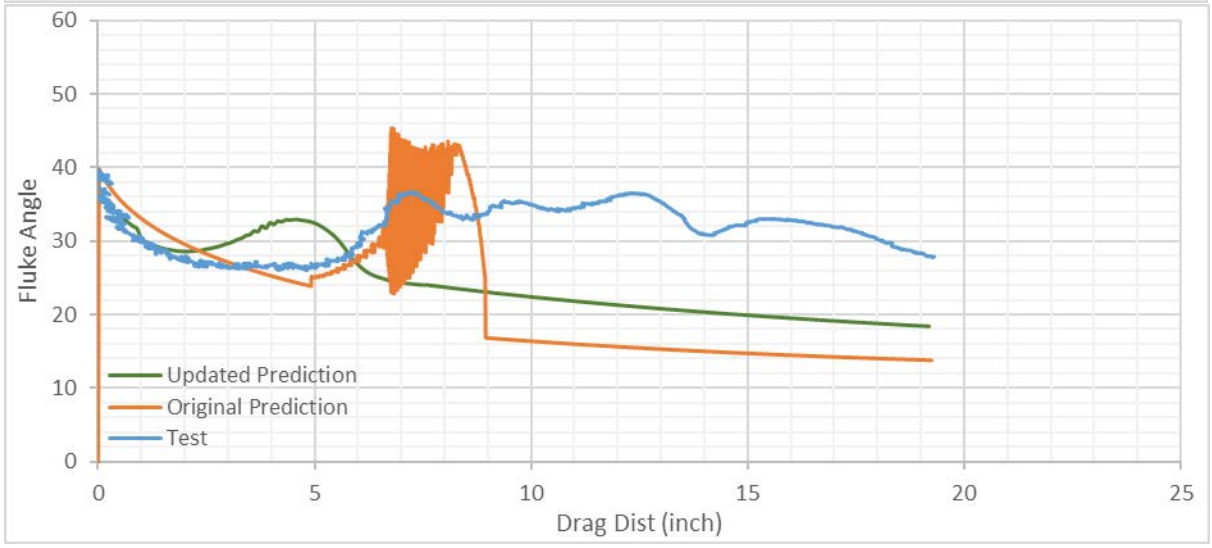

Case 7 Fourth Repeat

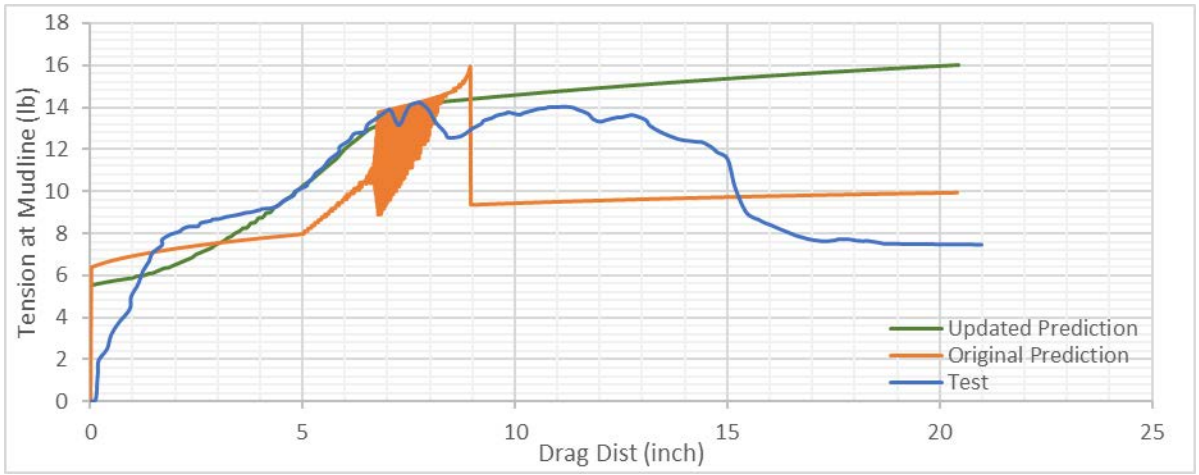

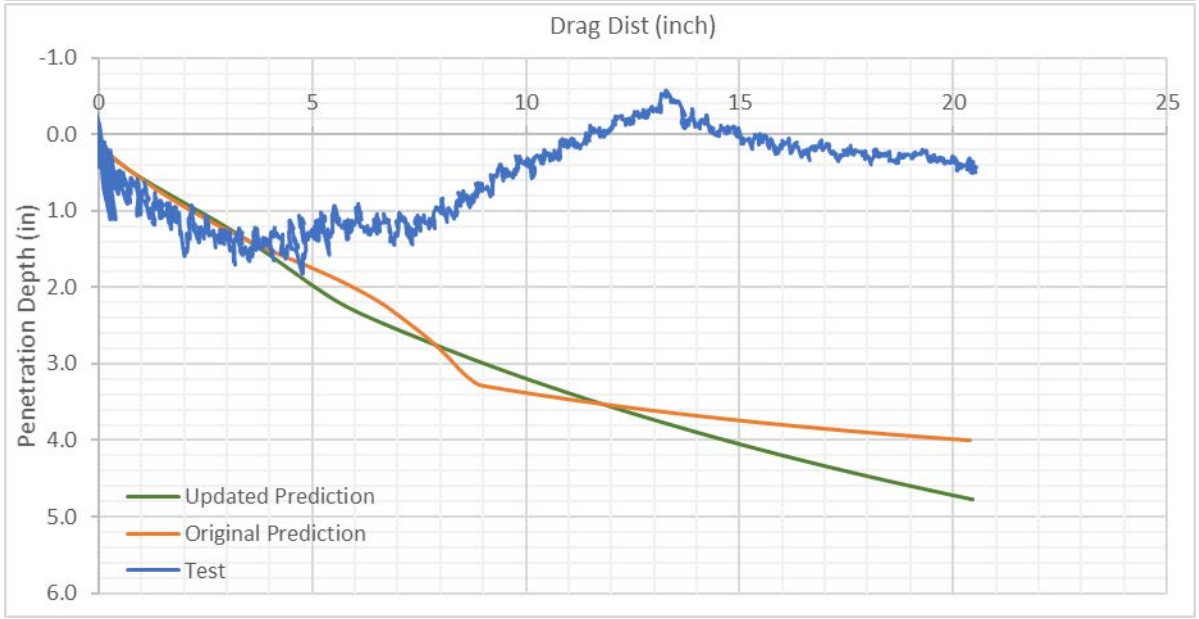

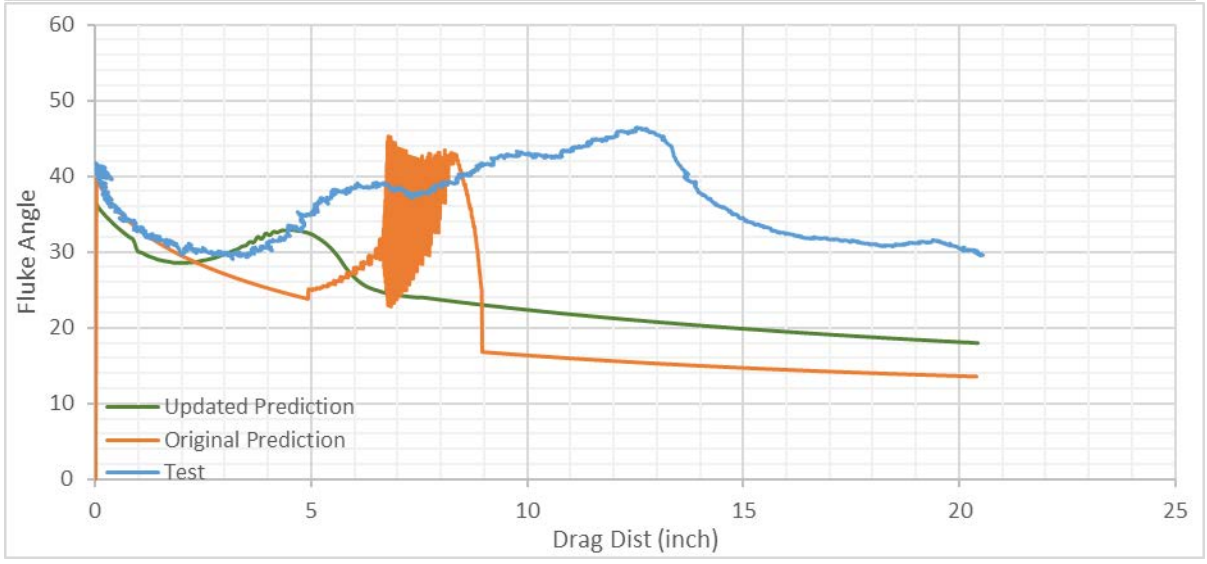

Case 8

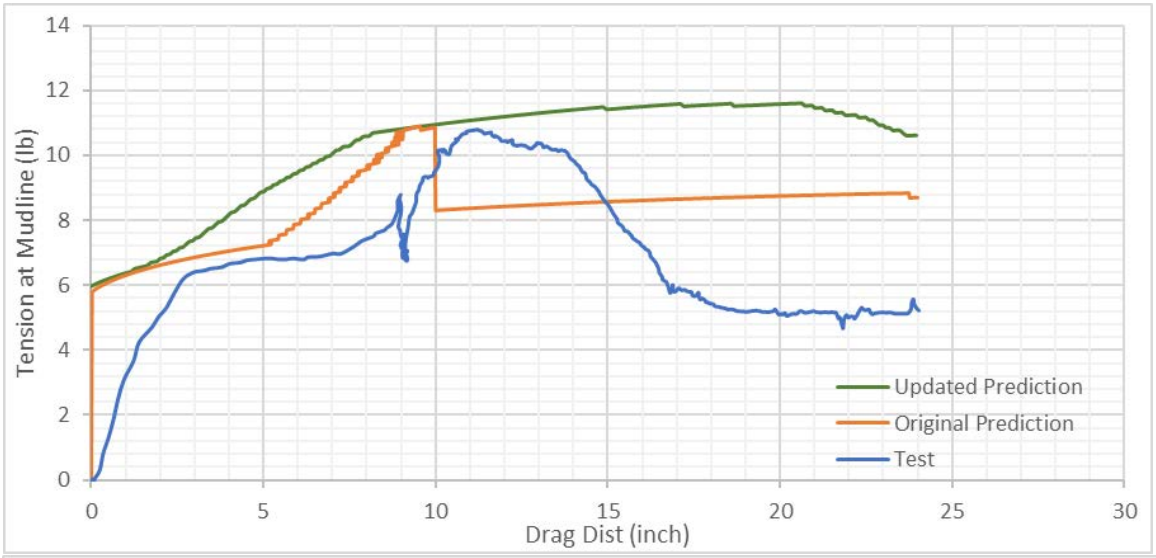
Tension at Mudline (lb)
Drag Dist (inch)
Updated Prediction
Original Prediction
Test

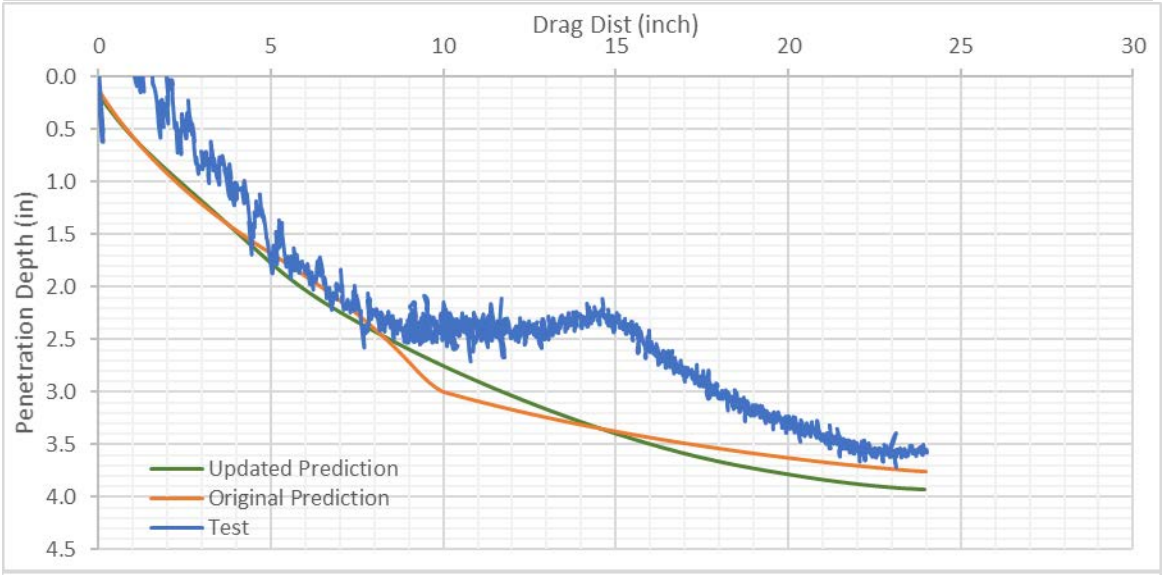
Drag Dist (inch)
Penetration Depth (in)
Updated Prediction
Original Prediction
Test

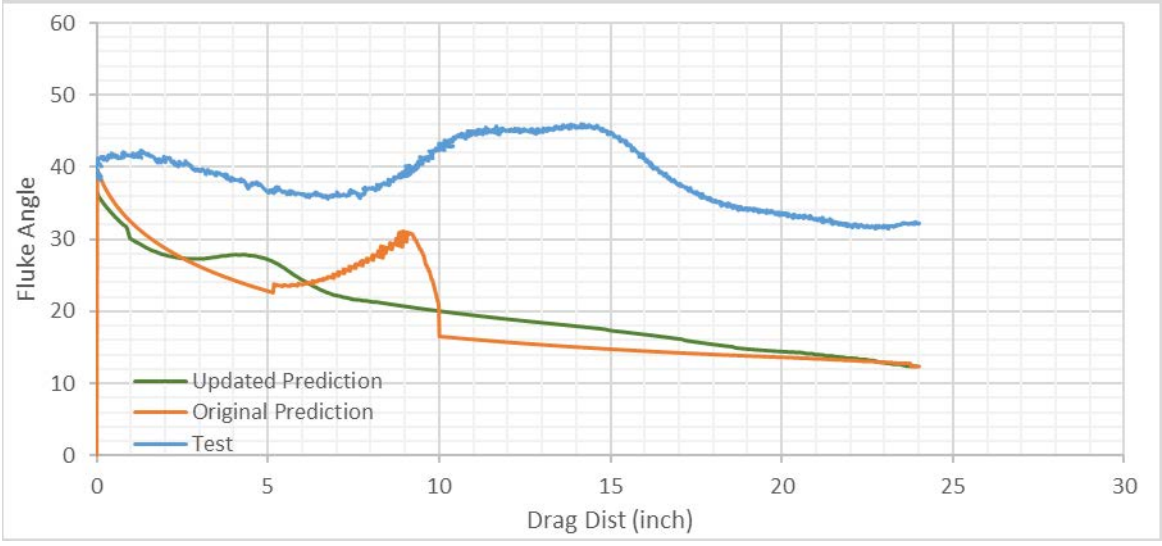
Fluke Angle
Drag Dist (inch)
Updated Prediction
Original Prediction
Test

Case 8 First Repeat

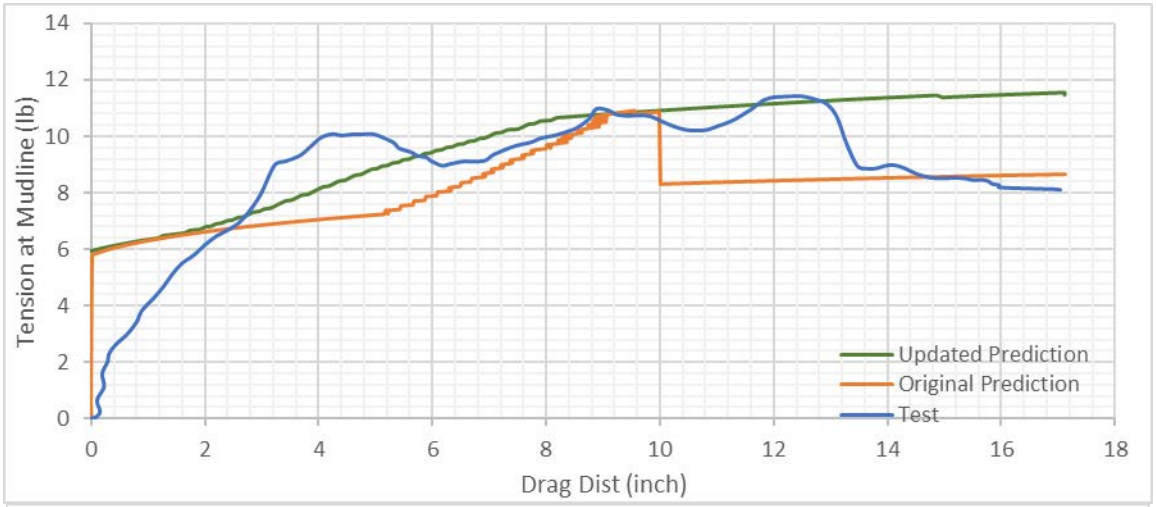

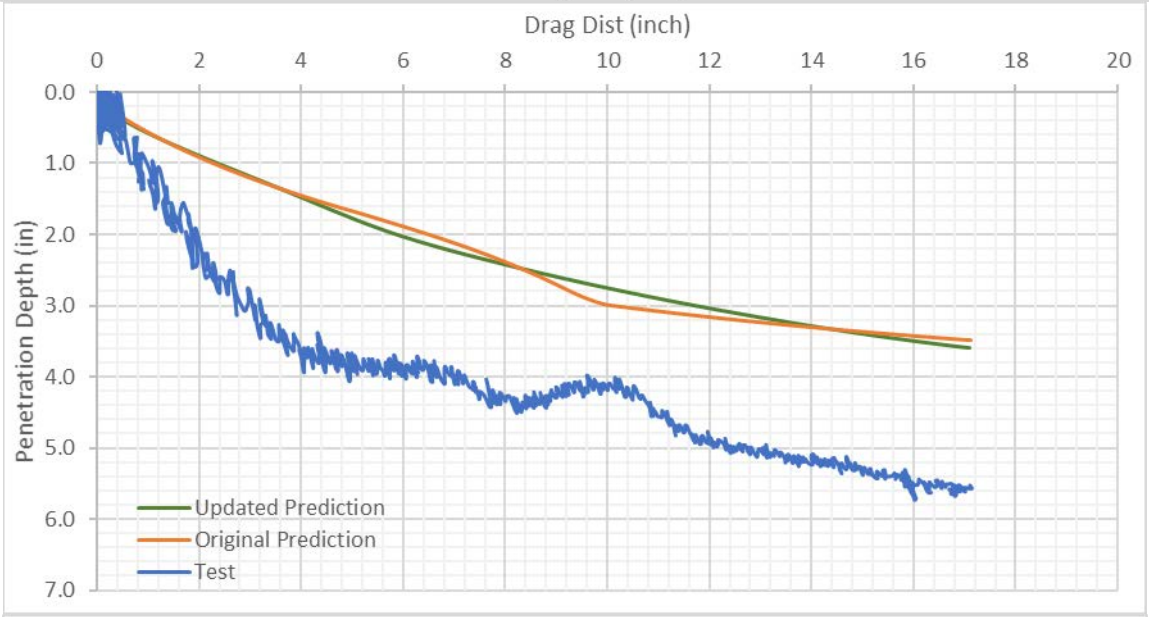

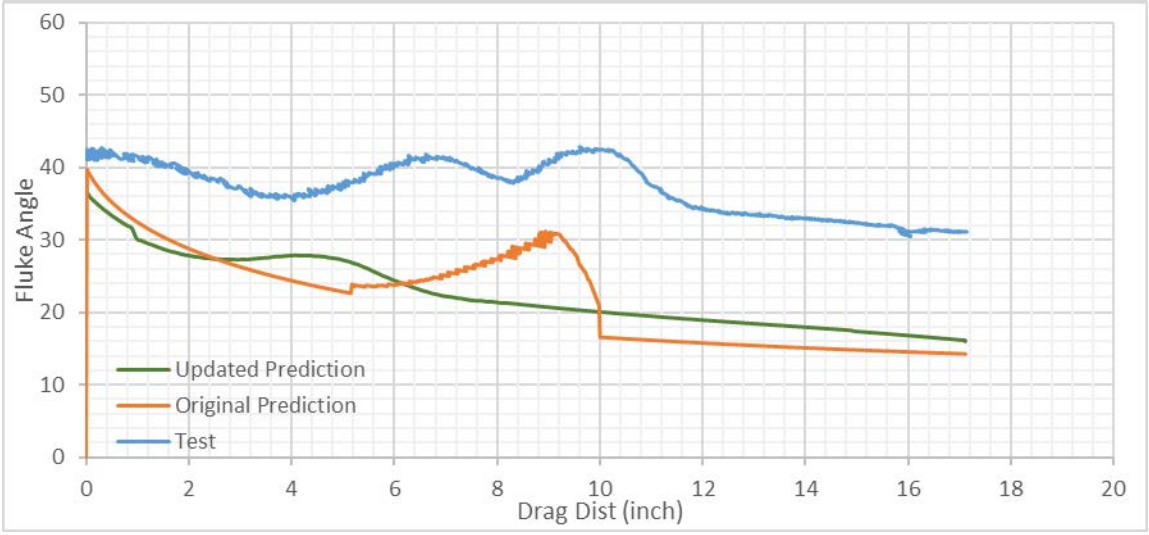

Case 8 Second Repeat

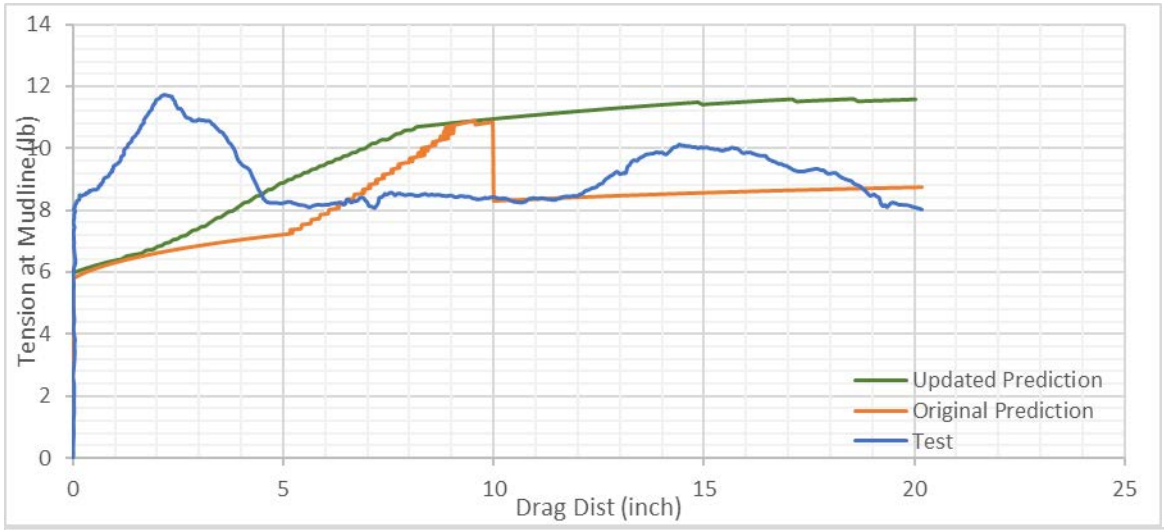

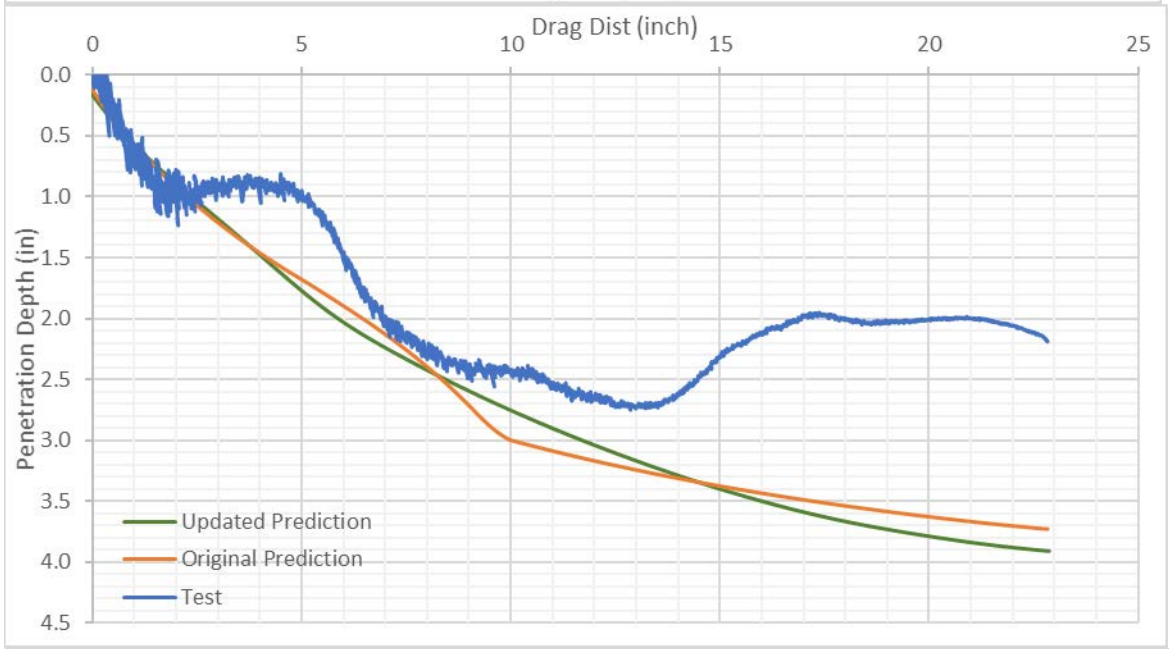

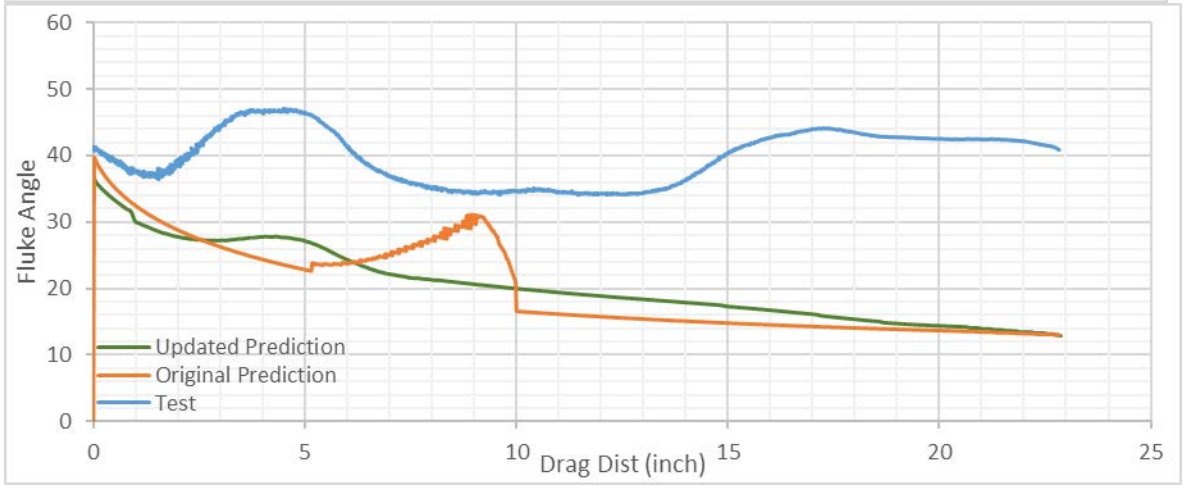

Case 8 Third Repeat

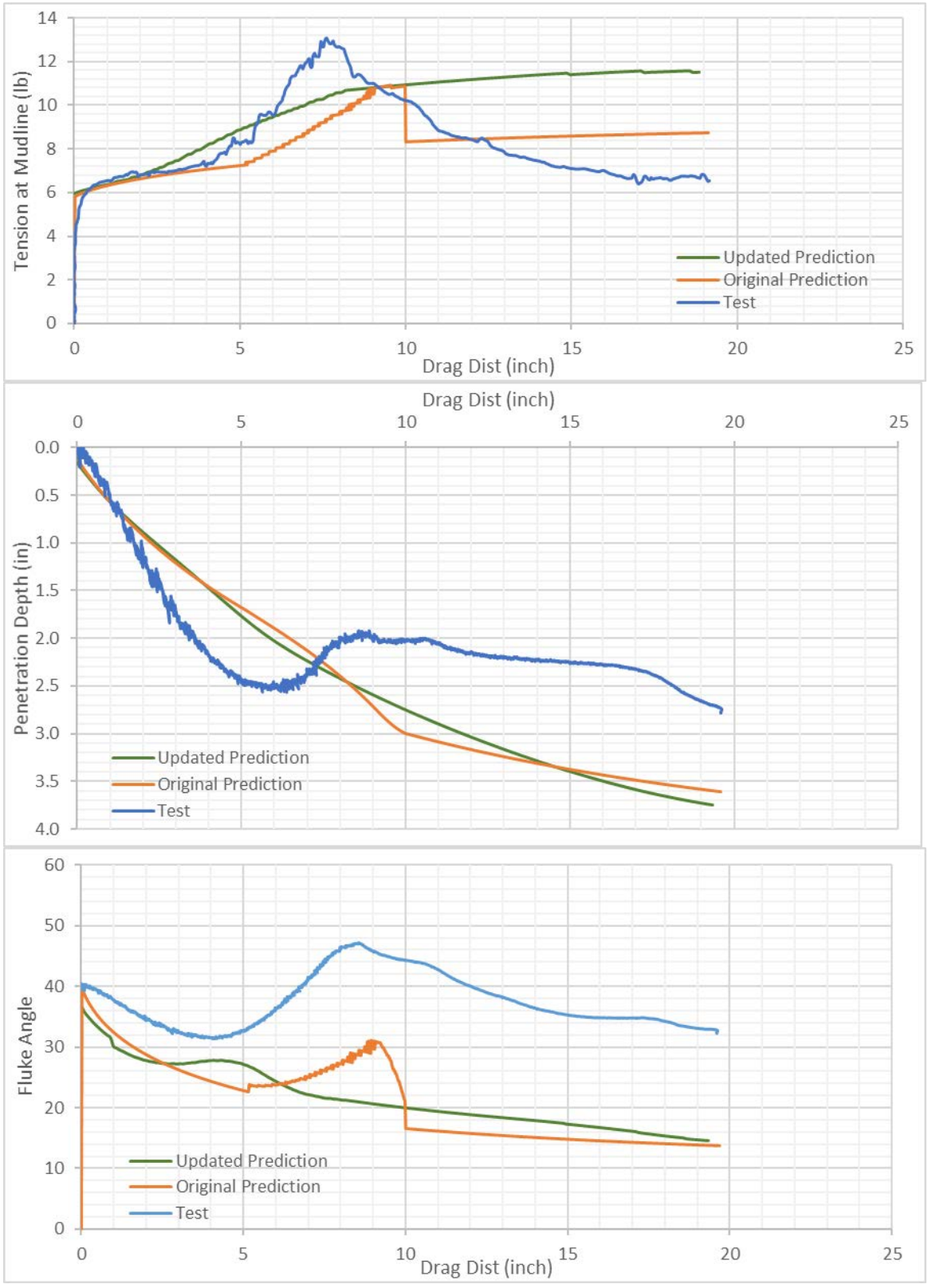

Case 8 Fourth Repeat

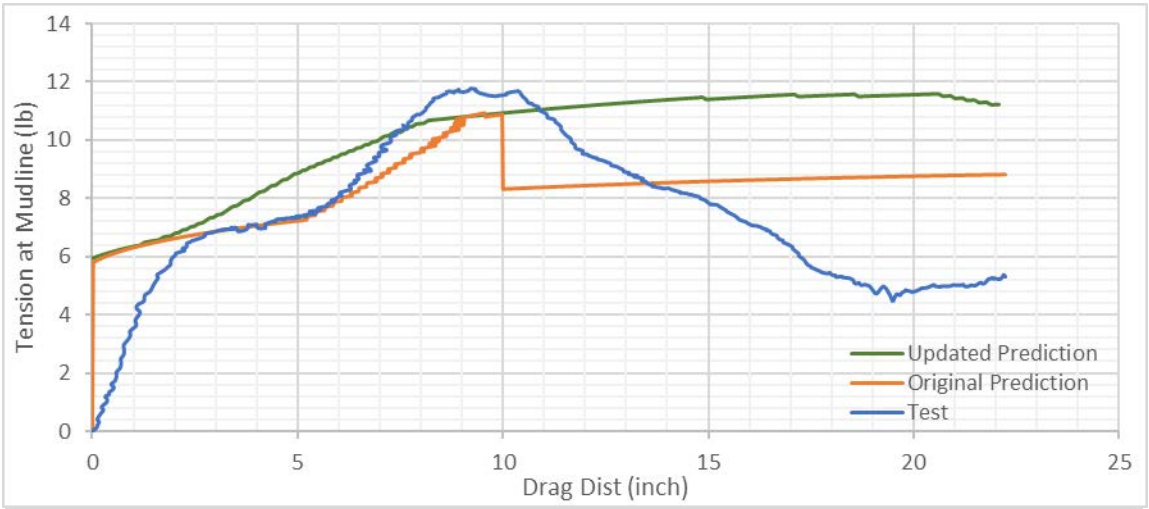

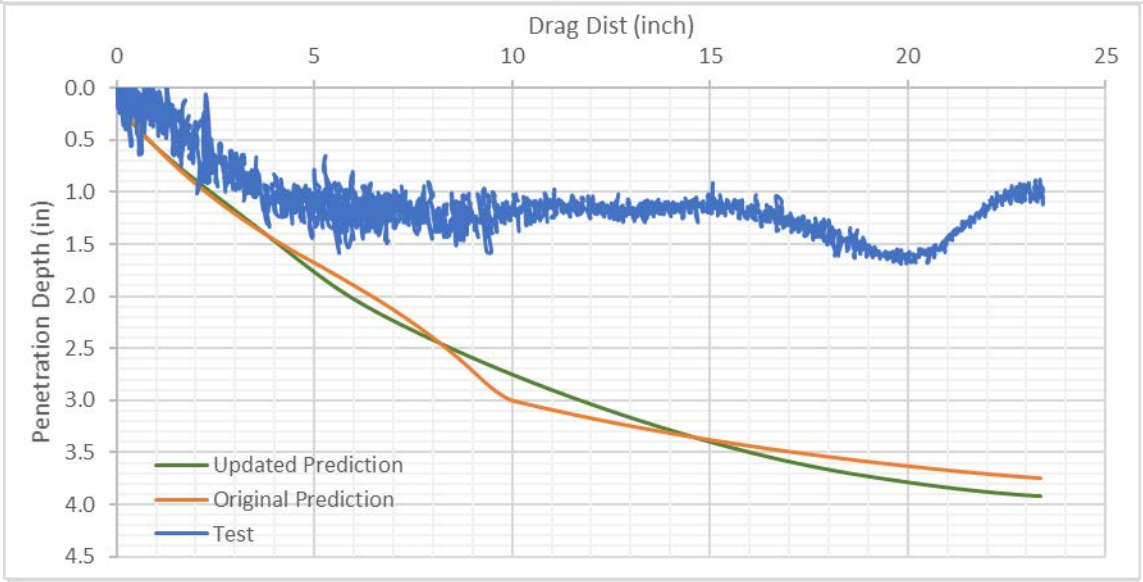

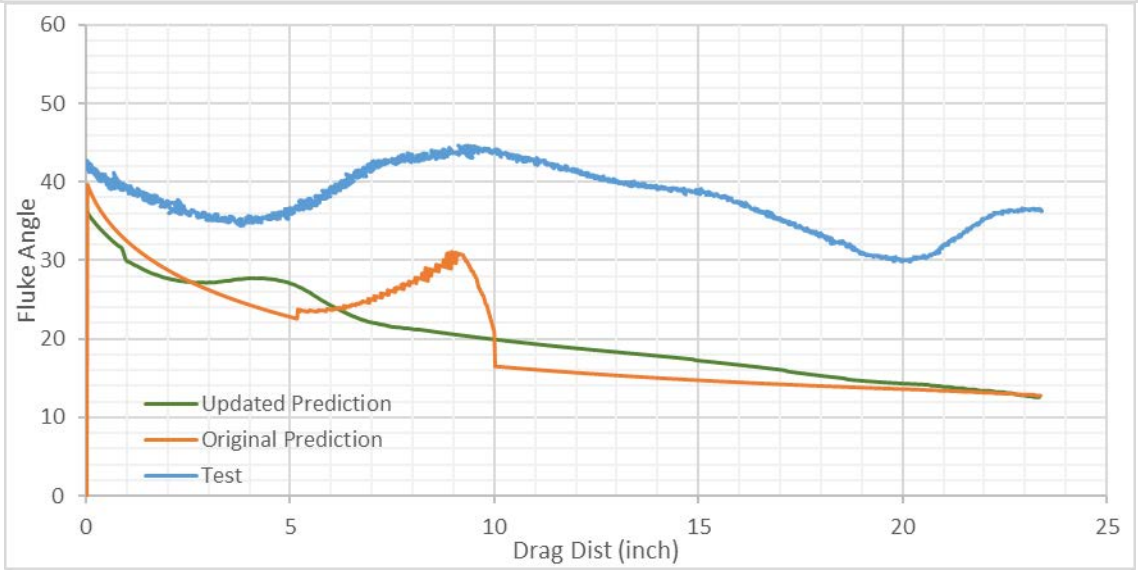

Appendix D. Comparison between Tandem System Anchor and a Single Drag Embedment Anchor

Case 1

Line Diameter (connecting two anchors)	0.19 inch
The 2nd anchor Attached to 1st Anchor's	Padeye
Spacing between two anchors	4.19 inch (1.16 fluke length)

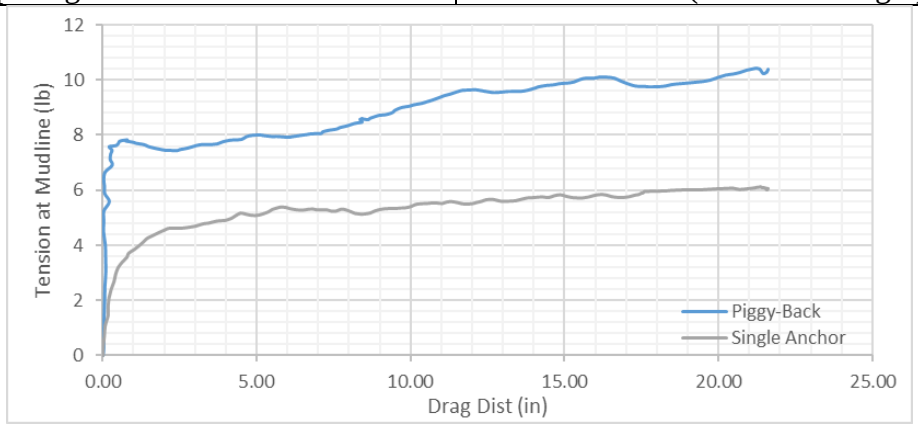

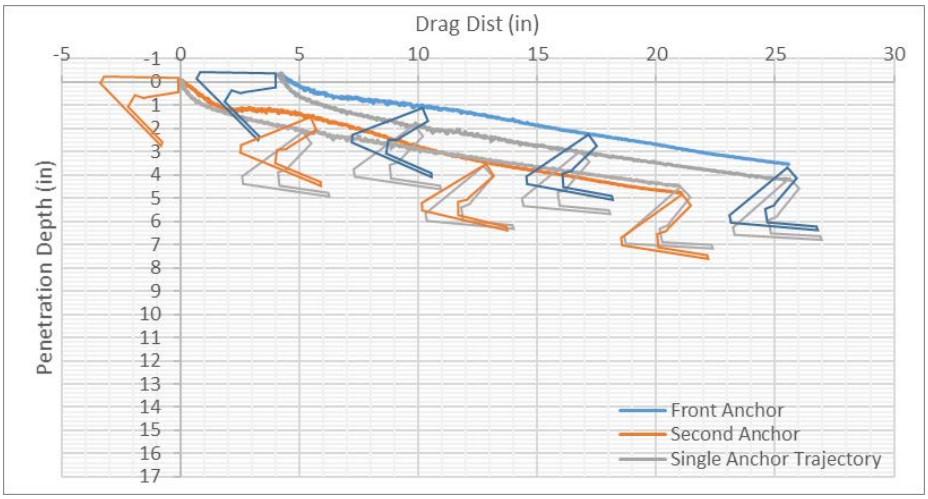

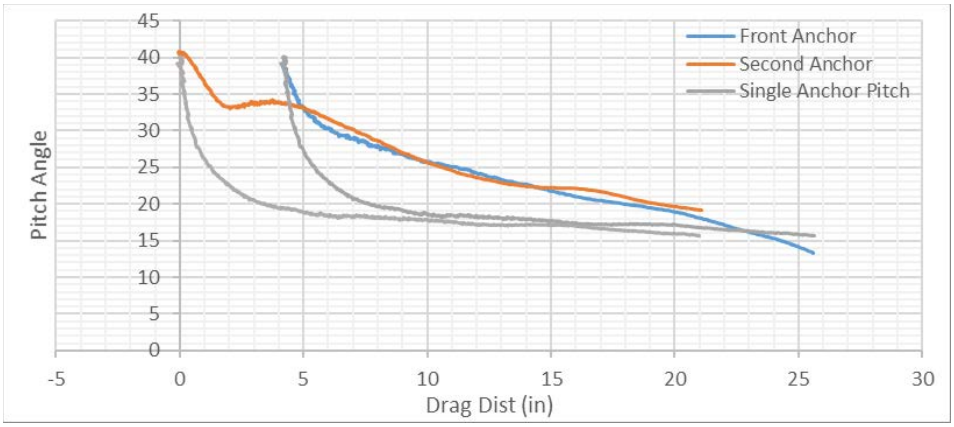

First Repeat test in Case 1

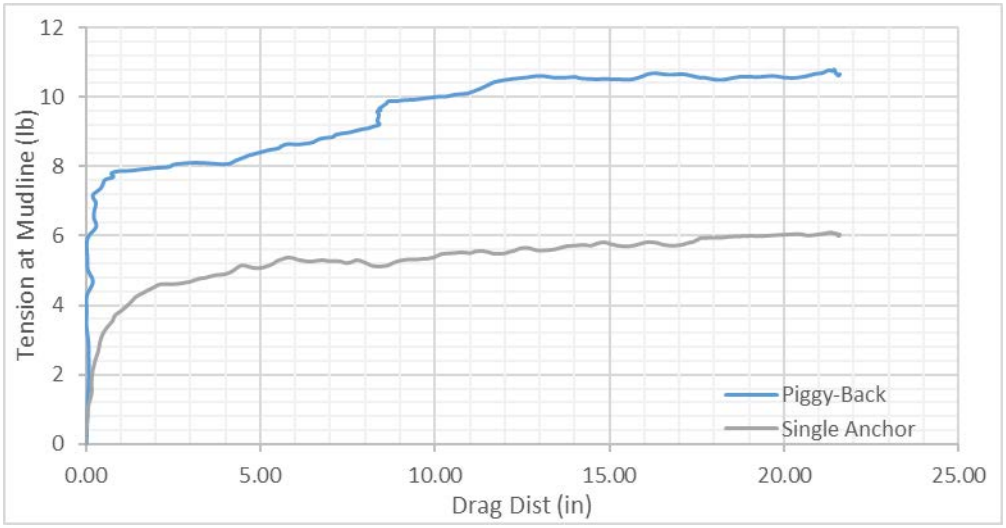

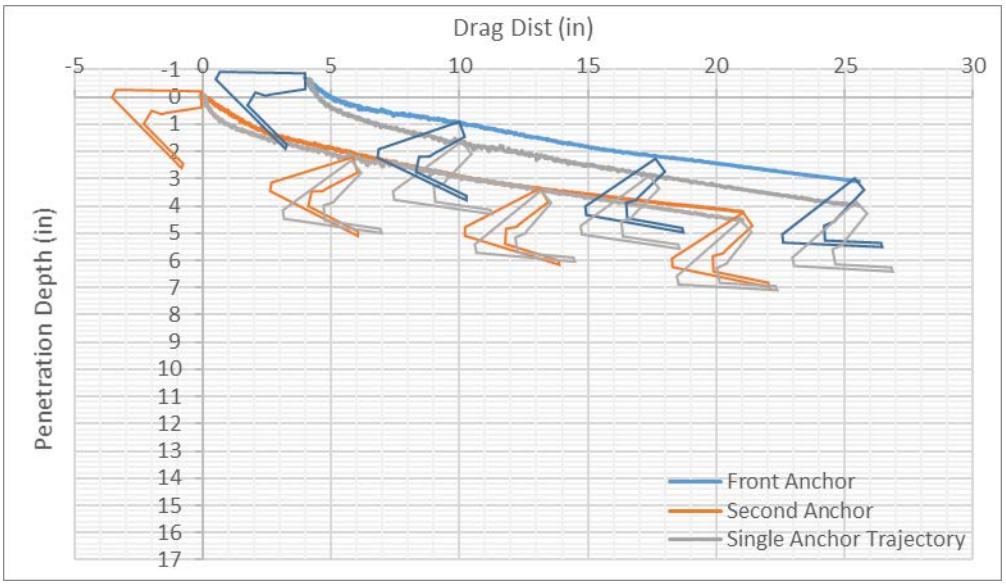

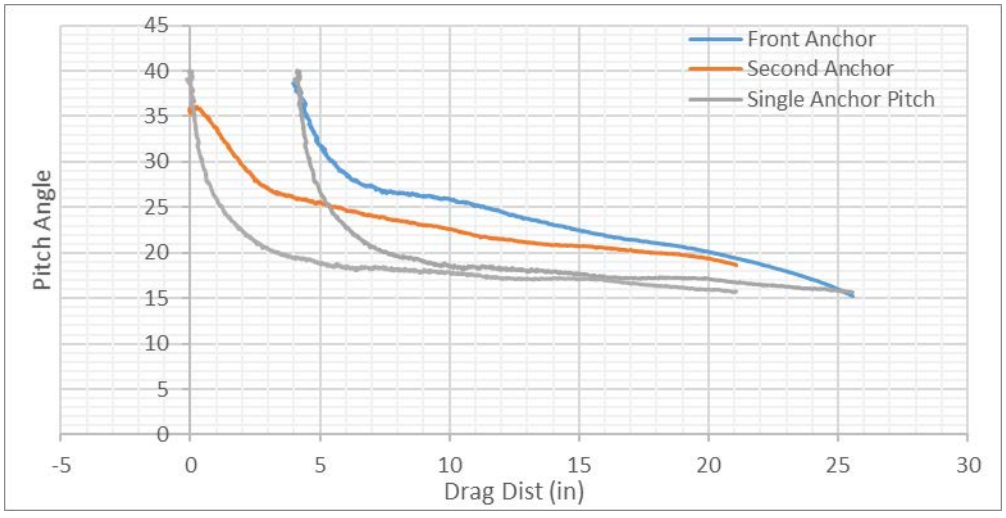

Second Repeat Test in Case 1

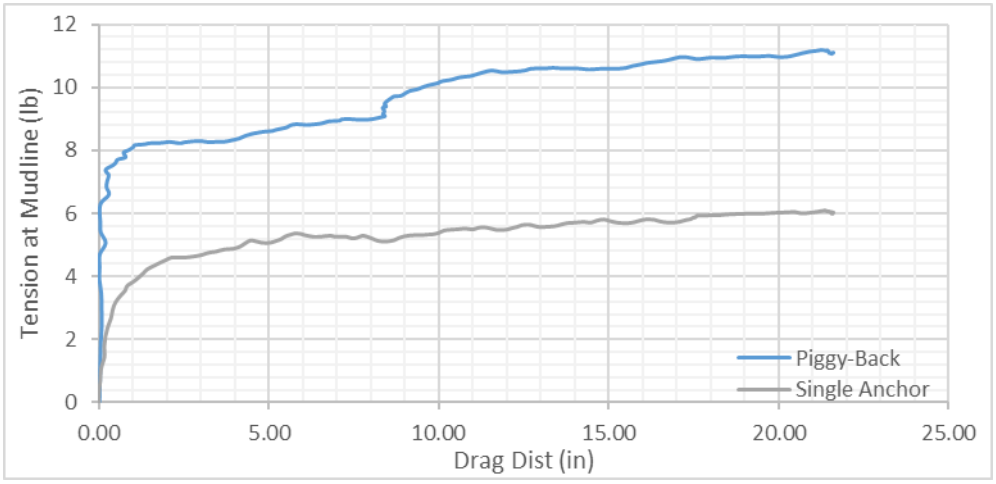

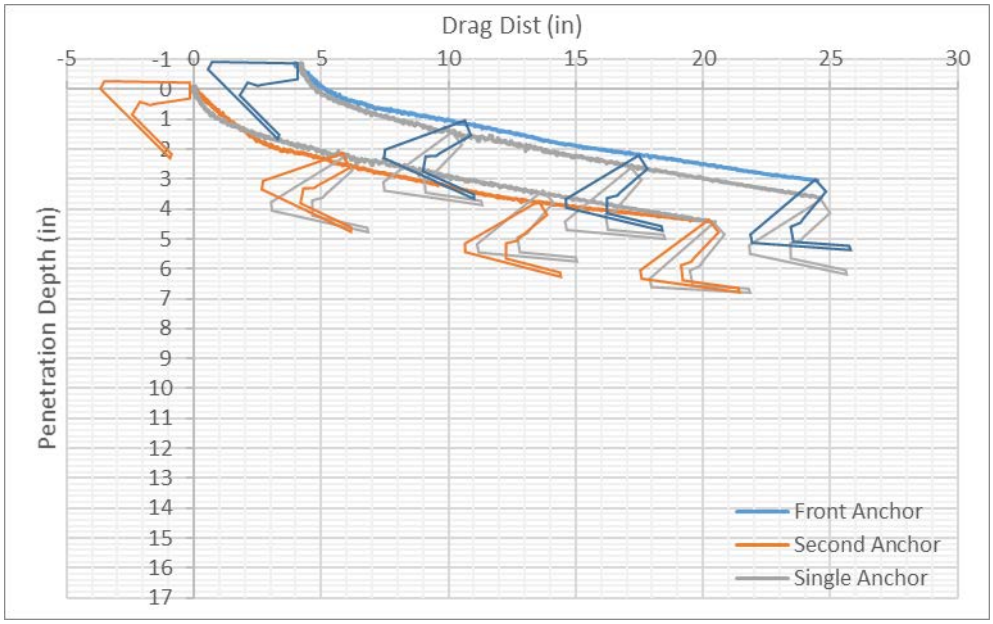

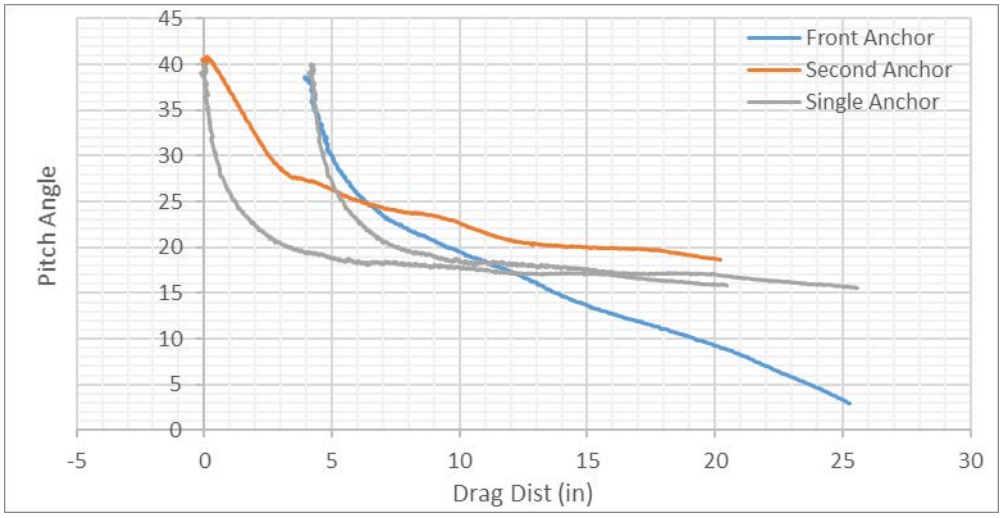

Case 2

Line Diameter (connecting two anchors)	0.19 inch
The 2nd anchor Attached to 1st Anchor's	Center of Back Fluke
Spacing between two anchors	6.40 inch (1.77 Fluke Length)

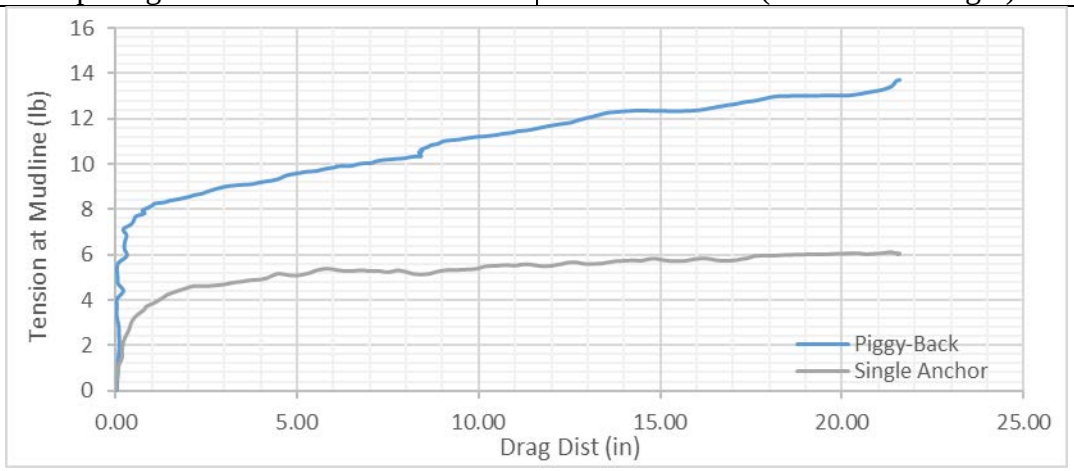

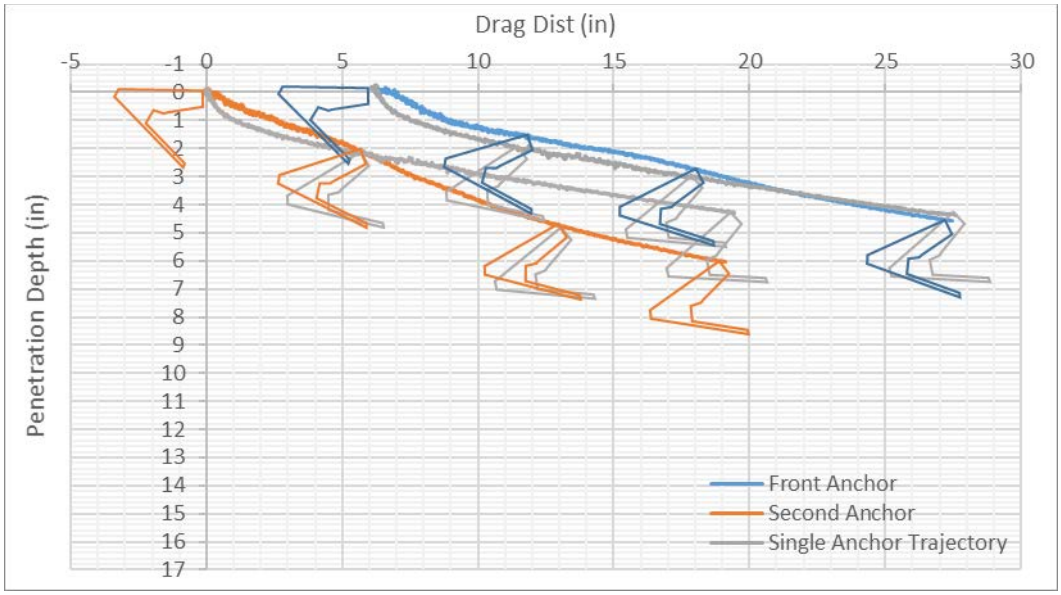

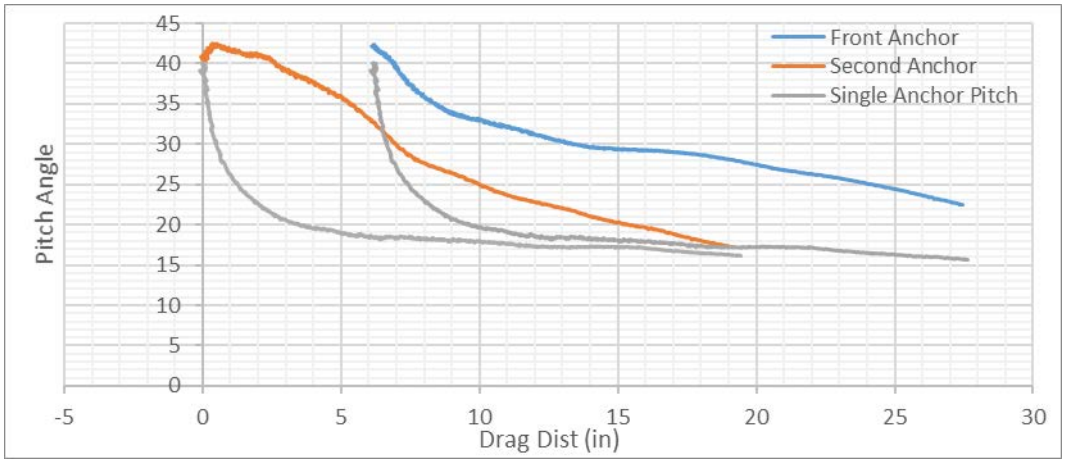

First Repeat test in Case 2

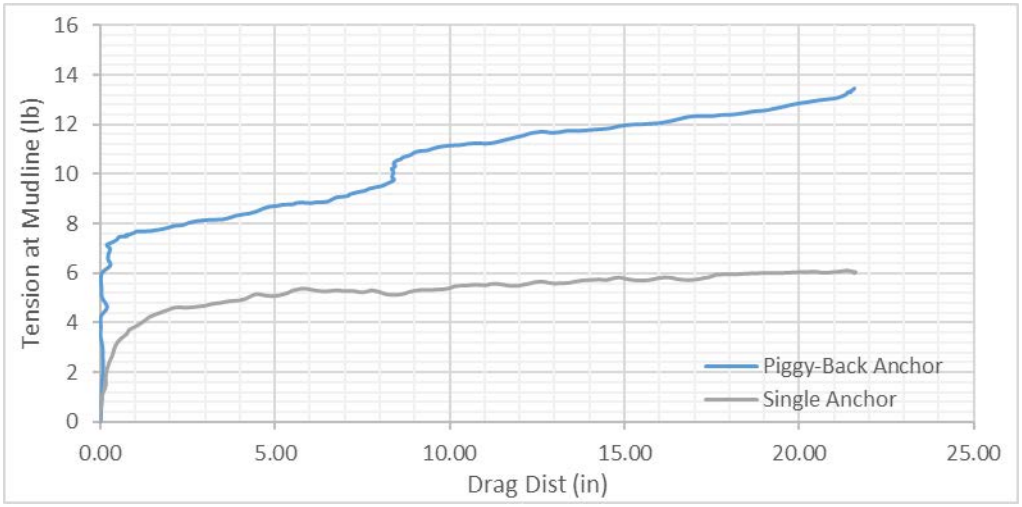

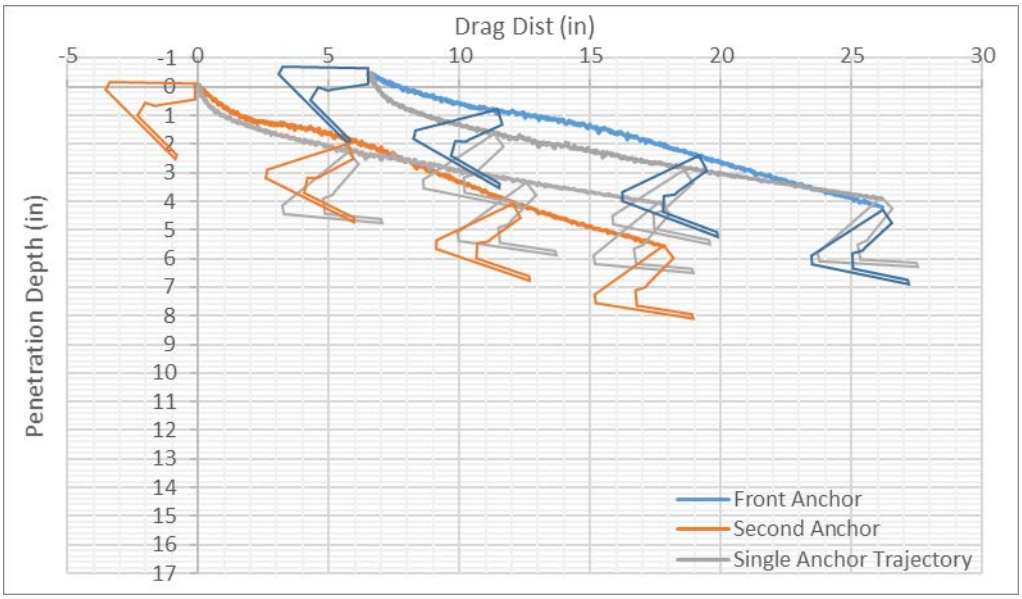

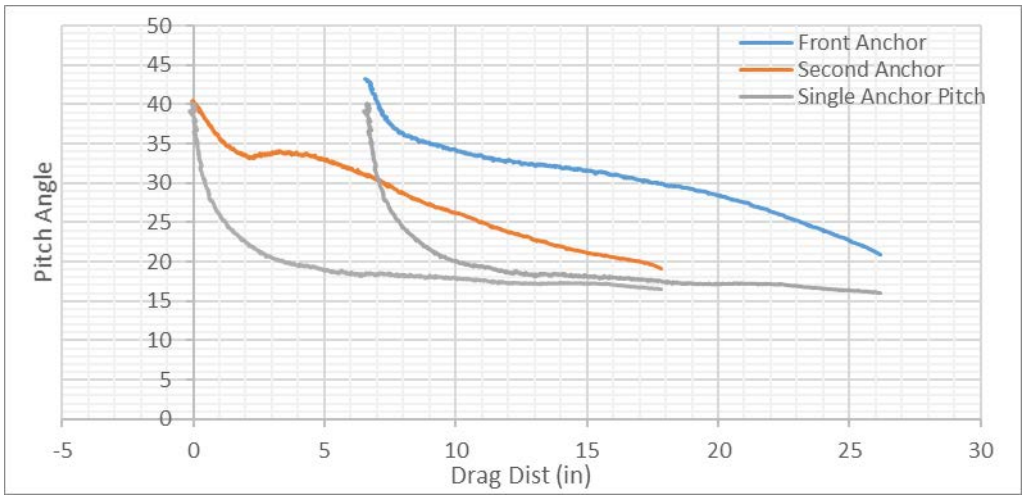

Case 3

Line Diameter (connecting two anchors)	0.19 inch
The 2nd anchor Attached to 1st Anchor's	Padeye
Spacing between two anchors	6.57 inch (1.81 Fluke Length)

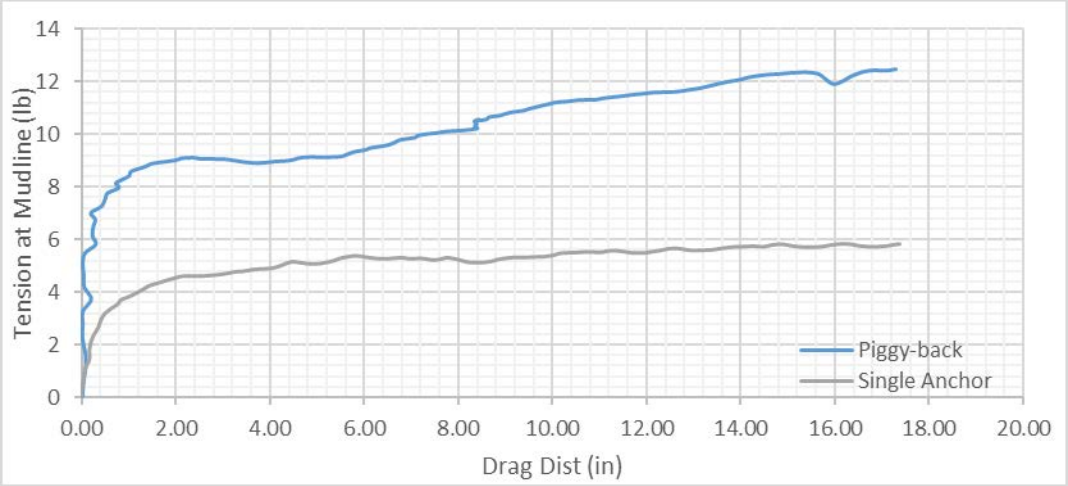

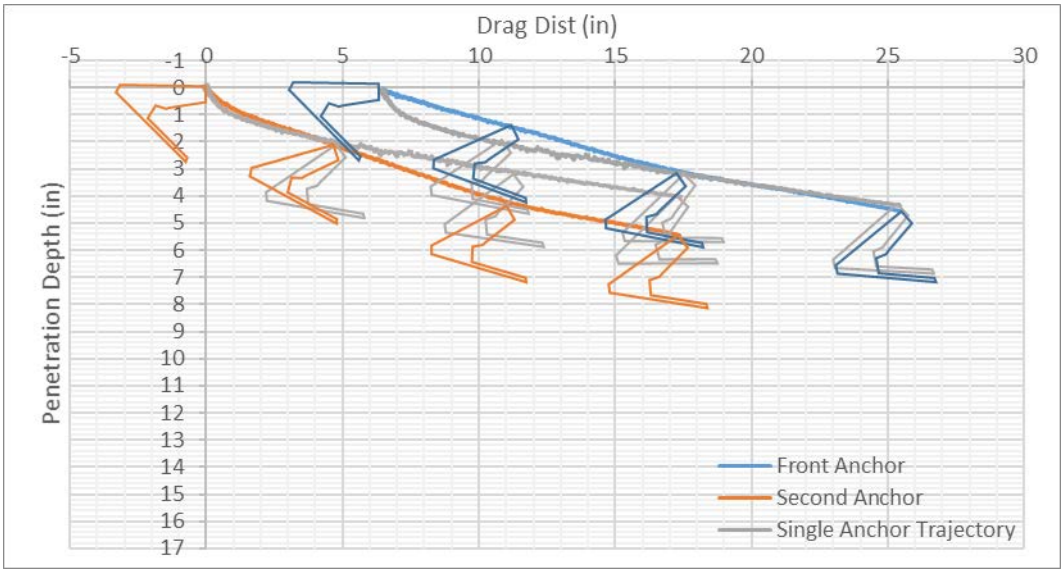

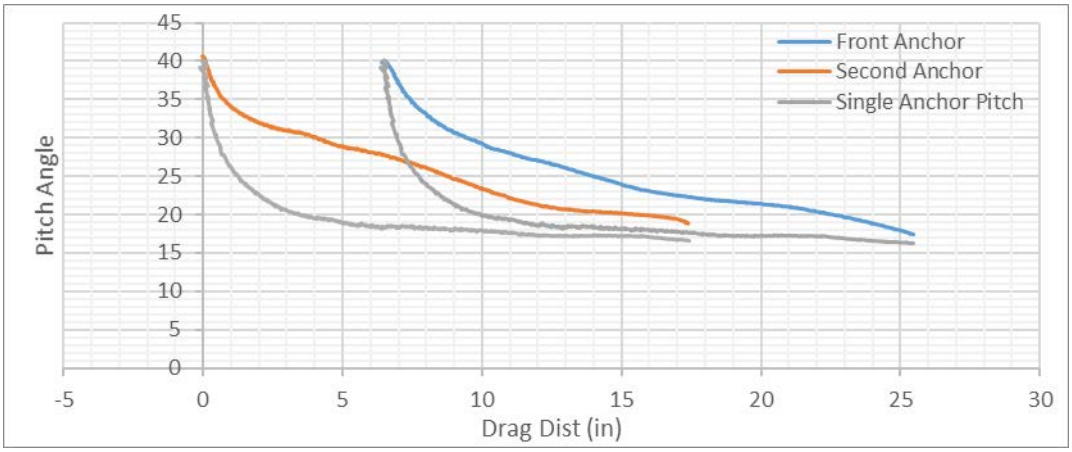

First Repeat test in Case 3

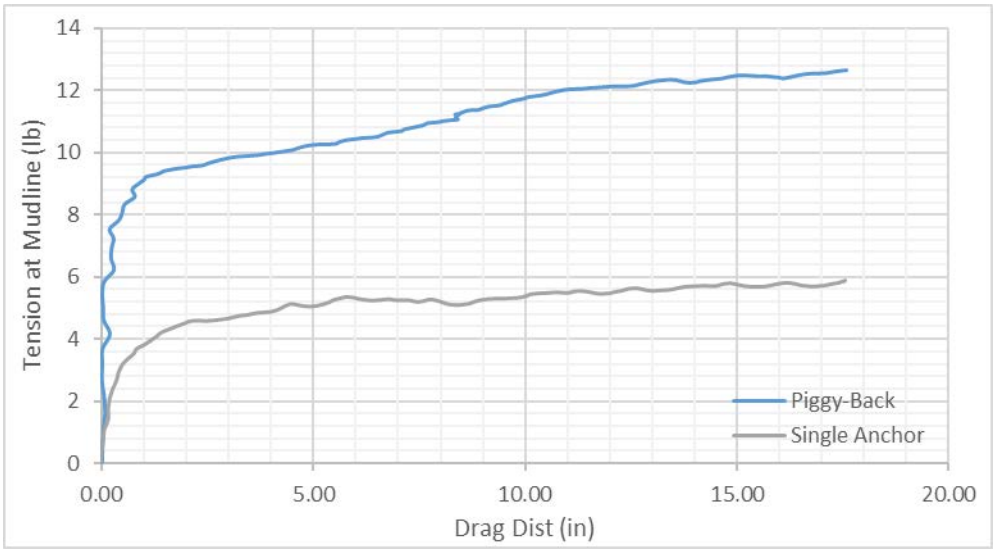

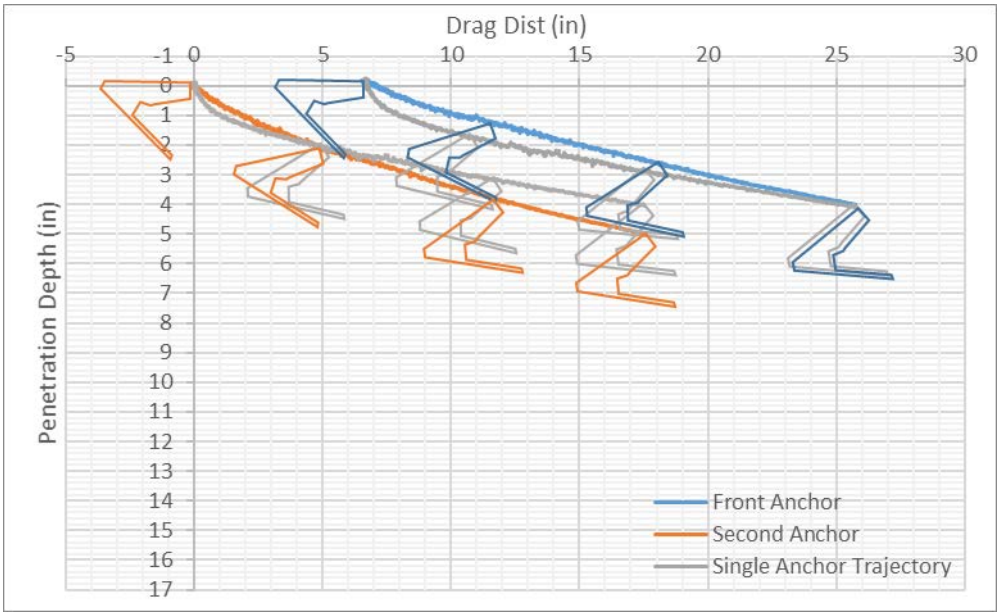

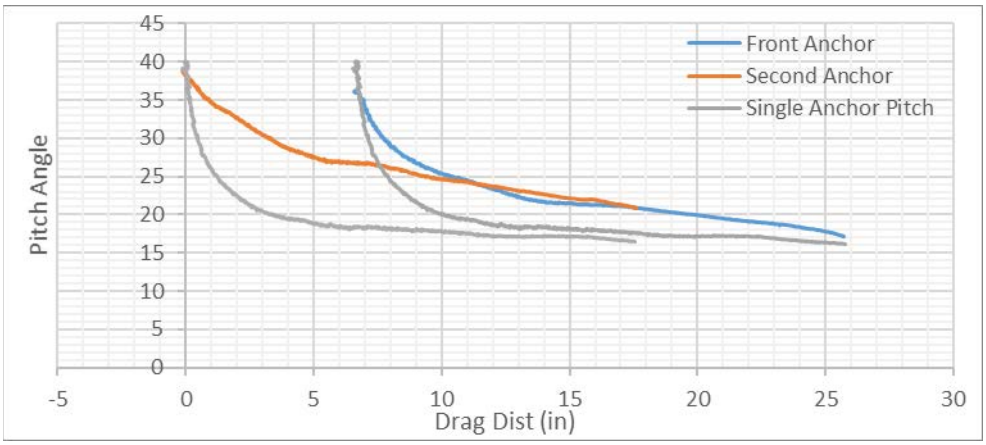

Second Repeat Test in Case 3

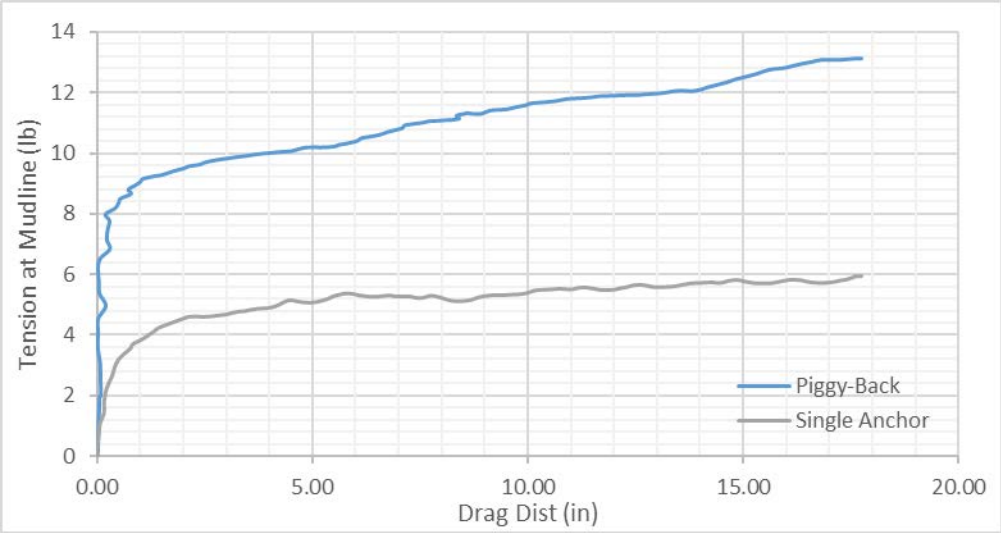

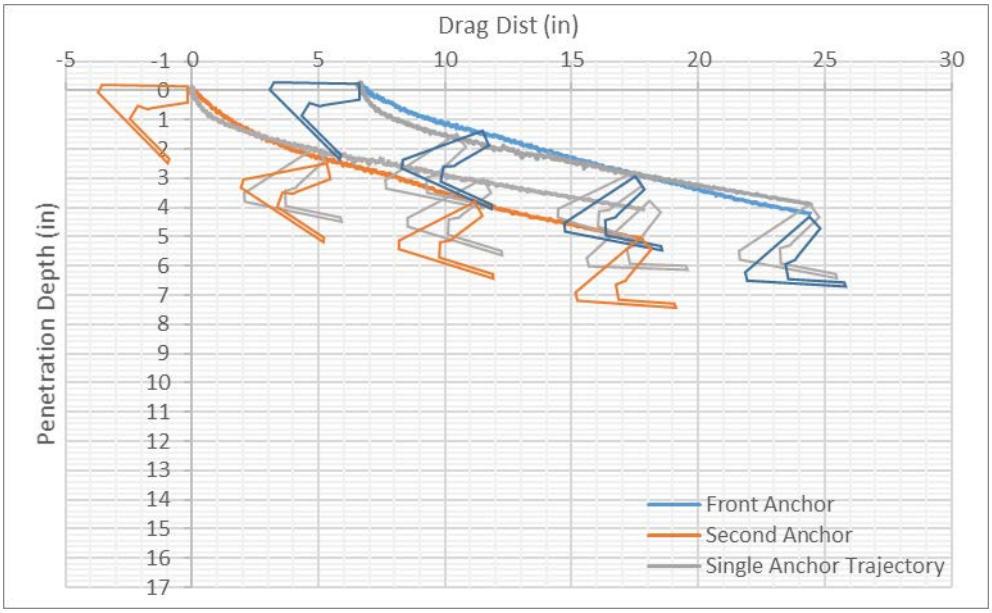

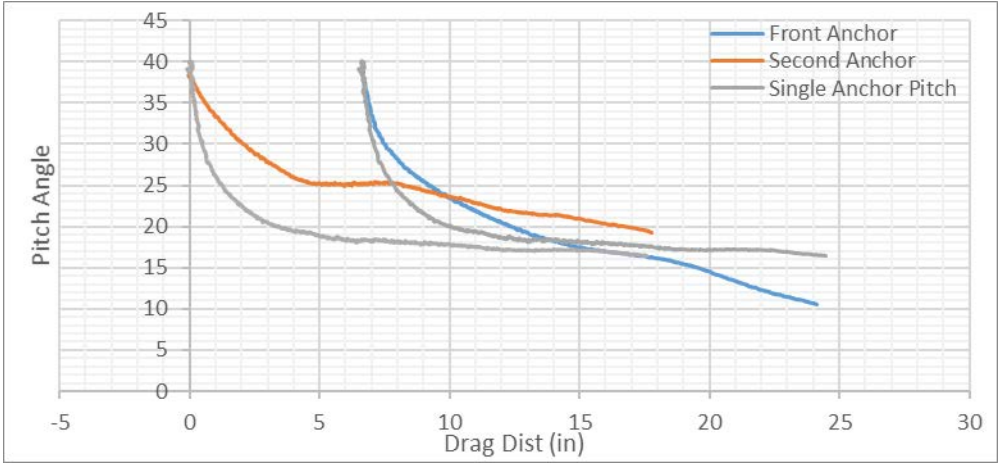

Case 4

Line Diameter (connecting two anchors)	0.05 inch
The 2nd anchor Attached to 1st Anchor's	Padeye
Spacing between two anchors	5.02 inch (1.38 Fluke Length)

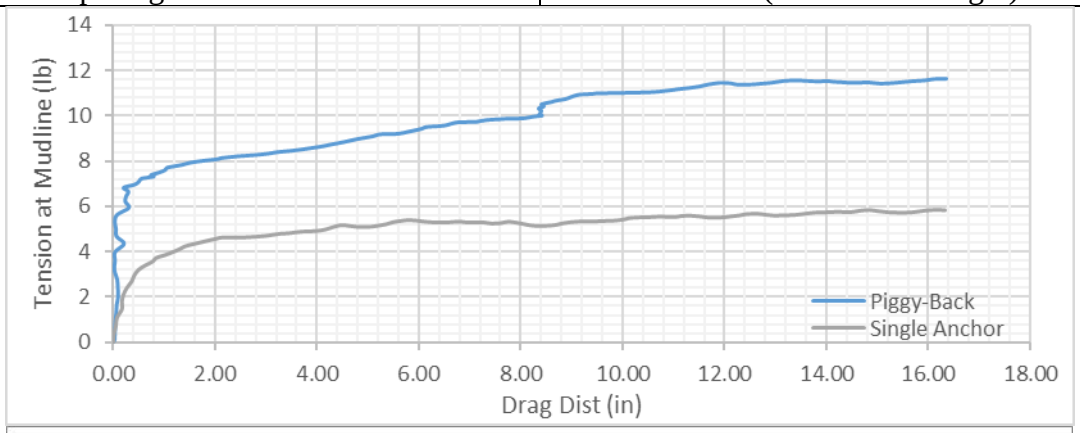

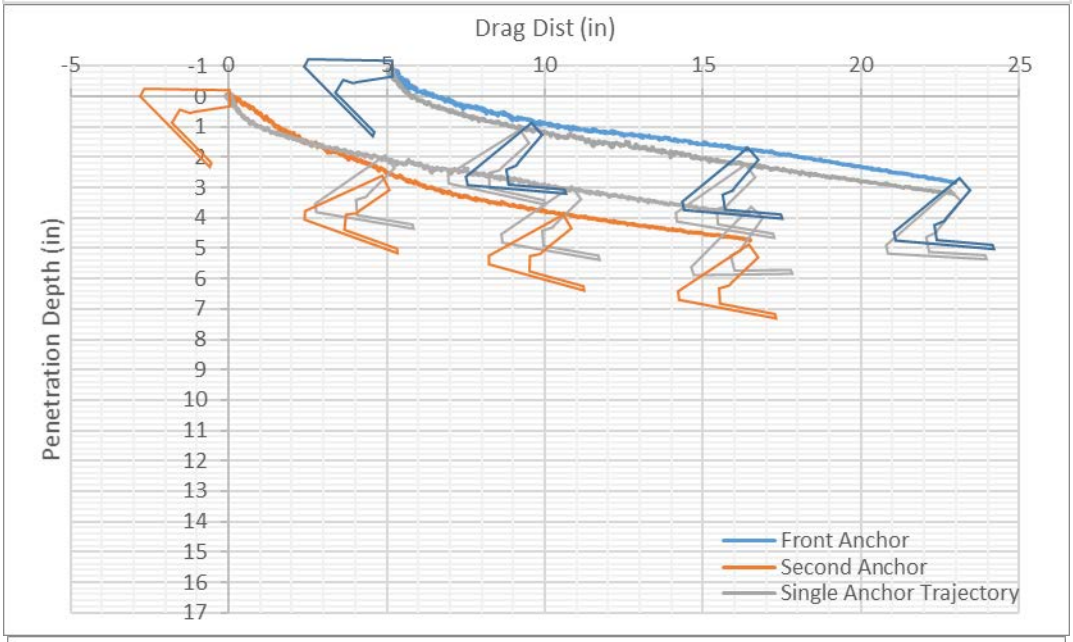

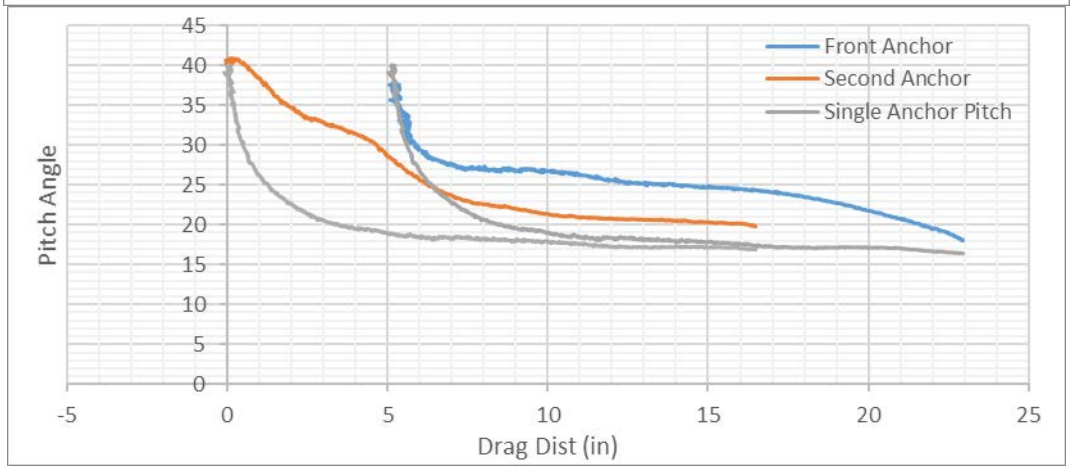

First Repeat test in Case 4

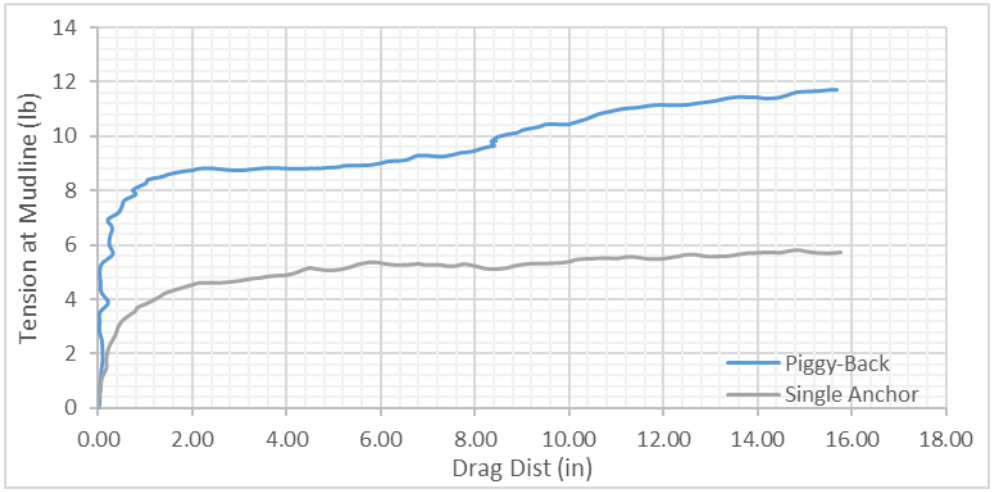

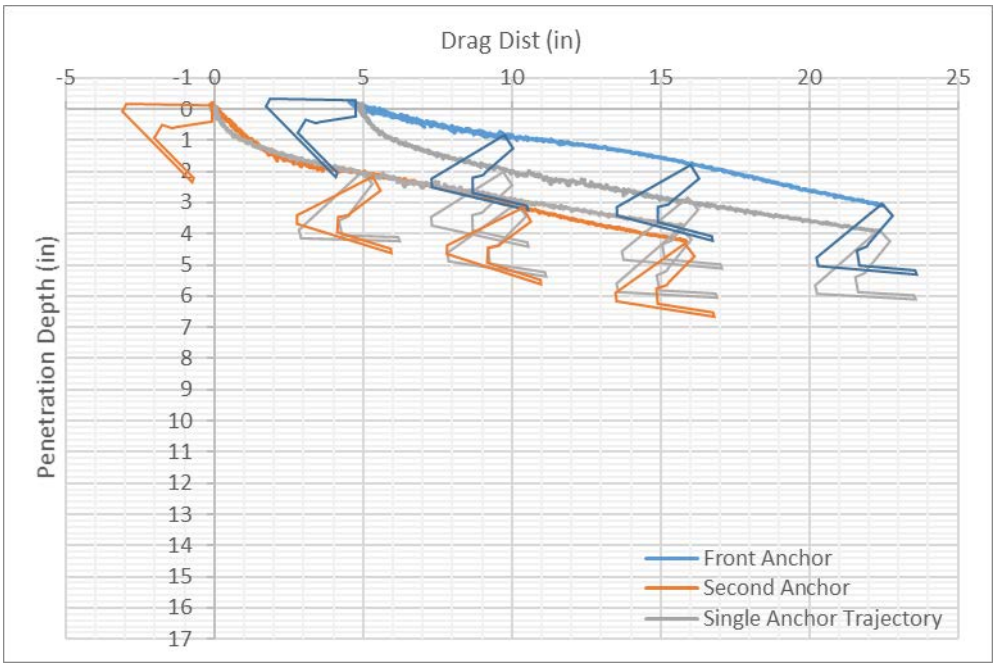

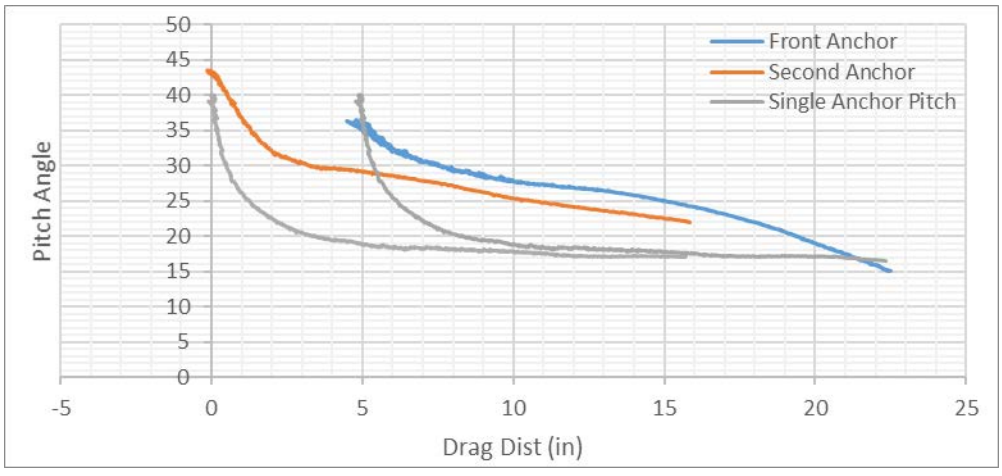

Case 5

Line Diameter (connecting two anchors)	0.19 inch
The 2nd anchor Attached to 1st Anchor's	Center of Back Fluke
Spacing between two anchors	10.42 inch (2.87 Fluke Length)

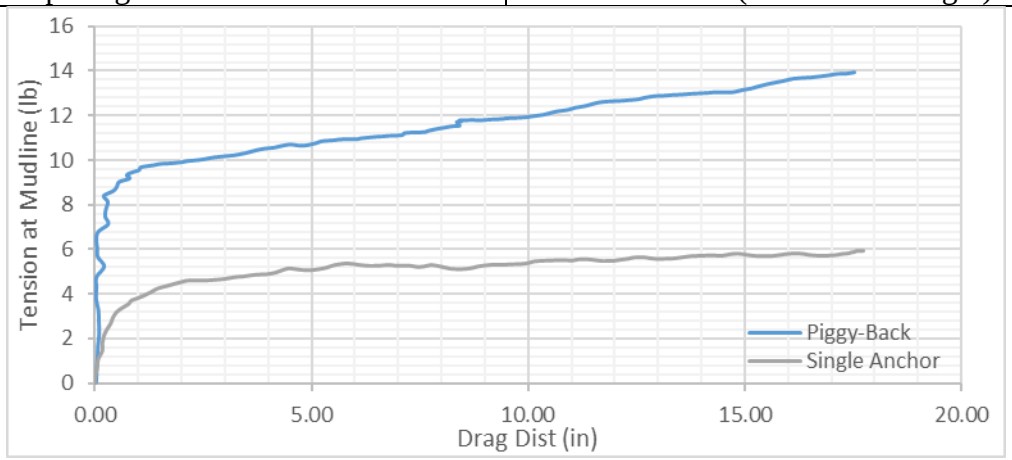

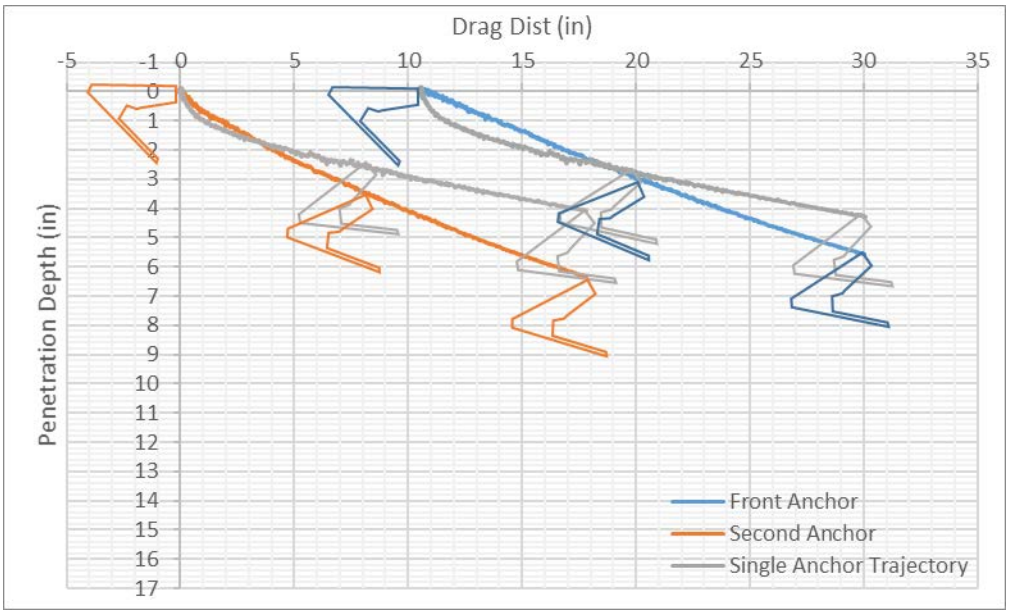

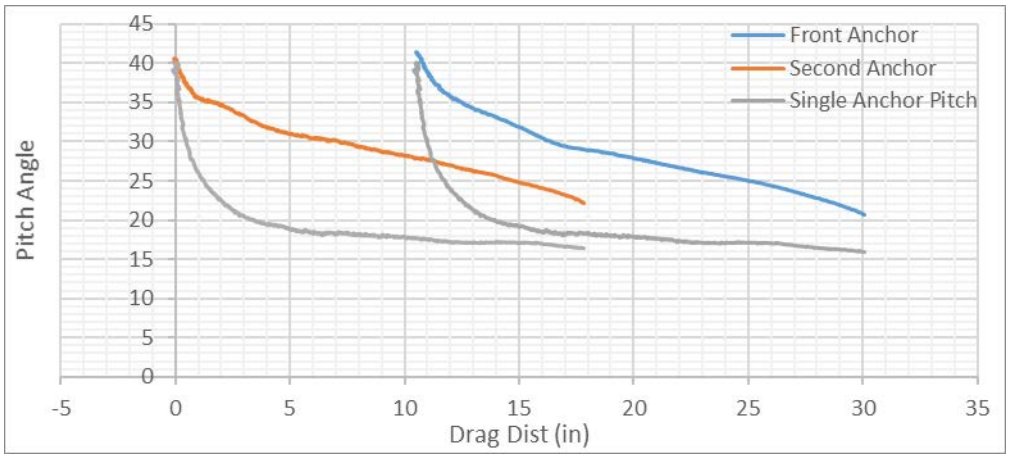

First Repeat test in Case 5

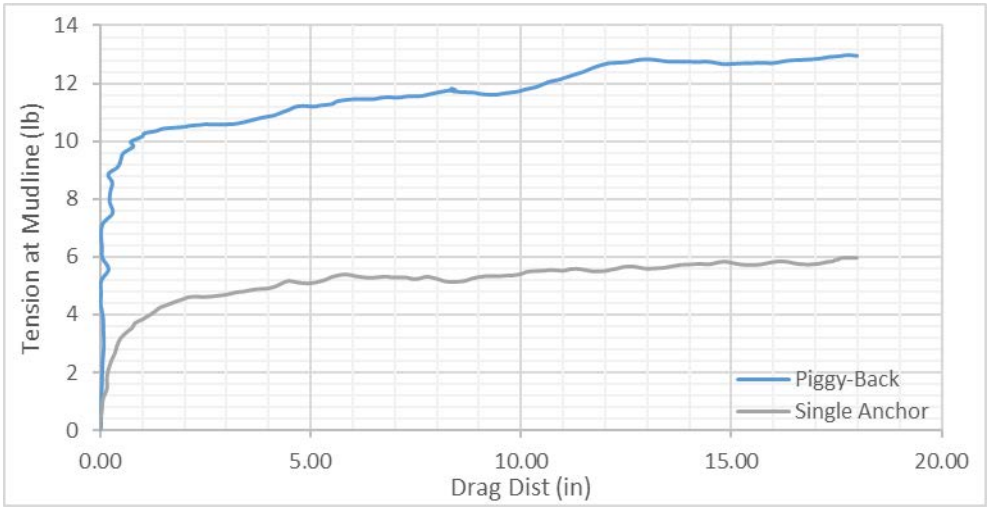

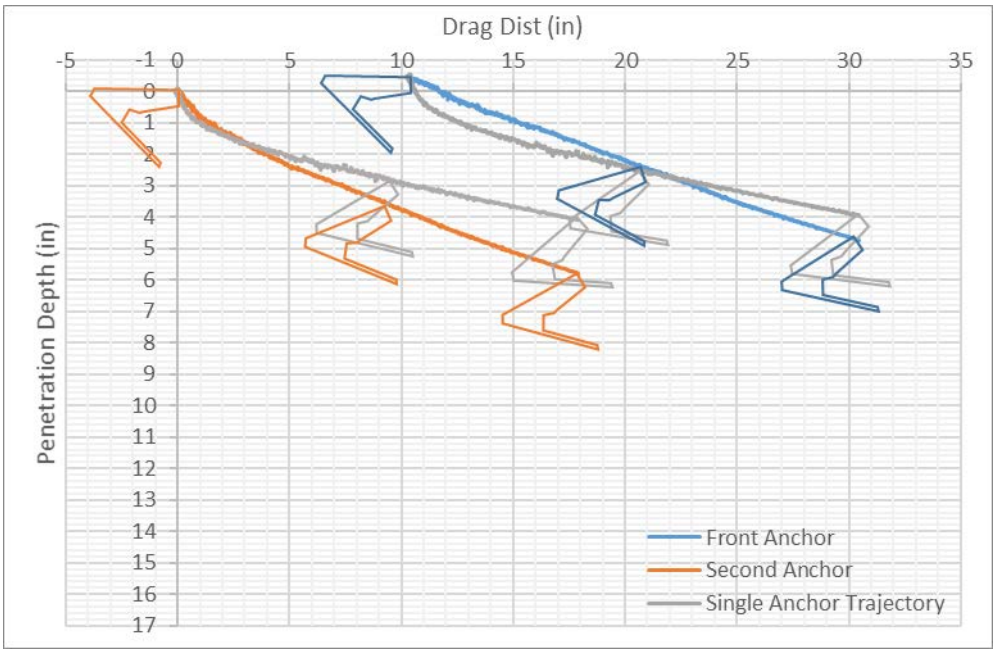

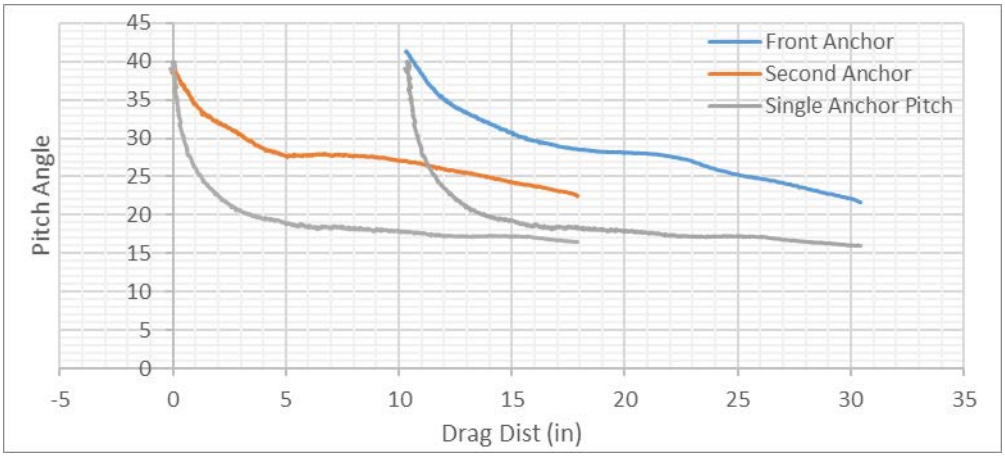

Second Repeat Test in Case 5

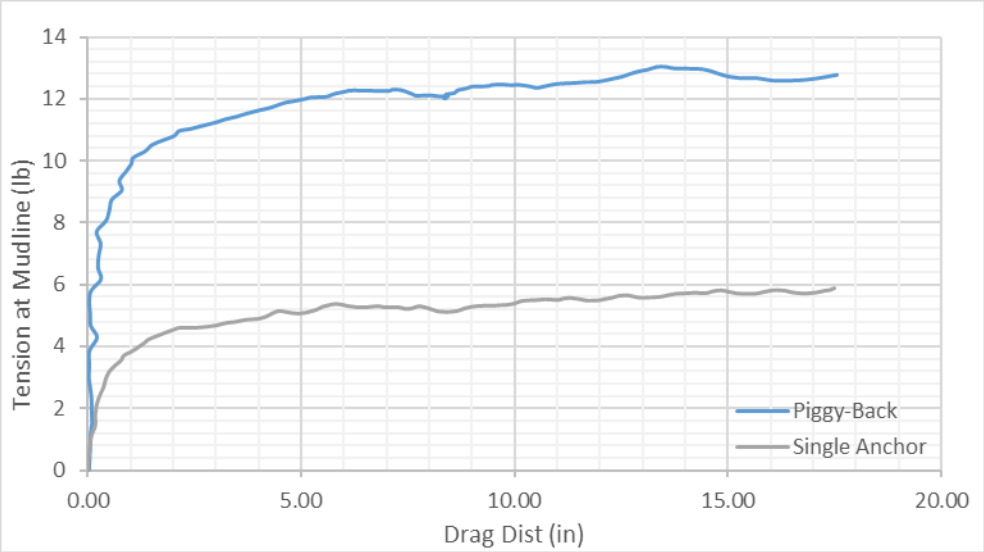

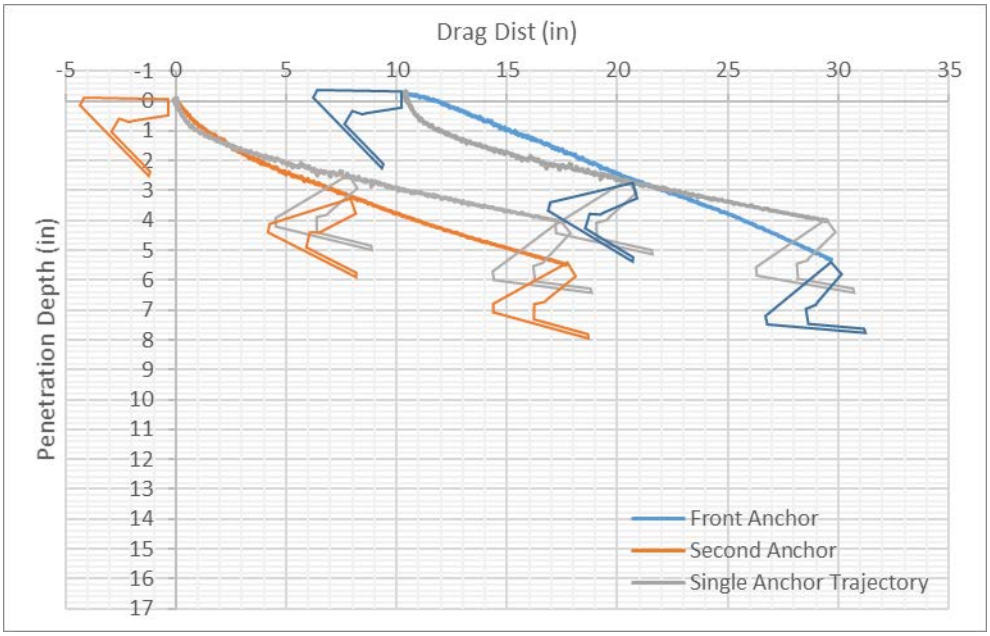

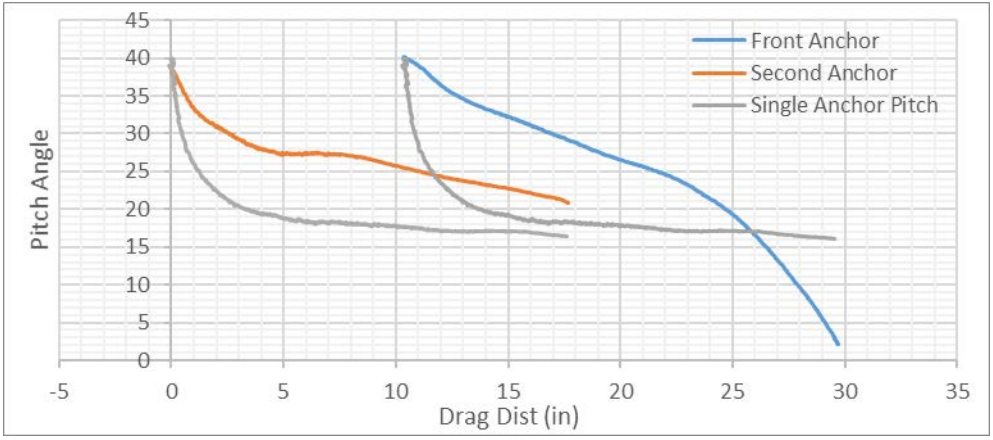

Case 6

Line Diameter (connecting two anchors)	0.05 inch
The 2nd anchor Attached to 1st Anchor's	Center of Back Fluke
Spacing between two anchors	11.38 inch (3.14 Fluke Length)

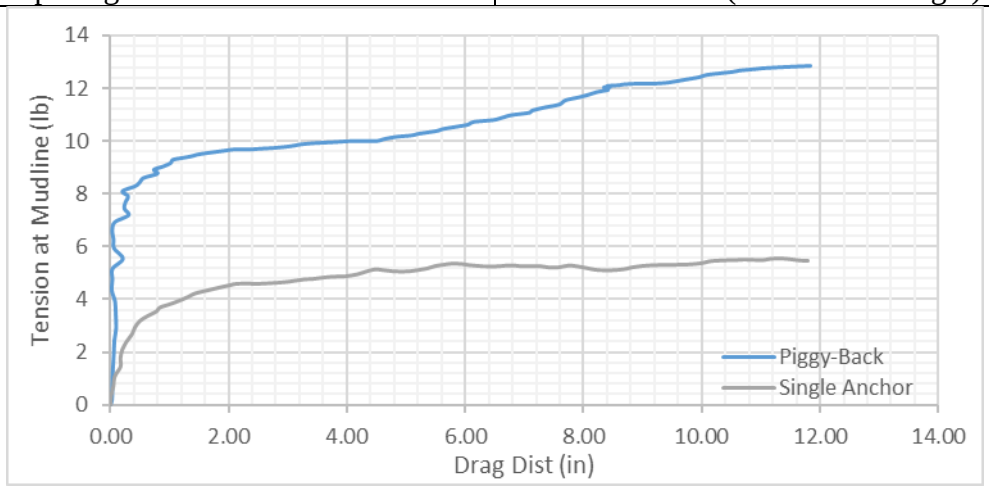

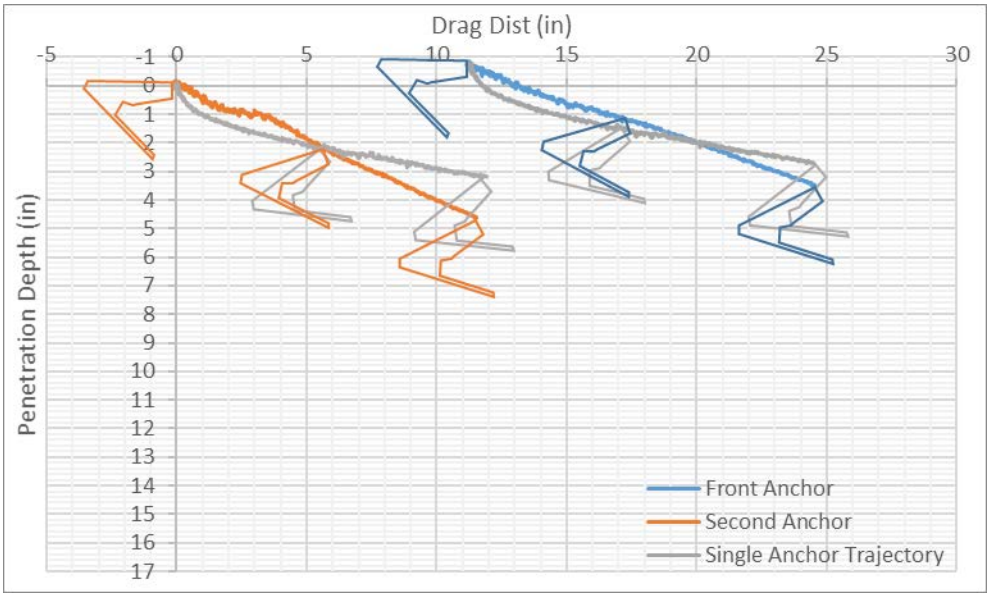

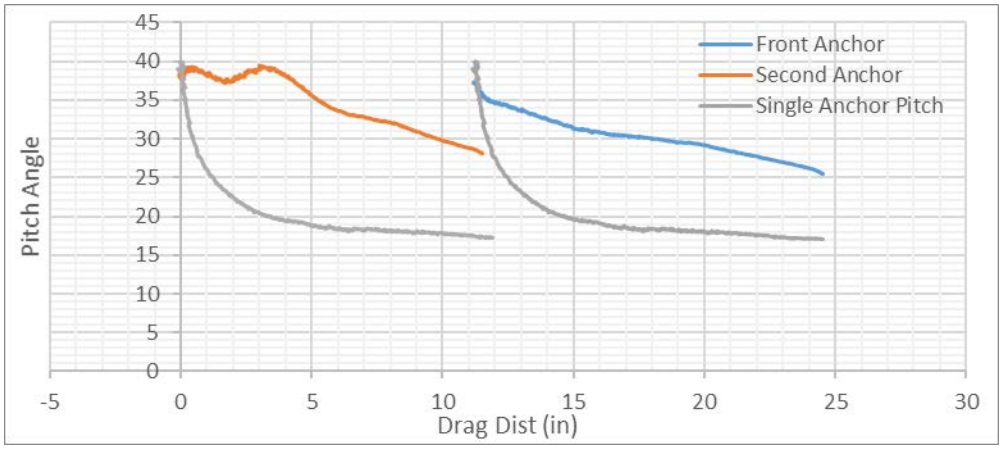

First Repeat test in Case 6

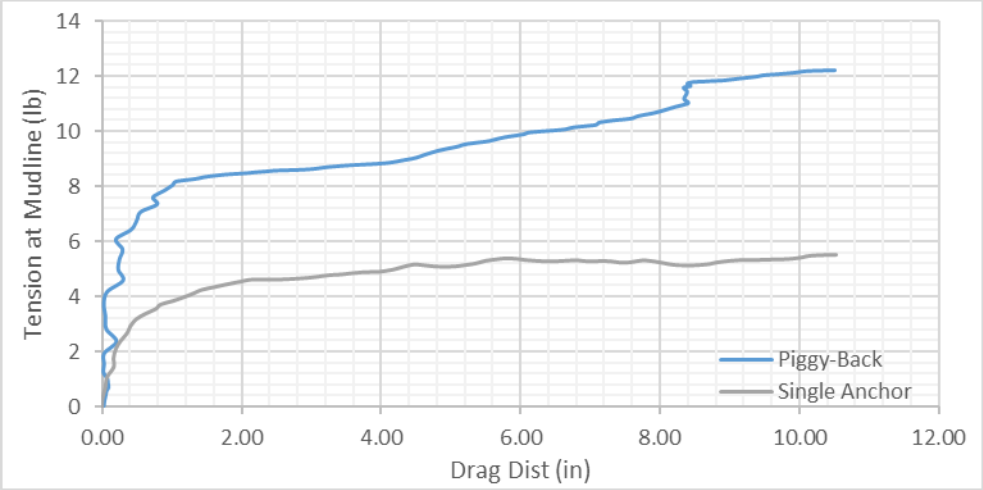

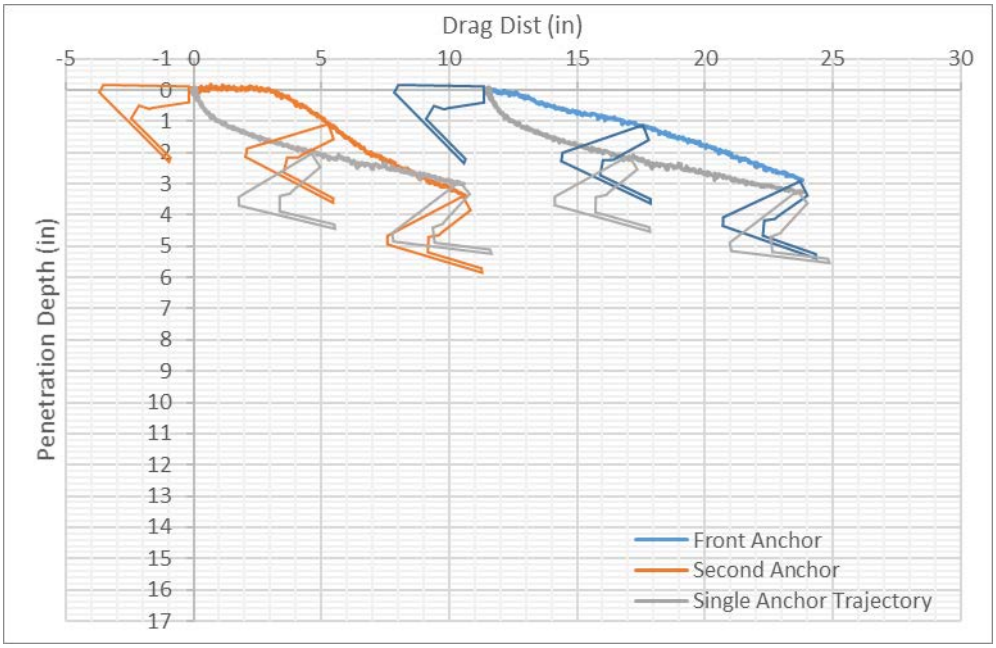

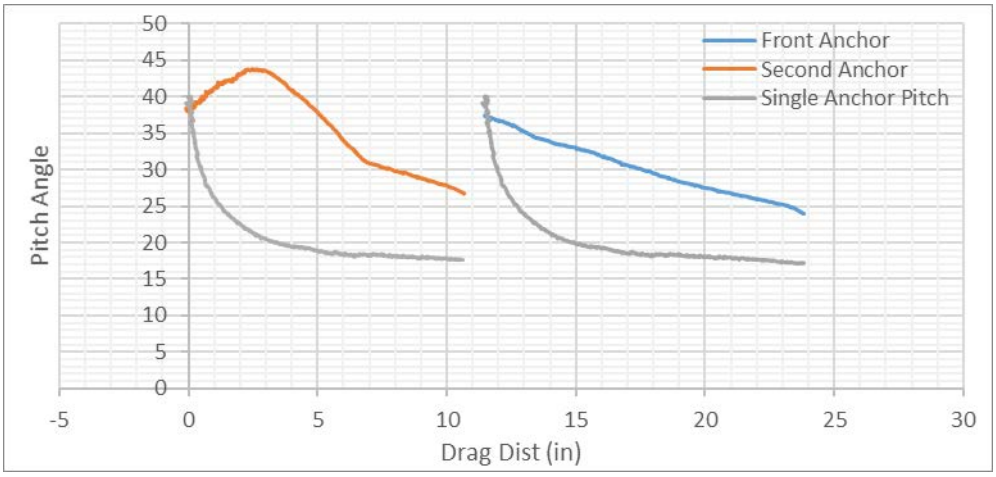

Second Repeat Test in Case 6

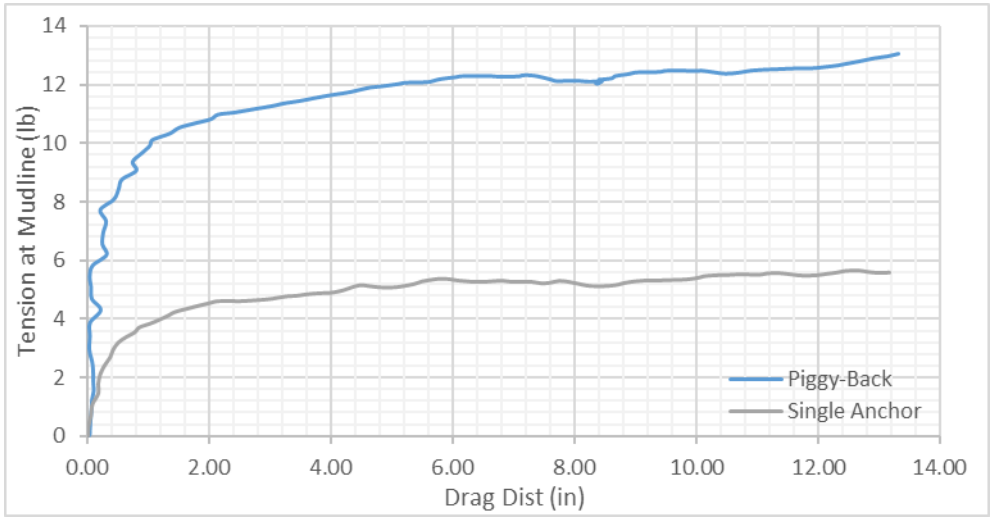

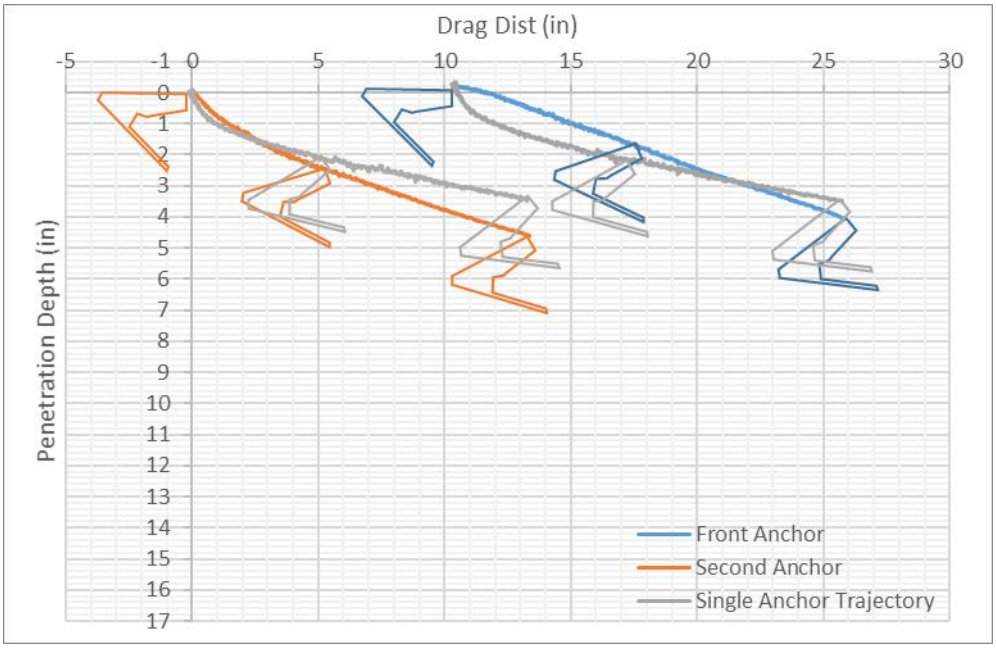

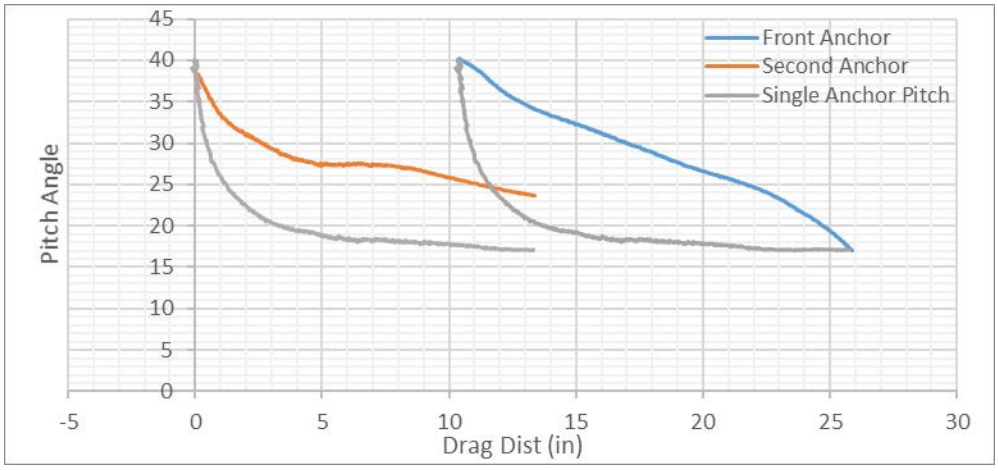

Case 7

Line Diameter (connecting two anchors)	0.19 inch
The 2nd anchor Attached to 1st Anchor's	Padeye
Spacing between two anchors	8.28 inch (2.28 Fluke Length)

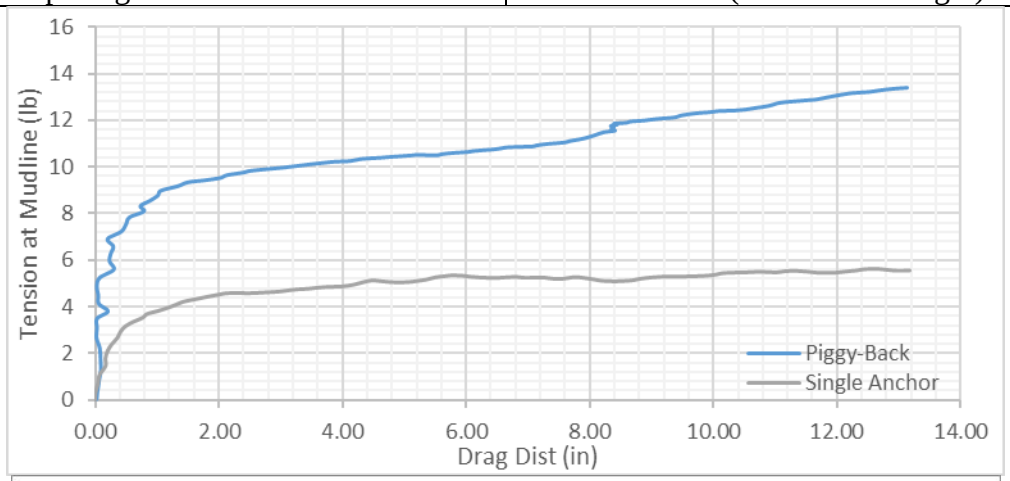

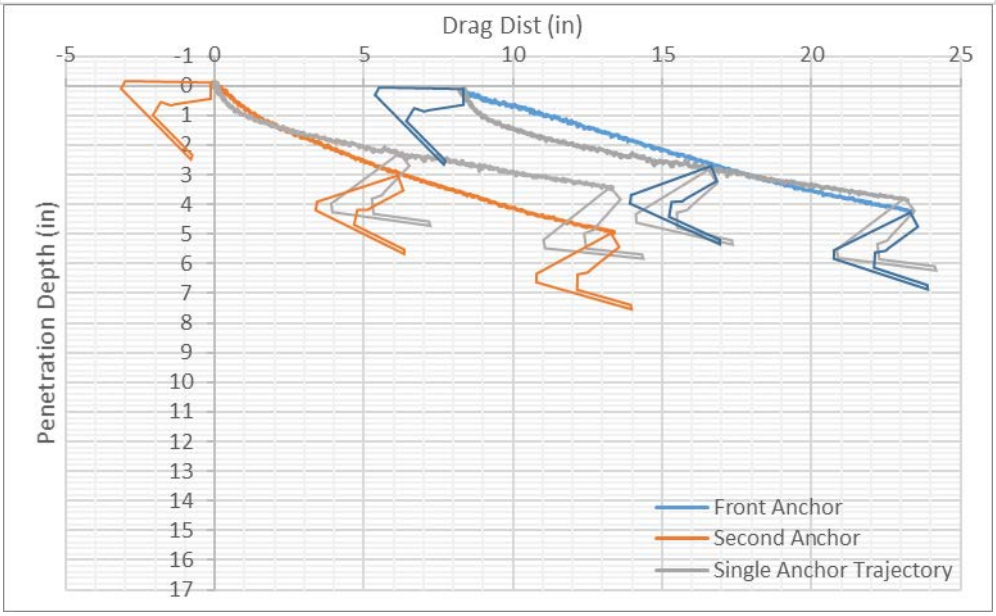

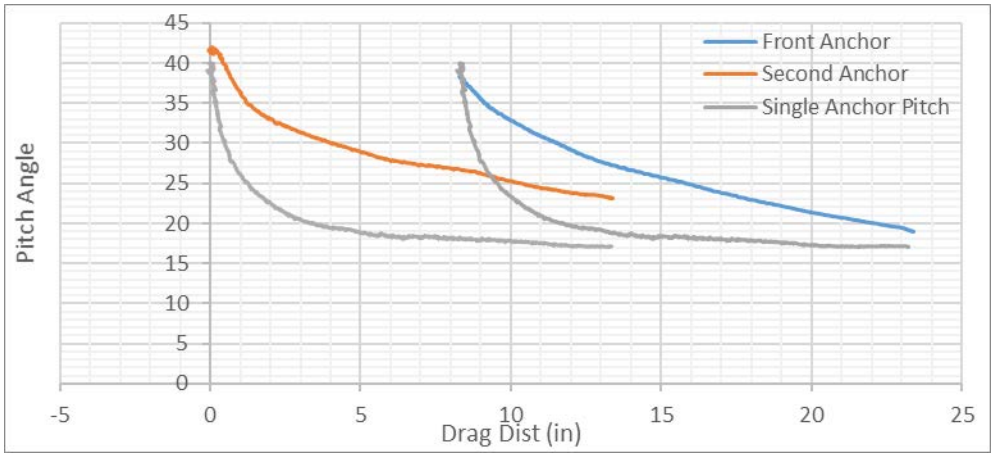

First Repeat test in Case 7

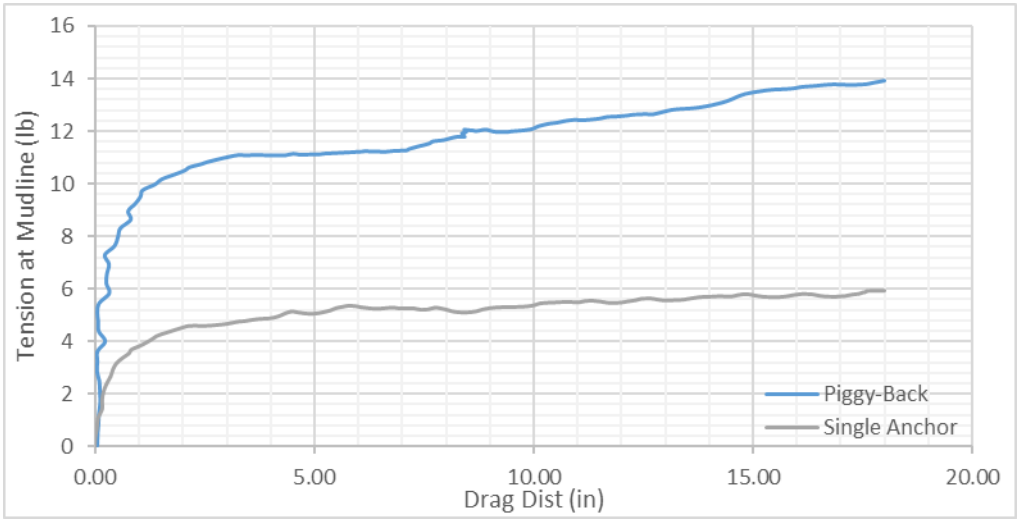

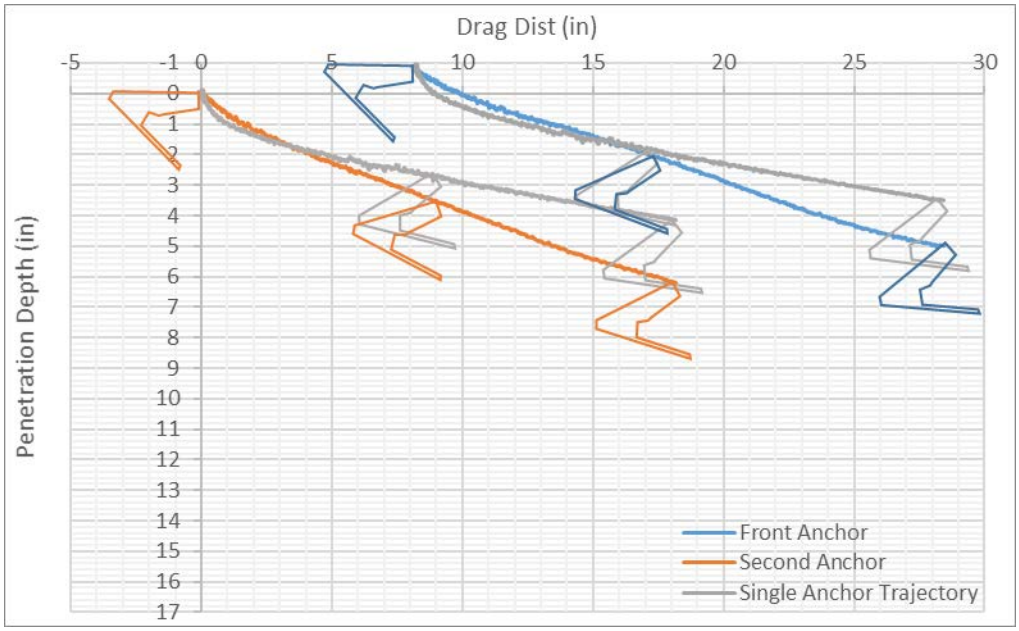

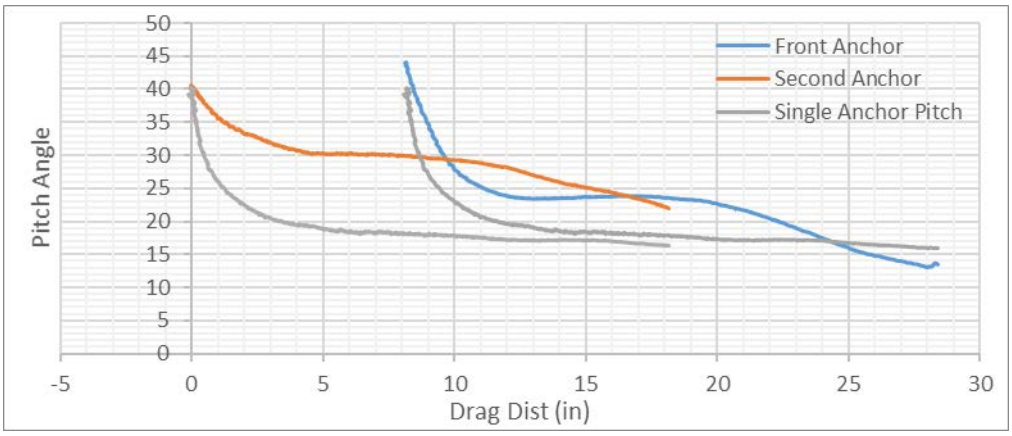

Second Repeat Test in Case 7

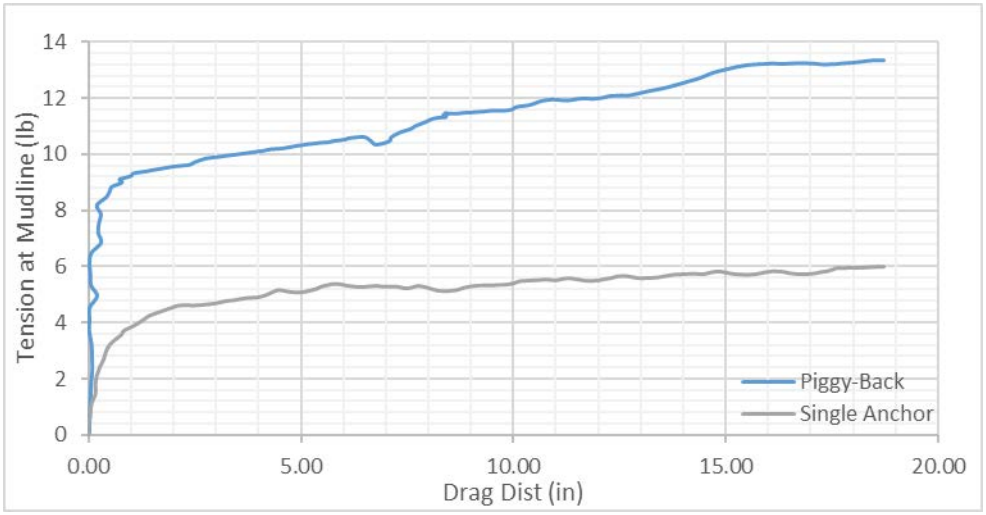

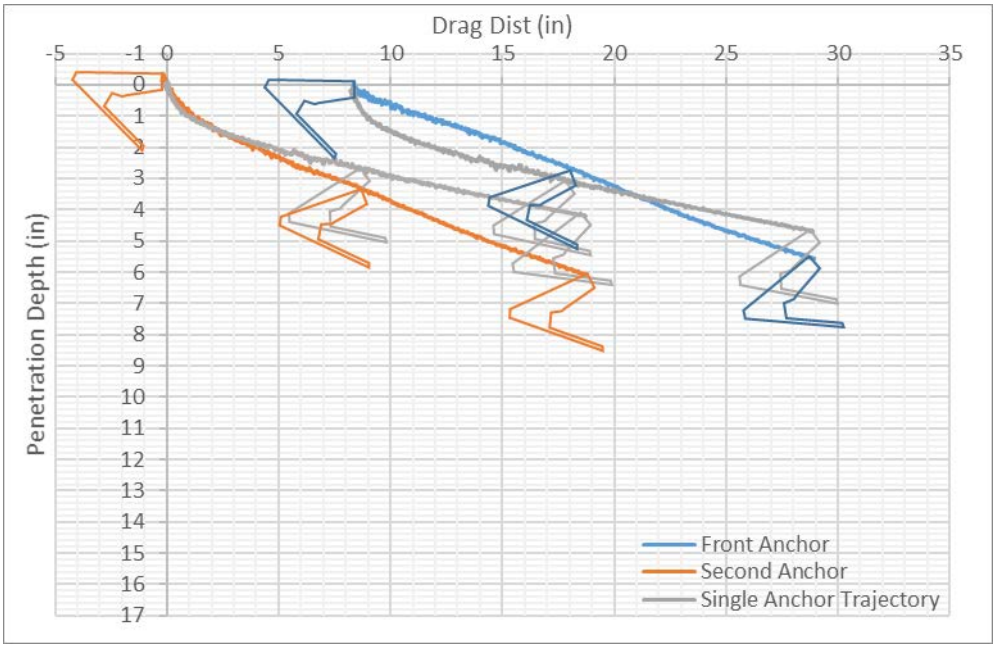

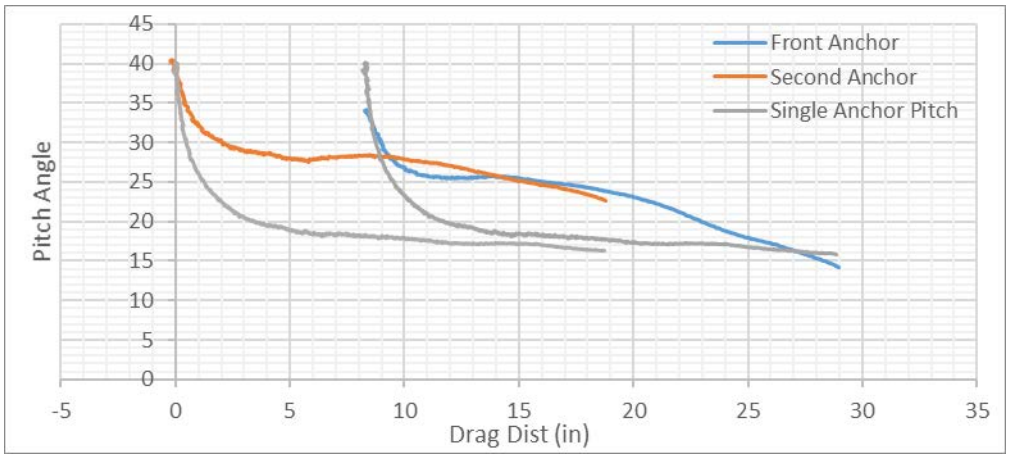

Third Repeat Test in Case 7

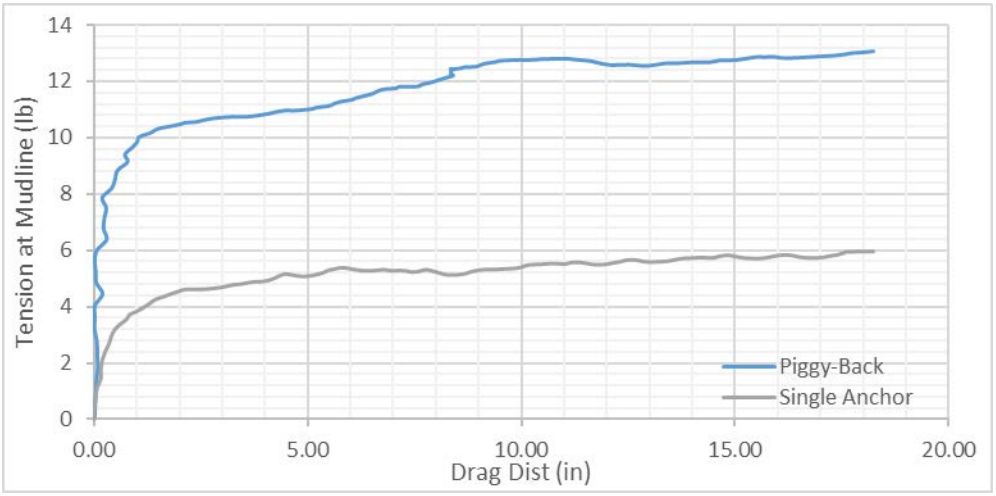

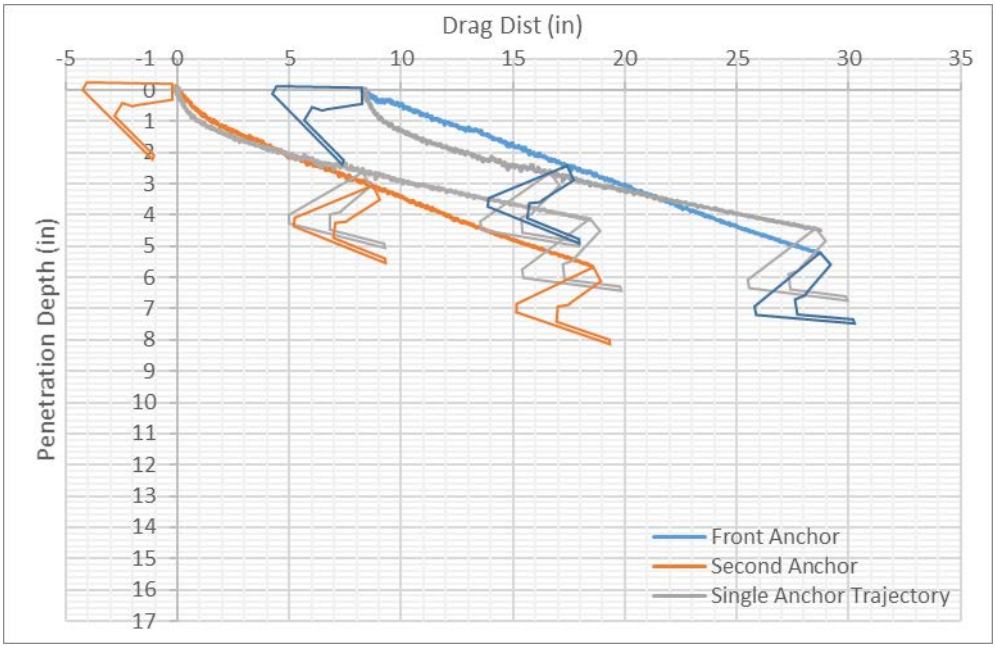

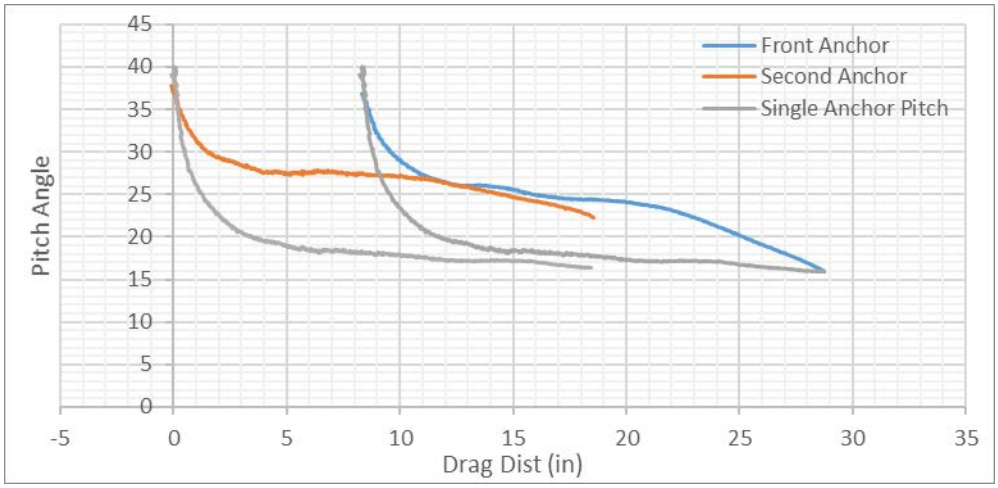

Case 8

Line Diameter (connecting two anchors)	0.05 inch
The 2nd anchor Attached to 1st Anchor's	Padeye
Spacing between two anchors	11.54 inch (3.18 Fluke Length)

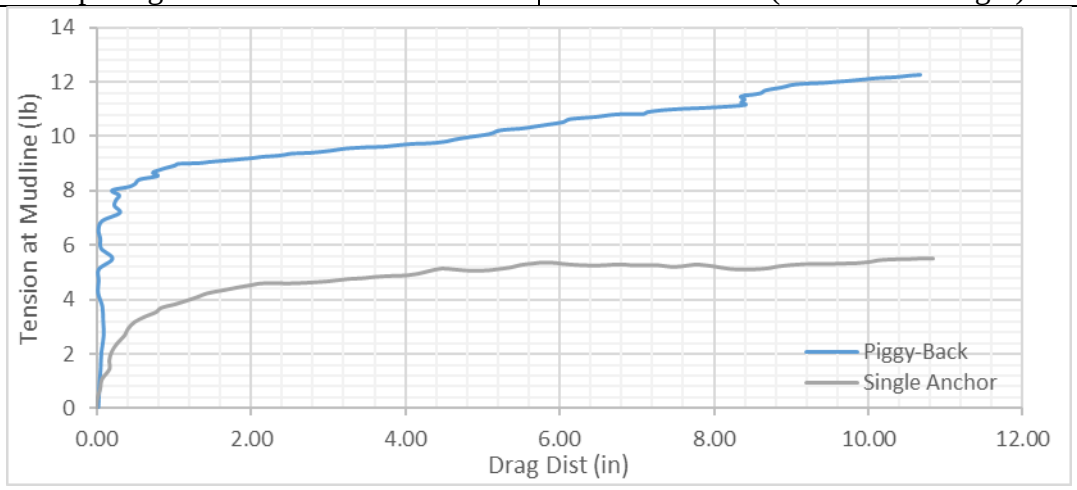

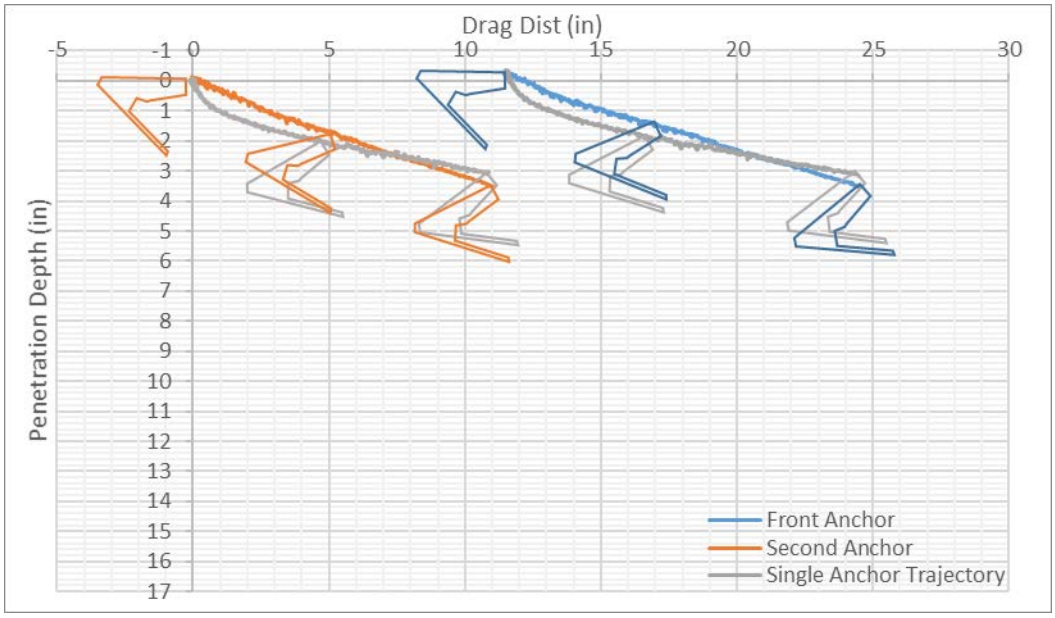

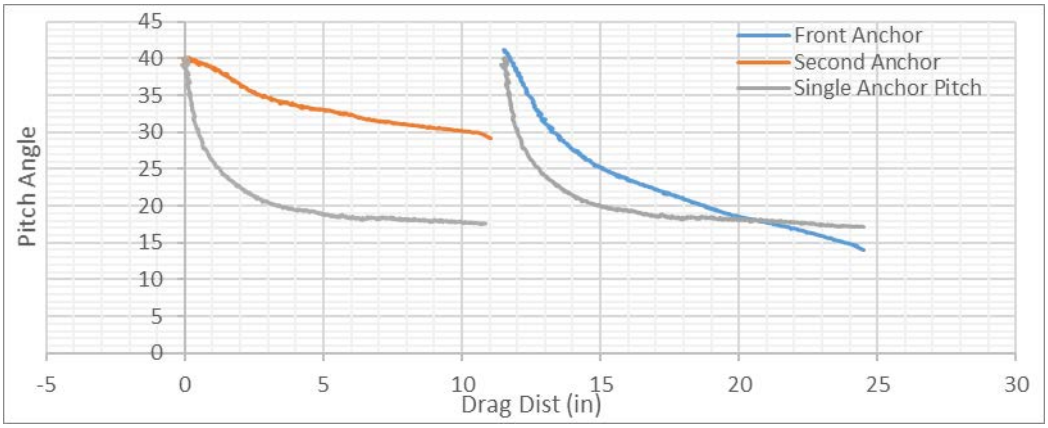

Case 9

Line Diameter (connecting two anchors)	0.19 inch
The 2nd anchor Attached to 1st Anchor's	Center of Back Fluke
Spacing between two anchors	12.28 inch (3.39 Fluke Length)

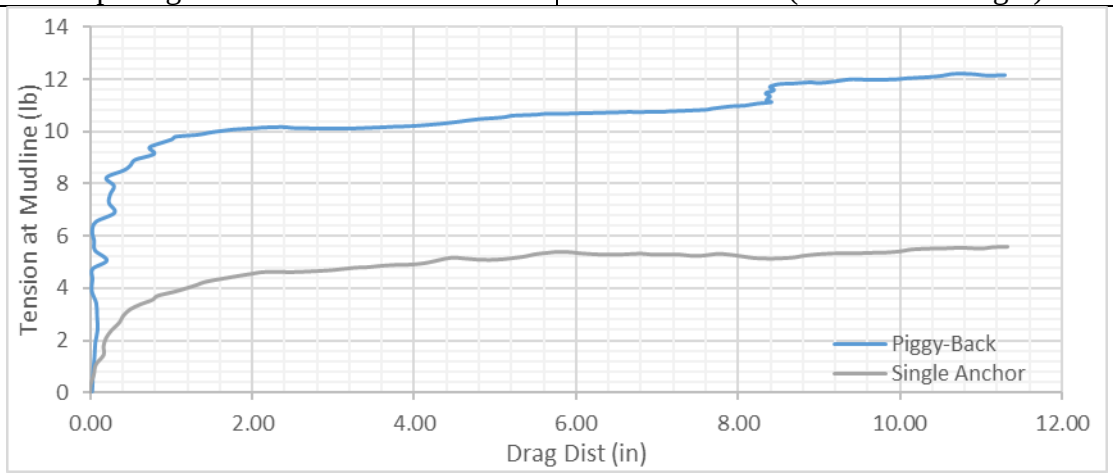

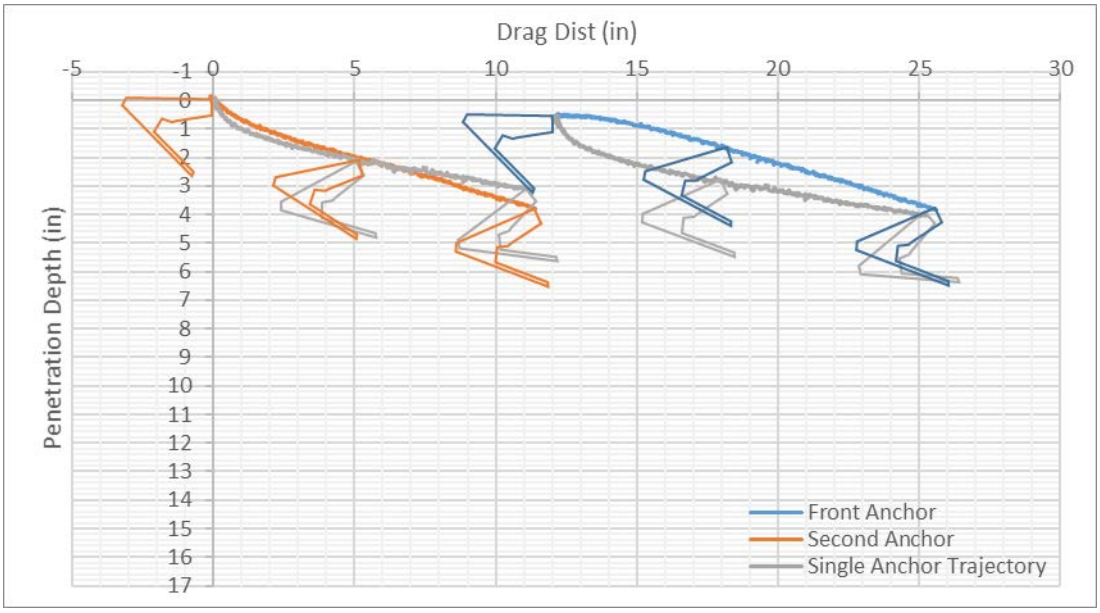

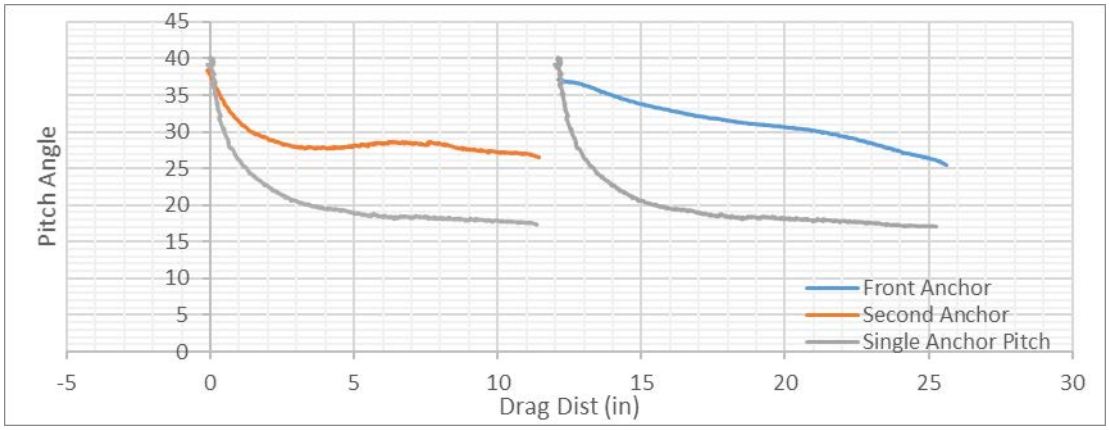

First Repeat test in Case 9

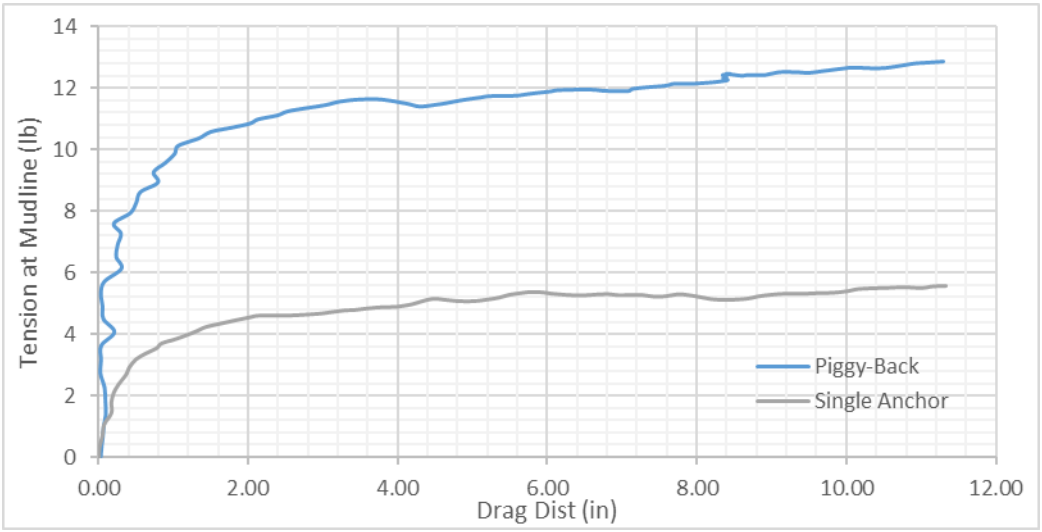

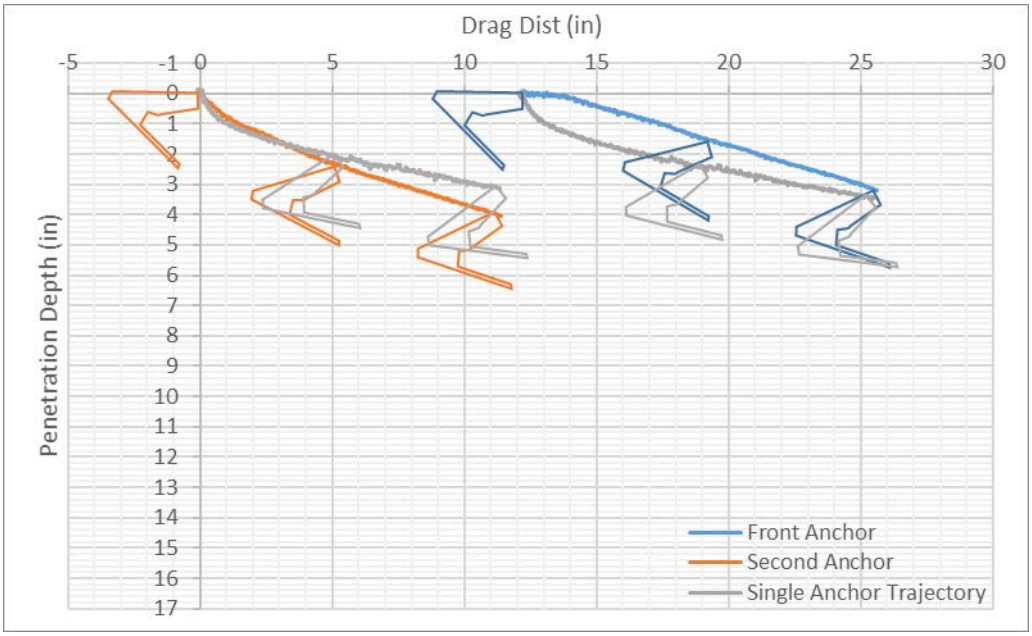

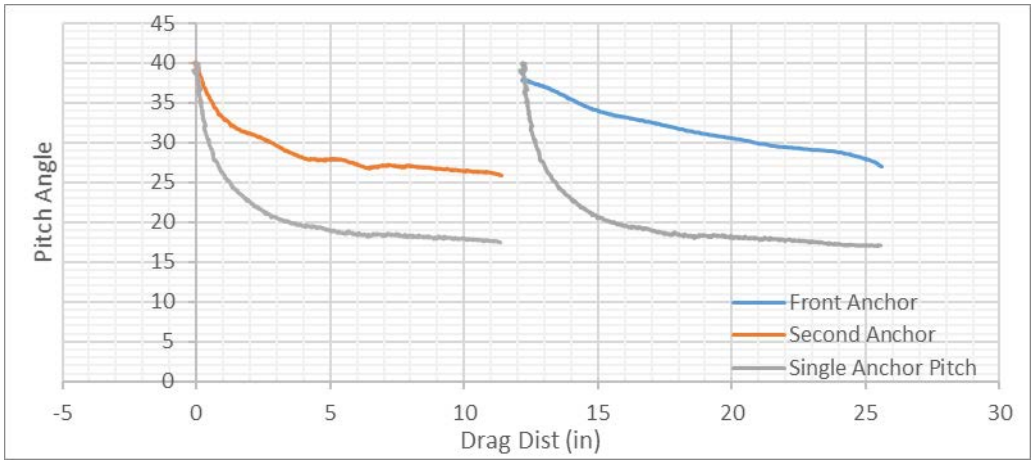

Second Repeat Test in Case 9

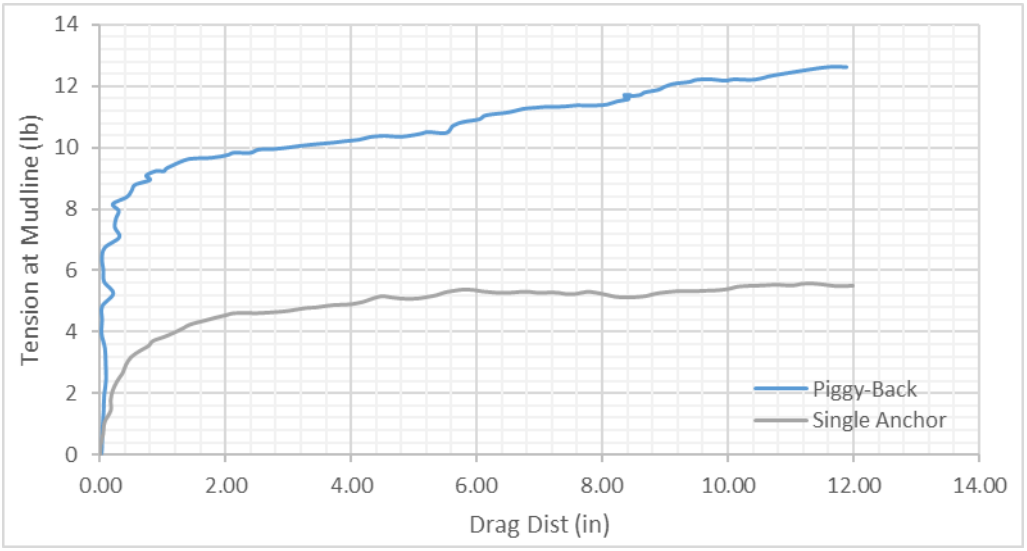

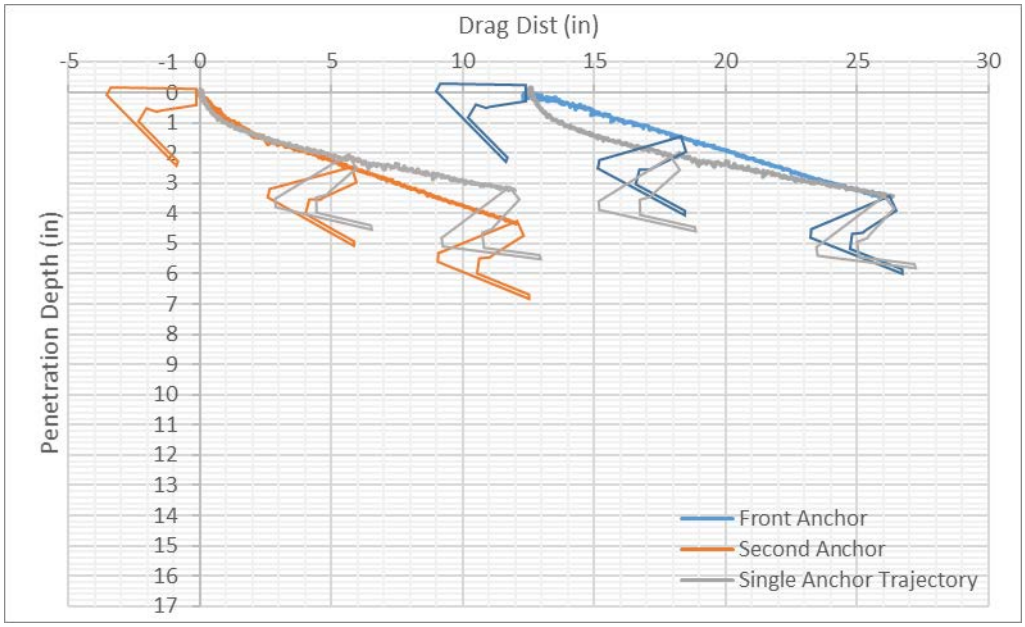

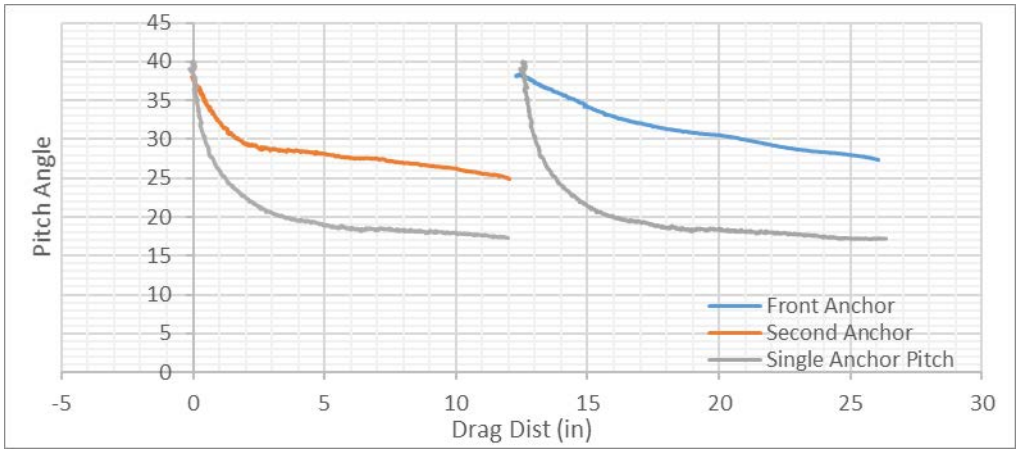

Case 10

Line Diameter (connecting two anchors)	0.05 inch
The 2nd anchor Attached to 1st Anchor's	Center of Back Fluke
Spacing between two anchors	14.62 inch (4.03 Fluke Length)

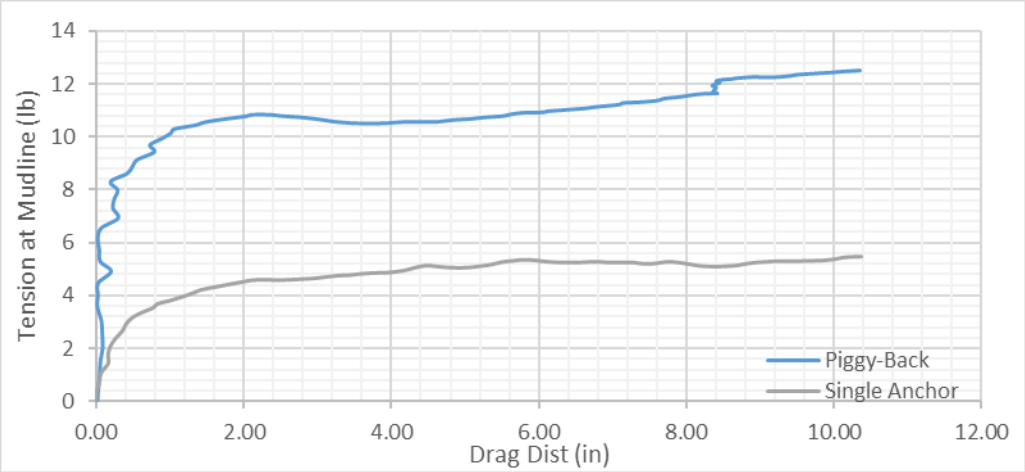

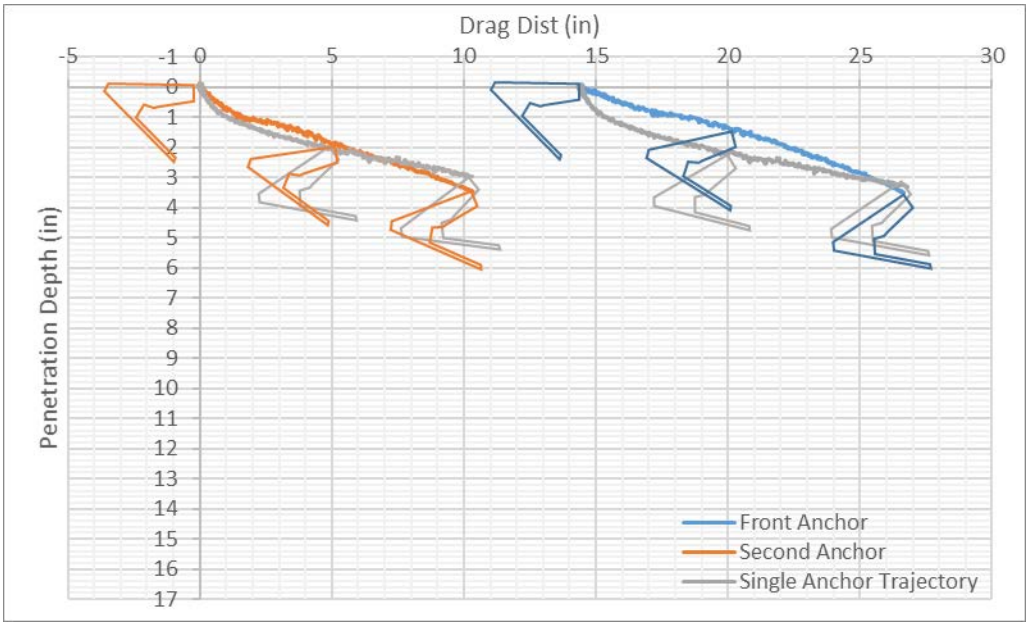

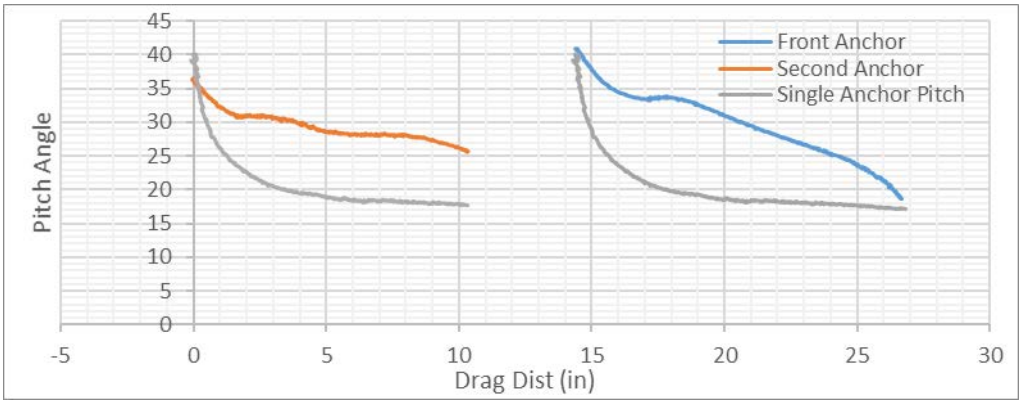

First Repeat test in Case 10

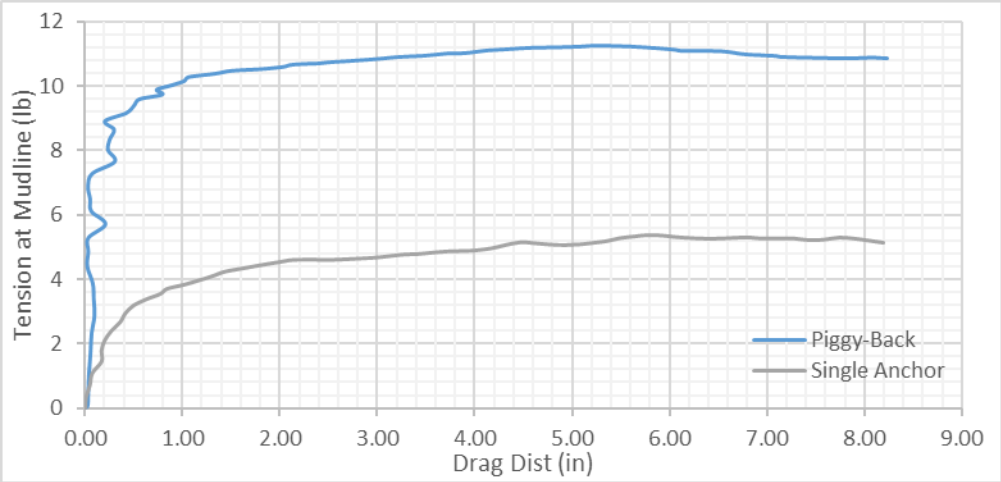

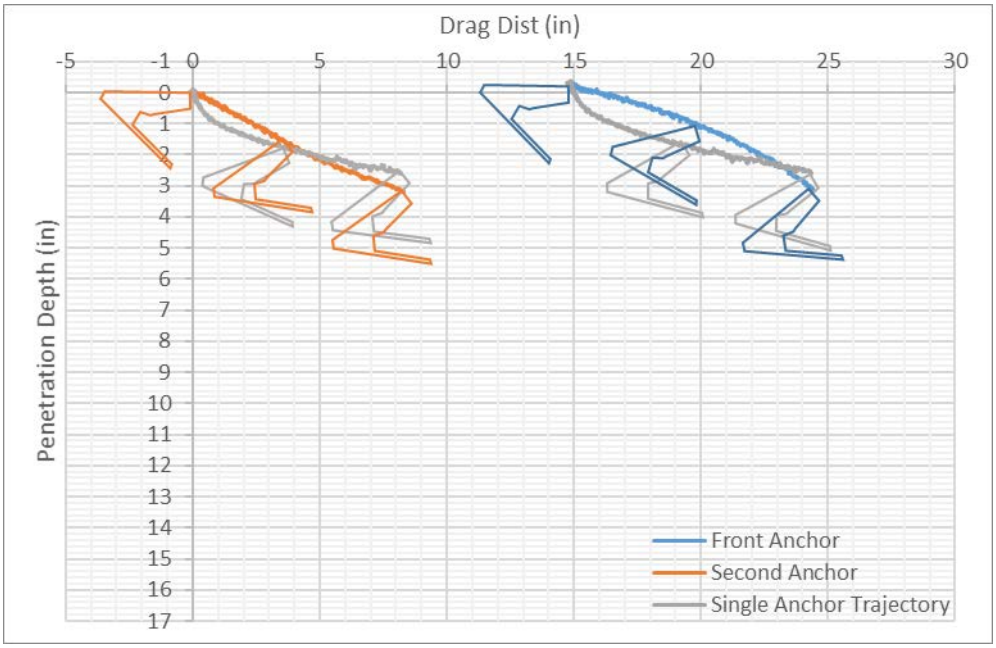

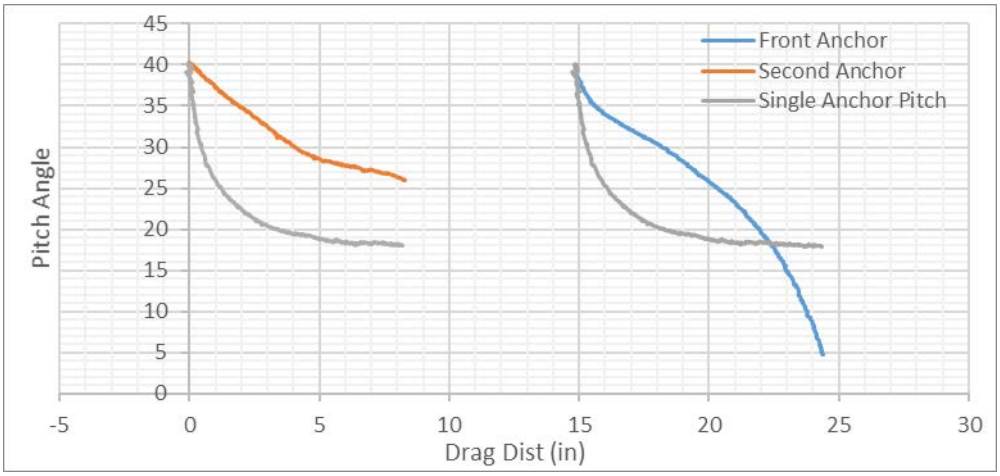

Case 11

Line Diameter (connecting two anchors)	0.05 inch
The 2nd anchor Attached to 1st Anchor's	Padeye
Spacing between two anchors	15.29 inch (4.24 Fluke Length)

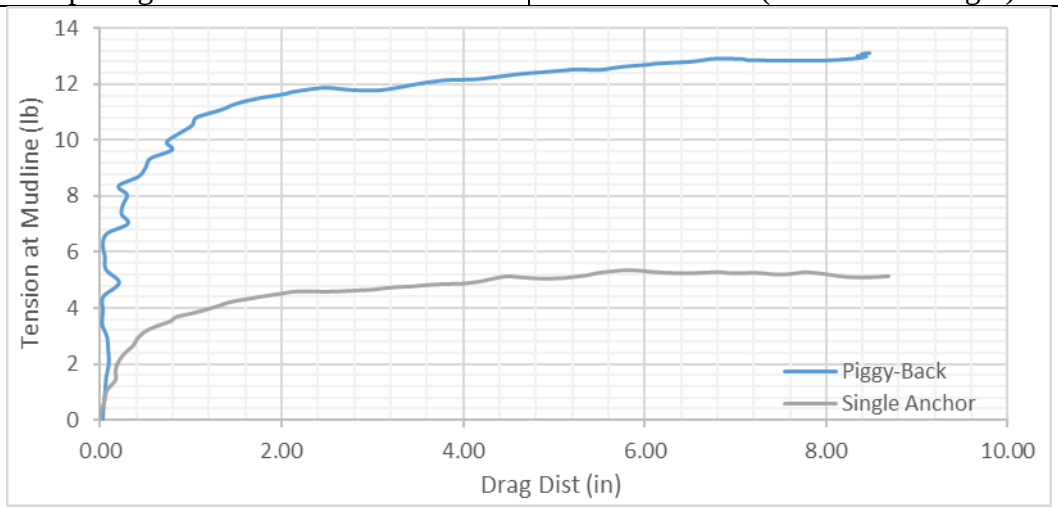

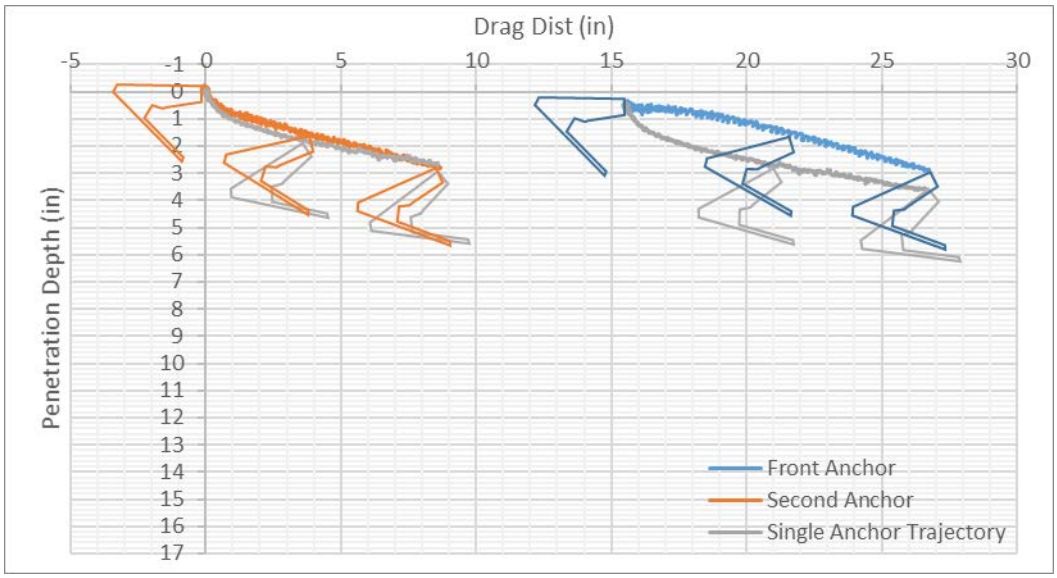

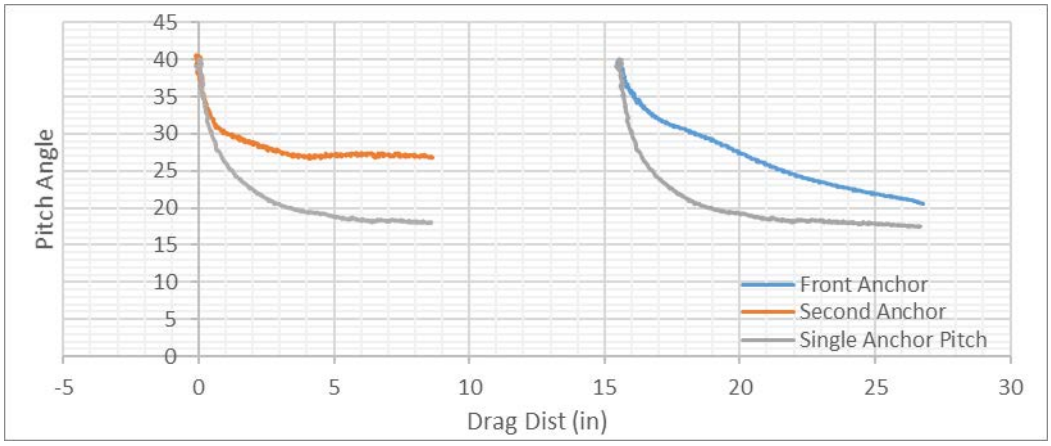

First Repeat test in Case 11

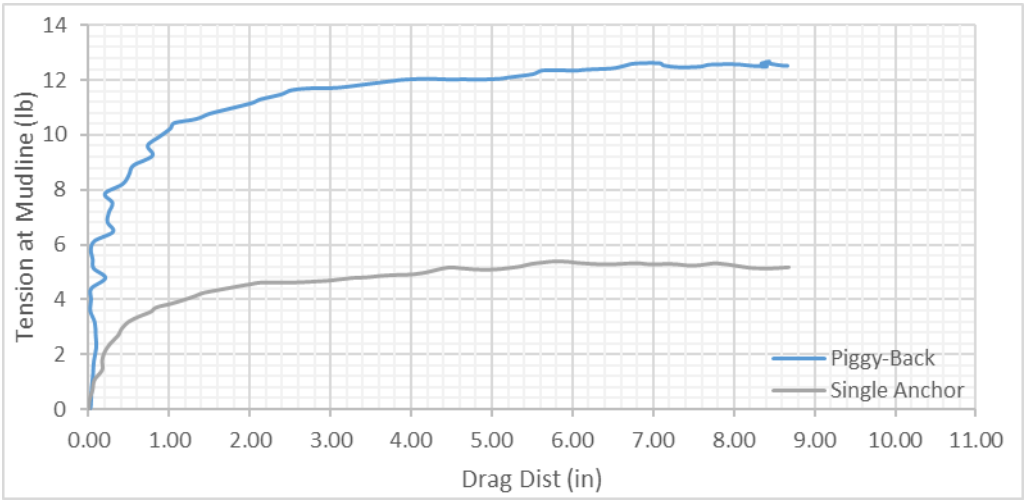

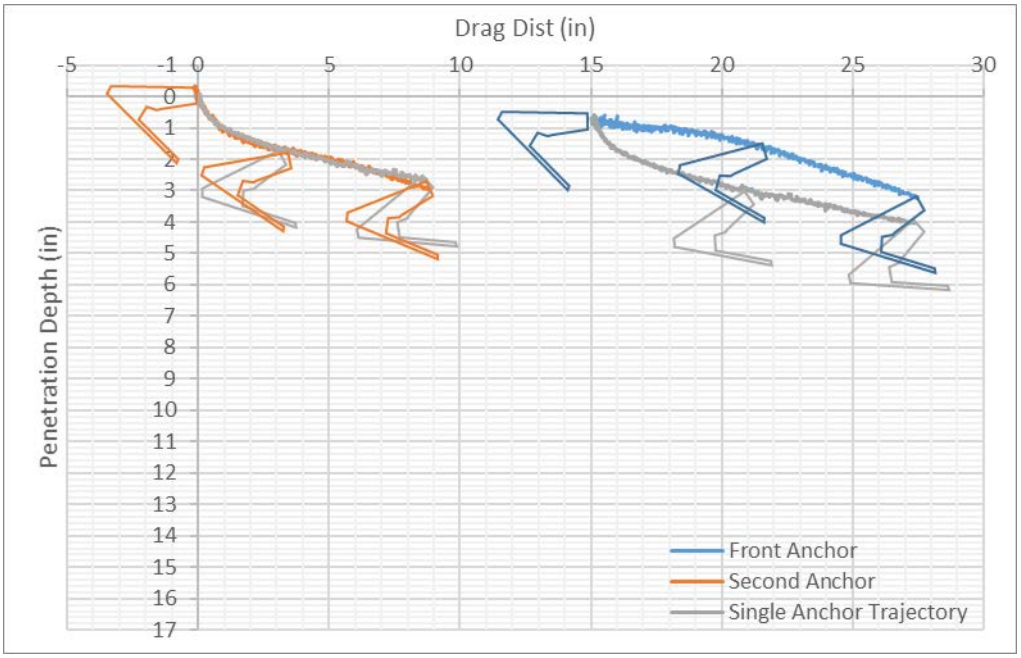

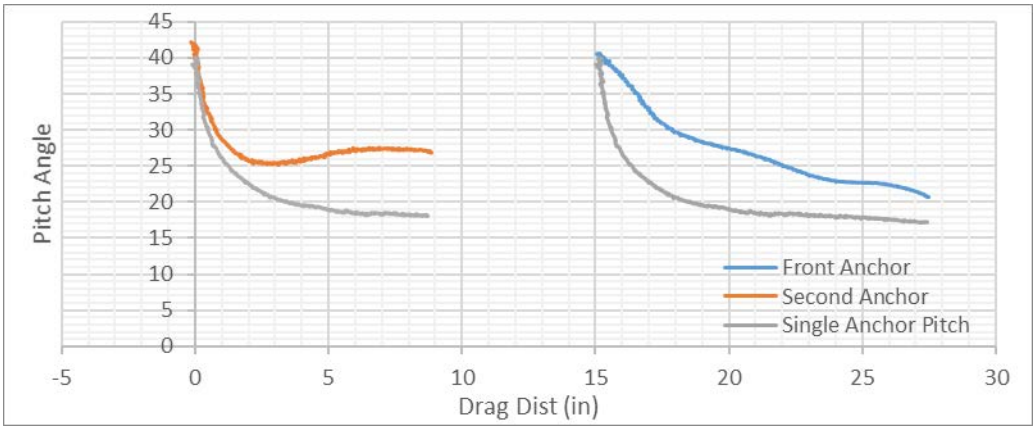

Second Repeat Test in Case 11

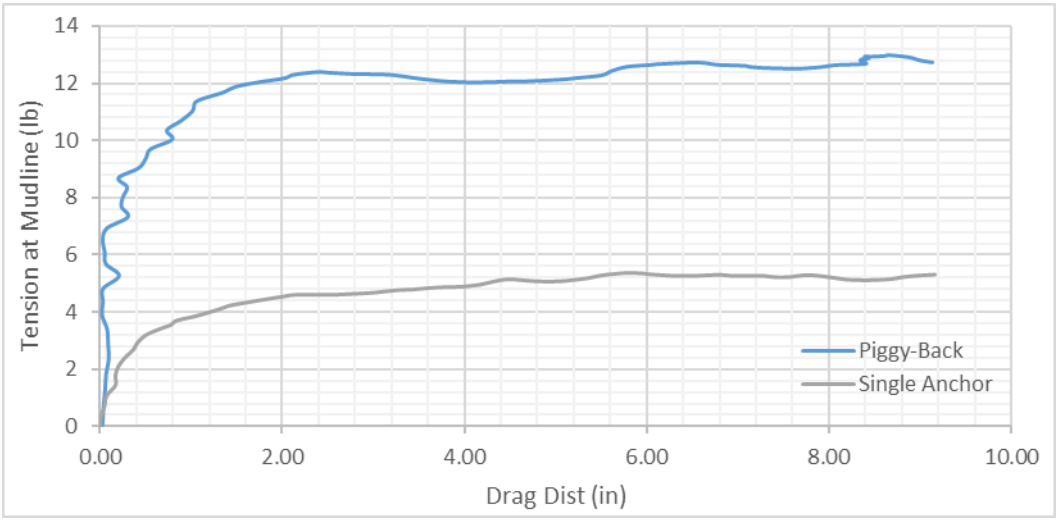

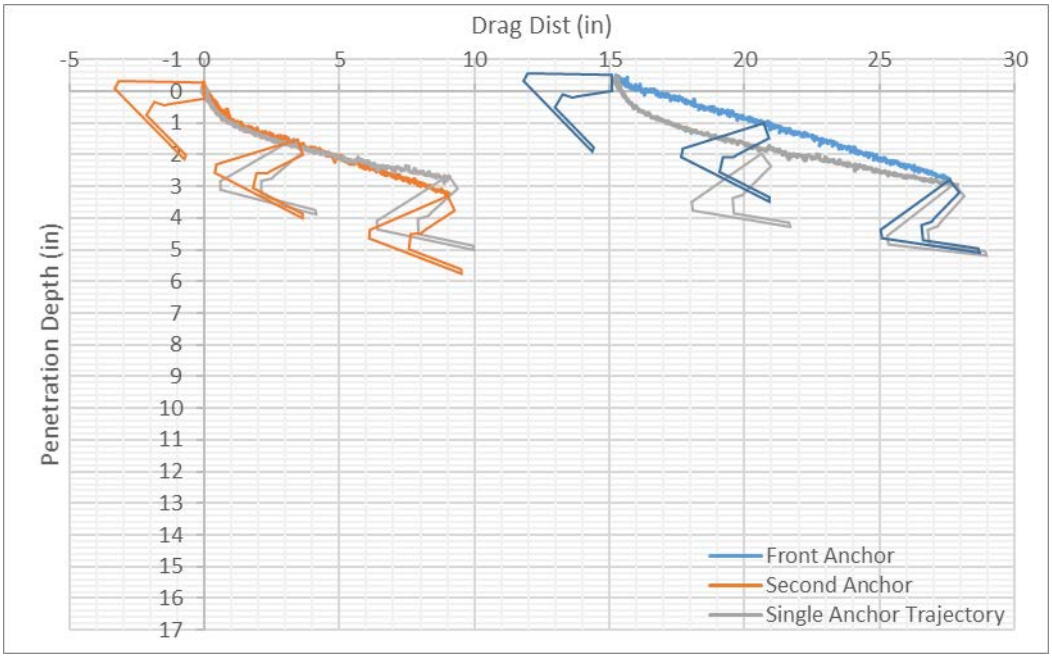

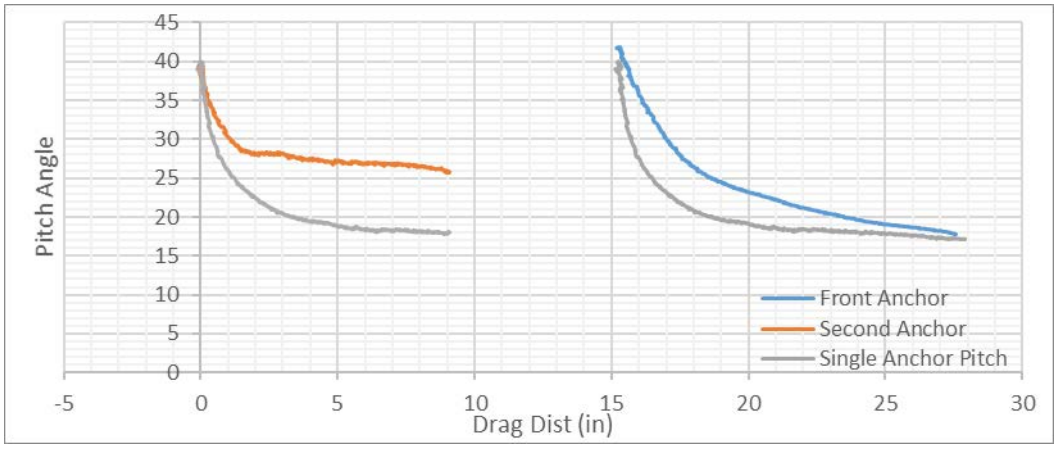

Third Repeat Test in Case 11

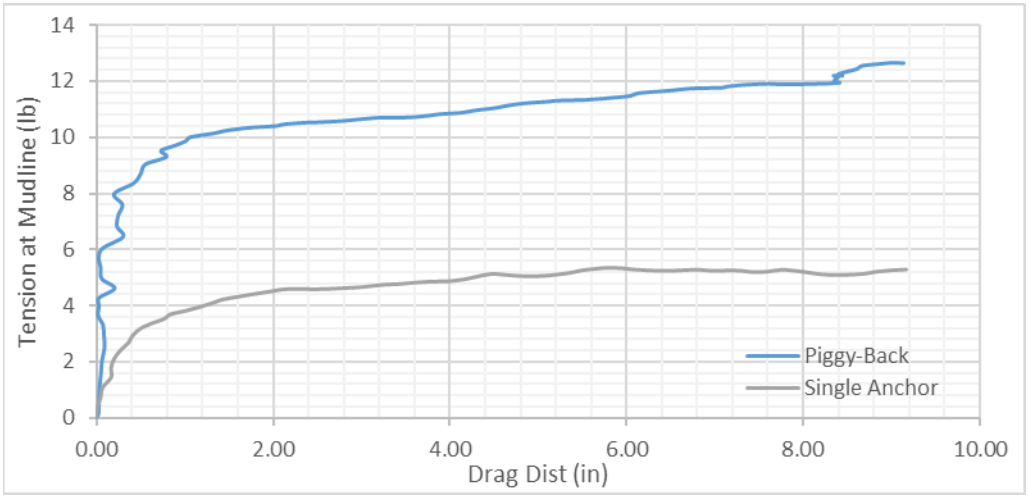

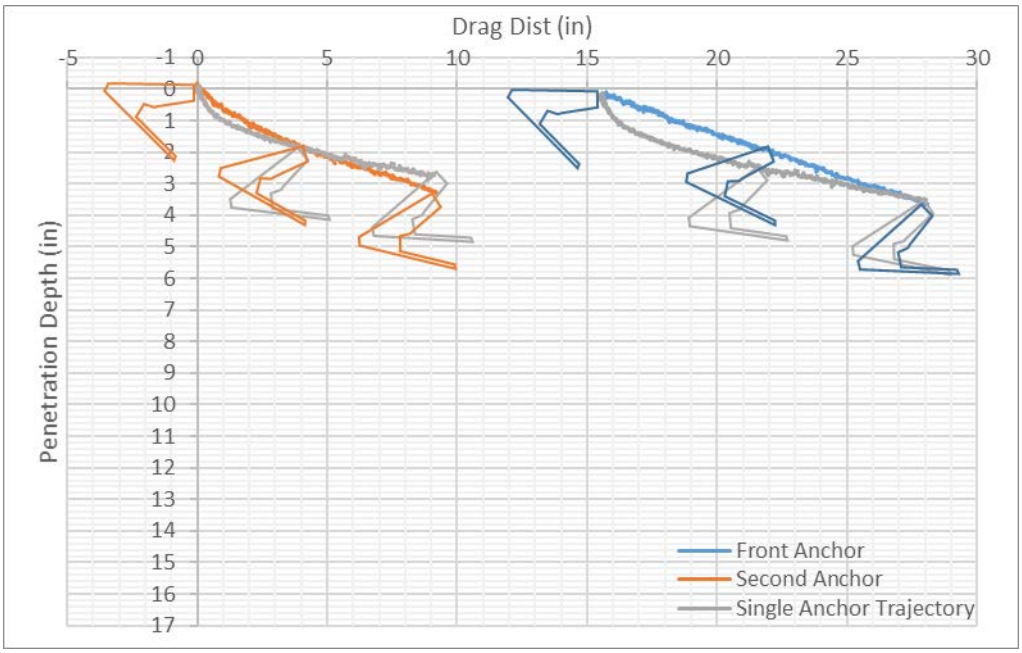

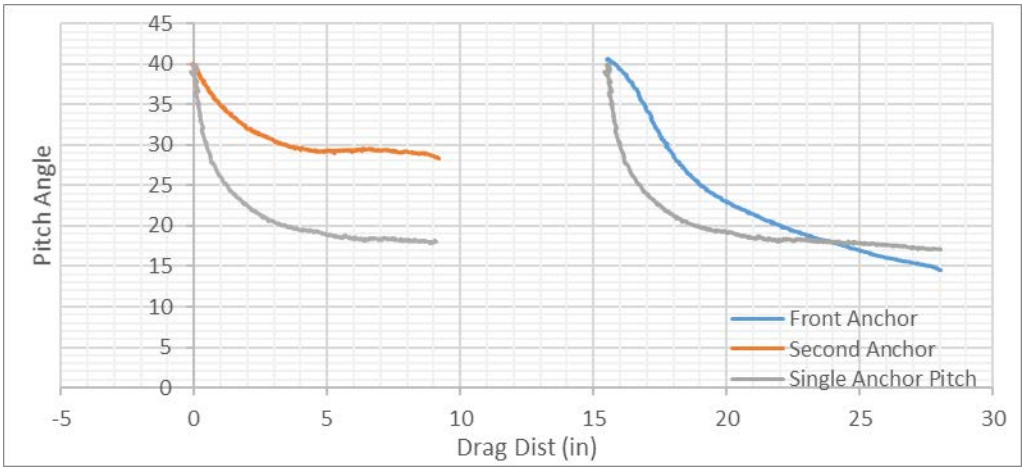

Case 12

Line Diameter (connecting two anchors)	0.19 inch
The 2nd anchor Attached to 1st Anchor's	Center of Back Fluke
Spacing between two anchors	19.53 inch (5.39 Fluke Length)

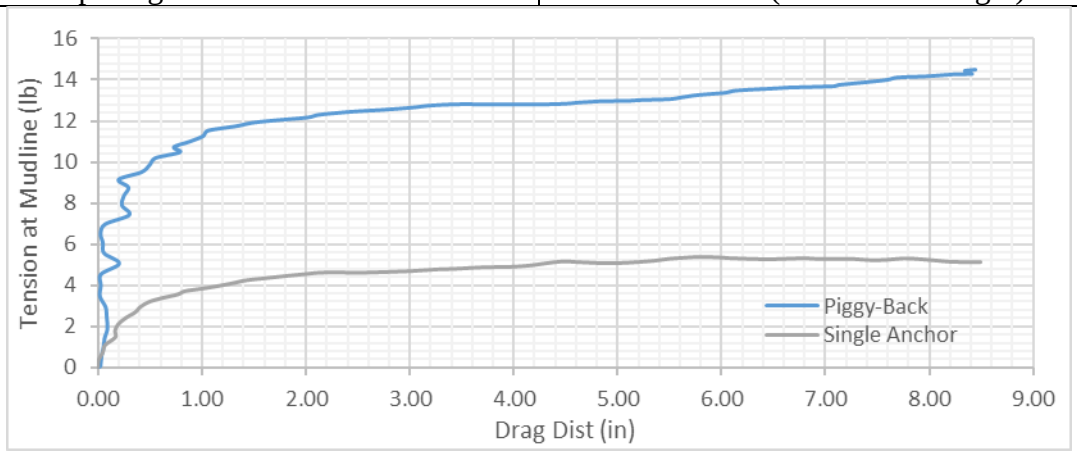

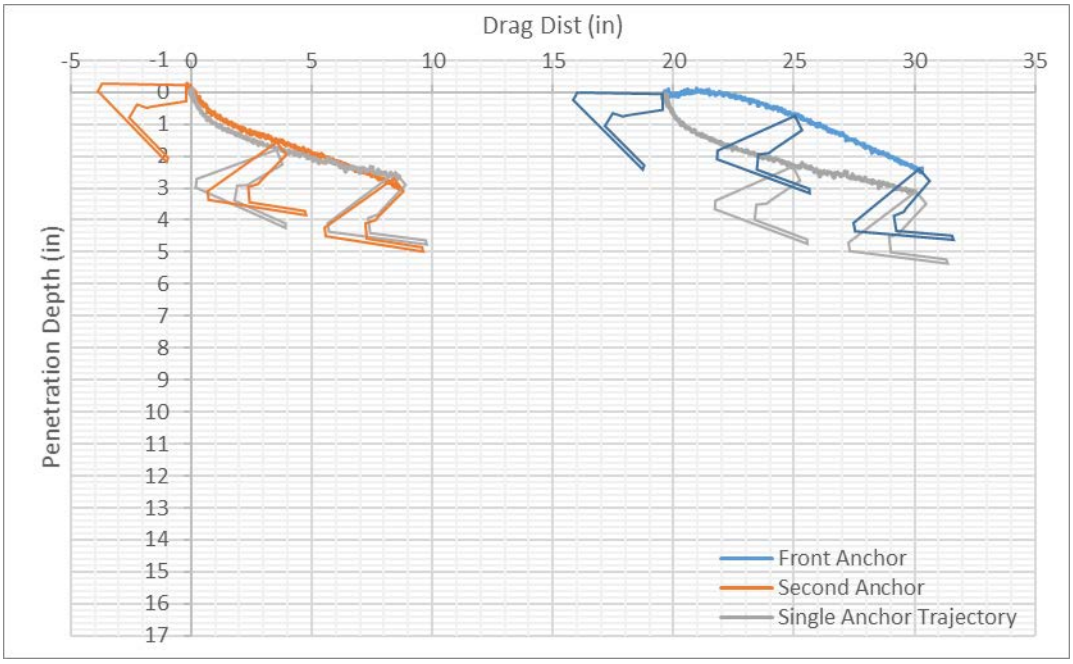

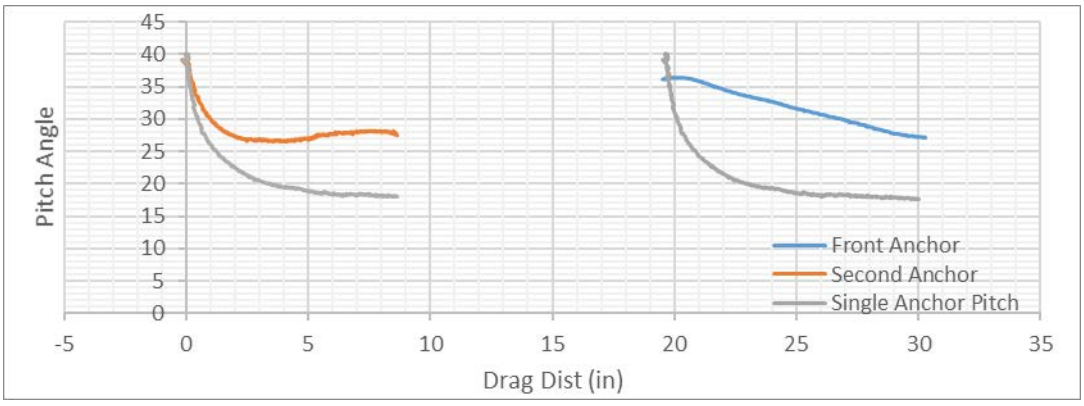

First Repeat test in Case 12

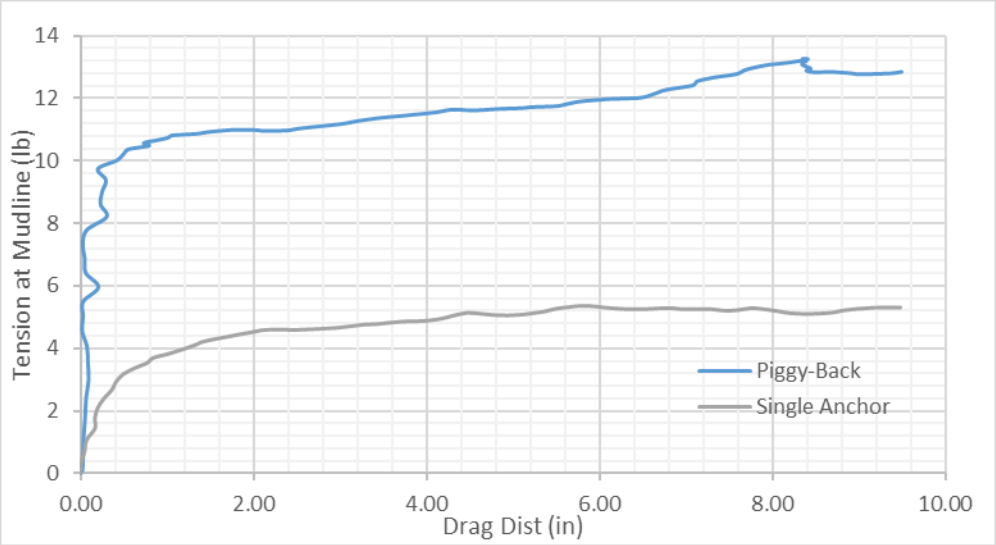

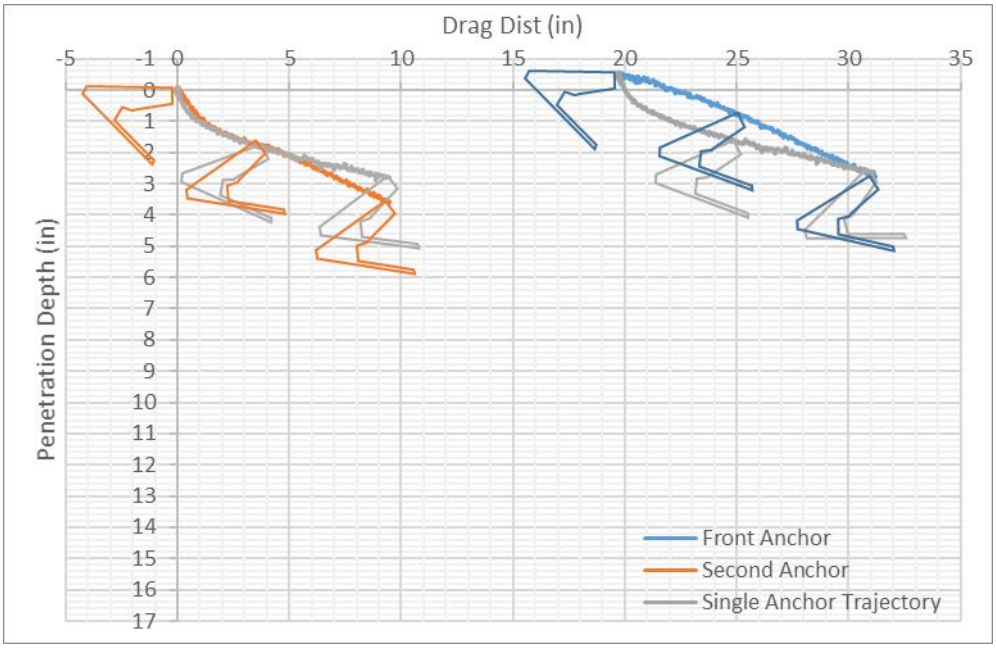

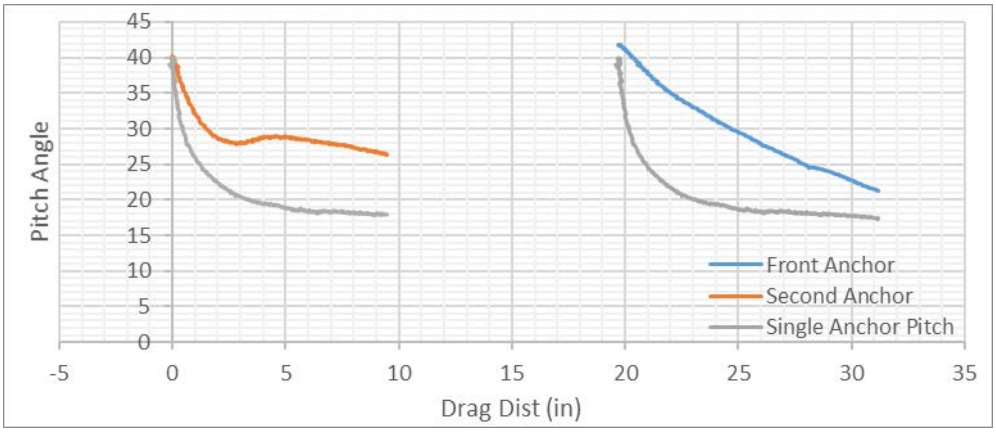

Second Repeat Test in Case 12

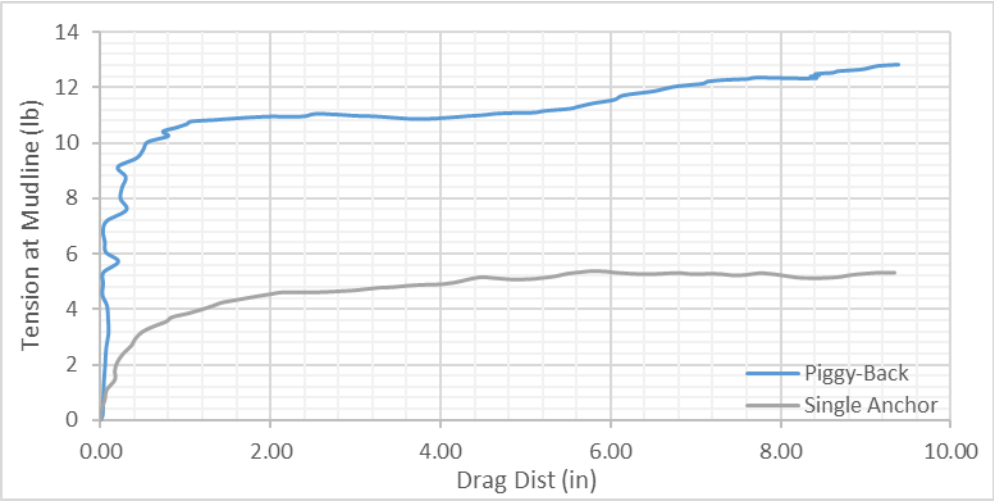

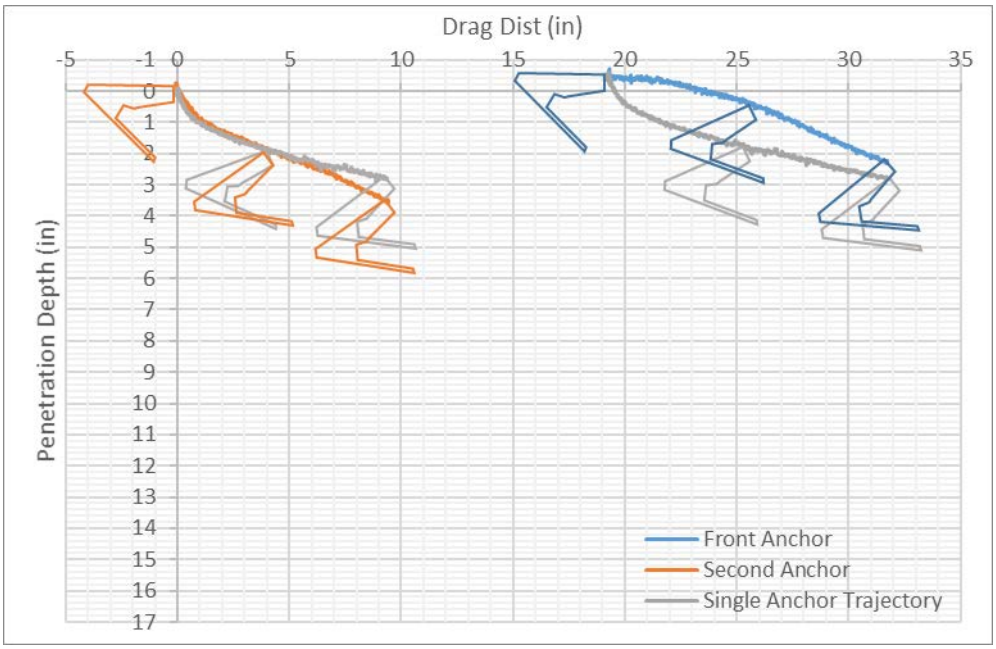

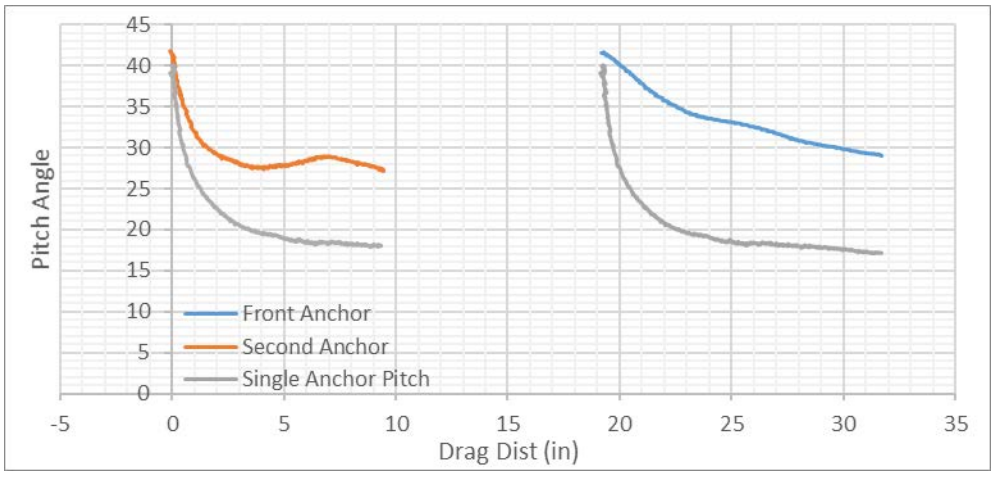

Case 13

Line Diameter (connecting two anchors)	0.05 inch
The 2nd anchor Attached to 1st Anchor's	Center of Back Fluke
Spacing between two anchors	15.23 inch (4.2 Fluke Length)

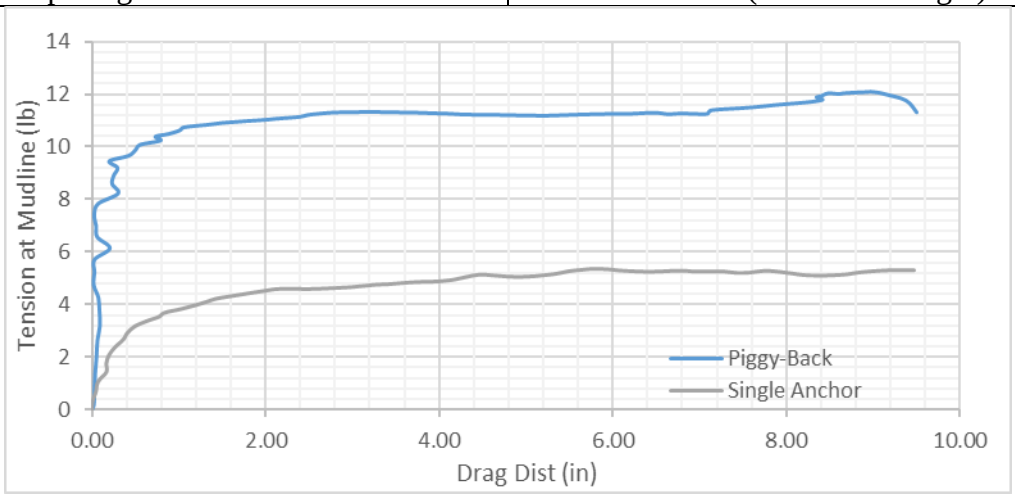

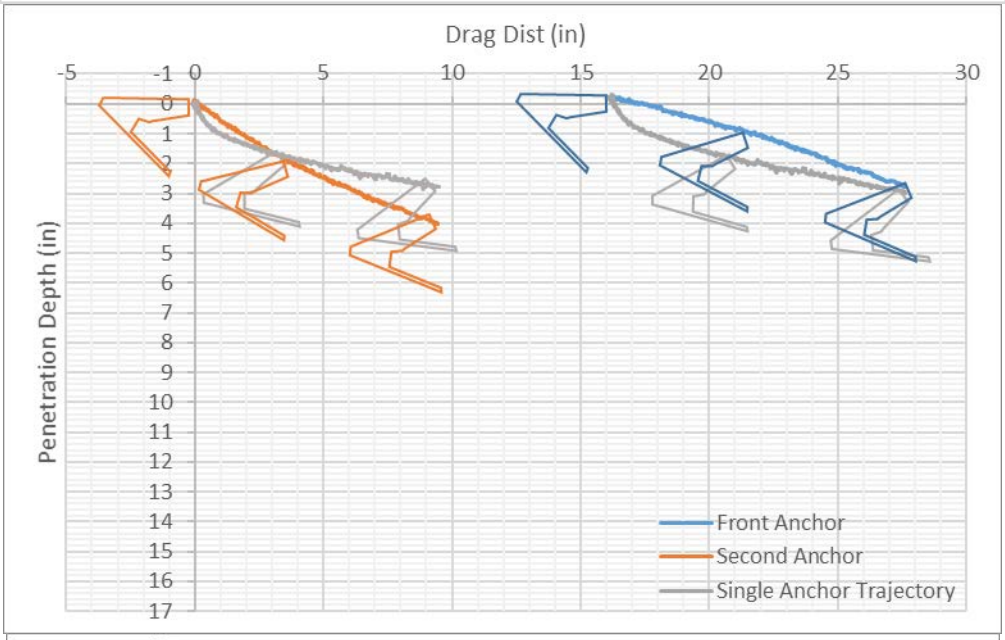

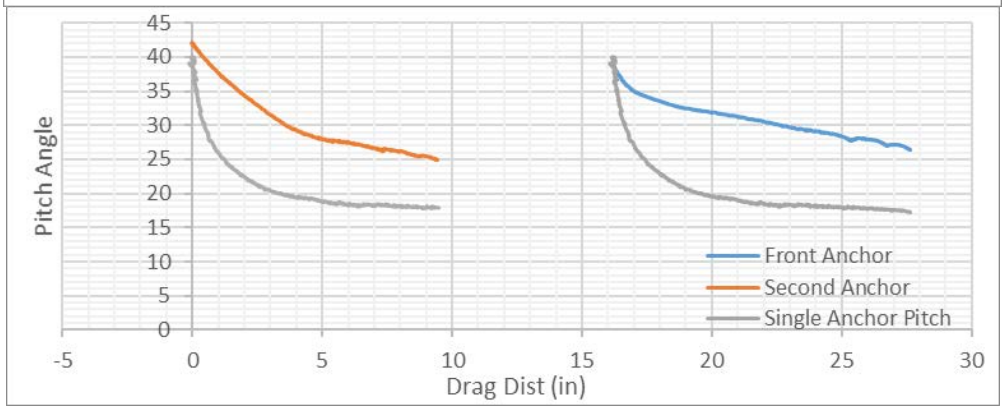

First Repeat test in Case 1

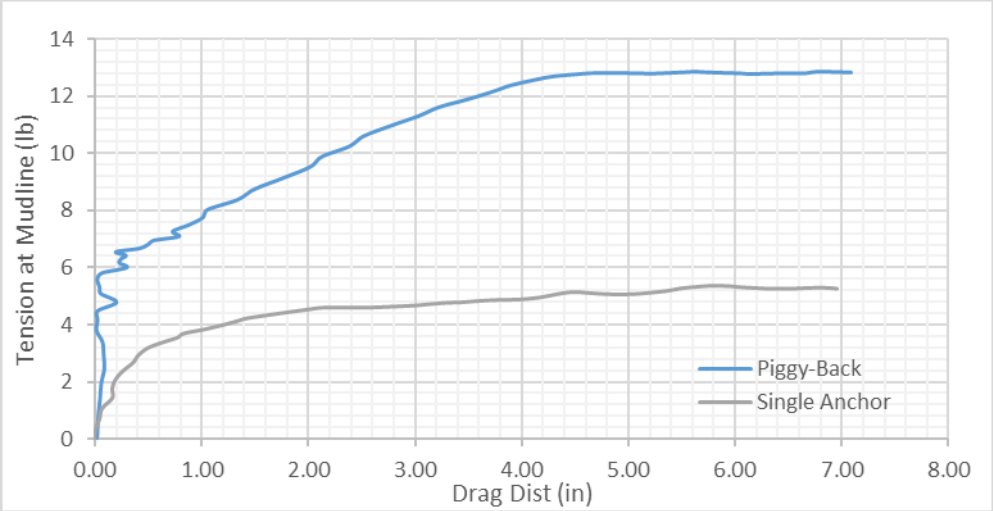

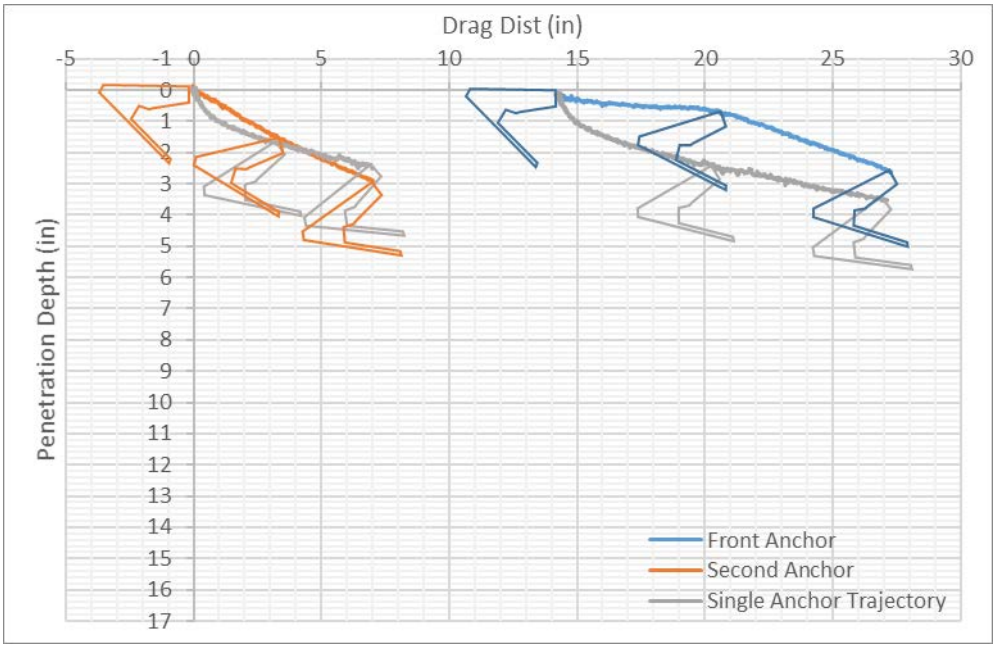

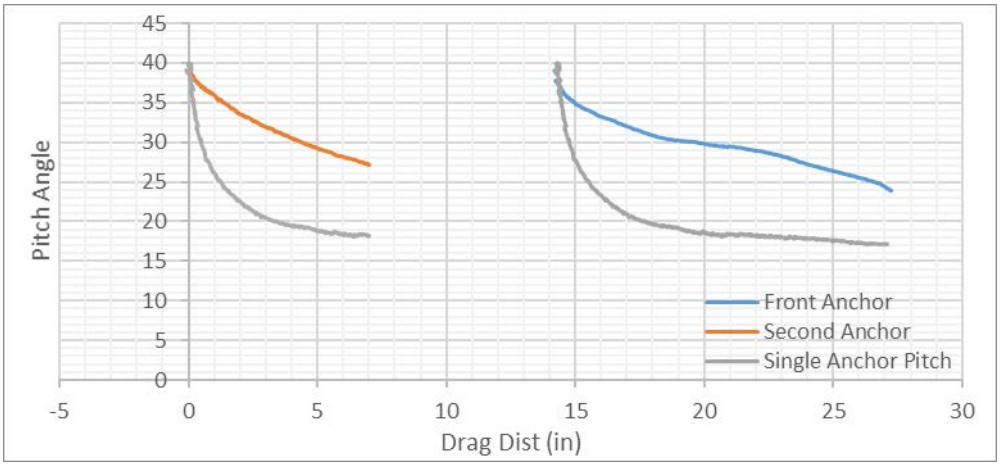

Case 14

Line Diameter (connecting two anchors)	0.05 inch
The 2nd anchor Attached to 1st Anchor's	Padeye
Spacing between two anchors	6.89 inch (1.9 Fluke Length)

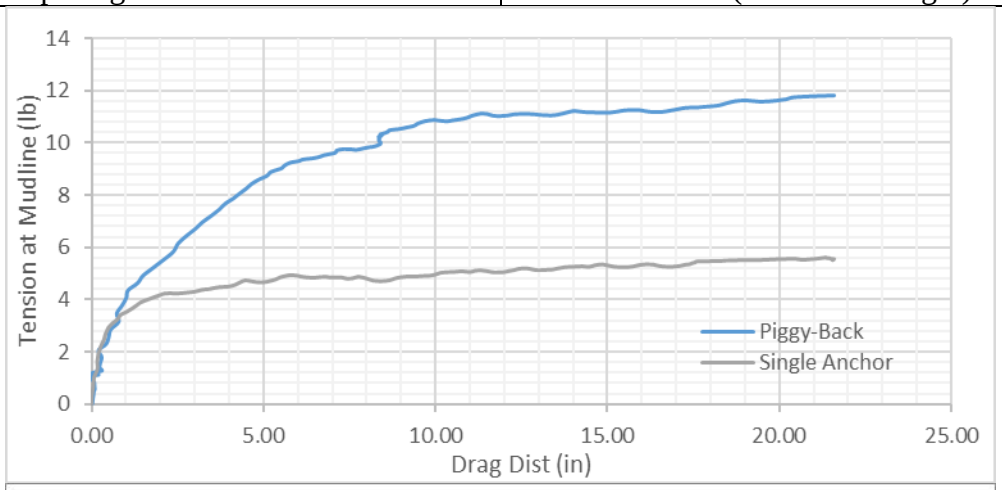

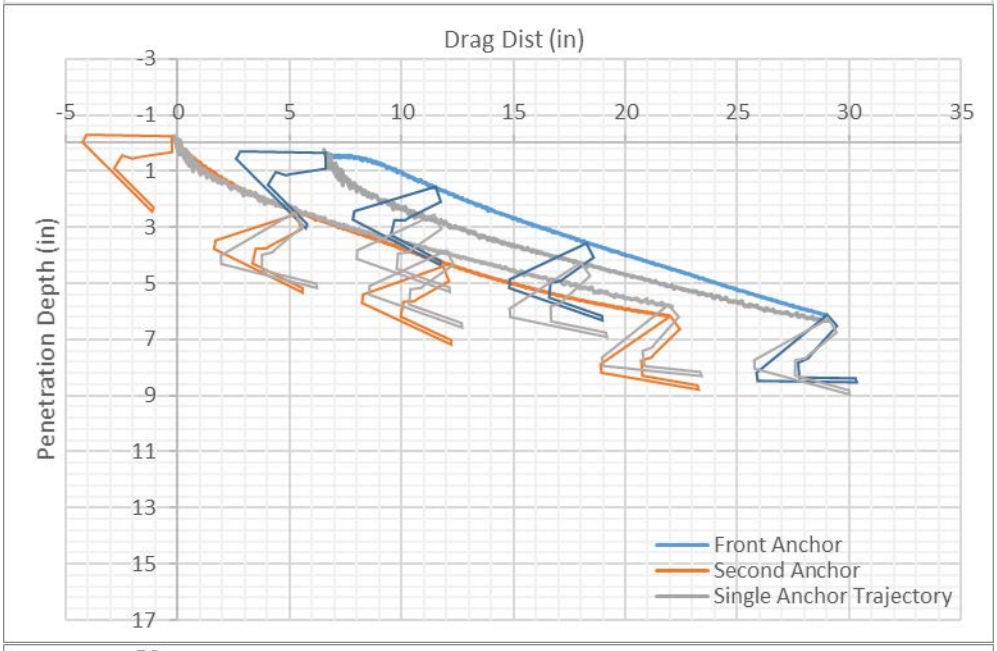

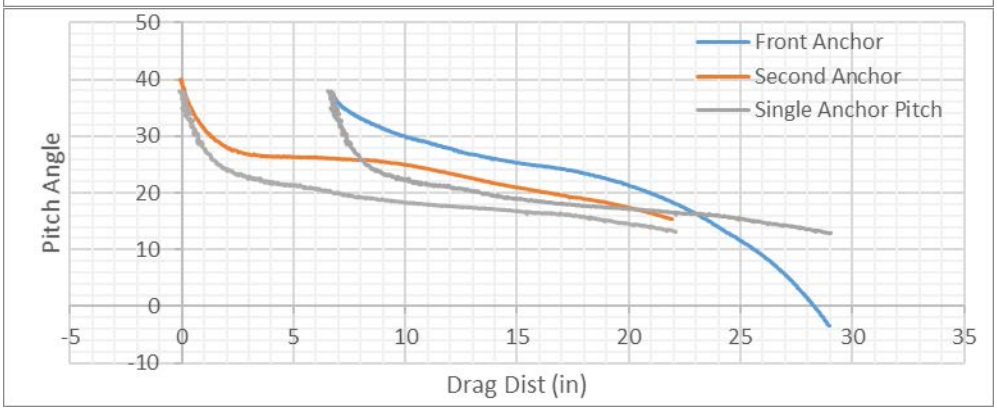

First Repeat Test in Case 14

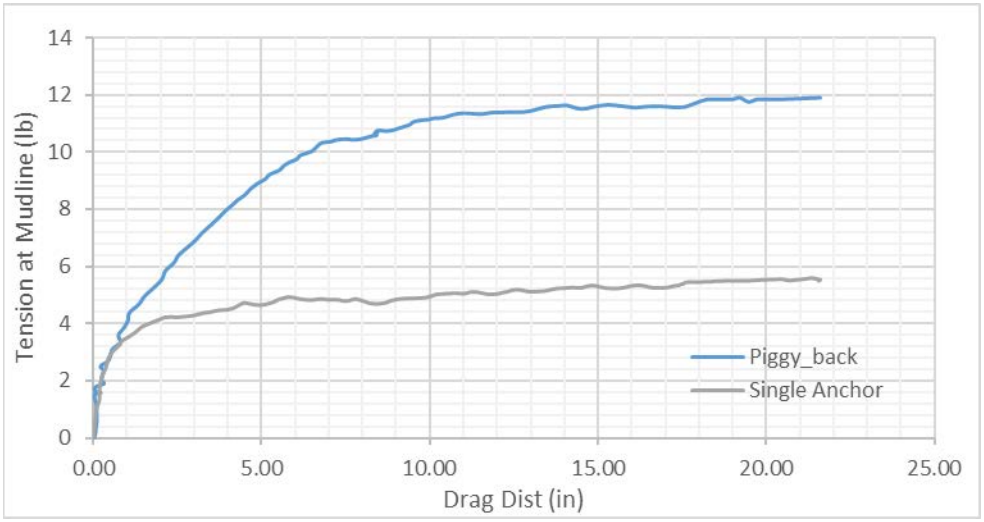

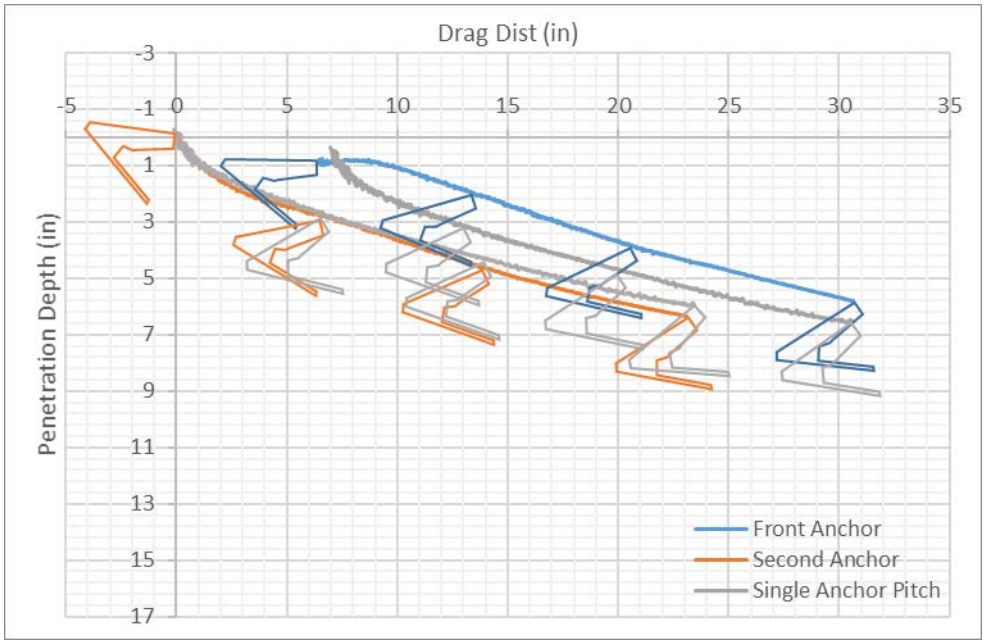

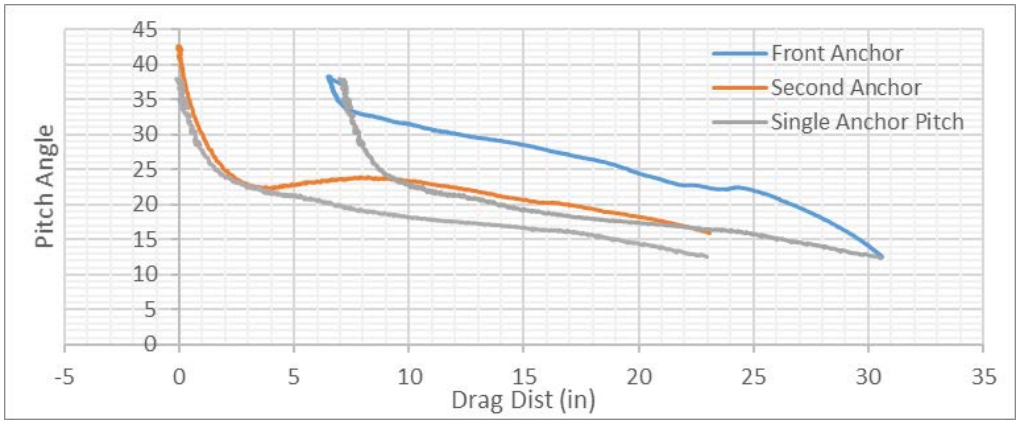

Second Repeat Test in Case 14

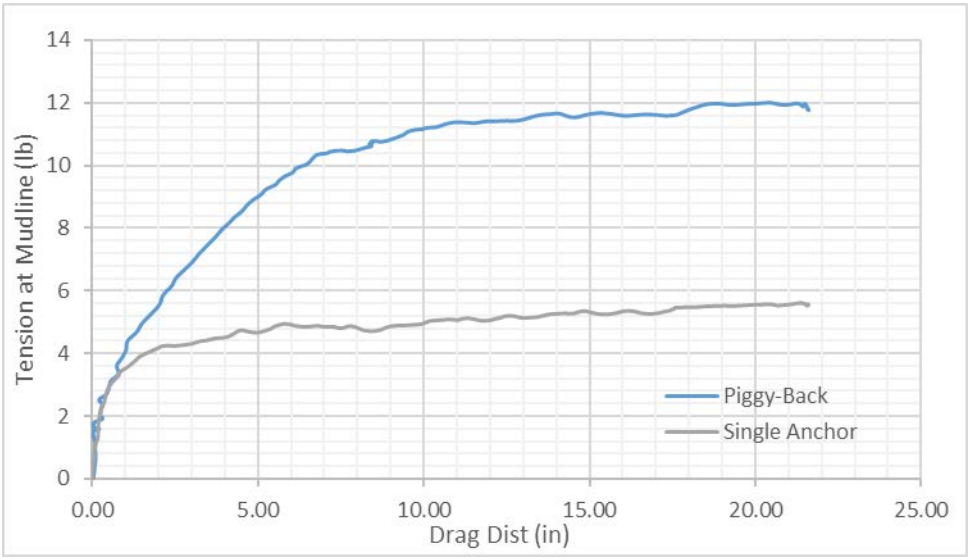

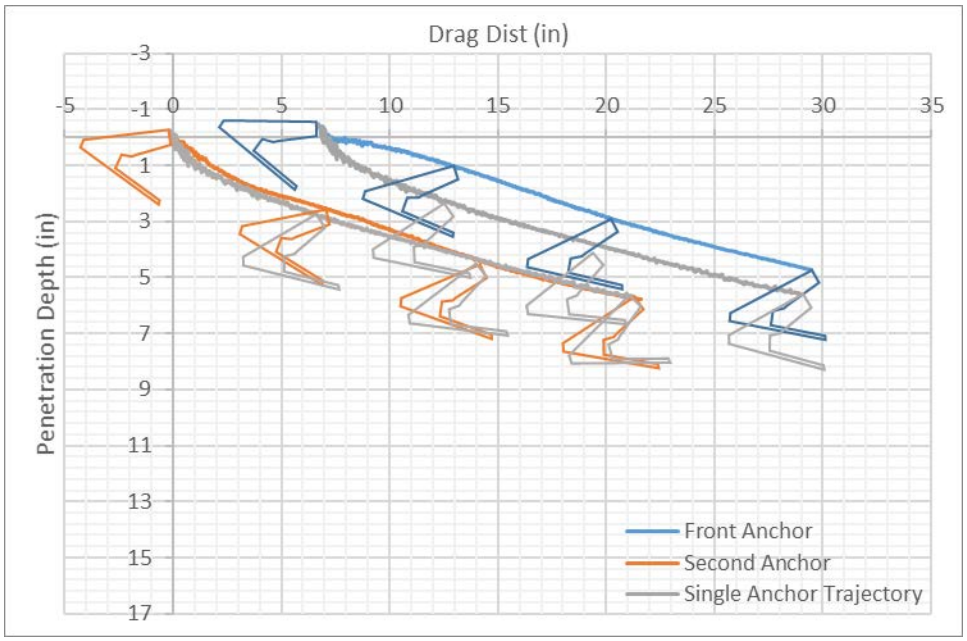

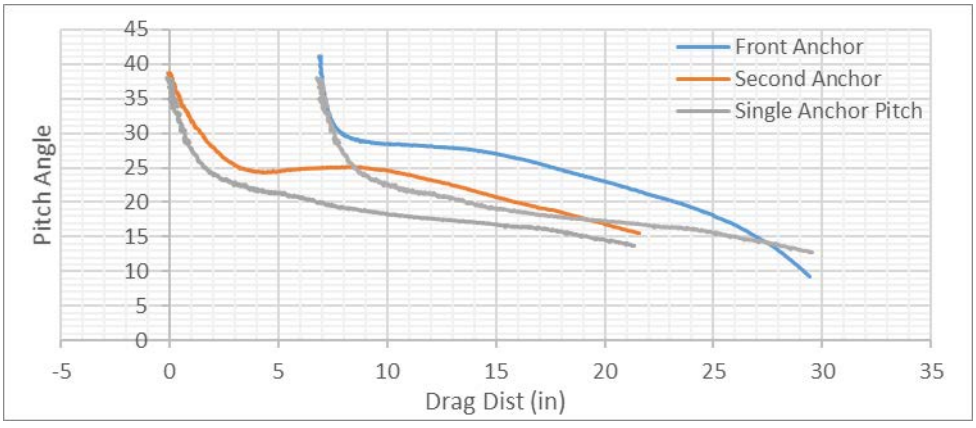

Case 15

Line Diameter (connecting two anchors)	0.19 inch
The 2nd anchor Attached to 1st Anchor's	Padeye
Spacing between two anchors	13.70 inch (3.78 Fluke Length)

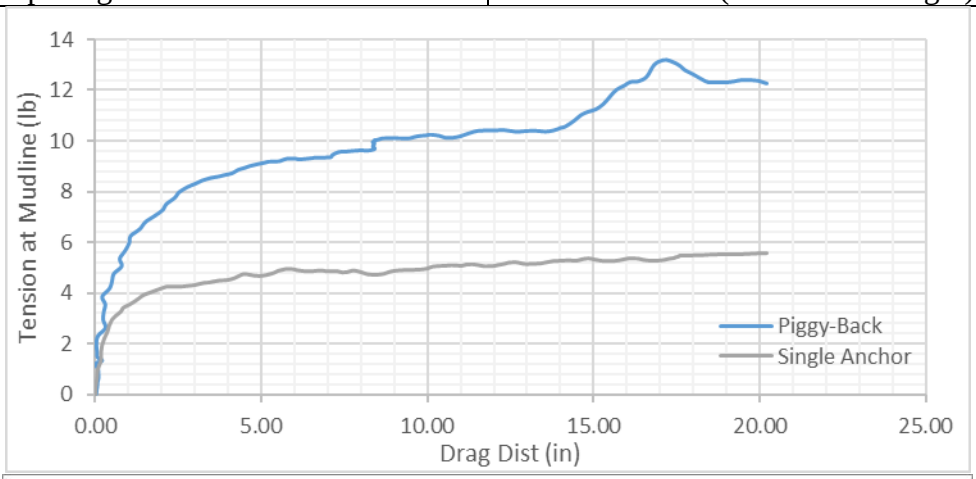

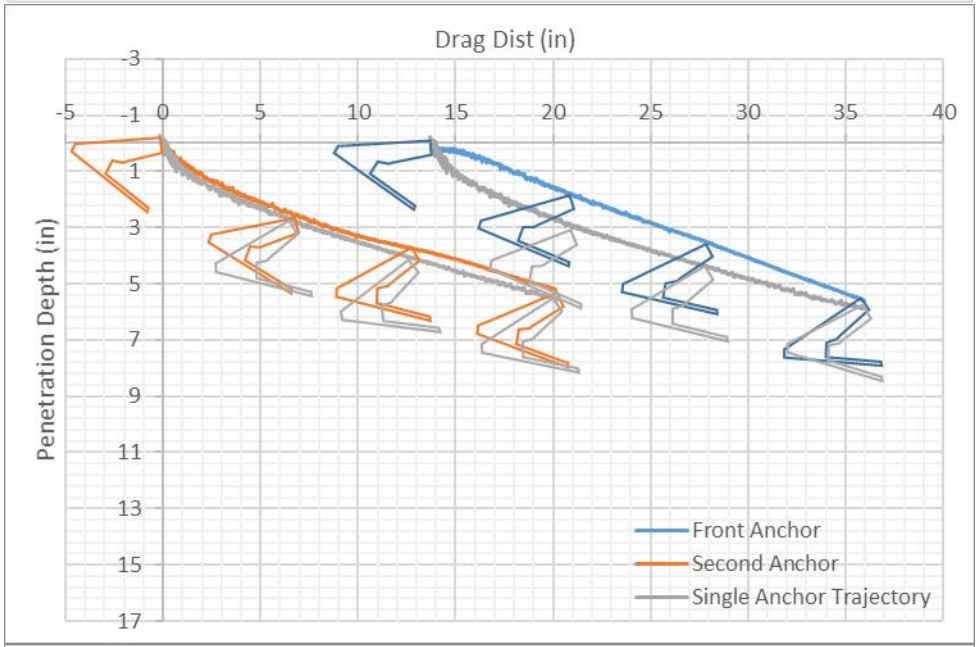

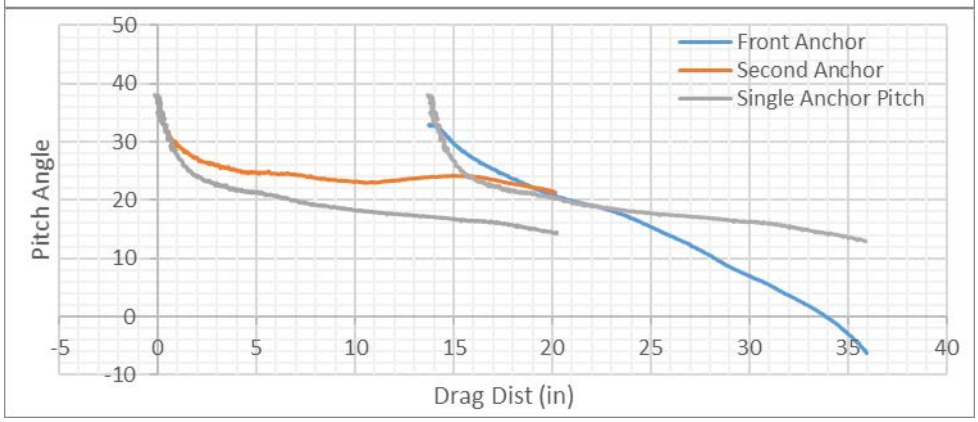

First Repeat Test in Case 15

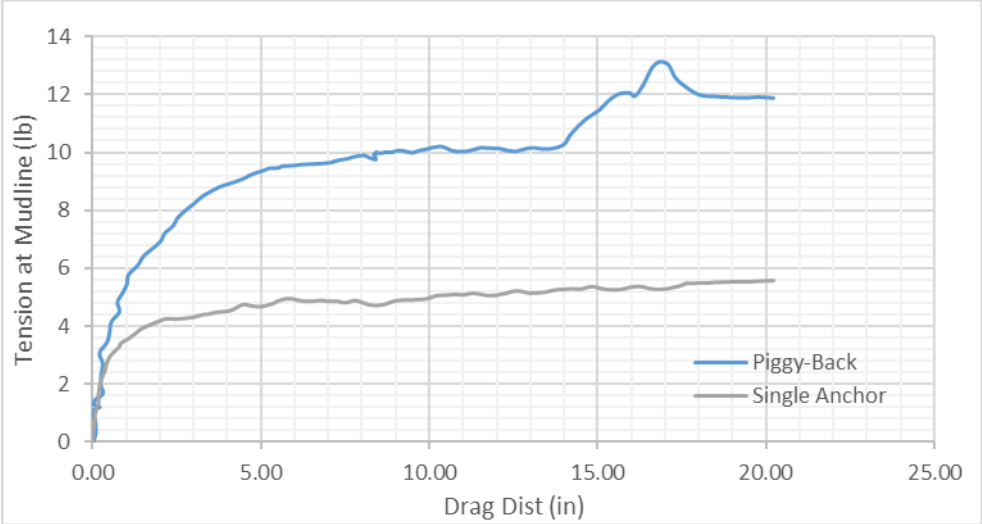

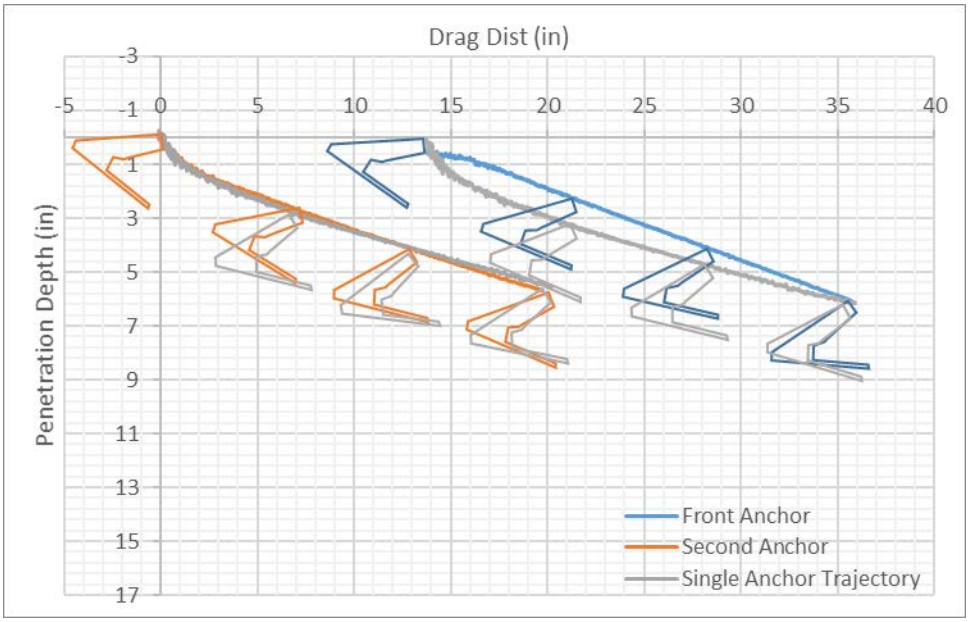

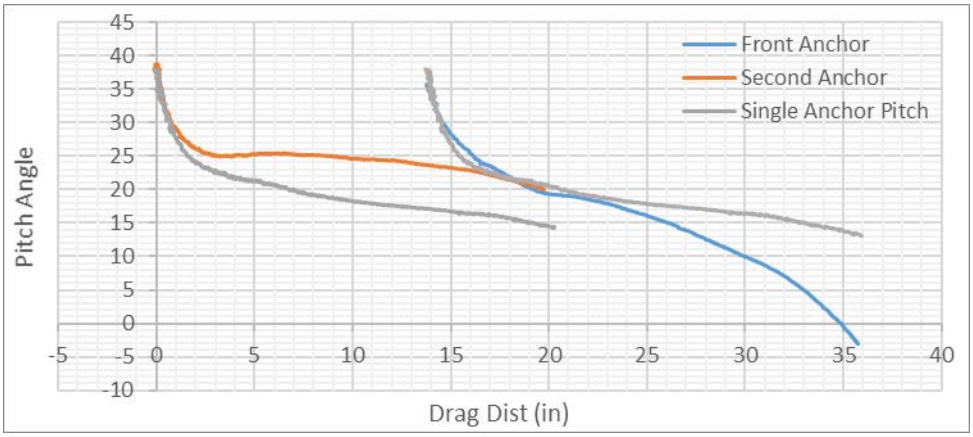

Second Repeat Test in Case 15

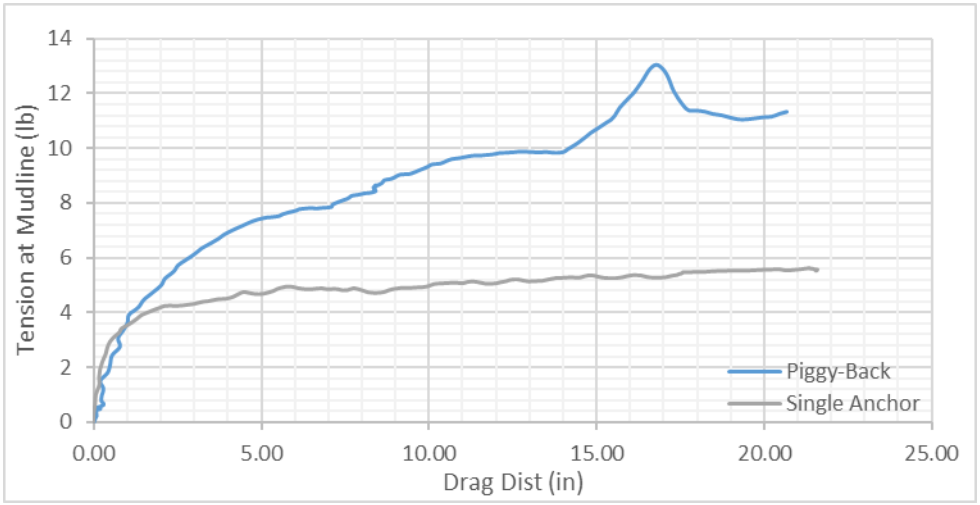

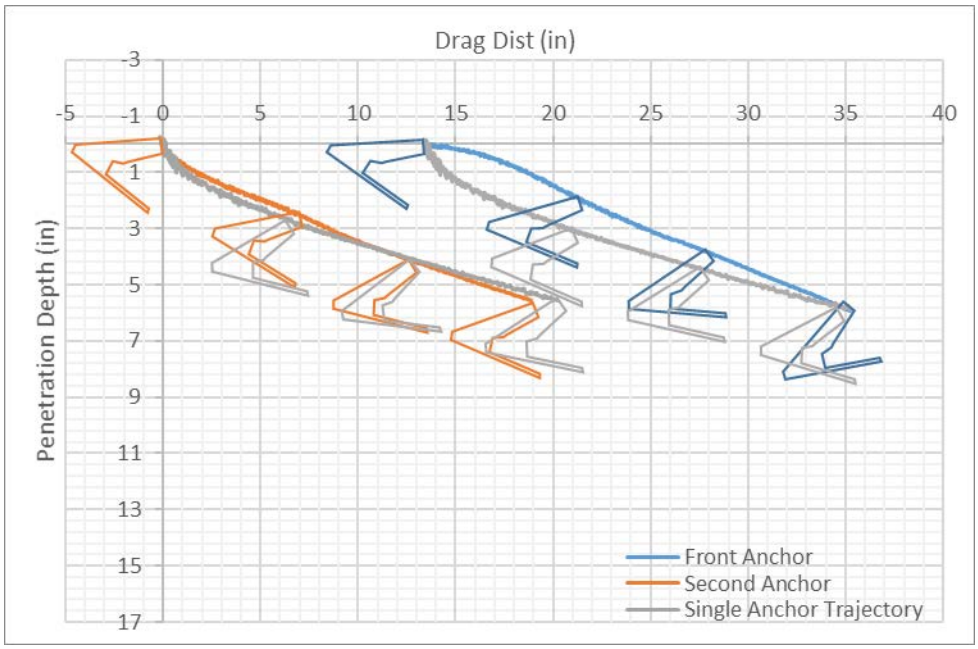

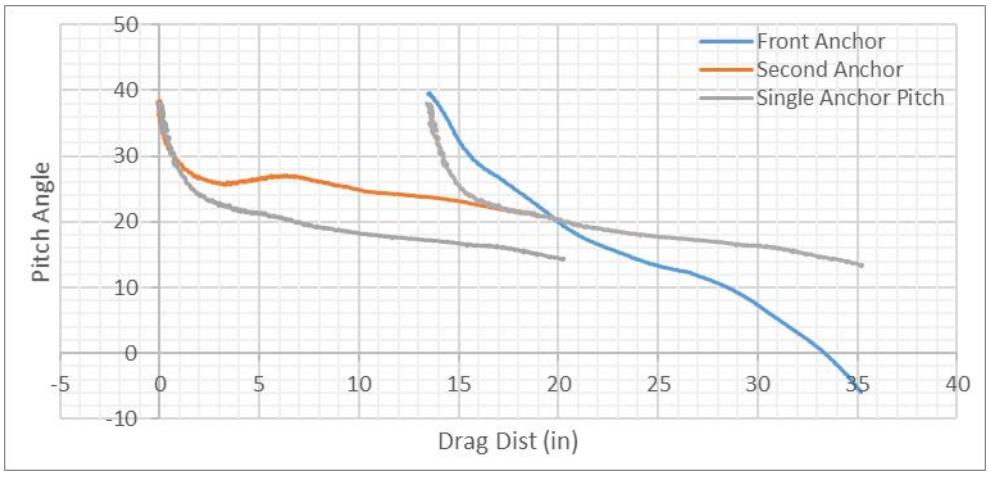

Case 16

Line Diameter (connecting two anchors)	0.19 inch
The 2nd anchor Attached to 1st Anchor's	Padeye
Spacing between two anchors	17.93 inch (4.95 Fluke Length)

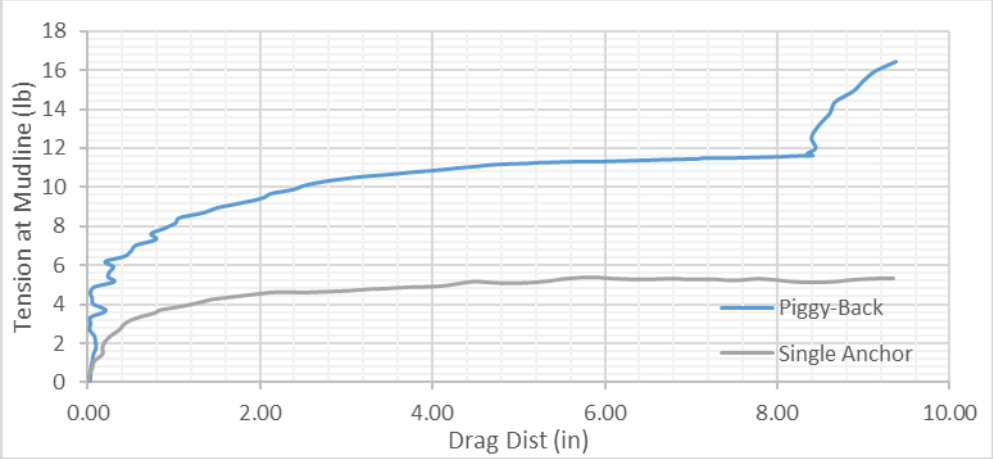

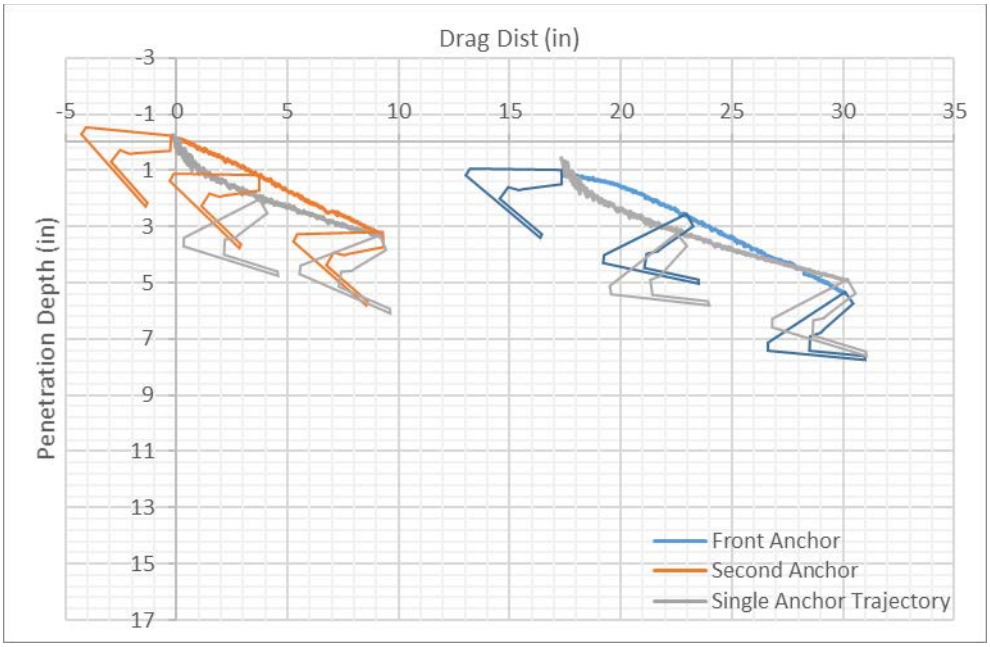

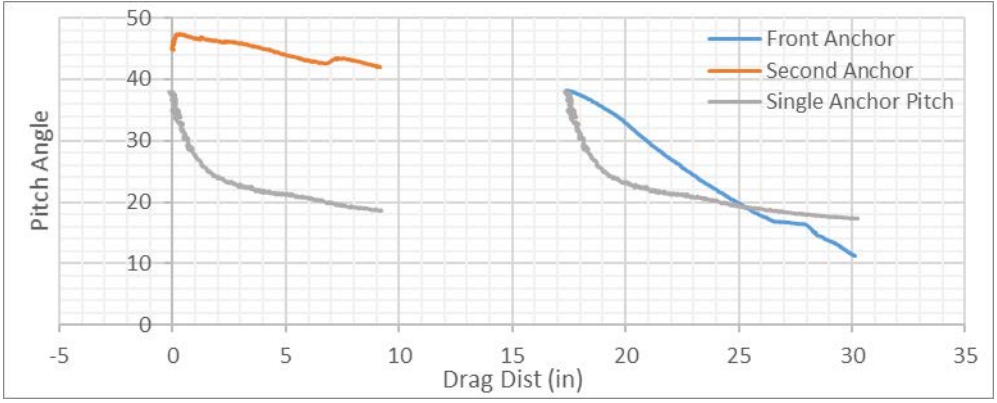

First Repeat Test in Case 16

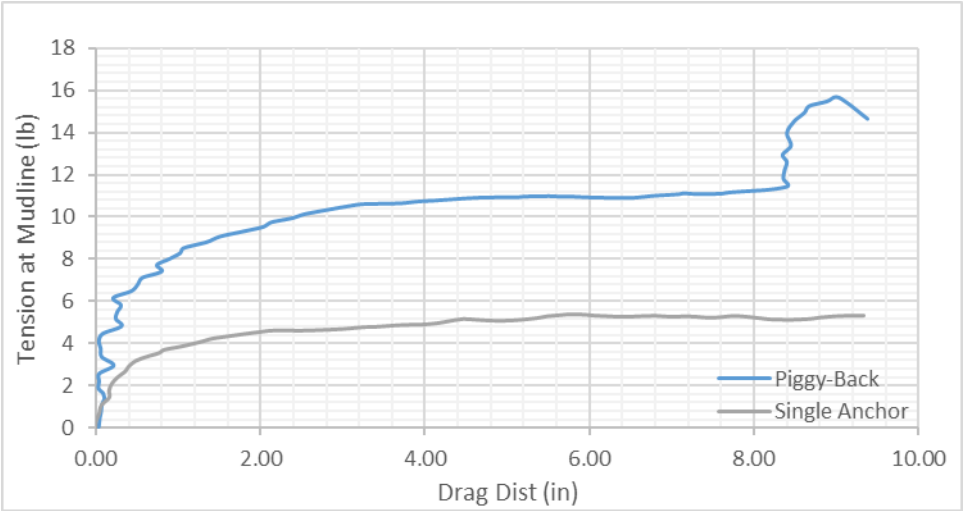

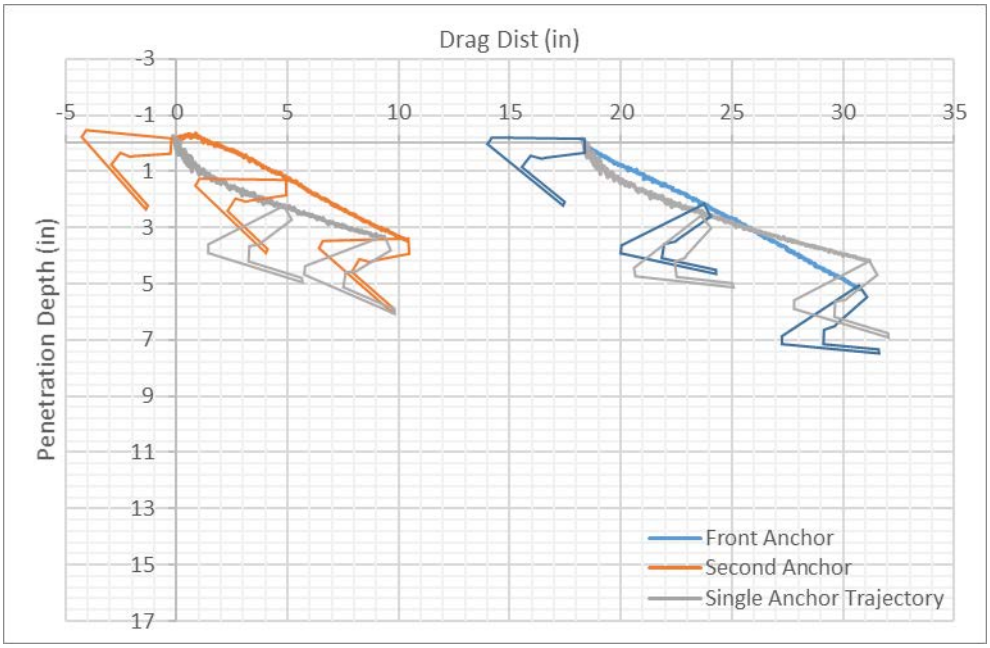

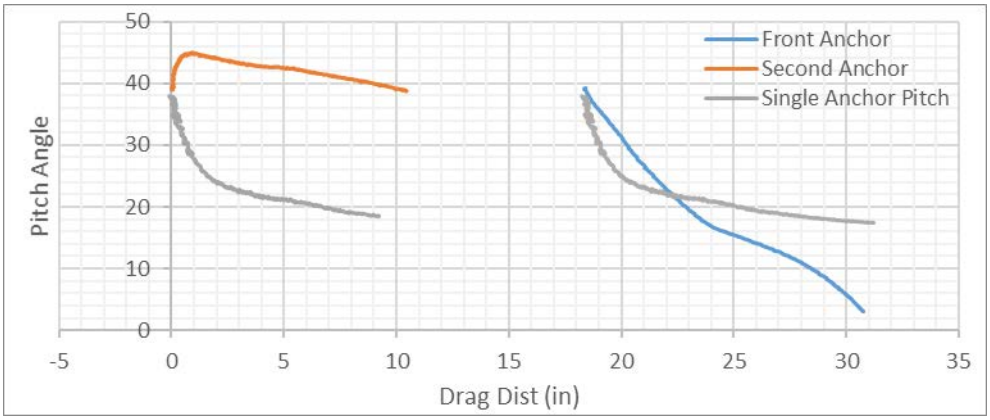

Second Repeat Test in Case 16

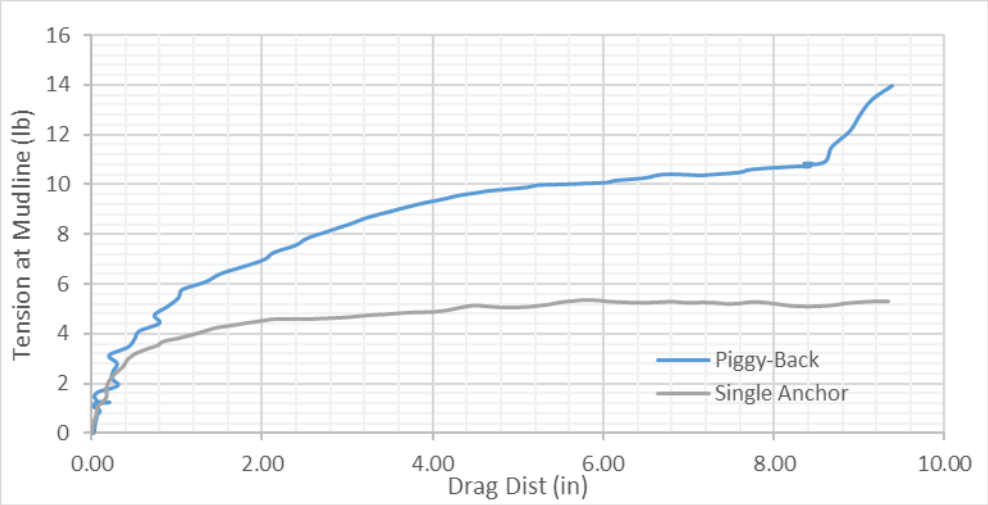
Tension at Mudline (lb)
16
14
12
10
8
6
4
2
0
0.00
2.00
4.00
6.00
8.00
10.00
Drag Dist (in)
Piggy-Back
Single Anchor

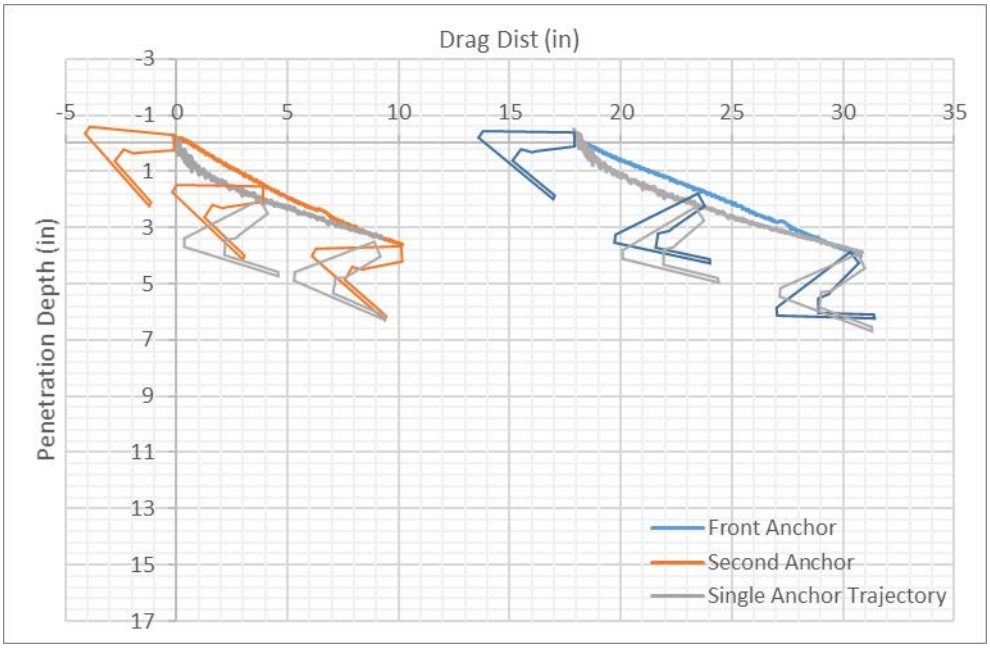
Drag Dist (in)
-5
-3
-1
0
1
3
5
7
9
11
13
15
17
5
10
15
20
25
30
35
Penetration Depth (in)
Front Anchor
Second Anchor
Single Anchor Trajectory

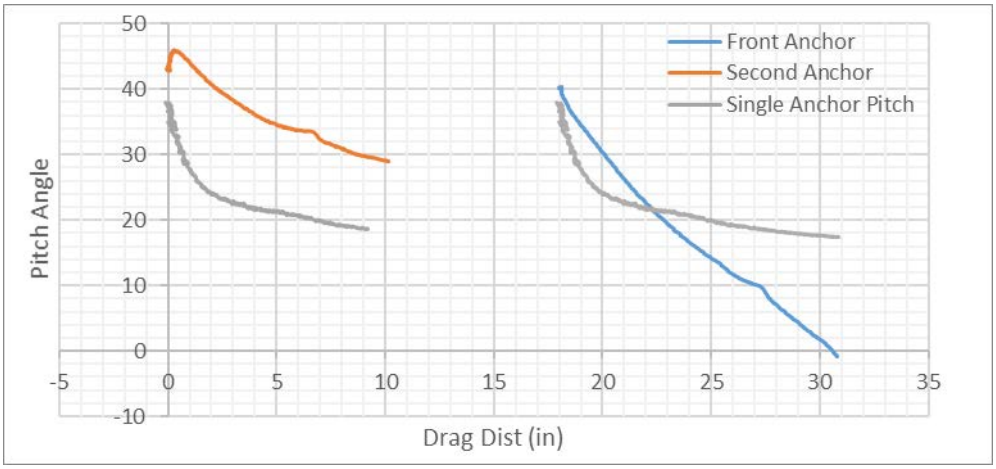
50
40
30
20
10
0
-10
-5
0
5
10
15
20
25
30
35
Pitch Angle
Drag Dist (in)
Front Anchor
Second Anchor
Single Anchor Pitch

Appendix E. Comparison between Analytical and Experimental Results of Tandem System Anchor

Case 2

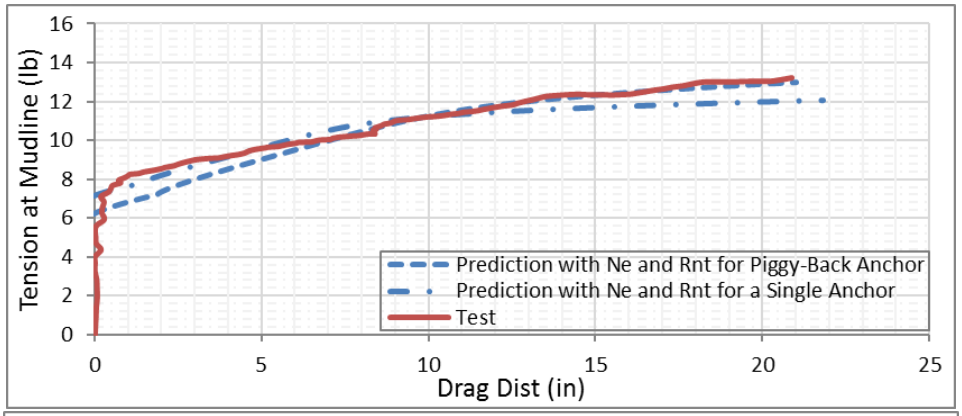

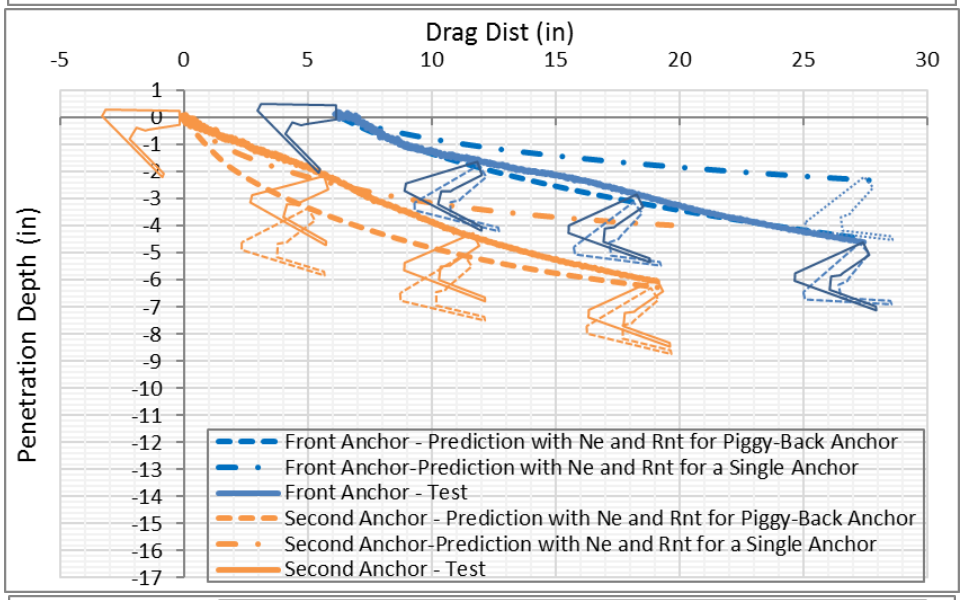

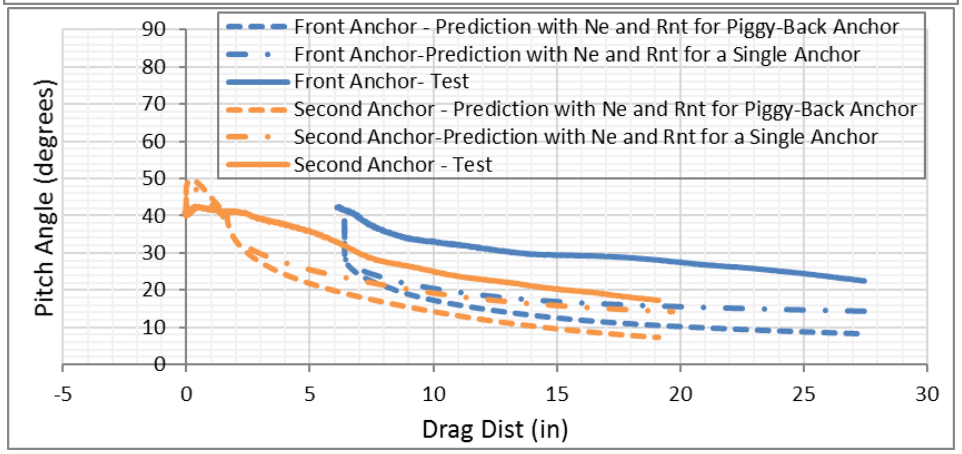

First Repeat Test in Case 2

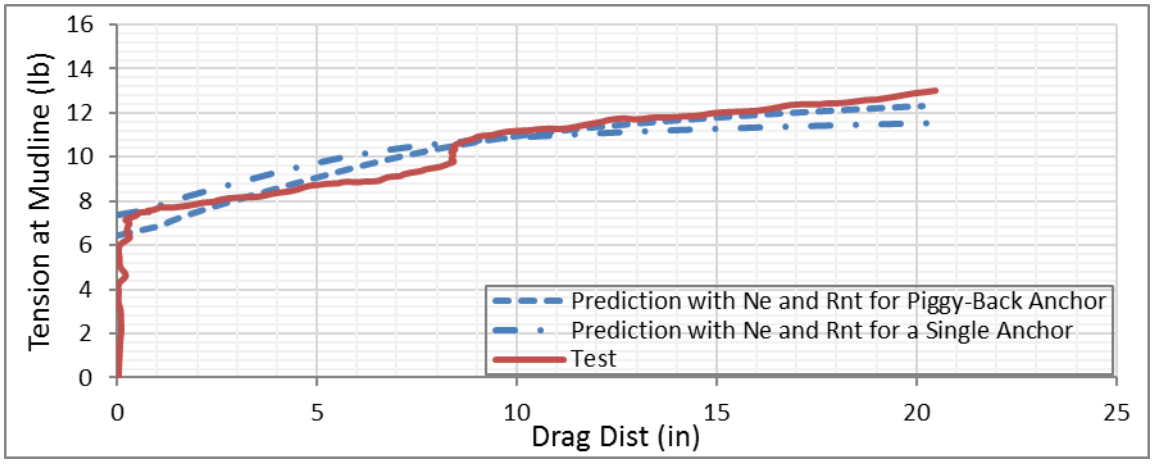

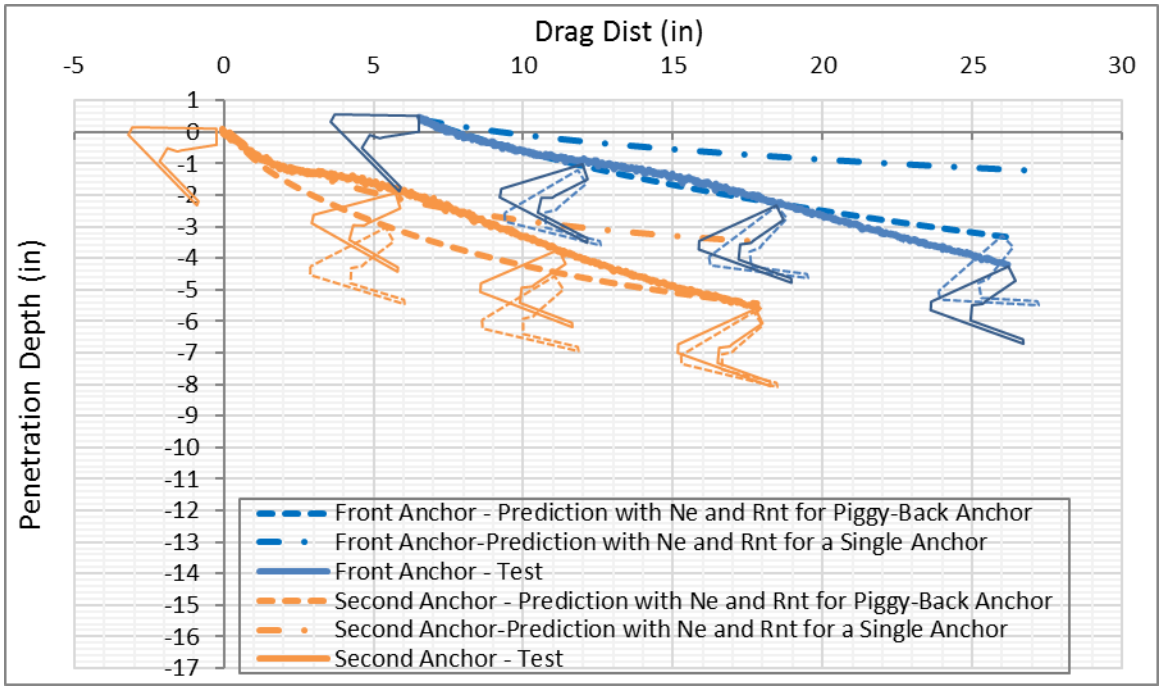

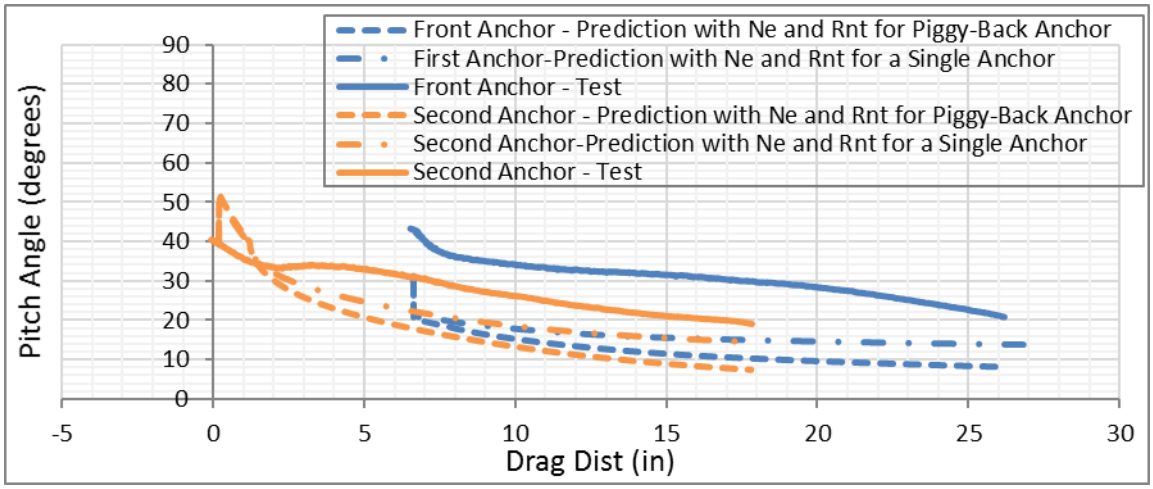

Case 5

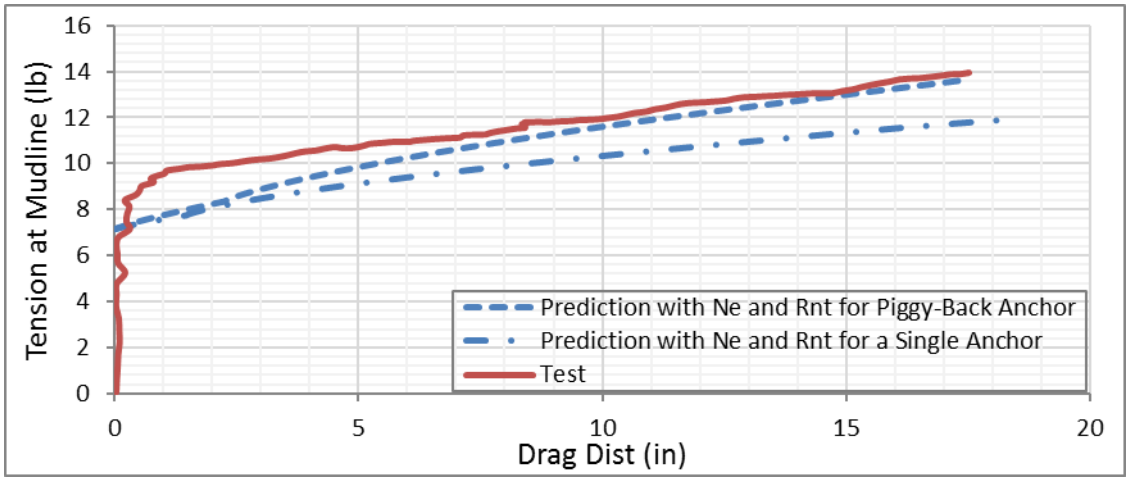
Tension at Mudline (lb)
Drag Dist (in)
Prediction with Ne and Rnt for Piggy-Back Anchor
Prediction with Ne and Rnt for a Single Anchor
Test

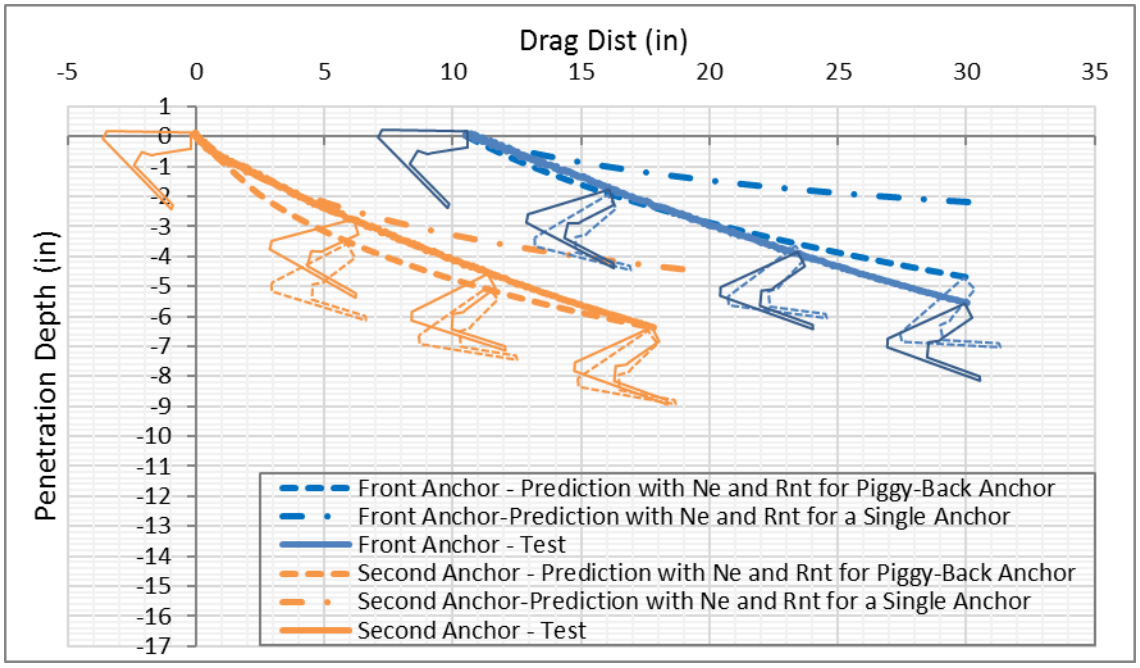
Drag Dist (in)
Penetration Depth (in)
Front Anchor - Prediction with Ne and Rnt for Piggy-Back Anchor
Front Anchor-Prediction with Ne and Rnt for a Single Anchor
Front Anchor - Test
Second Anchor - Prediction with Ne and Rnt for Piggy-Back Anchor
Second Anchor-Prediction with Ne and Rnt for a Single Anchor
Second Anchor - Test

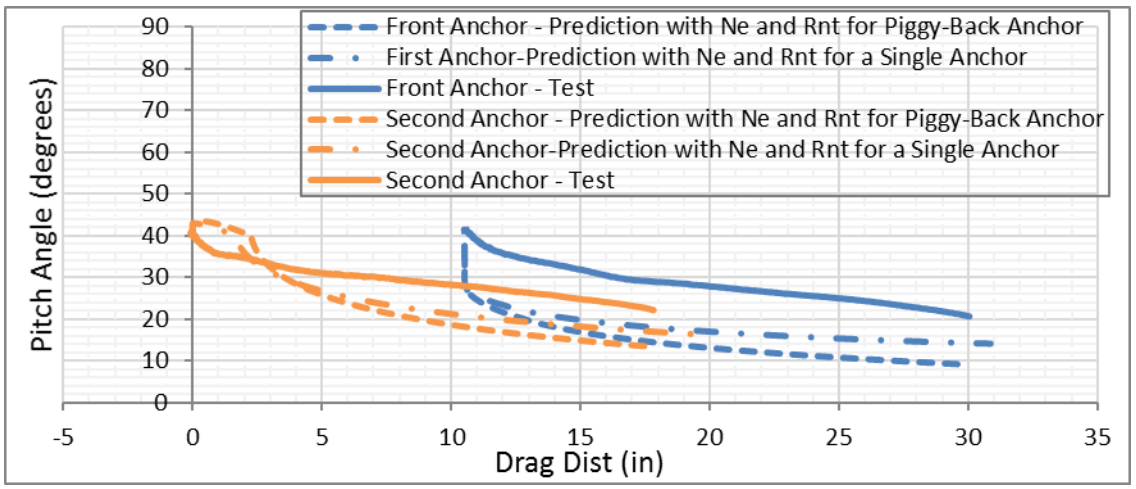
Pitch Angle (degrees)
Drag Dist (in)
Front Anchor - Prediction with Ne and Rnt for Piggy-Back Anchor
First Anchor-Prediction with Ne and Rnt for a Single Anchor
Front Anchor - Test
Second Anchor - Prediction with Ne and Rnt for Piggy-Back Anchor
Second Anchor-Prediction with Ne and Rnt for a Single Anchor
Second Anchor - Test

First Repeat Test in Case 5

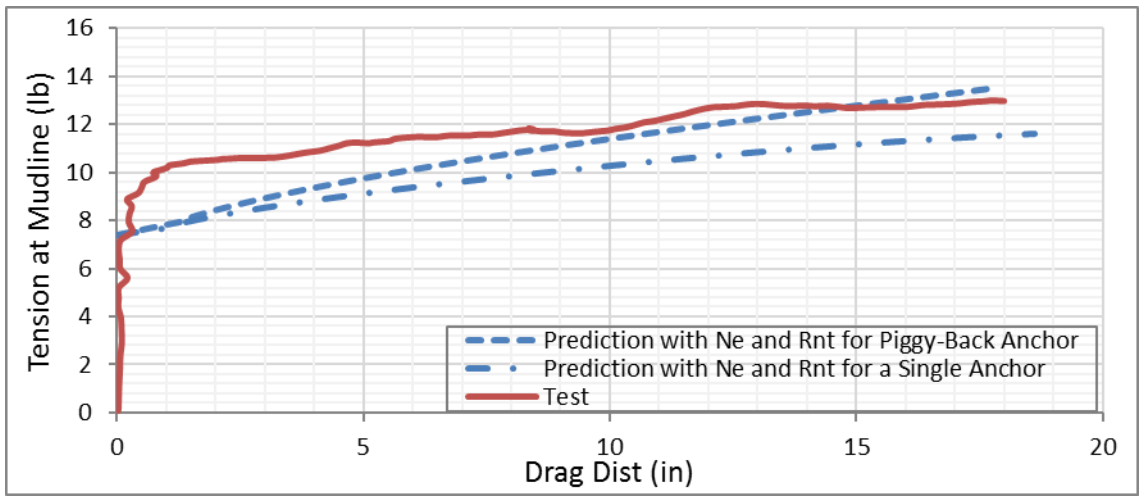

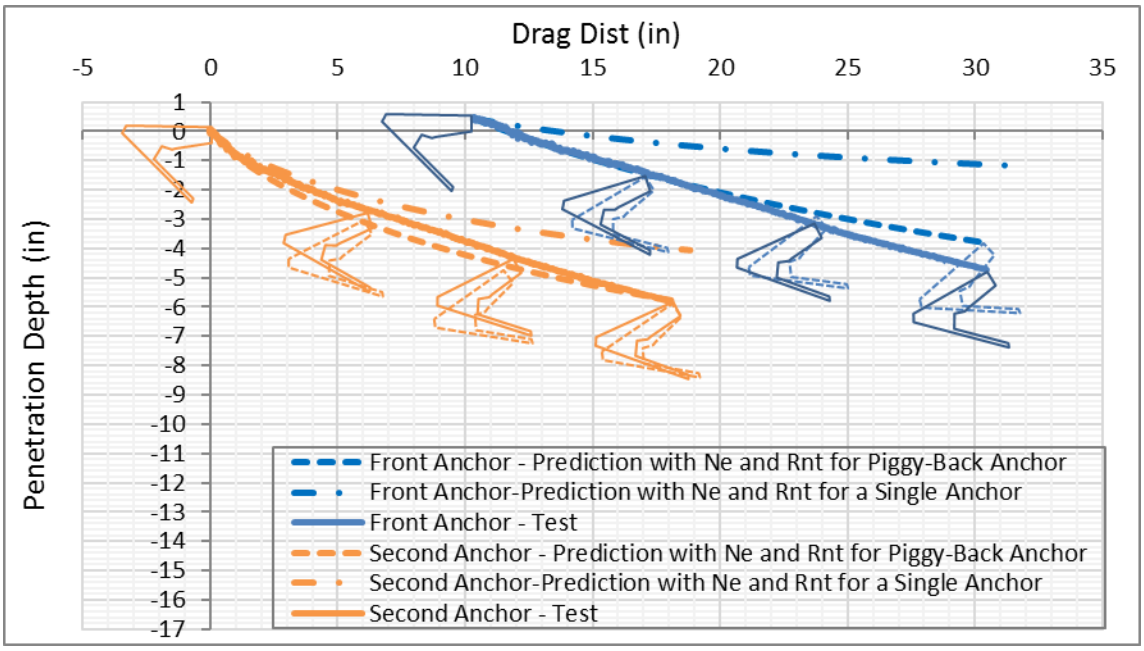

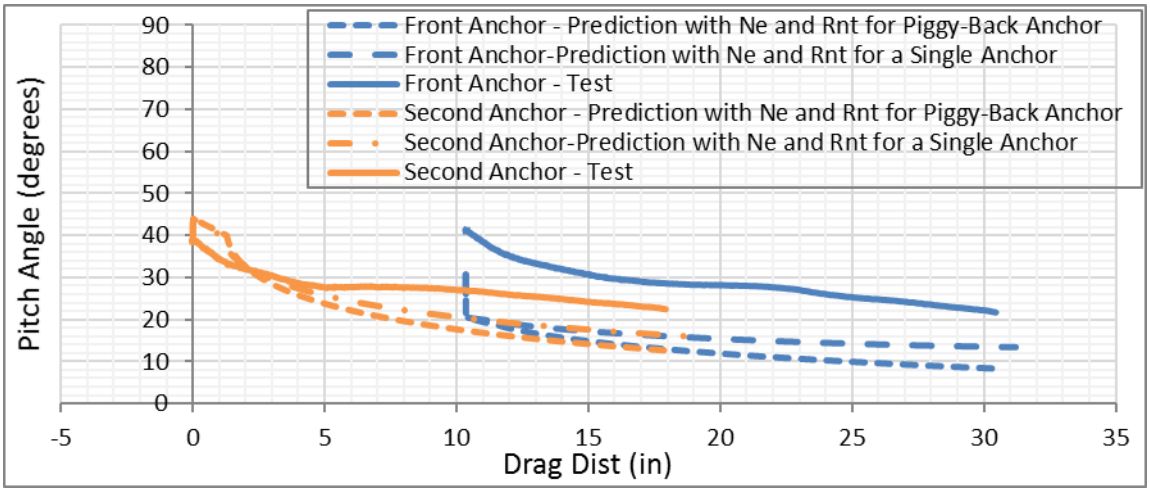

Second Repeat Test in Case 5

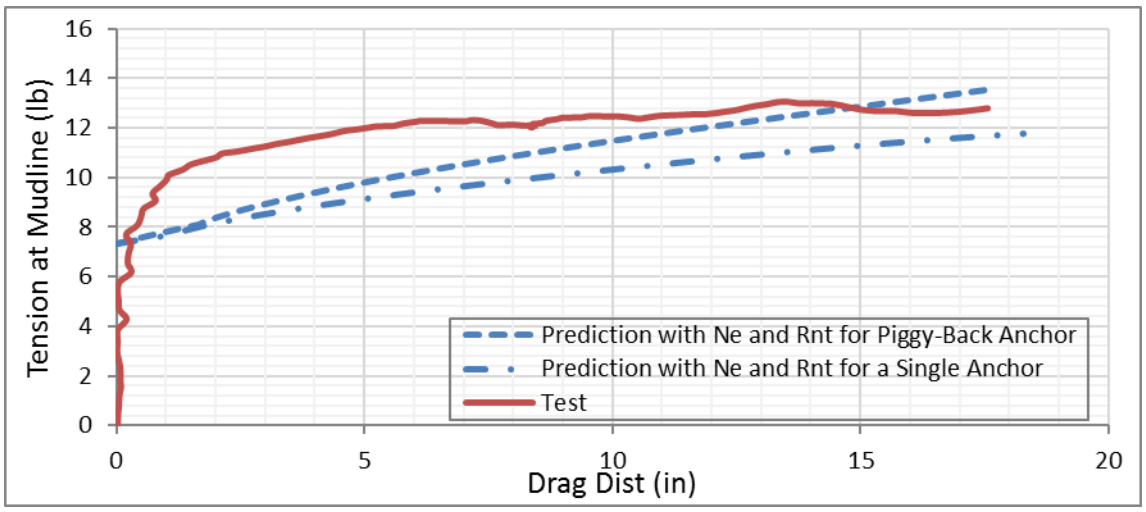

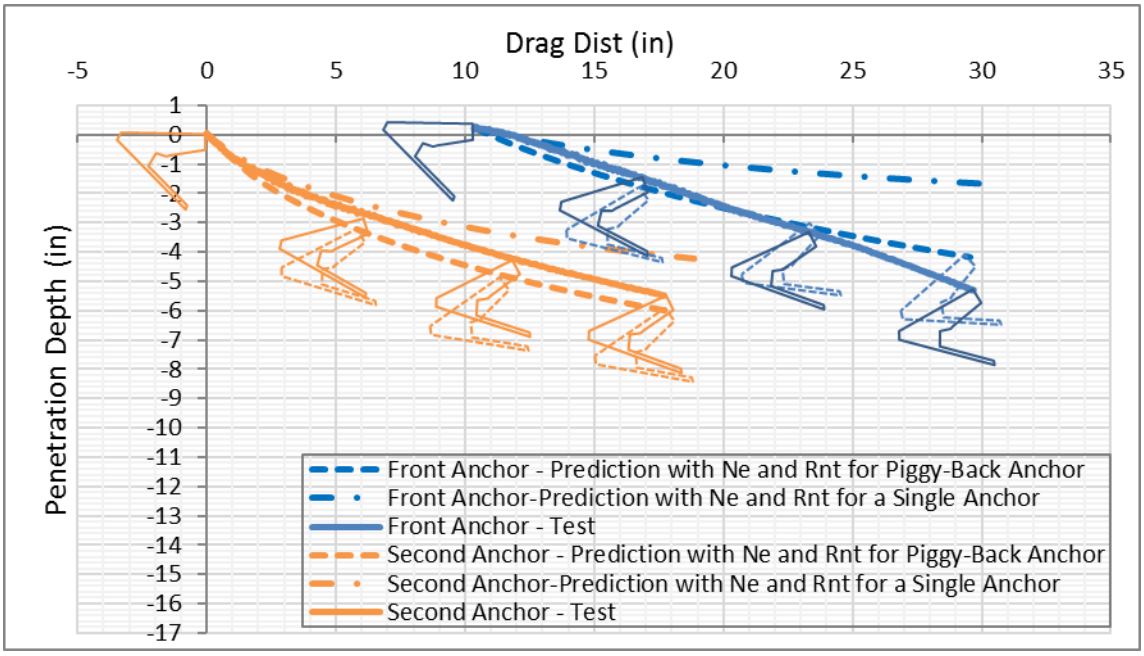

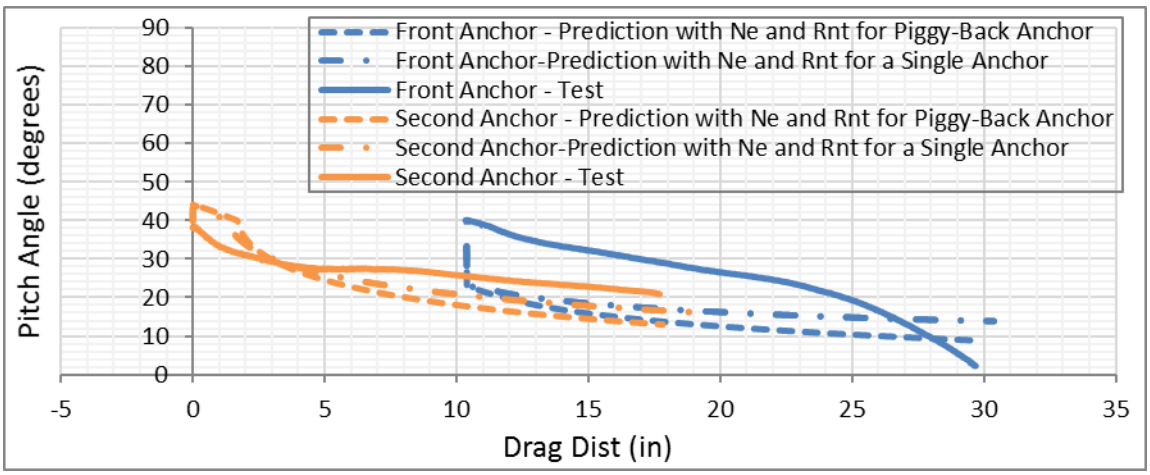

Case 6

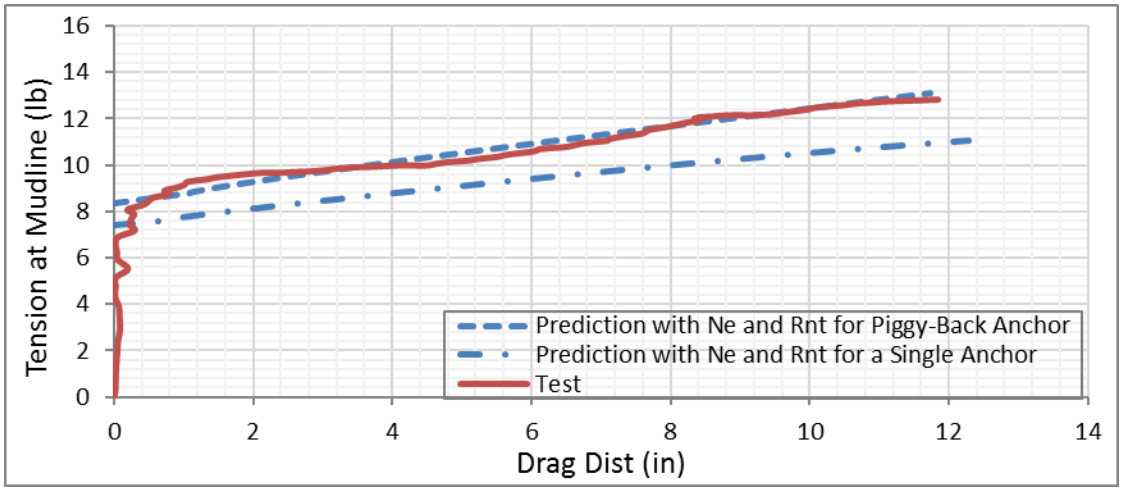
Tension at Mudline (lb)
Drag Dist (in)
Prediction with Ne and Rnt for Piggy-Back Anchor
Prediction with Ne and Rnt for a Single Anchor
Test

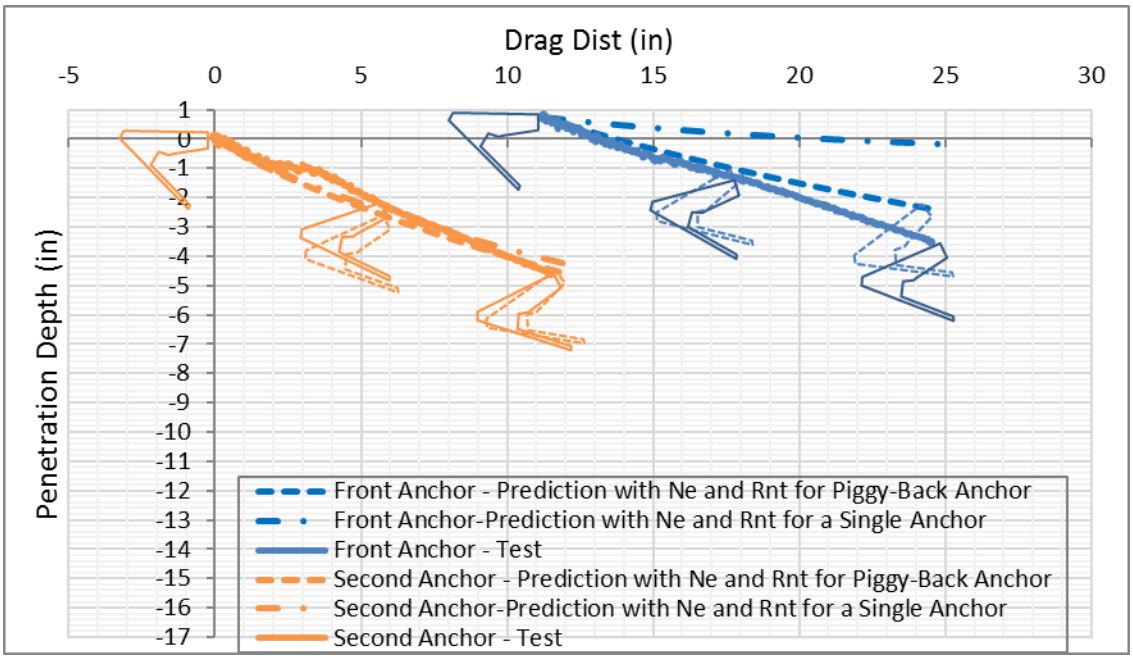
Drag Dist (in)
Penetration Depth (in)
Front Anchor - Prediction with Ne and Rnt for Piggy-Back Anchor
Front Anchor-Prediction with Ne and Rnt for a Single Anchor
Front Anchor - Test
Second Anchor - Prediction with Ne and Rnt for Piggy-Back Anchor
Second Anchor-Prediction with Ne and Rnt for a Single Anchor
Second Anchor - Test

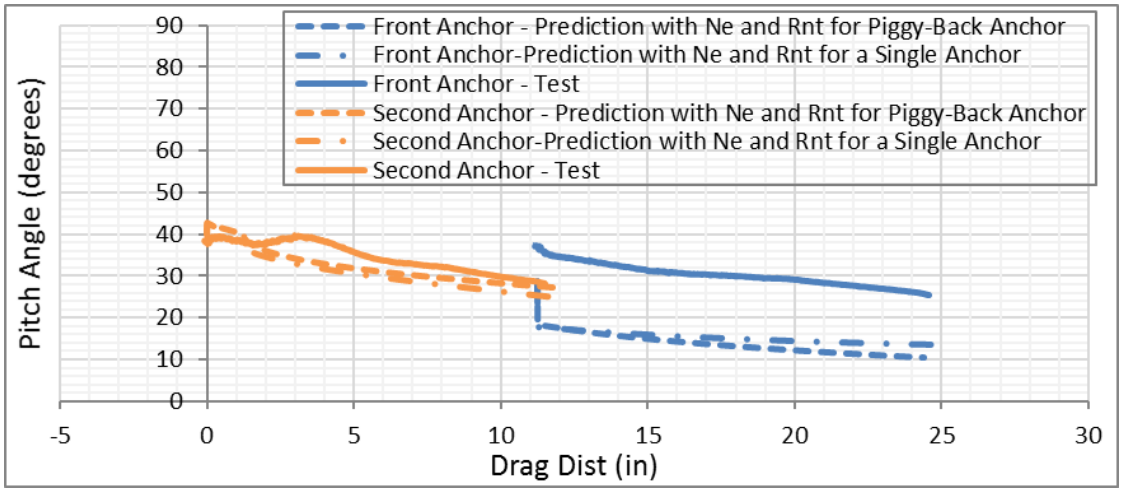
Pitch Angle (degrees)
Drag Dist (in)
Front Anchor - Prediction with Ne and Rnt for Piggy-Back Anchor
Front Anchor-Prediction with Ne and Rnt for a Single Anchor
Front Anchor - Test
Second Anchor - Prediction with Ne and Rnt for Piggy-Back Anchor
Second Anchor-Prediction with Ne and Rnt for a Single Anchor
Second Anchor - Test

First Repeat Test in Case 6

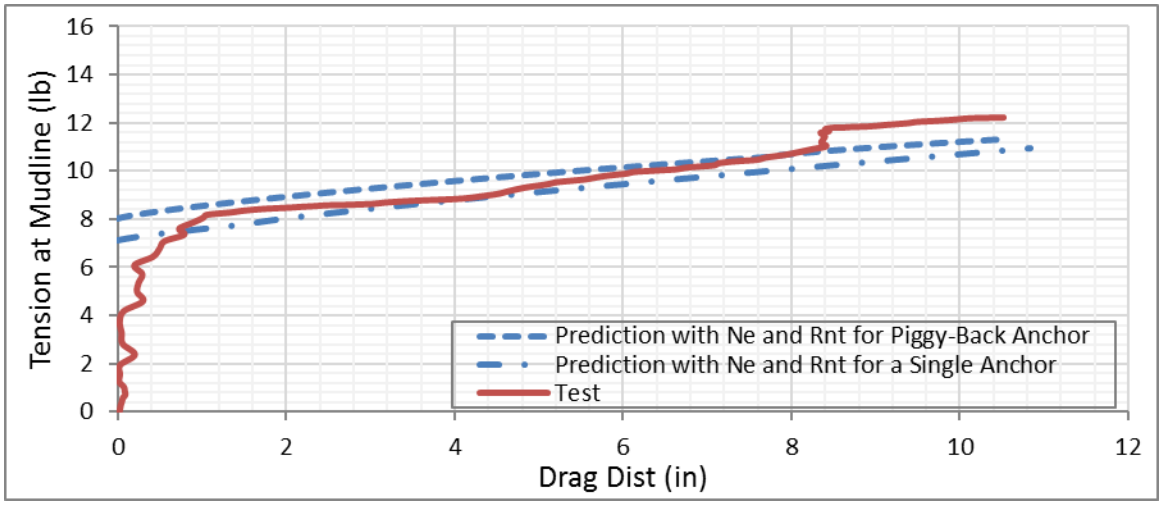

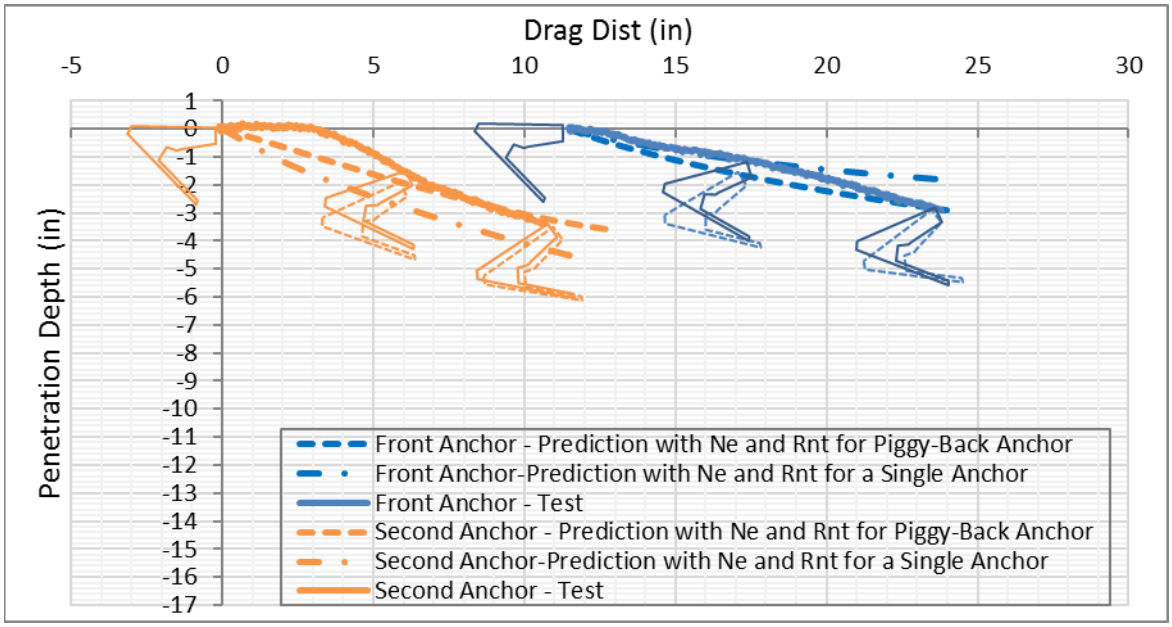

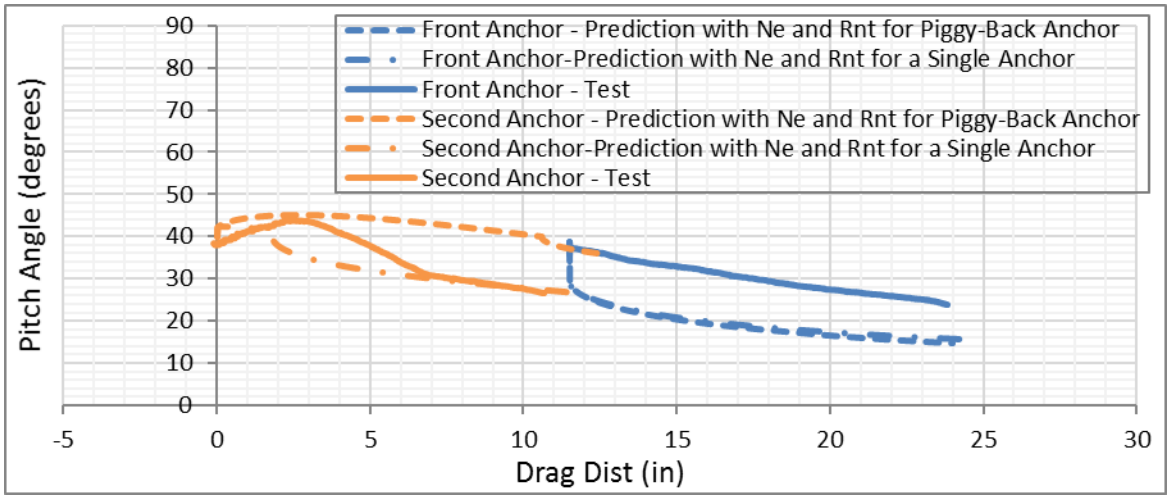

Second Repeat Test in Case 6

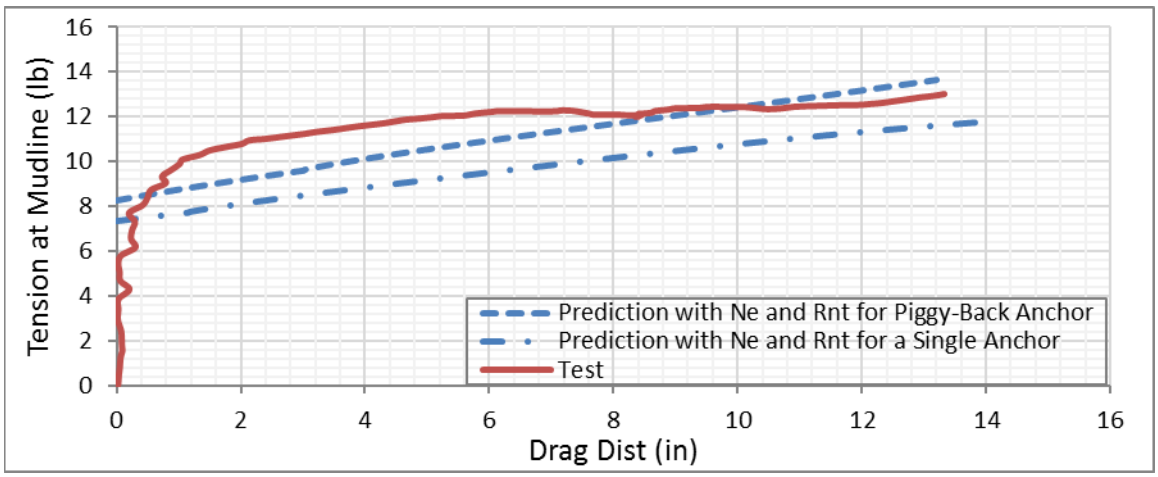

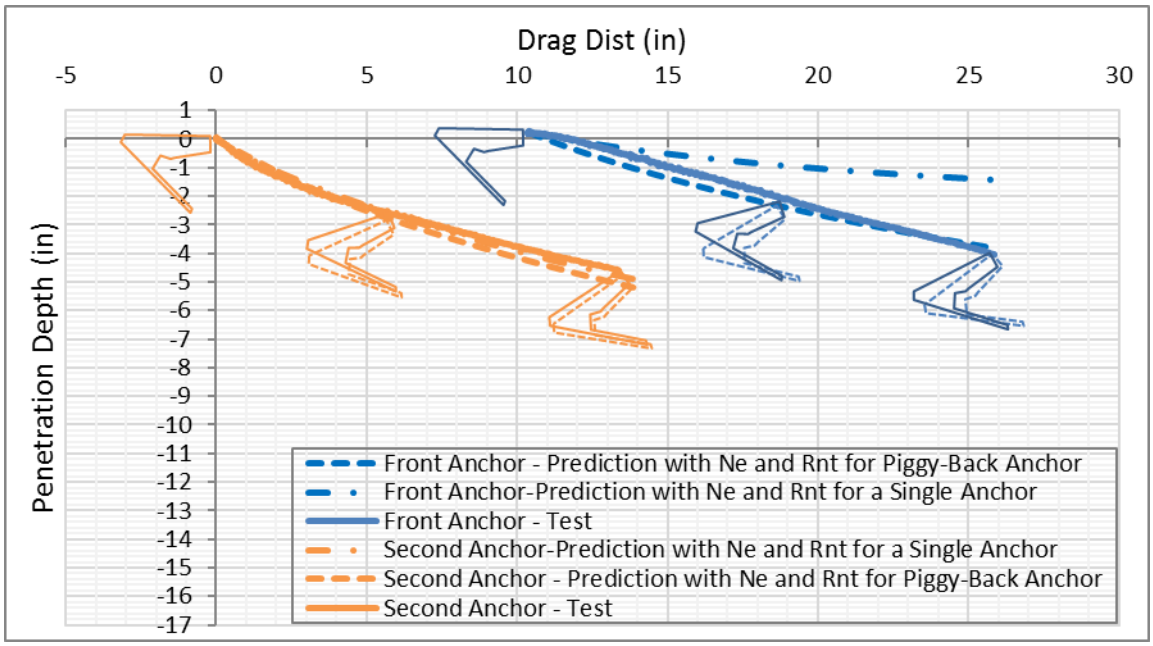

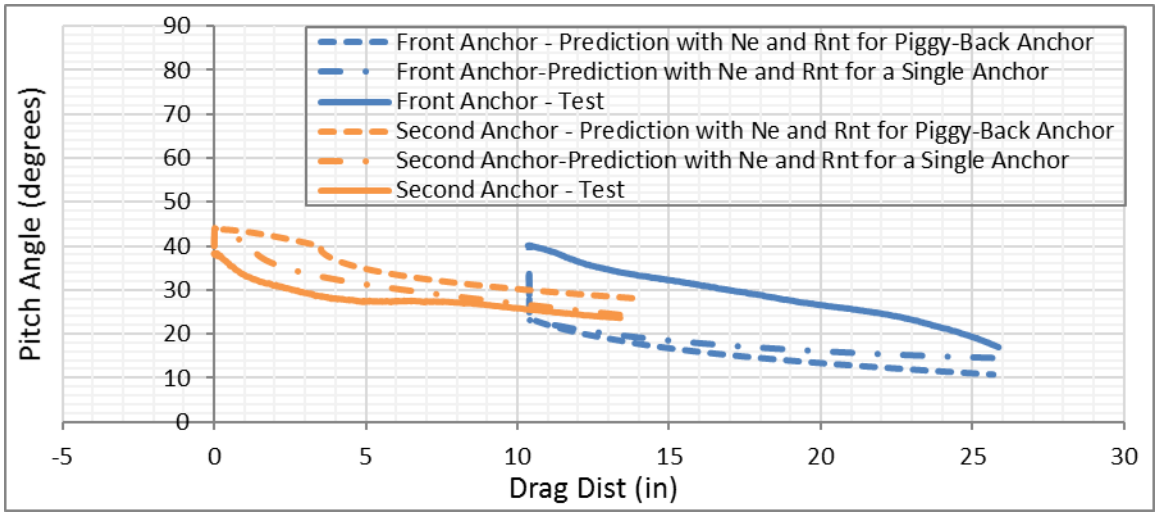

Case 9

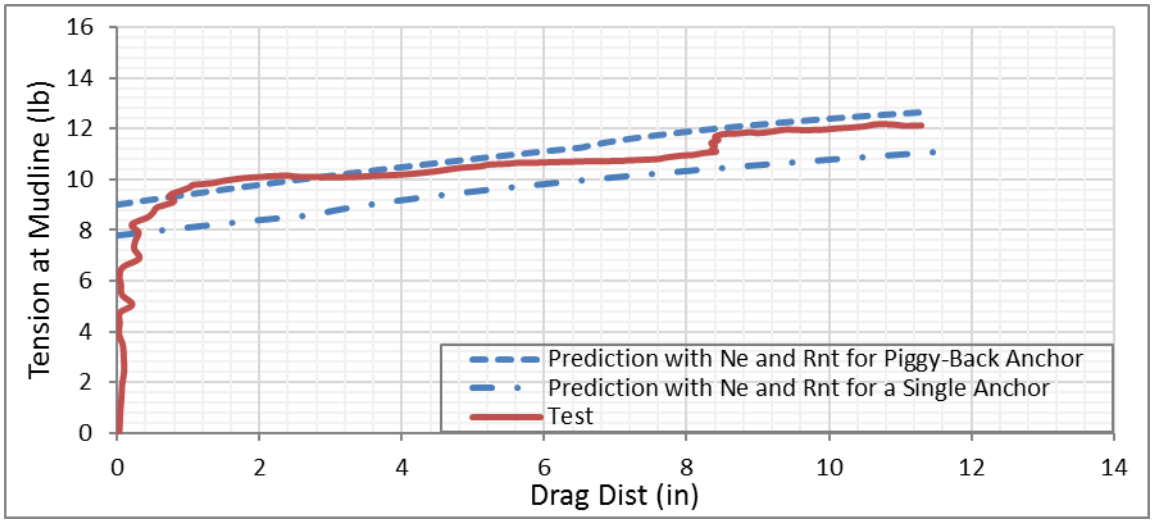
Tension at Mudline (lb)
Drag Dist (in)
Prediction with Ne and Rnt for Piggy-Back Anchor
Prediction with Ne and Rnt for a Single Anchor
Test

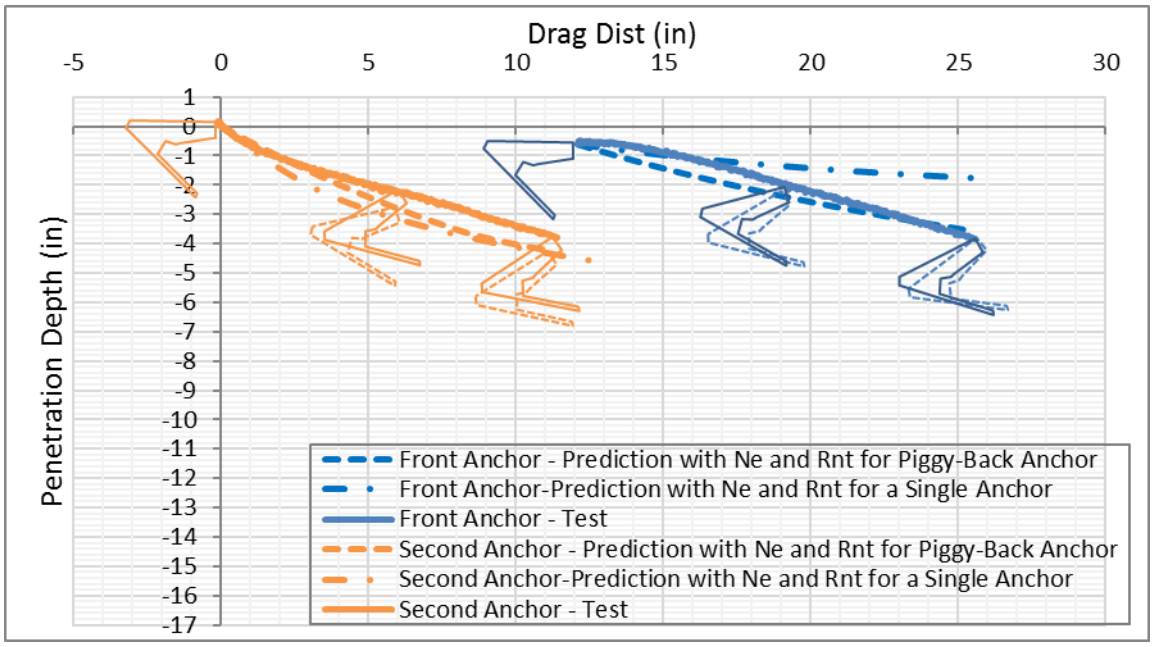
Drag Dist (in)
Penetration Depth (in)
Front Anchor - Prediction with Ne and Rnt for Piggy-Back Anchor
Front Anchor-Prediction with Ne and Rnt for a Single Anchor
Front Anchor - Test
Second Anchor - Prediction with Ne and Rnt for Piggy-Back Anchor
Second Anchor-Prediction with Ne and Rnt for a Single Anchor
Second Anchor - Test

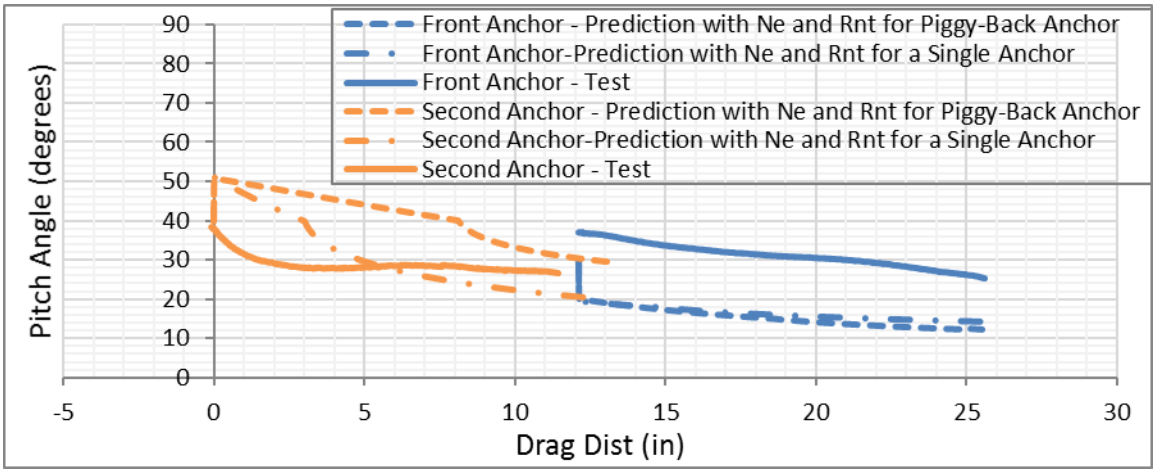
Pitch Angle (degrees)
Drag Dist (in)
Front Anchor - Prediction with Ne and Rnt for Piggy-Back Anchor
Front Anchor-Prediction with Ne and Rnt for a Single Anchor
Front Anchor - Test
Second Anchor - Prediction with Ne and Rnt for Piggy-Back Anchor
Second Anchor-Prediction with Ne and Rnt for a Single Anchor
Second Anchor - Test

First Repeat Test in Case 9

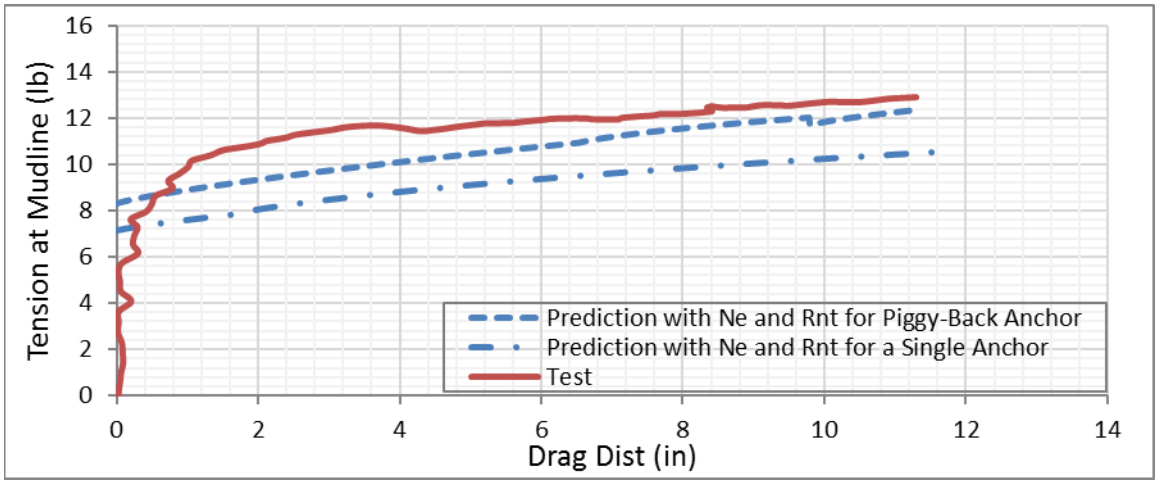

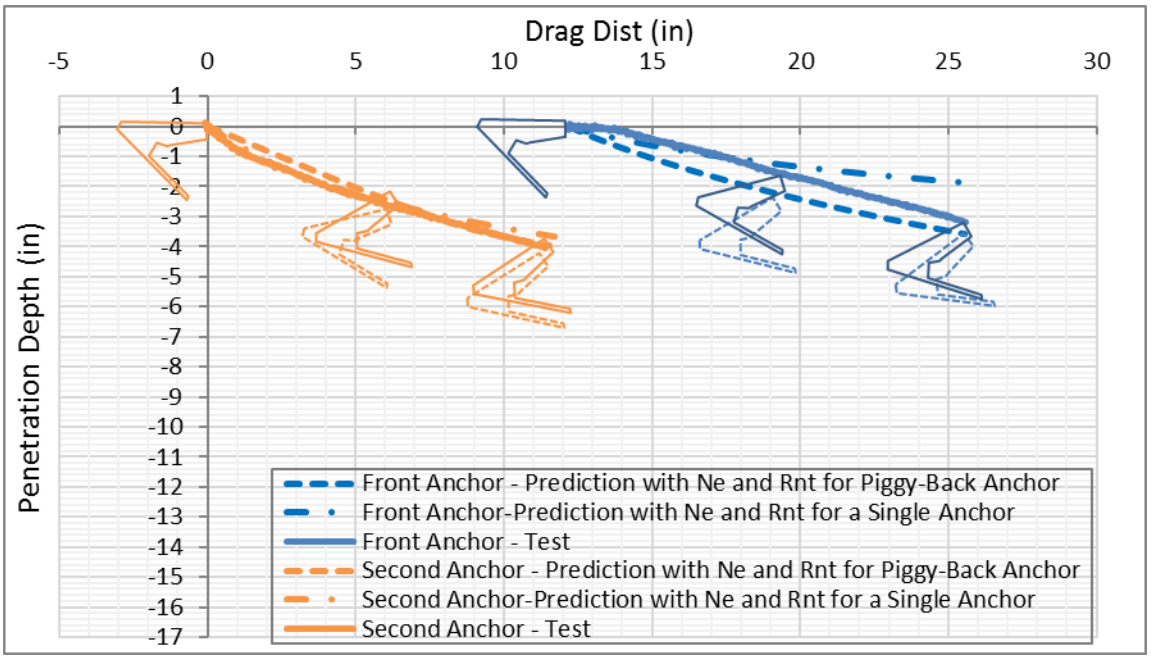

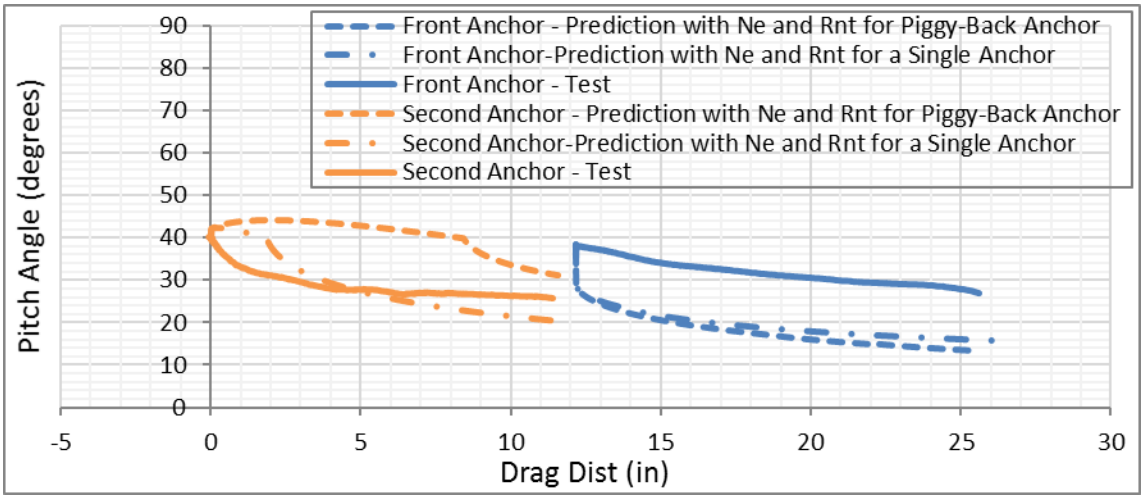

Second Repeat Test in Case 9

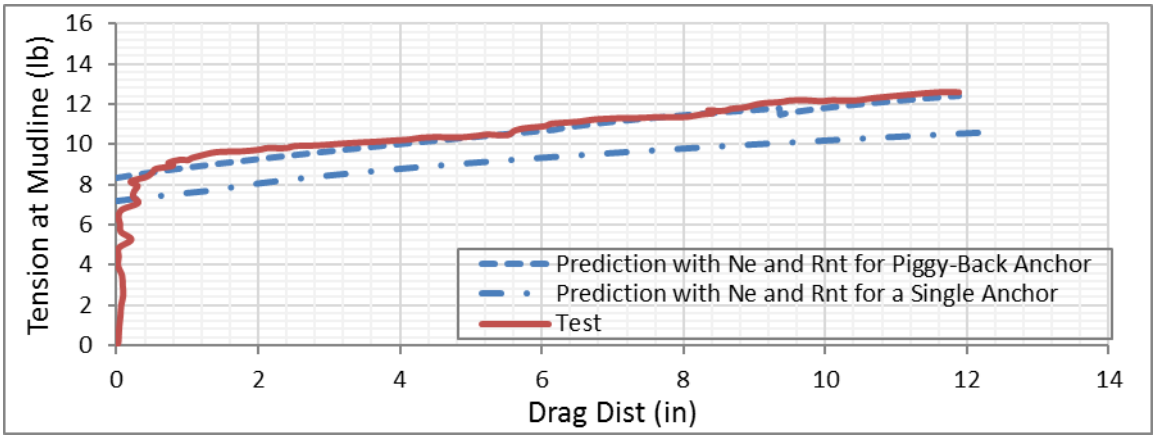

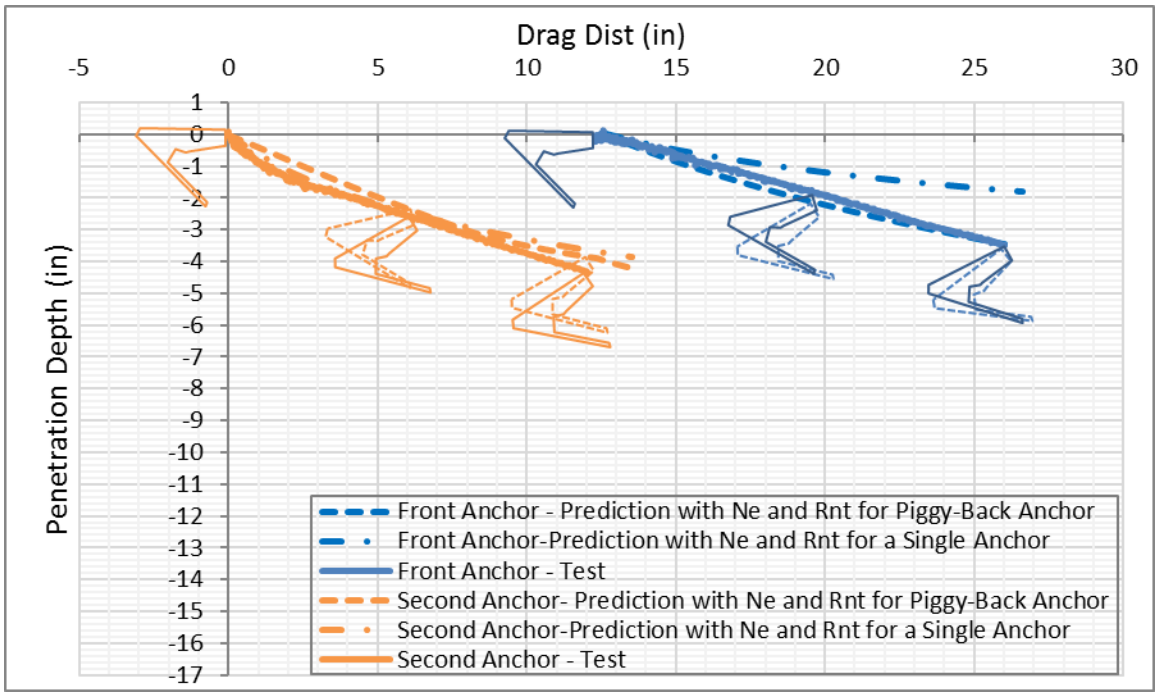

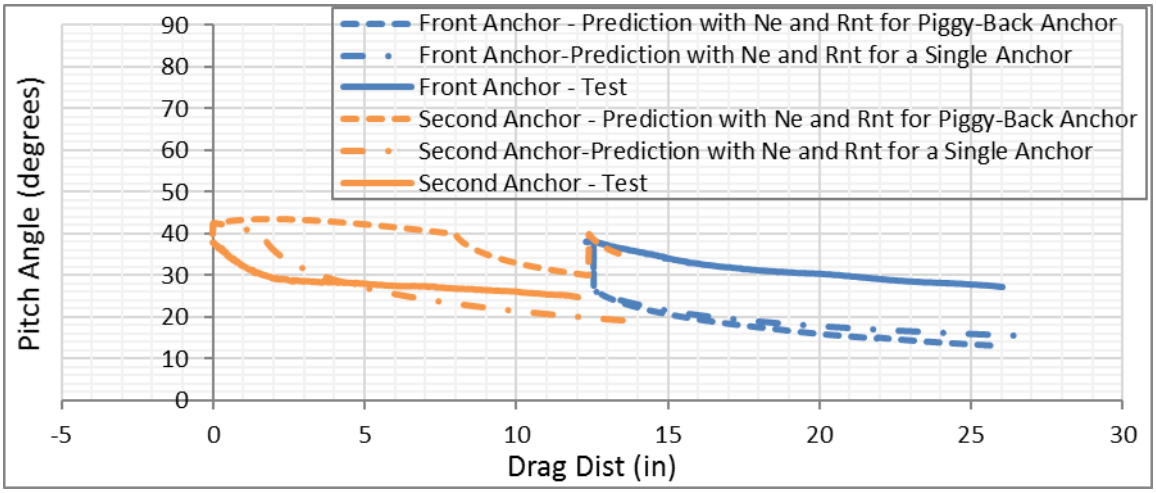

Case 10

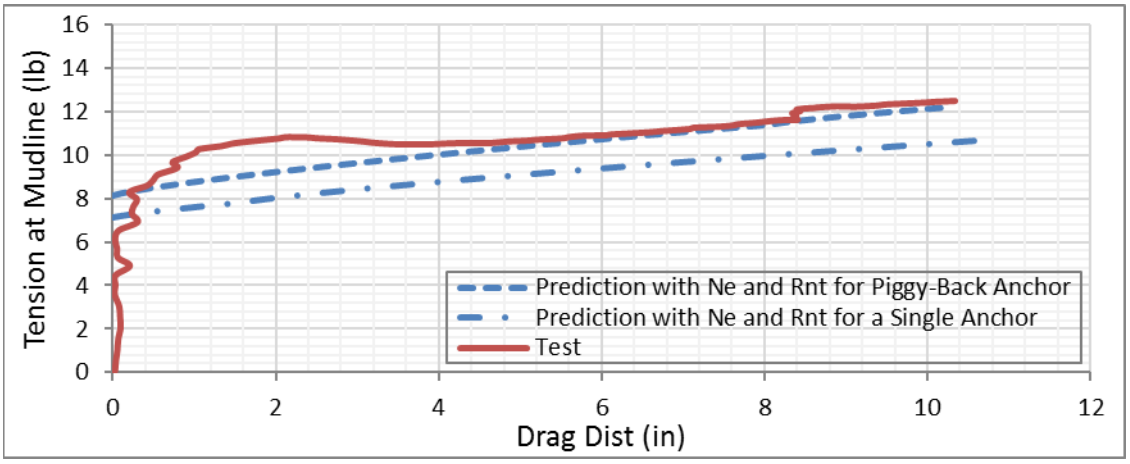
Tension at Mudline (lb)
Drag Dist (in)
Prediction with Ne and Rnt for Piggy-Back Anchor
Prediction with Ne and Rnt for a Single Anchor
Test

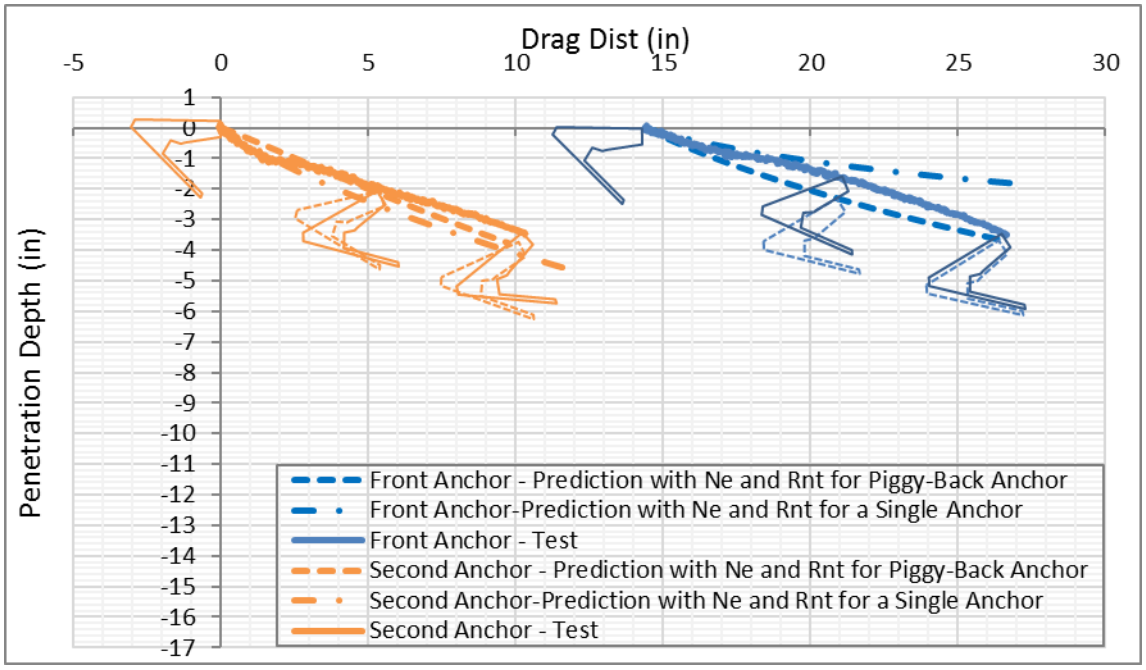
Drag Dist (in)
Penetration Depth (in)
Front Anchor - Prediction with Ne and Rnt for Piggy-Back Anchor
Front Anchor-Prediction with Ne and Rnt for a Single Anchor
Front Anchor - Test
Second Anchor - Prediction with Ne and Rnt for Piggy-Back Anchor
Second Anchor-Prediction with Ne and Rnt for a Single Anchor
Second Anchor - Test

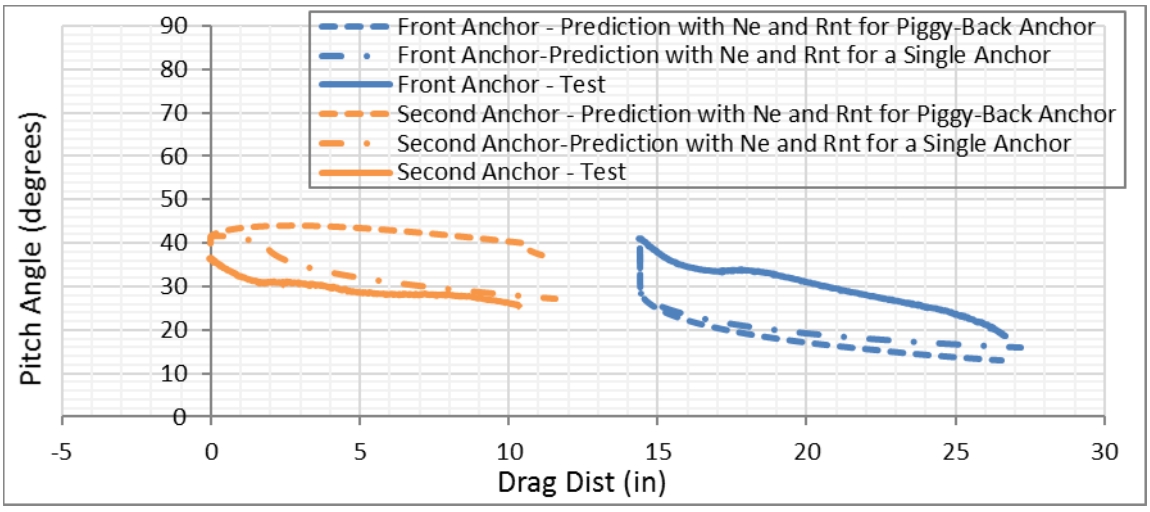
Pitch Angle (degrees)
Drag Dist (in)
Front Anchor - Prediction with Ne and Rnt for Piggy-Back Anchor
Front Anchor-Prediction with Ne and Rnt for a Single Anchor
Front Anchor - Test
Second Anchor - Prediction with Ne and Rnt for Piggy-Back Anchor
Second Anchor-Prediction with Ne and Rnt for a Single Anchor
Second Anchor - Test

First Repeat Test in Case 10

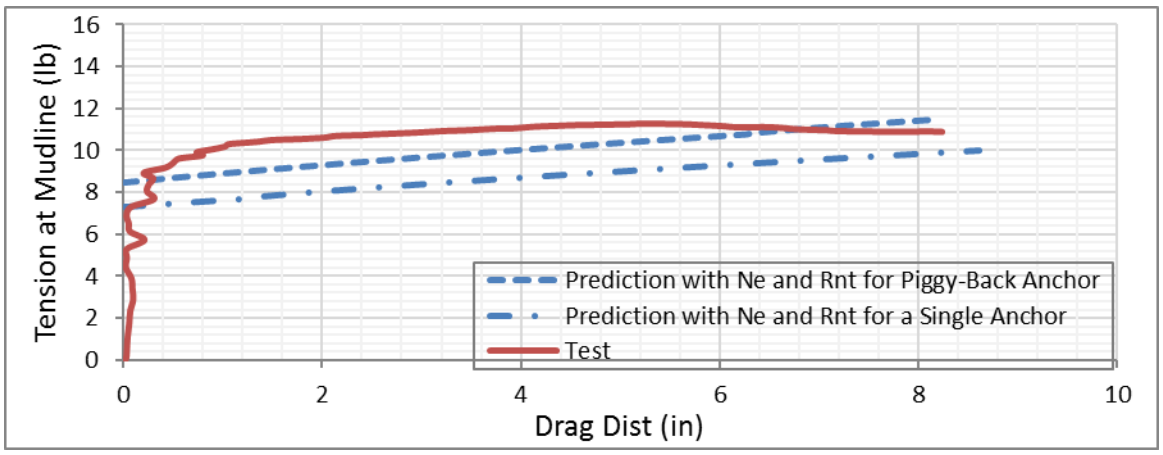

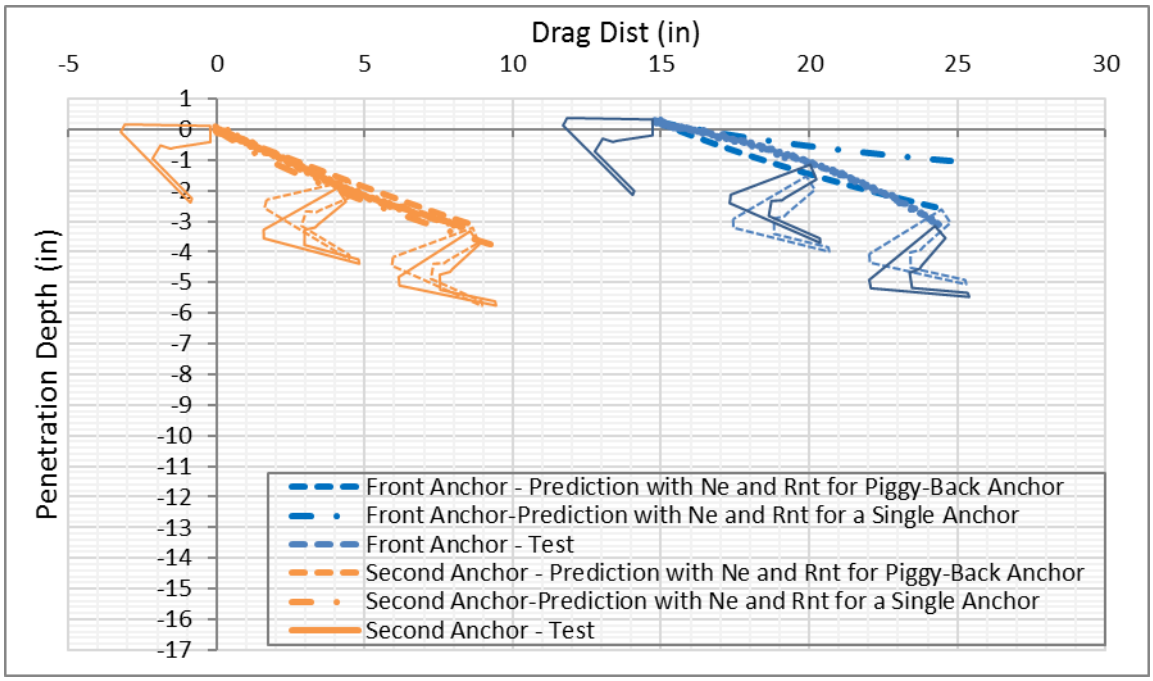

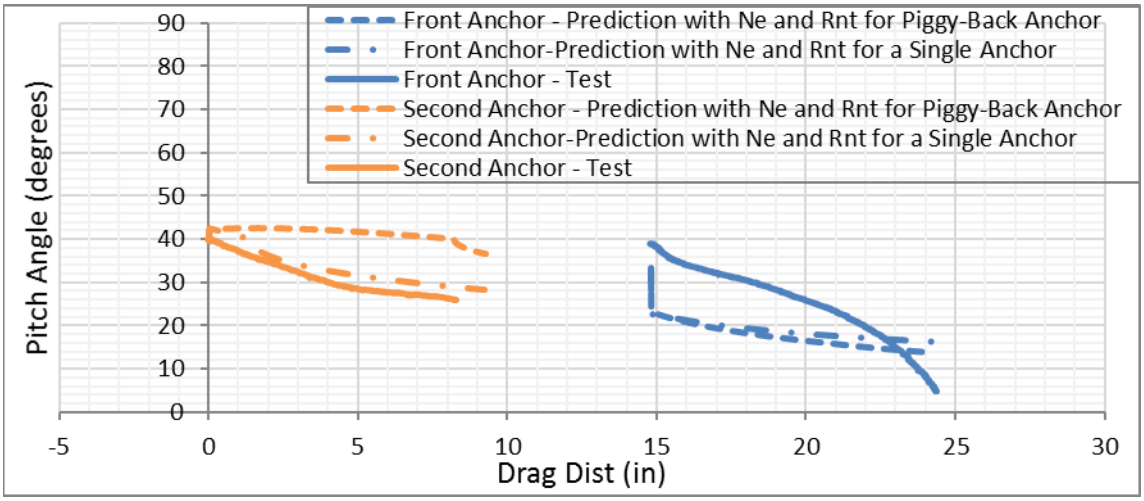

Case 12

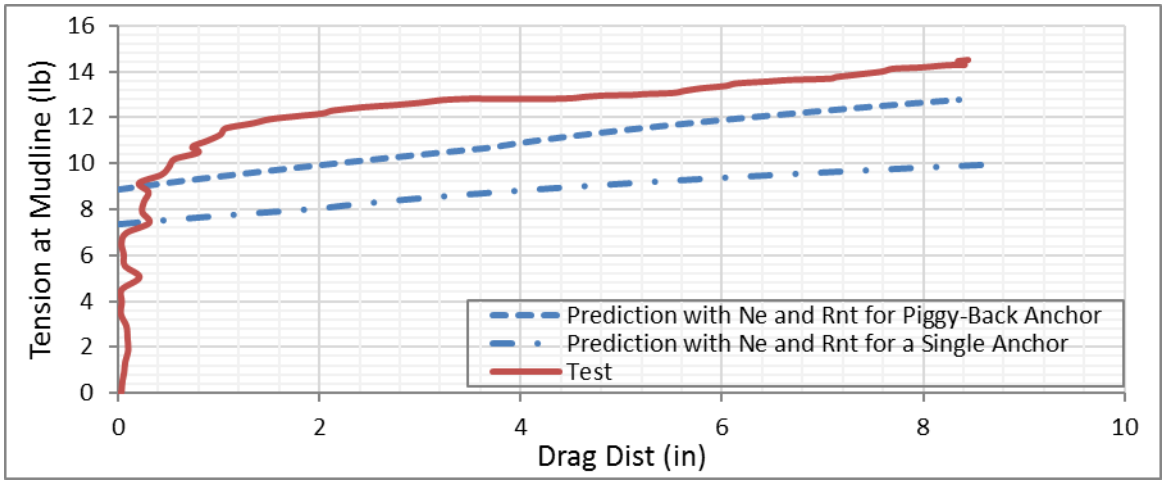
Tension at Mudline (lb)
Drag Dist (in)
Prediction with Ne and Rnt for Piggy-Back Anchor
Prediction with Ne and Rnt for a Single Anchor
Test

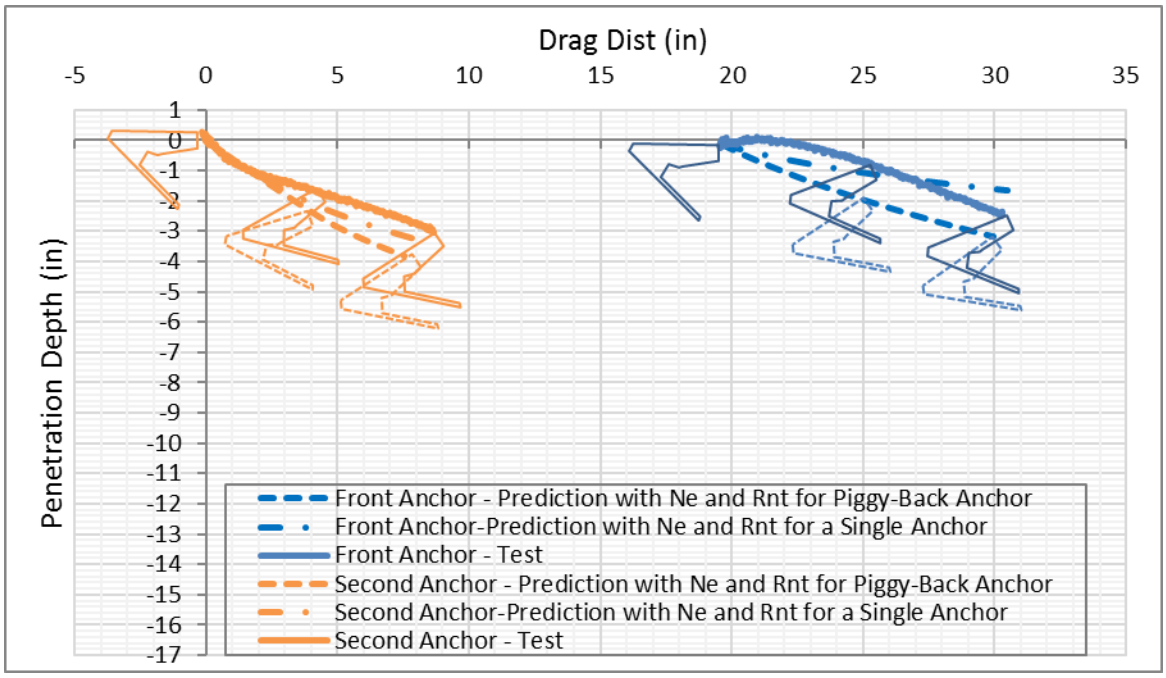
Drag Dist (in)
Penetration Depth (in)
Front Anchor - Prediction with Ne and Rnt for Piggy-Back Anchor
Front Anchor-Prediction with Ne and Rnt for a Single Anchor
Front Anchor - Test
Second Anchor - Prediction with Ne and Rnt for Piggy-Back Anchor
Second Anchor-Prediction with Ne and Rnt for a Single Anchor
Second Anchor - Test

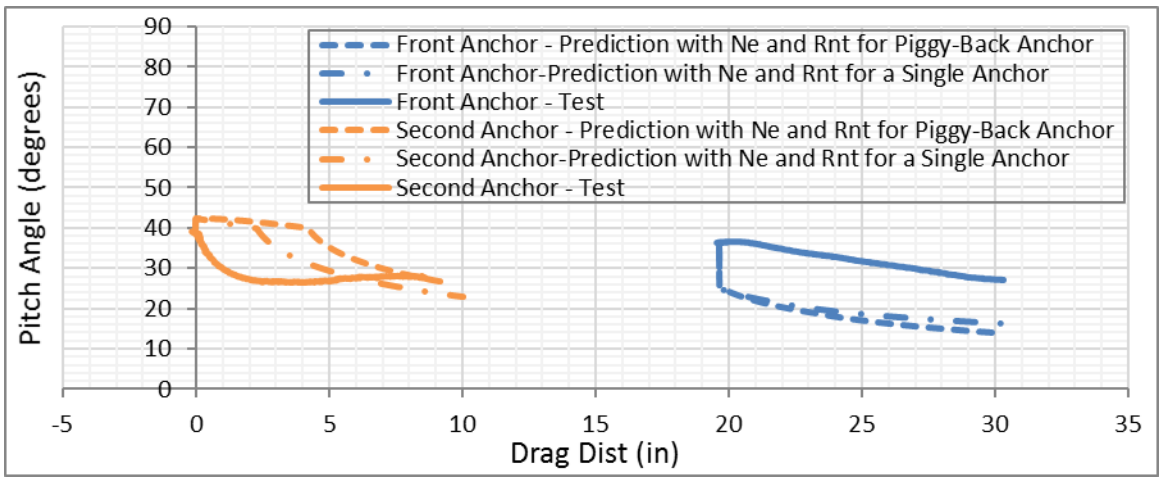
Pitch Angle (degrees)
Drag Dist (in)
Front Anchor - Prediction with Ne and Rnt for Piggy-Back Anchor
Front Anchor-Prediction with Ne and Rnt for a Single Anchor
Front Anchor - Test
Second Anchor - Prediction with Ne and Rnt for Piggy-Back Anchor
Second Anchor-Prediction with Ne and Rnt for a Single Anchor
Second Anchor - Test

First Repeat Test in Case 12

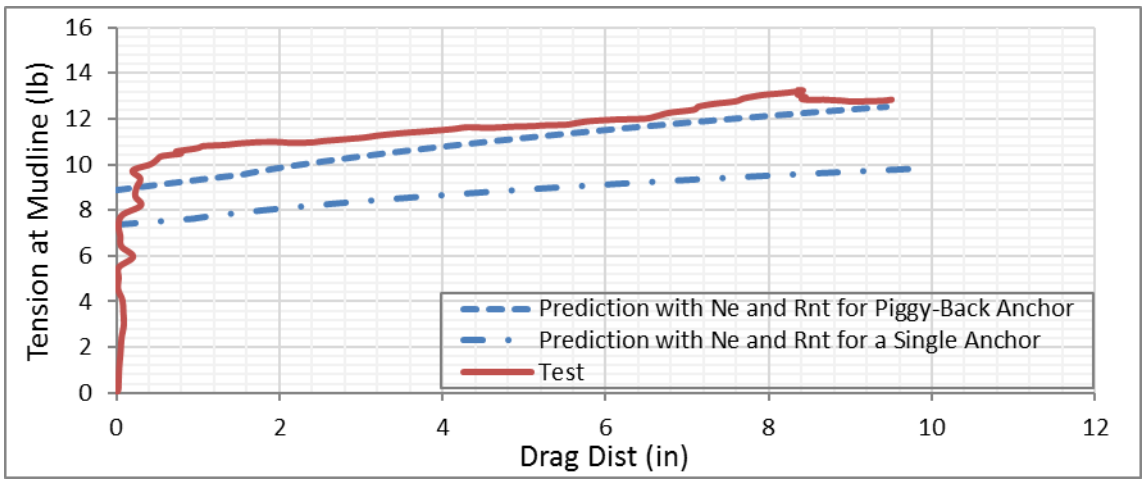

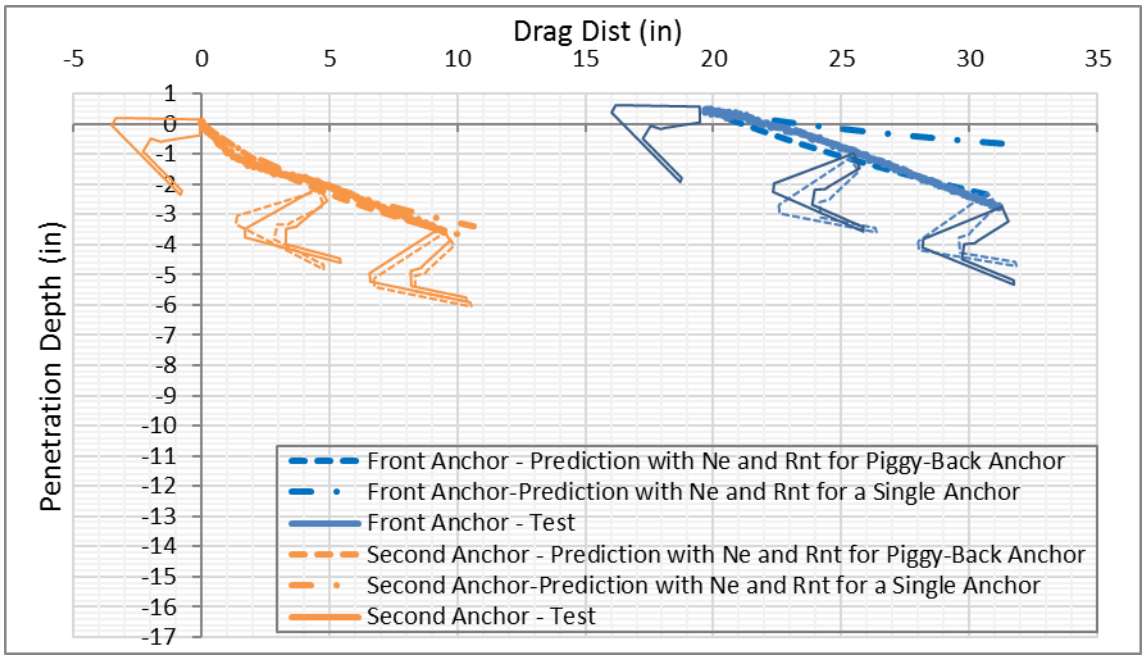

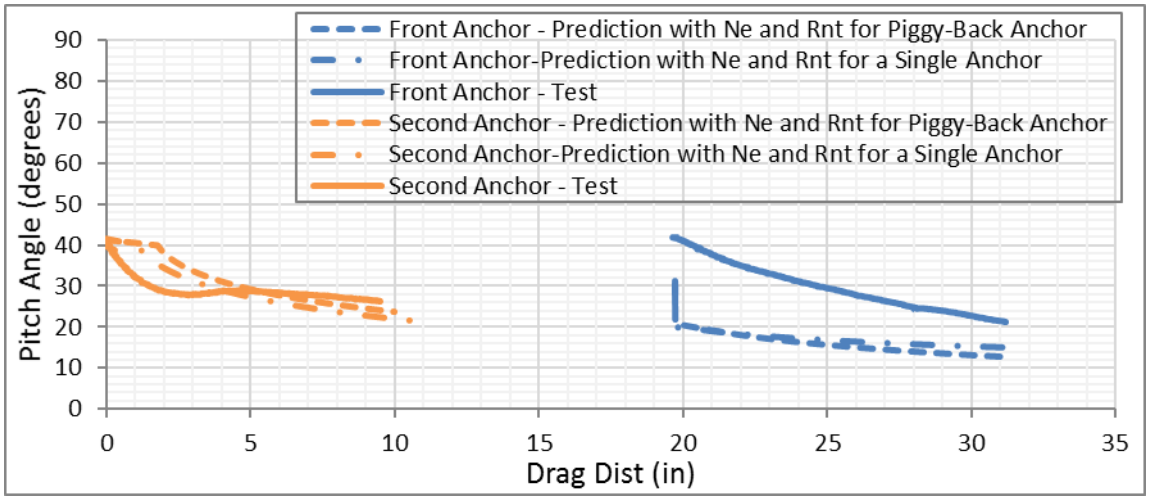

Second Repeat Test in Case 12

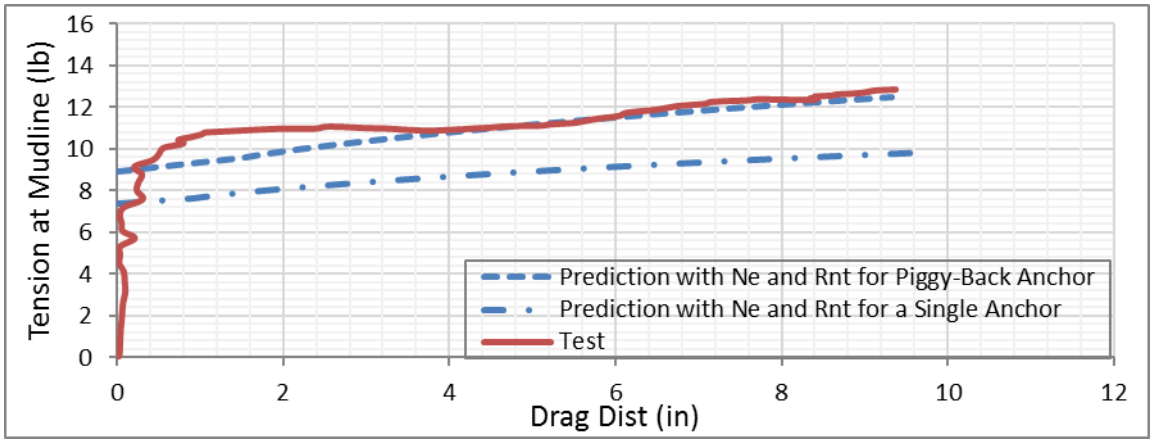

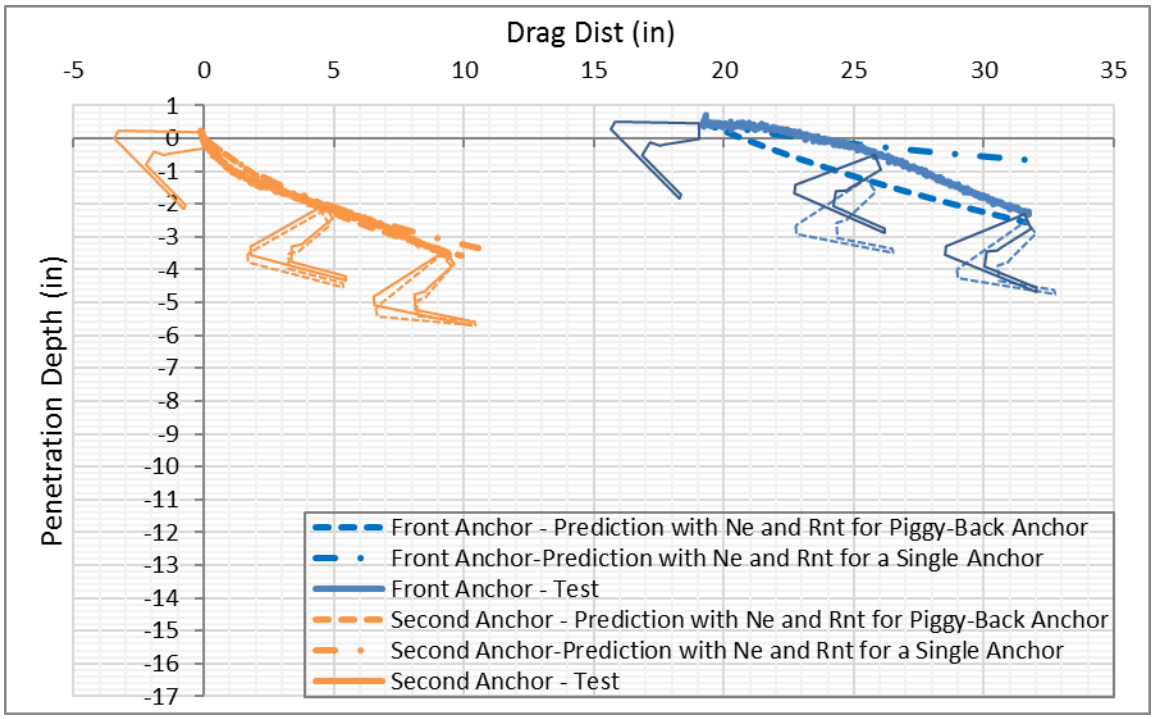

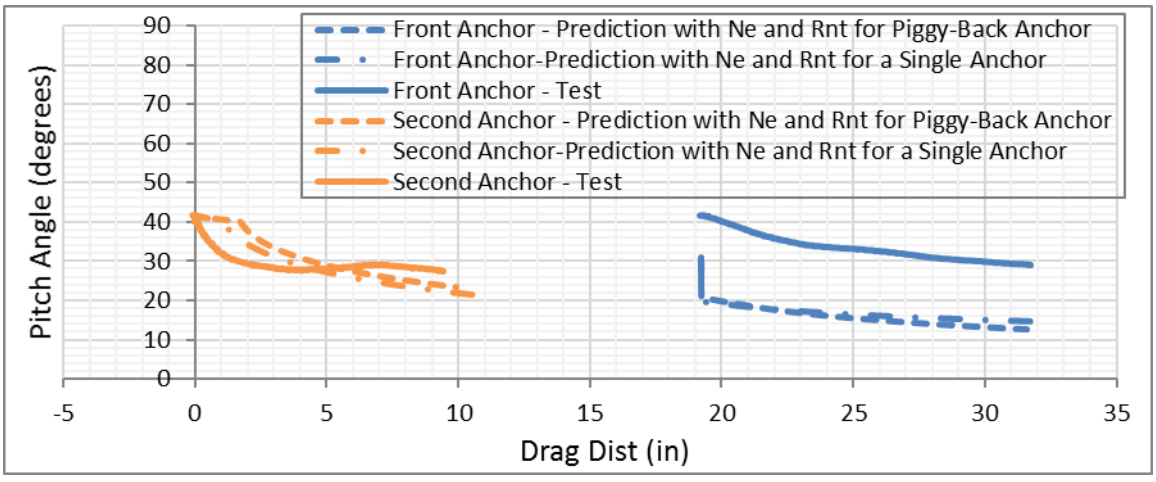

Case 13

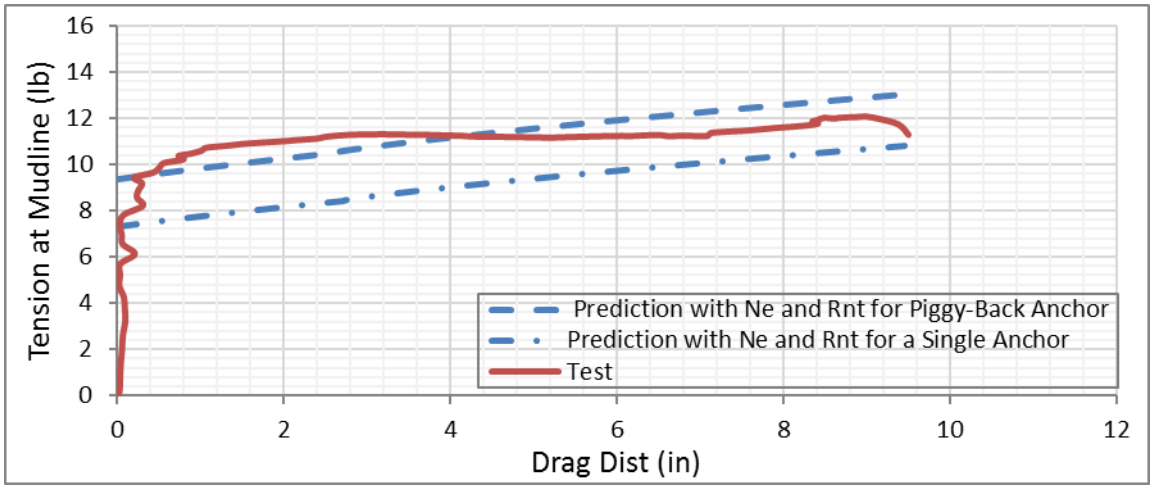
Tension at Mudline (lb)
Drag Dist (in)
Prediction with Ne and Rnt for Piggy-Back Anchor
Prediction with Ne and Rnt for a Single Anchor
Test

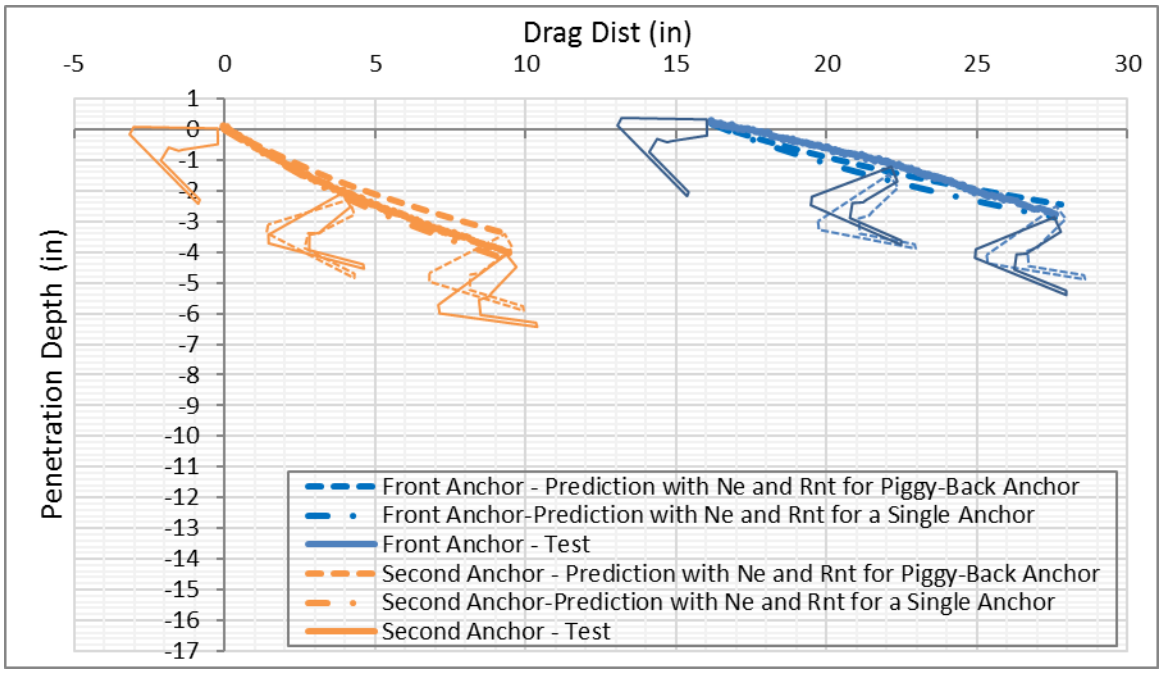
Drag Dist (in)
Penetration Depth (in)
Front Anchor - Prediction with Ne and Rnt for Piggy-Back Anchor
Front Anchor-Prediction with Ne and Rnt for a Single Anchor
Front Anchor - Test
Second Anchor - Prediction with Ne and Rnt for Piggy-Back Anchor
Second Anchor-Prediction with Ne and Rnt for a Single Anchor
Second Anchor - Test

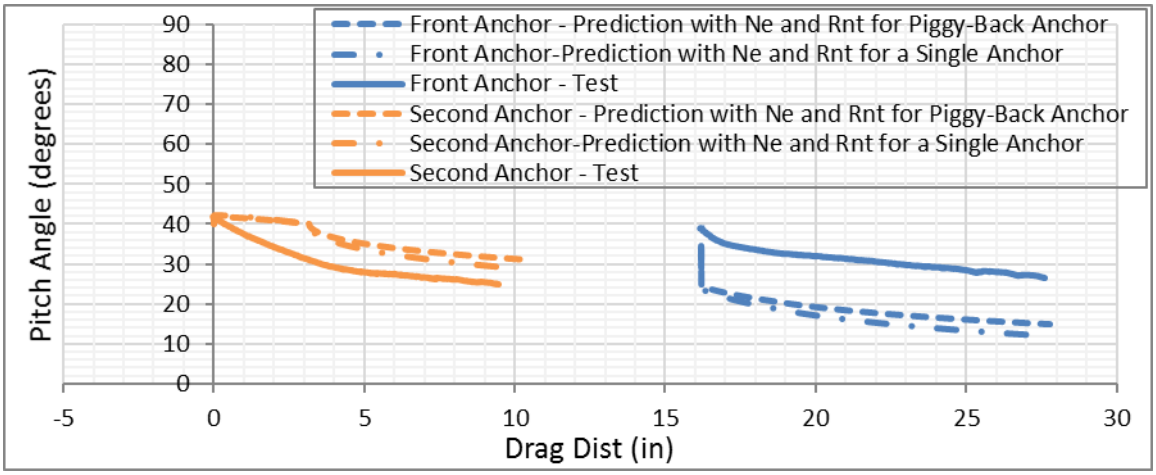
Pitch Angle (degrees)
Drag Dist (in)
Front Anchor - Prediction with Ne and Rnt for Piggy-Back Anchor
Front Anchor-Prediction with Ne and Rnt for a Single Anchor
Front Anchor - Test
Second Anchor - Prediction with Ne and Rnt for Piggy-Back Anchor
Second Anchor-Prediction with Ne and Rnt for a Single Anchor
Second Anchor - Test

First Repeat Test in Case 13

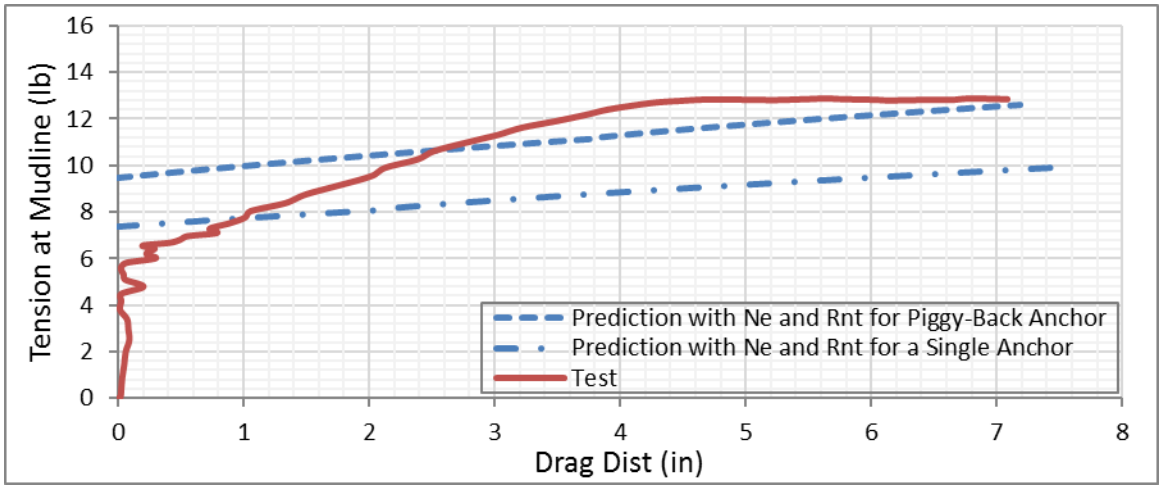

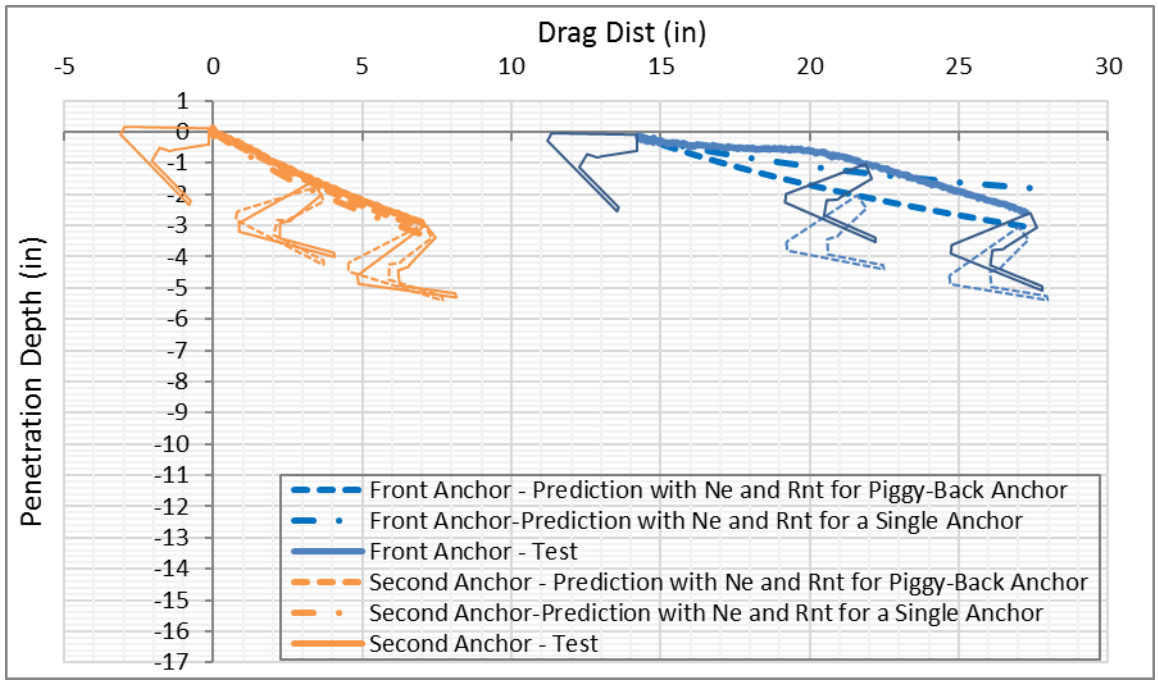

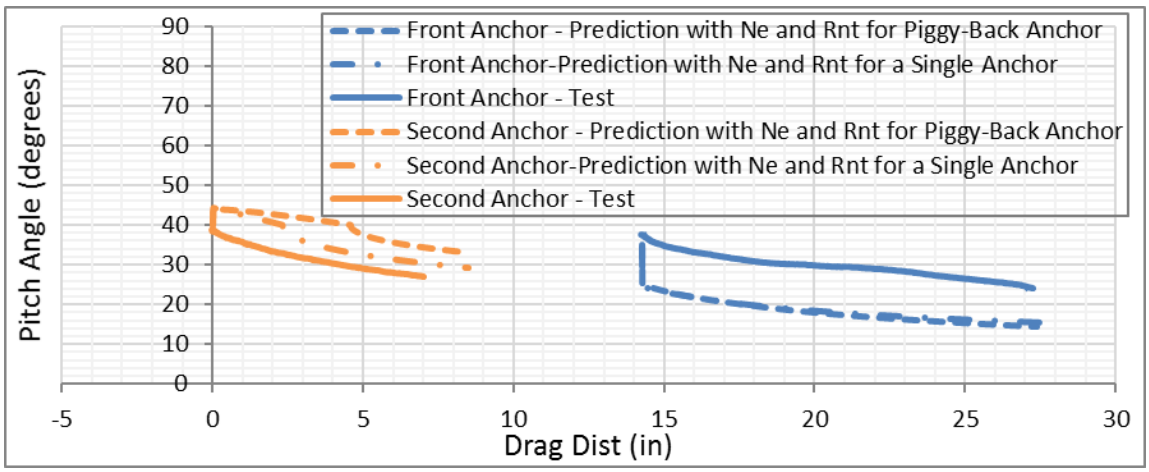

Appendix F. Free-Fall Penetration Tests with Flying Wing Anchor® in a Single Layer

Free-Fall Penetration with Flying Wing Anchor ® in a Single Layer

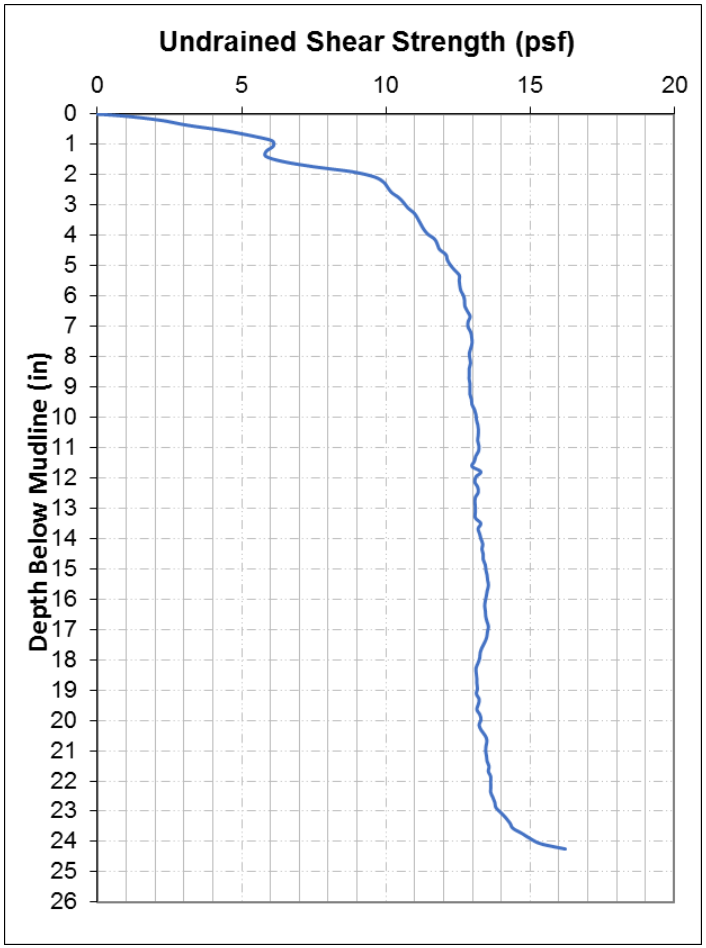

Free-Fall Penetration with Flying Wing Anchor ® in a Single Layer

Drop 1

	Impact v (ft/s)	Embedment D (L_f)	β	λ
Experiment	16.8	2.61	–	–
R_f in Power-Law	16.09	2.26	0.15	–
R_f in Semi-log	16.09	2.26	–	0.35

Prediction with R_f in power-law

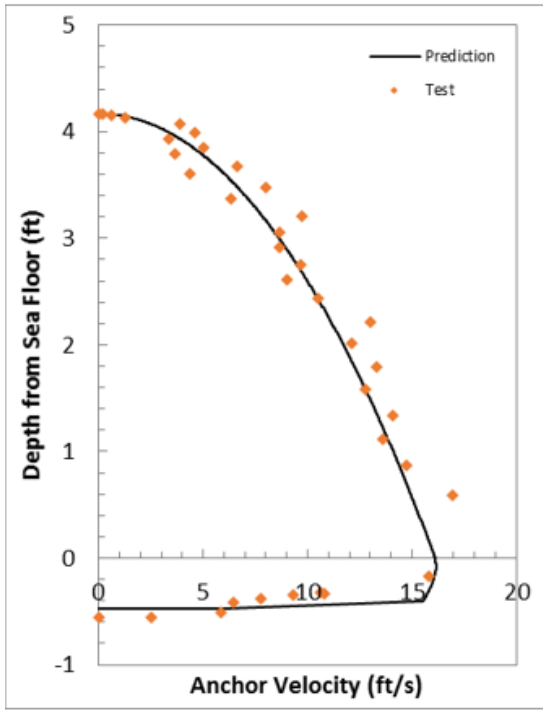

Prediction with R_f in semi-log

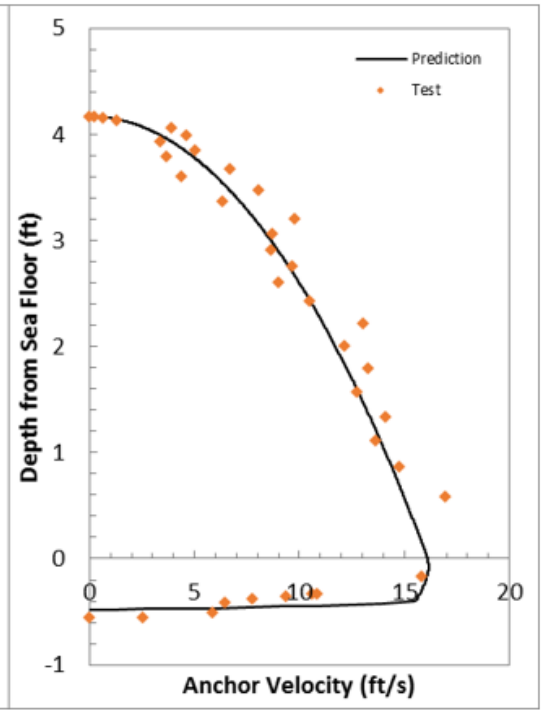

Free-Fall Penetration with Flying Wing Anchor ® in a Single Layer

Drop 2

	Impact v (ft/s)	Embedment D (L_f)	β	λ
Experiment	16.16	2.61	–	–
R_f in Power-Law	16.12	2.28	0.15	–
R_f in Semi-log	16.12	2.29	–	0.35

Prediction with R_f in power-law

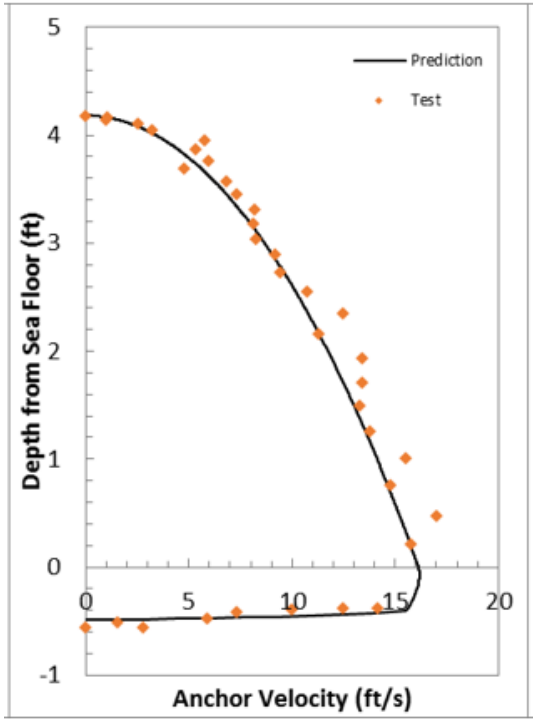

Prediction with R_f in semi-log

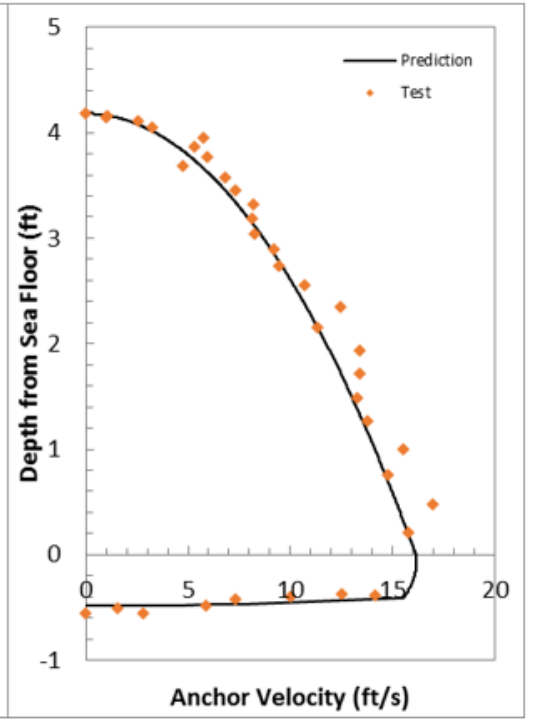

Free-Fall Penetration with Flying Wing Anchor ® in a Single Layer

Drop 3

	Impact v (ft/s)	Embedment D (L_f)	β	λ
Experiment	16.2	2.61	–	–
R_f in Power-Law	16.12	2.21	0.15	–
R_f in Semi-log	16.12	2.26	–	0.35

Prediction with R_f in power-law

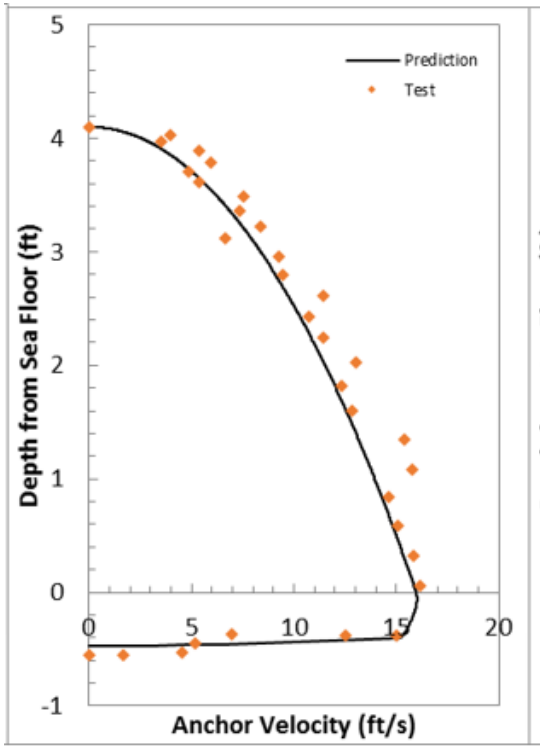

Prediction with R_f in semi-log

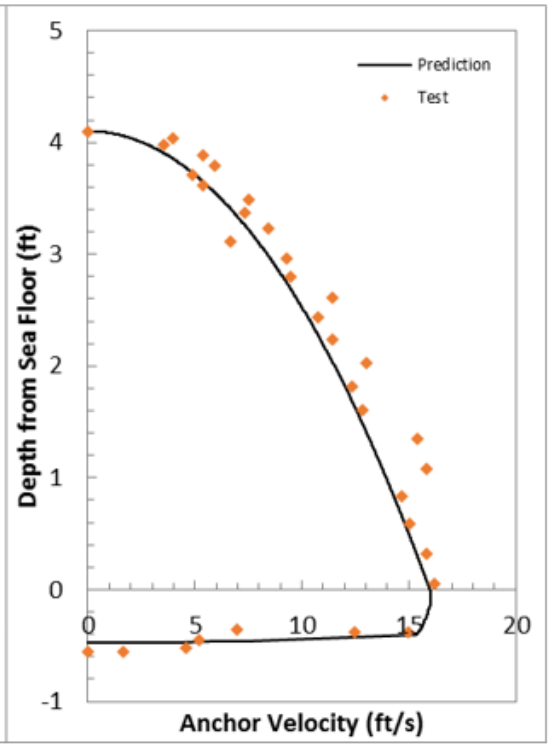

Free-Fall Penetration with Flying Wing Anchor ® in a Single Layer

Drop 4

	Impact v (ft/s)	Embedment D (L_f)	β	λ
Experiment	16.71	2.61	–	–
R_f in Power-Law	15.97	2.26	0.15	–
R_f in Semi-log	15.97	2.27	–	0.35

Prediction with R_f in power-law

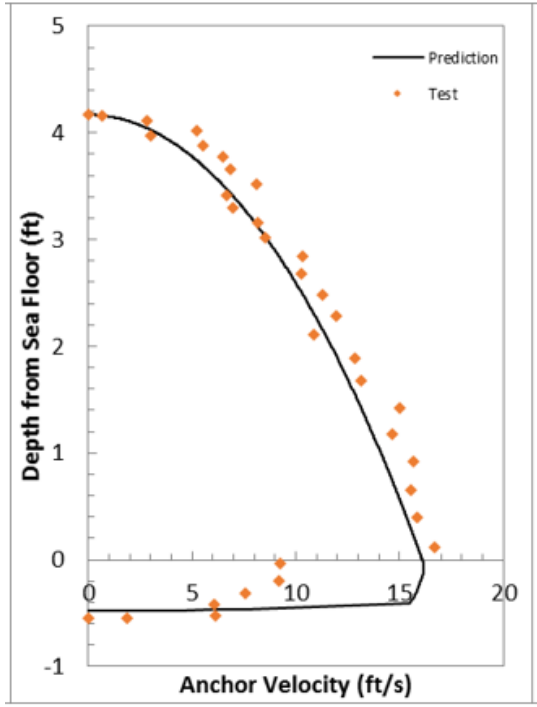

Prediction with R_f in semi-log

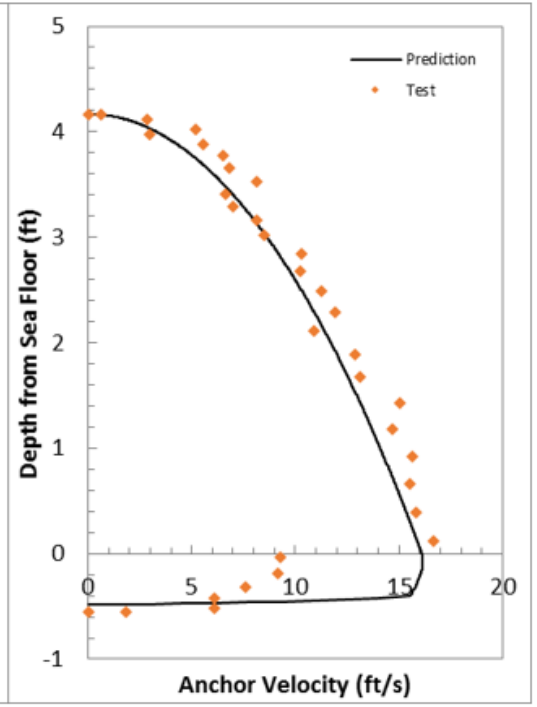

Free-Fall Penetration with Flying Wing Anchor ® in a Single Layer

Drop 5

	Impact v (ft/s)	Embedment D (L_f)	β	λ
Experiment	16.2	2.61	–	–
R_f in Power-Law	16.24	2.28	0.15	–
R_f in Semi-log	16.24	2.29	–	0.35

Prediction with R_f in power-law

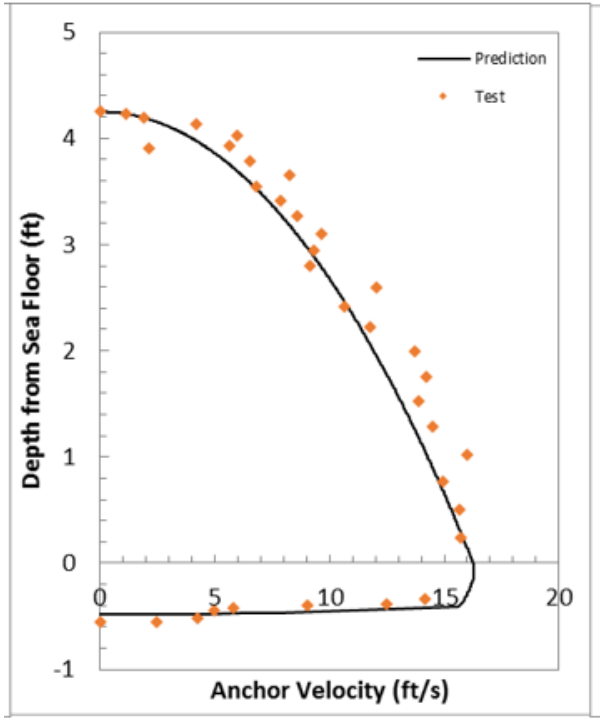

Prediction with R_f in semi-log

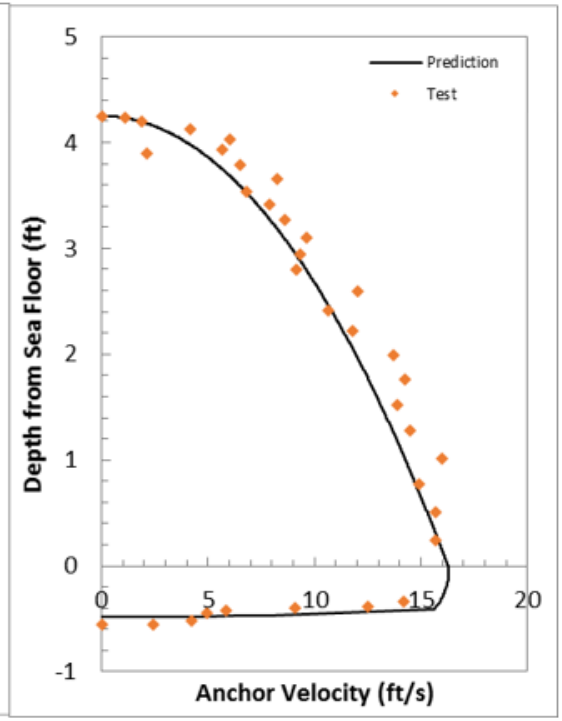

Free-Fall Penetration with Flying Wing Anchor ® in a Single Layer

Drop 6

	Impact v (ft/s)	Embedment D (L_f)	β	λ
Experiment	16.5	2.49	–	–
R_f in Power-Law	14.51	2.17	0.15	–
R_f in Semi-log	14.51	2.18	–	0.35

Prediction with R_f in power-law

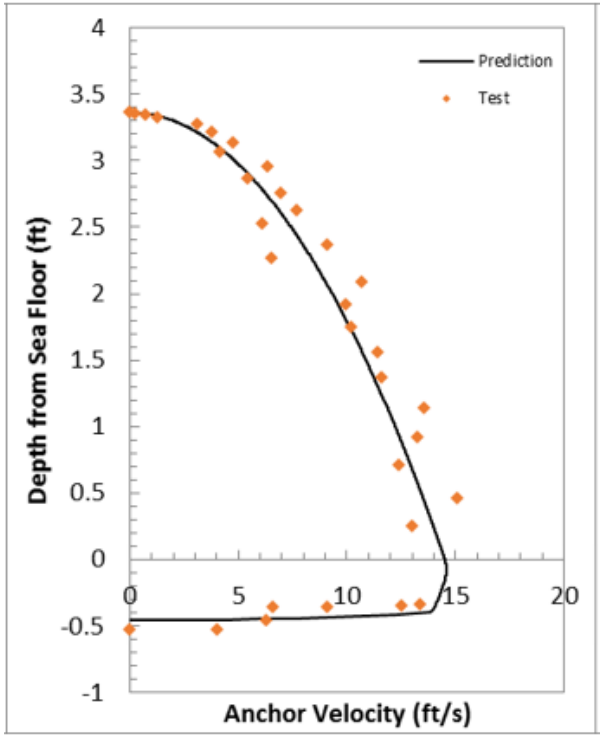

Prediction with R_f in semi-log

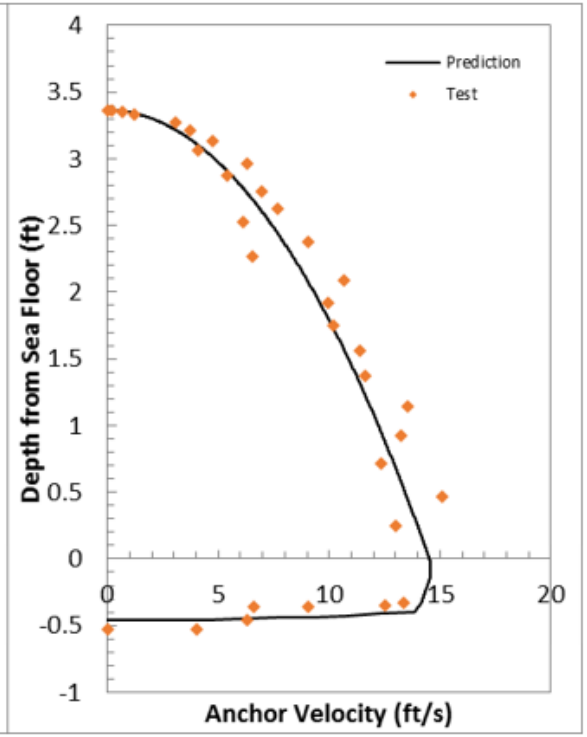

Free-Fall Penetration with Flying Wing Anchor ® in a Single Layer

Drop 7

	Impact v (ft/s)	Embedment D (L_f)	β	λ
Experiment	15.42	2.49	–	–
R_f in Power-Law	14.51	2.21	0.15	–
R_f in Semi-log	14.51	2.22	–	0.35

Prediction with R_f in power-law

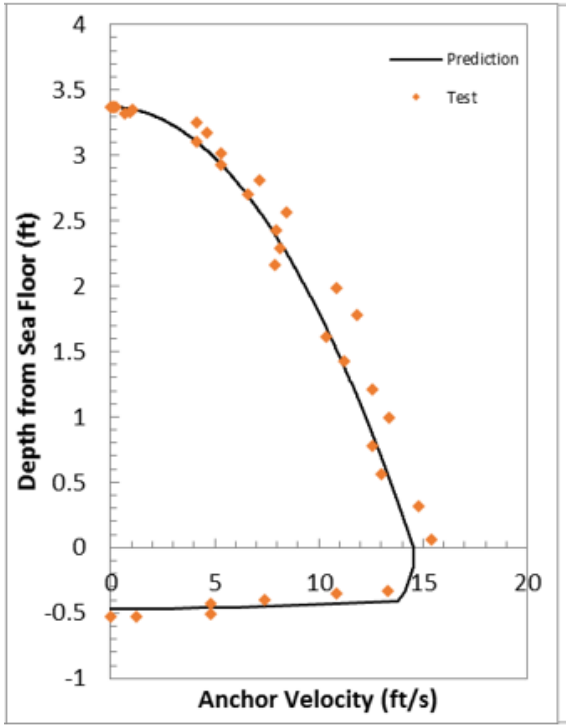

Prediction with R_f in semi-log

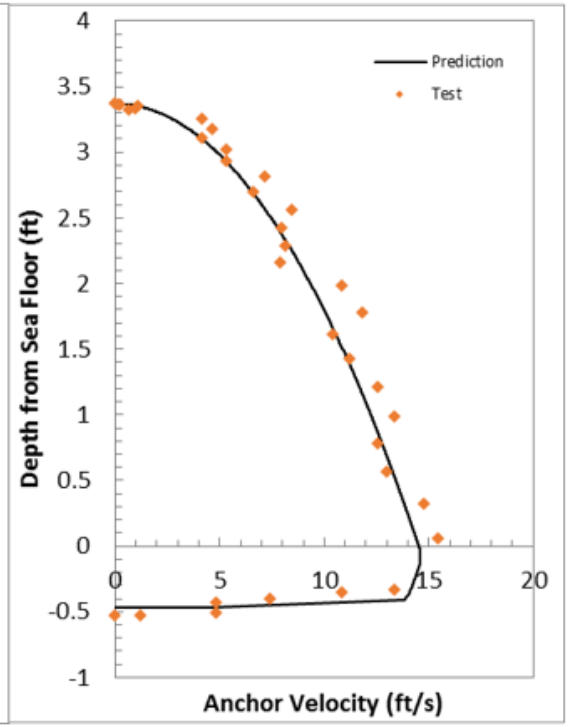

Free-Fall Penetration with Flying Wing Anchor ® in a Single Layer

Drop 8

	Impact v (ft/s)	Embedment D (L_f)	β	λ
Experiment	13.73	2.50	–	–
R_f in Power-Law	14.54	2.16	0.15	–
R_f in Semi-log	14.54	2.17	–	0.35

Prediction with R_f in power-law

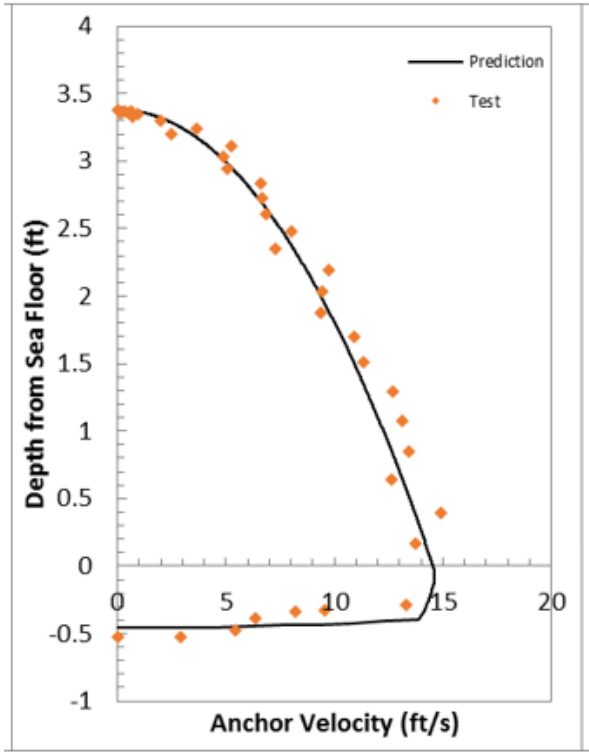

Prediction with R_f in semi-log

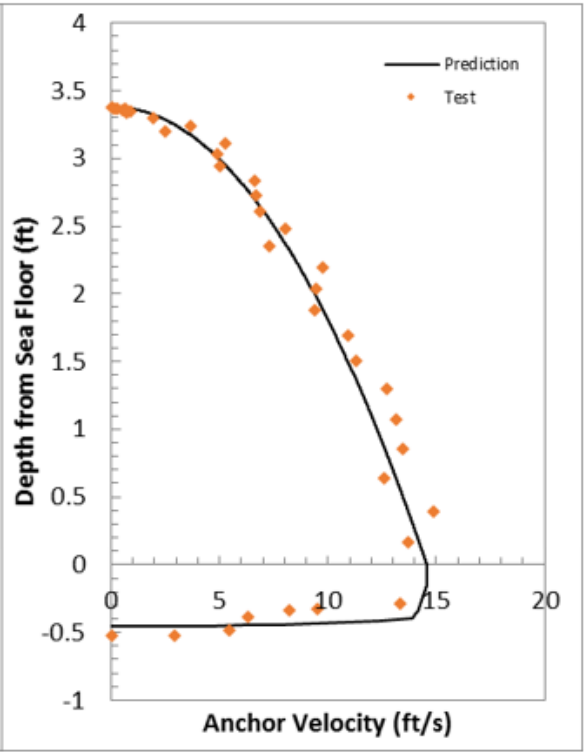

Free-Fall Penetration with Flying Wing Anchor ® in a Single Layer

Drop 9

	Impact v (ft/s)	Embedment D (L_f)	β	λ
Experiment	12.5	2.40	–	–
R_f in Power-Law	12.70	2.11	0.15	–
R_f in Semi-log	12.70	2.12	–	0.35

Prediction with R_f in power-law

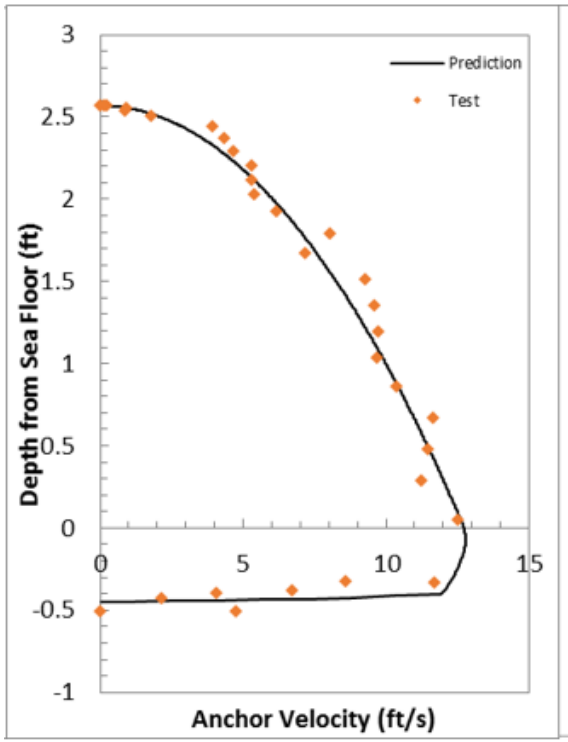

Prediction with R_f in semi-log

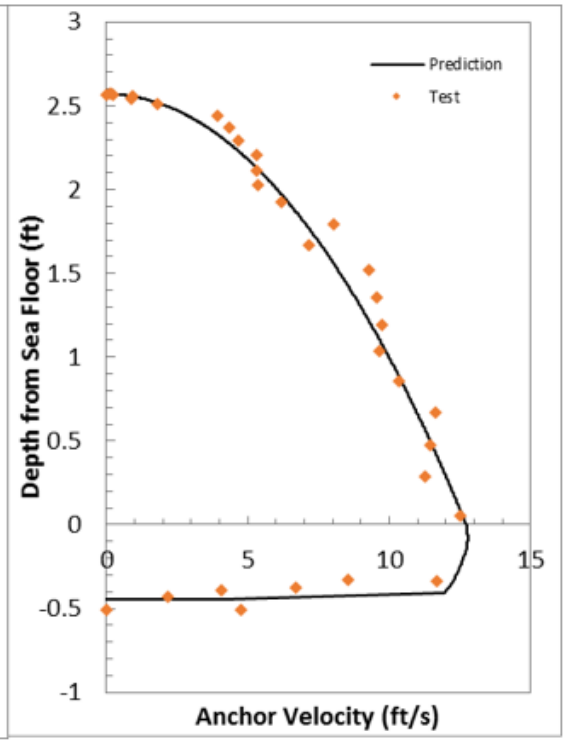

Free-Fall Penetration with Flying Wing Anchor ® in a Single Layer

Drop 10

	Impact v (ft/s)	Embedment D (L_f)	β	λ
Experiment	12.6	2.40	–	–
R_f in Power-Law	12.64	2.11	0.15	–
R_f in Semi-log	12.64	2.12	–	0.35

Prediction with R_f in power-law

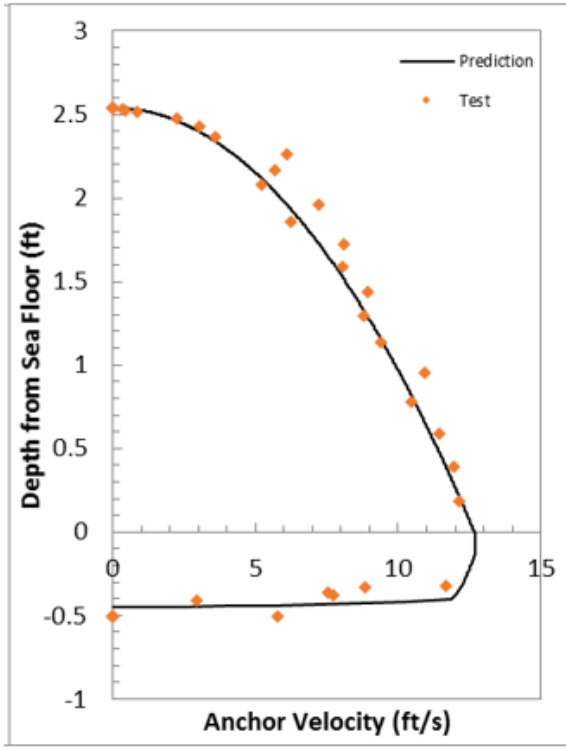

Prediction with R_f in semi-log

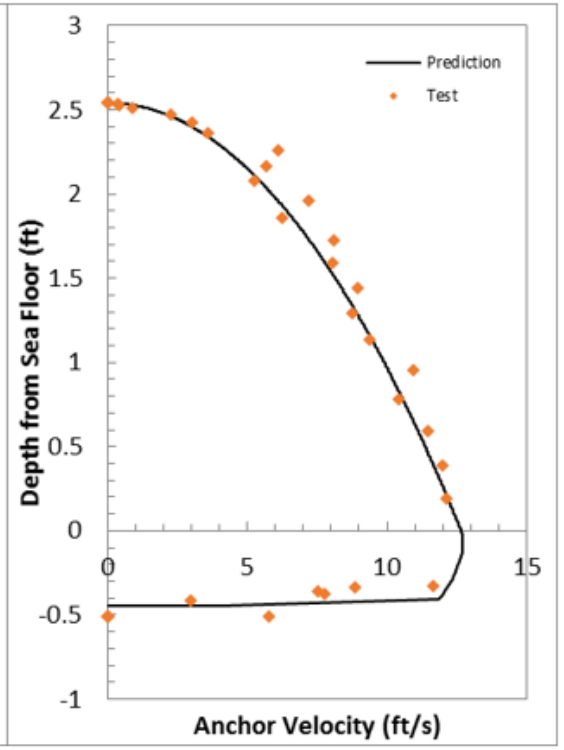

Free-Fall Penetration with Flying Wing Anchor ® in a Single Layer

Drop 11

	Impact v (ft/s)	Embedment D (L_f)	β	λ
Experiment	12.5	2.40	–	–
R_f in Power-Law	12.55	2.10	0.15	–
R_f in Semi-log	12.55	2.11	–	0.35

Prediction with R_f in power-law

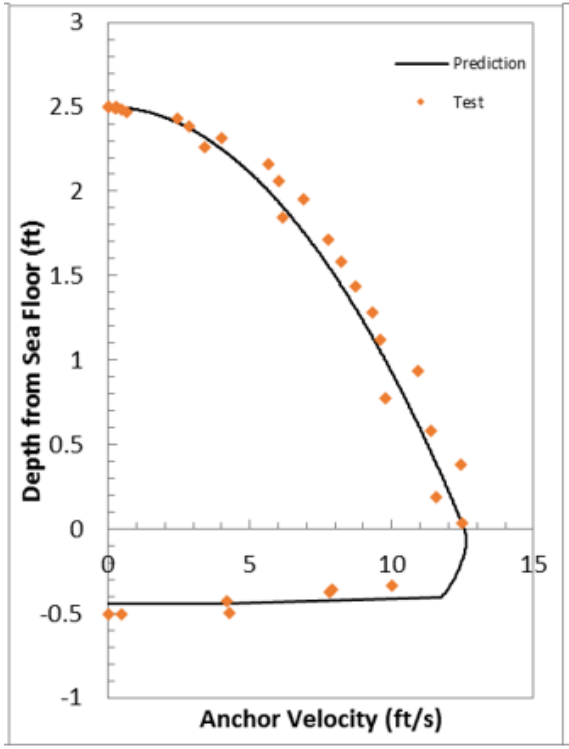

Prediction with R_f in semi-log

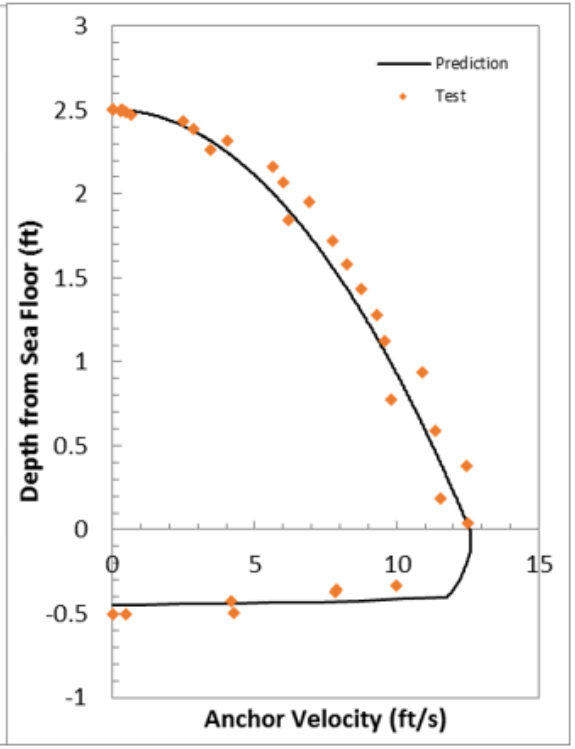

Free-Fall Penetration with Flying Wing Anchor ® in a Single Layer

Drop 12

	Impact v (ft/s)	Embedment D (L_f)	β	λ
Experiment	11.185	2.33	–	–
R_f in Power-Law	10.53	2.03	0.15	–
R_f in Semi-log	10.53	2.03	–	0.35

Prediction with R_f in power-law

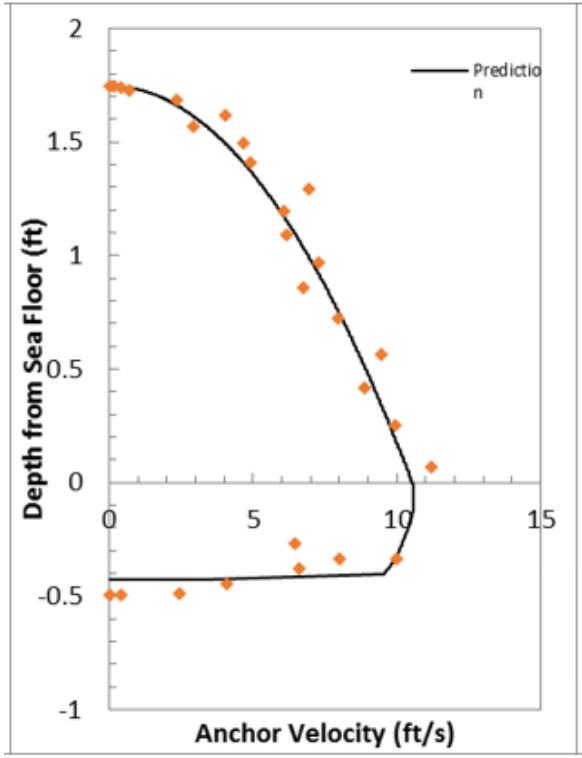

Prediction with R_f in semi-log

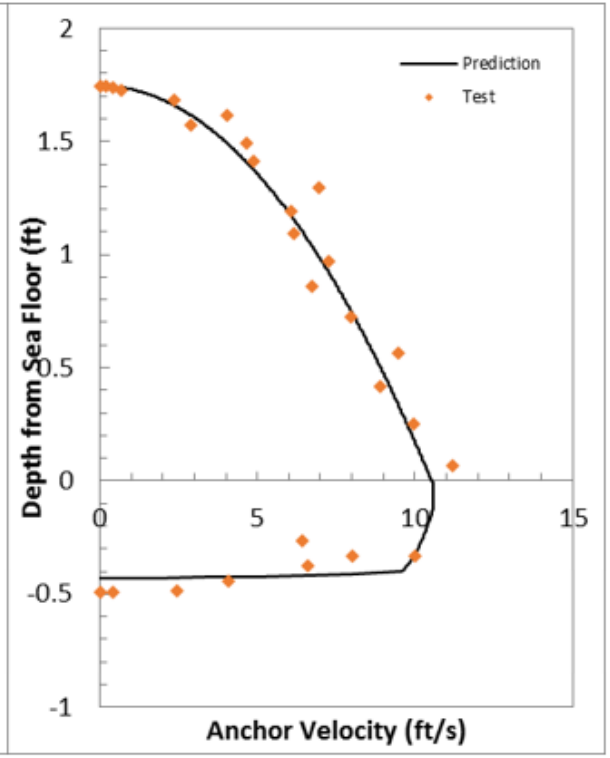

Free-Fall Penetration with Flying Wing Anchor ® in a Single Layer

Drop 13

	Impact v (ft/s)	Embedment D (L_f)	β	λ
Experiment	8.78	2.33	–	–
R_f in Power-Law	10.34	2.04	0.15	–
R_f in Semi-log	10.34	2.05	–	0.35

Prediction with R_f in power-law

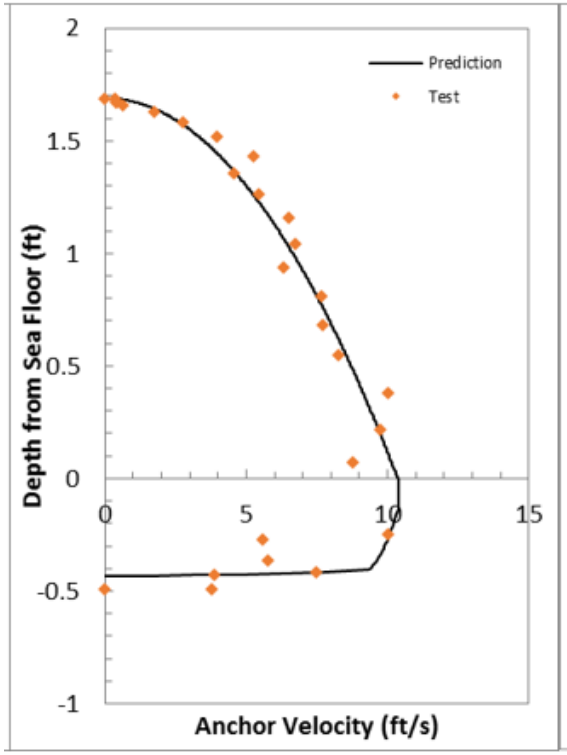

Prediction with R_f in semi-log

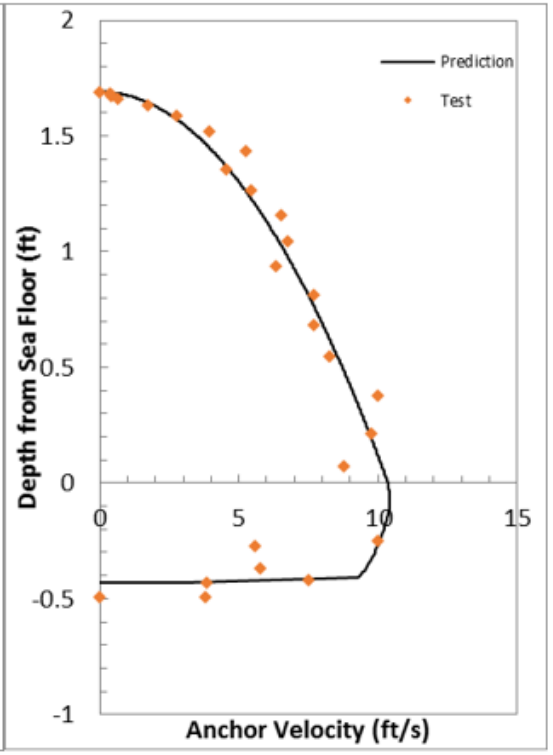

Free-Fall Penetration with Flying Wing Anchor ® in a Single Layer

Drop 14

	Impact v (ft/s)	Embedment D (L_f)	β	λ
Experiment	10	2.33	–	–
R_f in Power-Law	10.21	2.02	0.15	–
R_f in Semi-log	10.21	2.02	–	0.35

Prediction with R_f in power-law

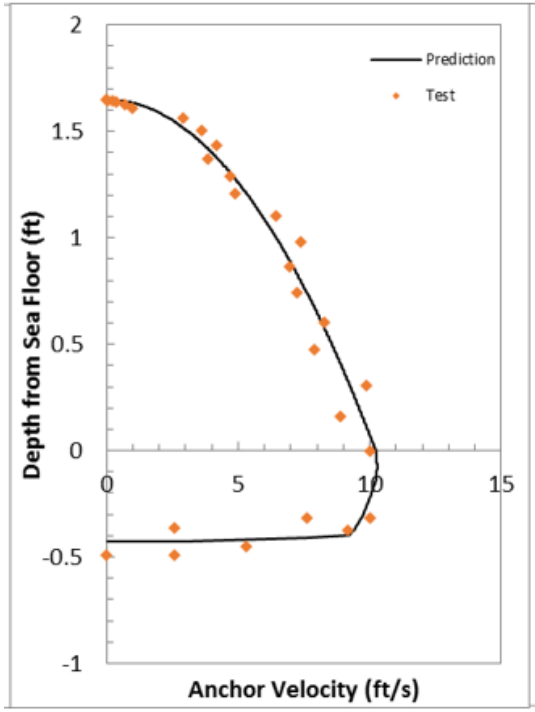

Prediction with R_f in semi-log

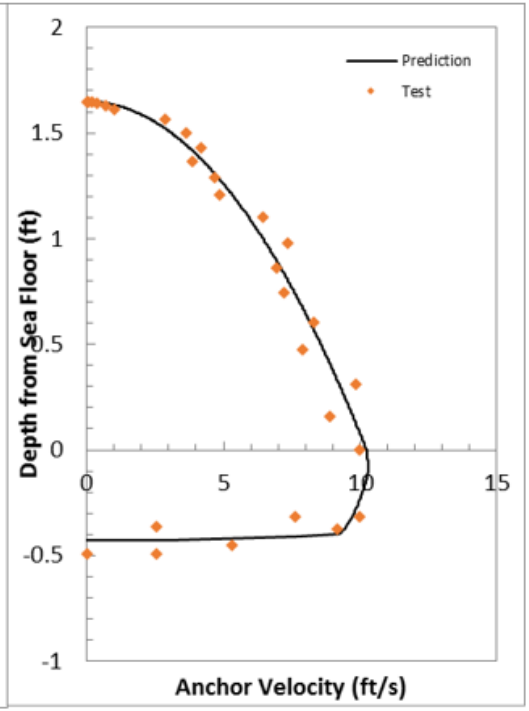

Free-Fall Penetration with Flying Wing Anchor ® in a Single Layer

Drop 17

	Impact v (ft/s)	Embedment D (L_f)	β	λ
Experiment	15.83	2.59	–	–
R_f in Power-Law	15.43	2.20	0.15	–
R_f in Semi-log	15.43	2.21	–	0.35

Prediction with R_f in power-law

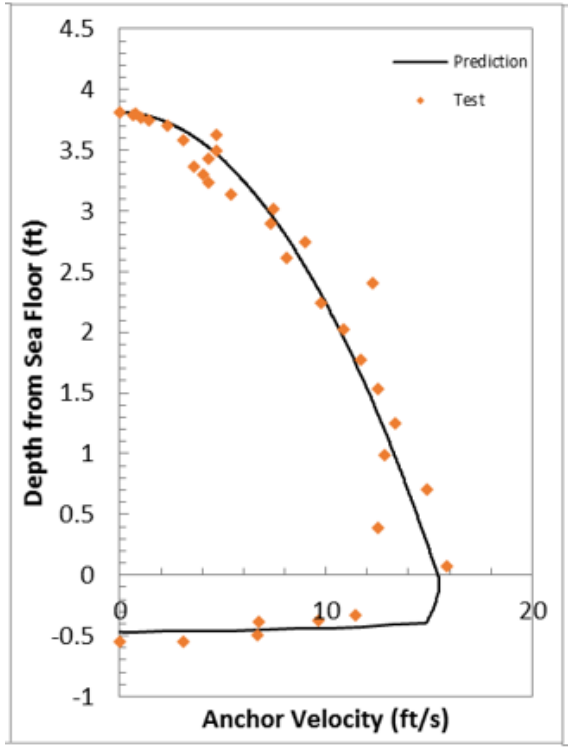

Prediction with R_f in semi-log

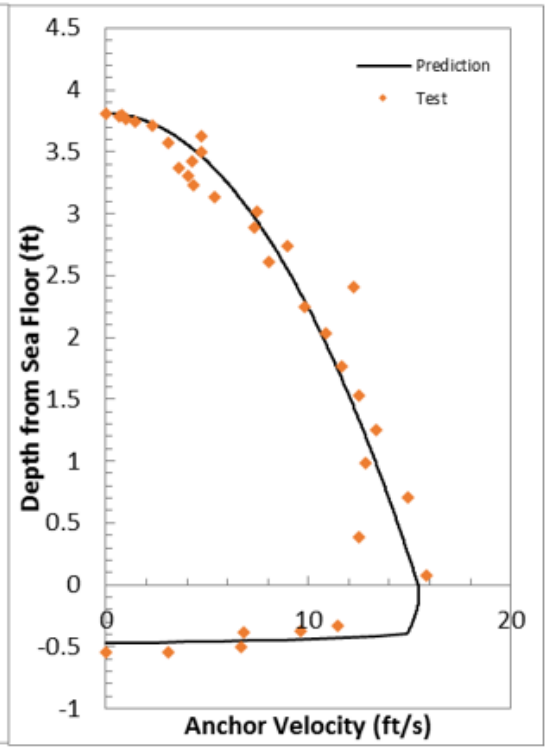

Free-Fall Penetration with Flying Wing Anchor ® in a Single Layer

Drop 18

	Impact v (ft/s)	Embedment D (L_f)	β	λ
Experiment	16.67	1.93	–	–
R_f in Power-Law	15.49	2.26	0.15	–
R_f in Semi-log	15.49	2.23	–	0.35

Prediction with R_f in power-law

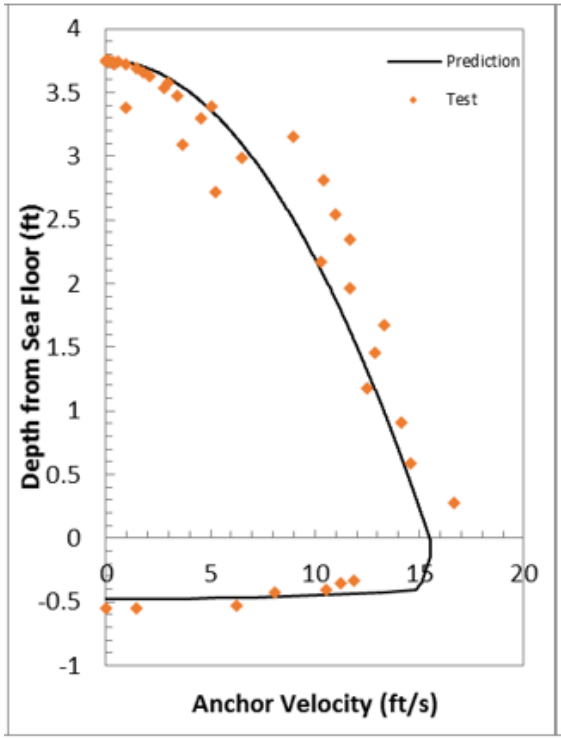

Prediction with R_f in semi-log

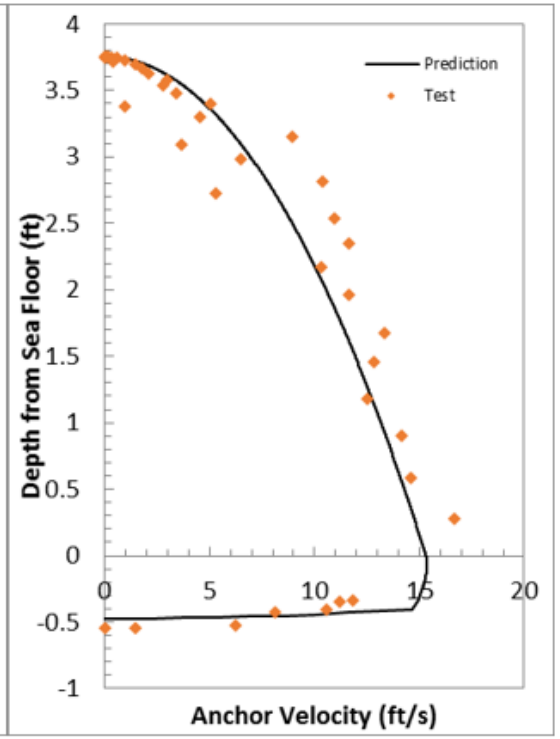

Free-Fall Penetration with Flying Wing Anchor ® in a Single Layer

Drop 19

	Impact v (ft/s)	Embedment D (L_f)	β	λ
Experiment	12.05	2.59	–	–
R_f in Power-Law	15.54	2.23	0.15	–
R_f in Semi-log	15.33	2.24	–	0.35

Prediction with R_f in power-law

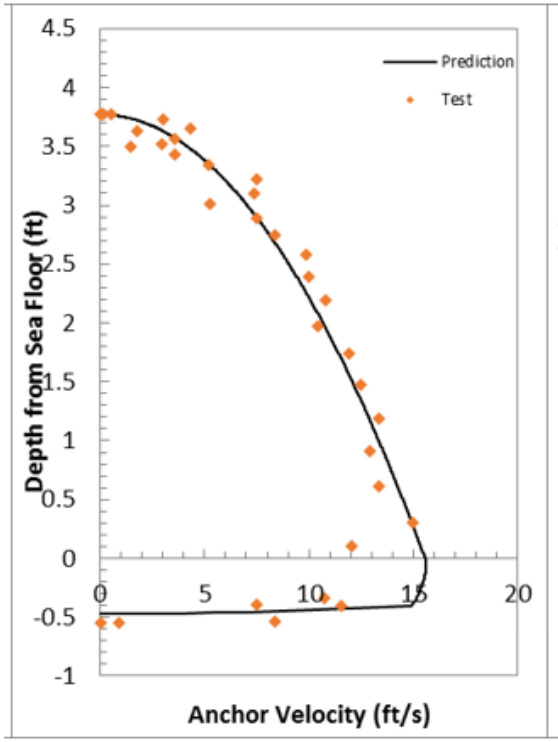

Prediction with R_f in semi-log

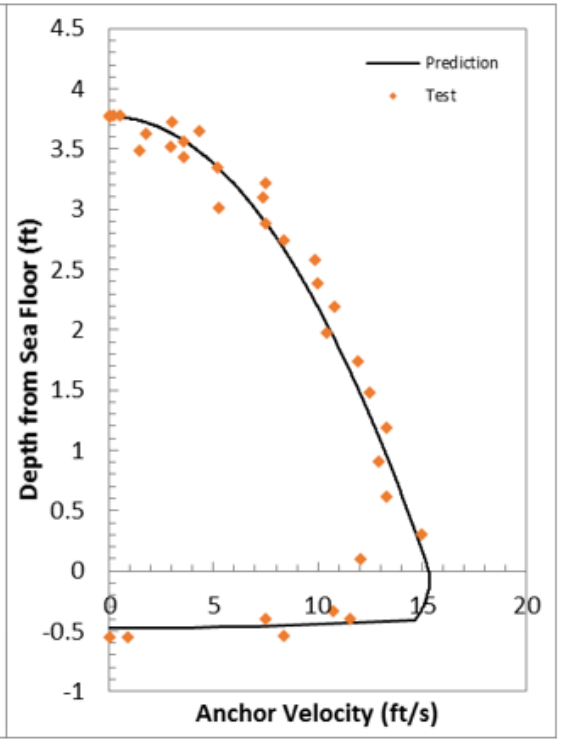

Appendix G. Free-Fall Penetration Tests with Flying Wing Anchor with Different Weight to Area Ratio

Free-Fall Penetration with Flying Wing Anchor ® in a Single Layer

Drop 20

	Impact v (ft/s)	Embedment D (L_f)	β	λ	Weight of Area Ratio = 22.13
Experiment	8.53	7.69	–	–	
R_f in Power-Law	10.40	8.23	0.15	–	
R_f in Semi-log	10.46	8.41	–	0.35	

Prediction with R_f in power-law Prediction with R_f in semi-log

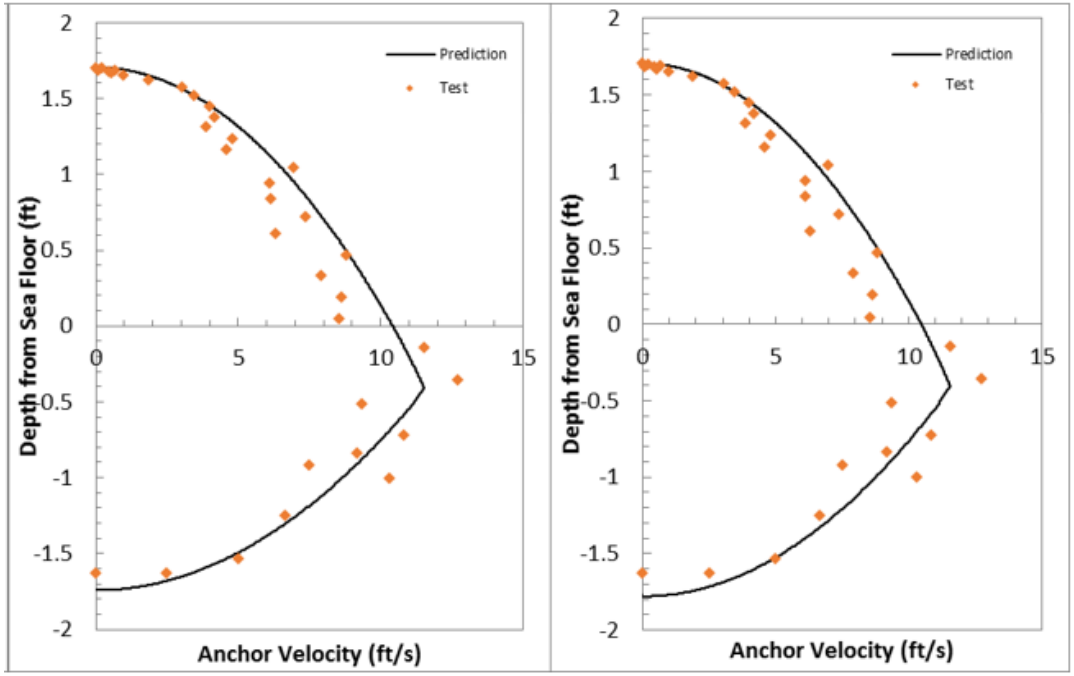

Free-Fall Penetration with Flying Wing Anchor ® in a Single Layer

Drop 21

	Impact v (ft/s)	Embedment D (L_f)	β	λ	Weight of Area Ratio = 22.13
Experiment	12.01	7.89	–	–	
R_f in Power-Law	10.49	8.54	0.15	–	
R_f in Semi-log	10.49	8.47	–	0.35	

Prediction with R_f in power-law

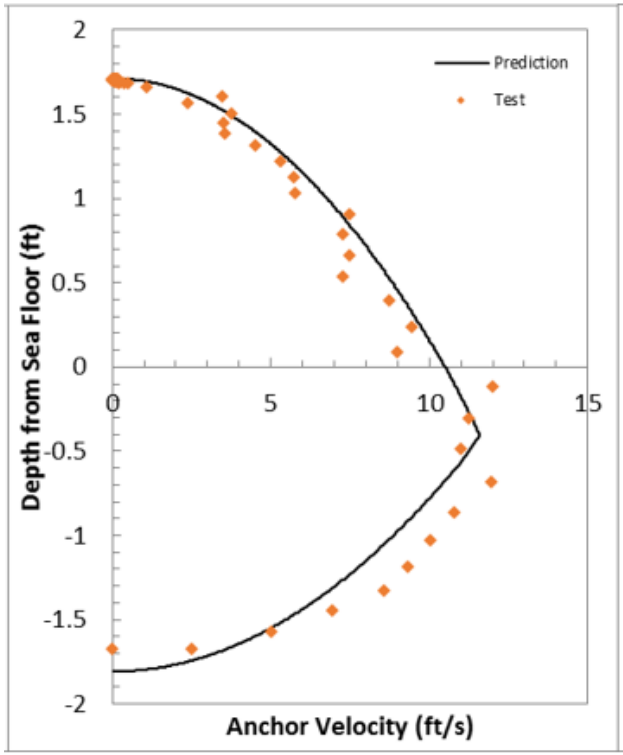

Prediction with R_f in semi-log

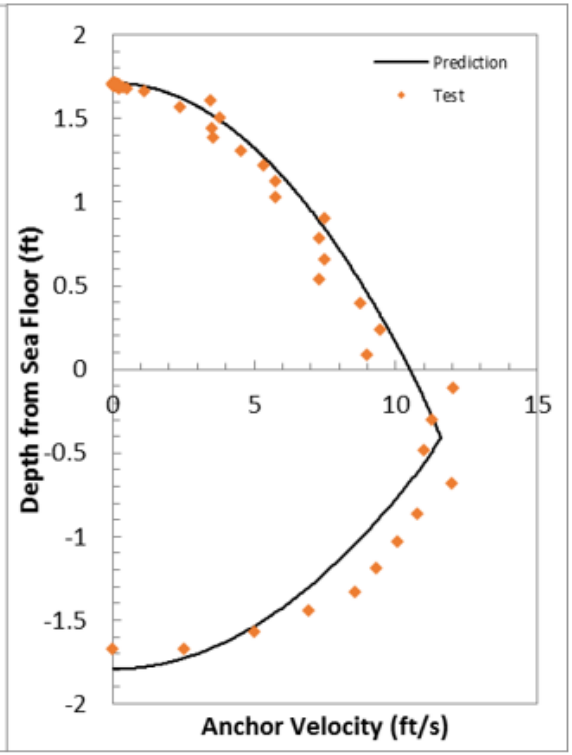

Free-Fall Penetration with Flying Wing Anchor ® in a Single Layer

Drop 22

	Impact v (ft/s)	Embedment D (L_f)	β	λ	Weight of Area Ratio = 22.13
Experiment	8.79	7.81	–	–	
R_f in Power-Law	10.40	8.40	0.15	–	
R_f in Semi-log	10.40	8.33	–	0.35	

Prediction with R_f in power-law

Prediction with R_f in semi-log

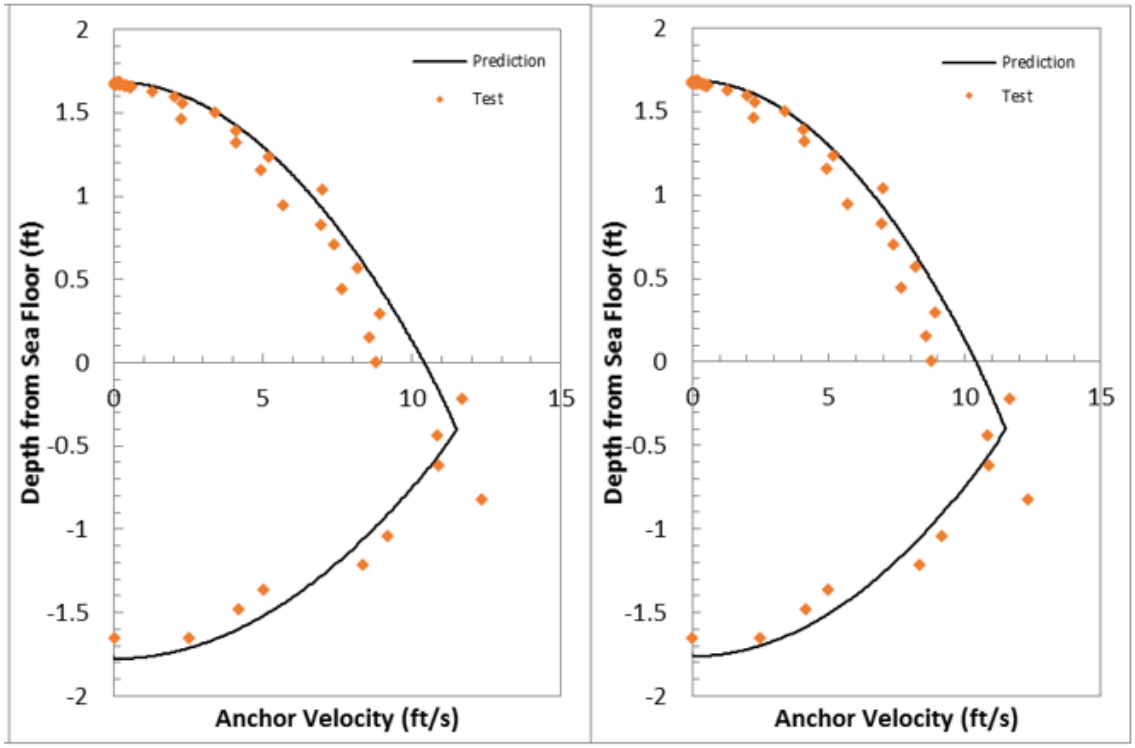

Free-Fall Penetration with Flying Wing Anchor ® in a Single Layer

Drop 23

	Impact v (ft/s)	Embedment D (L_f)	β	λ	Weight of Area Ratio = 9.5
Experiment	7.82	3.86	–	–	
R_f in Power-Law	10.49	3.94	0.15	–	
R_f in Semi-log	10.49	3.92	–	0.35	

Prediction with R_f in power-law

Prediction with R_f in semi-log

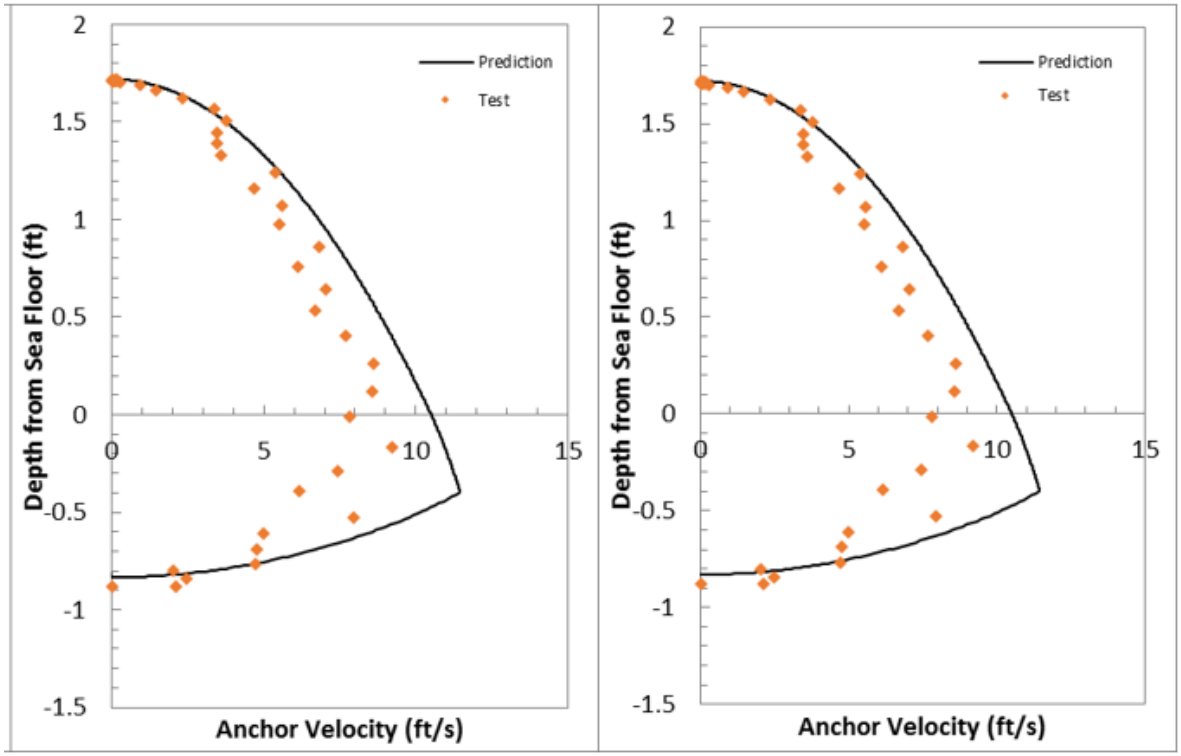

Free-Fall Penetration with Flying Wing Anchor ® in a Single Layer

Drop 24

	Impact v (ft/s)	Embedment D (L_f)	β	λ	Weight of Area Ratio = 9.5
Experiment	7.53	4.35	–	–	
R_f in Power-Law	10.52	3.95	0.15	–	
R_f in Semi-log	10.52	3.94	–	0.35	

Prediction with R_f in power-law

Prediction with R_f in semi-log

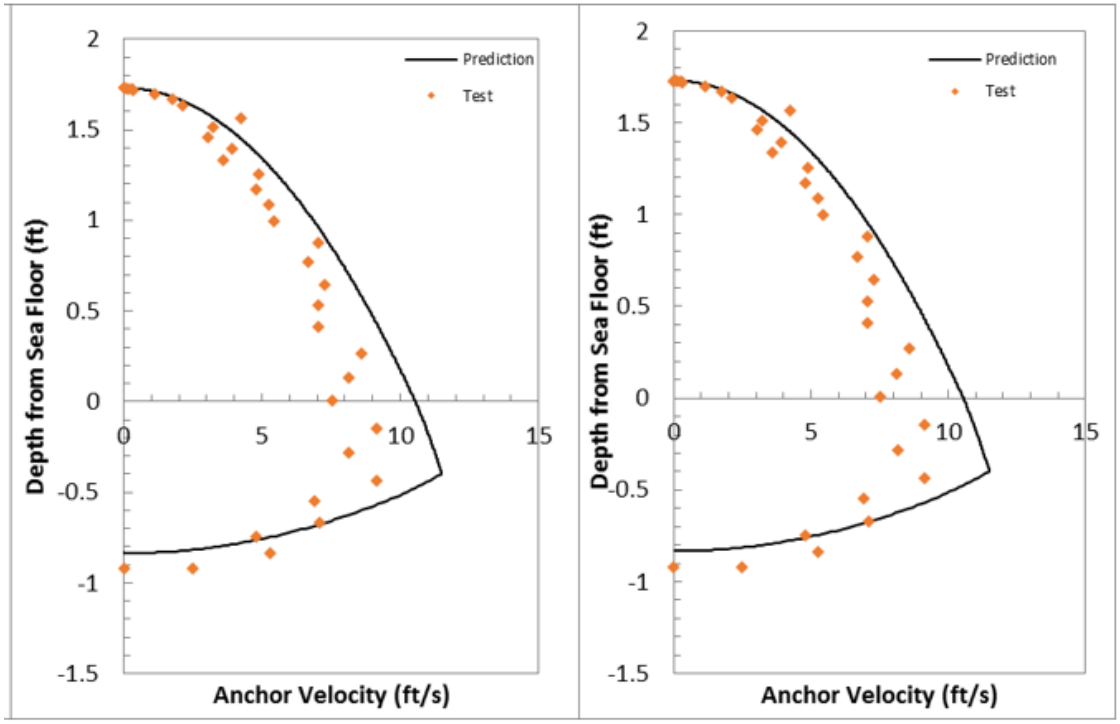

Free-Fall Penetration with Flying Wing Anchor ® in a Single Layer

Drop 25

	Impact v (ft/s)	Embedment D (L_f)	β	λ	Weight of Area Ratio = 9.5
Experiment	8.81	4.30	–	–	
R_f in Power-Law	10.42	3.93	0.15	–	
R_f in Semi-log	10.42	3.91	–	0.35	

Prediction with R_f in power-law

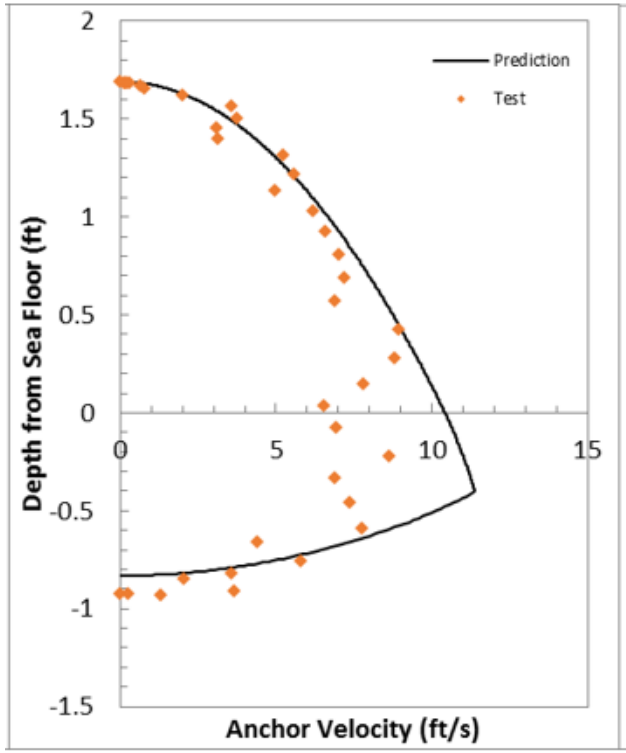

Prediction with R_f in semi-log

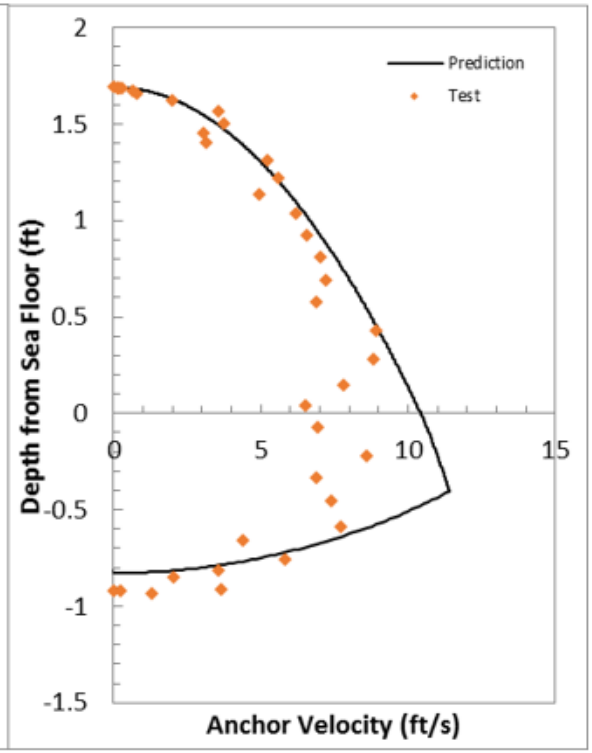

Free-Fall Penetration with Flying Wing Anchor ® in a Single Layer

Drop 26

	Impact v (ft/s)	Embedment D (L_f)	β	λ	Weight of Area Ratio = 6.32
Experiment	7.07	3.36	–	–	
R_f in Power-Law	10.48	3.17	0.15	–	
R_f in Semi-log	10.48	3.16	–	0.35	

Prediction with R_f in power-law

Prediction with R_f in semi-log

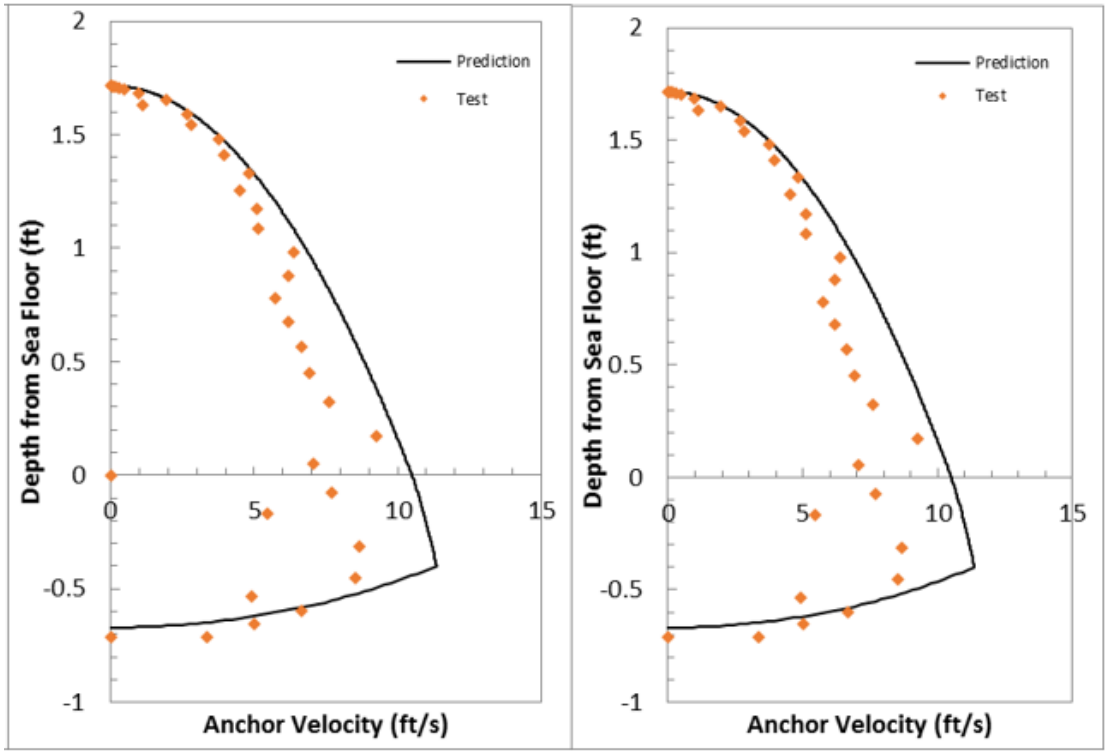

Free-Fall Penetration with Flying Wing Anchor ® in a Single Layer

Drop 27

	Impact v (ft/s)	Embedment D (L_f)	β	λ	Weight of Area Ratio = 6.3
Experiment	7.71	3.37	–	–	
R_f in Power-Law	10.58	3.21	0.15	–	
R_f in Semi-log	10.58	3.20	–	0.35	

Prediction with R_f in power-law Prediction with R_f in semi-log

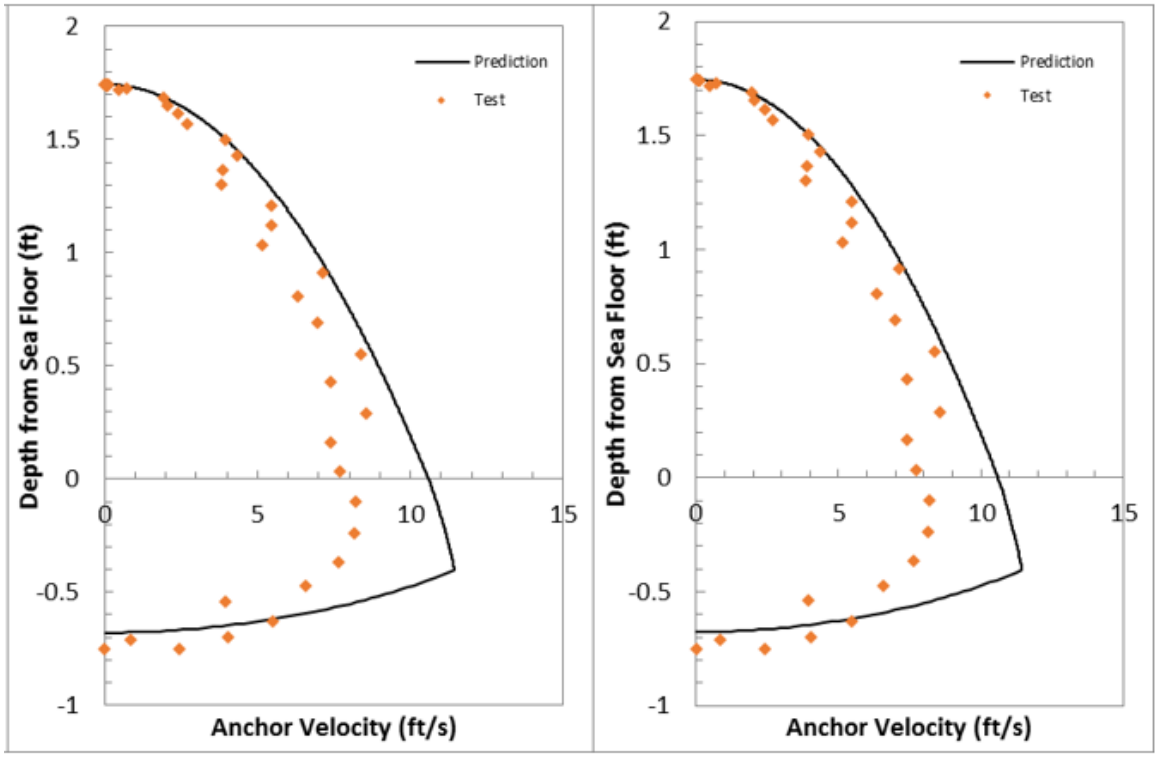

Free-Fall Penetration with Flying Wing Anchor ® in a Single Layer

Drop 28

	Impact v (ft/s)	Embedment D (L_f)	β	λ	Weight of Area Ratio = 6.3
Experiment	7.57	3.56	–	–	
R_f in Power-Law	10.42	3.16	0.15	–	
R_f in Semi-log	10.42	3.15	–	0.35	

Prediction with R_f in power-law

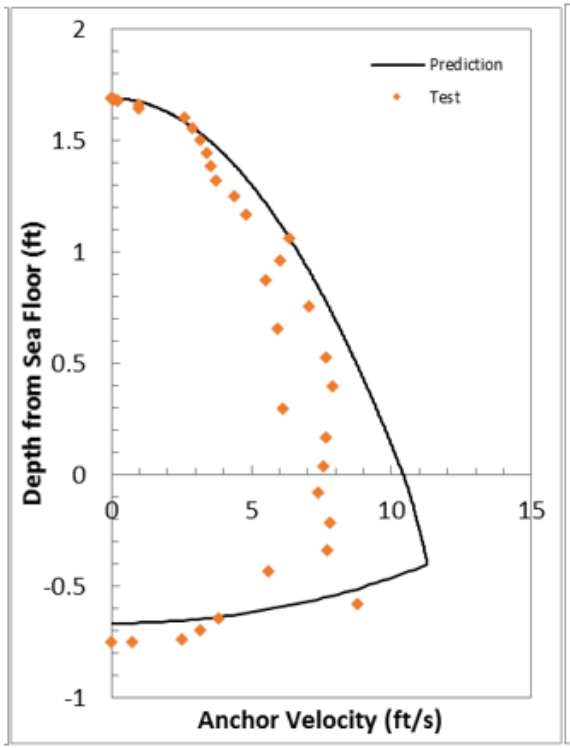

Prediction with R_f in semi-log

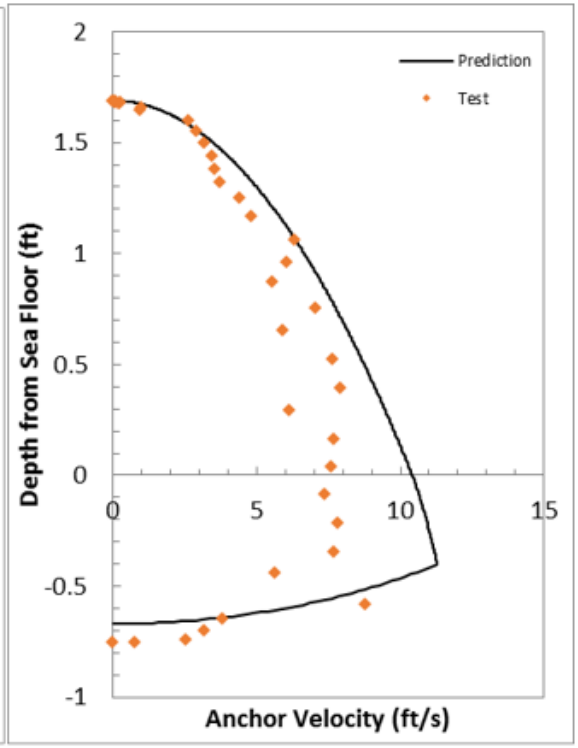

Appendix H. Free-Fall Penetration Tests with Flying Wing Anchor® in Layered Soil Profiles

Free-Fall Penetration with Flying Wing Anchor ® in Case 1 Layered Soil

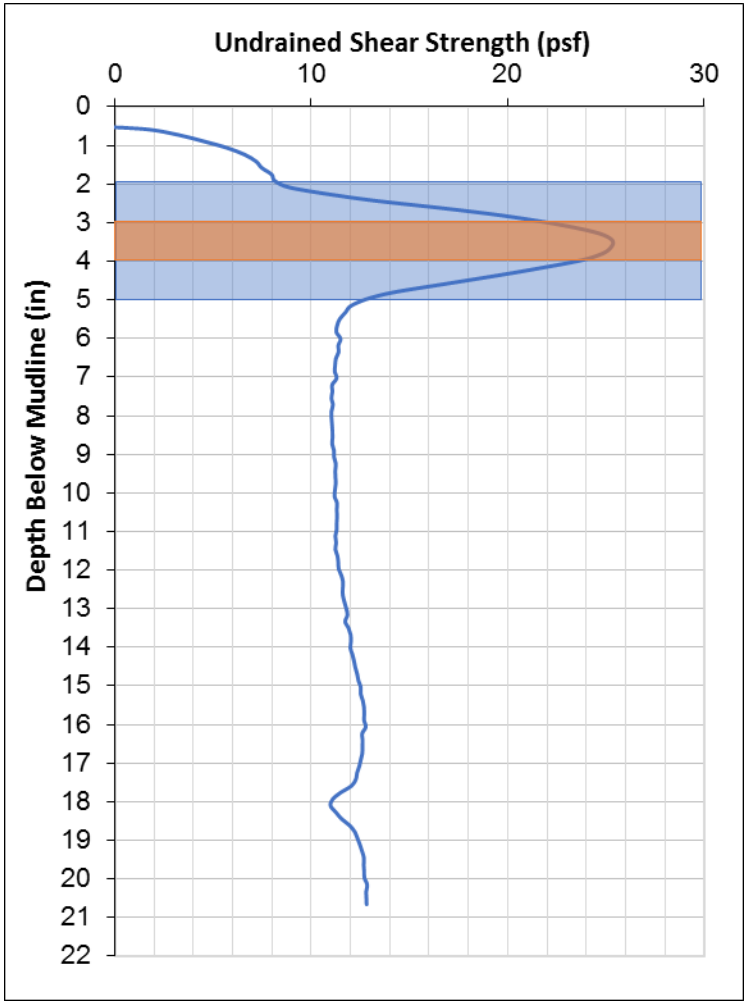

Free-Fall Penetration with Flying Wing Anchor ® in Case 1 Layered Soil

Drop 1

	Impact v (ft/s)	Embedment D (L_f)	β	λ
Experiment	15.2	2..93	–	–
R_f in Power-Law	14.42	2.01	0.15	–
R_f in Semi-log	13.86	2.01	–	0.35

Prediction with R_f in power-law

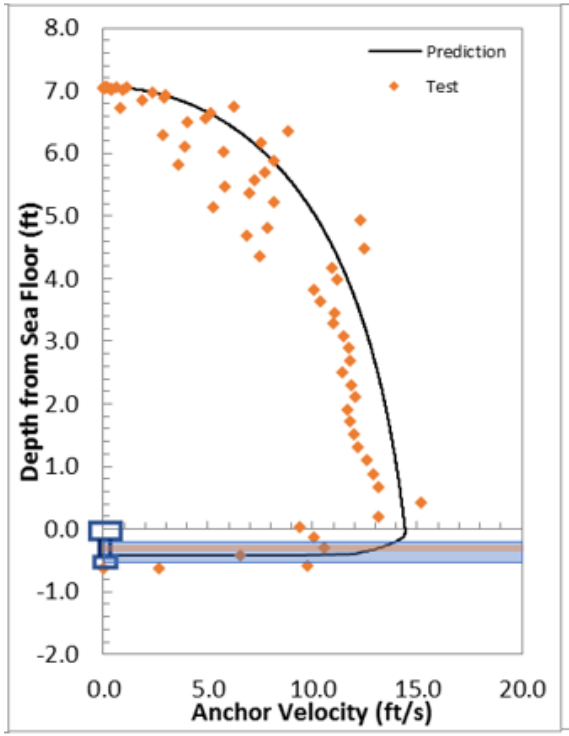

Prediction with R_f in semi-log

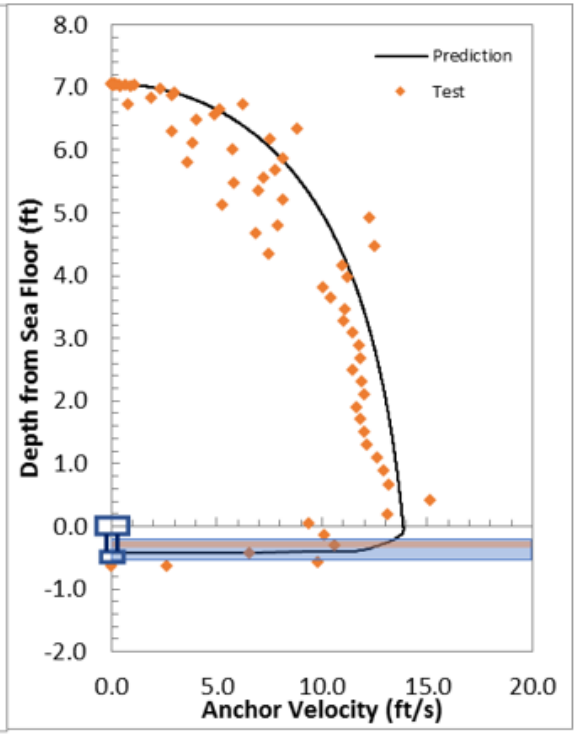

Free-Fall Penetration with Flying Wing Anchor ® in Case 1 Layered Soil

Repeat Test of Drop 1

	Impact v (ft/s)	Embedment D (L_f)	β	λ
Experiment	15.41	2.95	–	–
R_f in Power-Law	15.41	2.03	0.15	–
R_f in Semi-log	15.41	2.07	–	0.35

Prediction with R_f in power-law

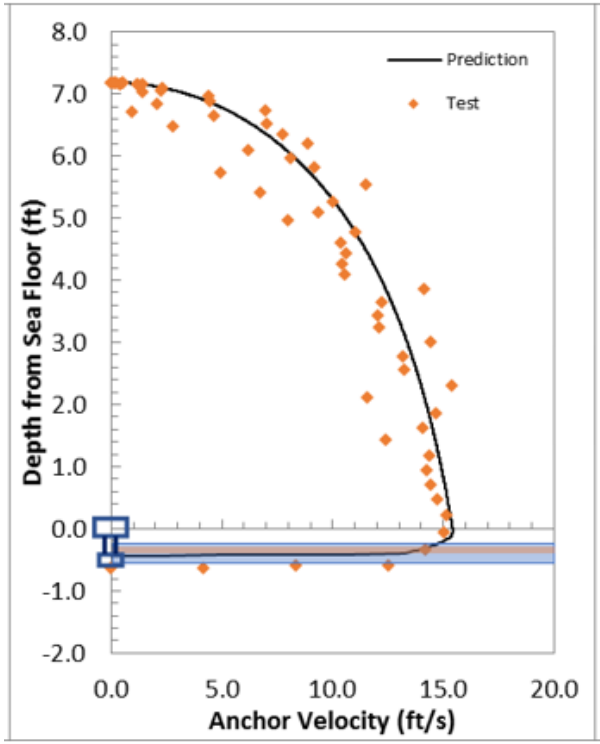

Prediction with R_f in semi-log

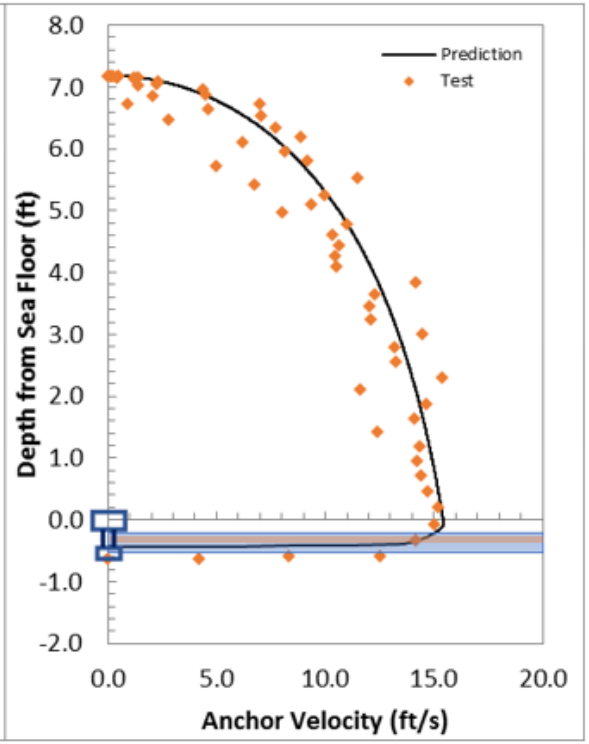

Free-Fall Penetration with Flying Wing Anchor ® in Case 1 Layered Soil

Drop 2

	Impact v (ft/s)	Embedment D (L_f)	β	λ
Experiment	12.5	1.89	–	–
R_f in Power-Law	13.58	2.04	0.15	–
R_f in Semi-log	13.58	2.04	–	0.35

Prediction with R_f in power-law

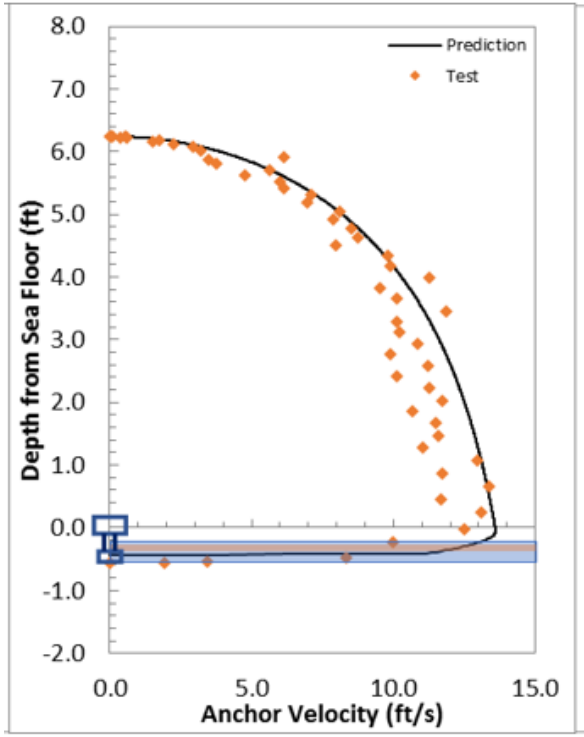

Prediction with R_f in semi-log

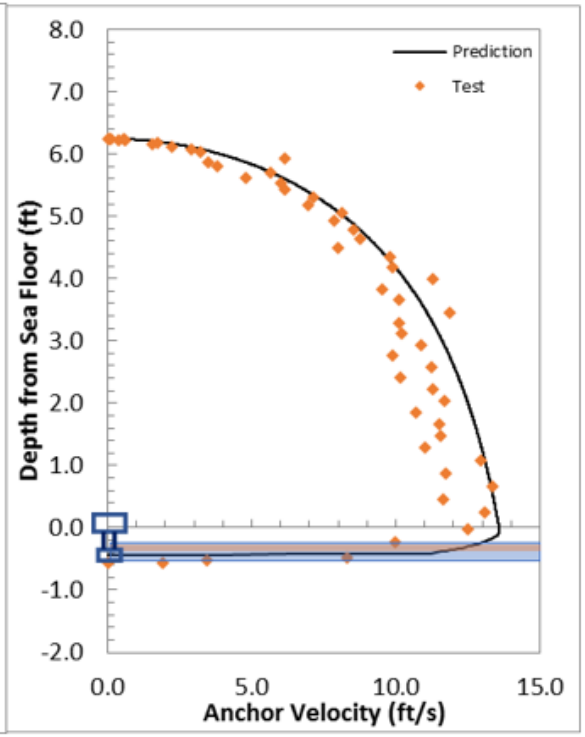

Free-Fall Penetration with Flying Wing Anchor ® in Case 1 Layered Soil

First Repeat in Drop 2

	Impact v (ft/s)	Embedment D (L_f)	β	λ
Experiment	15.79	2.86	–	–
R_f in Power-Law	15.79	2.06	0.15	–
R_f in Semi-log	15.79	2.07	–	0.35

Prediction with R_f in power-law

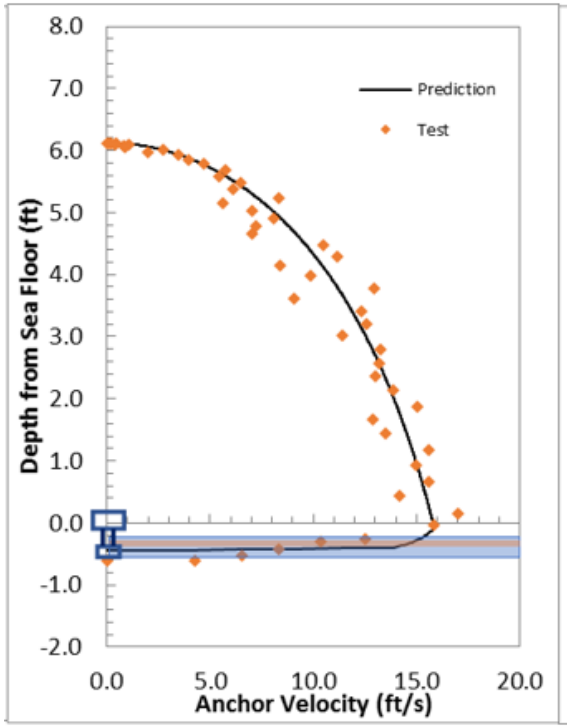

Prediction with R_f in semi-log

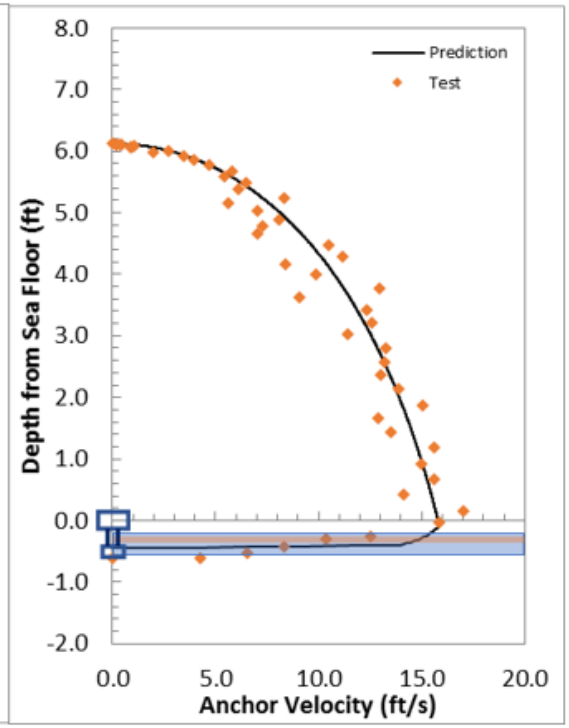

Free-Fall Penetration with Flying Wing Anchor ® in Case 1 Layered Soil

Second Repeat in Drop 2

	Impact v (ft/s)	Embedment D (L_f)	β	λ
Experiment	15.96	2.05	–	–
R_f in Power-Law	15.96	2.07	0.15	–
R_f in Semi-log	15.96	2.07	–	0.35

Prediction with R_f in power-law

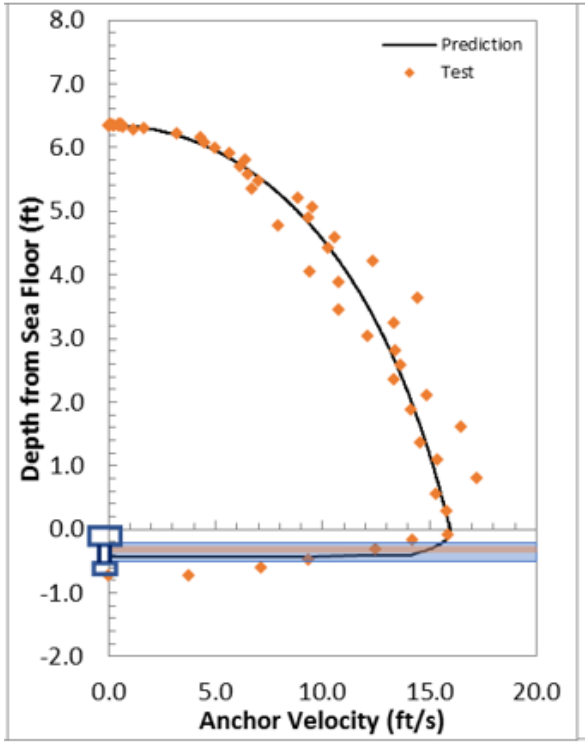

Prediction with R_f in semi-log

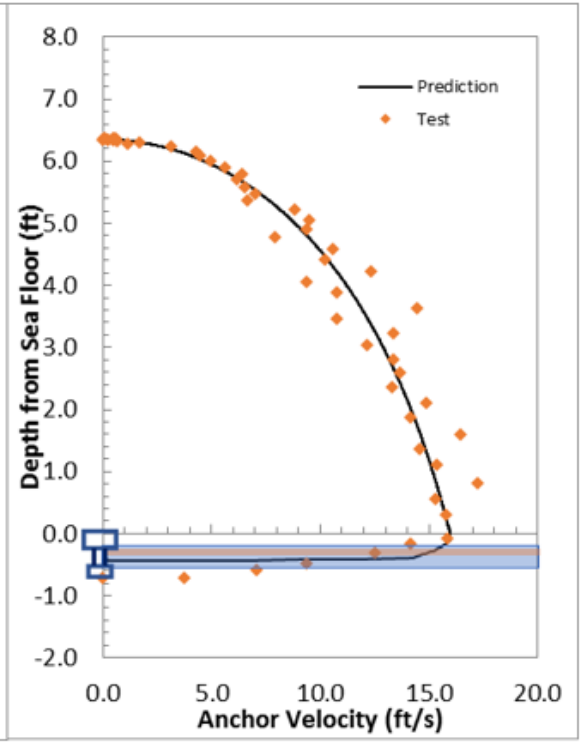

Free-Fall Penetration with Flying Wing Anchor ® in Case 1 Layered Soil

Third Repeat in Drop 2

	Impact v (ft/s)	Embedment D (L_f)	β	λ
Experiment	17.75	1.75	–	–
R_f in Power-Law	16.18	2.09	0.15	–
R_f in Semi-log	16.18	2.10	–	0.35

Prediction with R_f in power-law

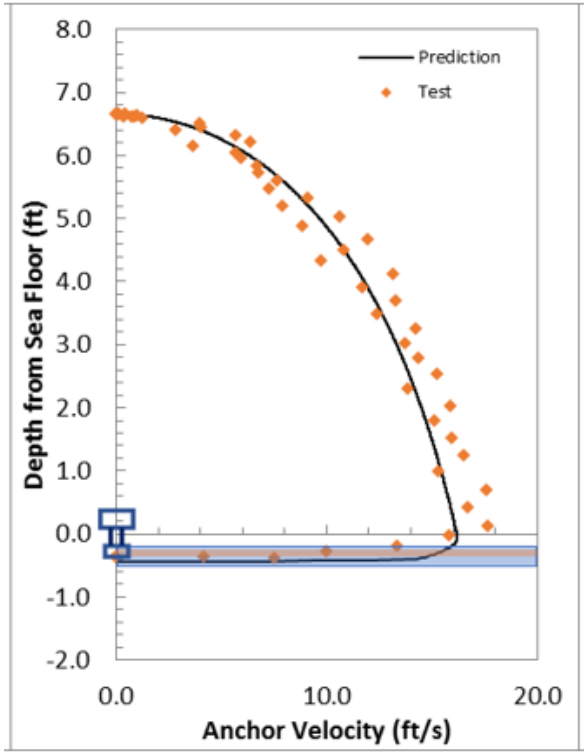

Prediction with R_f in semi-log

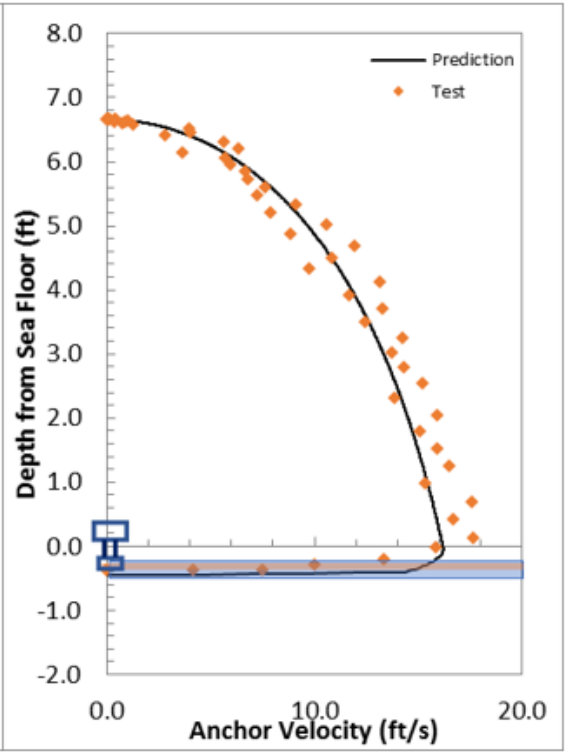

Free-Fall Penetration with Flying Wing Anchor ® in Case 1 Layered Soil

Drop 3

	Impact v (ft/s)	Embedment D (L_f)	β	λ
Experiment	14.17	1.90	–	–
R_f in Power-Law	14.46	1.90	0.15	–
R_f in Semi-log	14.46	1.96	–	0.35

Prediction with R_f in power-law

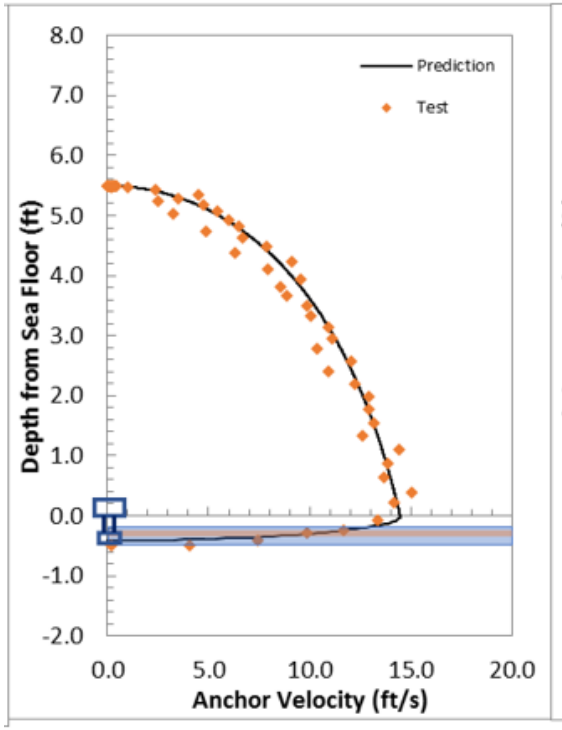

Prediction with R_f in semi-log

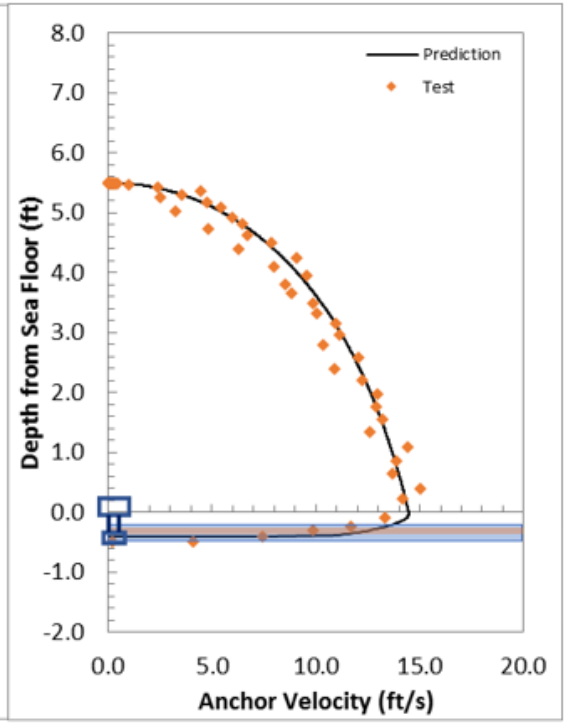

Free-Fall Penetration with Flying Wing Anchor ® in Case 1 Layered Soil

Repeat in Drop 3

	Impact v (ft/s)	Embedment D (L_f)	β	λ
Experiment	15.00	2.08	–	–
R_f in Power-Law	15.43	2.09	0.15	–
R_f in Semi-log	15.43	2.10	–	0.35

Prediction with R_f in power-law

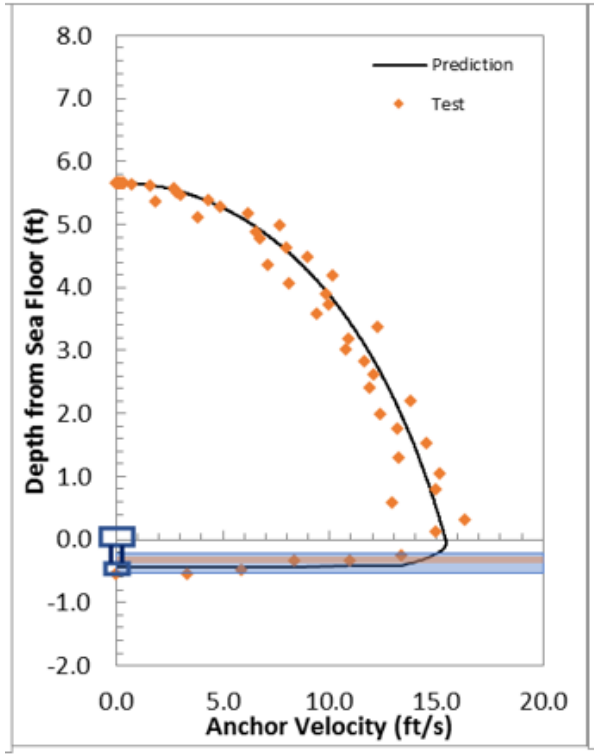

Prediction with R_f in semi-log

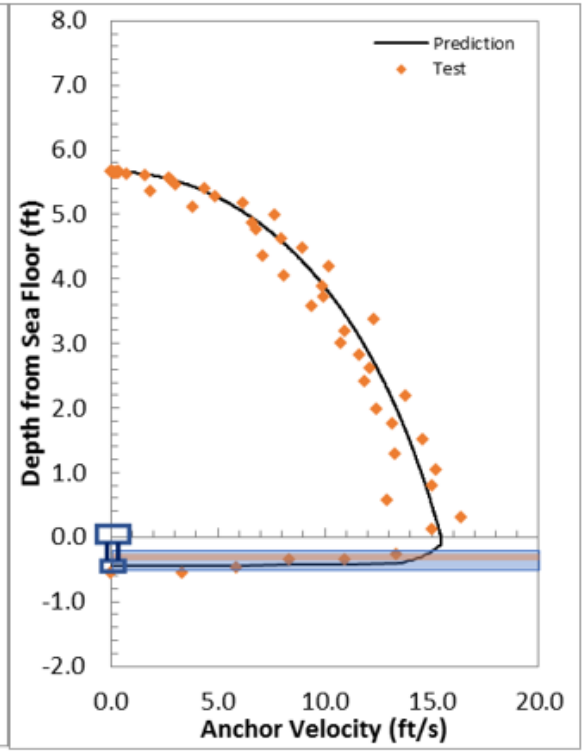

Free-Fall Penetration with Flying Wing Anchor ® in Case 2 Layered Soil

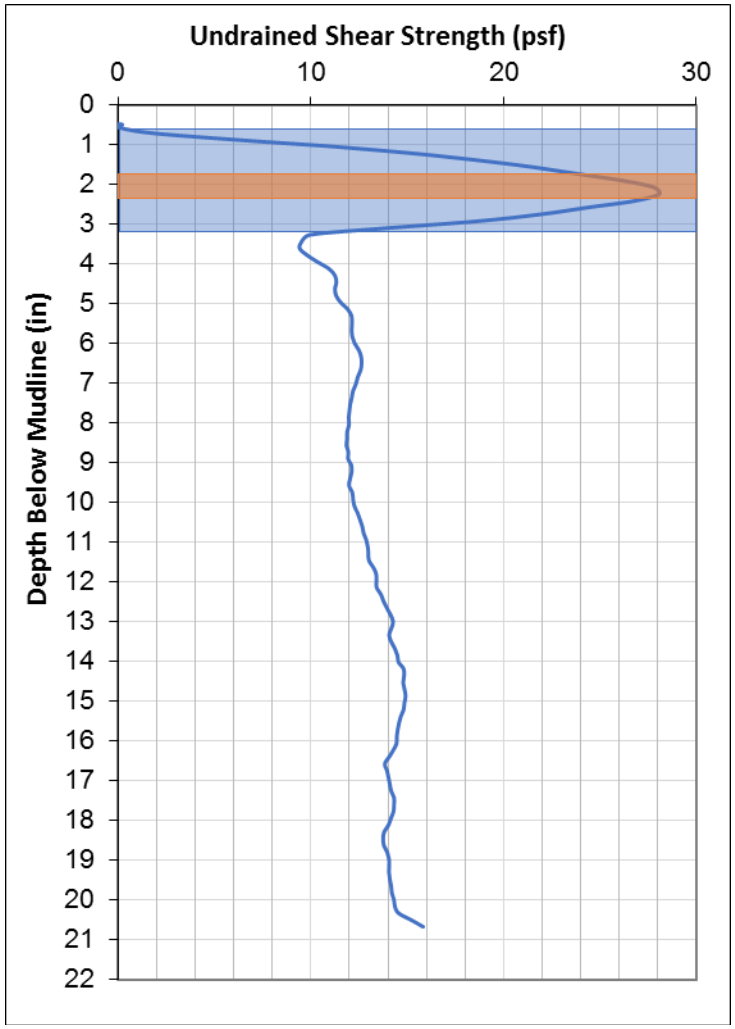

Free-Fall Penetration with Flying Wing Anchor ® in Case 2 Layered Soil

Drop 1

	Impact v (ft/s)	Embedment D (L_f)	β	λ
Experiment	18.87	1.91	–	–
R_f in Power-Law	17.81	1.95	0.15	–
R_f in Semi-log	17.81	2.11	–	0.35

Prediction with R_f in power-law

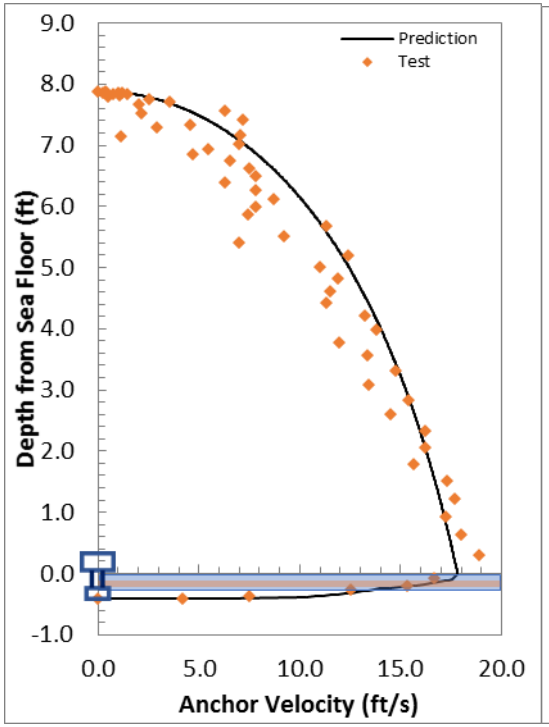

Prediction with R_f in semi-log

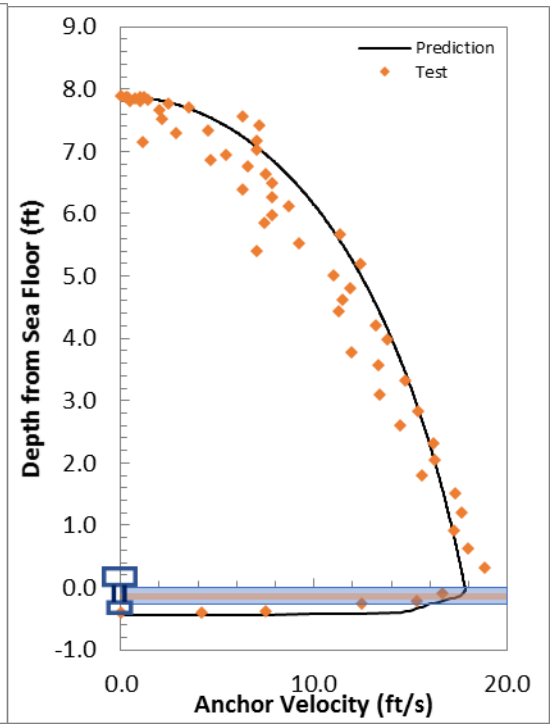

Free-Fall Penetration with Flying Wing Anchor ® in Case 2 Layered Soil

Repeat Test of Drop 1

	Impact v (ft/s)	Embedment D (L_f)	β	λ
Experiment	17.81	2.08	–	–
R_f in Power-Law	17.81	1.94	0.15	–
R_f in Semi-log	17.81	2.10	–	0.35

Prediction with R_f in power-law

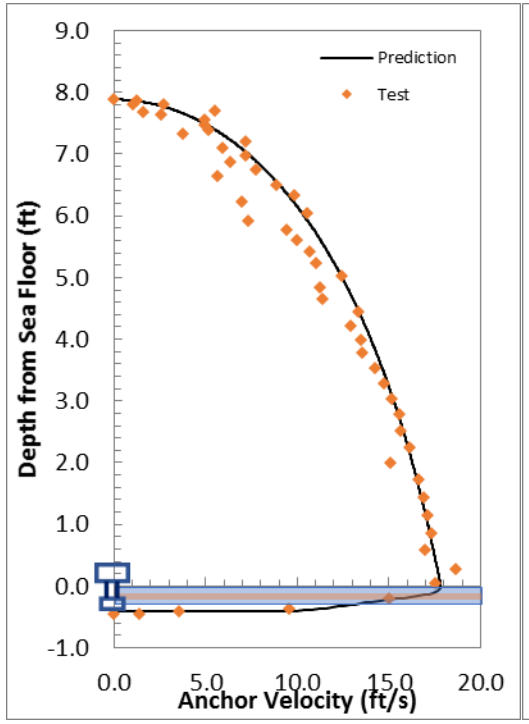

Prediction with R_f in semi-log

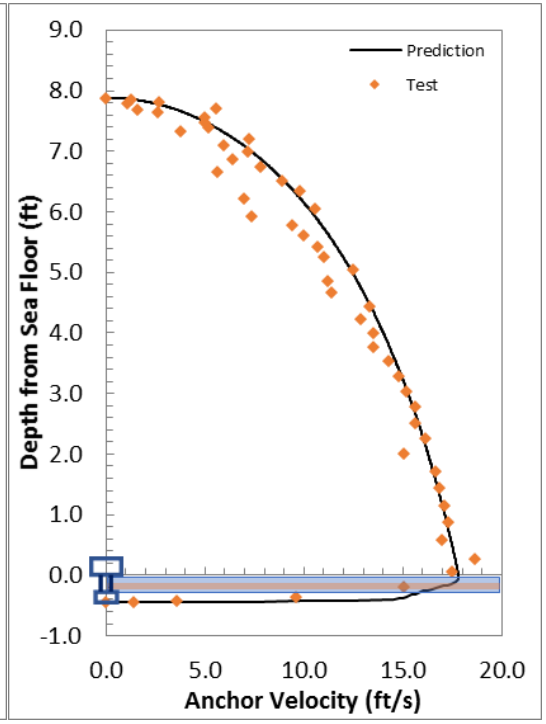

Free-Fall Penetration with Flying Wing Anchor ® in Case 2 Layered Soil

Drop 2

	Impact v (ft/s)	Embedment D (L_f)	β	λ
Experiment	17.93	1.86	–	–
R_f in Power-Law	17.14	1.93	0.15	–
R_f in Semi-log	17.14	2.12	–	0.35

Prediction with R_f in power-law

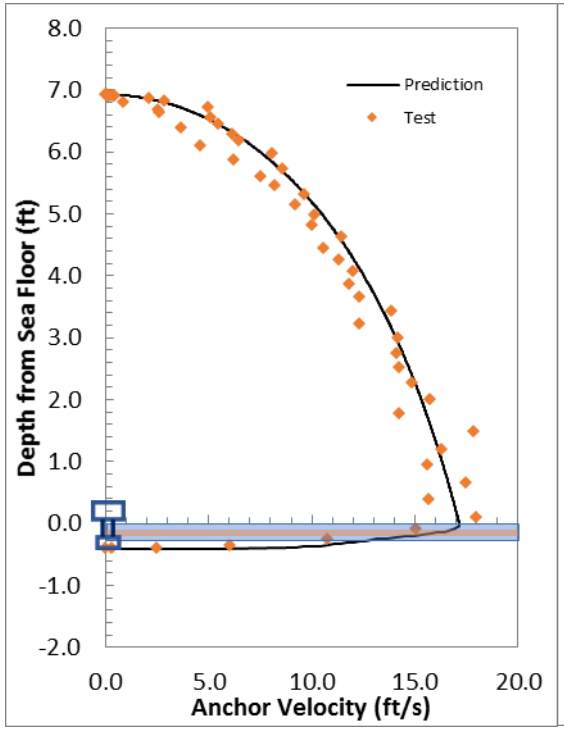

Prediction with R_f in semi-log

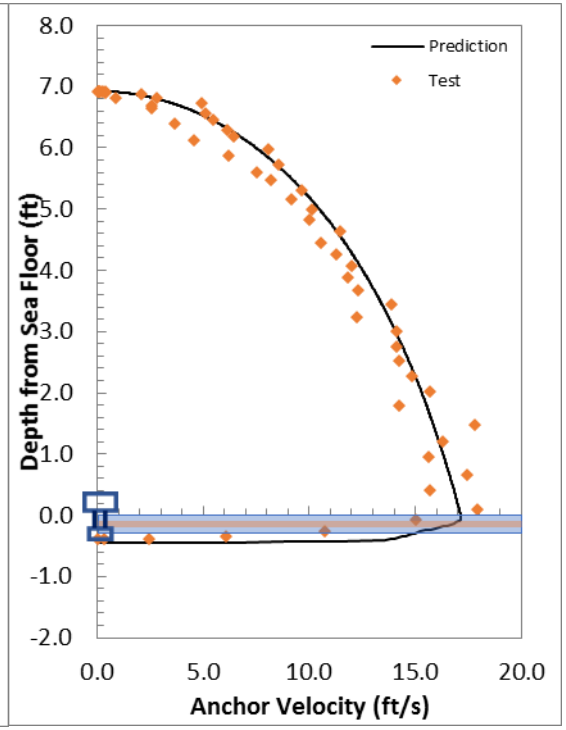

Free-Fall Penetration with Flying Wing Anchor ® in Case 2 Layered Soil

First Repeat in Drop 2

	Impact v (ft/s)	Embedment D (L_f)	β	λ
Experiment	17.19	2.08	–	–
R_f in Power-Law	17.19	1.94	0.15	–
R_f in Semi-log	17.19	2.08	–	0.35

Prediction with R_f in power-law

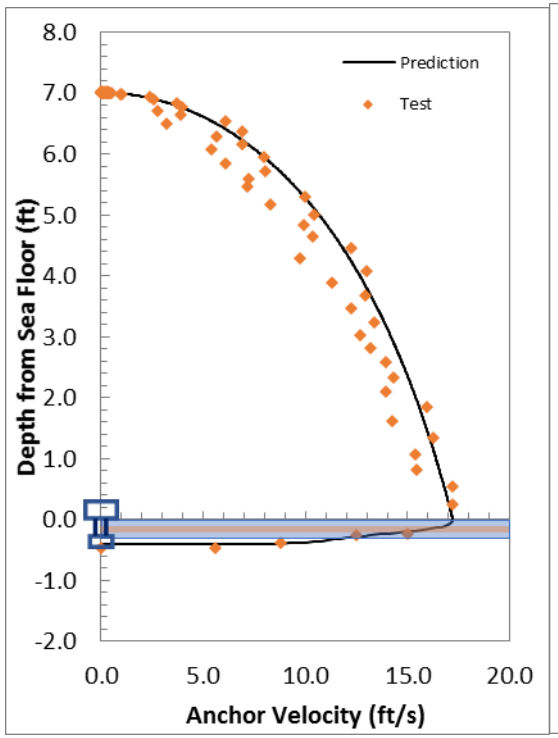

Prediction with R_f in semi-log

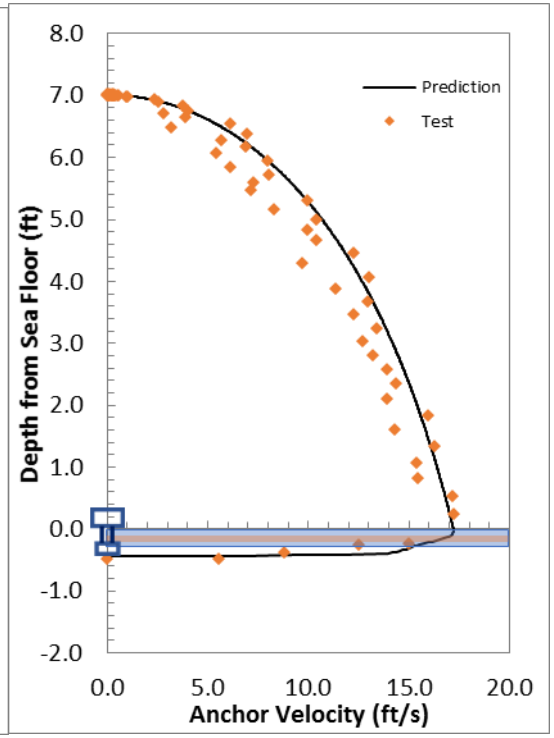

Free-Fall Penetration with Flying Wing Anchor ® in Case 2 Layered Soil

Drop 3

	Impact v (ft/s)	Embedment D (L_f)	β	λ
Experiment	15.00	1.41	–	–
R_f in Power-Law	16.49	1.67	0.35	–
R_f in Semi-log	16.49	1.97	–	0.5

Prediction with R_f in power-law

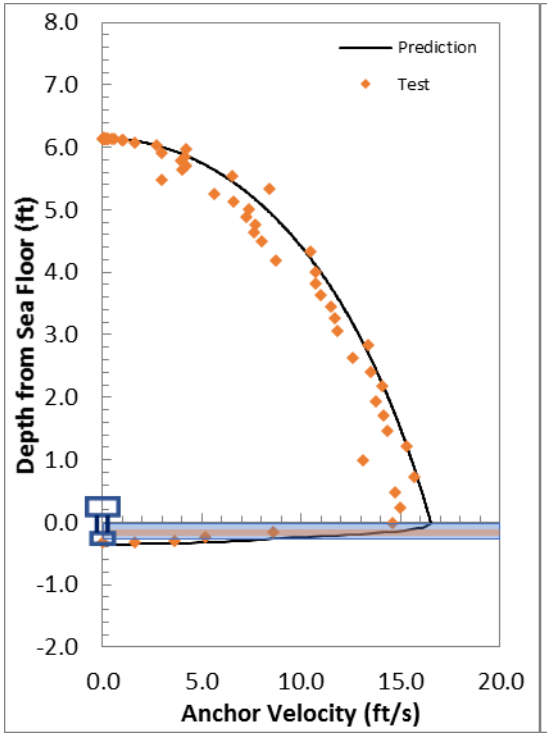

Prediction with R_f in semi-log

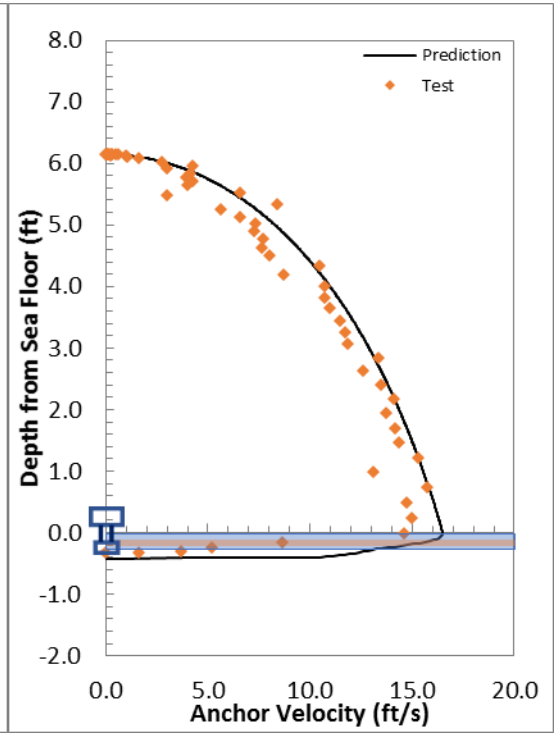

Free-Fall Penetration with Flying Wing Anchor ® in Case 2 Layered Soil

Repeat in Drop 3

	Impact v (ft/s)	Embedment D (L_f)	β	λ
Experiment	17.5	1.30	–	–
R_f in Power-Law	16.51	1.59	0.16	–
R_f in Semi-log	16.51	2.05	–	0.3

Prediction with R_f in power-law

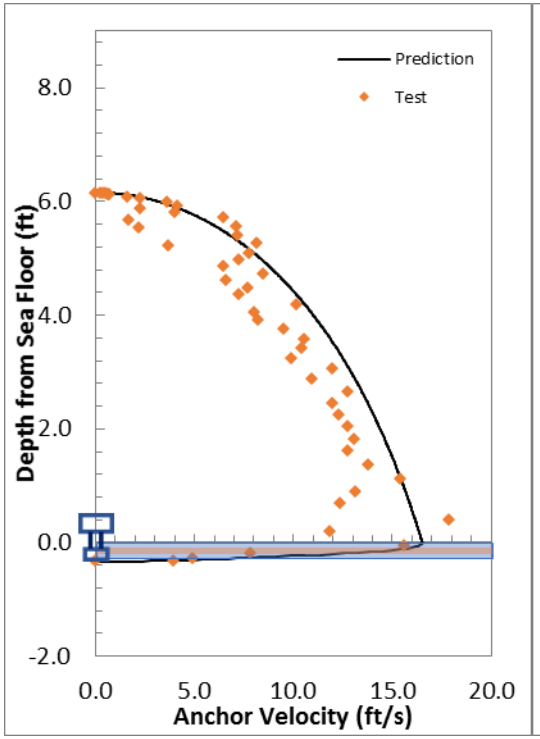

Prediction with R_f in semi-log

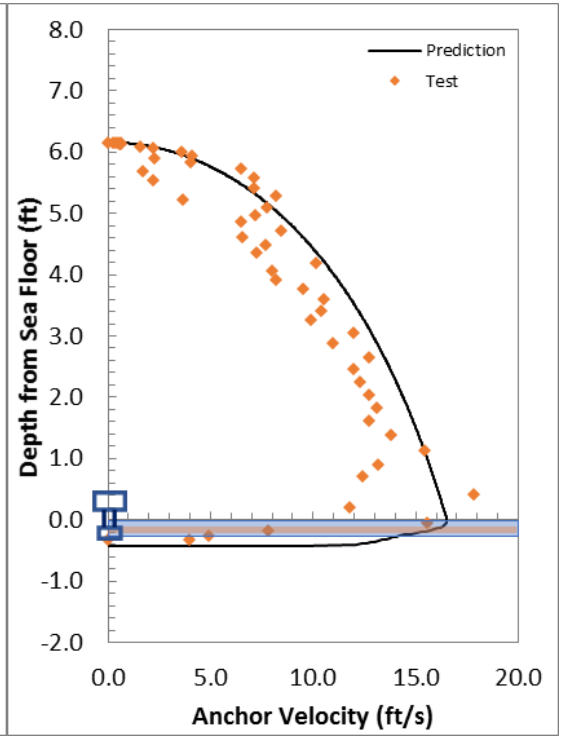

Free-Fall Penetration with Flying Wing Anchor ® in Case 3 Layered Soil

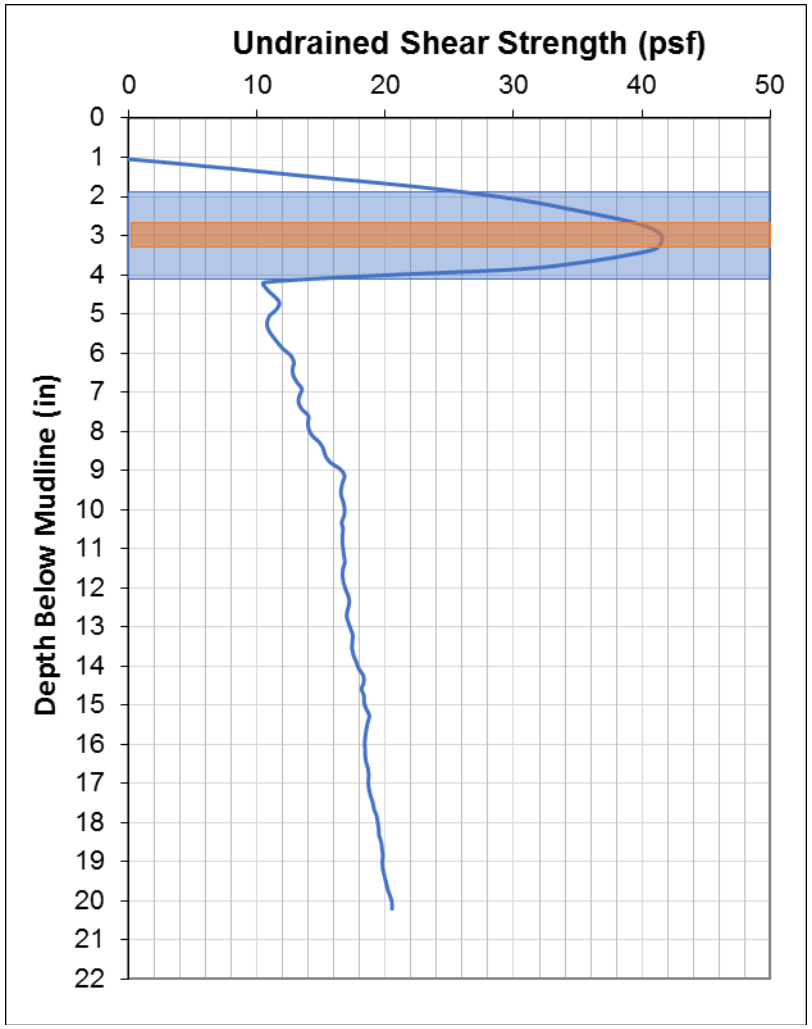

Free-Fall Penetration with Flying Wing Anchor ® in Case 3 Layered Soil

Drop 1

	Impact v (ft/s)	Embedment D (L_f)	β	λ
Experiment	17.6	1.45	–	–
R_f in Power-Law	17.62	1.34	0.2	–
R_f in Semi-log	17.62	1.92	–	0.3

Prediction with R_f in power-law

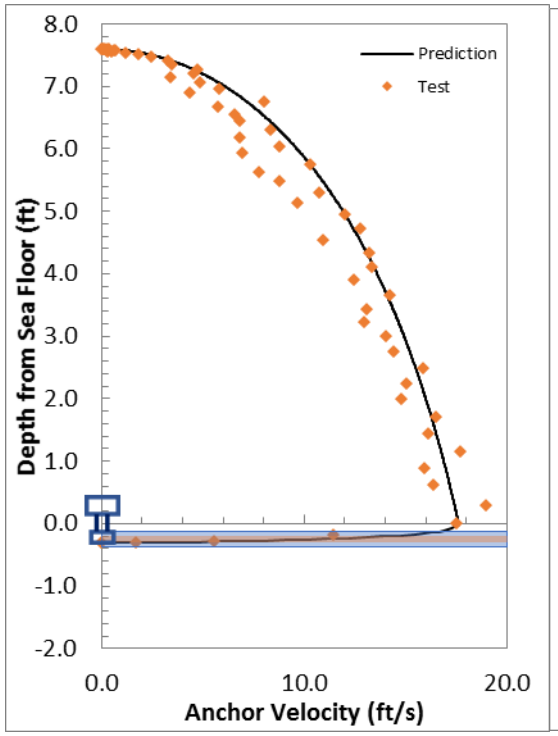

Prediction with R_f in semi-log

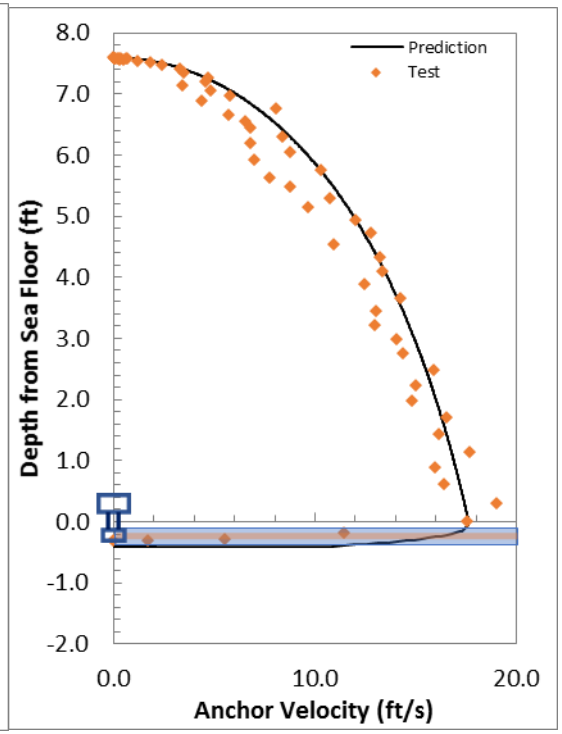

Free-Fall Penetration with Flying Wing Anchor ® in Case 3 Layered Soil

Repeat Test of Drop 1

	Impact v (ft/s)	Embedment D (L_f)	β	λ
Experiment	19.98	1.47	–	–
R_f in Power-Law	17.65	1.56	0.15	–
R_f in Semi-log	17.65	1.91	–	0.3

Prediction with R_f in power-law

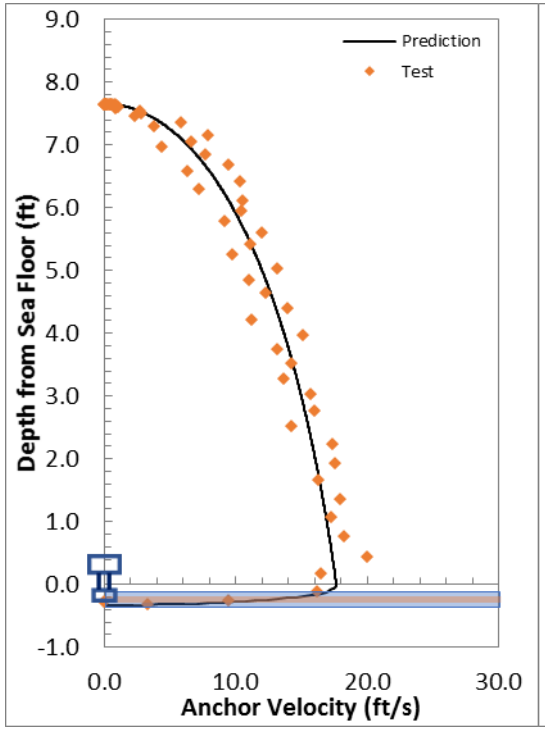

Prediction with R_f in semi-log

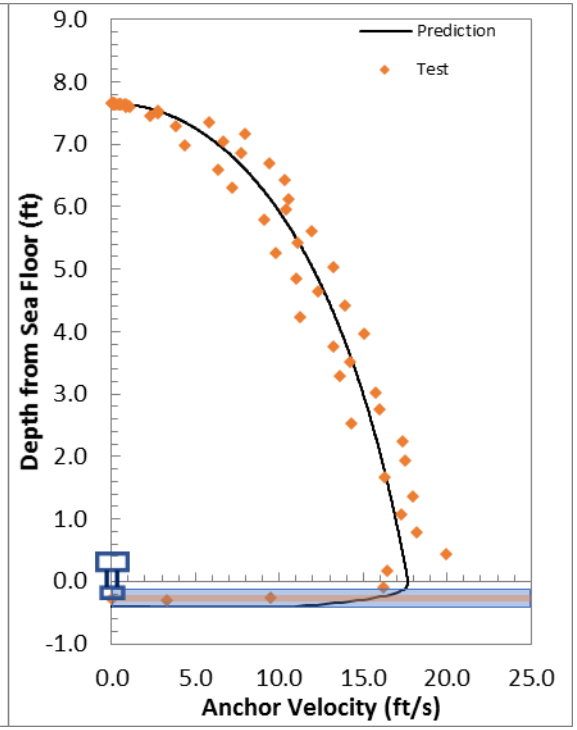

Free-Fall Penetration with Flying Wing Anchor ® in Case 3 Layered Soil

Drop 2

	Impact v (ft/s)	Embedment D (L_f)	β	λ
Experiment	16.8	1.17	–	–
R_f in Power-Law	17.06	1.31	0.2	–
R_f in Semi-log	17.06	1.91	–	0.3

Prediction with R_f in power-law

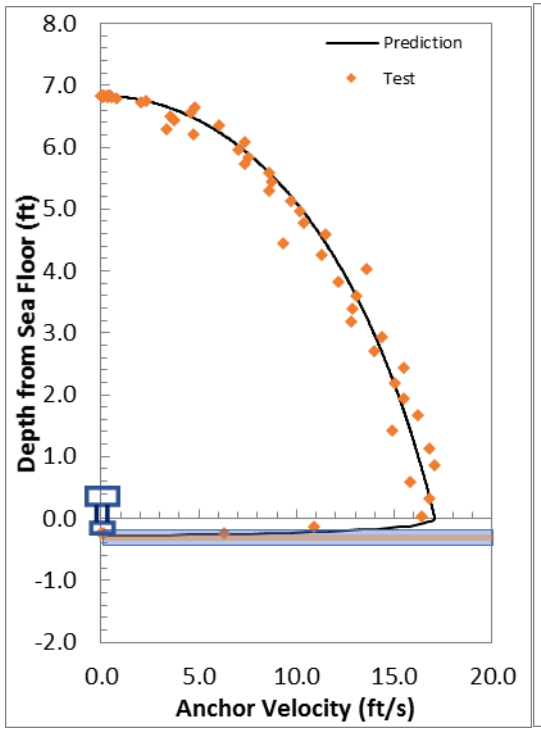

Prediction with R_f in semi-log

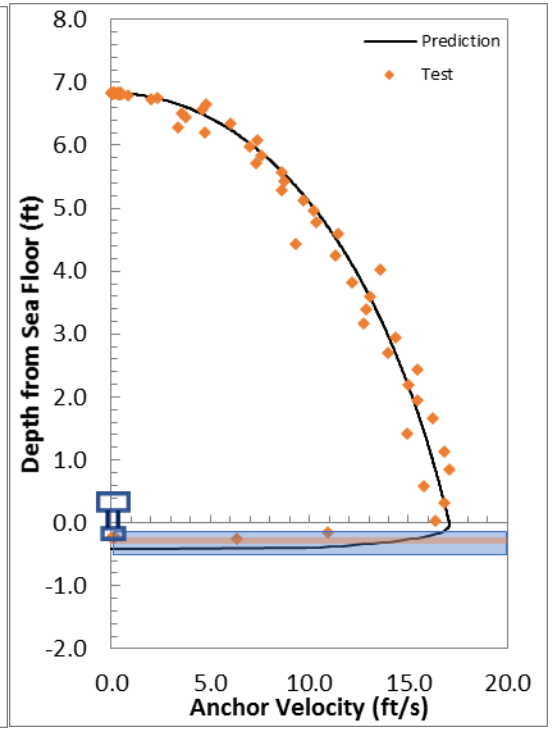

Free-Fall Penetration with Flying Wing Anchor ® in Case 3 Layered Soil

First Repeat in Drop 2

	Impact v (ft/s)	Embedment D (L_f)	β	λ
Experiment	16.48	1.15	–	–
R_f in Power-Law	17.14	1.56	0.15	–
R_f in Semi-log	17.14	1.96	–	0.35

Prediction with R_f in power-law

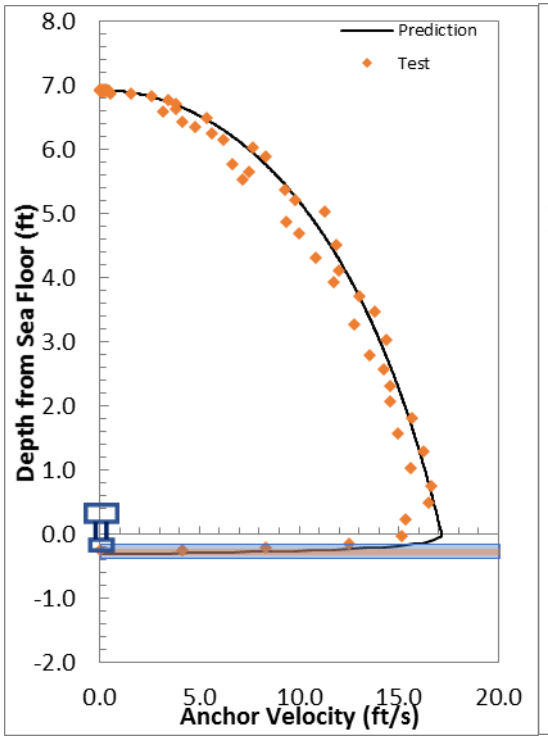

Prediction with R_f in semi-log

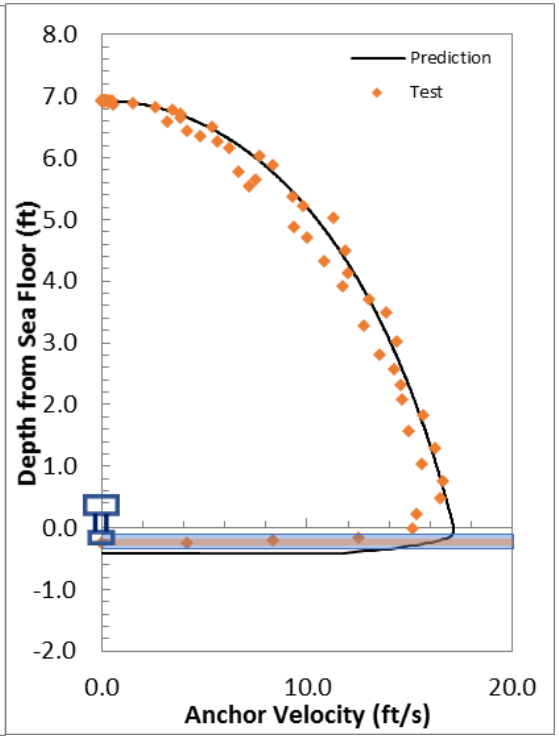

Free-Fall Penetration with Flying Wing Anchor ® in Case 3 Layered Soil

Second Repeat in Drop 2

	Impact v (ft/s)	Embedment D (L_f)	β	λ
Experiment	17.17	1.80	–	–
R_f in Power-Law	17.17	1.81	0.1	–
R_f in Semi-log	17.17	1.93	–	0.2

Prediction with R_f in power-law

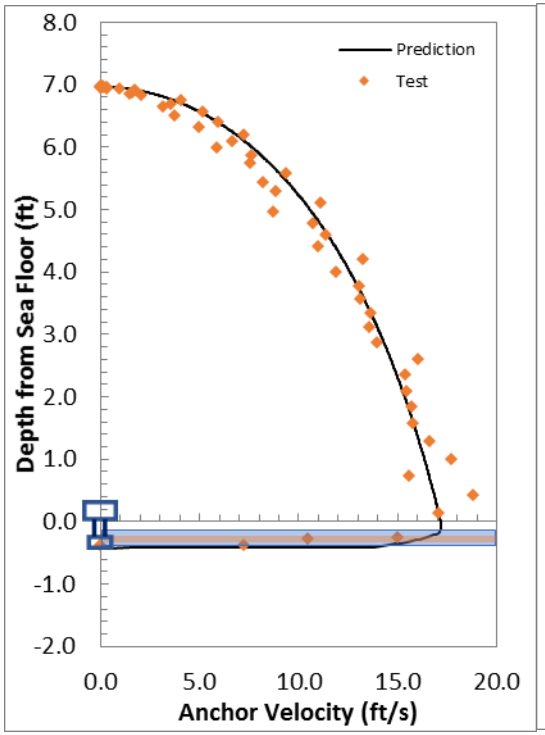

Prediction with R_f in semi-log

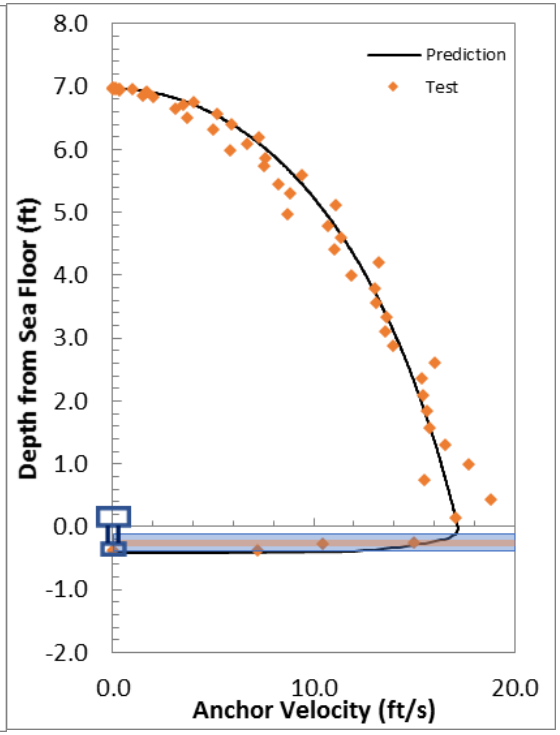

Free-Fall Penetration with Flying Wing Anchor ® in Case 3 Layered Soil

Drop 3

	Impact v (ft/s)	Embedment D (L_f)	β	λ
Experiment	16.41	0.8428	–	–
R_f in Power-Law	16.41	1.12	0.15	–
R_f in Semi-log	16.41	1.68	–	0.35

Prediction with R_f in power-law

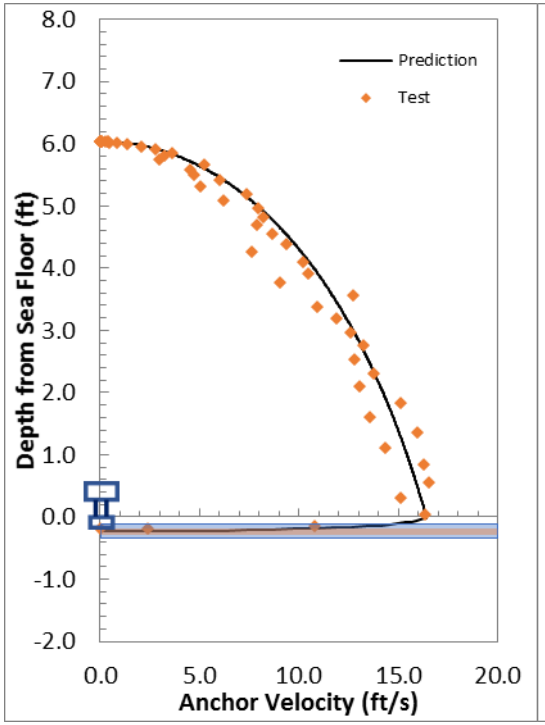

Prediction with R_f in semi-log

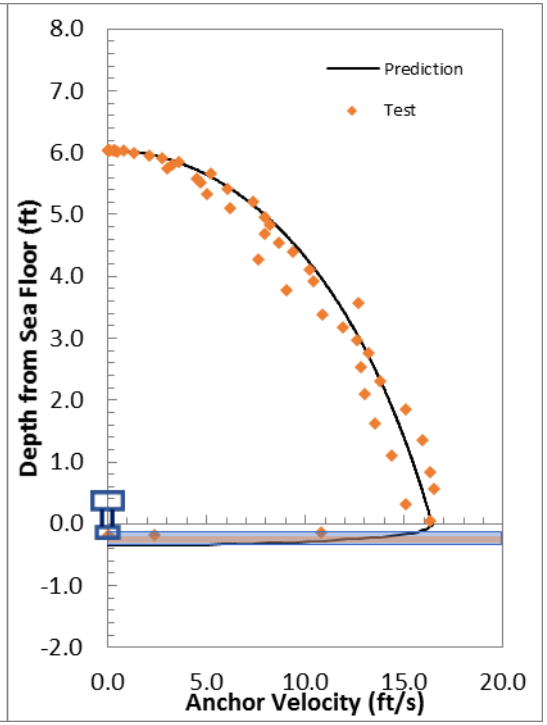

Free-Fall Penetration with Flying Wing Anchor ® in Case 3 Layered Soil

Repeat in Drop 3

	Impact v (ft/s)	Embedment D (L_f)	β	λ
Experiment	14.97	0.96	–	–
R_f in Power-Law	16.57	1.28	0.2	–
R_f in Semi-log	16.57	1.69	–	0.5

Prediction with R_f in power-law

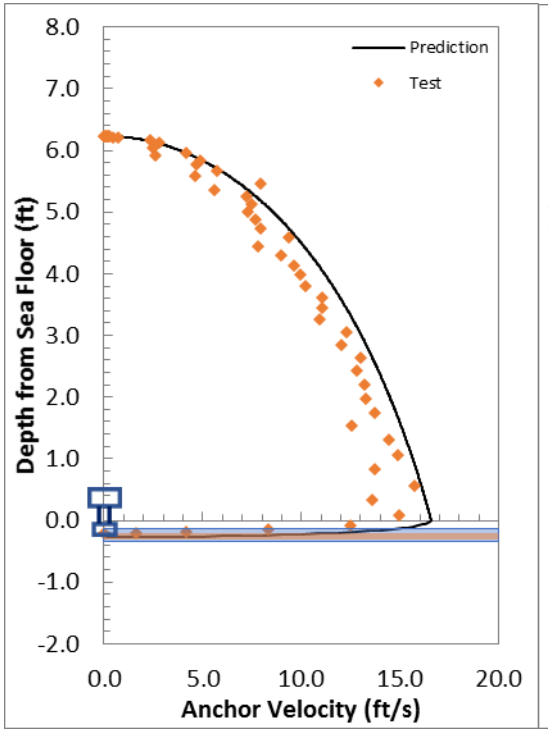

Prediction with R_f in semi-log

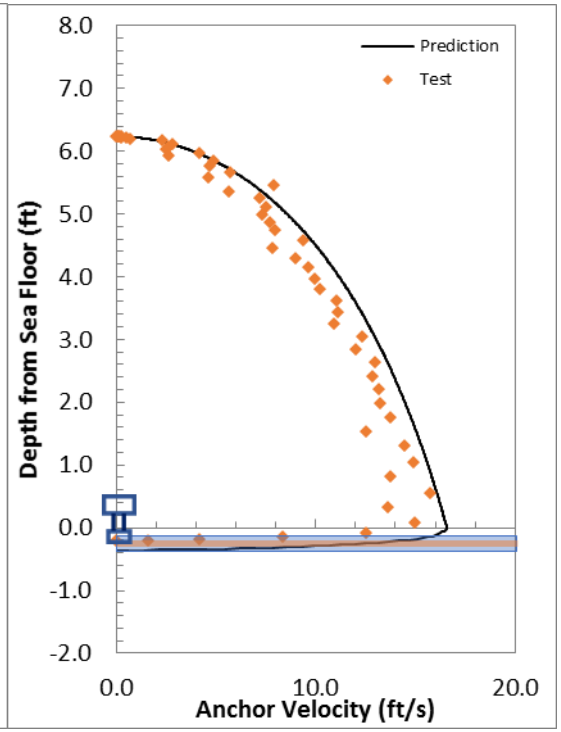

Free-Fall Penetration with Flying Wing Anchor ® in Case 4 Layered Soil

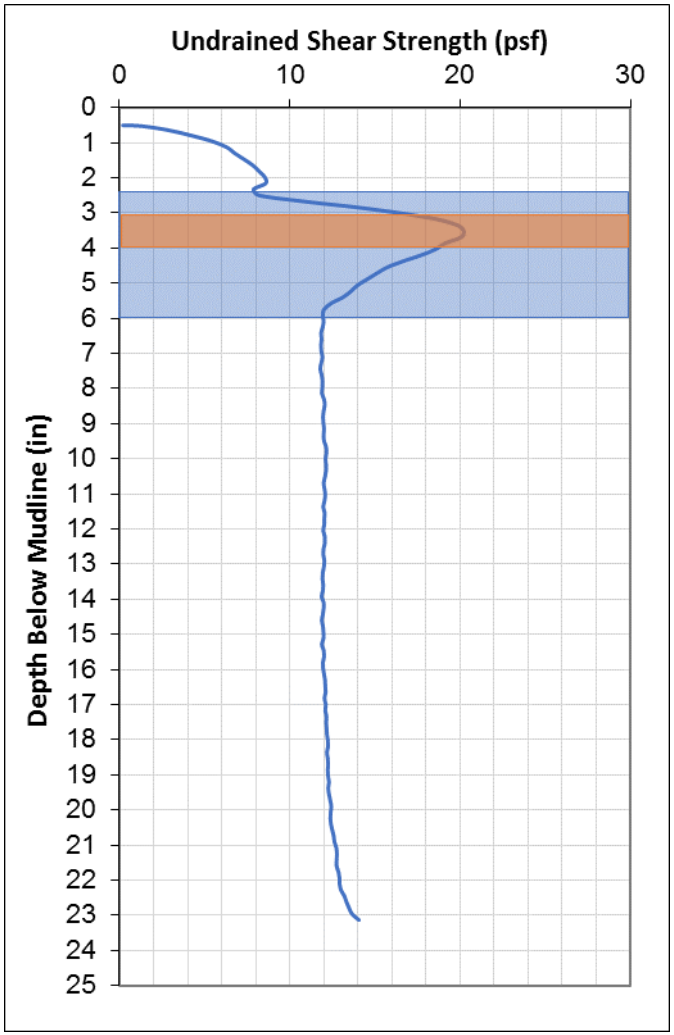

Free-Fall Penetration with Flying Wing Anchor ® in Case 4 Layered Soil

Drop 1

	Impact v (ft/s)	Embedment D (L_f)	β	λ
Experiment	18.24	3.17	–	–
R_f in Power-Law	17.66	2.24	0.1	–
R_f in Semi-log	17.66	2.25	–	0.2

Prediction with R_f in power-law

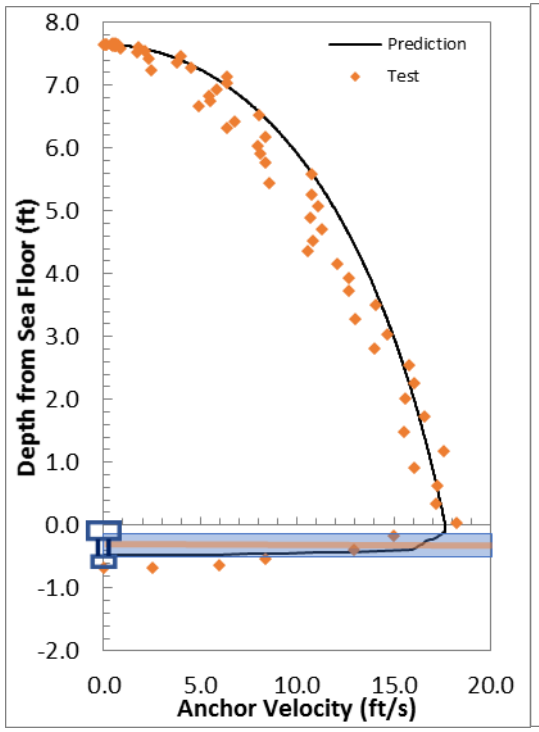

Prediction with R_f in semi-log

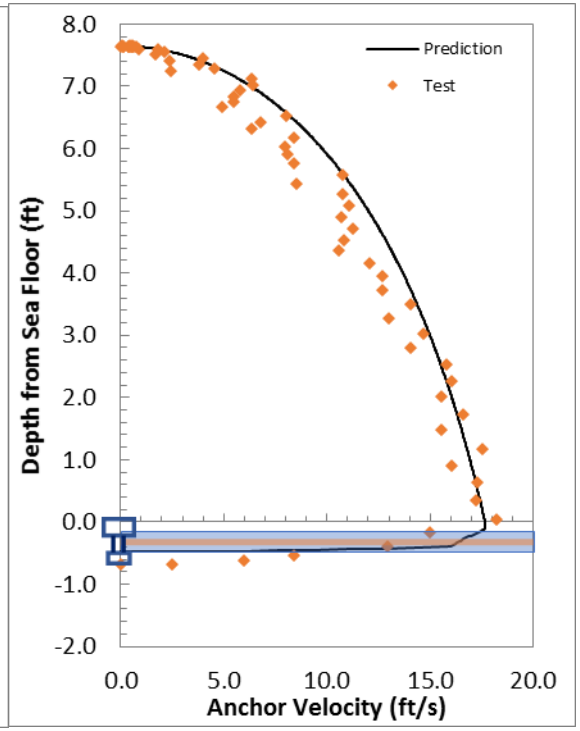

Free-Fall Penetration with Flying Wing Anchor ® in Case 4 Layered Soil

Repeat Test of Drop 1

	Impact v (ft/s)	Embedment D (L_f)	β	λ
Experiment	17.72	3.17	–	–
R_f in Power-Law	17.72	2.25	0.1	–
R_f in Semi-log	17.72	2.26	–	0.2

Prediction with R_f in power-law

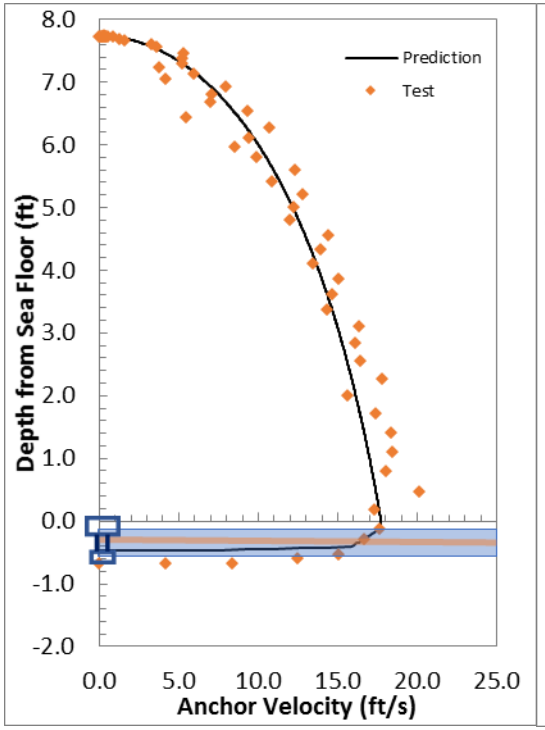

Prediction with R_f in semi-log

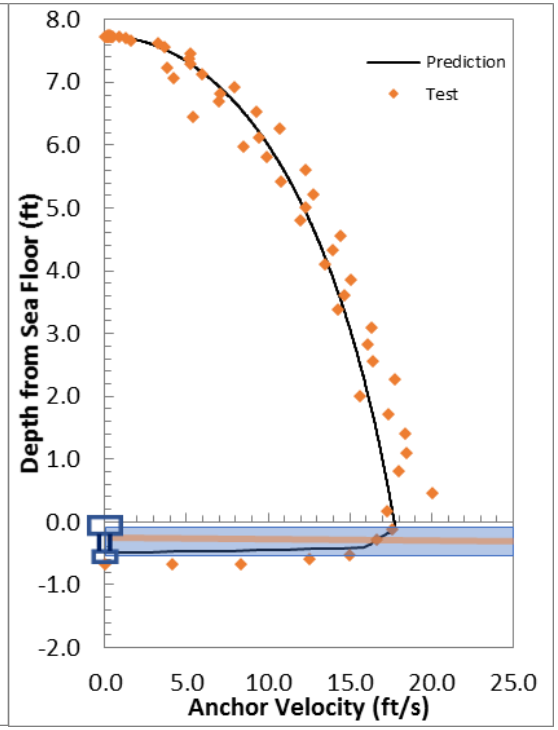

Free-Fall Penetration with Flying Wing Anchor ® in Case 4 Layered Soil

Drop 2

	Impact v (ft/s)	Embedment D (L_f)	β	λ
Experiment	18.57	2.97	–	–
R_f in Power-Law	17.02	2.20	0.1	–
R_f in Semi-log	17.02	2.21	–	0.2

Prediction with R_f in power-law

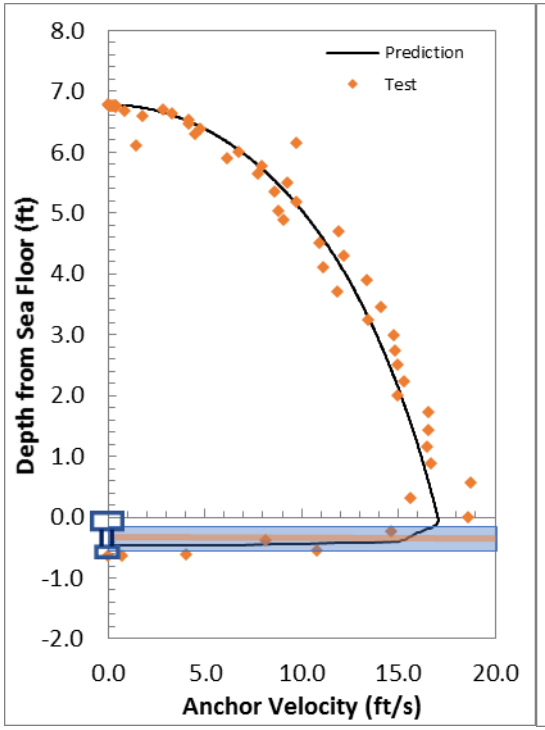

Prediction with R_f in semi-log

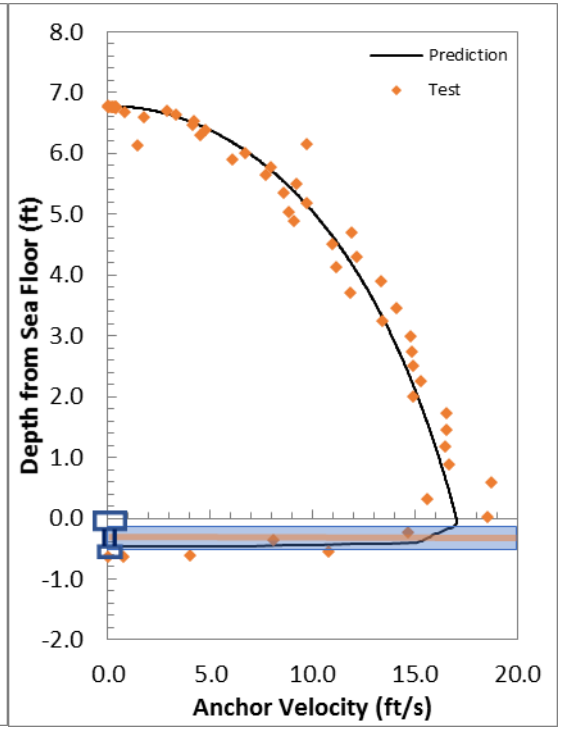

Free-Fall Penetration with Flying Wing Anchor ® in Case 4 Layered Soil

First Repeat in Drop 2

	Impact v (ft/s)	Embedment D (L_f)	β	λ
Experiment	18.15	2.97	–	–
R_f in Power-Law	17.08	2.23	0.1	–
R_f in Semi-log	17.08	2.24	–	0.2

Prediction with R_f in power-law

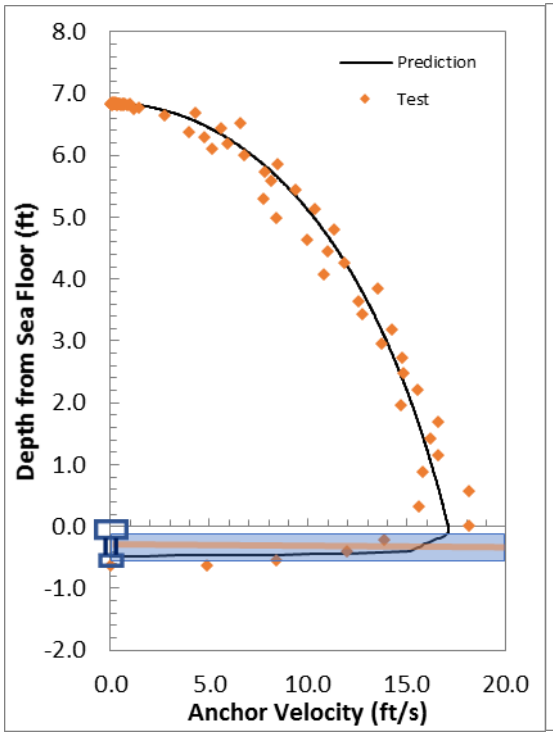

Prediction with R_f in semi-log

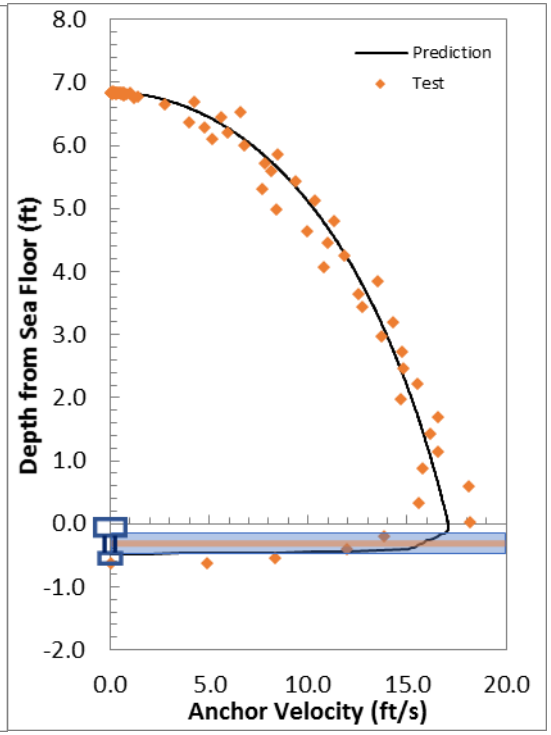

Free-Fall Penetration with Flying Wing Anchor ® in Case 4 Layered Soil

Drop 3

	Impact v (ft/s)	Embedment D (L_f)	β	λ
Experiment	15.22	2.77	–	–
R_f in Power-Law	15.86	2.17	0.1	–
R_f in Semi-log	15.86	2.18	–	0.2

Prediction with R_f in power-law

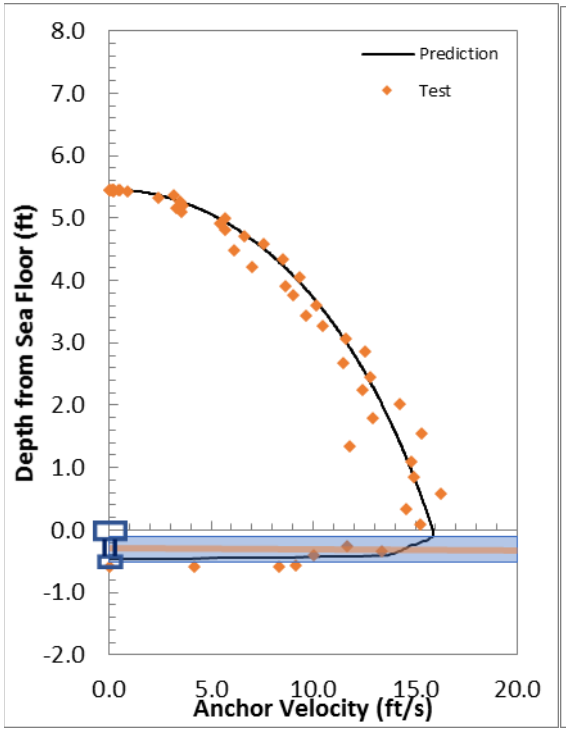

Prediction with R_f in semi-log

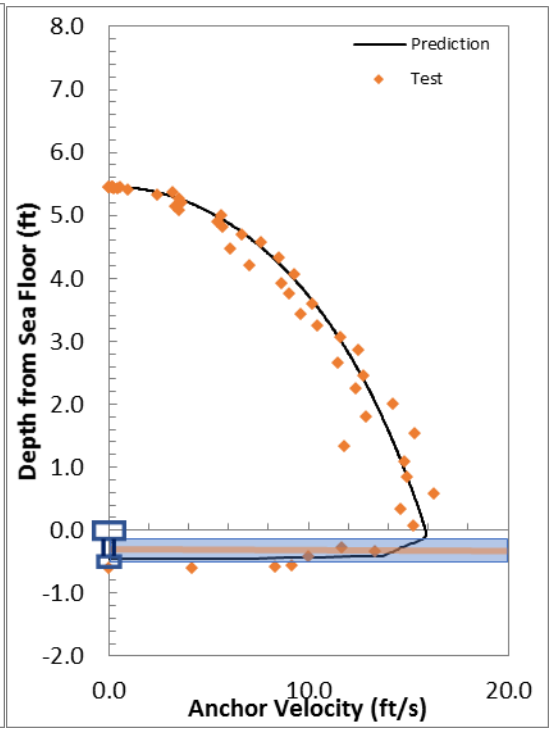

Free-Fall Penetration with Flying Wing Anchor ® in Case 4 Layered Soil

Repeat in Drop 3

	Impact v (ft/s)	Embedment D (L_f)	β	λ
Experiment	15.38	2.77	–	–
R_f in Power-Law	16.15	2.18	0.1	–
R_f in Semi-log	16.15	2.19	–	0.2

Prediction with R_f in power-law

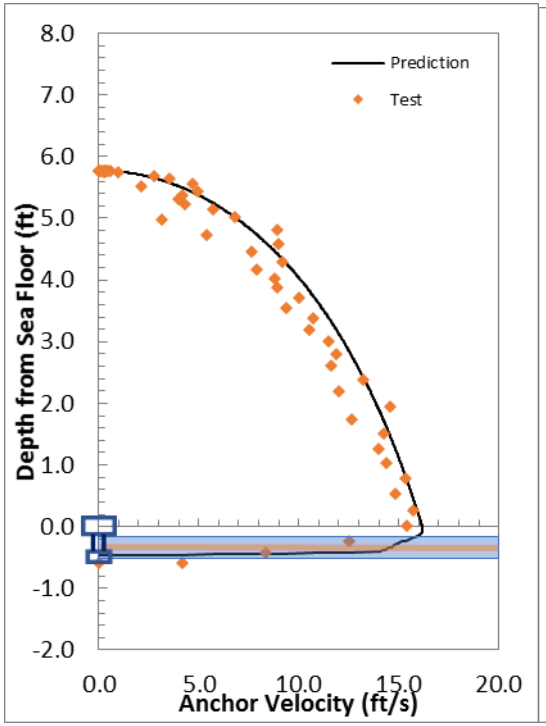

Prediction with R_f in semi-log

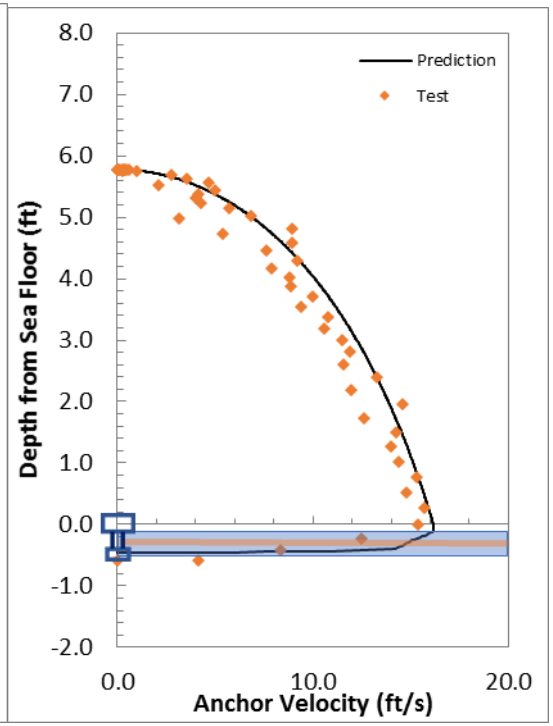

Free-Fall Penetration with Flying Wing Anchor ® in Case 5 Layered Soil

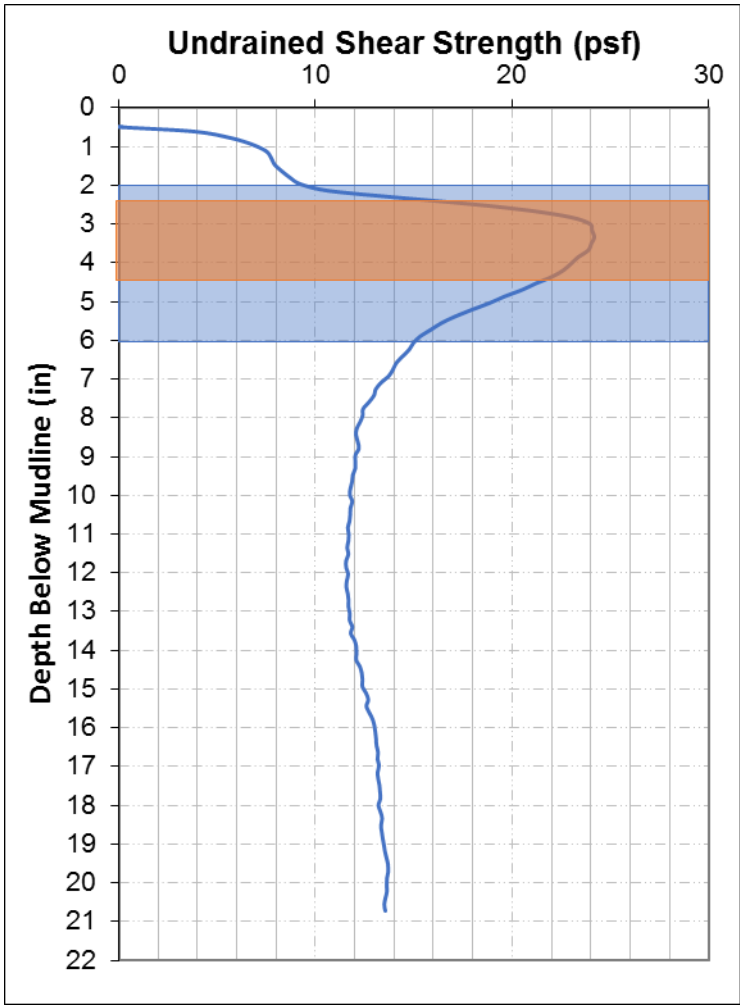

Free-Fall Penetration with Flying Wing Anchor ® in Case 5 Layered Soil

Drop 1

	Impact v (ft/s)	Embedment D (L_f)	β	λ
Experiment	16.54	2.97	–	–
R_f in Power-Law	17.61	2.27	0.15	–
R_f in Semi-log	17.61	2.13	–	0.35

Prediction with R_f in power-law

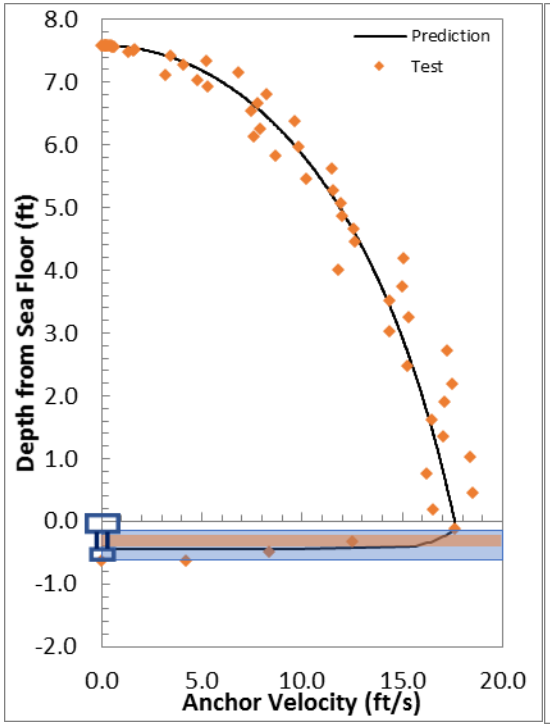

Prediction with R_f in semi-log

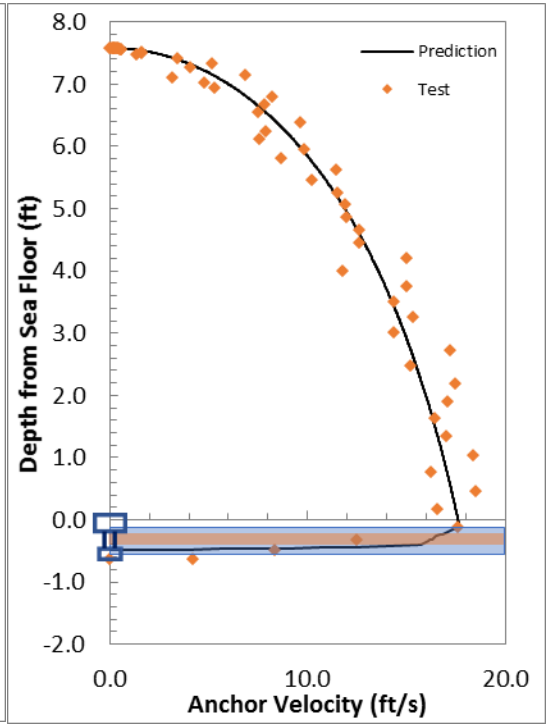

Free-Fall Penetration with Flying Wing Anchor ® in Case 5 Layered Soil

Repeat Test of Drop 1

	Impact v (ft/s)	Embedment D (L_f)	β	λ
Experiment	19.5	2.87	–	–
R_f in Power-Law	17.56	2.26	0.15	–
R_f in Semi-log	17.56	2.12	–	0.35

Prediction with R_f in power-law

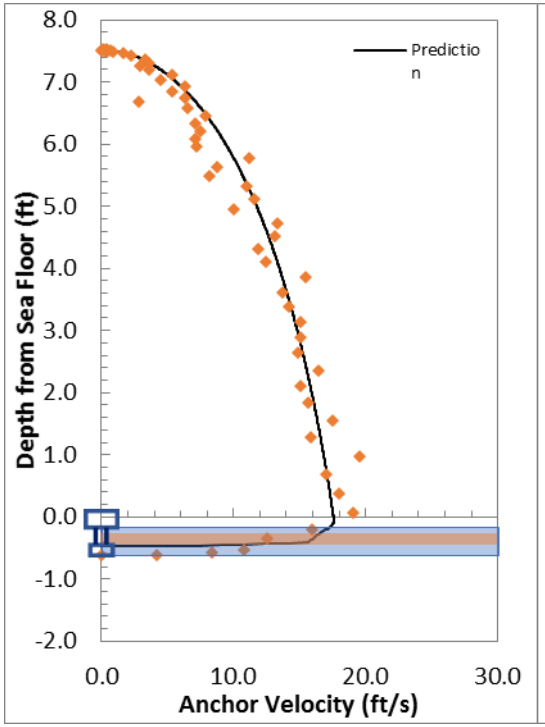

Prediction with R_f in semi-log

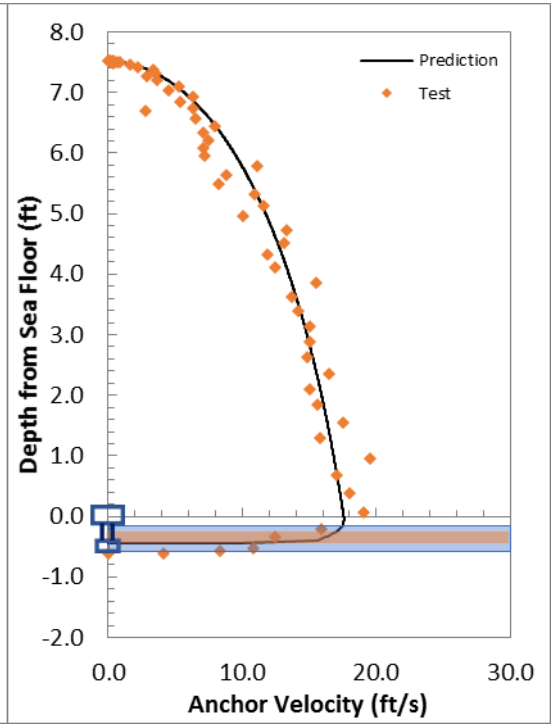

Free-Fall Penetration with Flying Wing Anchor ® in Case 5 Layered Soil

Drop 2

	Impact v (ft/s)	Embedment D (L_f)	β	λ
Experiment	16.85	2.59	–	–
R_f in Power-Law	16.93	2.20	0.15	–
R_f in Semi-log	16.93	2.00	–	0.35

Prediction with R_f in power-law

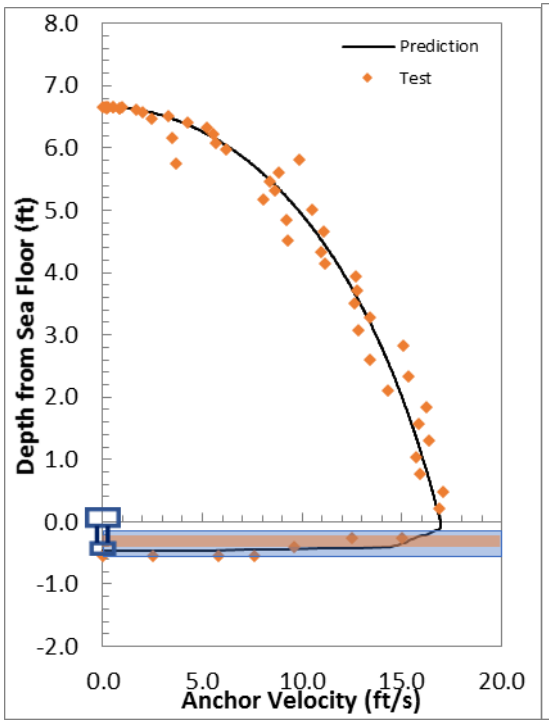

Prediction with R_f in semi-log

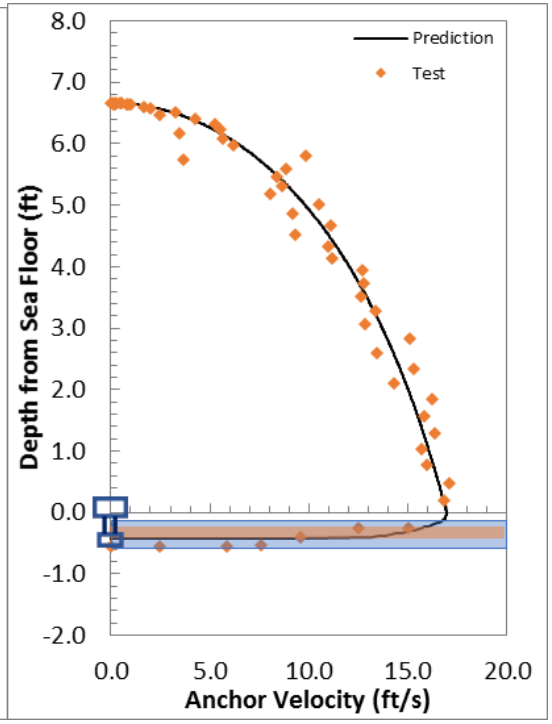

Free-Fall Penetration with Flying Wing Anchor ® in Case 5 Layered Soil

First Repeat in Drop 2

	Impact v (ft/s)	Embedment D (L_f)	β	λ
Experiment	16.87	2.67	–	–
R_f in Power-Law	16.87	2.24	0.15	–
R_f in Semi-log	16.87	2.05	–	0.35

Prediction with R_f in power-law

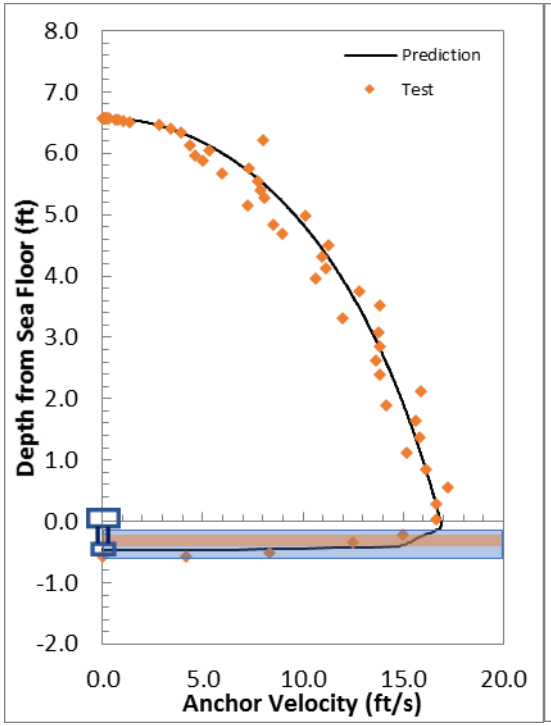

Prediction with R_f in semi-log

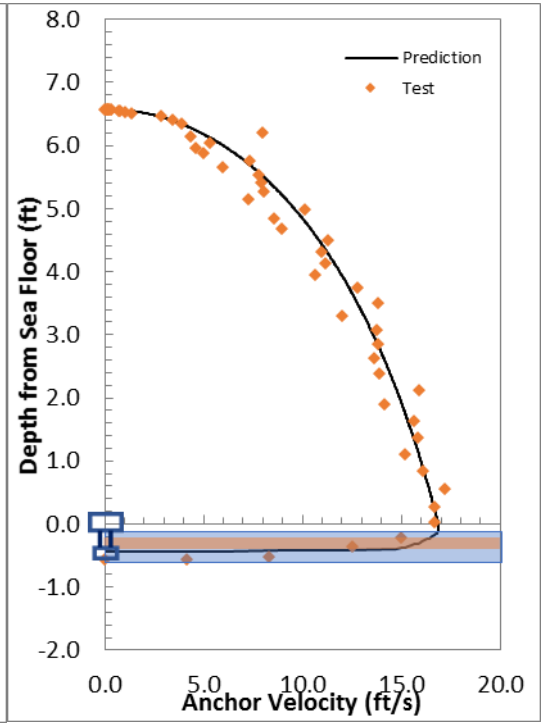

Free-Fall Penetration with Flying Wing Anchor ® in Case 5 Layered Soil

Drop 3

	Impact v (ft/s)	Embedment D (L_f)	β	λ
Experiment	16.67	2.58	–	–
R_f in Power-Law	16.12	2.16	0.15	–
R_f in Semi-log	16.12	2.03	–	0.35

Prediction with R_f in power-law

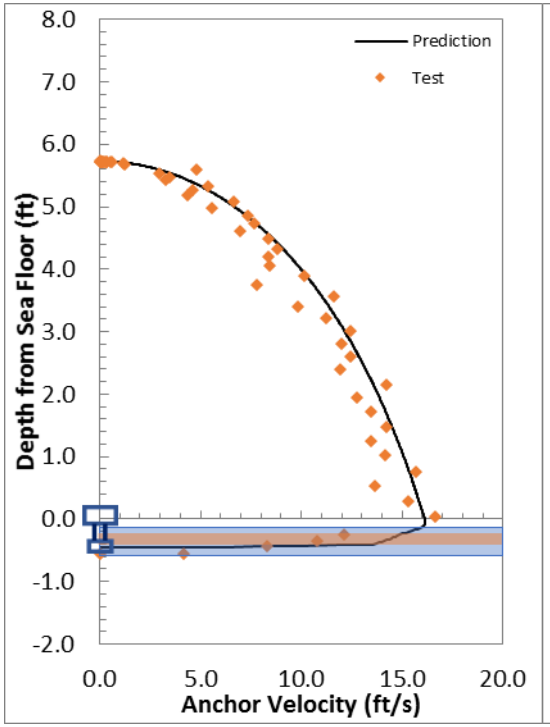

Prediction with R_f in semi-log

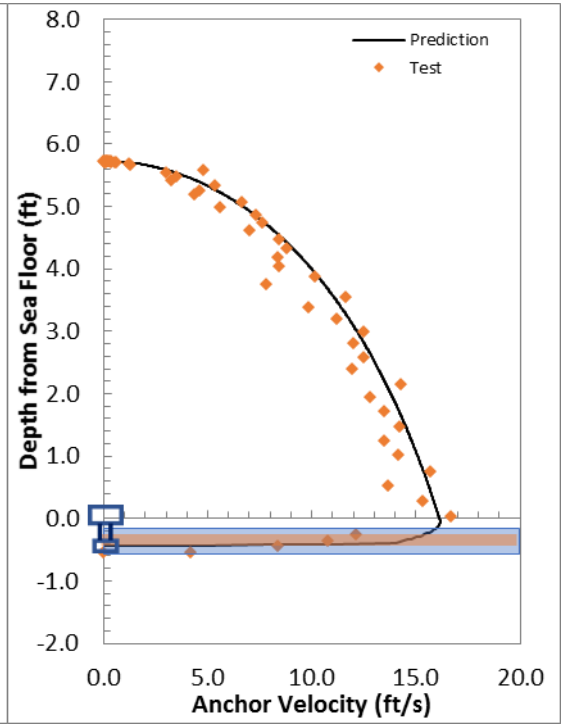

Free-Fall Penetration with Flying Wing Anchor ® in Case 5 Layered Soil

Repeat in Drop 3

	Impact v (ft/s)	Embedment D (L_f)	β	λ
Experiment	15.79	2.37	–	–
R_f in Power-Law	16.00	2.16	0.15	–
R_f in Semi-log	16.00	2.05	–	0.35

Prediction with R_f in power-law

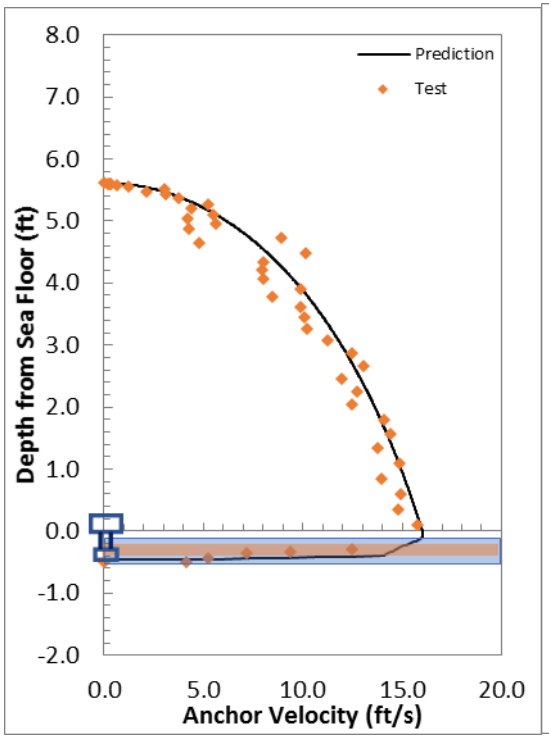

Prediction with R_f in semi-log

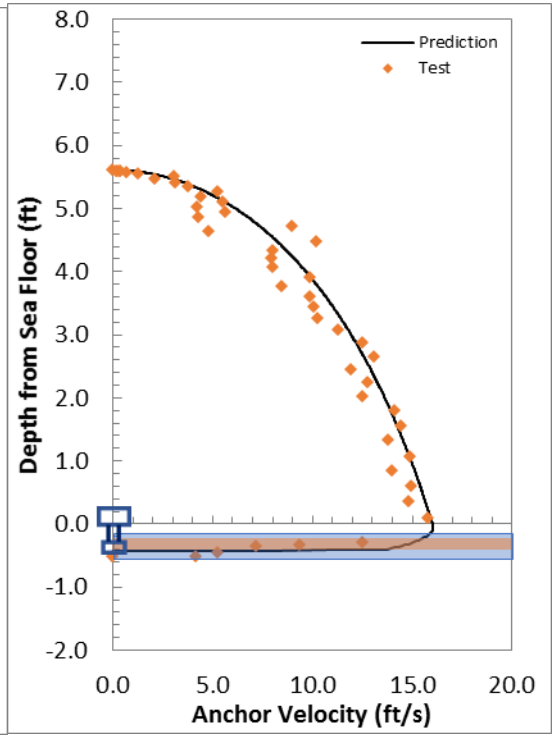

Free-Fall Penetration with Flying Wing Anchor ® in Case 6 Layered Soil

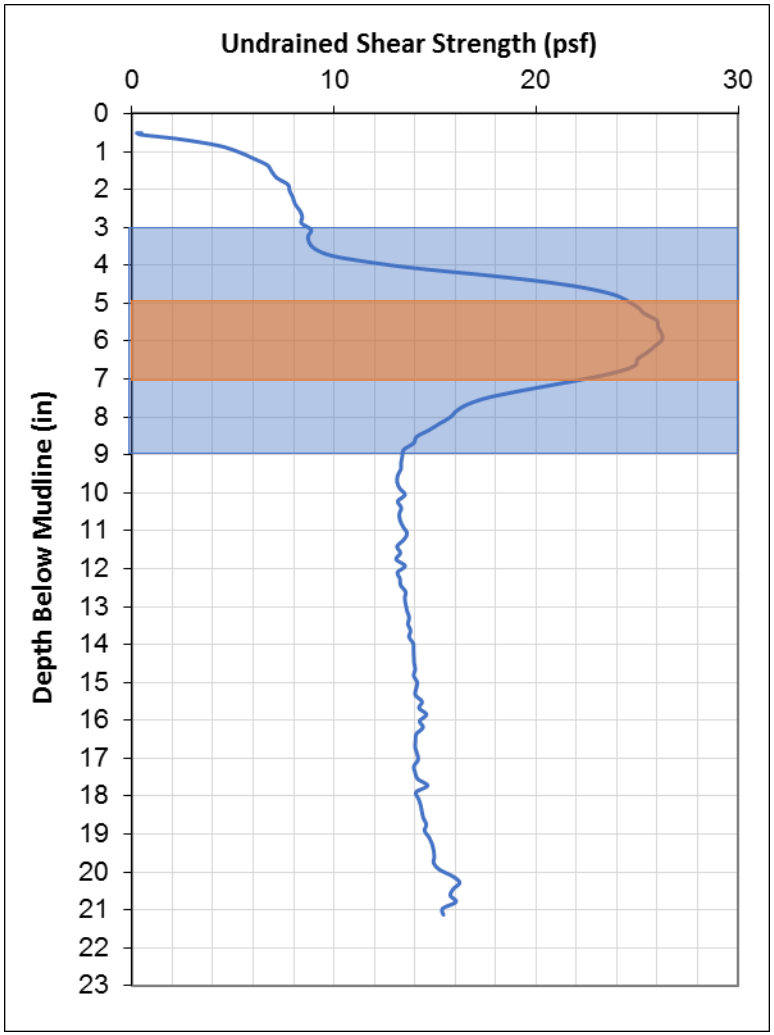

Free-Fall Penetration with Flying Wing Anchor ® in Case 6 Layered Soil

Drop 1

	Impact v (ft/s)	Embedment D (L_f)	β	λ
Experiment	17.90	3.21	–	–
R_f in Power-Law	17.43	2.26	0.15	–
R_f in Semi-log	17.43	2.27	–	0.35

Prediction with R_f in power-law

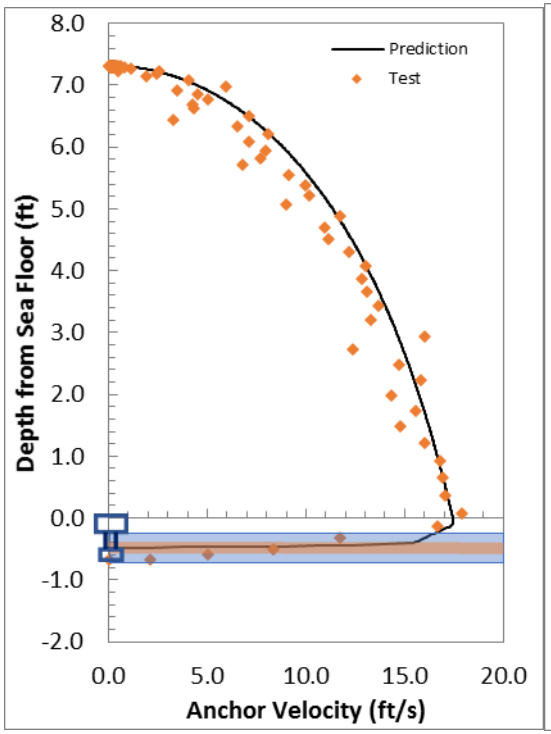

Prediction with R_f in semi-log

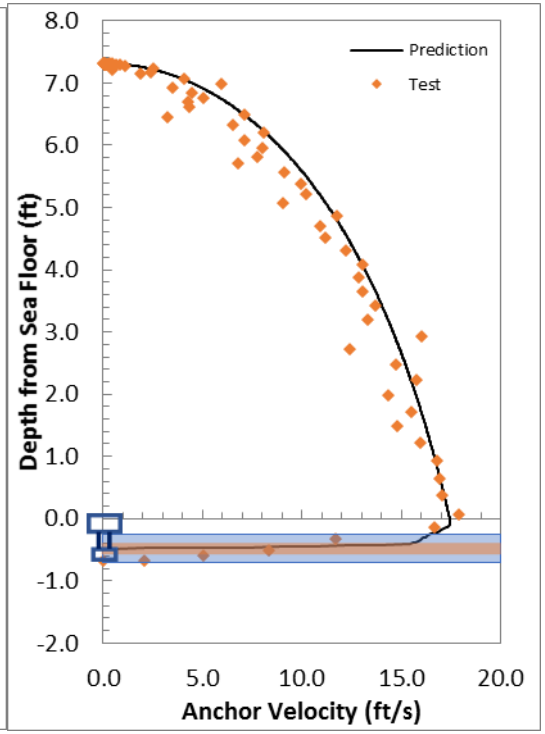

Free-Fall Penetration with Flying Wing Anchor ® in Case 6 Layered Soil

First Repeat Test of Drop 1

	Impact v (ft/s)	Embedment D (L_f)	β	λ
Experiment	16.98	3.31	–	–
R_f in Power-Law	17.61	2.24	0.15	–
R_f in Semi-log	17.61	2.25	–	0.35

Prediction with R_f in power-law

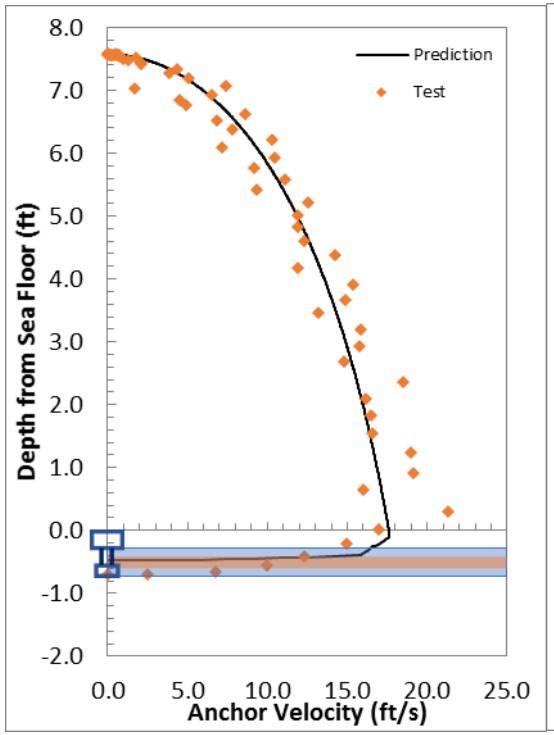

Prediction with R_f in semi-log

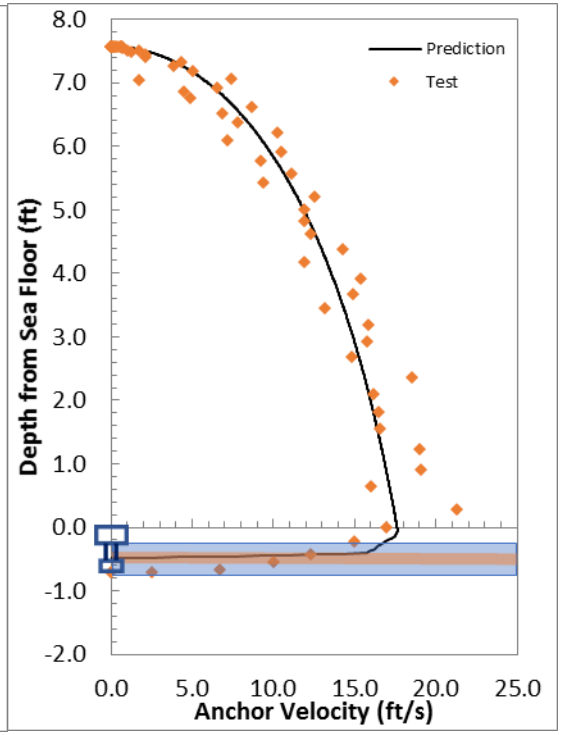

Free-Fall Penetration with Flying Wing Anchor ® in Case 6 Layered Soil

Second Repeat Test of Drop 1

	Impact v (ft/s)	Embedment D (L_f)	β	λ
Experiment	19.50	3.56	–	–
R_f in Power-Law	17.66	2.25	0.15	–
R_f in Semi-log	17.66	2.26	–	0.35

Prediction with R_f in power-law

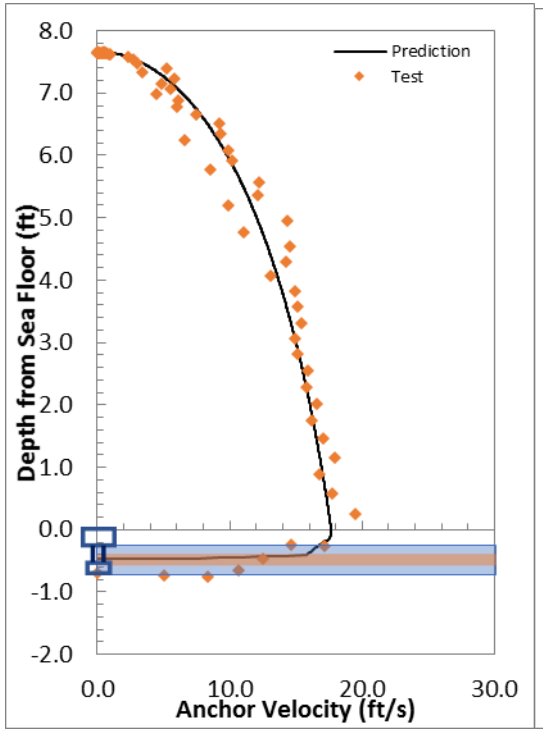

Prediction with R_f in semi-log

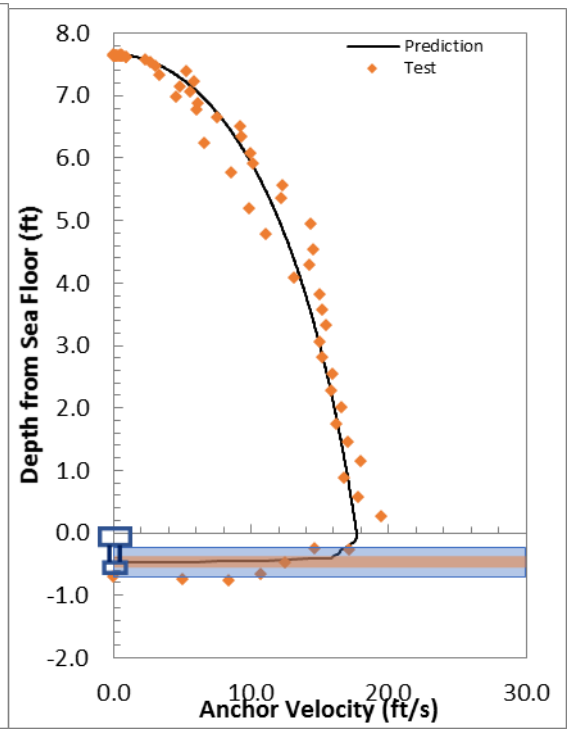

Free-Fall Penetration with Flying Wing Anchor ® in Case 6 Layered Soil

Drop 2

	Impact v (ft/s)	Embedment D (L_f)	β	λ
Experiment	16.3	3.07	–	–
R_f in Power-Law	16.9	2.23	0.15	–
R_f in Semi-log	16.9	2.24	–	0.35

Prediction with R_f in power-law

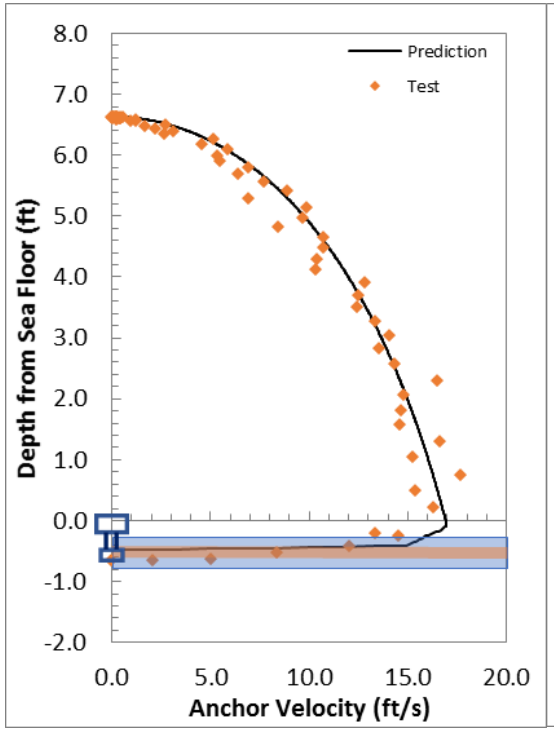

Prediction with R_f in semi-log

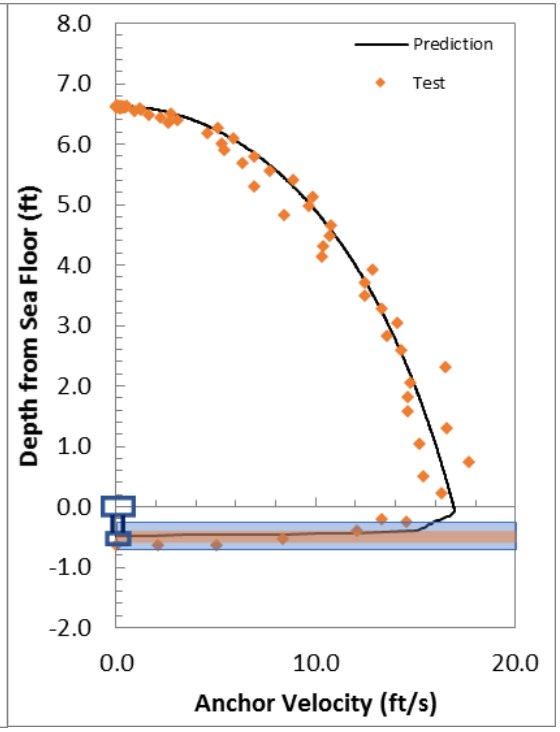

Free-Fall Penetration with Flying Wing Anchor ® in Case 6 Layered Soil

First Repeat in Drop 2

	Impact v (ft/s)	Embedment D (L_f)	β	λ
Experiment	17.33	3.06	–	–
R_f in Power-Law	16.84	2.21	0.15	–
R_f in Semi-log	16.84	2.22	–	0.35

Prediction with R_f in power-law

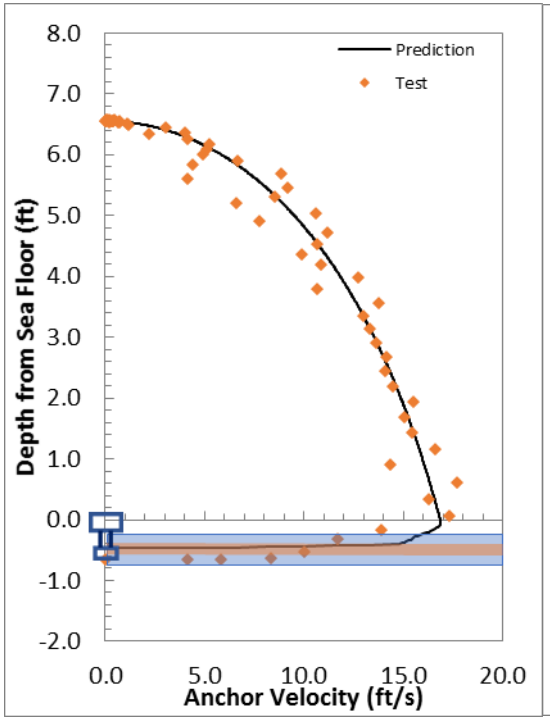

Prediction with R_f in semi-log

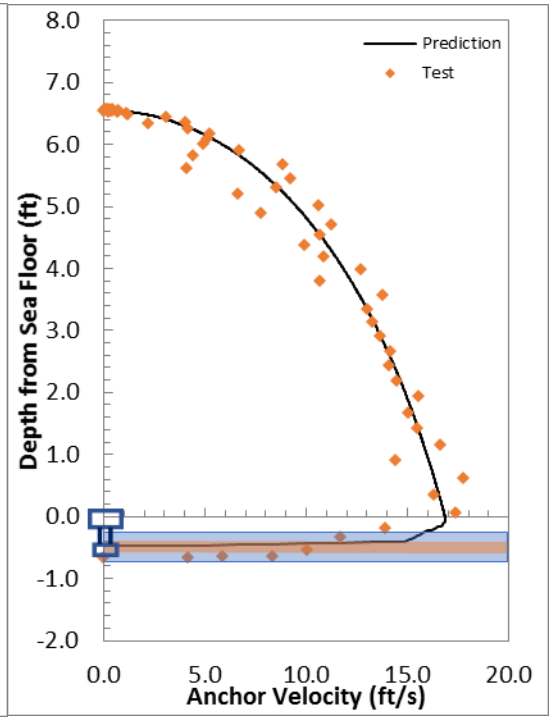

Free-Fall Penetration with Flying Wing Anchor ® in Case 6 Layered Soil

Drop 3

	Impact v (ft/s)	Embedment D (L_f)	β	λ
Experiment	16.3	2.92	–	–
R_f in Power-Law	16.84	2.45	0.15	–
R_f in Semi-log	16.84	2.25	–	0.35

Prediction with R_f in power-law

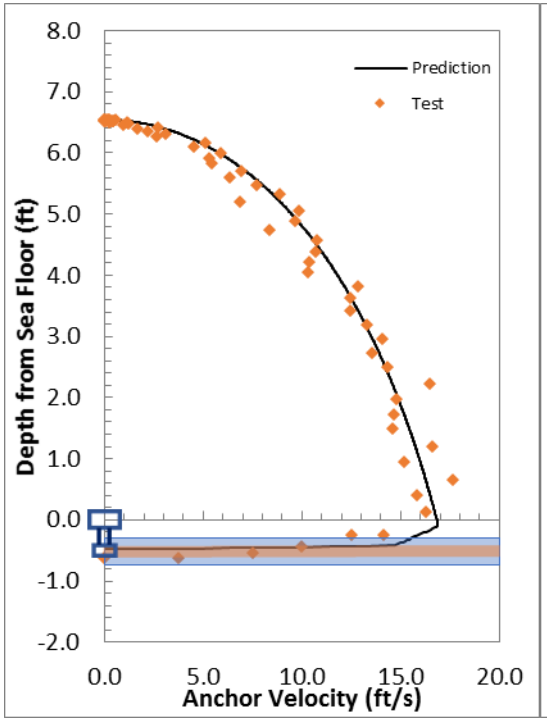

Prediction with R_f in semi-log

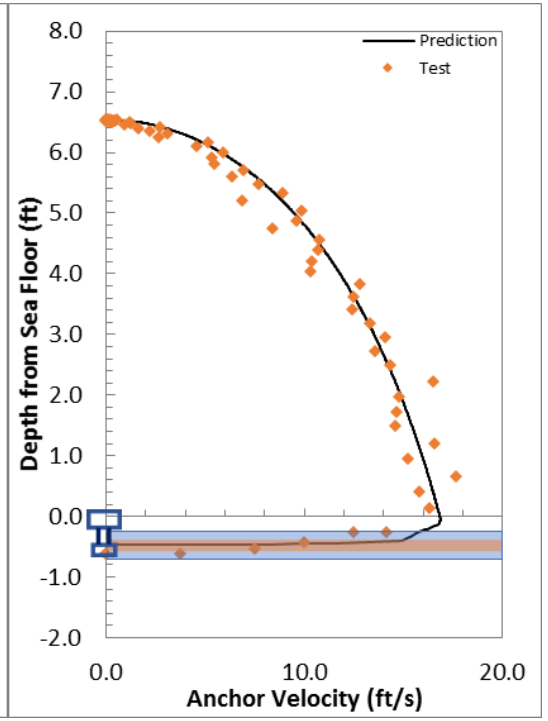

Free-Fall Penetration with Flying Wing Anchor ® in Case 6 Layered Soil

Repeat in Drop 3

	Impact v (ft/s)	Embedment D (L_f)	β	λ
Experiment	14.89	3.00	–	–
R_f in Power-Law	16.09	2.20	0.15	–
R_f in Semi-log	16.09	2.20	–	0.35

Prediction with R_f in power-law

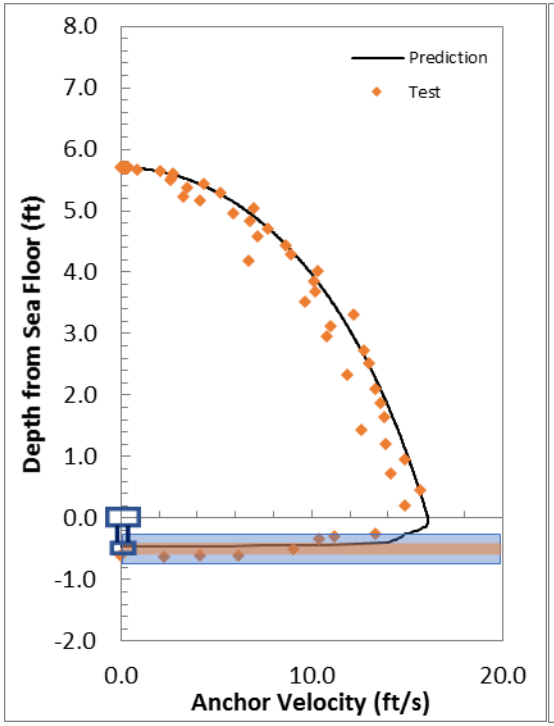

Prediction with R_f in semi-log

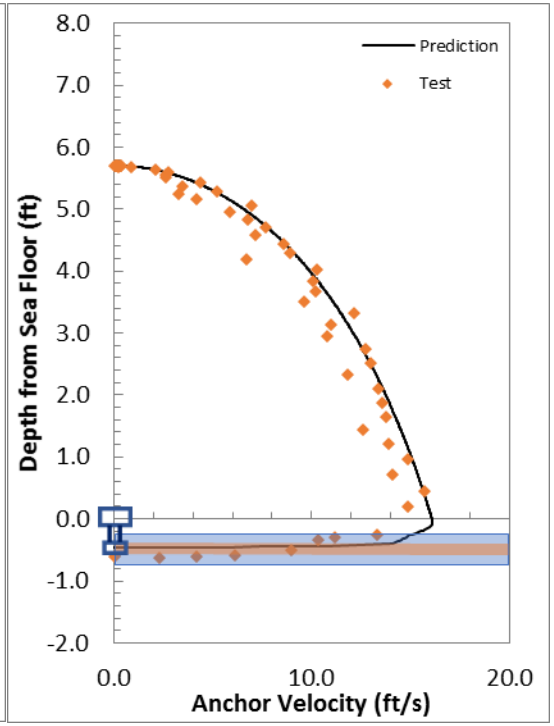

Free-Fall Penetration with Flying Wing Anchor ® in Case 7 Layered Soil

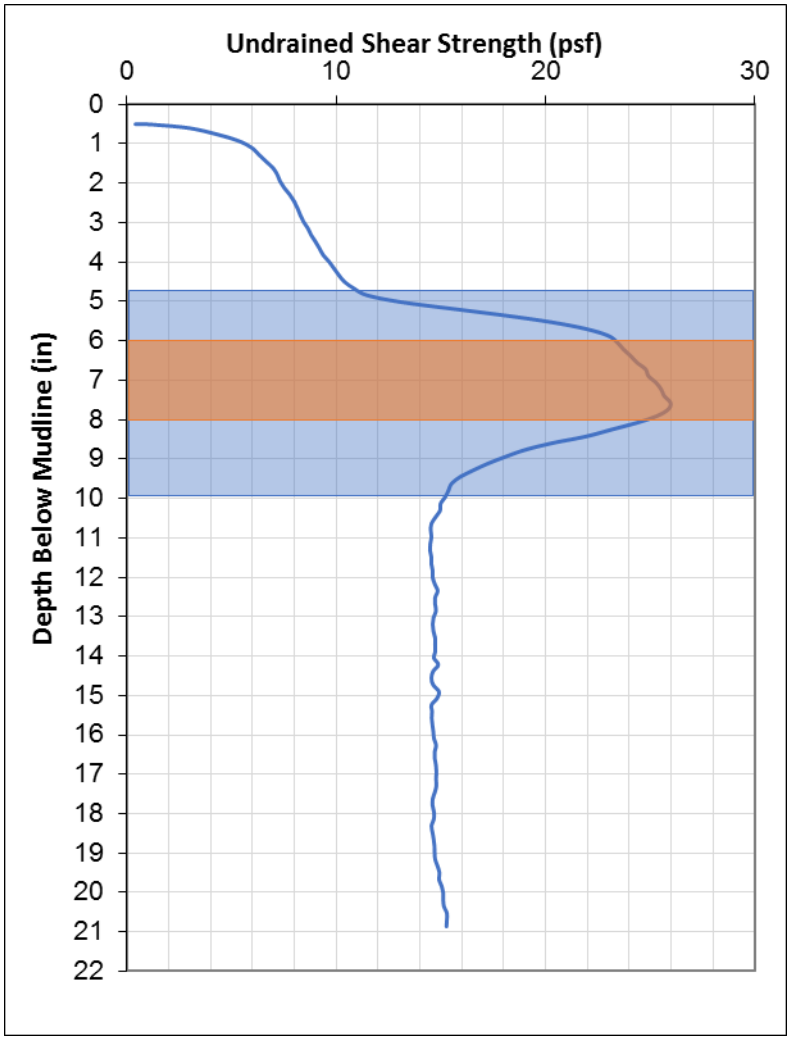

Free-Fall Penetration with Flying Wing Anchor ® in Case 7 Layered Soil

Drop 1

	Impact v (ft/s)	Embedment D (L_f)	β	λ
Experiment	17.67	3.26	–	–
R_f in Power-Law	17.45	2.23	0.15	–
R_f in Semi-log	17.45	2.24	–	0.35

Prediction with R_f in power-law

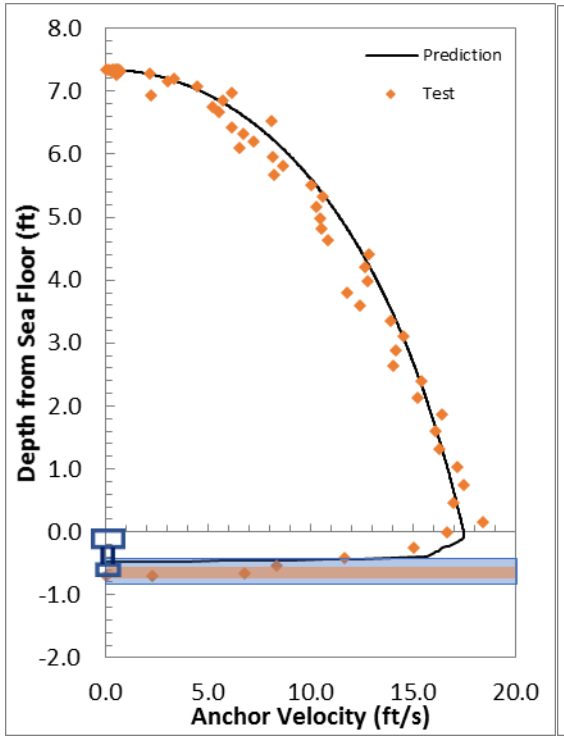

Prediction with R_f in semi-log

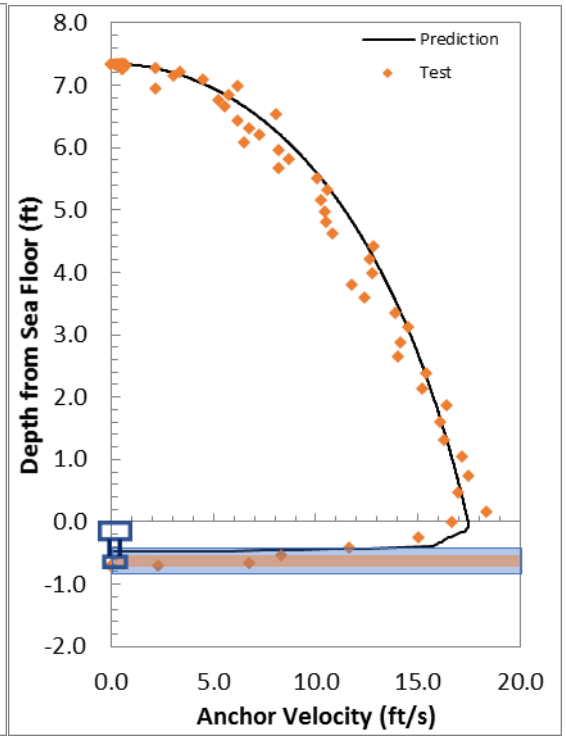

Free-Fall Penetration with Flying Wing Anchor ® in Case 7 Layered Soil

Repeat Test of Drop 1

	Impact v (ft/s)	Embedment D (L_f)	β	λ
Experiment	17.32	3.70	–	–
R_f in Power-Law	17.48	2.21	0.15	–
R_f in Semi-log	17.48	2.29	–	0.35

Prediction with R_f in power-law

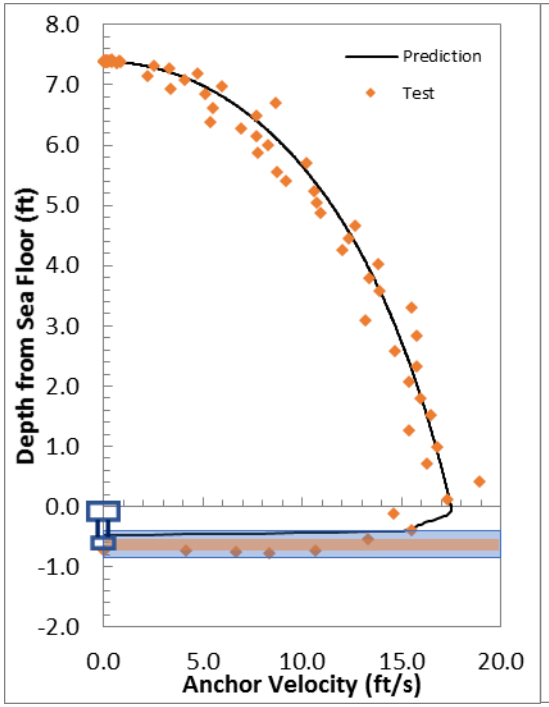

Prediction with R_f in semi-log

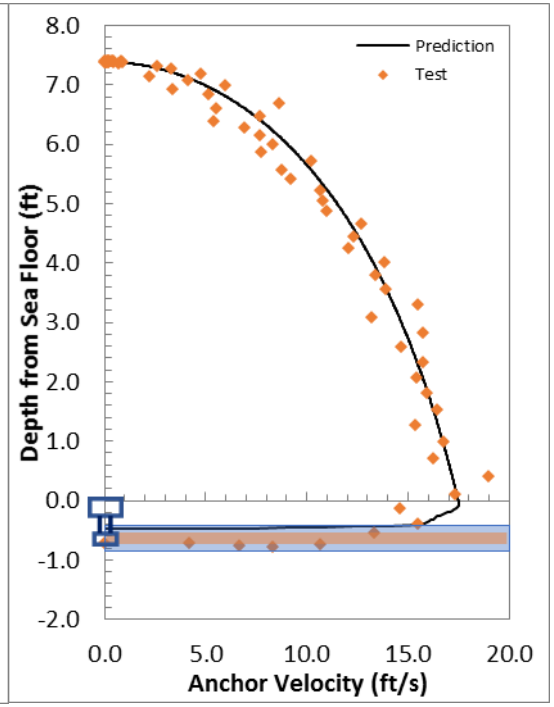

Free-Fall Penetration with Flying Wing Anchor ® in Case 7 Layered Soil

Drop 2

	Impact v (ft/s)	Embedment D (L_f)	β	λ
Experiment	16.99	2.97	–	–
R_f in Power-Law	16.70	2.29	0.15	–
R_f in Semi-log	16.70	1.08	–	0.35

Prediction with R_f in power-law

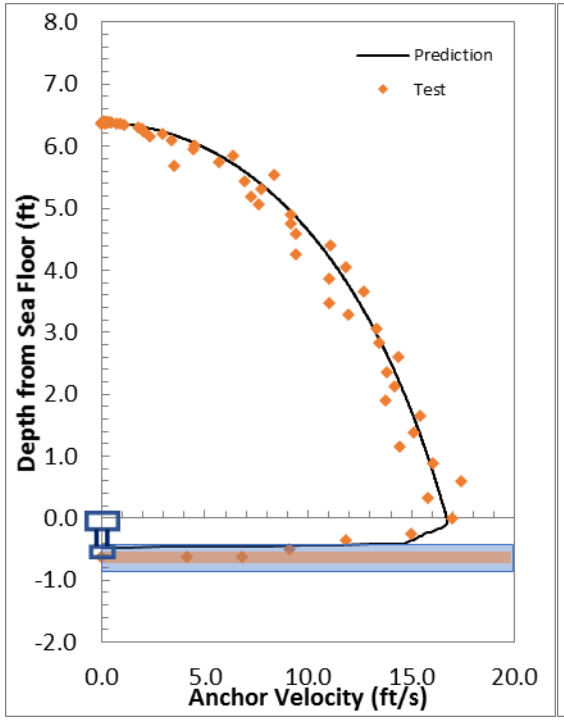

Prediction with R_f in semi-log

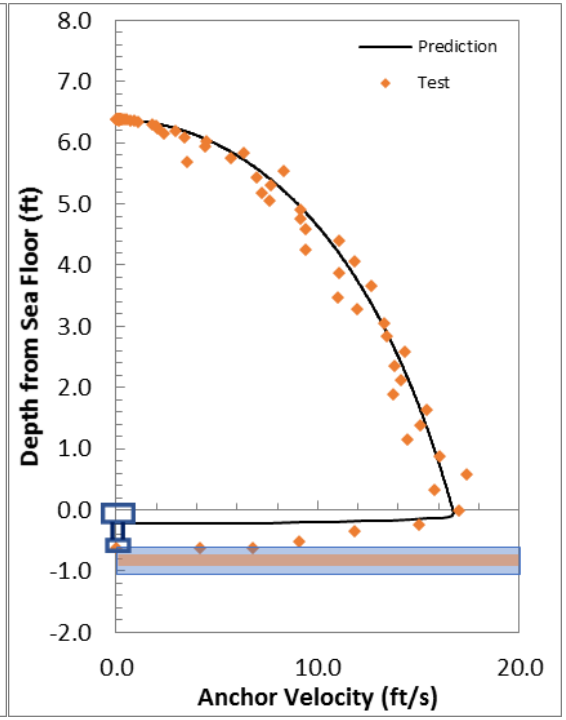

Free-Fall Penetration with Flying Wing Anchor ® in Case 7 Layered Soil

First Repeat in Drop 2

	Impact v (ft/s)	Embedment D (L_f)	β	λ
Experiment	16.67	3.07	–	–
R_f in Power-Law	17.06	2.21	0.15	–
R_f in Semi-log	17.06	2.21	–	0.35

Prediction with R_f in power-law

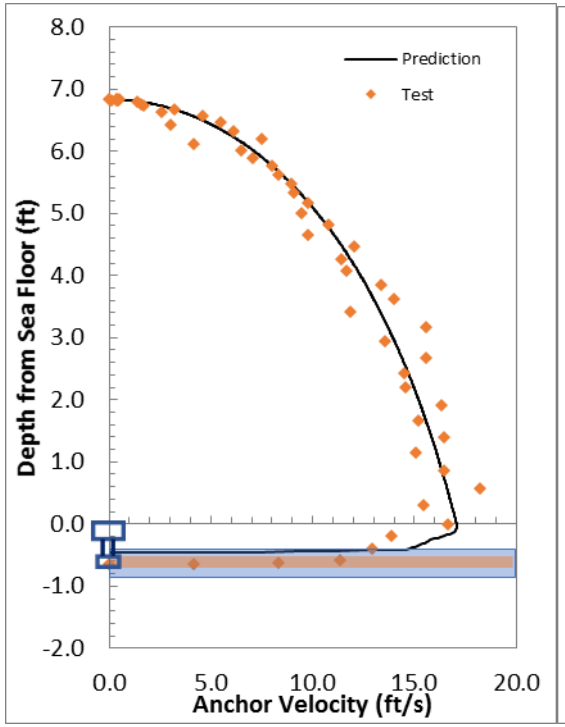

Prediction with R_f in semi-log

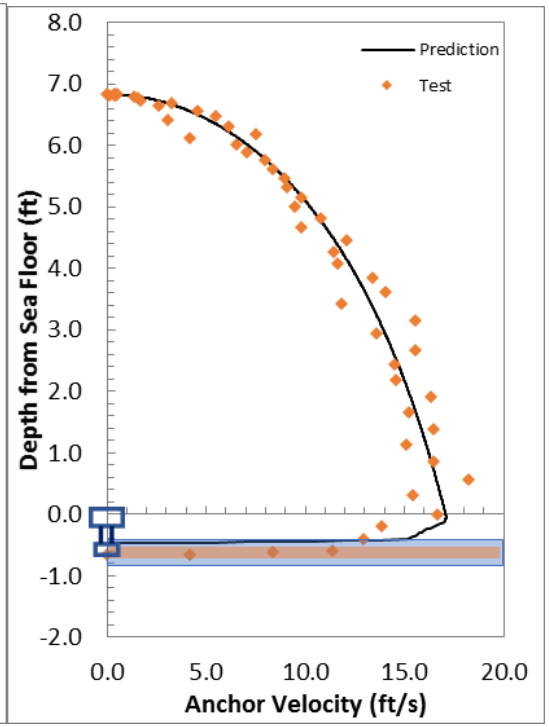

Free-Fall Penetration with Flying Wing Anchor ® in Case 7 Layered Soil

Second Repeat in Drop 2

	Impact v (ft/s)	Embedment D (L_f)	β	λ
Experiment	16.67	3.37	–	–
R_f in Power-Law	16.91	2.21	0.15	–
R_f in Semi-log	16.91	2.22	–	0.35

Prediction with R_f in power-law

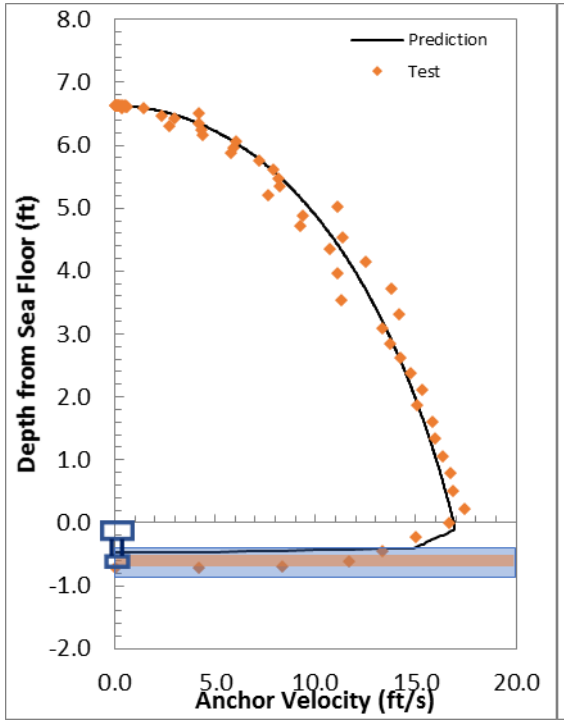

Prediction with R_f in semi-log

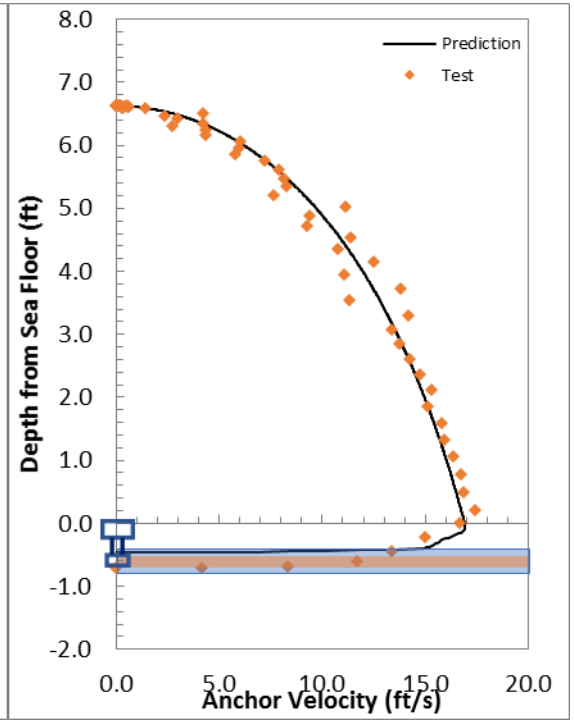

Free-Fall Penetration with Flying Wing Anchor ® in Case 7 Layered Soil

Drop 3

	Impact v (ft/s)	Embedment D (L_f)	β	λ
Experiment	16.67	2.87	–	–
R_f in Power-Law	16.11	2.17	0.15	–
R_f in Semi-log	16.11	2.05	–	0.35

Prediction with R_f in power-law

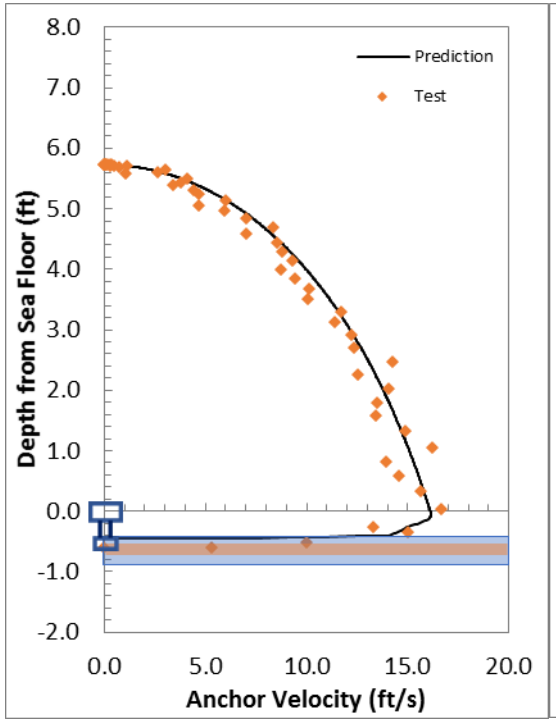

Prediction with R_f in semi-log

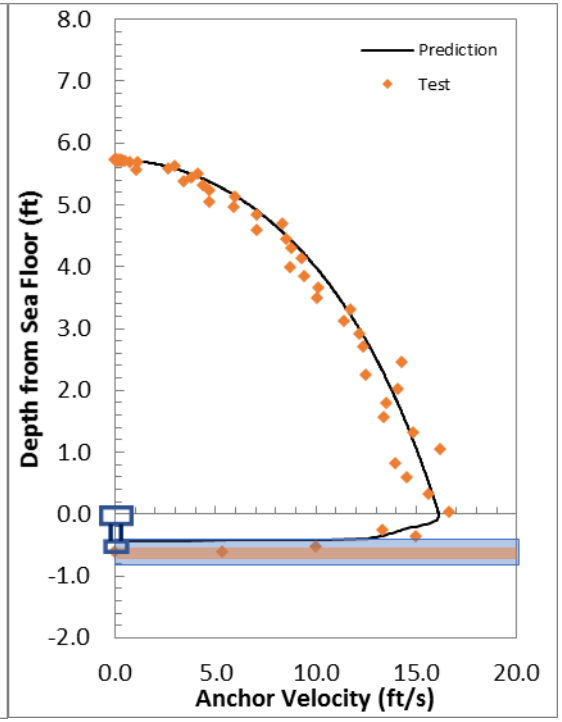

Free-Fall Penetration with Flying Wing Anchor ® in Case 7 Layered Soil

Repeat in Drop 3

	Impact v (ft/s)	Embedment D (L_f)	β	λ
Experiment	16.67	2.87	–	–
R_f in Power-Law	16.14	2.19	0.15	–
R_f in Semi-log	16.14	2.20	–	0.35

Prediction with R_f in power-law

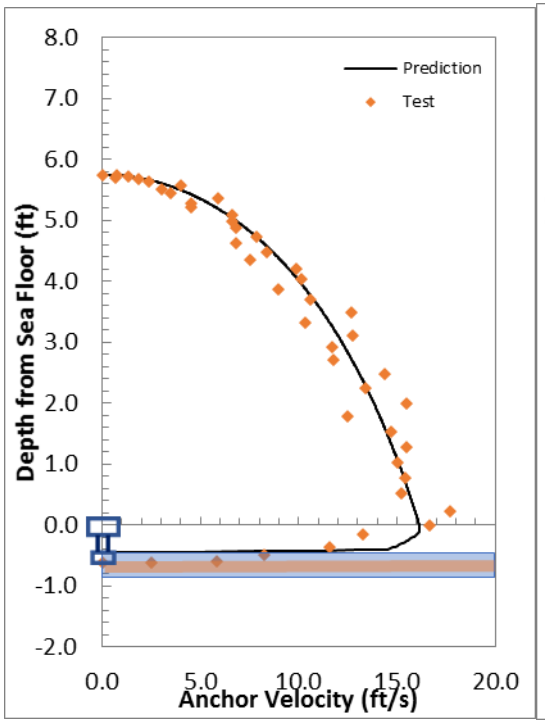

Prediction with R_f in semi-log

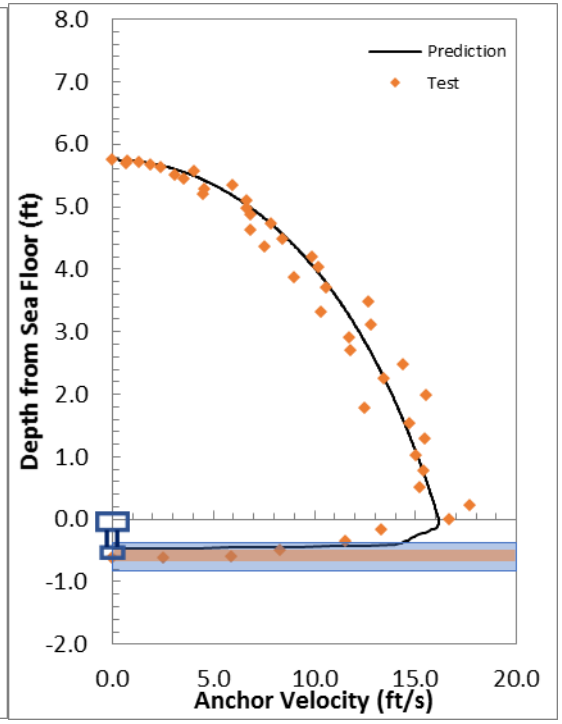

References

Abelev, A., & Valent, P. (2009). *Strain-Rate Dependency of Strength and Viscosity of Soft Marine Deposits of the Gulf of Mexico.* Biloxi, MS: Proc. of OCEANS 2009: Marine Technology for Our Future: Global and Local Challenges, MTS/IEEE Biloxi.

Achenbach, E. (1968). Distribution of Local Pressure and Skin Friction Around a Cylinder in Cross-flow up to Re = 5*10-6. *Journal of Fluid Mechanics, 34*(4), 625-639.

Achenbach, E. (1971). Influence of Surface Roughness on the Cross-Flow Around a Cylinder. *Journal of Fluid Mechanics, 46*(2), 321-335.

Acteon. (2009). Petrobra Awards Exclusive Torpedo Pile Technology Rights to InterMoor. *The Acteon Customer Magazine, 6*(9).

(November 30, 2009). *Advanced Anchoring and Mooring Study for Oregon Wave Energy Trust.*

Agnevall, T. (1998). Installation and Performance of the Petrobra P27 Stevmanta VLA Anchors. *2nd Annual Conference on Mooring and Anchoring.* Aberdeen.

American Petroleum Institute. (2002). *Recommended Practive for Planning, Designing and Constructing Fixed Offshore Platforms - Working Stress Design API RP 2A - WSD.* Washington D.C., USA.

Anderson, K., Murff, J., Randolph, M., Cluckey, E., Erbrich, C., Jostad, H., . . . Supachawarote, C. (2005). Suction Anchors for Deepwater Applications.

Proceedings of International Symposium Frontiers in Offshore Geotechnics, ISFPOG05, (pp. 3-30). Perth.

Araujo, J.B., Machado, R.D. and Medeiros, C.J. (2004). High Holding Power Torpedo Pile - Results From the First Long Term application. *Proc. International Conference on Offshore Mechanics and Arctic Engineering.* Vancouver.

Aubeny, C. (2017). *Piggy-back Trajectory-Load Capacity Prediction.* Texas A&M University.

Aubeny, C., & Chi, C. (2010). Mechanics of Drag Embedment Anchors in a Soft Seabed. *Journal of Geotechnical and Geoenvironmental Engineering, 136*(1), 51-68.

Aubeny, C., & Chi, C. (2014). Analytical Model for Vertically Loaded Anchor Performance. *Journal of Geotechnical and Geoenvironmental Engineering, 140*(1), 14-24.

Aubeny, C., & Dunlap, W. (2003). Penetration of Cylindrical Objects in Soft Mud. *Proceedings of IEEE OCeans, 4*, pp. 2068-2073.

Aubeny, C., & Shi, H. (2006). Interpretaion of Impact Penetration Measurements in Soft Clays. *Journal of Geotechnical and Geoenvironmental Engineering, ASCE, 132*(6), 770-777.

Aubeny, C., Gilbert, R., Randall, R., Zimmerman, E., McCarthy, K., Chen, C.-H., . . . Beemer, R. (2011). *The Performance of Drag Embedment Anchors (DEA). Contract Number M09PC00028, MMS Project Number 645, OTRC Project 32558-A6960, Minerals Management Service.*

Aubeny, C., Murff, J., & Kim, B. (2008). Prediction of Anchor Trajectory During Drag Embedment in Soft Clay. *Proceedings International Symposium on Frontiers in Offshore Geotechnics*, (pp. 314-319). Balkema, Perth, Australia.

Aubeny, C., Murff, J., & Roesset, J. (2001). Geotechnical Issues in Deep and Ultra Deep Waters. *International Journal of Geomechanics, 1*(2), 225-247.

Baglioni, V. P., Chow, G. S., & Endley, S. N. (1982). Jack-up Rig Foundation Stability in Stratified Soil Profiles. *Offshore Technology Conference.*

Beard, R. (1981). A Penetrometer for Deep Ocean Seafloor Exploration. *Proc. of OCEANS 1981: The ocean an International Workplace, MTS/IEEE*, (pp. 668-673). Boston, MA.

Beemer, R. D. (2011). *Analytical and Experimental Studies of Drag Embedment Anchors and Suction Caissons.* Texas A&M University.

Biscontin, G., & Pestana, J. (2001). Influence of Peripheral Velocity on Vane Shear Strength of an Artificial Clay. *Geotechnical Testing Journal, ASTM, 24*(4), 423-429.

Blake, A., & O'Loughlin, C. (2015). Installation of Dynamically Embedded Plate Anchors as Assessed Through Field Tests. *Canadian Geotechnical Journal, 52*, 1270-1282.

Blake, A., O'Loughlin, C., & Gaudin, C. (2015). Capacity of Dynamically Embedded Plate Anchors as Assessed Through Field Tests. *Canadian Geotechnical Journal, 52*(1), 87-95.

Blake, A., O'Loughlin, C., Morton, J., O'Beirne, C., Gaudin, C., & White, D. (2016). In Situ Measurement of the Dynamic Penetration of Free-Fall Projectiles in Soft Soils Using a Low Cost Intertial Measurement Unit. *Geotechnical Testing Journal, 39*(2), 235-251.

Brandão, F., Henriques, C., de Araújo, J., Ferreira, O., & Amaral, C. (2006). Albacora Leste Field Develpment - FPSO P-50 Mooring Syestem Concept and Installation. *In Proceedings of the 2006 Offshore Technology Conference,* (p. Paper No. OTC 18243). Houston, Texas, USA.

Bransby, M., & O'Neil, M. (1999). Drag Anchor Fluke Soil Interaction in Clays. *Proceedings International Symposium on Numerical Models in Geomechanics*, (pp. 489-494). Rotherdam, Netherlands: Balkema.

Bransby, M., & Randolph, M. (November 1997). Shallow Foundations Subject to Combined Loadings. *In Proceedings of the 9th International Conference on Computer Methods and Advances in Geomechanics. 3*, pp. 637-655. Wuhan: Edited by J. Yuan. A.A. Balkema, Rotterdam.

Brown, P., & Lawler, D. (2003). Sphere Drag and Settling Veloctiy Revisited. *Journal of Environmental Engineering*, 222-231.

Casagrande, A., & Wilson, S. (1951). Effect of rate of loading on the strength of clays and shales at constant water content. *Géotechnique, 2*(3), 251-563.

Casagrande, A., & Wilson, S. (1951). Effect of Rate of Loading on the Strength of Clays and Shales at Constant Water Content. *Géotechnique, 2*(3), 251-263.

Cenac II, W. (2011). *Vertically Loaded Anchor: Drag Coefficient, Fall Velocity and Penetration Depth Using Laboratory Measurements. Master's thesis.* College Station, USA: Texas A&M University .

Chen, W. (1975). *Limit Analysis and Soil Plasticity.* Eleservier, N.Y.

Chow, S., & Airey, D. (2013). Soil Strength Characterisation Using Free Falling Penetrometer. *Géotechnique, 63*(13), 1131-1143.

Chow, S., O'Loughlin, C., & Randolph, M. (2014). Soil Strength Estimation and Pore Pressure Dissipation for Free-Fall Piezocone in Soft Clay. *Géotechnique, 64*(10), 817-827.

Chung, S., Randolph, M., & Schneider, J. (2006). Effect of Penetration Rate on Penetrometer Resistance in Clay. *Journal of Geotechnical and Geoenvironmental Engineering, ASCE, 132*(9), 1188-1196.

Colliat, J.-L. (2002). Anchors for Deepwater to Ultradeepwater Moorings. *Proc. Offshore Technology Conference.* Houston, Texas: OTC 14306.

Colreavy, C., O'Loughlin, C., & Randolph, M. (2016). Experience with a dual pore pressure element piezoball. *International Journal of Physical Modelling in Geotechnics*.

Colreavy, C., O'Loughlin, C., & Randolph, M. (2016). Experience with a Dual Pore Pressure Element Piezoball. *International Journal of Physical Modelling in Geotechnics*.

Craig, W. (1994). Size Effects in Anchor Performance. *Canadian Geotechnical Journal*, 450-454.

Dayal, U., Allen, J., & Jones, J. (1975). Use of an Impact Penetrometer for the Evaluation of the In-Situ Strength of Marine Sediments. *Marine Georesources & Geotechnology*, *1*(2), 73-89.

Denney, D. (2007). Albacora Leste Filed -- P-50 FPSO Mooring System. An Overview of Paper No. OTC 18243. *The Journal of Petroleum Technology, 59*(2), 73-75.

DNV. (2000). *DNV Recommended Practice RP-E301 Design and Installation of Fluke Anchors in Clay.*

Ehlers, C., Young, A., & Chen, J. (2004). Technology Assessment of Deepwater Anchors. *Offshore Technology Conference OTC-16840-MS.* Houston, Texas.

Einav, I., & Randolph, M. (2006). Effect of Strain Rate on Mobilised Strength and Thickness of Curved Shear Bands. *Géotechnique*, *56*(7), 501-504.

Elkhatib, S., & Randolph, M. (2005). The Effect of Interface Friction on the Performance of Drag-in Plate Anchors. *Proceedings of International Symposium on Frontiers in Offshore Geotechnics (ISFOG).* London: Taylor & Francis.

Elkhatib, S., Lonnie, B., & Randolph, M. F. (2002). Installation and Pull-out Capacities of Drag-In Plate Anchors. *Proceedings of The Twelfth (2002) International Offshore and Polar Engineering Conference*, (pp. 648-654). Kitakyushu, Japan.

El-Sherbiny, R. (2005). Performance of Suction Caisson Anchors in Normally Consolidated Clay . *Ph.D. Dissertation*. The University of Texas at Austin.

Eltaher, A., Rajapaksa, Y., & Chang, K. (2003). Industry Trends for Design of Anchoring Systems for Deepwater Offshore Structures. *Proc. Offshore Technology Conference.* Houston, Texas: OTC 15265.

Erbrich, C. (2005). Australian Frontiers - Spudcans on the Edge. *Proc. 1st Int Symp. Frotiers in Offshore Geotechnics, Perth,* (pp. 49-74).

Freeman, T., & Schüternhelm, R. (1990). A Geotechnical Investigation of a Deep Ocean Site. *Geotechnical Aspects of Ocean Waste Disposal Symposium, ASTM STP 1087, Demars, K.R. and Chaney, R.C. Eds., American Siciety for Testing and Materials*, (pp. 255-275). Philadalphia.

Freeman, T., Murray, C., Francis, T., McPhail, S., & Schultheiss, P. (1984). Modelling Radiaoactie Watst DIsposal by Penetrator Experiments in the Abyssal Atlantic Ocean. *Letters to Nature, 310,* 130-133.

French, L., Richardson, G., Kazanis, E., Montgomery, T., Bohannon, C., & Gravois, M. (2006). *Deep Gulf of Maxico 2006: America's expanding frontier.* U.S. Department of Interior, Minerals Management Service, Report No. MMS 2006-022.

French, L., Richardson, G., Kazanis, E., Montgomery, T., Bohannon, C., & Gravois, M. (2006). *Deepwater Gulf of Mexico 2006: America's Expanding Frontier.* U.S. Department of Interior, Minerals Management Service, Report No. MMS 2006-022.

Ganjoo, K. (2010). *Experimental Testing of Pure Translation and Rotation Loading of Drag Anchors.* Master Thesis. The University of Texas at Austin.

Gaudin, C., Hossain, M., O'Loughlin, C., & Zimmerman, E. (2013). The Performance of Dynamically Embedded Anchors in Calcerous Silt. *In Proceedings of the 32nd International Conference on Ocean. Offshore and Arctic Engineering*, (pp. Paper No. OMAE 2013-10115). Nantes, France.

Gaudin, C., O'Loughlin, C., & Randolph, M. (2006). Centrifuge Tests on Suction Embedded Plate Anchors. *Proceedings of the 6th International Conference on Physical Modelling in Geotechnics, 6th ICPMG 06.* Hong Kong.

Gaudin, C., Simkin, M., White, D., & O'Loughlin, C. (2010b). Experimental Investigation into the Influence of a Keying Flap on the Keying Behavior of Plate Anchors. *Proceedings of the 20th International Offshore and Polar Engineering Conference.* Beijing, China.

Gerkus, H. (2016). *Model Experiments to Measure Yield Thresholds and Trajectories for Plate Anchors and Develop a New Anchor Concept.* Ph.D. Dissertation. The University of Texas at Austin.

Gerkus, H., Giampa, J., Senanayake, A., Lai, Y., Huang, Y., Iturriaga Flores, J., . . . Gilbert, R. (2016). Preliminary Development of a New Concept to Improve Sustainability of Offshore Foundations. *Geo-Chicago 2016: Sustainability, Energy, and the Geoenvironment.* Chicago, IL.

Gilbert, R. B., Lupulescu, C., Lee, C. H., Miller, J., Kroncke, M., Yang, M., . . . Murff, J. D. (2009). Analytical and Experimental Modeling for Out-of-Plane Loading of Plate Anchors. *Offshore Technology Conference.* Houston, TX.

Gilbert, R., Iturriaga Flores, J., & Gerkus, H. (2015). *Patent No. 10046-101PV2 United States of America.*

Gilbert, R., Morvant, M., & Audibert, J. (2008). *Torpedo Piles Joint Industry Project - Model Torpedo Pile Tests in Kaolinite Test Beds, Report No. 02/08B187.* Offshore Technology Center, Texas A&M University.

Graham, J., Crooks, J., & Bell, A. (1983). Time Effects on the Stress-Strain Behaviour of Natural Soft Clays. *Géotechnique, 33*(3), 327-340.

Horan, A. (2012). *The Mechanical Behavior of Normally Consolidated Soils as a Function of Pure Fluid Salinity. M.S. Thesis.* Massaachusetss Institute of Technology.

Hossain, M., & Randolph, M. (2011). Spudcan Foundations on Multi-Layered Soils with Interbedded Sand and Stiff Clay Layers. *Proc. Twenty-First International Offshore and Polar Engineering Conference*, (pp. 463-470). Maui, Hawaii, USA.

Hossain, M., Kim, Y., & Gaudin, C. (2014). Experimental Investigation of Installation and Pullout of Dynamically Penetrating Anchors in Clay and Silt. *Journal of Geotechnical and Geoenvironmental Engineering, 140*(7).

House, A. (1998). Drag Anchor and Chain Performance in Stratified Soils. *Australian Geomechanics*, 63-74.

Huang, Y. (2015). Designing a Laboratory Model Test Program for Developing a New Offshore Anchor. *M.Sc. Thesis*. The University of Texas at Austin.

Jeng, D. (2007). Potential of Offshore Wind Energy in Australia. *Offshore Technology Conference.* Houston, TX, USA.

Jose Eugenio Iturriaga Flores. (2016). *Risk-Informed Design of New Anchor Concept for Floating Energy Production Systems. Ph.D. Dissertation.* The University of Texas at Austin.

Lee, C. (2008). *Constructing Test Bed of Clay with a Specified Profile of Undrained sShear Strength Versus Depth. M.S. Thesis.* The University of Texas at Austin.

Lehane, B., O'Loughlin, C., Gaudin, C., & Randolph, M. (2009). Rate Effects on Penetrometer Resistance in Kaolin. *Géotechnique, 59*(1), 41-52.

Lelievre, B., & Tabatabaee, J. (1981). The Performance of Marine Anchors with Planar Fluke in Sand. *Canadian Geotech Journal, 18*, 520-534.

Lieng, J., Hove, F., & Tjelta, T. (1999). Deep Penetrating Anchor: Subseabed Deepwater Anchor Concept for Floaters and Other Installations. *In Proceedings of the 9th International Offshore and Polar Engineering Conference*, (pp. Paper No. ISOPE 1-99-093). Brest, France.

Lisle, T. (2001). *Rocket Anchors - A Deep Water Mooring Solution. Honour's thesis, The University of Western Australia.*

Low, H., Randolph, M., DeJong, J., & Yafrate, N. (2008). Variable Rate Full-Flow Penetration Tests in Intact and Remoulded Soil. *In Proceedings of the 3rd International Conference on Site Characterization*, (pp. 1087-1092). Taipei.

Martin, C., & Houlsby, G. (2001). Combined Loading of Spudcan Foundations on Clay; Numerical Modelling. *Géotechnique, 51*(8), 687-699.

McCarthy, K. (2011). *Experimental In-Plane Bahavior of a Generic Scale Model Drag Embedment Anchor in Kaolinite Test Beds.* Master Thesis. The University of Texas at Austin.

Medeiros Jr., C. (2001). Torpedo Anchor for Deep Water. *In Proceedings of the 2001 Deep Offshore Technology Conference.* Rio de Janeiro, Brazil.

Medeiros Jr., C. (2002). Low Cost Anchor System for Flexible Risers in Deep Waters. *In Proceedings of the 2002 Offshore Technology Conference.* Houston, Texas, USA.

Medeiros, C., Hassui, L., & Machado, R. (1997). *US Patent No. 6106199.*

Migliore, H., & Lee, H. (1978). *Seafloor Penetration Tests: Presentation and Analysis of Results.* Port Hueneme, California: Technical Note N-1178.

Morton, J., & O'Loughlin, C. (September 2012). Dynamic Penetration of a Sphear in Clay. *Proc. of the 7th International Conference in Offshore Site Investigation and Geotechnics*, (pp. 223-230). London, United Kindgom.

Murff, J. (1994). Limit Analysis of Multi-Footing Foundation Systems. *Proceedings of the 8th International Conference on Computer Methods and Advances in Geomechanics*, (pp. 233-244). Taylor & Francis, Abington, U.K.

Murff, J. (2005). Vertically Loaded Plate Anchors for Deepwater Applications. *Proc., Int. Symp. on Frountiers in Offshore Geotechnics, IS-FOG05,* (pp. 31-48). Balkema, Perth, Australia.

Murff, J., & Anderson, H. (2001). *Deepwater Anchor Design Practice-First Year Report to API.* College Station, Texas.: Offshore Technology Research Center, Texas A&M University.

Murff, J., Randolph, M., Elkhatib, S., Kolk, H., Ruinen, R., Strom, P., & Throne, C. (2005). Vertically Loaded Plate Anchors for Deepwater Applications. *Proc. Int. Symp. on Frontiers in Offshore Geotechnics ISFOG05*, (pp. 31-48).

Musial, W. and Butterfiled, Natl. (2006). Energy from offshore wind. *Offshore Technology Conference.*

NCEL. (1987). *Drag Embedment Anchors for Navy Moorings.* U.S. Navy, Port Hueneme, CA: Naval Civil Engineering Laboratory.

Neubecker, S., & Randolph, M. (1995). Profile and Frictional Capacity of Embedded Anchor Chains. *Journal of Geotechnical Engineering, 121*(11), 797-803.

Neubecker, S., & Randolph, M. (1996b). Performance of Embedded Anchor Chains and Consequences for Anchor Design. *Proceedings of the 28th Annual Offshore Technology Conference*, (p. OTC 7712). Houston, Texas.

O'Loughlin , C., Randolph, M., & Richardson, M. (2004a). Experimental and Theoretical Studies of Deep Penetrating Anchors. *In Proceedings of the 2004 Offshore Technology Conference, Paper No. OTC 16841.* Houston, Texas, USA.

O'Loughlin, C., Blake, A., & Gaudin, C. (2016). Géotechnique. *Towards a Simple Design Procedure for Dynamically Embedded Plate Anchors*.

O'Loughlin, C., Blake, A., & Gaudin, C. (2016). Towards a Simple Design Procedure for Dynamically Embedded Plate Anchors. *Géotechnique, 76*(9), 741-753.

O'Loughlin, C., Blake, A., Richardson, M., Randolph, M., & Gaudin, C. (2014). Installation and Capacity of Dyanmically Embedded Plate Anchors as Assessed Through Centrifuge Tests. *Ocean Engineering*, 201-213.

O'Loughlin, C., Lowmass, A., Gaudin, C., & Randolph, M. (2006). Physical Modelling to assess Keying Characteristics of Plate Anchors. *Proceedings of the International Conference on Physical Modelling in Geotechnics, 1*, pp. 659-665. Hong Kong.

O'Loughlin, C., Randolph, M., & Einav, I. (2004b). Physical Modelling of Deep Penetrating Anchors. *In Proceedings of the 9th Australian and New Zealand Conference on Geomechanics, 2*, pp. 710-716. Auckland, New Zealand.

O'Loughlin, C., Richardson, M., & Randolph, M. (2009). Centrifuge Tests on Dynamically Installed Anchors. *In Proceedings of the 28th International Conference on Ocean, Offshore and Arctic Engineering.* Honululu, Hawaii, USA.

O'Loughlin, C., Richardson, M., Randolph, M., & Gaudin, C. (2013). Penetration of Dynamically Installed Anchors in Clay. *Géotechnique, 63*(11), 909-919.

O'Neill, M., Bransby, M., & Randolph, M. (2003). Drag Anchor Fluke-Soil Interaction in Clays. *Canadian Geotechnical Journal, 40*, 78-94.

Ove Arup and Partners. (1982). *Ocean Disposal of High Level Radioactive Waste: Penetration Option - Studies Relevant to Emplacement in Deep Ocean Sediments.* Department of the Environment, Report No. DOE/RW/82.102.

Peuchen, J., & Mayne, P. (2007). Rate Effects in Vane Shear Testing. *In Proceedings of the 6th International Conference on Offshore Site Investigation and Geotechnics: Confronting New Challenges and Sharing Knowledge*, (pp. 187-194). London, UK.

Poorooshasb, F., & James, R. (1989). Centrifuge Modelling of Heat-Generating Waste Disposal. *Canadian Geotechnical Journal, 26*, 640-652.

Raie, M., & Tassoulas, J. (2009). Installation of Torpedo Anchors: Numerical Modelling. *Journal of Geotechnical and Geoenvironmental Engineering, 135*(12), 1805-1813.

Randolph, M and Gourvenec, S. (2011). *Offshore Geotechnical Engineering.*

Randolph, M., & White, D. (2012). Interaction Forces Between Pipelines and Submarine Slides - a Geotechnical Viewpoint. *Ocean Engineering, 48*, 32-37.

Rasulo, M., & Aubeny, C. (2017). *Trajectory Layered: User's Manual and Example Analyses.* Texas A&M University.

Richardson, M. (2008). *Dynamically Installed Anchors for Floating Offshore Structures. Ph.D. Thesis. University of Western Australia.*

Ruinen, R., & Degenkamp, G. (1999). First Application of 12 Stevmanta Anchors (VLA) in the P27 Taut Leg Mooring System . *Proceedings of Deep Offshore Technology.*

Sahdi, F., Gaudin, C., & White, D. (2014b). Strength Properties of Ultra-Soft Kaolin. *Canadian Geotechnical Journal, 51*(4), 420-431.

Schmid, W. (1969). The Penetration of Objects into the Ocean Bottom. *Civil Engineering in the Oceans II*, 167-208.

Sheahan, T., Ladd, C., & Germaine, J. (1996). Rate-Dependent Undrained Shear Behavior of Saturated Clay. *Journal of Geotechnical Engineering, 122*(2), 99-108.

Shelton, J. (2007). OMNI-Max Anchor Development and Technology. *In Proceedings of the Ocean Conference.* Vancouver, Canada.

Shelton, J., Nie, C., Shuler, D., & Delmar System Inc. (2011). Intallation Penetration of Gravity Installed Plate Anchors - Laboratory Study Results and Field History Data. *Offshore Technology Conference.* Rio de Janeiro, Brazil.

Skempton, A. (1951). The Bearing Capacity of Clays. *In Proceedings of the Building Research Congress, 1*, pp. 180-189. London.

Song, Z., Hu, Y., & Randolph, M. (2008). Numerical Simulation of Vertical Pullout of Plate Anchors in Clay. *Journal of Geotechnical and Geoenvironmental Engineering, ASCE, 134*(6), 866-875.

Steiner, A., Kopf, A., L'Heureux, J.-S., Kreiter, S., Stegmann, S., Haflidason, H., & Morez, T. (2014). In Situ Dynamic Piezocone Penetrometer Tests in Natural Clayey Soils - a Reappraisal of Strainrate Corrections. *Canadian Geotechnical Journal, 51*(3), 272-288.

Stewart, D., & Randolph, M. (1994). T-bar Penetration Testing in Soft Clay. *Journal of Geotechnical Engineering*, 2230-2235.

Stewart, W. (1992). Drag Embedment Anchor Performance Prediction in Soft Soils. *Proceedings of 24th Offshore Technology Conference*, (p. OTC 6970). Houston, Texas.

Sturn, H., Lieng, J., & Saygili, G. (2011). Effect of Soil Variability on the Penetration Depth of Dynamically Installed Drop Anchors. *In Proceedings of the Offshore Technology Conference*, (p. OTC 22396). Rio de Janeiro, Brazil.

Taylor, R. (1982). *Drag Embedment Anchor Tests in Sand and Mud.* NCEL.

Taylor, R. J. (1987). *Single and Tandem Anchor Performance of the New Navy Mooring Anchor: The NAVMOOR Anchor.* Naval Facilities Engineering Command and Naval Sea Systems Command.

Teh, K. L. (2006). Prediction of Punch-Through for Spudcan Penetration in Sand Overlying Clay. *Proc. Offshore Technology Coneference.* Houston.

Throne, C. (1998). Penetration and Load Capacity of Marine Drag Anchors in Soft Clay. *Jounrnal of Geotechnical and Geoenvironmental Enginering*, *124*(10), 943-953.

True, D. (1976). *Undrained Vertical Penetration into Ocean Bottom Soils. Ph.D. Thesis.* University of California, Berkeley.

Vryhof. (1999). *Vryhof Anchors, Krimpen ad Yssel.* The Netherlands.

Vryhof. (2015). *Anchor Manual 2015 - The Guide to Anchoring.*

Vryhof Anchor Manual. (2005). Krimpen ad Yssel, Netherlands.

Vryhof Anchors. (2010). *Vryhof Anchor Manual.* Krimpen ad Yssel, Netherlands.

Walker, G., & Taylor, R. (1983). Model Anchor Tests in Cohesionless Soil. *15th Annual OTC in Houston, Texas*, (pp. 143-149).

Waston, P. (2005). Geotechnical Interpretation for the Yolla A Platform. *Proc. 1st Int. Symp. Frontiers in Offshore Geotechnics, Perth, Australia*, (pp. 343-349).

Weimmie, A. (2003). *Experimental Investigations of a New Offshore Anchoring System - Deep Penetrating Anchors. Diploma Thesis, Hamburg University of Applied Science.*

Wilde, B. (2009). Torpedo Pile Anchors Enter the GoM. *Advances in Mooring Systems, E&P OCtober 2009 Issue.* Hart Energy Publishing, 1616S. Voss, Ste. 100, Houston.

Wilde, B., Hans, T., & Fulton, T. (2001). Field Testing of Suction Embedded Plate Anchors. *Proceedings of the Eleventh International Offshore and Polar Engineering Conference.* Stavanger, Norway.

Yang, M., Aubeny, C., & Murff, J. (n.d.). Behavior of Suction Embedded Plate Anchors During Keying Process. *Journal of Geotechnical and Geoenvironmental Engineering, 138*(2), 174-183.

Yang, M., Murff, J., & Aubeny, C. (2008). *Out of Plane Loading of Plate Anchors, Analytical Modeling.* College Station, Texas: Phase II Rep. Prepared for Offshore Technology Research Center, College Station, ABS Consulting.

Yang, M., Murff, J., & Aubeny, C. (2010). Undrained Capacity of Plate Anchor Under General Loading. *Journal of Geotechnical and Geoenvironmental Engineering, 136*(10), 1383-1393.

Young, C. (1969). Depth Prediction for Earth-Penetrating Projectiles. *Journal of the Soil Mechanics and Foundations Division, ASCE, 95*(SM3), 803-817.

Young, C. (1981). An Empirical Equation for Predicting Penetration Depth into Soft Sediments. *Proc. IEEE Oceans' 81*, (pp. 674-677).

Young, C. (October 1997). *Penetration Equations.* Albuquerque, New Mexico: Contracter Report SAND 97-2426, Sandia National Laboratories.

Zhu, H., & Randolph, M. (2011). Numerical Analysis of a Cylinder Moving Through Rate-Dependent Undrained Soil. *Ocean Engineering, 38*, 943-953.

Zimmerman, E., & Spikula, D. (2005). A New Direction for Subsea Anchoring and Foundations.

Zimmerman, E., Smith, M., Shelton, J., & Systems, D. (2009). Efficient Gravity Installed Anchor for Deepwater Mooring. *In Proceedings of the 2009 Offshore Technology Conference*, (p. Paper No. OTC 20117). Houston, Texas.